Lecture Notes in Civil Engineering

Marco di Prisco
Marco Menegotto *Editors*

Proceedings of Italian Concrete Days 2018

Springer

Lecture Notes in Civil Engineering

Volume 42

Lecture Notes in Civil Engineering (LNCE) publishes the latest developments in Civil Engineering - quickly, informally and in top quality. Though original research reported in proceedings and post-proceedings represents the core of LNCE, edited volumes of exceptionally high quality and interest may also be considered for publication. Volumes published in LNCE embrace all aspects and subfields of, as well as new challenges in, Civil Engineering. Topics in the series include:

- Construction and Structural Mechanics
- Building Materials
- Concrete, Steel and Timber Structures
- Geotechnical Engineering
- Earthquake Engineering
- Coastal Engineering
- Hydraulics, Hydrology and Water Resources Engineering
- Environmental Engineering and Sustainability
- Structural Health and Monitoring
- Surveying and Geographical Information Systems
- Heating, Ventilation and Air Conditioning (HVAC)
- Transportation and Traffic
- Risk Analysis
- Safety and Security

To submit a proposal or request further information, please contact the appropriate Springer Editor:

- Mr. Pierpaolo Riva at pierpaolo.riva@springer.com (Europe and Americas);
- Ms. Swati Meherishi at swati.meherishi@springer.com (India);
- Ms. Li Shen at li.shen@springer.com (China);
- Dr. Loyola D'Silva at loyola.dsilva@springer.com (S-E Asia and Australia/NZ).

Indexed by Scopus

More information about this series at http://www.springer.com/series/15087

Marco di Prisco · Marco Menegotto
Editors

Proceedings of Italian Concrete Days 2018

Springer

Editors
Marco di Prisco
Dipartimento Ingegneria Civile
Politecnico di Milano
Milan, Milano, Italy

Marco Menegotto
AICAP
Rome, Roma, Italy

ISSN 2366-2557 ISSN 2366-2565 (electronic)
Lecture Notes in Civil Engineering
ISBN 978-3-030-23747-9 ISBN 978-3-030-23748-6 (eBook)
https://doi.org/10.1007/978-3-030-23748-6

This Springer imprint is published by the registered company Springer Nature Switzerland AG
The registered company address is: Gewerbestrasse 11, 6330 Cham, Switzerland

Preface

"Structural concrete" indicates today structures and materials formerly referred to as reinforced, plain and prestressed concrete, as well as all modern fibre-reinforced in cementitious matrix ones. It represents by far the most popular structural means in building and civil engineering worldwide.

Applications concern not only new constructions, but more and more rehabilitation, conservation, strengthening and upgrading, of the existing structures, particularly in seismic areas. Requirements cover new aspects related to sustainability, including environmental friendliness, durability, adaptability to reuse (of materials, elements or entire structure).

Construction processes keep evolving, availing new working means, ideas, technologies, analytical and experimental tools, assessment criteria, standards for better measuring focused performances, controls. The material, too, undergoes remarkable development, differentiating itself for specific applications, up to the multiple today's concretes, binders, additives and reinforcements, metallic or composites.

aicap and **CTE**—both referring internationally to ***fib*** and having the same mission of promoting research, dissemination of knowledge and good use of structural concrete—after the great success of the first edition 2016, have organized ITALIAN CONCRETE DAYS 2018, offering to all players—such as industrialists of construction, producers of components, technology and materials, professionals of architecture and civil engineering, field technicians, researchers and academics—an opportunity for updating their cultural sight, establishing contacts, sharing information and opinions, discussing applications, proposing solutions and consolidating their own role awareness.

The ICD 18 proceedings, published in Italian language on digital media with ISBN 978-88-99916-11-4, contain over 128 technical and scientific papers, within the foreseen topics: theory and modelling, applications and realizations, materials and investigations, technology and construction techniques. They trace a state of the art open to international evolution and note the present position on the way of sustainability.

This volume represents a synthesis of the proceedings, aimed at an international promotion of the event, collecting a set of contributions, presented therein in English, which may deserve a wider international acquaintance.

We would like to take this opportunity to thank all the colleagues of the scientific committee, particularly the international experts, for reviewing and finalizing the papers in a tight time. Our sincere appreciation is also extended to the secretariats of both **aicap** and **CTE**, who were able to work in perfect cooperation, offering to the Italian Community a high-quality resume of many innovative activities which have mainly involved national experts. A special acknowledgement is addressed to the International Association of Structural Concrete ***fib***, for having supported this event in the perspective of an International Federation aimed at concrete structures improvement worldwide.

We hope that this volume can contribute to favouring the dialogue among the stakeholders acting in the construction field, in the new era of globalization and digitalization, and to further enhance in it the international cooperation.

Marco di Prisco
Marco Menegotto

Organization

Scientific Committee

Maria Antonietta Aiello
Franco Angotti
Luigi Ascione
Gyorgy N. Balazs
Gianni Bartoli
Beatrice Belletti
Andrea Benedetti
Gabriele Bertagnoli
Francesco Biasioli
Fabio Biondini
Fabio Bolzoni
Ezio Cadoni
Gianmichele Calvi
Giuseppe Campione
Roberto Cerioni
Bernardino Chiaia
Mario Chiorino
Piero Colajanni
Dario Coronelli
Hugo Corres Peiretti
Edoardo Cosenza
Piero D'Asdia
Andrea Dall'Asta
Gianmarco De Felice
Achille Devitofranceschi
Luigino Dezi
Marco di Prisco
Pierpaolo Diotallevi
Mauro Dolce
Luigi Evangelista
Giovanni Fabbrocino
Ciro Faella
Alessandro Fantilli
Roberto Felicetti
Liberato Ferrara
Giuseppe Ferro
Dora Foti
Paolo Franchin
Dante Galeota
Pietro Gambarova
Natalino Gattesco
Alessandra Gubana
Donatella Guzzoni
Lorenzo Jurina
Lidia La Mendola
Giuseppe Mancini
Gaetano Manfredi
Enzo Martinelli
Annibale Materazzi
Claudio Mazzotti
Alberto Meda
Marco Menegotto
Antonio Migliacci
Claudio Modena
Franco Mola
Pietro Monaco
Giorgio Monti
Giacomo Moriconi

Aurelio Muttoni
Antonio Nanni
Camillo Nuti
Antonio Occhiuzzi
Luciano Ombres
Maurizio Orlando Bruno Palazzo
Stefano Pampanin
Maurizio Papia
Maria Rosaria Pecce
Carlo Pellegrino
Francesco Pesavento
Mario P. Petrangeli
Paolo E. Pinto
Marco Andrea Pisani
Giovanni Plizzari
Cesare Prevedini
Andrea Prota
Roberto Realfonzo
Elena Redaelli
Zila Rinaldi
Paolo Riva
Gianpaolo Rosati
Anna Saetta
Marco Savoia
Nunzio Scibilia
Enzo Siviero
Enrico Spacone
Giuseppe Spadea
Luc Taerwe
Sergio Tattoni
Giandomenico Toniolo
Nerio Tullini
Michele Valente
Ivo Vanzi
Renato Vitaliani

Contents

Theory and Modeling Materials

Assessment of the Partial Safety Factor Related to Resistance Model Uncertainties in 2D NLFEAs of R.C. Systems

P. Castaldo(✉), D. Gino, D. La Mazza, G. Bertagnoli, V. I. Carbone, and G. Mancini

Department of Structural, Geotechnical and Buildings Engineering, Politecnico Di Torino, Turin, Italy
paolo.castaldo@polito.it

Abstract. This work estimates the partial safety factor corresponding to the resistance model uncertainties in non-linear finite element method analyses (NLFEAs) of reinforced concrete structures considering various structural typologies with different behaviours and failure modes (i.e., walls, deep beams, panels). The comparison between the two-dimensional NLFE structural model results and the experimental outcomes is carried out considering the possible solution strategies available to describe the mechanical behaviour of reinforced concrete members in different software codes. Several NLFE structural models are defined for each experimental test in order to investigate the resistance model uncertainty. Then, a consistent treatment of the resistance model uncertainties is proposed following a Bayesian approach identifying the mean value and the coefficient of variation of the resistance model uncertainties. Finally, in agreement with the safety formats for NLFEAs of reinforced concrete structures, the partial safety factor is calibrated.

Keywords: 2D NLFEA · Resistance model uncertainties · Partial safety factor · Reinforced concrete structure · Bayes approach · Global safety format

1 Introduction

The non-linear finite element method analyses (NLFEAs) are one of the most common and practical instruments able to model the actual mechanical response of reinforced concrete members and systems in conditions of both serviceability limit states (SLS) and ultimate limit states (ULS).

In general, the type of uncertainties affecting the structural analyses can be classified in two families: aleatory and epistemic. The aleatory uncertainties are related to the randomness of the variables that governs a specific phenomenon or a resisting mechanism, whereas the epistemic uncertainties are mainly related to the "lack of knowledge" in the characterization of the structural model (Kiureghian and Ditlevsen 2009; Mancini et al. 2017; Gino et al. 2017). The reliability assessment of a structural system by means of a NLFE analysis has to account for both such families of uncertainty.

M. di Prisco and M. Menegotto (Eds.): ICD 2018, LNCE 42, pp. 3–15, 2020.
https://doi.org/10.1007/978-3-030-23748-6_1

Guidelines for NLFE analyses have been recommended by fib Bulletin 45 (2008) and Belletti et al. (2011) in order to perform an accurate calibration of the structural finite element model. Contextually, different safety formats for NLFEAs have been proposed in the literature by several authors (Allaix et al. 2013; Shlune et al. 2012) and international codes (CEN EN 1992-2 2005; *fib* Model Code 2010). The different safety formats allow the calculation of the design structural resistance R_d, by means of Eq. (1):

$$R_d = \frac{R_{rep}}{\gamma_R \cdot \gamma_{Rd}} \tag{1}$$

where R_{rep} is the representative value of the structural resistance (intended as the global strength of the structural member or system) estimated by means of NLFEAs according to the mentioned above safety formats, γ_R is the partial safety factor accounting for the statistical variability of material properties (i.e., aleatory uncertainties), γ_{Rd} represents the partial safety factor accounting for the modelling uncertainties (i.e., epistemic uncertainties).

The present work calibrates the value of the partial safety factor related to the model uncertainties γ_{Rd} for two-dimensional (2D) non-linear finite element method analyses (NLFEAs) of reinforced concrete (r.c.) structures. In detail, twenty-one (21) experimental tests, related to various typologies of structures with different behaviours and failure modes (i.e., walls, deep beams, panels), have been reproduced by means of appropriate plane stress NLFE structural models and compared to the experimental results. Several NLFE structural models are defined for each experimental test in order to study the influence of the model uncertainties on the plane stress NLFE analysis of r.c. systems. Specifically, nine (9) plausible structural models (i.e., solution strategies) are defined adopting three (3) types of software and three (3) assumptions about the mechanical behaviours in tension for concrete. Successively, a consistent statistical treatment of the resistance model uncertainties is proposed according to Bayesian approach (Gelman et al. 2014). Firstly, the prior distributions of the resistance model uncertainties for the nine (9) different solution strategies are evaluated and, then, updated based on the average data coming from the other eight (8) NLFE models in order to assess the posterior distributions. Then, averaging the statistical parameters of the posterior distributions related to the nine (9) different structural models, the mean value and the coefficient of variation for the resistance model uncertainties have been characterised. Finally, in compliance with the safety formats for NLFEAs of r.c. structures (CEN EN 1992-2 2005; *fib* Model Code 2010), the partial safety factor related to the resistance model uncertainties is evaluated and proposed as a function of the pre-assigned reliability level for r.c. structures of new construction.

2 Characterization of the Model Uncertainties

As introduced in Sect. 1, the uncertainties related to the definition of the resistance model should be assessed by means of the comparison between the experimental outcomes and the results from numerical simulations. According to Holický et al. (2016),

the following aspects have to be considered in order to identify the resistance model uncertainties for NLFEAs:

- the set of the experimental data should contain the parameters necessary for the reproduction of the tests and for the definition of NLFE models;
- the experimental results should be differentiated concerning the typologies of structures and failure modes;
- a consistent statistic and probabilistic analysis of the observed model uncertainties needs to be performed to identify the most likely probabilistic distribution with the associated parameters.

In agreement to JCSS (2001), the resistance model uncertainty, ϑ_i, represents the ratio between the i-th actual resistance (response) estimated from an experimental test $R_{Exp,i}(X,Y)$ and the i-th resistance (or response) estimated by a NLFEA $R_{FEA,i}(X)$ and, may be expressed as follows:

$$\vartheta_i = \frac{R_{Exp,i}(X,Y)}{R_{FEA,i}(X)} \tag{2}$$

where X is a vector of basic variables included into the resistance model (i.e., NLFE model), Y is a vector of variables that may affect the resisting mechanism but are disregarded within the model. Note that the unknown effects of Y variables, if present, are indirectly incorporated by the characterisation of ϑ_i.

In the following, after a brief description of the experimental tests set considered for the investigation, the model uncertainties ϑ_i will be assessed differentiating between nine (9) different solution strategies.

3 NLFE Modelling and Case Studies

In this section, the experimental outcomes reported in the scientific literature (Filho 1995; Foster and Gilbert 1998; Lefas and Kotsovos 1990; Leonhardt and Walther 1966; Vecchio and Collins 1982) and related to 21 different typologies of structural members are considered and assumed as a benchmark test set. All these experimental tests, developed respectively on four shear panels, on five deep beams and on eleven walls, have been performed through a monotonic incremental loading process up to failure. The specimens have been realized in laboratory and supported by statically determined configurations. The experimental results, in terms of load vs displacement or shear stress vs angular distortion diagrams, are herein compared to the outcomes from the different NLFE simulations.

3.1 Definition and Differentiation of the Structural Numerical Models

Several solution methodologies are available in order to perform plane stress NLFEAs of r.c. structures. In this work, three common software codes, marked as Software A, Software B and Software C are adopted with the aim to reproduce the outcomes of the experimental tests set. Each software makes it possible to perform different choices

about the hypotheses related to equilibrium, compatibility and constitutive laws. Specifically, for each software, four-node quadrilateral iso-parametric plane stress finite elements, based on linear polynomial interpolation and 2 × 2 Gauss point's integration scheme are used for the numerical simulations. The assessment of the size of the FE meshes has been performed after an appropriate sensitivity analysis. The non-linear system of equations is solved by means of the standard Newton-Raphson iterative procedure based on the hypothesis of linear approximation (*fib* Bulletin 45 2008).

For each software, the following main characteristics for the finite element models are also assumed: concerning the concrete, non-linear behaviour in compression is considered, including softening with a reduction of the compression strength and shear stiffness (shear retention factor equal to 0.2) after cracking (Bertagnoli et al. 2015). The smeared cracking with fixed crack direction model (Bertagnoli et al. 2015) has been adopted; the steel reinforcements has been modelled with a three linear σ-ε curve (Bertagnoli et al. 2015); discrete and smeared models for the reinforcement assuming a perfect bond interaction (Bertagnoli et al. 2015) has been used; concerning Young's modulus and tensile strength of concrete, the material properties are derived as a function of the experimental compressive strength, according to CEN EN 1992-1-1 (2004). More details concerning the finite elements formulation, shape functions, constitutive models and convergence criteria related to Software A, B and C selected for the present work may be also acknowledged in (Bertagnoli et al. 2015).

In addition to the abovementioned differences concerning the three different software codes, another important differentiation between the NLFE models has been considered with respect to the concrete tensile mechanical behavior. In fact, the interaction between reinforcing bars and concrete between cracks gives rise to the "tension stiffening effect". Performing numerical simulations, this effect may be accounted for through a modification of the constitutive tensile behavior of concrete. This modification consists into the definition of a tension softening law in the post peak concrete tensile response.

In this paper, three different constitutive laws for concrete in tension are considered in order to cover different hypotheses accounting for the tension stiffening effect (Bertagnoli et al. 2015): elastic-brittle (i.e., Brittle), elastic-plastic (i.e., Plastic) and a linear tension softening (i.e., LTS). The constitutive law having a linear tension softening for the concrete tensile behavior has been calibrated in each software with the aim to best fit the experimental outcomes.

The nine different structural models can be defined combining the use of the three different software (i.e., Software A, B and C) with the three different concrete tensile behaviours (i.e., Brittle, Plastic and LTS). The scheme of the solution methodologies adopted in this work is depicted in Fig. 1.

Finally, the resistance model uncertainties can be identified and computed, according to Sect. 2, for the different experimental tests of the 21 r.c. members, leading to a total number of 189 NLFE simulations.

3.2 Experimental Tests Considered for the Investigation and Results

In this section, the experimental results reported in the scientific literature (Filho 1995; Foster and Gilbert 1998; Lefas and Kotsovos 1990; Leonhardt and Walther 1966;

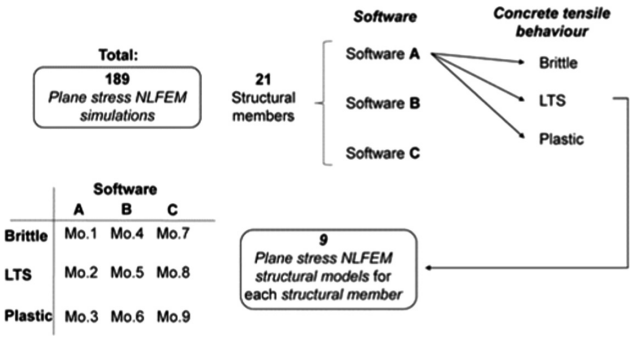

Fig. 1. Differentiation between structural models and summary of the benchmark NLFE simulations.

Vecchio and Collins 1982) and related to 21 different typologies of structural members are considered and assumed as the benchmark test set. All these experimental tests, developed respectively on four shear panels, on five deep beams and on eleven walls, have been performed through a monotonic incremental loading process up to failure. The specimens have been realized in laboratory and supported by statically determined configurations. The experimental results, in terms of load vs displacement or shear stress vs angular distortion diagrams, are compared to the outcomes from the total of 189 plane stress NLFE performed, as previously discussed.

More details on the experimental tests set may be acknowledged in the original papers and (Bertagnoli et al. 2015).

In Figs. 2, 3, 4, 5 and 6, the experimental and numerical tests results are reported, showing the numerical model schematization of each test with the application of the load "q" or of the shear stress τ. The complete results in terms of maximum load reached during the tests and within the simulation are reported in Table 1. In contrast with the simple geometry of the selected structural members, Figs. 2, 3, 4, 5 and 6 illustrate that it is very difficult to reproduce the actual behaviour. Furthermore, models with plastic and brittle concrete tensile behaviours, do not always represent the upper and the lower bound of the possible response, respectively, due also to the different failure modes. In fact, the resisting mechanism of the experimental test in Fig. 2 is characterised by the progressive yielding of the tensile reinforcements and concrete crushing in the column on the right side of the square opening. The failure mode of the experimental test in Fig. 3 is characterised by the progressive yielding of the tensile bottom reinforcements and concrete crushing at the top chord close to the column where the load is applied. The failure mode of the experimental test in Fig. 4 is characterised by the progressive yielding of the external reinforcements with concrete crushing in the right corner of the wall at the connection with the stiff foundation.

The failure modes of the experimental tests in Figs. 5 and 6 are characterised by the bottom reinforcement yielding and an arch-tie resisting mechanism with bar yielding, respectively. The results deriving from the mentioned above 189 NLFE simulations are

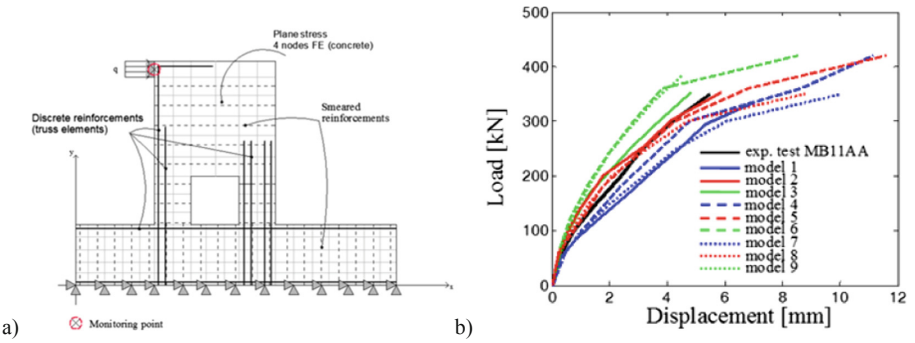

Fig. 2. Numerical model schematization (a) and load vs displacement curves for the specimen MB11AA.

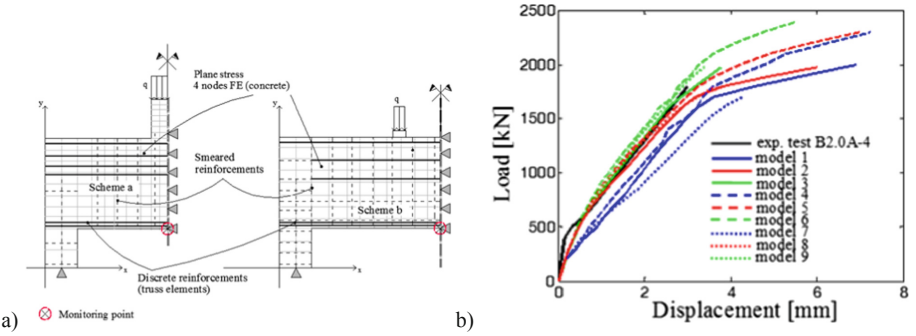

Fig. 3. Numerical model schematization (a) and load vs displacement curves for the specimen B2.0A-4.

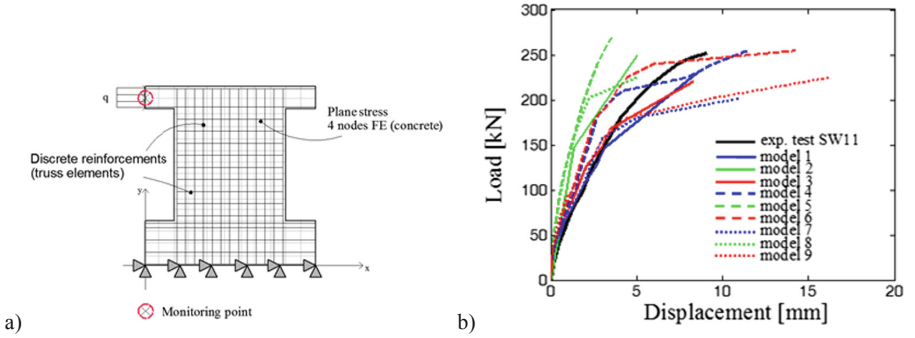

Fig. 4. Numerical model schematization (a) and load vs displacement curves for the specimen SW11.

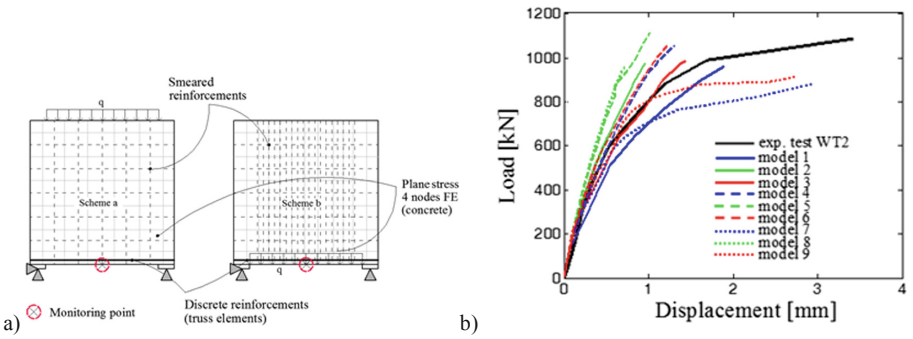

Fig. 5. Numerical model schematization (a) and load vs displacement curves for the specimen WT2.

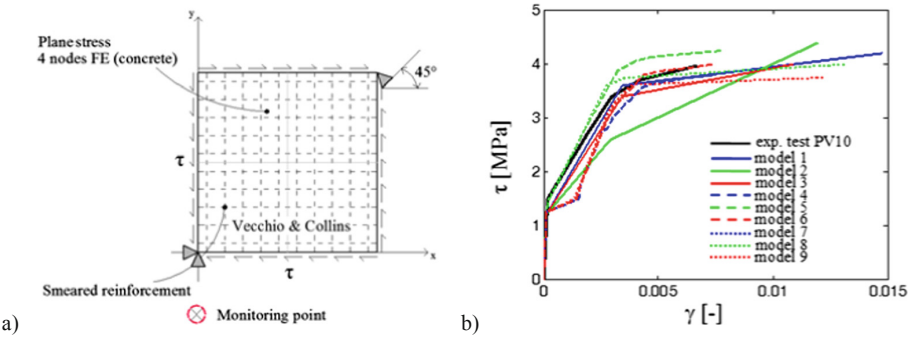

Fig. 6. Numerical model schematization (a) and load vs displacement curves for the specimen PV10.

useful to assess the resistance model uncertainties in plane stress NLFEAs of r.c. structures characterised by different failure modes. These results have demonstrated the need to calibrate appropriate values of the corresponding partial safety factor. In Table 2 the results in terms of the ratio $\vartheta_i = R_{EXP,i}/R_{FEA,i}$ are reported.

4 Statistical Processing for the Calibration of the Partial Safety Factor

The present section focuses on the statistical processing of the model uncertainties represented in Table 2 and on the assessment of the partial safety factor for model uncertainties related to plane stress NLFEAs of r.c. structures. As discussed in Sect. 3, the results differ significantly from one commercial software to the another highlighting that also the software selected in order to perform the NLFE simulations represents a source of uncertainty on the assessment of the structural resistance.

Table 1. Results of the investigation in terms of maximum load.

Ref.	Exp. test	Model uncertainties ϑ_i [–]								
		Mo. 1	*Mo. 2*	*Mo. 3*	*Mo. 4*	*Mo. 5*	*Mo. 6*	*Mo. 7*	*Mo. 8*	*Mo. 9*
Filho (1995)	MB1AA	1.04	0.99	0.99	0.83	0.83	0.83	1.00	1.00	0.91
	MB1AE	1.07	0.96	1.05	0.93	0.93	0.85	1.06	1.02	0.90
	MB1EE1	1.04	1.07	1.00	0.92	1.03	0.83	0.96	0.92	0.83
	MB1EE1	0.96	0.96	0.96	0.92	0.92	0.83	0.91	0.92	0.92
	MB4EE	1.04	1.08	0.98	0.88	0.95	0.88	1.00	1.00	0.89
Foster and Gilbert (1998)	B2.0A-4	0.90	0.91	0.91	0.78	0.78	0.75	1.05	1.00	0.91
	B3.0A-4	0.96	0.96	1.00	0.78	0.83	0.78	1.10	1.10	0.96
	B2.0-1	1.03	1.06	1.09	0.99	0.94	0.84	1.06	1.16	1.16
	B3.0-1	0.93	0.97	0.91	0.83	0.83	0.77	1.05	1.00	0.91
	B2.0-3	0.90	0.90	0.89	0.88	0.82	0.74	1.00	0.93	0.93
Lefas and Kotsovos (1990)	SW11	1.10	1.14	1.01	0.99	0.99	0.94	1.25	1.12	1.12
Leonhardt and Walther (1966)	WT2	1.13	1.10	1.12	1.03	1.03	0.97	1.23	1.19	1.13
	WT3	0.97	0.97	0.97	0.89	0.89	0.84	1.03	0.97	0.97
	WT4	1.06	1.06	1.05	0.88	0.88	0.88	1.34	1.25	0.95
	WT6	0.81	0.79	0.79	0.85	0.85	0.79	0.99	0.99	0.83
	WT7	0.86	0.83	0.92	0.86	0.86	0.86	1.00	1.00	0.89
Vecchio and Collins (1982)	PV10	0.95	0.99	0.90	1.04	0.99	0.93	1.06	1.06	0.99
	PV19	0.76	0.66	0.66	0.81	0.81	0.76	1.05	1.05	1.05
	PV21	0.73	0.73	0.73	0.82	0.82	0.81	1.09	1.09	1.06
	PV22	0.73	0.75	0.75	0.90	0.90	0.90	1.28	1.28	1.28

4.1 Probabilistic Model for Model Uncertainties

First of all, the probabilistic model (Castaldo et al. 2018a, b, c, d, e; Castaldo et al. 2013) for the random variable ϑ (i.e., model uncertainty random variable) should be defined. The probability plot, reported in Fig. 7, shows that the overall sample data of 189 results follow a unimodal lognormal distribution. Similar results are achieved for the sample of 21 results related to each model. This result is in compliance with JCSS (2001).

The Chi-square test has been performed for each structural model (Models 1 to 9) and for the overall sample confirming the assumption of unimodal lognormal distributions.

4.2 Bayesian Updating and Assessment of the Partial Safety Factor

The probabilistic assessment of the resistance model uncertainty for NLFEAs is performed by means of a Bayesian approach (Gelman et al. 2014), which makes it possible

Table 2. Results of the investigation: ratios $\vartheta_i = R_{EXP,i}/R_{FEA,i}$.

Ref.	Exp. test	Model uncertainties ϑ_i [–]								
		Mo. 1	*Mo. 2*	*Mo. 3*	*Mo. 4*	*Mo. 5*	*Mo. 6*	*Mo. 7*	*Mo. 8*	*Mo. 9*
Filho (1995)	MB1AA	0.91	0.91	0.78	0.78	0.75	1.05	1.00	0.91	0.90
	MB1AE	0.96	1.00	0.78	0.83	0.78	1.10	1.10	0.96	0.96
	MB1EE1	1.06	1.09	0.99	0.94	0.84	1.06	1.16	1.16	1.03
	MB1EE1	0.97	0.91	0.83	0.83	0.77	1.05	1.00	0.91	0.93
	MB4EE	0.90	0.89	0.88	0.82	0.74	1.00	0.93	0.93	0.90
Foster and Gilbert (1998)	B2.0A-4	0.99	0.99	0.83	0.83	0.83	1.00	1.00	0.91	1.04
	B3.0A-4	0.96	1.05	0.93	0.93	0.85	1.06	1.02	0.90	1.07
	B2.0-1	1.07	1.00	0.92	1.03	0.83	0.96	0.92	0.83	1.04
	B3.0-1	0.96	0.96	0.92	0.92	0.83	0.91	0.92	0.92	0.96
	B2.0-3	1.08	0.98	0.88	0.95	0.88	1.00	1.00	0.89	1.04
Lefas and Kotsovos (1990)	SW11	1.14	1.01	0.99	0.99	0.94	1.25	1.12	1.12	1.10
Leonhardt and Walther (1966)	WT2	1.10	1.12	1.03	1.03	0.97	1.23	1.19	1.13	1.13
	WT3	0.97	0.97	0.89	0.89	0.84	1.03	0.97	0.97	0.97
	WT4	1.06	1.05	0.88	0.88	0.88	1.34	1.25	0.95	1.06
	WT6	0.79	0.79	0.85	0.85	0.79	0.99	0.99	0.83	0.81
	WT7	0.83	0.92	0.86	0.86	0.86	1.00	1.00	0.89	0.86
Vecchio and Collins (1982)	PV10	0.95	0.99	0.90	1.04	0.99	0.93	1.06	1.06	0.99
	PV19	0.76	0.66	0.66	0.81	0.81	0.76	1.05	1.05	1.05
	PV21	0.73	0.73	0.73	0.82	0.82	0.81	1.09	1.09	1.06
	PV22	0.73	0.75	0.75	0.90	0.90	0.90	1.28	1.28	1.28

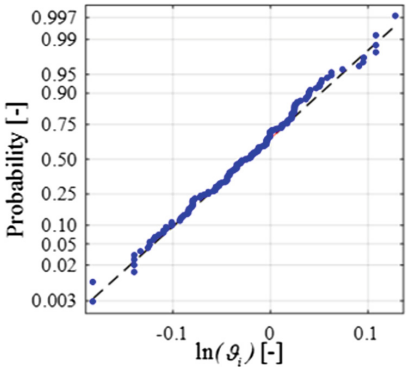

Fig. 7. Probability plot of $\ln(\vartheta_i)$ for all the models.

to update prior data through new information. Precisely, the prior information is characterised by the model uncertainty values conditional to the use of a specific structural model, that can be represented by its lognormal cumulative distribution function $F(\vartheta \mid M_j)$ (i.e., CDF) (Table 3), whereas the new information, which makes it possible to update the prior results, consists of the numerical outcomes related to the other eight (8) models. Specifically, the prior information for each structural model is updated on the basis of the data obtained from the other eight (8) models in order to evaluate the posterior distributions. Then, the parameters (summarized in the vector z_j for each structural model) of nine (9) distributions are defined and denoted as $F_{Mj}(\vartheta \mid z_j)$ and represent the new information for updating the prior distributions. By means of a Bayesian procedure, the posterior distribution functions $F(\vartheta \mid M_j, z_j)$ for each structural model Mj can be assessed. Since the purpose of this study is the development of a comprehensive probabilistic model, the resistance model uncertainty, after the Bayesian updating, has to be averaged over all the structural models that can be used by engineers.

Table 3. Parameters of both prior distributions estimated by means of the minimum likelihood technique.

Structural model	Mean μ_ϑ	Standard deviation σ_ϑ	Coefficient of variation V_ϑ
	[–]	[–]	[–]
	Prior conditioned distributions $F(\vartheta \mid M_j)$		
1	0.94	0.13	0.14
2	0.93	0.15	0.16
3	0.93	0.14	0.15
4	0.89	0.08	0.10
5	0.89	0.08	0.09
6	0.84	0.08	0.09
7	1.07	0.10	0.09
8	1.05	0.09	0.09
9	0.97	0.12	0.12

The posterior non conditioned distribution function $F(\vartheta \mid Z)$, having the distribution parameters (i.e., mean and standard deviation) summarized into the vector Z, can be evaluated averaging the statistical parameters of the nine posterior distributions conditioned to the different structural models $F(\vartheta \mid M_j, z_j)$. The parameters of posterior distributions are reported in Table 4. After the Bayesian updating, models 3, 6, 9 (plastic behaviour for concrete in tension) have shown the largest coefficient of variation. After that, averaging the statistical parameters of the posterior distributions related to the different structural models, the mean value and the coefficient of variation characterizing the resistance model uncertainties can be evaluated (Table 4).

Finally, in compliance with the hypothesis of log-normal distribution for the variable ϑ, the partial safety factor representative of the resistance model uncertainties γ_{Rd} can be determined, according to JCSS (2001), as follows:

Table 4. Parameters of both posterior distributions and averaged posterior distribution estimated by means of the minimum likelihood technique.

Structural model	Mean μ_ϑ	Standard deviation σ_ϑ	Coefficient of variation V_ϑ
	[–]	[–]	[–]
	Posterior conditioned distributions $F(\vartheta \mid M_j, z_j)$		
1	1.02	0.13	0.12
2	1.02	0.13	0.13
3	1.01	0.13	0.13
4	0.97	0.14	0.14
5	0.96	0.14	0.14
6	0.95	0.14	0.15
7	1.10	0.11	0.10
8	1.08	0.11	0.10
9	1.03	0.12	0.12
	Posterior distribution $F(\vartheta \mid z)$		
Average statistical parameters	1.01	0.13	0.12

$$\gamma_{Rd} = \frac{1}{\mu_\vartheta} \cdot \exp(\alpha_R \cdot \beta \cdot V_\vartheta) \tag{3}$$

where μ_ϑ is the mean value of the posterior averaged resistance model uncertainties distribution, V_ϑ is the coefficient of variation of the posterior averaged resistance model uncertainties distribution calculated as $\sigma_\vartheta/\mu_\vartheta$, α_R is the first-order-reliability-method (FORM) correction factor, assumed approximately equal to 0.8 and 0.32 as suggested by CEN EN 1992-2 (2005), *fib* Model Code (2010) and explained in the case of dominant and non-dominant resistance variable, respectively, β is the reliability index. The value of γ_{Rd}, in the hypothesis of non-dominant resistance variable according to CEN EN 1992-2 (2005) and *fib* Model Code (2010), with the FORM correction factor α_R equal to 0.32, for structures with an ordinary service life of 50 years and moderate consequences of structural failure (β = 3.8), can be set equal to 1.15.

5 Conclusions

The present investigation focuses on the evaluation the partial safety factor related to the model uncertainties for plane stress non-linear finite element method analyses of reinforced concrete systems. In particular, different experimental tests, concerning different typologies of structures with different behaviours and failure modes (i.e., walls, deep beams, panels), have been numerically simulated by means of appropriate two-dimensional FE structural models (i.e., plane stress configuration) and compared to

the experimental outcomes. The resistance model uncertainties have been characterised by appropriate lognormal distributions and, then, a consistent treatment has been proposed following a Bayesian approach. Specifically, the mean value and the coefficient of variation of the resistance model uncertainties are, respectively, equal to 1.01 and 0.12. Finally, concerning ordinary structures of new construction, according to the hypotheses of non-dominant resistance variable for model uncertainties, moderate consequences of structural failure and 50 years service life, the partial safety factor for the resistance model uncertainties in 2D NLFE simulations of reinforced concrete structures equal to 1.15 is proposed.

Acknowledgements. This work is part of the collaborative activity developed by the authors within the framework of the Committee 3 – Task Group 3.1: *"Reliability and safety evaluation: full-probabilistic and semi-probabilistic methods for existing structures"* of the International Federation for Structural Concrete (*fib*).

References

Allaix DL, Carbone VI, Mancini G (2013) Global safety format for non-linear analysis of reinforced concrete structures. Struct Concr 14(1):29–42

Belletti B, Damoni C, Hendriks MAN (2011) Development of guidelines for nonlinear finite element analyses of existing reinforced and prestressed beams. Eur J Environ Civ Engin 15 (9):1361–1384

Bertagnoli G, La Mazza D, Mancini G (2015) Effect of concrete tensile strength in non –linear analysis of 2D structures: a comparison between three commercial finite element softwares. In: Heft 178. 3rd international conference on advances in civil, structural and construction engineering, Rome, 10–11 December

Castaldo P, Calvello M, Palazzo B (2013) Probabilistic analysis of excavation-induced damages to existing structures. Comput Geotech 53:17–30

Castaldo P, Gino D, Bertagnoli G, Mancini G (2018a) Partial safety factor for resistance model uncertainties in 2D non-linear finite element analysis of reinforced concrete structures. Eng Struct 176:746–762

Castaldo P, Gino D, Carbone VI, Mancini G (2018b) Framework for definition of design formulations from empirical and semi-empirical resistance models. Struct Concr 19(4):980–987

Castaldo P, Jalayer F, Palazzo B (2018c) Probabilistic assessment of groundwater leakage in diaphragm wall joints for deep excavations. Tunn Undergr Space Technol 71:531–543

Castaldo P, Palazzo B, Alfano G, Palumbo MF (2018d) Seismic reliability-based ductility demand for hardening and softening structures isolated by friction pendulum bearings. Struct Control Health Monit 25(11):e2256

Castaldo P, Ripani M, Lo Priore R (2018e) Influence of soil conditions on the optimal sliding friction coefficient for isolated bridges. Soil Dyn Earthq Eng 111:131–148

CEN EN 1992-1-1 (2004) Eurocode 2, Design of concrete structures – Part 1-1. Brussels, CEN

CEN EN 1992-2 (2005) Eurocode 2, Design of concrete structures – Part 2: concrete bridges. Brussels, CEN

fib Bulletin N°45 (2008) Practitioner'guide to finite element modelling of reinforced concrete structures. State of the art report. Lausanne

fib (2010) Model Code for Concrete Structures 2010. *fib*, Lausanne

Filho JB (1995) Dimensionamento e comportamento do betao estrutural em zonas com discontinuitades. PhD Thesis, Universidade Tecnica de Lisbona

Foster SJ, Gilbert M (1998) Experimental studies on high strength concrete deep beams. ACI Struct J 95:382–390

Gelman A, Carlin JB, Stern HS, Dunson DB, Vehtari A, Rubin DB (2014) Bayesian data analysis, 3rd edn. CRC Press, Boca Raton

Gino D, Bertagnoli G, La Mazza D, Mancini G (2017) A quantification of model uncertainties in NLFEA of R.C. shear walls subjected to repeated loading. Ingegneria Sismica. Anno XXXIV Special Issue 79–91

Holický M, Retief JV, Sikora M (2016) Assessment of model uncertainties for structural resistance. Probab Eng Mech 45:188–197

JCSS (2001) Probabilistic model code. JCSS

Kiureghian AD, Ditlevsen O (2009) Aleatory or epistemic? Does it matter? Struct Saf 31:105–112

Lefas ID, Kotsovos MD (1990) Behaviour of reinforced concrete structural walls: strength, deformation characteristics and failure mechanism. ACI Struct J 87:23–31

Leonhardt F, Walther R (1966) Wandartige Träger. Deutscher Ausschuss für Stahlbeton. Heft 178. Ernst & Sons, Berlin, Germany

Mancini G, Carbone VI, Bertagnoli G, Gino D (2017) Reliability-based evaluation of bond strength for tensed lapped joints and anchorages in new and existing reinforced concrete structures. Struct Concr 19(3):904–917. https://doi.org/10.1002/suco.201700082

Shlune H, Gylltoft K, Plos M (2012) Safety format for non-linear analysis of concrete structures. Mag Concr Res 64(7):563–574

Vecchio FJ, Collins MP (1982) The response of reinforced concrete to in-plane and normal stresses. Department of Civil Engineering, University of Toronto, Toronto, Canada

Robustness of 3D Base-Isolated R.C. Systems with FPS

P. Castaldo[1(✉)], G. Mancini[1], and B. Palazzo[2]

[1] Department of Structural, Geotechnical and Building Engineering, Politecnico Di Torino, Turin, Italy
paolo.castaldo@polito.it
[2] Department of Civil Engineering, University of Salerno, Salerno, Italy

Abstract. This study evaluates the seismic robustness of 3D r.c. structures isolated with single-concave friction pendulum system (FPS) devices by computing the seismic reliability of different models related to different malfunction cases of the seismic isolators. Considering the elastic response pseudo-acceleration as the relevant random variable, the input data have been defined by means of the Latin Hypercube Sampling technique in order to develop 3D inelastic time-history analyses. In this way, bivariate structural performance curves at each level of the r.c. structural systems as well as seismic reliability-based design abacuses for the FP devices have been computed and compared in order to evaluate the robustness of the r.c. system considering different failure cases of the FP bearings. Moreover, the seismic robustness is examined by considering both a configuration equipped with beams connecting the sub-structure columns and a configuration without these connecting beams in order to demonstrate their effectiveness and provide useful design recommendations for base-isolated structural systems equipped with FPS.

Keywords: Seismic isolation · Friction pendulum devices · Seismic robustness · Structural performance · Connecting beams

1 Introduction

Over the last years, friction pendulum system (FPS) devices have become more and more an effective technique for the seismic protection of structures and infrastructure (Zayas et al. 1990). Several robustness and probabilistic analyses, structural reliability methods and reliability-based analyses (Chen et al. 2007; Kelly et al. 1987) by estimating the stochastic responses of base-isolated systems under random earthquake excitations as well as reliability-based optimizations of base-isolated structures including uncertainties such as isolator properties and ground motion characteristics (Alhan and Gavin 2005; Zou et al. 2010; Mishra et al. 2013; Zhao and Chen 2013) have been performed. The influence of the FPS properties on the seismic response of base-isolated systems has been presented by Castaldo and Tubaldi (2015) proposing a nondimensionalization of the motion equations for a two-degree-of-freedom system. Seismic reliability analyses of a reinforce concrete (r.c.) 3D base-isolated system with a lifetime of 50 years and located near L'Aquila site (Italy) have been performed in

M. di Prisco and M. Menegotto (Eds.): ICD 2018, LNCE 42, pp. 16–27, 2020.
https://doi.org/10.1007/978-3-030-23748-6_2

Castaldo et al. (2015) highlighting the influence of the bivariate correlation between the response parameters on the structural performance (SP) curves and proposing a seismic reliability-based design method to define the isolator dimensions. In Castaldo et al. (2016), the life-cycle cost analysis (LCCA) of a r.c. 3D system equipped with FP devices is discussed describing the positive benefits derived from increasing values of the isolation degree. For different structural properties, the seismic reliability-based design approach has been proposed in Castaldo et al. (2017a) with the scope to provide useful design solutions for the seismic devices. In Castaldo and Ripani (2016), the optimal friction values of FP isolators for the different soil conditions have been discussed and evaluated. Seismic reliability-based relationships between the strength reduction factors and the displacement ductility demand for base-isolated systems have been presented in Castaldo et al. (2017b). In addition, the robustness analysis of base-isolated high-rise buildings with friction-type bearings and a robust design optimization of base isolation system have been presented, respectively, in Takewaki (2008) and Roy and Chakraborty (2015).

This study evaluates the seismic robustness of a 3D r.c. base-isolated structure equipped with single-concave friction pendulum system (FPS) devices, designed according to NTC08 (NTC 2008) by estimating the seismic reliability in its design life (50 years) of different models related to different malfunction cases of the seismic isolators. For the seismic reliability assessment, the elastic response pseudo-acceleration corresponding to the isolated period is assumed as the relevant random variable, modeled through a Gaussian probability density function (PDF) (NTC 2008). By means of the Latin Hypercube Sampling (LHS) technique (Mckey et al. 1979, Celarec and Dolšek 2013), the input data have been defined for each model and 3D inelastic time-history analyses have been developed. In this way, bivariate structural performance (SP) curves at each level of the r.c. structure as well as seismic reliability-based design (SRBD) abacuses for the FP bearings have been computed and compared in order to evaluate the robustness of the system for the different failure cases considered. Moreover, the seismic robustness of the abovementioned r.c. structure has also been examined by considering both a configuration equipped with r.c. beams connecting the substructure columns and a configuration without these connecting beams in order to demonstrate their effectiveness in improving the seismic robustness.

2 Failure Cases and Uncertainties for the Seismic Robustness Assessment

The seismic robustness assessment of the base-isolated r.c. structure is herein developed in probabilistic terms estimating the seismic reliability in the performance space (Bertero and Bertero 2002) by means of a comparison between the performance objective (PO) curves and the SP curves of the different models representative of the different failure cases of the seismic devices. According to SEAOC-Vision (2000), CEN (2006), FEMA-274 (1997), relationships between the four structural PO levels, expressed in terms of the maximum interstory drift limits for each limit state (*LS*), and the corresponding probabilities exceeding the *LS* thresholds during the lifetime (50 years) of the structural system (Tena-Colunga and Escamilla-Cruz 2007), are

presented in Table 1, according to both American (FEMA-356 2000) and Italian seismic code (NTC 2008) provisions, respectively, for a fixed-base (FB) and a base-isolated (BI) structure. In this study, mono/bi-variate interstory drift δ for the sub/superstructure and mono/bi-variate relative displacement u for the FPS, respectively, are assumed as the engineering demand parameters (EDPs).

Table 1. Limit states in terms of maximum Interstory Drift Indices (IDI) and reliability indices in 50 years for fixed-base and base-isolated systems (Castaldo et al. 2017b; Tena-Colunga and Escamilla-Cruz 2007; FEMA-356 2000).

Limit state	Damage	FB structure IDI (%)	β	P_f	BI structure IDI (%) (NTC 08)	BI structure IDI (%) (FEMA-274)
LS1	Slight	0 < IDI < 0.3	0	$5.0 \cdot 10^{-1}$	0 < IDI < 0.2	0 < IDI < 0.1
LS2	Moderate	0.3 < IDI < 0.6	1	$1.6 \cdot 10^{-1}$	0.2 < IDI < 0.4	0.1 < IDI < 0.2
LS3	Heavy	0.6 < IDI < 1.5	2	$2.2 \cdot 10^{-2}$	0.4 < IDI < 1.0	0.2 < IDI < 0.5
LS4	Collapsed	IDI > 2	3	$1.5 \cdot 10^{-3}$	IDI > 1.3	IDI > 0.7

As for the structural systems, a four-story symmetric r.c. 3D frame building, shown in Fig. 1, with a lifetime of 50 years and located in L'Aquila site (geographic coordinates 41°58′25″ N, 13°24′00″ E, Italy), analysed in similar studies (Castaldo et al. 2015, 2016; Almazàn and De la Llera 2003a), has been considered in this work. Three (4^{th}, 3^{rd}, 2^{nd} stories) and one (1^{st} story) levels and the FPS isolation level compose the base-isolated r.c. structure. As already mentioned and also shown in Fig. 1, both a configuration equipped with beams connecting the substructure columns and a configuration without these connecting beams are considered. Assuming a radius of curvature $R = 1.5$ m and a design sliding friction coefficient equal to $\mu = 3\%$ (Castaldo et al. 2017b) for the FPS, the base-isolated r.c. structure has been designed in compliance with the life safety *LS* (Castaldo et al. 2017b; Kilar and Koren 2009; Naeim and Kelly 1999), considering a soil type B and a behavior factor $q = 1.5$ (NTC 2008). A post-yield stiffness ratio higher than 3% characterises the superstructure non-linear response along each direction. More details may be found in Castaldo et al. (2015, 2016).

Note that, in the design assumptions of the seismic hazard corresponding to L'Aquila site (Italy) and of the sliding friction coefficient $\mu = 3\%$, with reference to the both structural configurations, all the design and construction recommendations provided from both SEAOC-Vision (2000) and FEMA-356 (2000), related to the life safety *LS*, are respected as well as, regarding "*LS1*" and "*LS2*", the stiffness of the frames assures the respect of the more restrictive performance requirements for BI structures (NTC 2008; FEMA-356 2000) (Table 1) at each story, especially, in the configuration with the connecting beams (Fig. 1(a)). Moreover, note also that the lack of the connecting beams, having section dimensions 0.30 × 0.30 m (Fig. 1) and modelled as elastic axial bracing elements, at the substructure level does not modify the construction and design details of the super/sub-structure elements under the above-mentioned design assumptions ($\mu = 3\%$). A FEM model for each structural configuration has been defined in SAP2000 (2002) as shown in Fig. 1. From the eigenvalue

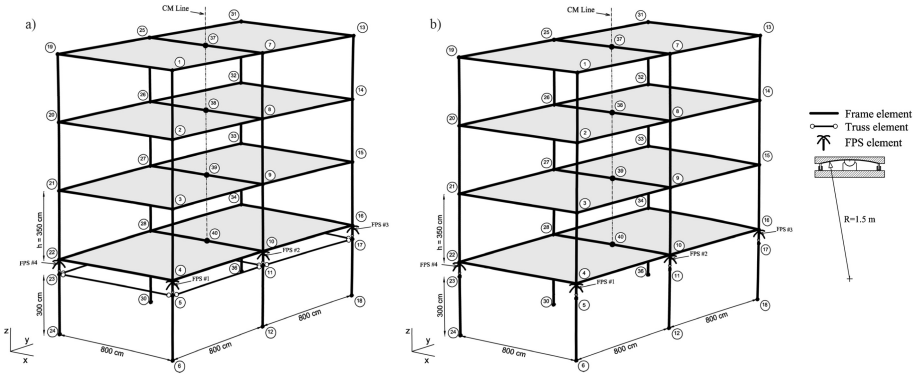

Fig. 1. Base-isolated structure configurations with (a) and without (b) the beams connecting the substructure columns.

analyses developed on the BI and FB structural system, the first period of the FB structure is equal to T_{fb} = 0.58 s, the first period of the BI system T_{is} is 2.58 s leading to a value of the isolation degree I_d higher than 3 (NTC 2008; FEMA-356 2000). Within a Rayleigh damping model, imposing a damping factor ξ_{is}= 2% on the first two modes of the 3D BI system (Alhan and Gavin 2005; Castaldo et al. 2015, 2016; Almazàn and De la Llera 2003a), mass proportional α and stiffness proportional β coefficients have been set equal to 0.0244 and 0.0041, respectively. In the FEM model, with reference to the non-linear behavior of each FPS device, the force is expressed as (Castaldo et al. 2015, 2016; Naeim and Kelly 1999):

$$F = \mu W \mathrm{sgn}(\dot{u}) + \frac{W}{R}u \tag{1}$$

in which, *sgn* denotes the signum function of the sliding velocity $\dot{u}$. In particular, the non-linear dependence of the friction coefficient μ on the sliding velocity of each frictional device, as described in Castaldo et al. (2015, 2016, 2017b), has been modelled as Constantinou et al. (1990, 2007), Mokha et al. (1990):

$$\mu = f_{\max} - (f_{\max} - f_{\min}) \exp(-\alpha \dot{u}) \tag{2}$$

where f_{max} and f_{min} represent, respectively, the sliding friction coefficients at large and nearly zero sliding velocities. The rate parameter "a" is set equal to 50 s/m (Constantinou et al. 1990, 2007). In order to take into account the stick-slip phenomenon, the abovementioned velocity-dependent equation can be modified as follows (Fagà et al. 2016):

$$\mu = f_{\max} - (f_{\max} - f_{rev}) \exp(-\alpha \dot{u}) \tag{3}$$

where f_{max} and f_{rev} represent the reference friction coefficient and the friction coefficient at motion reversals (stick-slip phases) (Fagà et al. 2016), respectively.

Regarding the inelastic behaviour of the r.c. structural members, a lumped plasticity approach has been adopted for each structural configuration (FEMA-356 2000) considering the interaction between the axial force and the bending moments ($P–M_y–M_x$) and the interaction between the bending moments ($M_y–M_x$) for the plastic hinges of the columns and of the beams, respectively.

With reference to the failure scenarios for the seismic robustness assessment, for each structural configuration, different models related to different malfunction cases of the FP devices are herein considered in order to evaluate the consequential damage to the structural system. In particular, different deterministic values of the sliding friction coefficient are assumed in order to take into account both the stick-slip phenomenon and the potential failure behaviour of an isolator, characterised by a very high friction coefficient. In Table 2, all the details related to the different models are reported according to Eq. (3) and to the numbering of both the devices and joints illustrated in Fig. 1. From the models reported in Table 2, note that a very influencing difference exists between an internal and corner device: the internal isolator is subjected to an almost double weight with respect to the corner device so that if a malfunction affects an internal isolator, a higher eccentricity between the forces of the isolation level, of the superstructure and of the substructure occurs.

Table 2. Friction coefficient properties for the different models.

Models	FPS#1 Properties (joint-5)	FPS#2 Properties (joint-11)	FPS#3 Properties (joint-17)	FPS#4 Properties (joint-23)	FPS#5 Properties (joint-29)	FPS#6 Properties (joint-35)
Model 1	$f_{max} = 0.03$ $f_{rev} = 0.03$	$f_{max} = 0.03$ $f_{rev} = 0.03$	$f_{max} = 0.03$ $f_{rev} = 0.03$	$f_{max} = 0.03$ $f_{rev} = 0.03$	$f_{max} = 0.03$ $f_{rev} = 0.03$	$f_{max} = 0.03$ $f_{rev} = 0.03$
Model 2	$f_{max} = 0.03$ $f_{rev} = 0.07$	$f_{max} = 0.03$ $f_{rev} = 0.07$	$f_{max} = 0.03$ $f_{rev} = 0.07$	$f_{max} = 0.03$ $f_{rev} = 0.07$	$f_{max} = 0.03$ $f_{rev} = 0.07$	$f_{max} = 0.03$ $f_{rev} = 0.07$
Model 3	$f_{max} = 0.03$ $f_{rev} = 0.07$	$f_{max} = 0.03$ $f_{rev} = 0.07$	$f_{max} = 0.03$ $f_{rev} = 0.07$	$f_{max} = 0.03$ $f_{rev} = 0.07$	$f_{max} = 0.03$ $f_{rev} = 0.07$	$f_{max} = 0.03$ $f_{rev} = 0.20$
Model 4	$f_{max} = 0.03$ $f_{rev} = 0.07$	$f_{max} = 0.03$ $f_{rev} = 0.07$	$f_{max} = 0.03$ $f_{rev} = 0.07$	$f_{max} = 0.03$ $f_{rev} = 0.07$	$f_{max} = 0.03$ $f_{rev} = 0.20$	$f_{max} = 0.03$ $f_{rev} = 0.07$
Model 5	$f_{max} = 0.03$ $f_{rev} = 0.07$	$f_{max} = 0.03$ $f_{rev} = 0.07$	$f_{max} = 0.03$ $f_{rev} = 0.07$	$f_{max} = 0.03$ $f_{rev} = 0.07$	$f_{max} = 0.03$ $f_{rev} = 0.07$	$f_{max} = 0.03$ $f_{rev} = 0.40$
Model 6	$f_{max} = 0.03$ $f_{rev} = 0.07$	$f_{max} = 0.03$ $f_{rev} = 0.07$	$f_{max} = 0.03$ $f_{rev} = 0.07$	$f_{max} = 0.03$ $f_{rev} = 0.07$	$f_{max} = 0.03$ $f_{rev} = 0.40$	$f_{max} = 0.03$ $f_{rev} = 0.07$

Finally, regarding the uncertainties, the elastic response pseudo-acceleration corresponding to the isolated structural period with an inherent damping factor of 2% is assumed as the main random variable, modelled by a Gaussian PDF (Castaldo et al. 2016; Cornell 1968; Luco and Cornell 2007), relevant to the structural performance (Castaldo et al. 2016). More details about the above mentioned Gaussian PDF, the sampling procedure and the registration selection criterion are described in (Castaldo et al. 2013, 2015; Castaldo 2018a, b, c, d, e, f). Within the 3D inelastic simulations, each earthquake event has been considered with its corresponding three components.

The details of the real registrations, selected from the European Strong-Motion Database (ESMD), may be found in Castaldo et al. (2015) and in Castaldo et al. (2016).

3 Seismic Reliability-Based Robustness Assessment

In order to estimate the seismic reliability-based robustness of the super/sub-structure and of the FP devices in the different failure cases, several inelastic dynamic simulations have been performed in SAP2000 (2002) for each corresponding structural model and for the both structural system configurations taking into account the seismic uncertainty. Indeed, for each numerical analysis, the peak interstory drifts, δ_x and δ_y, at each story of the super/sub-structure as well as the extreme relative displacements, u_x and u_y, of the FP device level have been computed along x and y directions, respectively. These EDPs have been fitted by means of bi/mono-variate lognormal distributions (Castaldo et al. 2016, 2017a, b) estimating, through the maximum likelihood estimation technique, the mean and standard deviation in both directions (x and y directions).

Figures 2–3 show the lognormal monovariate cumulative distribution functions (CDFs) in each direction for all the models and for the two structural configurations at the 4th level of the superstructure and at joint (# 29) of the substructure, respectively. At the superstructure along the both directions, Models 6 and 4 lead to the worst effects due to the high eccentricity between the forces of the isolation level and of the superstructure. Regarding the substructure, a failure case related to a substructure column causes the highest monovariate exceeding probabilities on the substructure column itself in both directions (Models 6 and 4 on joint-29) (Fig. 3). The connecting beams allow to strongly reduce the failure probabilities at the substructure level thanks to an increase of the structural redundancy among all the substructure columns.

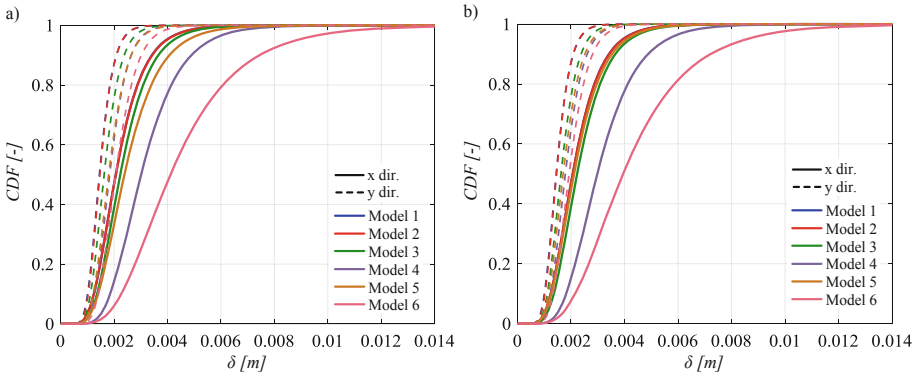

Fig. 2. Lognormal monovariate PDFs at the 4th story: structure with (a) and without (b) the connecting beams.

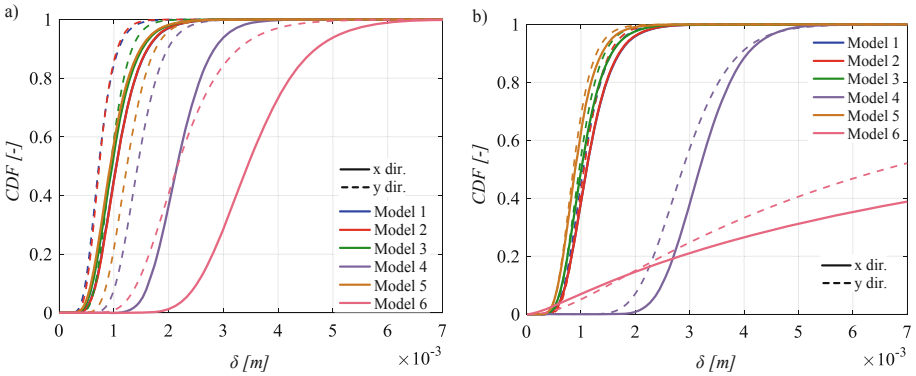

Fig. 3. Lognormal monovariate PDFs at the substructure-joint 29: structure with (a) and without (b) the connecting beams.

As demonstrated in Castaldo et al. (2015, 2016), the seismic reliability assessment has been carried out in terms of bivariate exceeding probabilities. The JPDFs corresponding to joint-29 of the substructure are shown in Fig. 4 as contour lines for Model 6. The statistical parameters of the JPDFs corresponding to the substructure columns strongly increase in the case without the connecting beams as illustrated in Fig. 4(b).

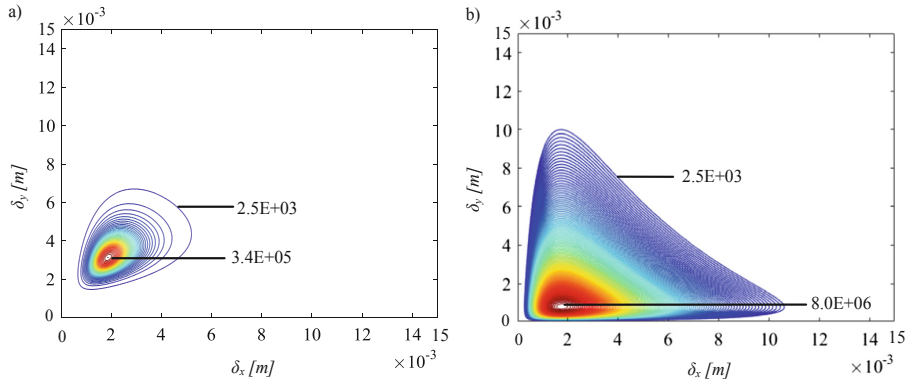

Fig. 4. Contour lines of lognormal bivariate PDFs at the substructure-joint 29, related to Model 6, for configuration with (a) and without (b) connecting beams.

Next, defining several *LS* functions as bi-dimensional domains on the bi-directional interstory drifts or displacements (bi-dimensional performance objectives POs), the bivariate seismic reliability of the 3D r.c. system has been estimated. Specifically, the no-exceeding bivariate probabilities have been evaluated as follows: for each JPDF, related to each model, configuration and story, the volume delimited by the cylinder representative of the corresponding bi-dimensional *LS* domain, expressed in terms of IDs for the super/sub-structure and of relative displacements for the FP devices, has

been numerically computed. After that, the bivariate exceeding probabilities (bivariate CCDFs), have been numerically calculated as the complementary values of the bivariate no-exceeding probabilities. Figures 5 and 6 show, in the performance space in logarithmic scale, the bivariate SP curves of the 4th level (superstructure) and of the joint-29 at 1st level (substructure), numerically computed for the different models and configurations, compared to the PO curves according to the both FEMA-274 and NTC08 provisions, as previously discussed. From the comparison, it is possible to evaluate the (bivariate) seismic reliability-based robustness of the overall system and observe that, for the both configurations, the stick-slip phenomenon and malfunction of the FP devices slightly decrease the bivariate seismic reliability of the superstructure, as shown in Fig. 5.

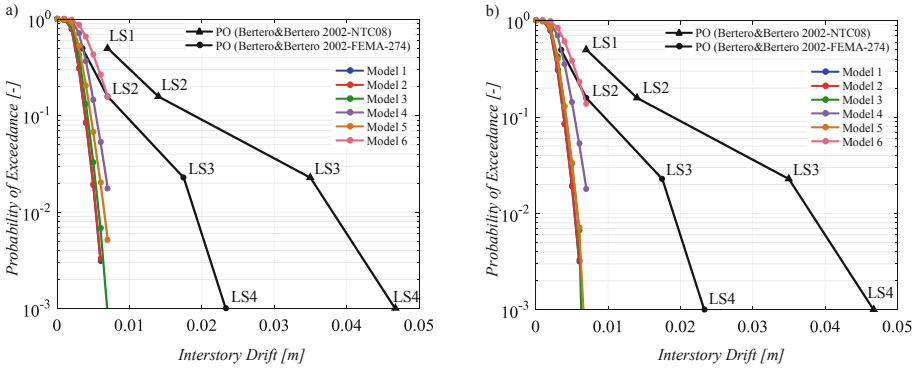

Fig. 5. Exceeding bivariate probabilities at the 4th story, related to configuration with (a) and without (b) the connecting beams.

With reference to the substructure, joint-29 (Fig. 6), Models 4 and 6, similarly to the monovariate assessment, lead to the lowest seismic reliability values so that the both *LS1* and *LS2*, related to the both PO curves defined according, respectively, to FEMA-274 and NTC08 provisions, are violated in the case without the connecting beams. Moreover, *LS3* and *LS4* according to FEMA-274 are also violated in the case without the connecting beams with the consequence that a severe damage to the substructure can occur. This also means that if a malfunction of an internal device causes a friction coefficient higher than 40%, the substructure column can really collapse leading to a disproportioned damage to the overall system in the case without the connecting beams.

Finally, Fig. 7 illustrates the bivariate SP curves of the FP devices showing that these results can be useful for their design (i.e. radius in plan r) within the approach of the seismic reliability-based design (SRBD) (Castaldo et al. 2015, 2016, 2017a, b). The R-square coefficients are higher than 0.97 for all the proposed regressions demonstrating their effectiveness. Form these regression curves, it is possible to observe that with the aim to achieve a given (bivariate) exceeding P_f, a higher radius in plan r is necessary in the case of a malfunction of a corner device. In particular, a failure

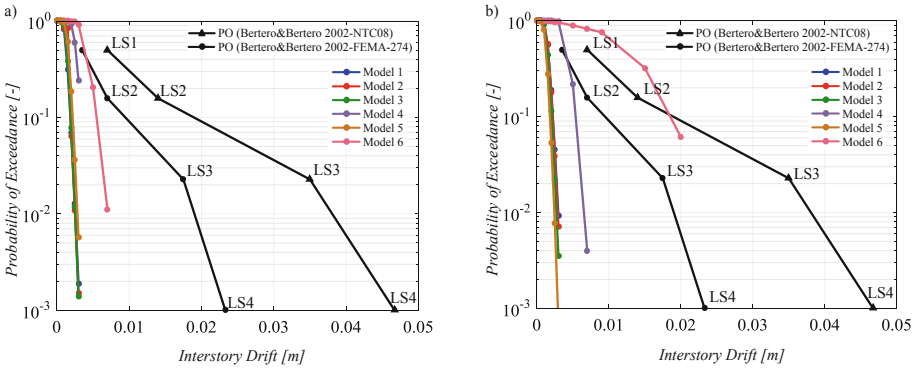

Fig. 6. Exceeding bivariate probabilities at the substructure-joint 29, related to configuration with (a) and without (b) the connecting beams.

probability of $P_f = 1.5 \cdot 10^{-3}$ (in 50 years) requires a radius in plan r ranging from 0.30 m to 0.40 m.

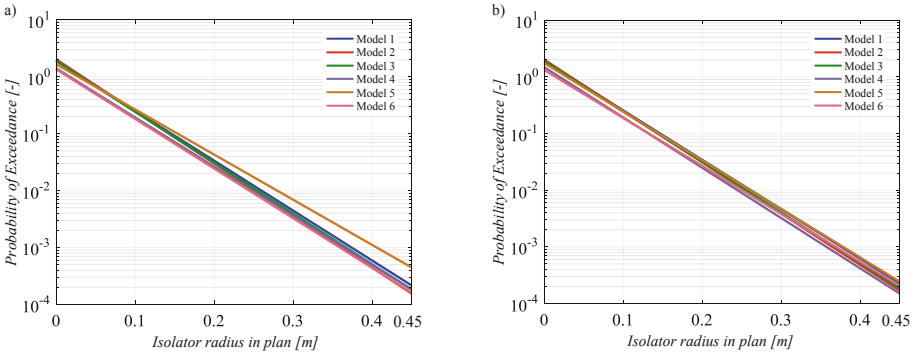

Fig. 7. Exceeding bivariate probabilities at the FP devices, related to configuration with (a) and without (b) the connecting beams.

4 Conclusions

The scope of this work is to estimate the seismic robustness of an ordinary 3D r.c. structure equipped with FP devices, in probabilistic terms, highlighting the importance of the connecting beams at the substructure story. In particular, different models related to different failure cases of the FP devices are presented and, assuming a lifetime of 50 years and L'Aquila (Italy) as reference site, the earthquake main characteristics are assumed as the relevant random variables. The seismic reliability-based results of the 3D r.c. structural system highlight that the presence of the connecting beams strongly improves the seismic reliability and robustness of the substructure by means of an increase of the structural redundancy allowing the respect of the limit states provided

by both NTC08 and FEMA-274 provisions. Moreover, it is also possible to declare that the connecting beams at the substructure level mainly increase the seismic robustness of the substructure without negatively modifying the seismic reliability of the superstructure and isolation level by means of an increase of the structural redundancy for a malfunction of a device. This improvement in terms of the seismic reliability and robustness of the substructure also leads to an increase of the foundation safety. Therefore, the diaphragm floor at the superstructure as well as the connecting beams at the substructure allow to avoid a damage disproportionate to the original cause and, so, can represent very useful design solutions and recommendations aimed at improving the robustness of base-isolated systems equipped with FPS in the case of a real malfunction of a seismic frictional device.

References

Alhan C, Gavin HP (2005) Reliability of base isolation for the protection of critical equipment from earthquake hazards. Eng Struct 27:1435–1449

Almazàn JL, De la Llera JC (2003a) Physical model for dynamic analysis of structures with FPS isolators. Earthquake Eng Struct Dynam 32:1157–1184. https://doi.org/10.1002/eqe.266

Almazàn JL, De la Llera JC (2003b) Physical model for dynamic analysis of structures with FPS isolators. Earthquake Eng Struct Dynam 32:1157–1184. https://doi.org/10.1002/eqe.266

Bertero RD, Bertero VV (2002) Performance-based seismic engineering: the need for a reliable conceptual comprehensive approach. Earthquake Eng Struct Dynam 31:627–652. https://doi.org/10.1002/eqe.146

Building Seismic Safety Council (1997) NEHRP commentary on the guidelines for the seismic rehabilitation of buildings. Provisions (FEMA-274). Washington, DC

Castaldo P, Amendola G, Palazzo B (2017a) Seismic fragility and reliability of structures isolated by friction pendulum devices: seismic reliability-based design (SRBD). Earthquake Eng Struct Dynam 46(3):425–446. https://doi.org/10.1002/eqe.2798

Castaldo P, Palazzo B, Della Vecchia P (2015) Seismic reliability of base-isolated structures with friction pendulum bearings. Eng Struct 95:80–93

Castaldo P, Palazzo B, Della Vecchia P (2016) Life-cycle cost and seismic reliability analysis of 3D systems equipped with FPS for different isolation degrees. Eng Struct 125:349–363

Castaldo P, Palazzo B, Ferrentino T (2017b) Seismic reliability-based ductility demand evaluation for inelastic base-isolated structures with friction pendulum devices. Earthquake Eng Struct Dynam 46(8):1245–1266

Castaldo P, Ripani M (2016) Optimal design of friction pendulum system properties for isolated structures considering different soil conditions. Soil Dyn Earthquake Eng 90:74–87

Castaldo P, Tubaldi E (2015) Influence of FPS bearing properties on the seismic performance of base-isolated structures. Earthquake Eng Struct Dynam 44(15):2817–2836

Castaldo P, Calvello M, Palazzo B (2013) Probabilistic analysis of excavation-induced damages to existing structures. Comput Geotech 53:17–30

Castaldo P, Gino D, Bertagnoli G, Mancini G (2018a) Partial safety factor for resistance model uncertainties in 2D non-linear finite element analysis of reinforced concrete structures. Eng Struct 176:746–762

Castaldo P, Gino D, Carbone VI, Mancini G (2018b) Framework for definition of design formulations from empirical and semi-empirical resistance models. Struct Concr 19(4):980–987

Castaldo P, Jalayer F, Palazzo B (2018c) Probabilistic assessment of groundwater leakage in diaphragm wall joints for deep excavations. Tunn Undergr Space Technol 71:531–543
Castaldo P, Mancini G, Palazzo B (2018d) Seismic reliability-based robustness assessment of three-dimensional reinforced concrete systems equipped with single-concave sliding devices. Eng Struct 163:373–387
Castaldo P, Palazzo B, Alfano G, Palumbo MF (2018e) Seismic reliability-based ductility demand for hardening and softening structures isolated by friction pendulum bearings. Struct Control Health Monit 25(11):e2256
Castaldo P, Ripani M, Lo Priore R (2018f) Influence of soil conditions on the optimal sliding friction coefficient for isolated bridges. Soil Dyn Earthquake Eng 111:131–148
Celarec D, Dolšek M (2013) The impact of modelling uncertainties on the seismic performance assessment of reinforced concrete frame buildings. Eng Struct 52:340–354
CEN (2006) European Committee for Standardization. Eurocode 0: basis of structural design. Final draft. Brussels
Chen J, Liu W, Peng Y, Li J (2007) Stochastic seismic response and reliability analysis of base-isolated structures. J Earthquake Eng 11:903–924
Constantinou MC, Mokha A, Reinhorn AM (1990) Teflon bearings in base isolation. II: modeling. J Struct Eng 116(2):455–474
Constantinou MC, Whittaker AS, Kalpakidis Y, Fenz DM, Warn GP (2007) Performance of seismic isolation hardware under service and seismic loading. Technical report MCEER-07-0012
Cornell CA (1968) Engineering seismic risk analysis. Bull Seismol Soc Am 58(5):1583–1606
ESMD http://www.isesd.hi.is/
Fagà E, Ceresa P, Nascimbene R, Moratti M, Pavese A (2016) Modelling curved surface sliding bearings with bilinear constitutive law: effects on the response of seismically isolated buildings. Mater Struct 49:2179. https://doi.org/10.1617/s11527-015-0642-2
FEMA-356 (2000) Prestandard and commentary for the seismic rehabilitation of buildings. Federal Emergency Management Agency, Washington, DC
Kelly J, Leitmann MG, Soldatos AG (1987) Robust control of base-isolated structures under earthquake excitation. J Optim Theory Appl 53(2):159–180
Kilar V, Koren D (2009) Seismic behaviour of asymmetric base isolated structures with various distributions of isolators. Eng Struct 31:910–921
Luco N, Cornell CA (2007) Structure-specific scalar intensity measures for near-source and ordinary earthquake ground motions. Earthquake Spectra 23(2):357–392
Mckey MD, Conover WJ, Beckman RJ (1979) A comparison of three methods for selecting values of input variables in the analysis from a computer code. Technometrics 21:239–245
Mishra SK, Roy BK, Chakraborty S (2013) Reliability-based-design-optimization of base isolated buildings considering stochastic system parameters subjected to random earthquakes. Int J Mech Sci 75:123–133
Mokha A, Constantinou MC, Reinhorn AM (1990) Teflon bearings in base isolation. I: testing. J Struct Eng 116(2):438–454
Naeim F, Kelly JM (1999) Design of seismic isolated structures: from theory to practice. Wiley, Chichester, UK
NTC08 (2008) Norme tecniche per le costruzioni. Gazzetta Ufficiale del 04.02.08, DM 14.01.08, Ministero delle Infrastrutture
Roy BK, Chakraborty S (2015) Robust optimum design of base isolation system in seismic vibration control of structures under random system parameters. Struct Saf 55:49–59
SAP 2000 (2002) Computers and Structures Inc., Berkley, CA
SEAOC-Vision 2000 Committee (1995) Vision 2000-a framework for performance-based earthquake engineering, vol 1. Structural Engineers Association of California, Sacramento, CA

Takewaki I (2008) Robustness of base-isolated high-rise buildings under code-specified ground motions. Tall Spec Build 17(2):257–271

Tena-Colunga A, Escamilla-Cruz JL (2007) Torsional amplifications in asymmetric base-isolated structures. Eng Struct 29(2):237–247

Zayas VA, Low SS, Mahin SA (1990) A simple pendulum technique for achieving seismic isolation. Earthquake Spectra 6:317–333

Zhao C, Chen J (2013) Numerical simulation and investigation of the base isolated NPPC building under three-directional seismic loading. Nucl Eng Des 265:484–496

Zou XK, Wang Q, Li G, Chan CM (2010) Integrated reliability-based seismic drift design optimization of base-isolated concrete buildings. J Struct Eng 136:1282–1295

A Model for the Analysis at ULS of Corroded RC Beams

A. Recupero[1], N. Spinella[1(✉)], and F. Tondolo[2]

[1] Department of Engineering, Università Di Messina, Messina, Italy
nino.spinella@unime.it
[2] Department of Structural, Geotechnical and Building Engineering, Politecnico Di Torino, Turin, Italy

Abstract. The proposed model is able to consider the interaction between bending, shear and normal forces. Some experimental tests present in the literature, where the structural behaviour of reinforced concrete beams in presence of corrosion of longitudinal and transversal rebar was investigated, were used in the present study in order to validate the proposed model. The numerical results seem to be in good agreement with the experimental ones.

Keywords: Shear-Moment interaction · Corrosion · Limit equilibrium theory · Curvature · Ductility

1 Introduction

The use of reinforced concrete (RC) in the structural field is, of course, a good compromise between costs and durability, being able to provide good performances even in aggressive environmental conditions.

However, concentrations of chlorides close to the rebar and/or carbonation of the cover concrete, together with corrosion due to hydrogen embrittlement, may cause the degradation of the mechanical characteristics of the materials.

Corrosion causes the expansion of rebar and, by the pressure on the surrounding concrete, cracks form in the material.

At the same time, the area of the rebar is reduced, together with the reduction of strength and ductility capacity of the steel. It follows, therefore, that the steel-concrete bond tends to be drastically depleted.

Some research works examined the behaviour of RC beams when stirrups and rebar are both corroded, highlighting as the elements can loss part of their load capacity under these conditions (Rodriguez et al. 1996; El Maaddawy et al. 2005; Alaskar 2013).

Furthermore, the non-uniform corrosion along the stirrups and the consequent loss of resistance and ductility, can change the beam failure mode, causing a brittle collapse and without any warning (Recupero et al. 2014; Cesetti et al. 2016; Colajanni et al. 2016).

Although in the literature are reported several experimental campaigns on beams with corroded rebar, there are few experimental works on the reduction of shear capacity of RC beams with corroded stirrups.

M. di Prisco and M. Menegotto (Eds.): ICD 2018, LNCE 42, pp. 28–39, 2020.
https://doi.org/10.1007/978-3-030-23748-6_3

Furthermore, in order to simulate the effects of corrosion, some models are available to reproduce the degradation of the mechanical capacities of the corroded elements and various theoretical models were developed using the Finite Element Method (FEM). However, they require detailed information on the damaged materials.

In this work, to estimate how the mechanical characteristics of the steel rebar are influenced by corrosion, a large database of tensile tests performed on corroded rebar was collected. Based on these data, a simple equation is proposed for estimating the decay of steel yield strength.

Furthermore, an analytical model was proposed for the evaluation of the shear-bending interaction domain of corroded RC beams.

The formulation takes into account the reduction of the strength of concrete and steel, also providing valuable information on the influence of corrosion on the curvature and the degradation of the ductility of the beam at the Ultimate Limit State (ULS).

2 Influence of Corrosion on the Mechanical Properties of Steel Rebar

When the steel rebar is affected by corrosion phenomena, these reduce the cross-section and cause an increase in the volume of the material affected by the corrosive attack.

This increase in volume generates tensile stresses in the surrounding concrete, with consequent spalling of the cover and reduction of the compressive strength of the material.

To account for these effects of corrosion on the mechanical properties of concrete, the reduced cylindrical compressive strength of concrete due to corrosion can be evaluated using the model proposed by Coronelli and Gambarova (2004).

In the same way, corrosion causes the decadence of the mechanical capacities of the steel rebar, together with the reduction of their cross-section. Therefore, to analytically reproduce the degradation of the yield strength of the corroded material, the linear relationship suggested by Cairns et al. (2005) was used:

$$f_{y,c}/f_y = 1 - \alpha_y Q_c \tag{1}$$

where $f_{y,c}$, and f_y represent, respectively, the yield strength of the corroded and nominal steel; Q_c is the percentage of corrosion; $\alpha_y = 0.012$ is an empirical coefficient determined by regression analysis (Cairns et al. 2005).

However, the empirical coefficient proposed by Cairns et al. (2005) can be improved thanks to the availability of new experimental campaigns subsequently carried out by various authors. At this aim, five recent experimental campaigns were considered in this work (Cobo et al. 2011; Zhang et al. 2012; Apostolopoulos et al. 2013; Fernandez et al. 2016; Imperatore et al. 2017) for a total of 230 specimens.

All tests showed that the mechanical properties were reduced with the increase in the degree of corrosion, and the degrading effects were greater when the diameter of the steel bar was smaller (Presti et al. 2017).

The numerical regression performed on the database of 230 specimens, has allowed to obtain a new value of the coefficient α_y of 0.0094, which is slightly lower than the one proposed by Cairns et al. (2005).

Figure 1 shows the comparison between experimental and theoretical values. The adopted linear model appears robust. In fact, the mean value of the error, defined as the ratio between the experimental and the theoretical value, is equal to 0.99 and the Coefficient of Variation (CoV) is equal to 0.15.

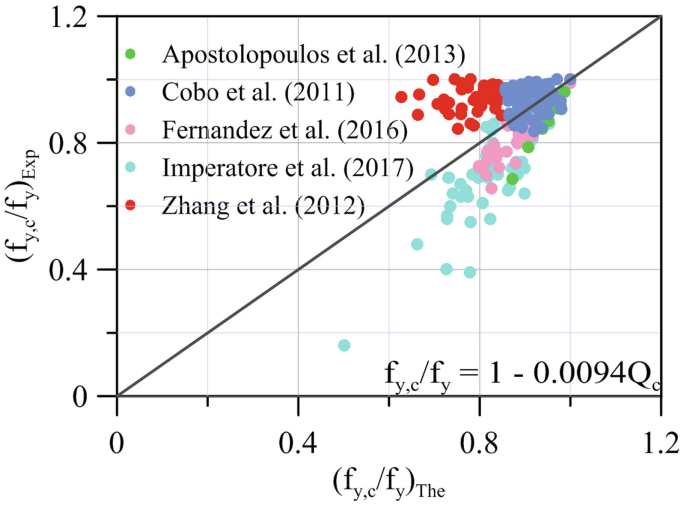

Fig. 1. Experimental versus theoretical yield strength of corroded rebar.

3 Shear-Bending Interaction of Corroded RC Beams

To define the shear-bending interaction domain of corroded RC beams, an already known model was used (Recupero et al. 2003, 2018; Colajanni et al. 2014, 2015, 2017). It is based on the theory of limit equilibrium, adapted to the case of corroded beams.

The influence of corrosion on the mechanical performance of the materials was taken into account by using the model proposed by Coronelli and Gambarova (2004) for the compressed concrete, and the linear model, here suitably calibrated, for the yield strength of the steel.

Furthermore, the concrete efficiency factor (η) was iteratively evaluated, in order to improve the original schema of the model and adequately simulate the strength of the concrete strut.

3.1 The Theoretical Model

The procedure for evaluating the shear-moment domain consists in dividing the cross-section of the beam into three layers of thickness not known a priori (y_i), which are subject to constant normal stress. In addition, the central layer is designed to resist at shear stress (Fig. 2).

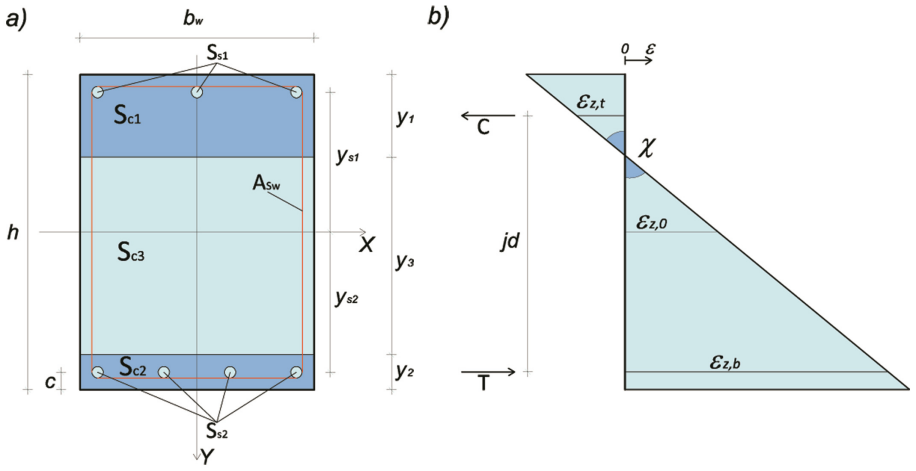

Fig. 2. (a) Cross-sectional model of the RC beam; and (b) strain field at ULS.

The three layers of concrete have areas S_{c1}, S_{c2} and S_{c3}, respectively. The longitudinal rebars are modelled as upper and lower truss elements having, respectively, area S_{s1} and S_{s2}.

The equilibrium equations between the internal and external forces (M_E), acting on the considered section and assuming a normal null force ($N_E = 0$), are the following:

$$\sigma_{c1}\int_{S_{c1}} dS_{c1} + \sigma_{c2}\int_{S_{c2}} dS_{c2} + \sigma_{S1}S_{S1} + \sigma_{S2}S_{S2} = V_R \cot\vartheta \tag{2}$$

$$\sigma_{c1}\int_{S_{c1}} y_c dS_{c1} + \sigma_{c2}\int_{S_{c2}} y_c dS_{c2} + \sigma_{S1}y_{s1}S_{S1} + \sigma_{S2}y_{s2}S_{S2} = M_E + V_R \cot\vartheta\left(\int_{S_{c3}} y_c dS_{c3} \Big/ \int_{S_{c3}} dS_{c3}\right) \tag{3}$$

where σ_{ci}, and σ_{si} are the normal stress of concrete and steel; y_c and y_{si} are the arms of the various layers from the centroid of the cross section of the beam.

Adopting the nominal values for the materials, f_{ym} for yielding steel, f_{cm} for the compressive strength of the concrete, the quantities relative to the areas S_{c1}, S_{c2} and S_{c3} depend on the thickness of the layers y_1, y_2 and y_3, which may vary according to the following geometrical conditions, to the limits imposed on the stresses and the $cot\theta$:

$$y_1 + y_2 + y_3 = h \tag{4.1}$$

$$-f_{cm} \leq \sigma_{ci} \leq 0 \tag{4.2}$$

$$-f_{ym} \leq \sigma_{si} \leq f_{ym} \tag{4.3}$$

$$\sigma_{cw} \leq -\eta f_{cm} \tag{4.4}$$

$$1 \leq \cot\theta \leq 3 \tag{4.5}$$

$$V_R = \min\left(V_{Rc} \vdots V_{Rs}\right) \tag{4.6}$$

The crisis of the beam can occur both by compression crushing of the concrete strut ($V_{Rc} = \sigma_{cw}\ S_{c3}\ cot\theta/(1 + cot^2\theta)$) and by yielding of the stirrups ($V_{Rs} = (A_{sw}/s_w)\sigma_{sw}\ y_3\ cot\theta$), according to the softened truss model.

To define the system of equations and inequalities, it is necessary to solve a linear programming problem where the objective function is represented by Eq. (4.6).

Assuming a value of the bending moment (M_E), we evaluate the thickness of the layers (y_1, y_2, y_3), the $cot\theta$ and the stresses (σ_{ci}, σ_{si}), simply by maximizing the shear strength (V_R) in the compliance with the conditions imposed (Eqs. 4.1–4.6).

3.2 The Effectiveness Factor

The effectiveness factor (η) takes into account the degradation of the compressive strength of the strut (σ_{cw}) caused by the transverse tensile strains.

In the theoretical model, as initially proposed, the effectiveness factor is assumed to be equal to a constant value as indicated by the various national and European codes (Recupero et al. 2003; Italian MIT 2008).

This assumption does not take into account the influence of the inclination of the strut (θ) and, more generally of the strain field at the ULS, on the effectiveness factor.

However, several researchers (Foster and Malik 2002; Bertagnoli et al. 2011; Spinella et al. 2019; Spinella 2019) have shown that the relationship between the compressive strength of the concrete and the effectiveness factor is weak, while the parameter that most influences the value of η is the inclination angle of the strut.

Recently, He et al. (2016) proposed a simple expression to evaluate η as a function of θ, deriving it from the modified compression field theory (MCFT) (Vecchio and Collins 1986):

$$\eta = \frac{1}{0.14 + 0.68\cot^2\theta} \tag{5}$$

In detail, in the MCFT foresees that the effectiveness factor η is calculated as a function of the principal tensile strain ε_1:

$$\eta = \frac{1}{0.8 + 170\varepsilon_1} \tag{6}$$

$$\varepsilon_1 = \varepsilon_{z,0}\left(\varepsilon_{z,0} + 0.002\right)\cot^2\theta \tag{7}$$

In Eq. (7), the centroidal axial strain $\varepsilon_{z,0}$ was assumed equal to the upper limit of the strain in the tensile part of the equivalent trusses (=0.002) (He et al. 2016). Therefore, simply by rearranging the Eqs. (6, 7), Eq. (5) is obtained.

In this work, these approximations were eliminated, and the strain field of the beam at the ULS was completely determined.

Once the forces resulting in concrete and steel, in equilibrium with the external bending moment M_E, were determined and consequently the shearing resistance V_R is known, the deformations of the upper ($\varepsilon_{z,t}$) and lower ($\varepsilon_{z,b}$) chord at the ULS can be obtained as follows:

$$\varepsilon_{z,t} = \left[-\frac{M_E}{jd} + V_R\cot\theta\left(\frac{1}{2} - \frac{y_2}{jd}\right)\right]\frac{1}{EA_t} \tag{8}$$

$$\varepsilon_{z,b} = \left[\frac{M_E}{jd} + V_R\cot\theta\left(\frac{1}{2} - \frac{y_1}{jd}\right)\right]\frac{1}{EA_b} \tag{9}$$

where $EA_t = E_c\,(S_{c1} - S_{s1}) + E_s\,S_{s1}$ e $EA_b = E_s\,S_{s2}$ are, respectively, the axial stiffness of the upper and lower chord, respectively; $jd = y_3 + (y_1 + y_2)/2$ is the lever arm (Fig. 2b).

Assuming that sections remain plane, the ultimate curvature and the centroidal axial strain are $\chi = (\varepsilon_{z,b} - \varepsilon_{z,t})/jd$ and $\varepsilon_{z,0} = \varepsilon_{z,t} + \chi\,(y_1 + y_3)/2$, respectively.

Therefore, the principal axial strain (ε_1) and the effectiveness factor (η) can be evaluated by the Eqs. (6, 7).

In summary, the procedure for the calculation of a point of the interaction domain involves the following steps:

1. assuming a value of M_E;
2. assuming a first value of variables set $X_0^T = [y_1, y_2, cot\theta, \sigma_{c1}, \sigma_{c2}, \sigma_{s1}, \sigma_{s2}]_0$;
3. the optimal values of variables set is found $X_{opt}^T = [y_1, y_2, cot\theta, \sigma_{c1}, \sigma_{c2}, \sigma_{s1}, \sigma_{s2}]_{opt}$. It provides the maximum shear V_R in the compliance of the imposed conditions;
4. jd, EA_t e EA_b are evaluated;
5. $\varepsilon_{z,t}$, $\varepsilon_{z,b}$, χ, $\varepsilon_{z,0}$, ε_1, η are evaluated;
6. a new value of $cot^2\theta_{new} = (\varepsilon_{z,0\text{-}0}.002)/(\varepsilon_1 + \varepsilon_{z,0\text{-}0}.004)$ is evaluated, on the base of compatibility conditions;
7. if $cot\theta_{new}$ is different from $cot\theta_{opt}$, it is back to step 2.

Usually few iterations are needed to achieve the convergence.

The proposed model provides a solution that respects the conditions of equilibrium and compatibility at the ULS. Furthermore, it provides valuable information on bending and shear strength as well as on the ductility of the cross-section in terms of ultimate curvature.

4 Shear-Bending Domain for Corroded Rc Beams

The procedure illustrated in the previous section allows the evaluation of the shear-bending interaction domains at the ULS.

A database of experimental tests on corroded beams available in the literature (Rodriguez et al. 1996; El Maaddawy et al. 2005; Alaskar 2013) was collected, in order to validate the proposed model.

In this section, the interaction domains obtained for the beams tested by El Maaddawy et al. (2005) are shown.

The specimens have size 152 × 254 × 3200 mm and were undergone to accelerated corrosion for a time varying between 50 and 310 days. Afterwards, four points tests were carried out.

In Fig. 3, the interaction domain Bending-Shear-Time of corrosion (M_E–V_R–t) are plotted.

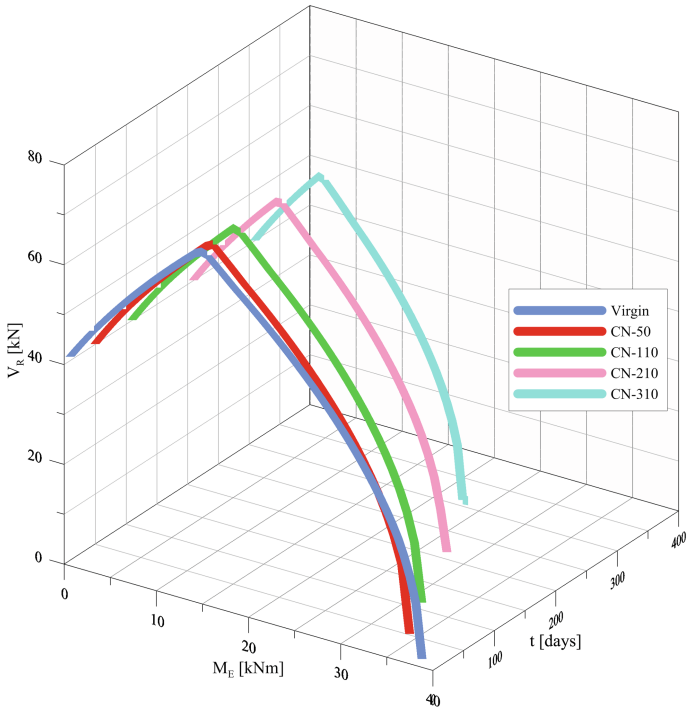

Fig. 3. Theoretical interaction M_E-V_R–t domains for the beams tested by El Maaddawi et al. (2005)

The proposed model also provides some valuable information on the ultimate curvature. In Fig. 4, the theoretical ultimate curvature as a function of moment and shear is plotted. As expected, the curvature decreases with the increase in the degree of

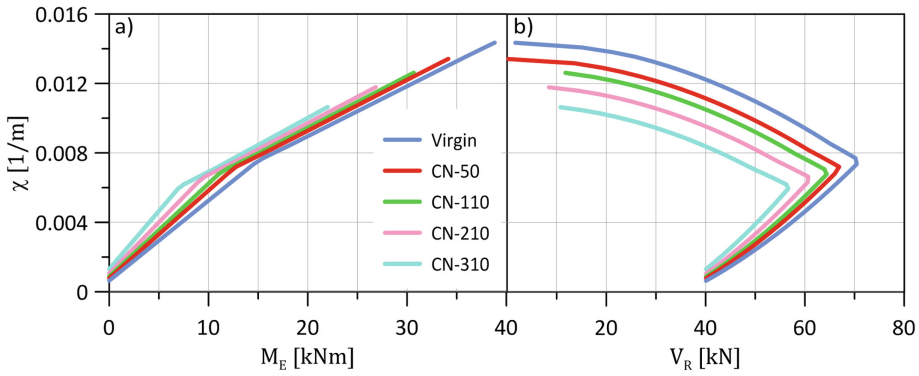

Fig. 4. Theoretical reduction of curvature at ULS as function of (a) moment and (b) shear strength for the beams tested El Maaddawi et al. (2005)

corrosion. Furthermore, the curvature reduction is almost constant for each shear value considered.

Therefore, the investigation on the capacity of structures subject to seismic action should take into account the interaction between shear and corrosion. In reality, most of the available software do not take these phenomena into account when estimating the ductility of the frame structures.

5 Validation of the Proposed Model

5.1 Experimental-Theoretical Shear Strength Comparison

In order to validate the proposed model, a database of experimental campaigns available in the literature was collected (Rodriguez et al. 1996; El Maaddawy et al. 2005; Alaskar 2013).

Experimental tests conducted by Rodriguez et al. (1996) concern RC beams subjected to electrochemical corrosion. The specimens were designed with high flexural reinforcement and with stirrups spacing close to $d/2$ (d: effective depth). The corrosion involved all the reinforcement (longitudinal and transversal).

The specimens are catalogued in different groups (11, 12, 13, 21, 31) as a function of the cylindrical compressive strength of the concrete (f_{cm}) and the geometrical percentage of the longitudinal (ρ_l) and transversal reinforcement (ρ_w).

In the tests by El Maaddawy et al. (2005) the corrosion was limited to the bottom longitudinal rebar. Furthermore, corrosion was uniformly induced only along the central part of the beams.

Finally, Alaskar (2013) has investigated the effect of the corrosion of the stirrups on the shear behaviour of slender RC beams. The specimens were catalogued on the basis of three variables: type of stirrups (none, 10 M improved adherence bars, smooth bars D12, smooth bars D6); corrosion rate (0%, 7.5% and 15%); stirrups spacing (100–200 mm).

Figure 5 shows the theoretical results provided by the proposed model. The theoretical shear (V_{the}) is compared with the experimental one (V_{exp}).

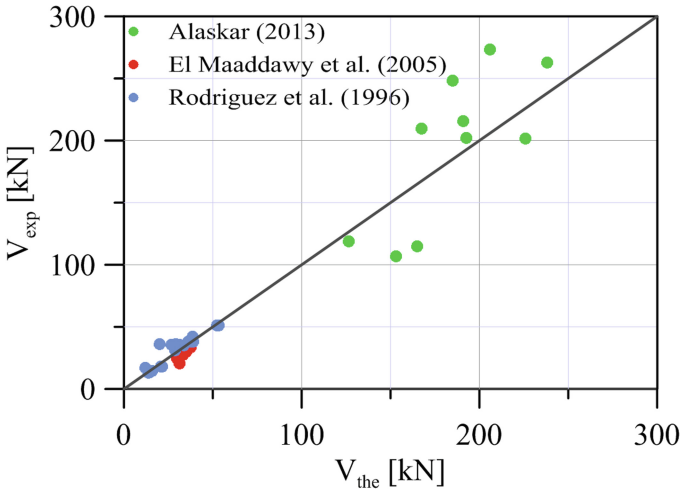

Fig. 5. Experimental versus theoretical shear strength of corroded beams

The statistical values of the experimental and theoretical shear strength (V_{exp}/V_{the}) provide an average of 1.00 and a coefficient of variation (CoV) equal to 0.21. Therefore, the proposed theoretical model shows a good reliability in predicting the shear strength of RC beams damaged by corrosion.

5.2 Influence of Corrosion on the Ultimate Curvature

Since the intensity of corrosion (i_{corr}) is constant for each of the experimental campaigns considered, and also assuming a linear penetration of corrosion in the steel as a function of the corrosion time, it was possible to plot in Fig. 6 the trend of the theoretical curvature (χ) to the ULS against to the corrosion time (t).

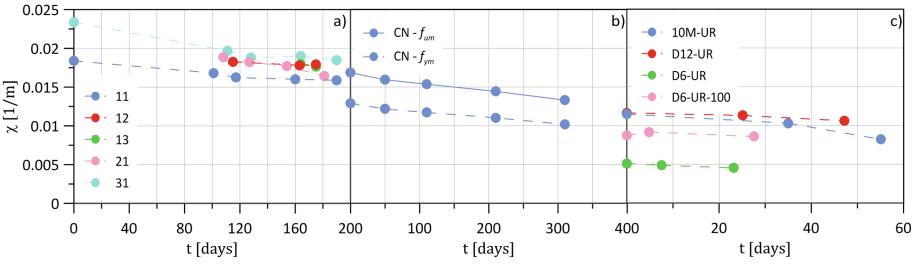

Fig. 6. Theoretical curvature at ULS versus time of corrosion: (a) Rodriguez et al. (1996); (b) El Maaddawy et al. (2005); and (c) Alaskar (2013)

The data were classified as proposed by the Authors in their research and on the basis of homogeneous groups of the main parameters (cylindrical compressive strength of concrete and geometrical percentage of reinforcement).

The trend of the curves shows how the proposed model provides a prediction of the degradation of the ultimate curvature as a function of the exposure of the specimens to the corrosion process. Further experimental studies are needed to validate the numerical prediction.

For both test campaigns by Rodriguez et al. (1996) and El Maaddawy et al. (2005), the decay of the curvature capacity at the ULS due to corrosion is about 21%.

The analysis of the tests carried out by Alaskar (2013) shows, instead, a smaller reduction of the last curvature for the three groups of beams D12-UR, D6-UR and D6-UR-100. While for the 10 M-UR group the ultimate curvature capacity is reduced by 28.4% due to corrosion.

The ultimate curvature is closely related to the ductility of the cross-section, so it is evident that corrosion causes not only a loss of load capacity, but also a reduced dissipation capacity of the structural element.

Therefore, the effects of corrosion should be considered for the design or evaluation of the seismic vulnerability of RC buildings.

6 Conclusions

In this research work an analysis of shear-flexural response of damaged-corrosion RC beams was performed.

The mechanical properties of materials subjected to the corrosion effects were adequately modelled with formulas taking into account the variability due to corrosion.

The damaging effect of corrosion on the yield strength of steel rebar was taken into account suitably improving a relationship proposed in literature.

A large database of tensile tests carried out on corroded steel rebar was collected and then a regression analysis was performed to obtain an empirical coefficient. The decay linear model proposed for the prediction of the yield strength of corroded steel rebar was proven to give satisfactory results.

A previous and consolidated theoretical model for the shear-flexural strength of structural elements was improved and adequate to the case of corroded RC beams.

A modified equation for the effectiveness factor for concrete was introduced in the solution procedure. It is function of the inclination angle of the compressive stress field at ULS. The procedure was generalized and the strain field at collapse was determined obtaining a compatible and a balanced solution. Moreover, the effects of corrosion on the steel rebar were taken into account and the linear decay model proposed was used.

The shear-flexural-time of corrosion domains obtained using the proposed model show how the corrosion effects influence the load bearing capacity of the structural elements.

In addition, the proposed model provides information about the curvature at ULS. The results of the numerical analysis highlight the decrease of the deformation capacity of the cross-section caused by different corrosion level.

Interesting results were obtained also in terms of interaction between shear strength and ultimate curvature, with an almost constant reduction of ULS curvature with a higher level of shear. The response behaviour of buildings subjected to seismic actions should be analysed considering corrosion effects also.

Finally, a database of tests available into literature of corroded RC beams subjected to transversal loads was collected and used to validate the proposed model. The numerical results were shown a good agreement with the experimental data.

Acknowledgements. The financial support from the Italian Ministry of Education, University and Research (PRIN Grant 2015HZ24KH – "*Failure mechanisms caused by corrosive degrade and by lack of constructive details in the existing structures in reinforced concrete.*") is gratefully acknowledged. The Corresponding Author wishes to express his personal gratitude to this research fund and also to the PRIN Grant 2015HZ24KH, through which a research fellow scholarship was awarded.

References

Alaskar A (2013) Shear behaviour of slender RC beams with corroded web reinforcement. Master's thesis, University of Waterloo

Apostolopoulos CA, Demis S, Papadakis VG (2013) Chloride-induced corrosion of steel reinforcement – mechanical performance and pit depth analysis. Constr Build Mater 38:139–146. https://doi.org/10.1016/J.CONBUILDMAT.2012.07.087

Bertagnoli G, Mancini G, Recupero A, Spinella N (2011) Rotating compression field model for reinforced concrete beams under prevalent shear actions. Struct Concr 12:178–186. https://doi.org/10.1002/suco.201000006

Cairns J, Plizzari GA, Du Y et al (2005) Mechanical properties of corrosion-damaged reinforcement. ACI Mater J 102:256–264. https://doi.org/10.14359/14619

Cesetti A, Mancini G, Tondolo F, Recupero A, Spinella N (2016) Physical model for structural evaluation of R.C. beams in presence of corrosion. In: Frank D, Beushausen H-D, Alexander MG, Moyo P (eds) Proceedings of the 4th international conference on concrete repair, rehabilitation and retrofitting, ICCRRR 2015. Leipzig, Germany, pp 107–114

Cobo A, Moreno E, Cánovas MF, Cánovas MF (2011) Mechanical properties variation of B500SD high ductility reinforcement regarding its corrosion degree. Mater Construcción 61:517–532. https://doi.org/10.3989/mc.2011.61410

Colajanni P, La Mendola L, Mancini G, Recupero A, Spinella N (2014) Shear capacity in concrete beams reinforced by stirrups with two different inclinations. Eng Struct 81:444–453. https://doi.org/10.1016/J.ENGSTRUCT.2014.10.011

Colajanni P, La Mendola L, Recupero A, Spinella N (2017) Stress field model for strengthening of shear-flexure critical RC beams. J Compos Constr 21(5):04017039. https://doi.org/10.1061/(asce)cc.1943-5614.0000821

Colajanni P, Recupero A, Ricciardi G, Spinella N (2016) Failure by corrosion in PC bridges: a case history of a viaduct in Italy. Int J Struct Integr 7:181–193. https://doi.org/10.1108/IJSI-09-2014-0046

Colajanni P, Recupero A, Spinella N (2015) Shear strength degradation due to flexural ductility demand in circular RC columns. Bull Earthquake Eng 13:1795–1807. https://doi.org/10.1007/s10518-014-9691-0

Coronelli D, Gambarova P (2004) Structural assessment of corroded reinforced concrete beams: modeling guidelines. J Struct Eng 130:1214–1224. https://doi.org/10.1061/(asce)0733-9445(2004)130:8(1214)

El Maaddawy T, Soudki K, Topper T (2005) Long-term performance of corrosion-damaged reinforced concrete beams. ACI Struct J 102:649–656. https://doi.org/10.14359/14660

Fernandez I, Bairán JM, Marí AR (2016) Mechanical model to evaluate steel reinforcement corrosion effects on σ–ε and fatigue curves. Experimental calibration and validation. Eng Struct 118:320–333. https://doi.org/10.1016/J.ENGSTRUCT.2016.03.055

Foster SJ, Malik AR (2002) Evaluation of efficiency factor models used in strut-and-tie modeling of nonflexural members. J Struct Eng 128:569–577. https://doi.org/10.1061/(asce)0733-9445(2002)128:5(569)

He Z-Q, Liu Z, John Ma Z (2016) Simplified shear design of slender reinforced concrete beams with stirrups. J Struct Eng 142:06015003. https://doi.org/10.1061/(ASCE)ST.1943-541X.0001394

Imperatore S, Rinaldi Z, Drago C (2017) Degradation relationships for the mechanical properties of corroded steel rebars. Constr Build Mater 148:219–230. https://doi.org/10.1016/J.CONBUILDMAT.2017.04.209

Italian MIT (2008) D.M. 14 January 2008. Nuove Norme tecniche per le costruzioni. Gazzetta Ufficiale, vol. 29 [in Italian]

Presti AL, Recupero A, Spinella N (2017) Influence of rebar corrosion on RC frame push-over response. In: High tech concrete: where technology and engineering meet - proceedings of the 2017 fib symposium, pp 2118–2126

Recupero A, D'Aveni A, Ghersi A (2003) N-M-V interaction domains for box and I-shaped reinforced concrete members. ACI Struct J 100(1):113–119. https://doi.org/10.14359/12445

Recupero A, Spinella N, Colajanni P, Scilipoti CD (2014) Increasing the capacity of existing bridges by using unbonded prestressing technology: a case study. Adv Civ Eng. https://doi.org/10.1155/2014/840902

Recupero A, Spinella N, Tondolo F (2018) A model for the analysis of ultimate capacity of RC and PC corroded beams. Adv Civ Eng. https://doi.org/10.1155/2018/8697109

Rodriguez J, Ortega LM, Casal J, Diez JM (1996) Assessing structural conditions of concrete structures with corroded reinforcement. In: Conference, concrete repair, rehabilitation and protection; E & FN Spon, Dundee, pp 65–78

Spinella N (2019) Modeling of shear behavior of reinforced concrete beams strengthened with FRP. Compos Struct 215:351–364. https://doi.org/10.1016/j.compstruct.2019.02.073

Spinella N, Colajanni P, Recupero A, Tondolo F (2019) Ultimate shear of RC beams with corroded stirrups and strengthened with FRP. Buildings 9(2):34. https://doi.org/10.3390/buildings9020034

Vecchio FJ, Collins MP (1986) The modified compression-field theory for reinforced concrete elements subjected to shear. ACI J Proc 83:219–231. https://doi.org/10.14359/10416

Zhang W, Song X, Gu X, Li S (2012) Tensile and fatigue behavior of corroded rebars. Constr Build Mater 34:409–417. https://doi.org/10.1016/J.CONBUILDMAT.2012.02.071

Criteria for the Structural Analysis of Precast Buildings with Dissipative Connection Systems of Cladding Wall Panels

G. Toniolo, F. Biondini, and B. Dal Lago(✉)

Department of Civil and Environmental Engineering,
Politecnico di Milano, Milan, Italy
brunoalberto.dallago@polimi.it

Abstract. With reference to the connections of cladding wall panels of precast buildings, different types of dissipative devices have been recently proposed. They have been developed based on a comprehensive theoretical study and experimental verification. A problem with the method of structural analysis is still pending to allow for practical application of these devices in the design and construction of the overall building in which they are installed. In general, non-linear time-history dynamic analysis can be applied on a 3-D model inclusive of frame, panels and their connections. However, this approach is demanding and not handy for the current design practice. A linear static or modal dynamic analysis based on the response spectrum could be applied, but at present the pertinent force-reducing behaviour factor is not given by the codes. Some simplified approximate approaches are hence presented in this paper, referring in particular to a friction based dissipative device to be used both in vertical and horizontal panels and to a plastic dissipative device to be used in horizontal panels. This latter, further to new constructions, can be applied also for the retrofitting or strengthening of existing buildings.

Keywords: Seismic performance · Cladding panel connections · Structural analysis · Precast structures

1 Introduction

In precast buildings the use of dissipative connections, placed between the wall panels or between panels and structure, introduces a source of friction or plastic hysteretic dissipation of energy in the dual wall-frame structural system. The contribution to energy dissipation of these connections in the seismic behaviour of the overall structural system depends on the magnitude of their deformation and force capacities with respect to those of the overall structural system in which they are installed.

To obtain a sensible force reduction, a suitable quantity of energy shall be dissipated. In the meantime, the stiffening effect which allows to sensibly reduce the displacements with respect to those of the bare frame comes from the total contribution given by the dissipative devices in terms of resisting force.

The friction-based devices (FBDs) shown in Fig. 1 are considered in this paper for the mutual joints of both vertical or horizontal panels. These devices have a very small

M. di Prisco and M. Menegotto (Eds.): ICD 2018, LNCE 42, pp. 40–55, 2020.
https://doi.org/10.1007/978-3-030-23748-6_4

initial elastic flexibility and a friction slide displacement capacity limited to few centimetres, with a constitutive law well represented by a rigid-pseudoplastic model (see Fig. 2).

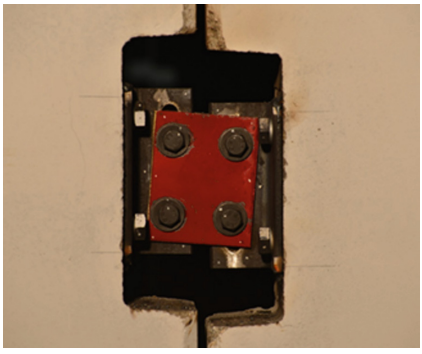

Fig. 1. Friction-based device "FBD" in operation

The seismic response of precast structures with FBDs has been investigated in Biondini et al. (2013). For the corresponding limited floor drifts, the columns, acting in parallel, remain usually within the elastic field and the dissipation of energy comes only from the dissipative devices up to their ultimate displacement capacity. Therefore, with respect to the overall seismic response of the initial stiff dual wall-frame system with fixed inter-panel connections, the force reduction effects can come only from the set of dissipative devices interposed between the panels when their slip threshold is attained. More information about the mechanical characterization of the FBDs considered in this paper can be found in Ferrara et al. (2011), Biondini et al. (2013), and Dal Lago et al. (2017).

The steel folded plate angles (FPAs) shown in Fig. 3 are also considered. These devices are placed at the ends of horizontal panels connecting them to the supporting lateral columns. They have a large initial elastic flexibility that modifies the vibration properties of the frame with the addition of a stiffening contribution. The subsequent plastic branch is also large, so that a certain contemporary contribution to energy dissipation at large displacements can come from both angles and columns. Figure 4 shows the cyclic behaviour of these folded plates, for which an elastic-plastic constitutive model can be assumed. More information about these elastic-plastic dissipative devices can be found in Dal Lago et al. (2018a). The general approach for the design of precast structures with dissipative systems of connections should be based on a nonlinear time-history dynamic analysis applied to the spatial model of the dual wall-frame structure where the panel connections are represented by their proper constitutive laws as presented before. However, this approach is computationally expensive and not handy in engineering practice.

As an alternative, the ordinary linear methods of seismic analysis could be applied based on the response spectrum and a proper estimation of the behaviour factor q which represents the force reduction due to the dissipative effects. In this way, the ordinary

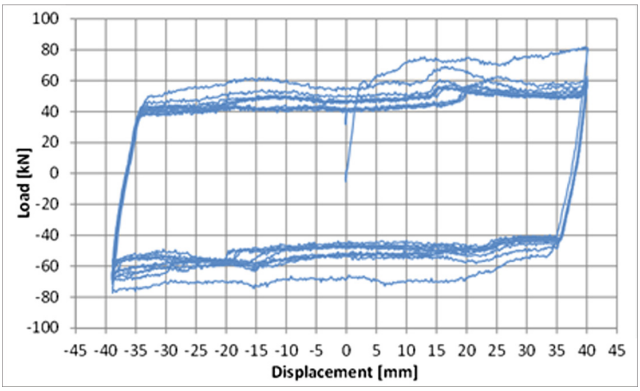

Fig. 2. Cyclic test on a single "FBD"

Fig. 3. Folded plate angle "FPA" installed between column and horizontal panel

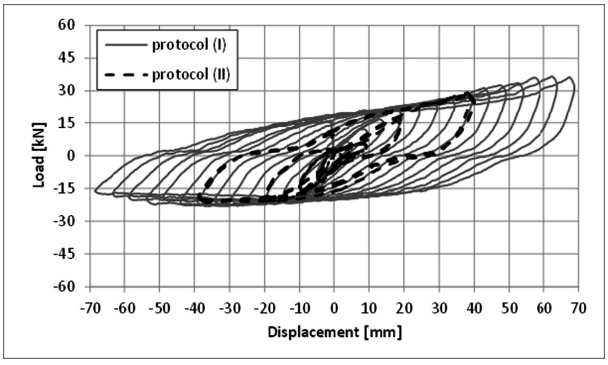

Fig. 4. Cyclic test on a single "FPA"

linear modal dynamic analysis of the frame structure can be performed. For the calibration of the behaviour factor, that is not presently regulated by the pertinent design codes, a preliminary parametric investigation should be made, comparing with a

probabilistic approach the results obtained by the non-linear and the linear dynamic analyses for a significant set of structural situations. Performance-based approaches more sophisticated than the linear analysis, but still of much easier implementation than a set of non-linear dynamic analyses, are discussed in Belleri (2017) and Dal Lago and Molina (2018). This paper presents some simplified approximate approaches with specific reference to FBDs and FPAs.

2 Friction-Based Dissipative Devices

The results of recent experimental and numerical investigations demonstrated that precast structures with dissipative friction-based inter-panel connections exhibit large ductility and dissipation capacity. This is shown by the hysteretic cycles of Fig. 5 registered for a full-scale prototype of precast structure submitted to a long series of tests at the European Laboratory for Structural Assessment (ELSA) of the Joint Research Centre (JRC) within the scope of the SAFECLADDING Project (see Colombo et al. 2014; EUR 27934 EN 2016; EUR 27935 EN 2016; Dal Lago et al. 2018b; Negro and Lamperti Tornaghi 2017, and Toniolo and Dal Lago 2017). In particular, the diagram of Fig. 5 refers to the cyclic test 1.18 performed on the quoted prototype provided with vertical panels and 3FBDs per joint, as described in Dal Lago et al. (2017) and Toniolo and Dal Lago (2017), where a detailed report of the quoted testing activity can be found. Following these results, it is suggested to adopt the behaviour factor of concrete frames as estimation of the behaviour factor of the dual wall-frame resisting system of precast structures with cladding panels provided with the dissipative connections of concern, under condition that the drift capacity of such connections is not exceeded.

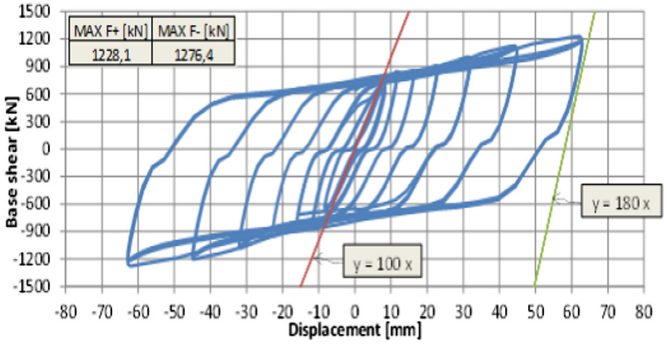

Fig. 5. Force displacement cycles with 3FBDs pendulum arrangement of vertical panels

Consequently, a simplified seismic analysis of the investigated systems could be carried out through the following steps:

1. definition of the elastic response spectrum of the site, to be read only in the plateau region because of the small natural vibration period expected for the stiff dual wall-frame resisting system;

2. definition of the design response spectrum based on a prescribed value of the behaviour factor q (as proposed in the following) and consequent evaluation of the seismic force;
3. static analysis, under this force, of the 3D model of the structure with the panels attached to each other with fixed connections;
4. evaluation from the above-mentioned analysis of the maximum forces in the inter-panel connections;
5. design of the dissipative devices so to have their friction threshold at about these forces;
6. evaluation of the maximum top displacement under a force corresponding to the actual friction threshold from a static analysis of the 3D model of the structure with the panels attached to each other with the FBDs provided with their initial elastic stiffness;
7. evaluation of the inelastic maximum top displacement of the dual wall-frame structure based on the criterion of equal energy associated with the prescribed value of the behaviour factor (elastic displacement of the stiff structure multiplied by $(1 + q^2)/2$);
8. evaluation of the corresponding relative displacements (joint drift) in the dissipative inter-panel devices, to be compared with their kinematic capacity;
9. overproportioning by capacity design of the other connections of the structural system to avoid early brittle failures;

For simple structures the forces in the inter-panel connections can also be evaluated on the basis of the maximum base shear calculated from a linear static analysis. Figure 6 shows the equilibrium conditions of the panels, each connected to the foundation with a central hinge and to the roof element with a shear key. The panels are provided with dissipative mutual connections where the maximum forces H and H' transmitted to their base are $H = Vb/h$ and $H' = Vb/(2\ h)$, where V is the slip threshold force of the joint devices.

2.1 Application of the Procedure

An example is discussed with reference to the concrete structural prototype tested at the ELSA laboratory (see Fig. 7). The structure has 3 + 3 columns 500 × 500 × 8000 mm (h = 7000 mm protruding from the foundation) and 6 + 6 vertical panels 160 × 2500 × 8400 mm, as shown in Fig. 8. Concrete Class 45/55 is used for all elements. A global weight of the vibrating mass of the building W = 1700 kN, placed at the level of the roof diaphragm and including the pertinent part of the mass of the cladding panels, is assumed.

The friction load threshold of the FBDs can be evaluated based on the tightening force $N = 0.7A_s f_{ub}/\gamma_7$ (EN 1993-1-8: 2004) of each pair of bolts (see Fig. 9):

$$V_z = N\frac{2\mu_d n k_s/\varphi}{\sqrt{1+\frac{e^2}{d^2}}}$$

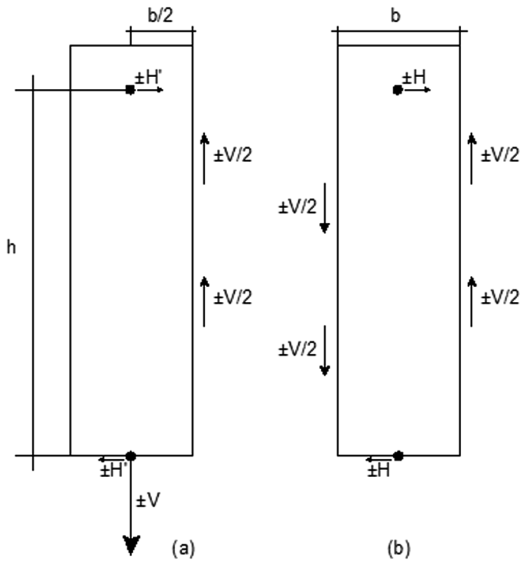

Fig. 6. Equilibrium of panels: (a) end panel; (b) internal panel (two devices per joint)

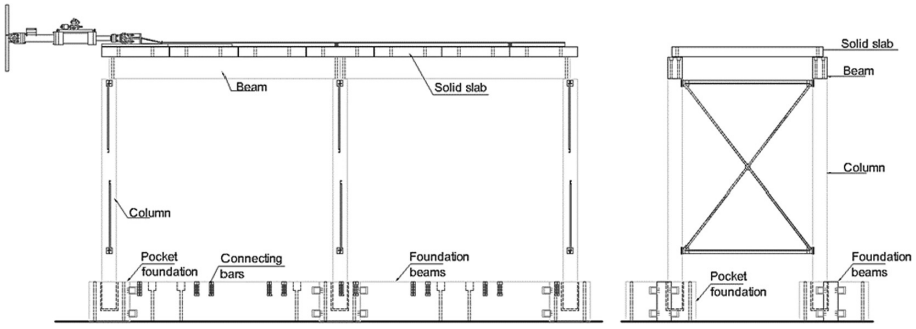

Fig. 7. Prototype of a precast structure tested at ELSA laboratory – longitudinal and transverse sections

where $n = 2$ is the number of active friction surfaces, and where the values $\mu_d = 0.44$ and $k_s = 0.63$ are assumed for the friction coefficient and the effectiveness factor of slotted holes, respectively. With respect to their random variability, these are lower side limit values that lead to overestimate the displacements of the structure. The φ-factor, assumed equal to 1.5, accounts for the friction losses when Belleville washers are used. With $e = 68.5$ mm and $d = 86$ mm, as shown in Fig. 9, the above formula simplifies in:

$$V_z = 0.578N$$

The maximum joint drift capacity is 50 mm.

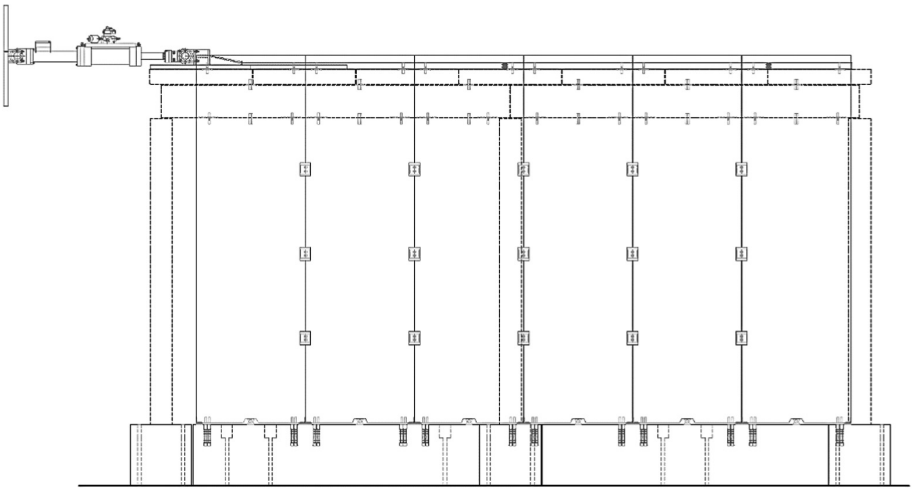

Fig. 8. Arrangement of the vertical panels in a lateral wall

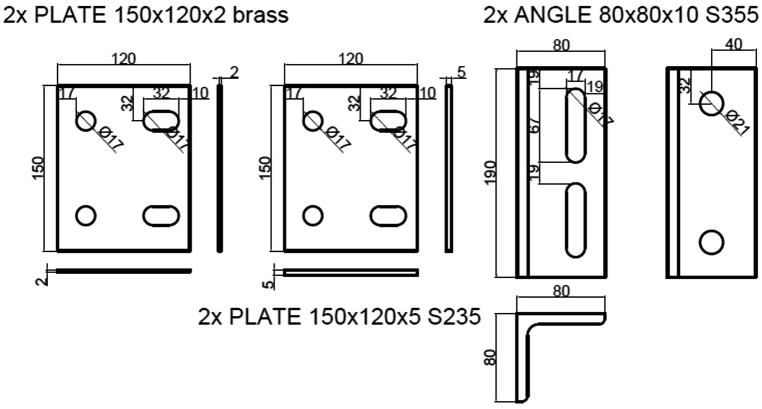

Fig. 9. Details of the FBD

Considering the number of panel interfaces of two walls $n_i = 10$ (see Fig. 8), the shear load V_z on a single device with n_j connections per interface is:

$$V_z = \frac{Fh}{n_i n_j b}$$

where F is the global force coming from the roof, b = 2.5 m is the width of a panel, and h = 7.0 m is the height of its upper fastening (h/b = 2.8).

The procedure is as follows:

Step 1

Considering the elastic response spectrum of Eurocode 8 (EN 1998-1:2004) for a site with a PGA equal to 0.30 g and a subsoil type B, the maximum elastic structural response is $S_e = 2.5 \times 1.2 \times 0.30\ g = 0.90\ g$.

Step 2

Assuming $q = 5$, the plateau value of the design spectrum becomes $S_d = 0.90\ g/5 = 0.18\ g$.

Step 3

The seismic force is: $F = 0.180 \times 1700 = 306$ kN.

Step 4

The shear load with $n_i = 5 + 5$ panel interfaces of the two walls and $n_j = 2$ connection devices per interface is $V_z = 2.8 \times 06/(10 \times 2) = 42.9$ kN.

Step 5

The tightening force with M16 bolts Class 8.8 is $N = 0.7A_s f_{ub}/\gamma = 0.7 \times 157\ 800/1.1/1000 = 79.9$ kN and the friction load threshold of one device is $V_{z0} = 0.578 \times 79.9 = 46.2$ kN. With $V_z/V_{z0} = 0.929$ the actual force reduction is $q_0 = 5\ 0.929 = 4.64$ and the seismic force is $F_0 = 306/0.929 = 329$ kN.

Step 6

The elastic drift d_e of the structure subjected to the horizontal force F_0 can be calculated on the basis of the stiffness $K_v = K_c + K_w$, that is the sum of the contributions of columns and walls working in parallel:

$$d_e = F_0/K_v$$

For a single column is $k_c = c3EI/h^3 = 442$ N/mm, where $c = 0.25$ is the value of the stiffness reducing factor of the cracked cross-section with 8ϕ24 reinforcing bars, $h = 7000$ mm is the free column height, $I = 57.76 \times 10^8$ mm^4 is the second order moment of the cross-section, inclusive of the reinforcement, and $E = 35000$ N/mm^2 is the elastic modulus of concrete. Being $n_c = 6$ the number of columns, the total stiffness is:

$$K_c = n_c k_c = 6 \times 442 = 2652\ \text{N/mm}.$$

This is confirmed with good accuracy by the cyclic test 1/06 reported in Toniolo and Dal Lago (2017), where the experimental stiffness of the structure with an isostatic panel connection system has been measured in about 2700 N/mm.

Neglecting the very small intrinsic deformability of the wall panels, their deformation can be concentrated at the interface dissipative connections as for a rigid rotation of the panels. Assuming $k' = 50000$ N/mm the intrinsic elastic stiffness of a single connection device as obtained by tests (see Dal Lago et al. 2018a), the global contribution of the walls is:

$$K_w = n_i n_j k'/(h/b)^2 = 127556\ \text{N/mm}$$

leading to K_v = 2652 + 127556 = 130208 N/mm. Note that the contribution of the column is limited to 2% and, therefore, could be neglected without introducing relevant approximations. The elastic drift is:

$$d_e = F_0/K_v = 329000/130208 = 2.5 \text{ mm}$$

Step 7

With $(1 + q_0^2)/2$ = 11.26 and with the plasticisation concentrated within the FBDs, the elastic-plastic top displacement is d = 2.5 × 11.26 = 28.5 mm. This limit corresponds to a fully elastic structural behaviour and to post-earthquake operability.

Step 8

The joint drift in the inter-panel devices is:

$$d' = 28.5/2.8 = 10.2 \text{ mm}$$

This value is lower than the kinematic maximum capacity $d_{\max}$ = 50 mm of the device.

Step 9

Finally, assuming the upper side limit values for the friction parameters with a global factor ρ equal to 1.6 (see Dal Lago et al. 2017), one obtains an upper bound estimation of the seismic force:

$$F_0 = 1.6 \times 1.5 \times 329 = 790 \text{ kN}$$

This force has to be used to perform the overproportioning by capacity design of the other connections of the structural system.

It is worth noting that the mean of the lower and upper values of the seismic force F_0 roughly corresponds to what actually measured in the test 1/11 reported in Toniolo and Dal Lago 2017.

Assuming q = 10 and n_j = 1, the above calculations can be adjusted as follows:

Step 2 S_d = 0.09 g
Step 3 F = 153 kN
Step 4 With n_j = 1 is V_z = 42.9 kN
Step 5 With M16 bolts Class 8.8 is:

$$N = 79.9 \text{ kN}$$
$$V_{z0} = 0.578 \times 79.9 = 46.2 \text{ kN}$$
$$V_z/V_{z0} = 42.9/46.2 = 0.929$$
$$q_0 = 10 \times 0.929 = 9.3$$
$$F_0 = 153/0.93 = 165 \text{ kN}$$

Step 6 With K_v = 66427 N/mm is: d_e = 165000/66427 = 2.5 mm
Step 7 With $(1 + q_0^2)/2$ = 43.7 the elastic-plastic top displacement is: d = 2.5 × 43.7 = 109 mm

Step 8 The joint drift in the inter-panel devices is:

$$d' = 109/2.8 = 39.1 \quad \text{mm}$$

Step 9 The upper estimation of the seismic force is: $F_0 = 1.6 \times 1.5 \times 165 = 395$ kN

The joint drift is still lower than the kinematic maximum capacity of 50 mm of the device $d_{\max}$. However, in this case the drift of $100 \times 109/7000 = 1.56\%$ is around the yielding limit of the columns ($\approx 1.5\%$), and therefore corresponds to a post-earthquake scenario of moderate structural damage.

These calculations are valid as long as the equal energy criterion can be applied for the evaluation of the elastic-plastic top displacement of the structure.

2.2 Comparative Behaviour

The response obtained by computation for the structure provided with the dissipative friction devices in terms of seismic force and top displacement should be compared with what would be obtained by computation for the same structure without such devices. In this latter case the seismic resisting system is a pure frame without any stiffening contribution of the wall panels attached as they are with an isostatic pendulum connection system.

Firstly, a standard design is performed following the rules of Eurocode 8 (EN 1998-1:2004). With the same data of the presented example, but assuming a translation stiffness of the columns $k_c = c3EI_c/h^3$ calculated with $c = 0.5$ and $I_c = 500^4/12$ ($K_c = n_c k_c$), the natural vibration period of the frame structure is:

$$T = 2\sqrt{\frac{W}{K_c}} = 2\sqrt{\frac{1700}{4783}} = 1.19\text{s}$$

and the corresponding elastic spectral acceleration is:

$$S_e = 0.9g\frac{0.5}{1.19} = 0.378g$$

leading to an elastic force:

$$F_e = 1700 \times 0.378 = 642.8\,\text{kN}$$

The top displacement is:

$$d = 642.8/4.783 = 134\,\text{mm}$$

The reinforcement of the columns could be proportioned so to obtain a design resisting force:

$$F_d = F_e/q$$

where for instance a value $q = 3$ could be assumed for the behavior factor, without changing the expected value of the top displacement of the considered flexible frame

structure (equal displacement range). The flexural strength of the base section of one of the 6 columns 7.0 m high, with F_d = 214.3 kN, should be:

$$M_r = 214.3 \times 7.0 / 6 = 250 \text{ kNm}$$

This standard design, with an over-estimation of the flexural stiffness of the cracked columns, would lead to an under-estimation of the top displacement.

With a more reliable calculation, that allows also a direct comparison with what obtained with the test 0/02 on the bare structure presented in Toniolo and Dal Lago (2017), a value K_c = 2652 N/mm before defined leads to T = 1.60 s with an elastic spectral acceleration S_e = 0.281 g. Therefore, the elastic seismic force is:

$$F_e = 1700 \times 0.281 = 477.7 \text{ kN}$$

and the top displacement is:

$$d = 477.7/2.652 = 180 \text{ mm}$$

with a drift of 100 × 180/7000 = 2.57% sensibly larger than the yielding limit of the columns and corresponding to a post-earthquake scenario of extensive structural damage.

Referring to the actual reinforcement of the tested prototype (8ϕ24 chosen for the general purposes of the experimental program) that gives, with γ_s = 1.0 and with the actual material strength, a resistant moment M_r = 560 kNm, the resisting design force is:

$$F_d = 560 \times 6/7.0 = 480 \text{ kN}$$

as confirmed by the cyclic test 0/04 on the bare frame structure presented in Toniolo and Dal Lago (2017), and it is almost equal to the calculated elastic value. The values obtained by the pseudo-dynamic test 0/02 already quoted gives instead d = 220 mm and F = 460 kN.

The direct comparison gives the following response parameters (force and displacement round figures):

with 2FBDs $q = 5$	329 (to 790)	kN	29	mm	(0.4%)
with 1FBD $q = 10$	165 (to 395)	kN	109	mm	(1.6%)
without FBDs	480	kN	180	mm	(2.6%)

This comparison shows that, at the ultimate limit state of no-collapse, the frame structure of concern without FBDs is affected by large damage, while the same structure has little damage if provided with one FBD per interface and has no damage at all if provided with two FBDs per interface; but this in counterbalanced by a higher force engagement of all the structural connections.

3 Folded Plate Angles

For an ordinary proportioning, the folded plate angles here proposed have an initial phase of elastic behaviour that covers the elastic phase of the columns with which they work in parallel. For large displacements they have a subsequent plastic behaviour that joins the plastic phase of the columns.

It is to be reminded that, with respect to the ordinary steel angles that provide panel-to-column fixed connections leading to a wall resistant system with very high forces, the flexible folded plate angles limit these joint forces to much lower values corresponding to their yielding threshold, preserving in this way the frame behaviour and the integrity of the connections. In the meantime, with respect to an isostatic panel-to-column fastening arrangement, the folded plate angles add their stiffness to the column one, decreasing the structural deformations.

This contribution can be expressed in terms of the top displacement d of the structure and the elastic stiffness k of the single angle. With the kinematic model of Fig. 10, where the actual curved deformation of the column is approximated to a rigid body rotation $\phi = d/h$ and the panel deformation is neglected, assuming n superimposed horizontal panels connected close to the four corners to the adjacent columns, any angle displays a deformation $s = \phi a/2$, of elongation at one side and shortening at the other side, with a corresponding force $f = ks$. So every panel renders to the column a restoring moment $w = fa = kda^2/(2\,h)$. In total from the n panels the restoring moment is nw with a restoring top force:

$$H = \frac{nw}{h} = \frac{1}{2} nk \frac{a^2}{h^2} d = K\,d$$

which doubles if there are panels connected from both sides of the column.

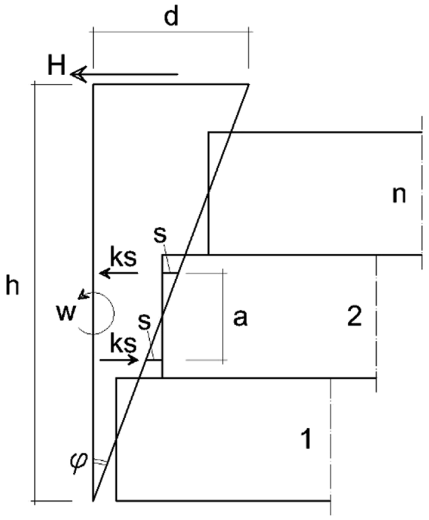

Fig. 10. Approximate kinematic model of the deformed structure

This contribution is to be added to the elastic translation stiffness $k_c = 3EI/h^3$ of the column leading to an increased stiffness. Adding up the increased stiffness of all the columns, one obtains the global stiffness of the structural system with which the first natural vibration period can be computed.

The design calculations can then be performed with reference to the typical procedure for flexible frame structures, where their energy dissipation capacity is not sensibly modified by the contribution of the FPAs.

3.1 Application of the Procedure

In the following an example of such calculation is reported with reference to the same structure considered in 2.1 where the vertical panels are replaced by 8 + 8 horizontal panels 160 × 2100 × 8400 mm. Of the 4 superimposed panels of any span, only the 3 lower ones are connected to the columns ($n = 3$) with the FPAs spaced by $a = 1800$ mm (Fig. 10). The upper one goes over the column height and has an isostatic arrangement of fasteners to the structural elements that doesn't give any stiffening contribution.

The FPA chosen is described in Fig. 11. It is 8 mm thick; it provides a first yielding load of $f_y = 10.2$ kN, a maximum load of $f_{max} = 36.0$ kN for symmetrically opposed coupling and a maximum drift of ±70 mm with an intrinsic initial elastic stiffness for out-of-plane restrained condition $k = 2600$ N/mm (see Dal Lago et al. 2018a).

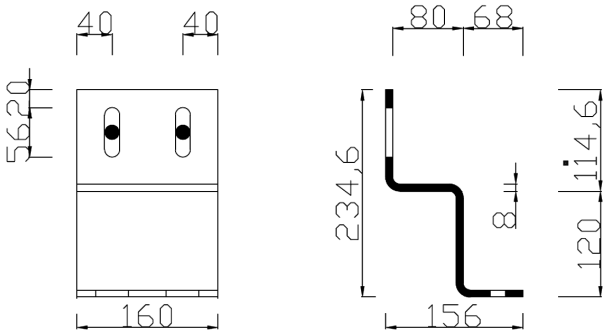

Fig. 11. Details of the FPA

With $a/h = 0.257$, for any restrained column side, one has the following stiffening contribution:

$$K = 3 \times 2600 \times 0.257^2/2 = 257.6\,\text{N/mm}$$

that in total, for the 8 restrained column sides, leads to $K_j = 8 \times 257.6 = 2060$ N/mm. The structural stiffness is:

$$K_v = K_c + K_j = 2652 + 2060 = 4713\,\text{kN/mm}$$

This value is in accordance with the results of test 2/09 of Toniolo and Dal Lago (2017) that shows an elastic stiffness of about 4500 N/mm.

To be noted that the stiffening contribution of the FPDs is of the same magnitude order of that of the columns in cracked elastic phase.

With the same data of the first example, but with a little higher weight W = 1750 kN of the vibrating mass due to the higher weight of the horizontal panels, the natural vibration period of the frame structure is:

$$T = 2\sqrt{\frac{1750}{4713}} = 1.22\,s$$

and the associated elastic acceleration read in correspondence of the abscissa T in the response spectrum is:

$$S_e = 0.9g \times 0.5/1.22 = 0.369\,g$$

that leads to the force:

$$F_e = 0.369 \times 1750 = 645.5 \quad \text{kN}$$

and to the displacement:

$$d = 645500/4713 = 137 \text{ mm}$$

which corresponds to 2.0% of column drift. This displacement would remain the same for any value of chosen *q-factor*. The deformation of the FPA is:

$$s = \frac{1}{2}\frac{a}{h}d = 0.5 \times 0.257 \times 137 = 17.6 \text{ mm}$$

about 4.5 times its yielding limit d_y = 3.9 mm, but still well below the maximum displacement capacity.

With reference to the maximum experimental force measured in test 2.08 as 417 kN, it seems that the dissipation effects of the FPAs, added to the unintended friction effects of the hanging connection system of the panels, can be represented in an approximate way with a force reducing factor of 1.5. This in fact would take the computed force to 645.5/1.5 = 430 kN. A certain unexplained difference remains between the computed and the measured displacements (137 mm against 93 mm).

3.2 Comparative Behaviour

The example above shows that the use of FPAs modifies the behaviour of the frame structure increasing its stiffness without changing relevantly its energy dissipation capacity. It provides a simple and cheap technique to fasten the cladding panels to the frame structure, alternative to the use of sliding connection device, and simple to be applied for the retrofitting of existing structures, avoiding its transformation in a dual

wall-frame system with all the related problems of very high forces and possible connection failures.

The comparison of the main response parameters of the structure (forces and displacements) with and without FPAs, where the latter ones have been calculated in the previous chapter, is shown here under:

with FPAs	430	kN	137	mm	(1.96%)
without FPAs	480	kN	180	mm	(2.57%)

4 Conclusions

Innovative technological solutions for dissipative panel connections have been proposed within the European research project Safecladding. For precast structures with such dissipative connections the seismic design should be made with proper nonlinear time-history dynamic analyses under prescribed ground motions. Nevertheless, this approach is computationally expensive and not handy in engineering practice. As an alternative, the linear methods of seismic analysis could be still applied if proper values of the behaviour factor are estimated on the basis of proper criteria formulated on the safe side.

Based on the large ductility and dissipation capacity experimentally measured for this type of systems, in this paper it is suggested to adopt the behaviour factor of concrete frames, provided the displacement capacities of the dissipative devices are fulfilled. In particular, this simplified procedure has been described for a type of friction-based dissipative device (FBD) to be used mainly in vertical panels. Guidelines are provided also for a type of folded plate angle (FPA), that can provide plastic dissipation of energy, to be used for the connections of horizontal panels.

Acknowledgements. This research work has been funded mainly by the European Commission within the FP7-SME-2011 SAFECLADDING research project (Grant agreement No. 314122, 2012), and partially by the Italian Department of Civil Protection (DPC) and the Italian Laboratories University Network of Earthquake Engineering (ReLUIS) within the research program DPC-ReLUIS 2014–2016. The financial supports of the funding institutions are gratefully acknowledged.

References

Belleri A (2017) Displacement based design for precast concrete frames with not-emulative connections. Eng Struct 141:228–240

Biondini F, Dal Lago B, Toniolo G (2013) Role of wall panel connections on the seismic performance of precast structures. Bull Earthq Eng 11(4):1061–1081

Colombo A, Negro P, Toniolo G (2014) The influence of classings on the seismic response of precast structures: the Safecladding project. In: Proceedings of the 2nd European Conference on Earthquake Engineering and Seismology, Istanbul, Turkey, 25–29 August, Paper No. 1877

Dal Lago B, Biondini F, Toniolo G (2017) Friction based dissipative devices for precast concrete panels. Eng Struct 147:356–371

Dal Lago B, Biondini F, Toniolo G (2018a) Experimental investigation on steel W-shaped folded plate dissipative connectors for precast cladding panels. J Earthquake Eng 22(5):778–800

Dal Lago B, Biondini F, Toniolo G (2018b) Seismic performance of precast concrete structures with energy dissipating cladding panel connection systems. Struct Concr 19:1908–1926

Dal Lago B, Molina FJ (2018) Assessment of a capacity spectrum design approach against cyclic and seismic experiments on full-scale precast RC structures. Earthq Eng Struct Dynam 47 (7):1591–1609

EN 1993-1-8:2004 Eurocode 3: Design of steel structures. Part 1-8: Design of joints. European Committee for Standardization, Brussels, Belgium

EN 1998-1:2004 Eurocode 8: Design of structures for earthquake resistance. Part 1: General rules, seismic actions and rules for buildings. European Committee for Standardization, Brussels, Belgium

EUR 27934 EN (2016) Design guidelines for precast structures with cladding panels. Publications Office of the European Union, Colombo A, Negro P, Toniolo G, Lamperti Tornaghi M (eds)

EUR 27935 EN (2016) Design guidelines for wall panel connections. Publications Office of the European Union, Colombo A, Negro P, Toniolo G, Lamperti Tornaghi M (eds)

Ferrara L, Felicetti R, Toniolo G, Zenti C (2011) Friction dissipative devices for cladding panels in precast buildings. Eur J Environ Civ Eng 15(9):1319–1338

Negro P, Lamperti Tornaghi M (2017) Seismic response of precast structures with vertical cladding panels: the SAFECLADDING experimental campaign. Eng Struct 132:205–228

Toniolo G, Dal Lago B (2017) Conceptual design and full-scale experimentation of cladding panel connection systems of precast buildings. Earthq Eng Struct Dynam 46(14):2565–2586

The Effect of Infill Walls on the Structural Identification of an Existing RC Frame Building

A. De Angelis(✉) and M. R. Pecce

Department of Engineering, University of Sannio, Benevento, Italy
adeangelis@unisannio.it

Abstract. A large number of Reinforced Concrete (RC) frames buildings containing unreinforced masonry infill walls are commonly used in structural system around the world. Earthquakes revealed that the performance of this type of buildings can be significantly affected by infill walls according their type and distribution in plane and along the height. The paper describes the experimental and analytical modal analysis of an existing RC framed building underling the influence of infill walls and partitions. An ambient vibration test was carried out and analysed by OMA; a 3D finite element model, comprehensive of infill walls and partitions, was successfully updated manually based on the in-situ test global modes. The progressive introduction of the infill walls and partitions, with the updating of their characteristics, allowed to demonstrate their essential effect on the elastic dynamic response of the structure and the necessity of their modelling to attain a reliable structural identification and model assessment.

Keywords: Infill walls · Structural identification · Model updating

1 Introduction

Recent earthquakes have revealed how the presence of infill walls in Reinforced Concrete (RC) buildings may significantly affect the seismic performance of buildings, both in terms of seismic demand and capacity. In particular, it was observed that the presence of correctly distributed infill elements can mitigate horizontal displacements and increase the overall resistance to horizontal actions. Conversely many existing RC buildings consist of structures designed prior to the enactment of current seismic design procedures, and therefore they consist of gravity-load-designed frames considering unreinforced masonry infill walls as nonstructural components.

Alternately, an uneven distribution in the plane and elevation of infill walls might lead to negative effects, such as a torsional mode shape in the plane and the soft storey mechanism.

Moreover, infill walls are vulnerable to damage during a seismic event because of intrinsic weak material properties or due to an ineffective link with the frame. The loss of exterior and interior infill walls has serious implications not only for life safety but also for the functionality of the building. Additionally, the loss of infill walls changes

M. di Prisco and M. Menegotto (Eds.): ICD 2018, LNCE 42, pp. 56–68, 2020.
https://doi.org/10.1007/978-3-030-23748-6_5

the dynamic behaviour of the building in terms of stiffness, natural frequency, damping and overall structural behaviour.

In the last five decades, many research studies have been carried out concerning the influence of infill walls on the behaviour of framed structures, individuating a huge number of parameters influencing the global coupled behaviour. In the case of existing structures, many of those parameters are difficult to measure in real situations, for example, the mechanical properties of masonry, which are strongly affected by the scatter of bricks, mortar characteristics, building techniques adopted by workers, details around the openings, and efficiency of the connection to the structures.

Therefore, because it is clear that infill walls have a role in the seismic response of frame structures, it is important to identify the actual structural behaviour of a building by taking into account the infills' contribution.

In this paper, the results of the structural identification of a case study of a framed RC building taking into account the infill walls and the internal partitions are reported as a first step of the procedure for assessing a reliable model of the building.

Other studies have already been developed on this topic (Ventura et al. 2002; Demetriu and Aldea 2012), but in few cases the internal partitions have been considered (Butt and Omenzetter 2014), as well as examining the single contribution of the perimetral and internal walls via a step-by-step updating. Even the details of the locations of the walls within the RC frames (the thickness restrained by the frame) are considered, and the in-plane deformability of the floor is introduced due to the relative high transversal stiffness of the building given by the walls.

1.1 The Case Study

The analysis case is a building located in Benevento (Campania, Southern Italy) designed in the early '60s according to old approaches and code provisions.

The building has a semi-basement, a ground floor and 2 storeys; the main in-plan dimensions are approximately Lx = 14.10 m and Ly = 44.10 m, and the inter-storey height is 4.00 m for the semi-basement and 3.80 m for the other storeys. The structure is made of RC frames; in particular, there are 3 longitudinal frames (NW-SE direction), each with 12 equal bays of 4.70 m in span and only 4 transversal frames (NE-SW direction) with 3 unequal bays of 5.40 m, 3.40 m and 4.80 m. In Fig. 1, the structural plan of the first floor of the building is drawn.

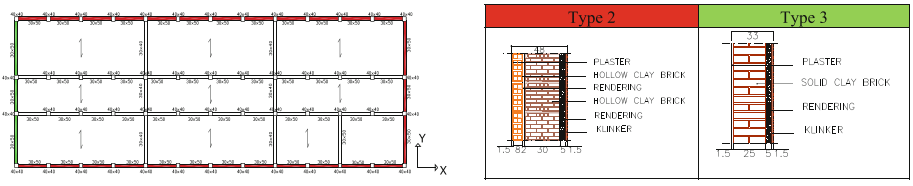

Fig. 1. The structural plan of the first floor of the building.

The structure was designed to bear only gravity loads by the longitudinal frames (NW-SE direction). Two frames in the transversal direction (NE-SW) are located at the ends of the buildings (external frames), and the other 2 divide the plan into 3 parts. The columns have a square cross-section with variable dimensions along the height at each floor; in particular, at the semi-basement floor, the columns have a square cross-section of 50 cm × 50 cm, and at the ground floor, first floor and second floor, the column sections have dimensions of 40 cm × 40 cm, 35 cm × 35 cm and 30 cm × 30 cm, respectively. In the longitudinal direction (NW-SE), the beams are 30 cm wide and 50 cm high; along the transversal direction (NE-SW), they are 30 cm × 35 cm at the second floor and 30 × 40 cm at the other floors, with the exception of the two extreme beams, whose cross-section dimensions are 30 cm × 50 cm at all levels. The floors are made of cast-in-place RC and hollow clay bricks for lightening, for a total height of 22 cm and an RC slab of 4 cm.

It should be remarked that a complete and reliable prediction of the structural response can be obtained only if the structural parameters of the infill walls and reinforced concrete frames are introduced based on in situ investigation and tests.

The original design is not available, and therefore an adequate investigation was carried out to identify the geometry and the reinforcement of all structural elements. Destructive and non-destructive tests were carried out to evaluate material mechanical properties and reinforcement details. To evaluate the compressive strength of concrete, 7 cores were extracted and 28 SonReb tests were conducted, obtaining a mean value of 15.4 MPa.

Regarding the steel reinforcement, some specimens were extracted by the structural elements, obtaining an average yielding strength of 299 MPa, and some essays were carried out to identify the structural detailing of the members, such as longitudinal and transverse reinforcement.

Regarding the infill walls and partitions, some essays were carried out specifically to determine the internal geometry and the characteristics of materials (bricks, hollow bricks, concrete blocks, etc.). The infill walls and partitions were grouped into categories to limit the number of essays according to the result of a preliminary thermographic study, with an essay for each category. Six different typologies of walls were identified in the structure, comprising solid block infill walls, hollow clay brick infill walls and double-leaf infill walls, as reported in Table 1.

1.2 The Dynamic Test

The aim of the dynamic test was to determine the dynamic characteristics of the case study building through AVT (Ambient Vibration Test). The dynamic in situ test was commissioned by the University Administration and was performed by the S2X company, which also carried out the data processing with software developed in the LabView Environment (Rainieri 2008; Rainieri and Fabbrocino 2015).

The roof, second, first and ground levels were instrumented in two corners with two monoaxial accelerometers measuring in two orthogonal directions (along the transverse direction, NE-SW, and the longitudinal direction, NW-SE) to capture the translational and torsional modes of the building.

Table 1. Description of the infill typologies detected

Type	Thickness [cm]	Layers (from the inward to the outward)
1	38	Plaster (1.5 cm); Hollow clay brick (30 cm); Rendering (5 cm); Klinker (1.5 cm)
2	48	Plaster (1.5 cm); Hollow clay brick (8 cm); Rendering (2 cm); Hollow clay brick (30 cm); Rendering (5 cm); Klinker (1.5 cm)
3	33	Plaster (1.5 cm); Solid clay brick (25 cm); Rendering (5 cm); Klinker (1.5 cm)
4	36	Plaster (1.5 cm); Hollow clay brick (12 cm); Air gap (4 cm); Solid clay brick (12 cm); Rendering (5 cm); Klinker (1.5 cm)
5	33	Plaster (1.5 cm); Hollow clay brick (30 cm); Plaster (1.5 cm)
6	33	Plaster (1.5 cm); Hollow clay brick (25 cm); Rendering (5 cm); Klinker (1.5 cm)

The sensors' locations and orientations are indicated by the red arrows in Fig. 2; however, because the roof floor was inaccessible for measurements, the sensors at that level (#1, #2, #3, #4) were fixed at the soffit of its floor. To evaluate the in-plane behaviour of the floor (rigid or flexible floor), pairs of sensors were added in the centre of the first (#15, #16) and second levels (#9, #10). The measurement equipment for the AVT consisted of 20 uniaxial piezoelectric accelerometers, which were mounted on levelled base plates to ensure accurate alignment. Data acquisition was carried out using a 24-bit modular acquisition system type Compact DAQ_1 with 32 channels, which was controlled by a laptop PC. The piezoelectric accelerometers are a type of commonly used uniaxial sensor that is characterized by high sensitivity and low background noise.

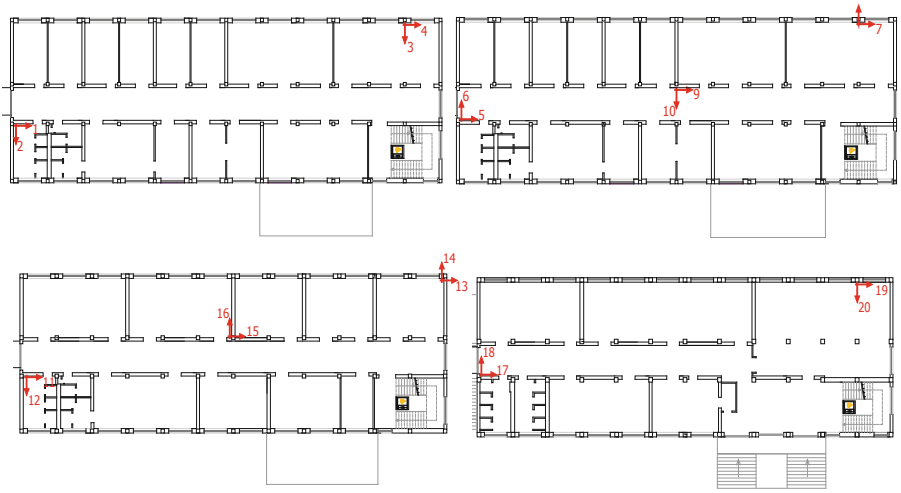

Fig. 2. The set-up at each level.

In Fig. 3, the graphical representations of the first three global mode shapes (with the deformed configurations in red) are shown; the first mode is translational in the transversal direction (NE-SW); the second mode is torsional, while the third one is translational in the longitudinal direction (NW-SE) coupled with torsion. The higher modes are local and associated with independent movements of the individual alignments of frames, perhaps due to the deformability of the floors in its plane.

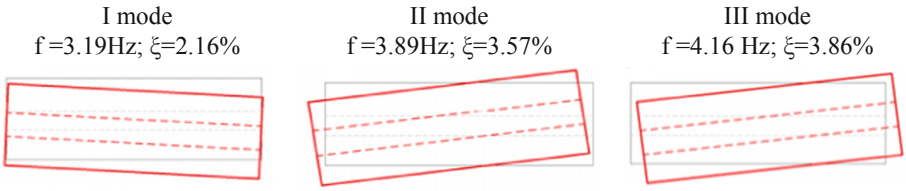

Fig. 3. Graphic representation of the experimental mode shapes.

2 The Structural Identification of the Case Study Building

The structural identification through dynamic in situ tests requires the development of an adequate numerical model that has to be updated considering the most important parameters governing the behaviour of the construction. Additionally, the role of infill walls and partitions on the dynamic response of an RC framed structure is examined in detail to calibrate the FE model of the building. To achieve this aim, the complete FE model of the case study was developed according to the following key steps:

1. The FE model of the RC structure (beams, columns and shear walls) was implemented.
2. The macroupdating of this model was progressively developed, including the nonstructural elements (infill walls and partitions), to understand their effects on the global dynamic behaviour of the structure.
3. A process of microupdating was carried out whereby the properties of the structural and nonstructural elements were adjusted systematically to obtain the best possible match with the measured modal properties.

2.1 Finite Element Models

Three FE models with different levels of sophistication were implemented to simulate the actual building using the software SAP2000 (CSI 2016):

(1) the bare 3D frame model with in-plane rigid floors (Model 1);
(2) the 3D frame model with infill walls and partitions and rigid floors (Model 2);
(3) the 3D frame model with infill walls and partitions and flexible floors (Model 3).

Even though the building's floor diaphragms play a critical role in distributing the horizontal actions among the resistant vertical elements, it is a common practice in the numerical simulation of buildings to model the floor diaphragms as a rigid horizontal plate

to reduce the computational efforts. However, this simplification may cause errors in the analyses when the building has a special shape, such as a long, narrow rectangular floor plan with a large length/width aspect ratio, which is the case of the considered building structure (Jain and Jennings 1985; Pan et al. 2006). In the first step, regarding the bare frame model, columns and beams were modelled by beam elements, while RC walls were modelled by shell elements. For the RC elements, an elastic modulus of 25000 N/mm^2, based on the results of the in situ characterizations, and a mass density of 2400 kg/m^3 were assumed. The floors were assumed to be rigid in their plane; the foundation was excluded from the model, and the structural elements were fully restrained. Figure 4(a) shows the 3D view of the model. The masses were directly associated with the structural elements according to the density and geometric dimensions; a uniform area mass was assigned to the floors according to their weight. For the self-weight of the infill walls and partitions, a linear load was applied. No live loads were applied, in accordance with the current state of the structure during the dynamic test. To introduce the infill walls and partitions in the linear model, diagonal struts were adopted. The elastic lateral stiffness of the panel was evaluated according to Eq. (1) (Dolsek and Fajfar 2008),

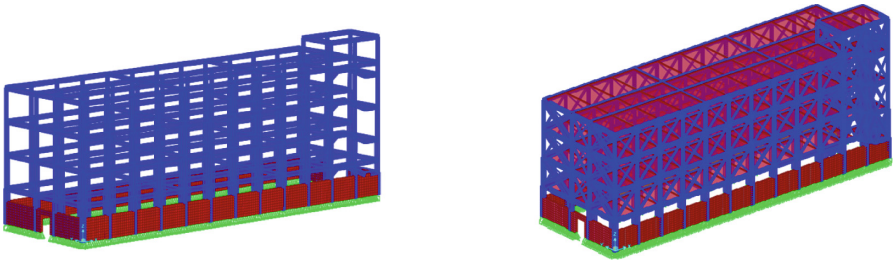

a) b)

Fig. 4. (a) The bare frame model; (b) the infilled frame model.

$$K_i = \frac{G_m \cdot L_w \cdot t_w}{H_w} \tag{1}$$

where G_m is the shear modulus of the wall, assumed equal to 0.4 E_m; L_w and H_w and t_w are the length, height and thickness of the panel, respectively. The thickness of each strut coincides with that of the correspondent masonry panel, and the length is equal to the diagonal of the panel. The influence of openings such as doors or windows was taken into account by using the factor λ proposed by Asteris *et al.* (2011), as a function of the opening percentage (opening area/infill wall area) according to Eq. (2),

$$\lambda = 1 - 2 \cdot \alpha_w^{0.54} + \alpha_w^{1.14} \tag{2}$$

in which α_w is the infill wall opening percentage (area of the opening to the area of the infill wall).

2.2 Macroupdating of the Model

The main objectives of a first macro-updating are the evaluation of the influence of nonstructural components, such as infill walls and partitions, on the dynamic behaviour of the structure and the assessment of the sensitivity to the in-plane flexibility of the floors.

Therefore, the following series of finite element models were considered:

- Stage I: three-dimensional bare frame model (Model 1) with rigid floors;
- Stage II: only the external infill walls were modelled using diagonal struts (Model 2.1), while for the unreinforced masonry partition walls, only the self-weight was taken into account;
- Stage III: The partition walls were added to the model using diagonal struts (Model 2.2). In this stage, the wall thickness was assumed to be equal to the entire depth of the walls;
- Stage IV: The thickness of the partition walls partially external to the frames was assumed to be equal to the depth restrained by the columns, and they were modelled using diagonal struts (Model 2.3);
- Stage V: The assumption of rigid floors was relaxed, and the floor slabs were modelled by shell elements to consider three different values of the equivalent thickness.

In stage I, the 3D bare frame model was analysed; the fundamental mode is in the transversal direction with a frequency of 0.95 Hz, followed by the torsional mode and translational mode in the longitudinal direction with frequencies of 1.25 Hz and 1.80 Hz, respectively.

The correlation between the experimental and numerical modes was investigated by comparing natural frequencies and MAC values, as shown in Table 2. The comparison between natural frequencies revealed the higher trend for numerical frequencies than for experimental ones. The differences for the first transverse, torsional and longitudinal modes are −70.2%, 67.4% and 56.7%, respectively, which are too approximate. The modal assurance criterion (MAC) values show a poor correlation between mode shapes, with the lowest value being 35.9% for the third mode.

Table 2. Comparison between experimental and numerical modes (Model 1).

Experimental		Numerical		Δf [%]	MAC [%]
Mode shape	f [Hz]	Mode shape	f [Hz]		
Transv.	3.19	Transv.	0.95	–70.2	72.4
Torsional	3.89	Torsional	1.26	–67.4	69.6
Longit. + torsional	4.16	Longit.	1.80	–56.7	35.9

Moreover, it can be observed that the FE model has lower natural frequencies, and hence the real structure is stiffer or the mass is lower. Therefore, it is necessary to consider the potential contribution of nonstructural elements to the stiffness of the structure. Thus, in stage II, at first only the external infill walls were modelled, while for the non-modelled partition walls, only the self-weight was taken into account as in the bare framed model; thus, a Model 2.1 with external infill walls modelled as diagonal struts was developed.

The first three mode frequencies are 2.73 Hz, 3.51 Hz and 4.39 Hz. The infill walls increased the model frequencies dramatically. For example, the first transversal mode frequency was increased from 0.95 Hz to 2.73 Hz, accounting for an increment of 188%, in agreement with the studies available in the literature (Oliveira and Navarro 2009); furthermore, the second mode was shifted from the torsional mode to the longitudinal mode, and the torsional mode appears only as the third mode of the model. The correlation between the natural frequencies of Model 2.1 and the experimental frequencies of the building is generally much better than the bare frame model. As shown in Table 3, the maximum difference of the first three mode frequencies is only 14.4%. However, there is a poor correlation for the fundamental mode (1st transverse mode), while for the other modes, it is not possible to evaluate the correlation since the modes are not matched.

Table 3. Comparison between experimental and numerical modes (Model 2.1).

Experimental		Numerical		Δf [%]	MAC [%]
Mode shape	f [Hz]	Mode shape	f [Hz]		
Transv.	3.19	Transv.	2.73	–14.4	34
Torsional	3.89	Longit.	3.51	–9.7	–
Longit. + torsional	4.16	Torsional.	4.39	–5.5	–

To better capture the mode shapes, in stage III, the partition walls, modelled as diagonal struts, were also added (Model 2.2). The correlation between the natural frequencies of Model 2.2 and the experimental frequencies of the building is shown in Table 4. It can be noted that the inclusion of the partition walls restores the sequence of the captured global modes and modifies the frequency by 15%, which is not negligible, conversely to the common idea of the negligible effect of internal partitions. Moreover, the correlation of the model with the experimental results is still not acceptable.

Table 4. Comparison between experimental and numerical modes (Model 2.2).

Experimental		Numerical		Δf [%]	MAC [%]
Mode shape	f [Hz]	Mode shape	f [Hz]		
Transv.	3.19	Transv.	3.43	7.4	30
Torsional	3.89	Torsional	4.50	15.7	25
Longit. + torsional	4.16	Longit.	5.35	28.6	25

Observing the architectural and structural drawing (see Fig. 5), it can be noted that many internal walls are partially offset from the main columns lines, and so they can partially contribute to the stiffness of the structure. Therefore, at stage IV, in Model 2.3, their thickness was taken as 0.19 m, which is the thickness restrained by the columns. The fundamental mode is in the transversal direction with a frequency of 3.41 Hz. It is followed by the torsional mode and translational mode in the longitudinal direction with frequencies of 4.48 Hz and 4.99 Hz, respectively. As reported in Table 5, the differences for the first transverse, torsional and longitudinal modes are 6.8%, 15.1% and 19.9%, respectively. The modal assurance criterion (MAC) values still show a poor correlation between mode shapes, with the lowest value being 28% for the second mode.

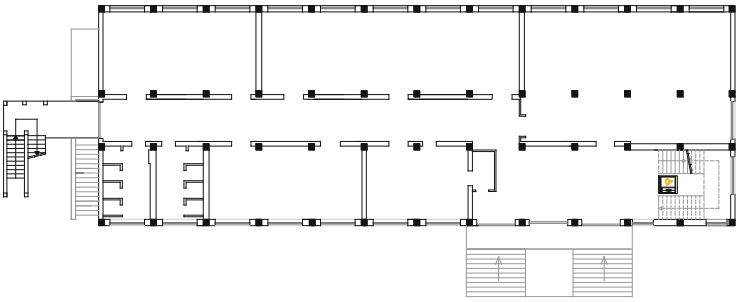

Fig. 5. Architectural drawing of the ground floor.

However, all experimental modes show diaphragm deformation. Thus, at the final stage V, to improve the model, the assumption of a rigid diaphragm is relaxed, and the floor slabs are added explicitly to the model using shell elements with a thickness equal to 100 mm (Model 3). The first three natural frequencies are 3.25 Hz, 4.37 Hz, and 4.83 Hz; they are associated with the mode shapes in the transversal, torsional and longitudinal direction coupled with torsional, respectively, which are now consistent with the experimental results. The matching of the natural frequencies between Model 3 and the experimental results is quite good (see Table 6). The introduction of a bi-dimensional in-plane model of the floors, able to take into account the flexibility of the floors, affects the fourth and fifth modes of the building. Alternately, the first three modes of the model, where the floors behave rigidly, are less affected by this model modification; their frequencies decreased only slightly: 4.7% for mode 1, 2.5% for mode 2 and 3.2% for mode 3.

2.3 Microupdating of the Model

The microupdating (i.e., changing of properties of the already included structural and nonstructural elements) was carried out in two main steps. First, a sensitivity analysis (Maia and Silva 1997) was carried out to examine in detail the effects of the various uncertain parameters on the numerical modes; then, the identified parameters were used to guide the further manual updating of the model.

Table 5. Comparison between experimental and numerical modes (Model 2.3).

Experimental		Numerical		Δf [%]	MAC [%]
Mode shape	f [Hz]	Mode shape	f [Hz]		
Transv.	3.19	Transv.	3.41	6.8	30
Torsional	3.89	Torsional	4.48	15.1	28
Longit. + torsional	4.16	Longit.	4.99	19.9	31

Table 6. Comparison between experimental and numerical modes (Model 3).

Experimental		Numerical		Δf [%]	MAC [%]
Mode shape	f [Hz]	Mode shape	f [Hz]		
Transv.	3.19	Transv.	3.13	–1.77	36
Torsional	3.89	Torsional	4.16	6.88	34
Longit. + torsional	4.16	Longit.	4.47	7.39	32

2.3.1 Sensitivity Analysis

In the case study, the following six key parameters were considered: the elastic modulus "E_{cls}" and the mass density "ρ_{cls}" of the structural elements, i.e., beams, columns and shear walls; the elastic modulus "E_{infill}" and the mass density "ρ_{infill}" of the infill walls and partitions; and the equivalent thickness "t_{floor}" and the dead loads "W_{floor}" of the floor.

The sensitivity analysis was carried out to compute the sensitivity coefficients (in percentage) of the various parameters that represent the ratio between the percentage change in the modal parameter $\Delta R_i^{num}/R_i^{num}$ and the percentage change of the parameter $\Delta X_i/X_i$ as reported in Eq. (3).

$$S_{i,j} = 100 \times \frac{\Delta R_i^{num}}{R_i^{num}} \Big/ \frac{\Delta X_i}{X_i} \tag{3}$$

In sensitivity analyses, only one parameter was varied at a time, and the others were kept constant with the same value assumed in the starting FE model; a step variation of 1% was assigned for each variable. The target responses, which were investigated in this sensibility analysis, were the first three natural frequencies and mode shapes of the global modes.

The computed sensitivity coefficients against the selected structural parameters and modal responses (frequencies and MAC Values) of the first three modes are reported in Table 7. It was found that the elastic modulus of the RC elements (beams, columns, and shear walls) affects all the frequencies of the target modes in the same direction with $S_{i,j}$ of 24–30%. Regarding the mode shape (i.e., the MAC value), the highest sensitivity of 32% was obtained with the second mode (i.e., the torsional mode). Instead, the second and third modes (i.e., the torsional and longitudinal + torsional modes) are most sensitive to the elastic modulus of the masonry walls with an $S_{i,j}$ of

22–26%. For the mode shapes, the sensitivity coefficients have the same values obtained for the elastic modulus of the RC elements but with the opposite effect.

Table 7. Sensitivity coefficients

	Mode 1		Mode 2		Mode 3	
Parameter	Frequency	MAC value	Frequency	MAC value	Frequency	MAC value
E_{cls}	30.23	13.75	27.46	32.29	23.84	28.43
ρ_{cls}	−11.11	1.25	−11.93	−2.05	−11.05	−15.05
E_{infill}	19.55	−13.65	22.36	−32.16	25.99	−28.27
ρ_{infill}	−14.20	−35.04	−15.72	22.71	1.79	−48.97
t_{floor}	6.49	0.35	3.46	4.47	3.03	5.75
W_{floor}	−19.87	−37.64	−18.14	18.69	−19.41	−6.62

2.3.2 Manual Updating

The manual tuning involves manual changes of the model geometry and mechanical characteristics by trial and error, guided by engineering judgement. The aim of this procedure is to bring the numerical model closer to the experimental results.

The starting model for the manual updating is Model 3. The key parameters, already introduced and discussed in the previous sensitivity analysis, were manually adjusted to obtain a good correlation with the test results; the starting and updated values of all the parameters are presented in Table 8.

The correlation between the final updated FE model and the test results are shown in Table 9; as seen, all three relevant natural frequencies are matched within 5%, and the high MAC values of 88% or more show a good correlation between experimental and numerical mode shapes. This yielded high confidence in the final updated FE model and its ability to give insight into appropriate parameters for modelling the building comprehensive of nonstructural elements.

3 Conclusions

In the case of existing structures, especially for RC framed constructions designed for vertical loads, an efficient procedure to estimate the effect of infill walls is to realize a dynamic test coupled with a structural identification by the updating of a numerical model, which can take into account the infill walls and partitions. The analysis of ambient vibration measurements conducted on the proposed case study allowed for calibration of a numerical model confirming the importance of the infill walls and partitions. In particular, the following results can be summarized:

– the contribution of the nonstructural walls to the lateral stiffness of the building in the elastic field can be up to 3 times that of the bare framed structure, especially for this type of building designed for gravity loads that have slender columns with

respect to the case of seismic design and have frames only in one of the two principal directions;
- also, internal partitions can be important for the thickness constrained between frames; furthermore, the structural response is influenced by their location within the RC frames (i.e., the restrained thickness);
- the stiffening effect of the nonstructural walls make the floor flexible, giving an error when the hypothesis of rigid floor is assumed.

Table 8. Variation of key parameters in the FE model.

Parameters updated	Starting values	Updated values	Change [%]
E_{cls} [MPa]	25000	25500	2.00
ρ_{cls} [kg/m^3]	2.40	2.24	−6.77
t_{floor} [m]	0.10	0.09	−10.00
W_{floor} [kN/m^2]	4.7	3.1	−34.04
$E_{infill\ (type\ 1)}$ [MPa]	2600	1200	−53.85
$E_{infill\ (type\ 2)}$ [MPa]	2263	1137	−49.76
$E_{infill\ (type\ 3)}$ [MPa]	5000	3800	−24.00
$E_{infill\ (type\ 4)}$ [MPa]	3000	2300	−23.33
$E_{infill\ (type\ 5)}$ [MPa]	2600	1200	−53.85
$E_{infill\ (type\ 6)}$ [MPa]	4000	2000	−50.00
$E_{infill\ (type\ 7)}$ [MPa]	2600	1200	−53.85
$\rho_{infill\ (type\ 1)}$ [kg/m^3]	0.88	1.06	20.46
$\rho_{infill\ (type\ 2)}$ [kg/m^3]	0.88	1.07	21.25
$\rho_{infill\ (type\ 3)}$ [kg/m^3]	1.55	1.55	0.26
$\rho_{infill\ (type\ 4)}$ [kg/m^3]	1.00	1.13	12.75
$\rho_{infill\ (type\ 5)}$ [kg/m^3]	0.80	1.00	25.64
$\rho_{infill\ (type\ 6)}$ [kg/m^3]	0.86	1.06	23.81
$\rho_{infill\ (type\ 7)}$ [kg/m^3]	1.36	1.67	23.31

Table 9. Comparison between experimental and updated numerical modes.

Experimental		Numerical		Δf [%]	MAC [%]
Mode shape	f [Hz]	Mode shape	f [Hz]		
Transv.	3.19	Transv.	3.03	−4.94	97
Torsional	3.89	Torsional	4.09	5.07	91
Longit. + torsional	4.16	Longit.	4.14	−0.51	88

The next step of this research is to improve the calibrated model with nonlinear modelling of the RC frames and masonry walls to study the behaviour of the building under a severe earthquake to check the role of the walls on the structure response and also the safety of these elements, confirming the importance of each step of the structural identification and modelling updating.

Acknowledgements. The authors gratefully would like to thank the financial support from the Project Smartcase, MIUR - Italian Ministry of Education, Universities and Research, Managerial Decree n.789 06/03/2014 (ID Number of the Project PON03PE_00093_1).

References

Asteris PG, Antoniou ST, Sophianopoulos DS, Chrysostomou CZ (2011) Mathematical macromodeling of infilled frame: state of art. J Struct Eng 137(12):1508–1517

Butt F, Omenzetter P (2014) Seismic response trends evaluation and finite element model calibration of an instrumented RC building considering soil-structure interaction and non-structural components. Eng Struct 65:111–123. https://doi.org/10.1016/j.engstruct.2014.01.045

Computers and Structures (2016) SAP2000 version 18. Walnut Creek, CA

Demetriu S, Aldea A (2012) Modal parameters of RC frame structure identified from ambient vibration measurements. In: 15th WCEE, Lisboa

Dolsek M, Fajfar P (2008) The effect of masonry infills on the seismic response of a four-storey reinforced concrete frame—a deterministic assessment. Eng Struct 30(7):1991–2001

Jain SK, Jennings PC (1985) Analytical models for low-rise buildings with flexible floor diaphragms. Earthquake Eng Struct Dynam 13:225–241

Maia NMM, Silva JMM (1997) Theoretical and experimental modal analysis. Research Studies Press, Taunton

Oliveira CS, Navarro M (2009) Fundamental periods of vibration of RC buildings in Portugal from in-situ experimental and numerical techniques. Bull Earthq Eng 8(3)

Pan T-C, Xuting You X, Brownjohn JMW (2006) Effects of infill walls and floor diaphragms on the dynamic characteristics of a narrow-rectangle building. Earthquake Eng Struct Dynam 2006(35):637–651

Rainieri C, Fabbrocino G (2015) Development and validation of an automated operational modal analysis algorithm for vibration-based monitoring and tensile load estimation. Mech Syst Sig Process 60–61:512–534

Rainieri C (2008) Operational modal analysis for seismic protection of structures. PhD thesis, University of Naples, Naples, Italy

Ventura CE, Lord JF, Simpson R (2002) Effective use of ambient vibration measurements for modal updating of a 48 storey building in Vancouver. In: Proceedings of the 3rd international conference on structural dynamics modelling - test, analysis, correlation and validation, Portugal

Influence of the Modelling Approach on the Failure Modes of RC Infilled Frames Under Seismic Actions

G. Blasi[1(✉)], D. Perrone[2], and M. A. Aiello[1]

[1] Department of Innovation for Engineering, University of Salento, Lecce, Italy
gianni.blasi@unisalento.it
[2] University School for Advanced Studies IUSS Pavia, Pavia, Italy

Abstract. The influence of the masonry infills on the seismic performances of Reinforced Concrete (RC) frames is generally evaluated in analytical and numerical studies by adopting the equivalent strut model; it is based on experimental observations showing that at the onset of damage, stresses migrate to the diagonal of the panel and are transferred to the surrounding frame through the contact zones at the corners. Above the different equivalent strut models available in literature, single-strut models are generally used to evaluate the global behaviour, while multi-strut approaches are preferred to investigate on local interaction phenomena between panel and frame. In case of existing buildings, with poor transversal reinforcement of the columns, the presence of the infills can lead to pre-emptive brittle failure. The present study is aimed at evaluating the influence of the modelling approach on the evaluation of the seismic performance both in terms of global and local behaviour. Nonlinear dynamic analyses have been performed on an 8-storey infilled RC frame, following the Incremental Dynamic Analysis procedure, in order to evaluate structural performances depending on the model adopted to simulate the infills.

Keywords: Equivalent strut · Infilled frames · Brittle failure of columns

1 Introduction

The investigation on local interaction between the infill panel and the surrounding frame is fundamental in the performance analysis of existing reinforced concrete (RC) buildings. In fact, post-earthquake loss estimations show how the infills significantly affect structural performances (Ricci et al. 2011). Despite the presence of the panel significantly increases the global strength and stiffness of the structure (Dolšek and Fajfar 2008; Gallipoli et al. 2009; Perrone et al. 2016) the local interaction between the panel and the column can lead to brittle failure of the latter in case of poor transversal reinforcement (Verderame et al. 2016).

Numerical analysis of RC frames conducted in the literature, generally adopt simplified models to simulate the behaviour of the infills (Jeon et al. 2015; Perrone et al. 2017). The numerical models developed by many researchers during last decades are based on experimental observations (Mehrabi et al. 1996) showing that by increasing the lateral load magnitude, stresses distribution in the panel migrate to the

M. di Prisco and M. Menegotto (Eds.): ICD 2018, LNCE 42, pp. 69–81, 2020.
https://doi.org/10.1007/978-3-030-23748-6_6

diagonal region. The equivalent truss macro-model, has been introduced by Polyakov (1960), and is nowadays the most adopted in numerical and analytical studies. Depending on the number of trusses simulating the panel, different model were developed to investigate on specific phenomena characterizing the behaviour of infilled RC frames (Chrysostomou et al. 2002; Crisafulli and Carr 2007; Rodrigues et al. 2008).

The single-strut model is generally preferred in global analyses (Kose 2009; Perrone et al. 2017), due to its simplicity and the reduction of the numerical efforts with respect to the multi-strut approach, the latter being most appropriate to investigate on local interaction between the panel and the surrounding frame (Asteris et al. 2011; Burton and Deierlein 2013; Verderame et al. 2011).

The parametric analysis conducted in the present study is aimed at evaluating the influence of the mechanical properties of masonry infills, on the failure modes of RC frames designed for gravity loads; in order to investigate both on global and local behaviour the multi-strut approach has been adopted in this study. Since the main parameter influencing the shear transferred to the column by the panel is the shear strength of the masonry, four different values of shear strength have been considered in the analysis, in accordance with the properties of the masonry panels characterizing Mediterranean regions. A numerical model of a gravity load designed RC infilled frame was developed and Incremental Dynamic Analysis (Vamvatsikos and Cornell 2001) was performed. IDA curves obtained show that the global performances of existing structures can significantly vary, depending on the shear strength of the infills influencing the failure modes of the columns.

2 Numerical Modelling of 8-Storey Infilled Frame

According to the 14th census ISTAT (2001), most of Italian existing buildings have been built before the introduction of seismic prescriptions in building codes. In existing buildings, only gravity loads were usually considered for the design of the columns, which consequently are characterized by poor transversal reinforcement; this feature often encourages brittle failure mechanisms due to the low shear strength of columns, particularly in the case of local interaction with the infills.

In order to reproduce the structural configuration of existing Italian buildings, an 8-storey infilled RC frame was analysed in the present work, designed according to R.D. L. 2229/1939 (1939), that regulated the design of RC buildings in Italy up to 1970. Four bays for each floor were considered, with span equal to 4.5 m, while inter-storey height was assumed to be 3.4 m. The area of the infill panels was reduced of 20% to account for openings in external walls.

2.1 Numerical Modelling of the RC Frame

A lumped plasticity approach was adopted for the numerical modelling of the frames, using the OpenSees platform (McKenna et al. 2000); linear elastic beam elements with flexural and shear springs connected in series were adopted for columns to take into account both flexural and shear failure (Fig. 1), while only flexural hinges were modelled in the beams.

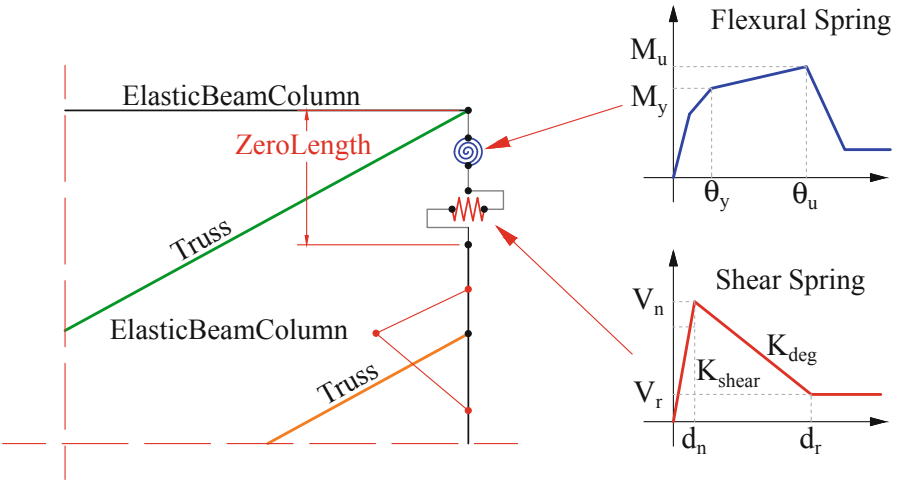

Fig. 1. Configuration of the numerical model adopted for the columns.

The moment-rotation (M-θ) nonlinear behaviour of the frames was evaluated according to Eurocode 8 (EN 1998-3 2005); the influence of the axial load on the flexural response of the columns was also considered.

The cyclic response of the flexural springs was defined according to the formulation proposed by Takeda et al. (1970), adopting the *Pinching4* Uniaxial material (Lowes and Altoontash 2003) available in OpenSees, Fig. 2 shows an example of the hysteretic curve calibrated for a column.

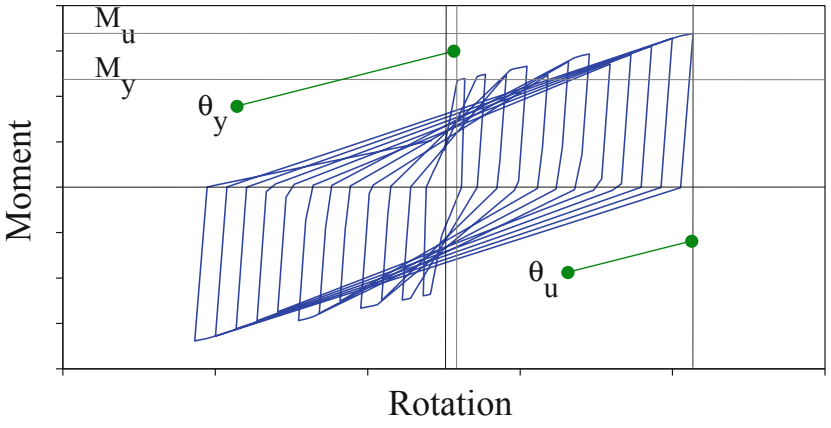

Fig. 2. M-θ hysteretic behaviour adopted for flexural springs.

The shear springs were defined assuming a linear elastic response up to the attainment of the maximum shear strength of the column, defined according to the formulation proposed by Sezen and Moehle (2004):

$$V_n = k\frac{A_t f_{yt} d}{s} + k\left(\frac{0.5\sqrt{f_c}}{\frac{a}{d}}\sqrt{1+\frac{N_{ed}}{0.5\sqrt{f_c}A_c}}\right)0.8A_c \quad (1)$$

In Eq. (1), k is a ductility factor varying within the range [0.7;1], A_t, f_{yt}, and s are the cross section area, yielding strength and spacing of the transversal reinforcement, respectively; A_c and d are the cross section area and effective depth of the column, f_c is the compressive strength of the concrete, and N_{ed} is the axial load.

The shear failure of the column is considered in the model by defining a post-peak softening slope, as reported in Fig. 1. The displacement at shear failure d_n is defined by the rate V_n/K_{shear}, where K_{shear} is the shear stiffness of the column, evaluated as $A_c \cdot G/h$, being G the tangent modulus of the concrete and h the height of the column.

2.2 Numerical Modelling of the Infill Panel

The response of the equivalent strut model is defined through a piecewise linear load-displacement behaviour, according to the formulation proposed by Panagiotakos and Fardis (1996). The first cracking strength F_{cr} is evaluated as the product of the shear strength of the panel τ_w, and the cross-section $A_w = L_w \cdot t_w$. The initial stiffness of the panel K_1 and the post cracking stiffness are calculated with Eqs. (2) and (3). In Eq. (2), G_W is the tangent modulus of the infill and L_W, t_W and h_W are the length, thickness and height of the panel, respectively.

$$K_1 = \frac{G_w t_w L_w}{h_w} \quad (2)$$

$$K_2 = \frac{E_w b_w t_w}{d_w} \quad (3)$$

K_2 is determined by the Young's modulus (E_W), the diagonal length (d_w) of the panel and the width of the equivalent truss section, b_W, evaluated according to Mainstone (1971), as:

$$\frac{b_w}{d_w} = 0.175\lambda h_w^{-0.4} \quad (4)$$

In Eq. (4), λ expresses the relative panel-to-frame stiffness, which was defined according to Eq. (5) by Stafford Smith and Carter (1969):

$$\lambda = \sqrt[4]{\left(\frac{E_w t_w \sin(2\theta)}{4EIh_w}\right)} \quad (5)$$

where θ is the angle of the diagonal dimension of the panel, while E and I are the Young's modulus of the concrete and the moment of inertia of the cross section of the RC frame columns.

The peak shear strength at the end of the hardening branch F_m is equal to 1.3 F_{cr}, while the softening slope is assumed equal to 0.02 K_1.

In order to evaluate the local interaction between panel and column, the infill panel is modelled by adopting the three-strut approach (Fig. 3) proposed by Chrysostomou (1991).

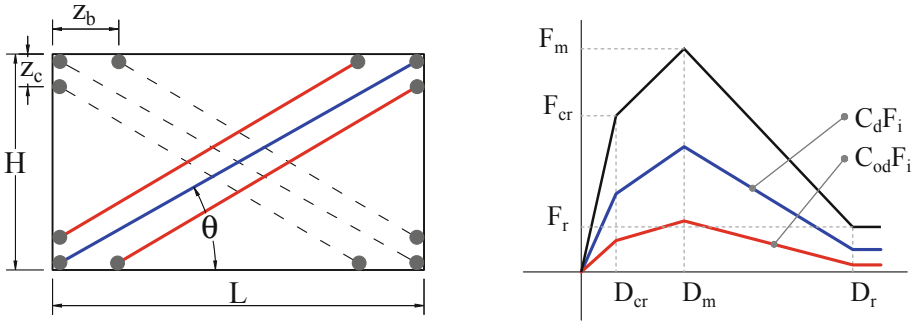

Fig. 3. Description of the model adopted to simulate the presence of the panel (from Chrysostomou et al. 2002).

According to the original formulation, 50% of the total stiffness of the panel was assigned to the central truss, while the remaining 50% was equally divided among the off-diagonal trusses.

According to the approach proposed by Al-Chaar (Al-Chaar et al. 2002), the off-diagonal trusses are connected to the columns and the beams at a distance from the joints equal to z_c and z_b, respectively (Eqs. (6) and (7)). Basing on the stiffness distribution, the coefficients C_d and C_{od} are equal to 0.50 and 0.25, which are assigned to the central and the off-diagonal struts, respectively.

$$z_c = \frac{C_d b_w + C_{od} b_w}{2cos\theta} \tag{6}$$

$$z_b = \frac{C_d b_w + C_{od} b_w}{2sin\theta} \tag{7}$$

3 Numerical Analysis Setting

The main parameter influencing the failure modes related to local interaction between frame and infill panel is the shear strength (τ_w) of the latter. According to the analytical formulation proposed by Panagiotakos and Fardis (1996), the variation of τ_w,

significantly modifies the Force-displacement response of the panel. In order to evaluate the influence of τ_w on the seismic response of the analysed RC frame, it was varied considering the masonry typically used in the Italian and European context. Hollow clay brick panels are mostly diffused in the Mediterranean areas, while solid concrete and clay bricks are generally preferred in the northern Europe (Ganz 2003; Watt 1990).

Depending on the mechanical properties of the bricks and the quality of mortar, the value of τ_w usually ranges between 0.1 and 0.4 MPa (EN 1996-1-2 2005); thus, four types of infilled frames were considered in the present study, having infill panels with shear strength equal to 0.1, 0.2, 0.3, and 0.4 MPa (named T1, T2, T3 and T4, respectively).

A set of 10 spectrum compatible ground motions was selected to perform the Incremental Dynamic Analysis (IDA). The generated ground motions are referred to a high hazard seismic zone of Italy (Benevento, Campania), considering a return period equal to 475 years. (i.e. referred to life-safety performance level design, according to Italian building code NTC-18 (NTC-2018 2018)) The elastic 5% damping spectra related to the selected ground motions are reported in Fig. 4.

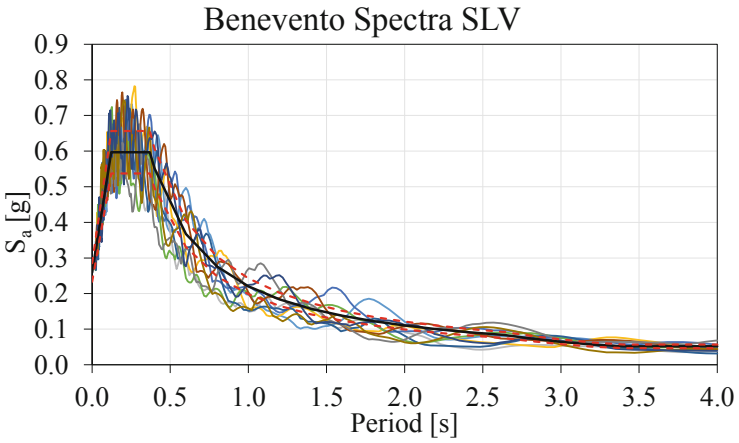

Fig. 4. Elastic spectra (5% damping) referred to ground motions selected for IDA (Black line is referred to the design spectrum).

The Incremental Dynamic Analyses are performed by increasing the intensity of the input motion up to the attainment of the life-safety performance level by a non-negative factor [0, +∞). In order to consider the failure modes related to the local interaction between panel and column, the life-safety performance level (PL) was evaluated by recording at each intensity of the input motion (i.e. at each IDA step) the status of flexural and shear springs of the column. Therefore, life-safety PL was attained once either flexural or shear failure of the column occurred.

4 Analysis Results

4.1 IDA Curves

The IDA curves report the relationship between the intensity measure, expressed in terms of spectral acceleration at the first period of the structure (S_a (T_1)) and the structural response. At each step, the structural response (performance level parameter) was assessed evaluating, for each column, the ratio between the maximum displacement/rotation recorded during the analysis and the displacement/rotation capacity. This ratio was calculated to assess both the shear and flexural behaviour. If the maximum ratio was obtained in flexural springs, the parameter was called maximum rotation factor (MRF), while in case of maximum ratio obtained in shear springs, it was called maximum shear factor (MSF).

According to the proposed approach, once MRF is equal to one, the flexural failure is obtained, while MSF = 1 means shear failure.

The choice of not monitoring the inter-storey drift to define the PL (as usually done in IDA) is related to the need of evaluating both the global behaviour of the structure and the local interaction due to the presence of the infills. While the drift is expressed by the chord rotation of the column and, as consequence, can be monitored by the MRF, for the adopted modelling approach no correlation exists between the MSF and the drift. Thus, the assumption of a unique parameter to define the PL wouldn't have been able to discern the failure mechanism.

Figures 5, 6, 7, 8 report the obtained results depending on the shear strength of the panel, while in Table 1, the average S_a (T_1) corresponding to the failure (i.e. either corresponding to MRF or MSF equal to one) is reported.

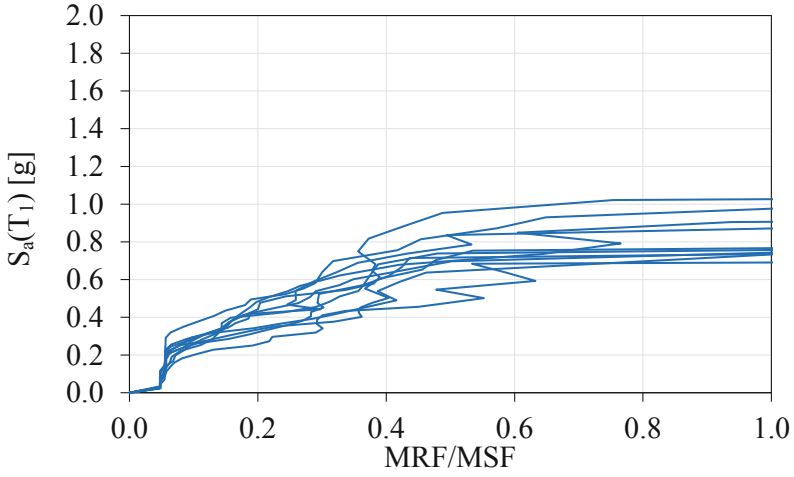

Fig. 5. IDA curves obtained for T1 (Blue line = MRF).

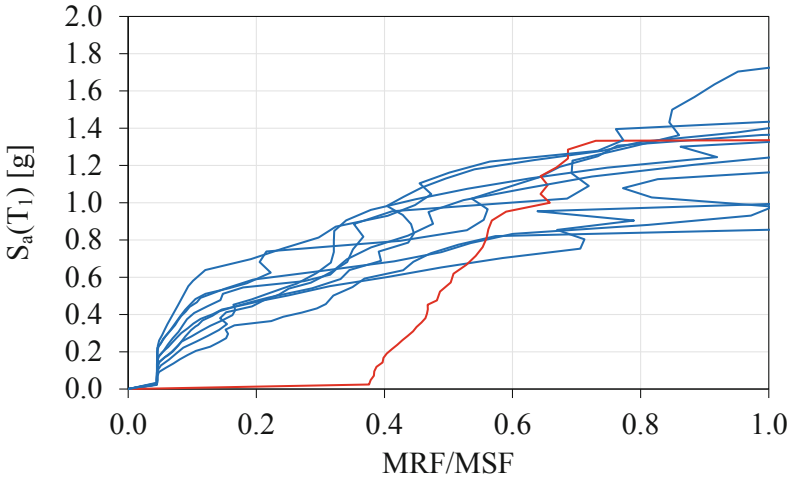

Fig. 6. IDA curves obtained for T2 (Blue line = MRF, red line = MSF).

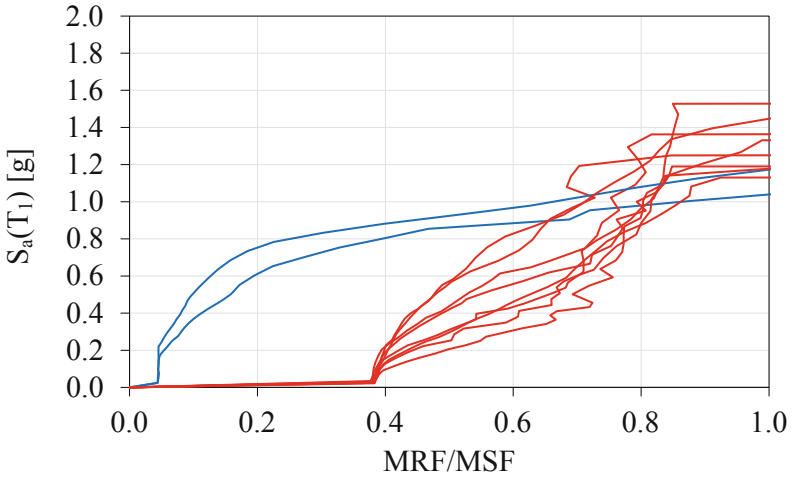

Fig. 7. IDA curves obtained for T3 (Blue line = MRF, red line = MSF).

The lower performances in terms of spectral acceleration capacity of the structure are obtained for τ_w = 0.4 MPa (Fig. 8), due to increase of shear transferred to the column by the infill panel, which led to early brittle failure. In this case the median S_a (T_1) at the collapse is equal to 0.84 g, for all considered ground motions the collapse is achieved due to the shear failure of the columns.

By reducing the strength to 0.3 MPa (Fig. 7), a significant increase of the structural performances is obtained (median S_a (T_1) at the collapse equal to 1.34 g), which can be related both to the reduction of the local interaction effect and the high contribute in

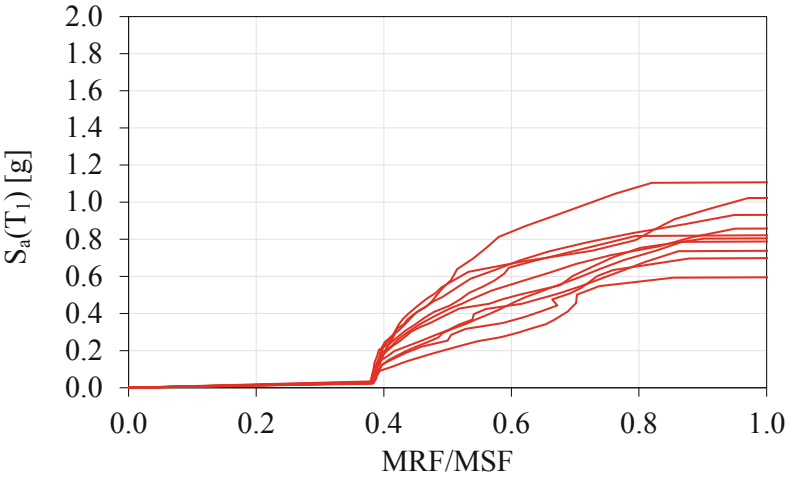

Fig. 8. IDA curves obtained for T4 (red line = MSF).

Table 1. Average values of $S_a(T_1)$ at collapse along with COV obtained for the analysed structures.

Frame	$S_a(T_1)$	COV
	g	%
T1	0.85	16
T2	1.28	19
T3	1.34	17
T4	0.84	18

terms of global strength due to the presence of the panel. For this configuration, only in two cases the collapse was recorded for flexural failure of the columns.

The IDA curves obtained show that the increase of the shear strength of the panel leads to a variation of the failure mode of the column, since for lower values, mainly flexural failures are obtained, while shear failure is the dominant mechanism by increasing τ_w. The lowest capacity was obtained for T1 and T4; in the first case, this is due to the low contribute of the infills in terms of global strength, while for T4 (Fig. 8), the brittle failure of the columns due to local interaction affected the global performances.

Referring to T2 and T3, a significant increase of the performances is obtained both comparing to T1 and T4. In fact, for intermediate values of τ_w, even if the shear in the column is higher comparing to T1, local interaction is not significant enough to lead to early shear failure and, consequently, the global performances are increased because of the contribute of the infills in terms of strength.

An interesting feature characterizing the observed performance is the dependence between the shape of the IDA curves and the parameter considered to define the PL (i.e.

MRF or MSF). In case of shear failure of the columns causing the collapse of the structure, high values of MSF are observed even for near-zero ground motion intensity, which means that the shear in the column due to gravity loads is already relevant compared to the shear strength. On the other hand, if collapse is attained for flexural failure, the MRF value associated to low S_a (T_1) is significantly lower.

This feature confirms that in case of existing buildings, shear failure rather than flexural one is the most likely to occur and suggests that the presence of strong infills can significantly increase the probability of collapse due to local interaction.

4.2 Failure Modes

Despite the correlation between the spectral acceleration capacity and the shear strength of the panel is not clearly defined observing IDA curves, the failure mode of the column is significantly influenced by τ_w.

Referring to τ_w = 0.1 MPa, only flexural failure was observed in the columns, for all the ground motions considered, while, by increasing the shear strength of the panel, shear failure rather than flexural ones occurs.

In order to obtain a simplified definition of the ductile behaviour of the structure analysed, depending on the shear strength of the panel, the value of MRF at failure was recorded for each IDA carried out.

Since MRF = 1 at failure means that flexural failure is obtained, in this case a ductile mechanism is considered, while if MRF at failure is lower than one (i.e. shear failure occurs), the dissipation capacity of the structure is reduced and a brittle behaviour is observed.

Figure 9 reports the recorded value of MRF at failure for each analysis conducted, clearly showing that the increase of shear strength of the panel leads to a significant reduction of the ductility capacity of the structure.

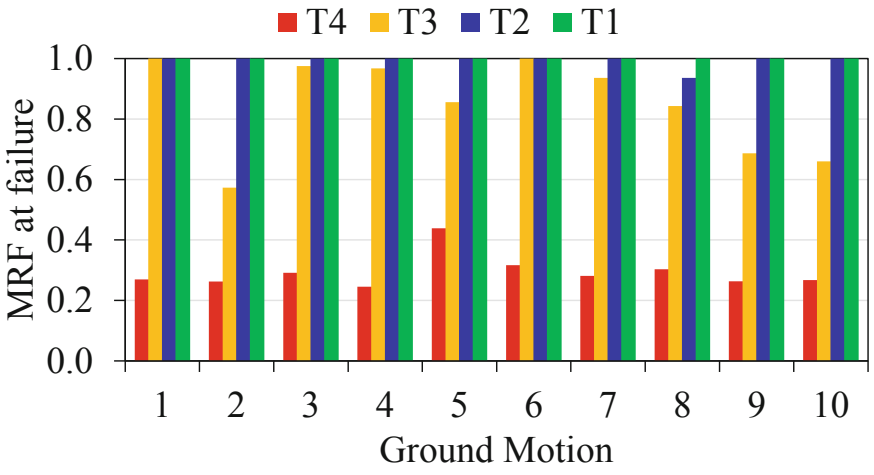

Fig. 9. MRF at failure obtained depending on τ_w.

As said before, referring to $\tau_w = 0.1$ MPa, flexural failure was obtained for all the ground motions considered, while, for $\tau_w = 0.2$ MPa, only in one case MRF was slightly lower than 1 at collapse (0.94).

By increasing the shear strength of the panel, a significant reduction of MRF at collapse is observed; for $\tau_w = 0.3$ MPa the average value obtained is 0.85, with COV equal to 0.18, while for $\tau_w = 0.4$ MPa, an average of 0.29 with COV equal to 0.19 is observed.

5 Conclusions

Despite the introduction of the performance-based-design represents a great improvement in the field of earthquake engineering, in most of Mediterranean countries, the majority of the buildings was designed before the upgrade of the building codes.

For this reason, civil engineers often deal with the seismic vulnerability assessment of existing buildings, whose performances are significantly different compared to new ones. The results obtained in the present study are consistent with experimental and numerical investigations from literature, which assessed that for existing buildings, the presence of the infill panel significantly modifies the structural performances.

The influence of the shear strength of the panel is the main issue addressed in the present work; well consolidated formulations from literature were adopted to develop a numerical model aimed at accurately reproduce the phenomena related to local interaction between panel and RC frame.

The incremental dynamic analyses carried out demonstrated that the properties of the infills could significantly influence failure modes of the columns. Flexural failure is the main mode observed in case of low shear resistance of the panels, while shear failure of columns was encouraged by the increase of the shear strength, leading to a reduction of the spectral acceleration capacity of the structure.

Considering the high uncertainty in the evaluation of mechanical properties of each element/material adopted in existing buildings, this study points out the need of further improvement of building design codes, in order to consider different features related to the presence of the infills in the seismic performance assessment of existing RC frames. Furthermore, the accurate definition of the model for the simulation of the masonry panel was found to be relevant for the prediction of brittle failure of the columns, which wouldn't have been captured adopting a single-strut approach, as usually done in global analyses.

References

Al-Chaar G, Issa M, Sweeney S (2002) Behavior of masonry-infilled nonductile reinforced concrete frames. J Struct Eng 128(8):1055–1063

Asteris PG, Antoniou ST, Sophianopoulos DS, Chrysostomou CZ (2011) Mathematical macromodeling of infilled frames: state of the art. J Struct Eng 137(12):1508–1517

Burton H, Deierlein G (2013) Simulation of seismic collapse in non-ductile reinforced concrete frame buildings with masonry infills. J Struct Eng 140(8):A4014016

Chrysostomou CZ (1991) Effects of degrading infill walls on the nonlinear seismic response of two-dimensional steel frames. Cornell University, Ithaca
Chrysostomou CZ, Gergely P, Abel JF (2002) A six-strut model for nonlinear dynamic analysis of steel infilled frames. Int J Struct Stab Dyn 2(3):335–353
Crisafulli FJ, Carr AJ (2007) Proposed macro-model for the analysis of infilled frame structures. Bull NZ Soc Earthq Eng 40(2):69–77
Dolšek M, Fajfar P (2008) The effect of masonry infills on the seismic response of a four-storey reinforced concrete frame - a deterministic assessment. Eng Struct 30(7):1991–2001
EN 1996-1-2 (2005) Eurocode 6 - Design of masonry structures - Part 1-2: General rules - Structural fire design. European Standard
EN 1998-3 (2005) Eurocode 8: Design of structures for earthquake resistance - Part 3: Assessment and retrofitting of buildings. European Standard
Gallipoli MR, Mucciarelli M, Vona M (2009) Empirical estimate of fundamental frequencies and damping for Italian buildings. Earthq Eng Struct Dynam 38:973–988
Ganz HR (2003) Post-tensioned masonry structures. VSL International LTD
ISTAT (2001) 14° Censimento Generale Della Popolazione E Delle Abitazioni. Retrieved dawinci.Istat.it
Jeon J-S, Park J-H, DesRoches R (2015) Measuring bias in structural response caused by ground motion scaling. Earthq Eng Struct Dynam 44:1783–1803
Kose MM (2009) Parameters affecting the fundamental period of RC buildings with infill walls. Eng Struct 31(1):93–102
Lowes LN, Altoontash A (2003) Modeling reinforced-concrete beam-column joints subjected to cyclic loading. J Struct Eng 129:1686–1697
Mainstone RJ (1971) On the stiffnesses and strengths of infilled frames. Proc Inst Civ Eng 49 (2):57–90
McKenna F, Fenves GL, Scott MH, Jeremir B (2000) Open system for earthquake engineering simulation, OpenSEES. University of Berkeley
Mehrabi AB, Shin PB, Schuller MP, Noland JL (1996) Experimental evaluation of masonry infilled RC frames. J Struct Eng 122(3):228–237
NTC-2018 (2018) Aggiornamento Delle «Norme Tecniche per Le Costruzioni». D.M. 17 gennaio 2018, Italy
Panagiotakos TB, Fardis MN (1996) Seismic response of infilled RC frame structures. In: 11th world conference on earthquake engineering. Acapulco, MX, June 23–28
Perrone D, Leone M, Aiello MA (2016) Evaluation of the infill influence on the elastic period of existing RC frames. Eng Struct 123:419–433
Perrone D, Leone M, Aiello MA (2017) Non-linear behaviour of masonry infilled RC frames: influence of masonry mechanical properties. Eng Struct 150:875–891
Polyakov SV (1960) On the interaction between masonry filler walls and enclosing frame when loading in the plane of the wall. Earthquake Engineering Research Institute
R.D.L 2229/39 (1939) Norme per L'esecuzione Di Opere in Conglomerato Cementizio Semplice O Armato. R.D.L. Italy, 16 novembre 1939
Ricci P, De Luca F, Verderame GM (2011) 6th April 2009 L'Aquila earthquake, Italy: reinforced concrete building performance. Bull Earthq Eng 9(1):285–305
Rodrigues H, Varum H, Costa A (2008) A non-linear masonry infill macro-model to represent the global behaviour of buildings under cyclic loading. Int J Mech Mater Des 4(2):123–135
Sezen H, Moehle JP (2004) Shear strength model for lightly reinforced concrete columns. J Struct Eng 130(11):1692–1703
Stafford Smith B, Carter C (1969) A method of analysis for infilled frames. Proc Inst Civ Eng 44 (1):31–48

Takeda T, Sozen MA, Nielsen NN (1970) Reinforced concrete response to simulated earthquakes. J Struct Div 96(12):2557–2573

Vamvatsikos D, Cornell CA (2001) Incremental dynamic analysis. Earthq Eng Struct Dynam 31 (3):491–514

Verderame GM, De Luca F, Ricci P, Manfredi G (2011) Preliminary analysis of a soft-storey mechanism after the 2009 L'Aquila earthquake. Earthq Eng Struct Dynam 40(8):925–944

Verderame GM, Ricci P, Del Gaudio C, De Risi MT (2016) Experimental tests on masonry infilled gravity- and seismic-load designed RC frames. In: 16th international brick and block masonry conference. Padova (IT)

Watt KA (1990) Nineteenth century brickmaking innovations in Britain: building and technological science. University of York: Institute of advanced architectural studies

Nonlinear Modeling Approaches for Existing Reinforced Concrete Buildings: The Case Study of De Gasperi-Battaglia School Building in Norcia

C. Lima[1], M. Angiolilli[2], F. Barbagallo[3], B. Belletti[4(✉)], A. V. Bergami[5], G. Camata[6], C. Cantagallo[6], M. Di Domenico[8], G. Fiorentino[5], A. Ghersi[3], A. Gregori[2], D. Lavorato[5], R. Luciano[7], E. M. Marino[3], E. Martinelli[1], C. Nuti[5], P. Ricci[8], L. Rosati[8], S. Ruggieri[9], S. Sessa[8], E. Spacone[6], M. Terrenzi[6], G. Uva[9], F. Vecchi[4], and G. M. Verderame[8]

[1] DICiv Università degli Studi di Salerno, Fisciano, Italy
[2] DICEAA Università degli Studi dell'Aquila, L'Aquila, Italy
[3] DICAR Università degli Studi di Catania, Catania, Italy
[4] DIA Università di Parma, Parma, Italy
beatrice.belletti@unipr.it
[5] Università degli Studi di Roma 3, Rome, Italy
[6] INGEO Università G. d'Annunzio di Chieti-Pescara, Chieti, Italy
[7] DICM Università di Cassino e del Lazio meridionale, Cassino, Italy
[8] DIST Università degli Studi di Napoli Federico II, Naples, Italy
[9] DICATECH, Politecnico di Bari, Bari, Italy

Abstract. This paper reports on a collaborative activity developed as part of the DPC-ReLUIS Research Project, year 2017. It aims at comparing the results obtained by considering alternative options in the definition of the nonlinear FEM model employed in pushover analyses for seismic assessment of existing RC frames. Specifically, the RC frame structure of the De Gasperi-Battaglia school building located in Norcia, Italy, is considered as a relevant case-study. This structure has been designed in the '60s of the past century according to the seismic code of the time and, hence, without taking into account the principles of Capacity Design. Although the building was actually retrofitted before the 2016 Central Italian earthquake, in this paper its original configuration has been considered. The nonlinear behaviour of the frame structure has been modelled by both following alternative approaches and employing different analysis codes. Therefore, this paper proposes an overview about how different the simulation output can be as a result of different modelling and analysis choices. In doing that, the work can be relevant to practitioners, as they may be warned about the consequences of those choices in terms of seismic vulnerability evaluation.

Keywords: RC existing buildings · Non-linear analysis · Pushover · Finite element method · Frame structure

M. di Prisco and M. Menegotto (Eds.): ICD 2018, LNCE 42, pp. 82–95, 2020.
https://doi.org/10.1007/978-3-030-23748-6_7

1 Introduction

Seismic assessment of existing buildings is a challenging task for practitioners, as it is influenced by a number of problematic aspects (Franchin et al. 2010), such as uncertainties about relevant geometric quantities (Silva et al. 2012), limited knowledge of structural detailing (Jalayer et al. 2010) and high variability in material properties (De Stefano et al. 2013) possibly affected by both the original workmanship practice (Tabbakhha and Modaressi-Farahmand-Razavi 2016) and eventual degradation phenomena (Li 2004). Moreover, when it comes to Reinforced Concrete (RC) structures, specific concerns arise with respect to the actual accuracy and reliability of capacity models, namely those mathematical relationships intended at determining the members' strength and ductility based on the available knowledge about materials properties and structural detailing (fib 2003). Furthermore, a significant variability in the results of seismic assessment may derive from the adoption of alternative analysis methods chosen among those generally accepted for the seismic simulation of structures (Fragiadakis et al. 2013).

This paper aims at summarizing the work made by several research groups as part of WP2 of the DPC-ReLUIS research project (year 2017) about the comparison of seismic simulation results obtained from alternative modelling approaches about both capacity models and numerical techniques for seismic analysis. Specifically, the results of pushover analyses run by considering either lumped- or distributed-plasticity models are proposed and discussed with the aim to highlights their potential and drawbacks. Since those analyses are performed by using commercial analysis codes, such as OpenSEES (Mazzoni et al. 2010), Abaqus (Dassault Systèmes Simulia Corp. 2017), MidasGen (CSPFEA 2018) and SAP2000 (Brunetta et al. 2006), the proposed results and comments are intended as a tutorial guide for practitioners in their everyday work.

Section 2 outlines the general theoretical bases of the various modelling approaches targeted in this study. Then, to make things clearer, Sect. 3 proposes a relevant case study (namely, the De Gasperi - Battaglia school building located in Norcia): the RC structure is described into details in its "as-built" configuration designed and realized in the '60s of the past century and, hence, without considering the recently completed seismic upgrading intervention. Section 4 highlights the main lessons learnt from this study and discloses the main ideas about the future developments of the present collaborative research.

2 Nonlinear Modelling of Materials and Elements

Seismic analysis of structures, especially those executed on existing ones and aimed at determining their seismic vulnerability, are generally carried out on nonlinear Finite Element (FE) models employed either in static (namely pushover) or dynamic (namely time-history) simulations of the response under actions induced by earthquake shaking.

However, several levels of detailing can be chosen in FE models, depending, on the one hand, on the actual accuracy of the available data (in terms of geometry, material properties and structural detailing) and, on the other hand, on the computational efforts that can be afforded. Ferretti et al. (2002) propose a possible classification of the FE

employed in structural and seismic analyses in a decreasing order of accuracy and computational effort:

- general purpose *3D elements* capable of simulating the structural response under the general assumption of continuum mechanics with non-linear constitutive laws: Abaqus (Dassault Systèmes Simulia Corp. 2017) is one of the most widely employed codes featuring these kinds of models;
- *fiber beam elements* formulated by assuming either the kinematic (displacement-based elements) or the equilibrium (force-based elements) conditions assumed in common beam theories (e.g. the Timoshenko theory) with non-linear properties implemented by means of 1D stress-strain relationships referred to the *fibers* of specific transverse sections selected throughout the beam axis and assumed as sampling points: this approach, generally referred to as "distributed plasticity approach" is available in various codes, among which the OpenSEES (Mazzoni et al. 2010) and MidasGen (CSPFEA 2018);
- *sectional beam elements*, similar to the aforementioned fiber-beam models, in which the nonlinear behavior is defined in terms of moment-curvature relationship in specific sampling points through the element's axis: although they are based on a distributed plasticity approach, relevant aspects of the mechanical behavior (such as the M-N interaction on both moments and curvatures) cannot be generally taken into account (elements of this sort were employed within the code IDARC (Reinhorn et al. 2009), among the first made available to the scientific community for performing nonlinear seismic analyses);
- *plastic-hinge beam elements*, in which the nonlinear behavior is *concentrated* (or *lumped*) in specific sections (e.g. the extreme sections of columns) whose moment-rotation relationship simulate the non-linear structural response: these elements are employed in several FE codes, among which SAP2000 (Brunetta et al. 2006); the N-M interaction can be taken into account in advanced formulations of this class of elements by either defining a family of moment-rotation curves obtained at different values of axial force (SAP2000) or updating "run-time" those curves by means of a fiber-discretization of the plastic-hinge sections (OpenSEES).

2.1 Concrete

The mechanical behavior of concrete is characterized by complex non-linearities, both in compression and in tension.

Concrete under compressive stress shows an elastic-linear behavior up to about 1/3 of the maximum resistance: non-linear behavior takes place due to the cracking processes that, after the peak in strength, originates softening phenomena. Post peak softening behavior is strongly influenced by both size of the specimen and boundary conditions (fib-MC2010 2012). The simulation of seismic response of existing buildings is generally referred to the average compressive strength f_{cm} whose relationship with the other materials' properties is described by well-established laws provided by various documents, such as NTC (2008) and fib-MC2010 (2012).

Moreover, transversal confinement influences displacement and force capacity of RC members. General models are available in the literature for simulating the response

of concrete subjected to tri-axial stress states (Kupfer et al. 1969). However, due to weak and widely spaced stirrups generally adopted in existing structures, the effect of confinement is often neglected in seismic assessment analysis.

Concrete behavior in tension is even more complex, as tension-induced cracks are discrete in nature, whereas FE models are generally based on assuming the continuity of displacement and force fields' FE This makes inappropriate the adoption of the classical "deformation" assessment in case of cracked concrete, for which the crack localization effect is fundamental in FEM analysis (fib 2008; Bazant and Oh 1983). An approach based on crack opening is provided by fib-MC2010 (2012). Generally, these techniques are based on the definition of fracture energy G_f, which can be determined through experimental tests or calculated in accordance to specific formulations, such as those provided by fib-MC2010 (2012): $G_f = 73\ f_{cm}^{0.18}$. Moreover, the concrete average tensile strength f_{ctm} can be calculated as suggested by fib-MC2010 (2012).

2.1.1 Uniaxial Laws

Several uniaxial σ-ε laws describing the behavior of concrete are available in the literature. For instance, the work by Kent and Park (1971) was further developed by Scott and Park (1982) considering the cross-section confinement, which represents a very important factor in case of cyclic loads. However, this model does not take into account the tensile contribution offered by concrete. Popovics (1973) proposed a (σ-ε) relationship similar to Kent and Park's one, in which no hysteretic cycles are considered in the unloading/loading branches. However, in this case, the tensile strength of concrete is not neglected. Compared to Kent and Park's model, the number of parameters required for this new model is higher and the shape of the softening branch can be varied. Mander et al. (1984) proposed a model capable of simulating the hysteretic behavior of confined and unconfined concrete under cyclic compression and tension. The description of the cyclic behavior is based on the statistical regression analysis of cyclic tests.

2.2 Steel

Generally, the mechanical behavior of steel reinforcement can be assumed symmetrical in compression and in tension. In monotonic load conditions, this behavior is characterized by a linear elastic initial branch up to the yielding point, after which a plastic-behavior first and a subsequent hardening phase are later noticed till the failure is reached.

As for the cyclic behavior, in case no sign reversal, loading-unloading curves correspond each other, with almost no hysteresis effects. Therefore, monotone σ-ε curve correspond to the envelope of the cyclic behavior. Conversely, in the case of load reversals, a gradual decrease in yield strength is noticed, together with non-linear phases characterized by a progressive loss in stiffness (Bauschinger effect). Since existing reinforced buildings are characterized by very low amount of transversal reinforcement, constitutive law for longitudinal reinforcement should also take into account buckling phenomenon as well. The monotonic post-buckling behavior varies with slenderness of the longitudinal reinforcement, defined as $\lambda = L/D$, in which L represents transversal stirrups spacing and D is the diameter of longitudinal rebars.

Mander et al. (1984), Mau and El-Mabsout (1989) and Monti and Nuti (1992) have studied the influence of the possible buckling of rebars in RC sections. The value $\lambda = 5$ has been identified as the upper limit of slenderness for the rebar not to exhibit buckling. This value is however influenced by the actual mechanical properties of steel (Bae et al. 2005).

Dhakal and Maekawa (2002) demonstrated that compressive behavior of a steel rebar subject to buckling depends on both its yield tension and slenderness, so that different steel grades can generate identical tension-deformation curve if combined parameter $L/D\sqrt{f_y}$ results the be the same. A wide investigation on steel reinforcements used in Italy till the '70s (smooth rebars) are presented by Cosenza and Prota (2006), in which a slenderness-ratio between 5 and 70 have been reported together with a new constitutive model for smooth rebars prone to buckling effects. Prota et al. (2009) reported experimental results highlighting that cyclic behavior of longitudinal rebars characterized for high values of slimness presents marked pinching.

2.2.1 Uniaxial Laws

Concerning the steel behavior, several uniaxial constitutive laws are found in literature. A brief overview follows.

Bilinear Elastic-Plastic Model with Kinematic and Isotropic Hardening

This model considers the cyclic behavior of steel in a simplified way. The bilinear σ-ε relationship is defined by two straight lines, whose slopes are Es e $E_{sh} = b \cdot E_s$, b being a dimensionless parameter. The intersection of the two lines represents the yielding point, defined by the yield strength f_y at the yielding deformation ε_y. The characterization of the isotropic hardening requires the definition of additional parameters, depending on the hypothesis of symmetrical behaviour or not.

Menegotto-Pinto Model (1973)

This model, later modified by Filippou et al. (1983), aims to simulate the cyclic behavior of steel and capture the Baushinger effect and the kinematic hardening (Menegotto and Pinto 1973) and its optionally isotropic nature (Filippou et al. 1983).

The cyclic behaviour is governed by several variables, such as ε_r and σ_r are related to the previous loading and unloading story and represent the deformation and the stress at the inversion-load points; another parameter (R) governs the evolution of the constitutive law curvature.

2.3 Modeling of Bending and Combined Compression and Bending Mechanisms

As already mentioned at the beginning of Sect. 2, alternative approaches can be followed with the aim to simulate the nonlinear response of members and structures under seismic actions. For instance, an empirical lumped plasticity macro-modelling

approach (referred to as "UNINA-Verderame" in the following) can be used in addition to fiber-based approaches. Nonlinear moment-chord rotation springs are adopted at the end of beam/column (elastic) elements; the backbone of these moment-chord rotation relationships simulate the key points of the non-linear response (cracking, yielding, maximum, "ultimate" (20% strength drop) and zero resistance). They are defined through the empirical expressions proposed by Verderame and Ricci (2017) calibrated for RC members with smooth rebars and calculated assuming the axial load value due to gravity loads and shear span equal to half the clear length of the element.

3 Case Study

3.1 General Description

The building studied in the present work is the De Gasperi-Battaglia school Institute located in Norcia (Italy). It is a four-storey RC framed structure with a rectangular shape in plan (12.8 × 59.8 m) and a maximum height of about 16.10 m measured from the foundation level. The entire building consists of three blocks, divided among them by two technical gaps arranged in parallel to the shorter direction. The floor slabs are made in RC with lightweight clay blocks and are arranged in order to transmit vertical loads to transversal frames. Figure 1 depicts the front view of the building in which the two technical gaps are highlighted, while Fig. 2 shows the structural scheme in plan (Fig. 2a), section (Fig. 2b) and the tridimensional model (Fig. 2c) of the left block as, in this work, it is analyzed only.

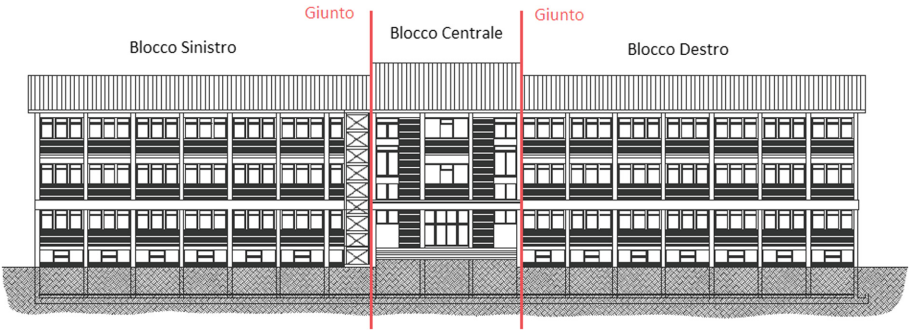

Fig. 1. Front view of the structure with the identification of the 3 blocks.

The technical gap that separate the structure under investigation from the central building is a Gerber system transmitting vertical loads of half a bay on the right of the frame T7 to the central block, whereas the total amount of the seismic mass is supported by columns of the investigated building.

The geometric and mechanical properties of the structure (i.e. sections of beam and columns, amount of reinforcement, concrete compressive strength, yielding stress of steel, and so on) results from the "*Seismic Identification Campaign*" performed in 1999

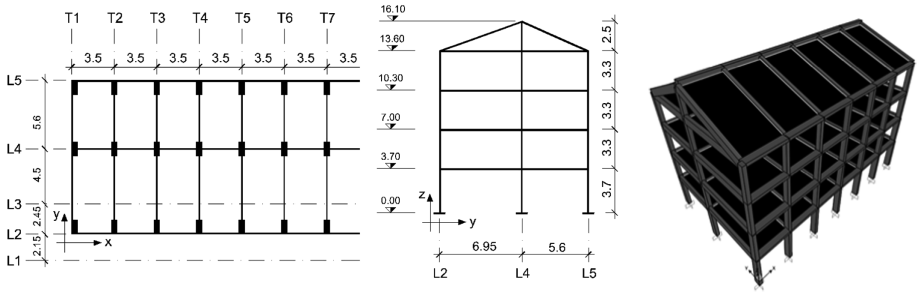

Fig. 2. Structural scheme of the analyzed structure: plan view (a), section (b) and tridimensional model (c).

and the design documents of the "*Retrofitting intervention*" developed in 2003 and 2010. Further details are herein omitted for sake of brevity.

3.2 Description of Numerical Models

Numerical models are developed by the Research Units (UR) involved within the DPC-ReLUIS Project without considering the beams of the last bay connecting the analyzed structure with the central building. Therefore, the related loads are applied as concentrated forces on the beam-to-column nodes of the transversal frame labelled T7 (Fig. 2a).

As far as the foundations are concerned, the hypothesis of fixed constrain at the base is assumed.

Moreover, at this stage of the activities, the mechanical contribution of masonry infills is neglected in the structural model and brittle mechanisms (shear failure of beams, columns and joints) are not considered.

The mass of the structure is evaluated according to the seismic combination (Eq. 2.5.5 of NTC 2008) assigning partial coefficients equal to 0.6 for variable school loads and 1 for gravitational loads. Floor masses result equal to 313.33 ton, 312.27 ton, 309.45 ton and 439.14 ton, respectively at the 1st, 2nd, 3rd and 4th floor. Pushover analyzes, which results are reported in Sect. 3.3, are performed by applying a horizontal force distribution proportional to the floor masses. Table 1 summarizes the nonlinear characteristics of the models and the seismic analysis code adopted by each UR.

UnivAQ and PoliBA work with a concentrate plasticity model (plastic hinges) in SAP2000 software. However, UnivAQ analyses are performed considering FEMA356 (2000) moment-rotation law for plastic hinges located at both ends of beams and columns. The floors are simulated as rigid diaphragms. Conversely, the PoliBA model accounts for M-θ laws adopted by NTC (2008) and each floor in the model is simulated by means of shell elements with thickness equal to the one of the RC slab. UniCH takes into account three different models: two of them are developed in MidasGen software considering concentrated (plastic hinges according FEMA356) or distributed plasticity (fiber elements), while the other one is developed in OpenSEES using fiber elements in

Table 1. Modeling features used by UR (NL = type of plasticity, ST = Section-type, C = Concentrated, D = Distributed, Mθ = Moment-curvature law, F = Fiber section)

UR	Software	Beam		Column	
		NL	ST	NL	ST
UnivAQ	SAP2000	C	Mθ	C	Mθ
UniPR	Abaqus	C	Mθ	C	Mθ
UniCH	MidasGen MidasGen OpenSEES	C C D	Mθ Mθ F	C D D	Mθ F F
UniSA	OpenSEES	C	F	C	F
UniNA Verderame	OpenSEES	C	Mθ	C	Mθ
UniNA Rosati	OpenSEES	D	F	D	F
UniRM3	OpenSEES	D	F	D	F
UniCT	OpenSEES	C	F	C	F
PoliBA	SAP2000	C	Mθ	C	Mθ

both beams and columns. Rigid diaphragms are included in all models for simulating the presence of RC floors.

UniRM3 and UniNA-Rosati analyze in OpenSEES a model with distributed plasticity elements similar to the one used by UniCH.

UniCT and UniSA develop very similar models in OpenSEES adopting concentrated plasticity elements. The non-linearity is concentrated at both ends of beams and columns in which the plastic hinges is modelled with fiber elements (namely "beamWithHinges" element in OpenSEES). Different approaches are used in order to simulate the floors: UniCT develops a model with rigid diaphragms and axial load releases for beams (Barbagallo et al. 2018), while UniSA adopt equivalent elastic trusses.

Models with rigid floor diaphragms are also developed and the effects of this a different simulation are discussed in the following section.

UniPR use the software Abaqus and adopt a model with plastic hinges including M-θ laws by NTC (2008). Finally, the model developed by UniNA-Verderame in OpenSEES accounts for a novel concentrated plasticity approach proposed by Verderame and Ricci (2017) to which readers can refer for further details.

3.3 Analysis of Results

The comparisons of the results obtained by different UR in terms of capacity curves are reported in Figs. 3 and 4 for the analyses performed along the Y- and X-direction, respectively.

Considering the two analyzed directions, significant differences can be observed in terms of both maximum strength and stiffness.

Seismic resistant frames are disposed along the Y-direction resulting in higher stiffness and strength than X-direction along which only thick beams are present.

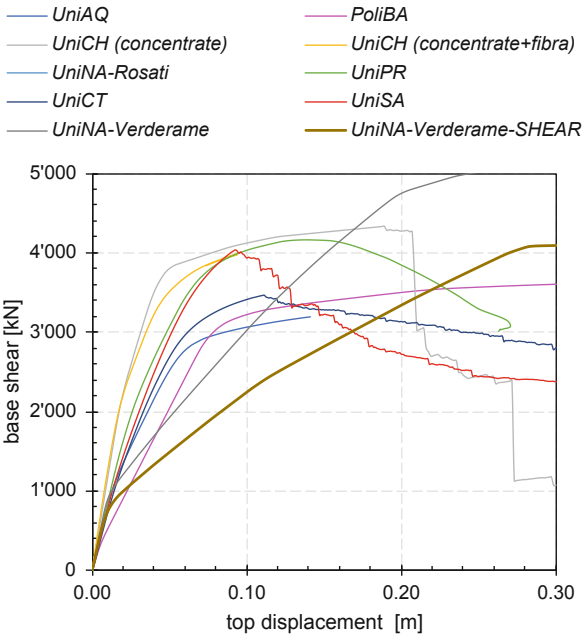

Fig. 3. Capacity curves along Y-direction.

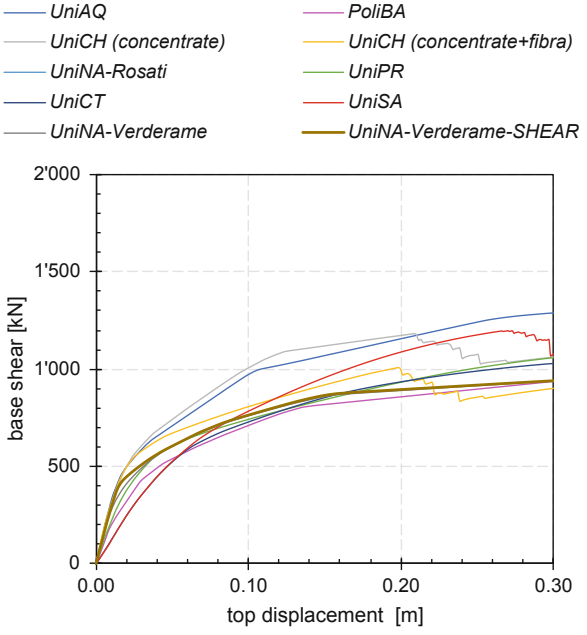

Fig. 4. Capacity curves along the X-direction.

Moreover, column cross-sections are all disposed with the strong axis along the Y-direction.

A substantially equal response in term of stiffness and strength is observed considering the results outlined by the various UR. As expected the initial stiffness is quite equal along both the Y- (Fig. 3) and X-direction (Fig. 4), while relevant differences are obtained in terms of maximum strength especially along the Y-direction (Fig. 3).

Similar strength and peak load displacement are observed for distributed plasticity models accounting only for members' flexural response. With respect to such models, different strength and peak load dis-placement are registered when adopting a lumped plasticity model based on empirical formulations dedicated to RC elements with plain bars (Verderame and Ricci 2017) accounting also for their deformability due to shear and fixed-end rotation.

3.3.1 Influence of the "Fictitious Compression" of Beams Related to the Rigid Floor Diaphragms Modelling

Floor slabs in RC buildings are usually characterized by high stiffness in their own plane. This may be simulated by introducing rigid diaphragms that constraint mutual displacements between nodes of the same floor. On the other hand, beams are often modelled as one-dimensional elements connected at their ends to the floor nodes.

Figures 5 and 6 report the capacity curves along the Y- and X-direction, respectively, derived by the UR which simulate the RC floors by means of rigid diaphragms. The curves are compared with the ones already depicted in Figs. 3 and 4 referring to the basic models used by UR. Such curves are reported in grey in Figs. 5 and 6 with the aim of highlight the effects obtained as a result of the fictitious compression induced in beams by the rigid constraint. The interaction between beam elements and the rigid diaphragm may distort the response of the beams in which the elongation under flexural actions of the center fiber (as after cracking the neutral axis shifts from the center of the section and the longitudinal axis of the beams tends to elongate) is prevented by the rigid diaphragm which in turn transmits a fictitious (compression) axial force to the beam. This axial force leads to the overestimation of the bending moment resistance, which in turn determines an inaccurate prediction of the structural response and modify the collapse mechanism. Such an effect is more relevant along the X-direction where there are not seismic resistant frames.

The drawback described above may be overcome by introducing an additional element in the FE model, named "axial buffer element" (Barbagallo et al. 2018), which is a Zero-Length element that connects one end of each beam to the corresponding node in the rigid diaphragm.

The axial stiffness of the buffer element is very low in order to allow the beams to deform axially freely and prevent the development of the fictitious axial force. Instead, the shear and flexural stiffnesses of this element are very high to restore the continuity of the structure and ensure the transmission of shear force and bending moment.

The nonlinear analysis executes by OpenSEES numerical models subjected to seismic excitation shows that the use of the buffer element leads to a more reliable estimation of the bending moment resistance of the beams and to a more accurate prediction of the seismic response of the structure.

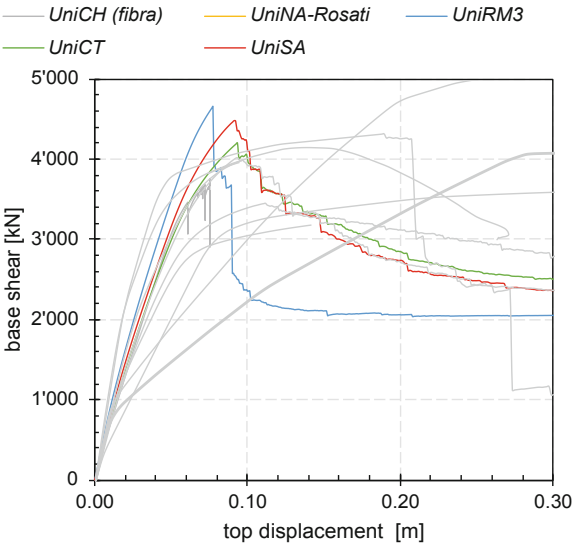

Fig. 5. Capacity curve along Y-direction in models with rigid diaphragm.

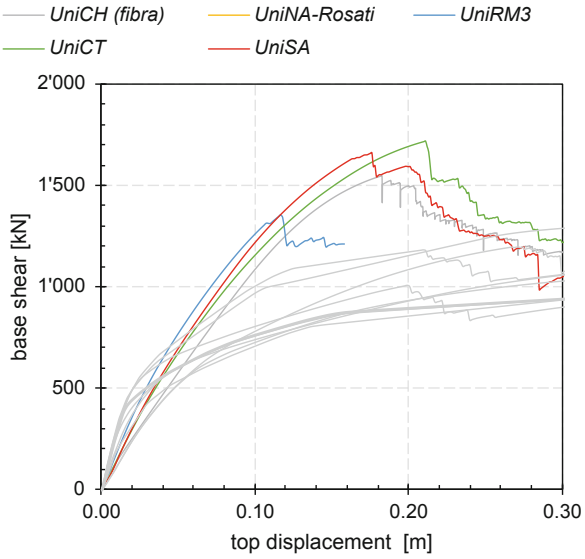

Fig. 6. Capacity curve along X-direction in models with rigid diaphragm.

A different approach is adopted by UniSA in order to reduce the development of the fictitious axial force. Specifically, floor slabs are modelled with elastic equivalent truss elements and, as it emerges from Figs. 5 and 6, such a simulation leads to accurate

prediction of the seismic response of the structure which results to be close to the one obtained by using the more refined "axial buffer element".

4 Conclusions

The present work outlines the non-linear modeling techniques adopted by the WP2 group of the ReLUIS Research Project 2017 in order to perform pushover analysis on representative numerical models of an existing structure not designed according to the principles of Capacity Design. The collaboration between the research units (UR) about the definition of the relevant input data, made it possible to minimize the uncertainties (e.g. geometric dimensions, applied loads, mechanical properties of the materials) and obtain a realistic assessment of the numerical model associated with the use of different modeling techniques.

Therefore, the work is intended as a tutorial guide to technicians working on seismic assessment of existing RC buildings through non-linear analyses. The differences in the results obtained using different modeling techniques and different seismic analysis codes show a non-negligible sensitivity to the numerical prediction of the structural response both in terms of resistance and deformation capacity. Relevant is the study of the effect on the structural response of the floor stiffness simulation by diaphragm constraint, which can introduce a fictitious compression in beams altering their bending strength and therefore led to unrealistic estimations of both the structure response and the collapse mechanism.

Acknowledgements. The authors wish to thank UniRM3, FIP Industriale, and designers involved in the retrofitting intervention for making available the relevant data of the De Gasperi-Battaglia structure. Moreover, they gratefully acknowledge the DPC-ReLUIS consortium for the financial support within the framework of the 2014-2018 Research Project, which this work belongs to.

References

Bae S, Mieses AM, Bayrak O (2005) Inelastic buckling of reinforcing bars. J Struct Eng 131 (2):314–321

Barbagallo F, Bosco M, Ghersi A, Marino E, Rossi P (2018) The combined effect of rigid diaphragm and beam modelling in rc buildings under pushover analysis. In: 16th European Conference on Earthquake Engineering. Thessaloniki, Greece

Bazant Z, Oh B (1983) Crack band theory for fracture of concrete. Mater Struct 16:155–177

Cosenza E, Prota A (2006) Experimental behaviour and numerical modelling of smooth steel bars under compression. J Earthq Eng 10(3):313–329

Brunetta M, Bandini L, De Lorenzi M (2006) SAP2000, analisi lineare/non lineare integrata con verifiche per strutture tridimensionali. CSI Computer and Structures Inc. http://www.csi-italia.eu/software/sap2000/. Accessed 1 Mar 2018

CSPFEA (2018) Midas Gen FX Manual, CSPFEA Engineering solutions. http://www.cspfea.net/portfolio_page/midas-gen-fx/. Accessed 1 Mar 2018

Dassault Systèmes Simulia Corp. (2017) Abaqus/CAE user's guide, Providence, RI, USA. https://www.3ds.com/it/prodotti-e-servizi/simulia/prodotti/abaqus/. Accessed 1 Mar 2018
De Stefano M, Tanganelli M, Viti S (2013) Effect of the variability in plan of concrete mechanical properties on the seismic response of existing RC framed structures. Bull Earthq Eng 11(4):1049–1060
Dhakal R, Maekawa K (2002) Modeling for postyield buckling of reinforcement. J Struct Eng 128(9):1139–1147
FEMA356 (2000) Prestandard and commentary for the seismic rehabilitation of buildings. Federal Emergency Management Agency, Washington
Ferretti D, Iori I, Morini M (2002) La stabilità delle strutture. Il caso delle costruzioni in cemento armato (in Italian). McGraw-Hill Companies, ISBN 9788838660337
fib (2003) Seismic assessment and retrofit of reinforced concrete buildings. fib Bulletin No. 24, Lausanne
fib (2008) International federation of structural concrete practitioners' guide to finite element modelling. Fib Bulletin n°45, Lausanne
fib-MC2010 (2012) International federation of structural concrete. Model Code 2010. Final draft. Fib Bulletin No. 65 & 66, Lausanne. Vol. 1, 2
Filippou F, Popov E, Bertero V (1983) Effects of bond deterioration on hysteretic behavior of reinforced concrete joints. Report EERC 83-19, Earthquake Engineering Research Center, University of California, Berkeley
Fragiadakis M, Vamvatsikos D, Aschheim M (2013) Application of nonlinear static procedures for seismic assessment of regular RC moment frame buildings. Earthq Spectra 30(2):767–794
Franchin P, Pinto PE, Rajeev P (2010) Confidence factor? J Earthq Eng 14(7):989–1007
Jalayer F, Iervolino I, Manfredi G (2010) Structural modeling uncertainties and their influence on seismic assessment of existing RC structures. Struct Saf 32:220–228
Kent D, Park R (1971) Flexural members with confined concrete. J Struct Div 97(7):1969–1990
Kupfer H, Hilsdorf H, Rusch H (1969) Behavior of concrete under biaxial stresses. ACI J 66:656–666
Li CQ (2004) Reliability based service life prediction of corrosion affected concrete structures. J Struct Eng 130(10):1570–1577
Mander J, Priestley M, Park R (1984) Theoretical stress-strain model for confined concrete. J Struct Eng ASCE 114(3):1804–1826
Mau S, El-Mabsout M (1989) Inelastic buckling of reinforcing bars. J Eng Mech 115(1):1–17
Mazzoni S, McKenna F, Fenves GL (2010) Getting started with OpenSees manual. Pacific Earthquake Engineering Research Center University of California, Berkeley. http://opensees.berkeley.edu/wiki/index.php/Getting_Started. Accessed 1 Mar 2018
Menegotto M, Pinto P (1973) Method of analysis for cyclically loaded reinforced concrete plane frames including changes in geometry and non-elastic behavior of elements under combined normal force and bending. In: International Association of Bridge and Structural Engineering. Lisbon, Portugal, 13: 15–22
Monti G, Nuti C (1992) Nonlinear cyclic behavior of reinforcing bars including buckling. J Struct Eng 118(12):3268–3284
NTC (2008) Norme tecniche per le costruzioni, D.M. 14/01/2008. Gazzetta Ufficiale n. 29 del 04.02.2008, Suppl. Ord. n.30
Popovics S (1973) A numerical approach to the complete stress strain curve for concrete. Cem Concr Res 3(5):583–599
Prota A, De Cicco F, Cosenza E (2009) Cyclic behavior of smooth steel reinforcing bars: experimental analysis and modeling issues. J Earthq Eng 13(4):500–519

Reinhorn AM, Roh H, Sivaselvan M, Kunnath SK, Valles RE, Madan A, Li C, Lobo R, Park YJ (2009) IDARC2D Version 7.0: A program for the inelastic damage analysis of structures, MCEER-09-0006 | 7/12/2009 | 406 pages

Scott, Park R (1982) Stress-strain behavior of concrete confined by overlapping hoops at low and high strain rates. ACI Struct J 79(1):13–27

Silva V, Varum H, Crowley H, Pinho R (2012) Extending displacement-based earthquake loss assessment (DBELA) for the computation of fragility curves. In: Proceedings of the 15th ECEE, Lisbon (PT), 24–28 September 2012

Tabbakhha M, Modaressi-Farahmand-Razavi A (2016) Analyzing the effect of workmanship quality on performance of unreinforced masonry walls through numerical methods. Comput Struct 167:1–14

Verderame GM, Ricci P (2017) An empirical-based approach for modeling and assessment of RC columns with plain bars. VI COMPDYN, Rhodes, Greece, June 2017

Modeling the Seismic Response of Vertical Concrete Cladding Panels

G. Menichini[1(✉)] and T. Isaković[2]

[1] Department of Civil and Environmental Engineering, University of Florence, Florence, Italy
giovanni.menichini@unifi.it
[2] Faculty of Civil and Geodetic Engineering, University of Ljubljana, Ljubljana, Slovenia

Abstract. During the recent earthquakes in Northern Italy many RC precast industrial buildings were seriously damaged. Amongst different types of damage, many falls of cladding panels were occurred. Consequently, many doubts about current knowledge about their seismic behaviour have been expressed.

To study the seismic response of claddings in real conditions and their influence on the system response of whole structure a series of full-scale shake table tests was performed by the University of Ljubljana in cooperation with IZIIS, Macedonia. The results of these experimental campaign were used to define and calibrate appropriate numerical models for the main structure, claddings and cladding-to-structure connections. These models are presented in the paper.

Keywords: Seismic response · Precast RC buildings · Vertical cladding panels · Mechanical connections · Hammer-head-straps · Numerical models · Nonlinear response history analysis

1 Introduction

In May 2012, the Emilia region was hit by two strong earthquake events. It was not historically considered as seismic, although also in the past it was affected by some intense earthquakes, such as that of Ferrara surroundings in 1570–1574. For these reasons, almost all the precast industrial buildings stroked by the earthquake had been designed without considering the effect of horizontal forces. It has been estimated that in these industrial areas, a large number of precast buildings suffered total failure or have been severely damaged, resulting in an important economic loss due to the interruption of production activities (Magliulo et al. 2013). These collapses confirmed that structures which are not properly designed are very vulnerable to the seismic actions. The connections failure between the various monolithic parts of buildings has been the main cause of most collapses. The large story drifts at the top caused the loss of support of the precast beams from the columns or of roofing tiles from the beams.

M. di Prisco and M. Menegotto (Eds.): ICD 2018, LNCE 42, pp. 96–109, 2020.
https://doi.org/10.1007/978-3-030-23748-6_8

In particular, collapses involving RC precast panels were caused by the inadequacy of their fastening systems on the support elements. Indeed, the connections of cladding panels to structural system were never explicitly designed for seismic load in the plane of panels, because of the lack of knowledge and understanding of the complexity of the problem (Bournas et al. 2014). For these reasons were some doubts about the seismic behaviour of these buildings and their panel to main frame connections. With the aim to better understand the behaviour of connection and to improve some results obtained by means of experiments performed on single components or subassemblies, a shaking table investigation campaign was performed at University of Ljubljana in cooperation with IZIIS, Macedonia. The experimental campaign was carried out in July 2017. In the paper, numerical modelling of the experiment is presented. In the following, Sect. 2 a brief description of experiment is displayed. Two types of vertical panels' configurations (fixed and rocking) and two types of connection were tested. In Sect. 4 mainly modeling of fixed panel is presented and hysteretic model of connection is explained. In Sect. 5 some possibilities and initial questions about numerical model of rocking panels are illustrated.

2 Brief Overview of the Experimental Study

2.1 Tests Set-Up

The tested full-scale prototype consisted of four 4.5 m high RC columns (30 ×30 cm) casted together with pad foundations, an RC slab and two vertical 15 cm thick concrete cladding panels (Fig. 1) for all elements, the class of concrete is 40/50 and the class of steel is S 500B. The mass of the slab was 8.6 t. The mass of one column was 1 t. The total height of each panel was 5.65 m and its mass were 3.6 t.

Typical mechanical connections, mostly used in West and Central Europe, were implemented to attach the cladding panels to the main structure. Two types of connection were applied and tested: the existing hammer-head-strap and the innovative one. Each vertical panel was attached to the RC slab by means of two hammer-head strap connections. Four configurations of vertical panels were tested, which differed in the type of connections between the panel and the slab and between the panel and the steel plate (Table 1).

2.2 Claddings – Main Structure Connections

In detail, the top connections consisted of a special steel strap (TA-210 or TA-290), a toothed washer, a bolt and two hot rolled steel channels with anchors, which were installed before casting the elements. One of the channels was casted in the panel whereas the other was casted in the slab.

Finally, the head of the strap was fixed inside the channel, which was casted in the panel (Fig. 2). In this way, the connection between the panel and the slab was created.

The design of the models was performed at the University of Ljubljana, Faculty of Civil and Geodetic Engineering, while the building of the prototype and panels was carried out in Kolektor CPG d.d, Nova Gorica, Slovenia.

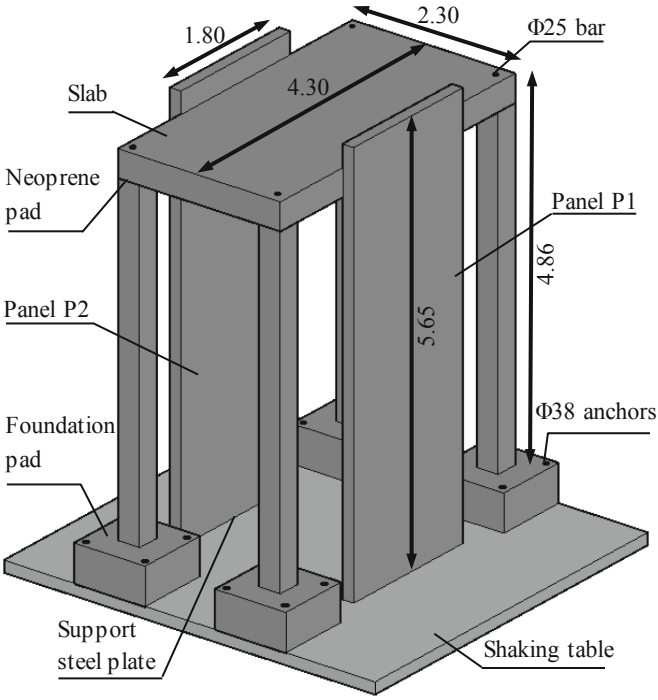

Fig. 1. Geometry and configuration of the tested specimen

Table 1. Summary of the tested configuration.

Label	Claddings-Structural connection	Claddings-ground connections	Number of panels
V1	Hammer-Head strap (TA 290)	Rocking	2
V1e*	Hammer-Head strap (TA 290)	Rocking	1
V2	Hammer-Head strap (TA 210)	Rocking	2
V2e*	Hammer-Head strap (TA 210)	Rocking	1
V3	Hammer-Head strap (TA 210)	Fixed	2
V4	Hammer-Head strap (TA 290)	Fixed	2

*The subscript "e" accounts for eccentricity in the model (removing one panel)

2.3 Shaking Table Characteristics and Input Acceleration

The IZIIS' 5 DOF seismic shaking table is proportioned 5.0×5.0 m in plan and is characterized by a play load of 40.0 t. The shake table tests were performed in several steps increasing the input intensity of the earthquake and monitoring the values of measured physical parameters necessary to assess the performance of the connection and of the entire structure. Petrovac E-W ground motion record was used in all test. The record was modified to match the Eurocode 8 spectrum. Starting from selected accelerogram, a series of scaled acceleration, form 0.1 g to 0.5 g were imposed to the shake table until severe damage or failure was reached in panels-structure connections.

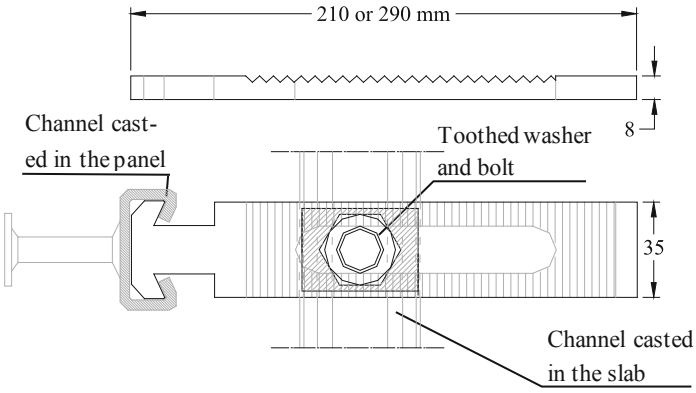

Fig. 2. Dimension of straps in the connection

3 Description of Numerical Models

3.1 Overview of Models

The computational framework Open System for Earthquake Engineering Simulation (OpenSees) (Mazzoni et al. 2009) was used to develop a numerical model of the structure panels and connections. The program has a large library of finite elements that can be employed for nonlinear analysis. Forced based elements were used to model columns also considering the P-Delta effect. The zero length elements were used to represent connection and elastic support, as shown in Fig. 3 below.

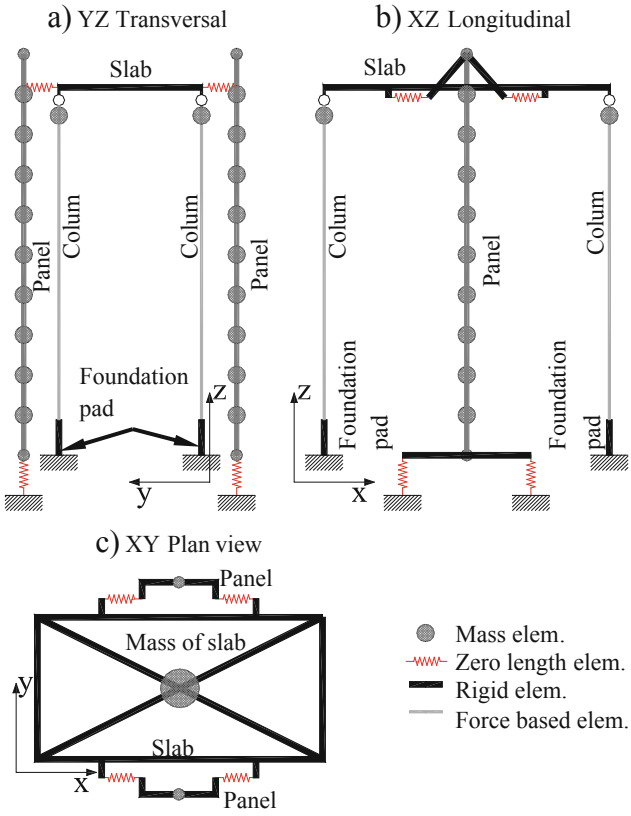

Fig. 3. Numerical model outline

More details about numerical modeling are presented in the next subsections. The modeling and the discretization of the masses are described in subsect. 3.2. Model for panels is explained in subsect. 3.3, while the model for columns in 3.4. Connections mechanism and modeling are explained in subsects. 3.5 and 3.6.

3.2 The Model of Masses

The masses were schematically lumped in the model nodes.

Mass of the slab was concentrated in the central node at the roof level (Fig. 3c), i.e. the mass centre, was assumed as the geometrical centroid of the roof slab.

The panels' mass was clearly distributed uniformly over their height. To catch an accurate response the panels, the mass was idealized using an 11-node lumped-mass model (Fig. 3a, b).

For the columns, their half mass is lumped to element ends (Fig. 3a, b).

Assumed values for the lumped masses are listed in the following Table 2.

Table 2. Masses position and value

Mass position		Mass value [t]
Centre of slab	m_s	8.60
Top of columns	m_c	0.50
Top and bottom of panels	$m_{p,tb}$	0.18
Middle joints of panels	$m_{p,m}$	0.36

3.3 The Model of Panels

In the panels, no yielding and no plastic deformations were observed during the all performed tests. For this reason, OpenSees' *elasticBeamColumn* element was used to model the panels. This type of element has a completely elastic behaviour. In the table below (Table 3) the properties of the cross-section are presented:

Table 3. Inertial characteristic of panel's elastic section

Properties	A [m^2]	J [m^4]	I_z [m^4]	I_y [m^4]
Panel	0.27	$2.02 \cdot 10^{-3}$	0.07	$5.06 \cdot 10^{-4}$

where: A is the area of cross-section, J is the torsional moment of inertia and I_z, I_y are the bending moments of inertia respect to the main axes of the section. The elastic modulus od C45/50 concrete is assumed 34.64 GPa and the shear modulus, with a Poisson coefficient $\nu = 0.2$, is G = 14.43 GPa.

Also, the rigid members were modelled with an *elasticBeamColumn* element type by assigning to them a quite large inertial characteristic.

3.4 The Model for Columns

To model the columns, three different types of elements were taken into consideration and compared:

1. A classic fiber model element (Spacone et al. 1998).
2. An element with concentrated plasticity, where the response of the non-linear hinges was defined by Takeda's hysteretic rule (Takeda et al. 1970).
3. A nonlinear force-based element where the non-linear response was defined with moment-curvature behaviour.

1. The first approach is widely used due to its capability of describing nonlinear structural behaviour. This type of model is quite able to accommodate random fields of structural properties of RC frame members. In the test, the initial stiffness was much lower than that correspond to gross cross-section. It has been an issue to reduce the initial stiffness in the fiber model. Some numerical issues were also observed in this model: a quite large and unreal vertical acceleration were observed using this model.

2. The second approach has the advantage of the simplicity of the formulation and a considerably reduction of the computational cost. On the other hand, the length of the plastic hinge is not a priori known, and it should be estimated. For this purpose the formulation that can be found in the literature, can be used, i.e. from Paulay and Priestley (1992).
3. The third approach is intermediate solution between the two described above.

The third approach was adopted to model the columns of the structure. The *forceBeamColumn* element was chosen from OpenSees' element library at each integration point, the response was defined by the moment curvature relationship, provided as input data.

In order to obtain the moment-curvature diagram, an OpenSees procedure was used, considering, among those available in the program library, the Popovics model (Mander et al. 1988) both for unconfined and confined concrete and Giuffré-Menegotto-Pinto model (Filippou et al. 1983) for S500 reinforcement steel.

Subsequently, the curve was bilinearized through the principle of equivalence of the areas. In the presented (2) and (3) approaches, the initial stiffness was possible easily to reduce without numerical problem. The reduction can be obtained by modifying the slope of the bilinear elastic branch, as shown in Fig. 4.

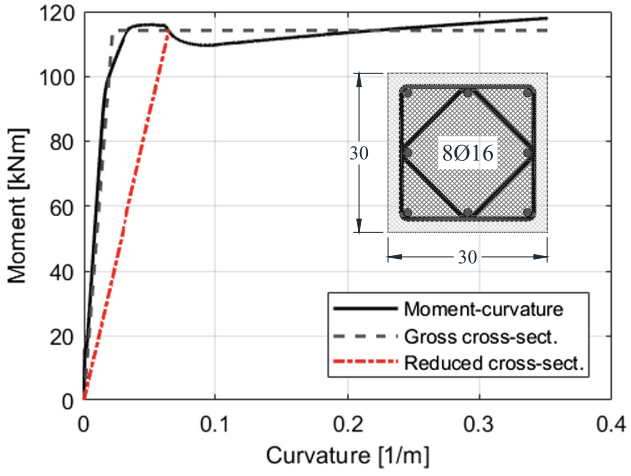

Fig. 4. Colum's section moment-curvature relationship

Although in all performed shaking table test, no yielding and no plastic deformations were observed, it was decided to prepare the numerical model for further analysis in nonlinear field, so a non-linear behaviour for columns was chosen.

3.5 The Model of Panels' Connection with Foundations

Two elastic springs were placed at the base of the panels (Fig. 3b). In case of fixed panels (test V3 and V4) the stiffness given to the springs was considerably high such that these could be considered as full fixed restraints. In the case of rocking panels, a nonlinear elastic behaviour was assigned to the panel's base spring such that they had a high stiffness in compression and very low stiffness in tension. In this way, the two springs were able to simulate a unilateral support to allow the panel to freely uplift.

3.6 The Model of Panels' Connection with the Main Structure

The model was defined based on the previous research performed by Zoubek et al. (2016). There are two important modifications of this model:

1. Due to the force applied perpendicular to the panel, resulting from a realistic seismic excitation, some stiffness of the connections was activated from the very beginning of the response, because the strap was almost immediately in contact with the channel casted in the panel. This stiffness limits the strap's rotation around the fixing bolt.
2. Before the failure of the strap at the large displacement demand, the stiffness was considerably increased due to the impact between the panes and the strap. This was taken into account in the numerical model.

The complete cyclic response of connection can be simulated by combining four different hysteretic models, which are included in the OpenSees materials library: *Elastic*, *ElasticPP*, *ElasticPPgap* and *Hysteretic*.

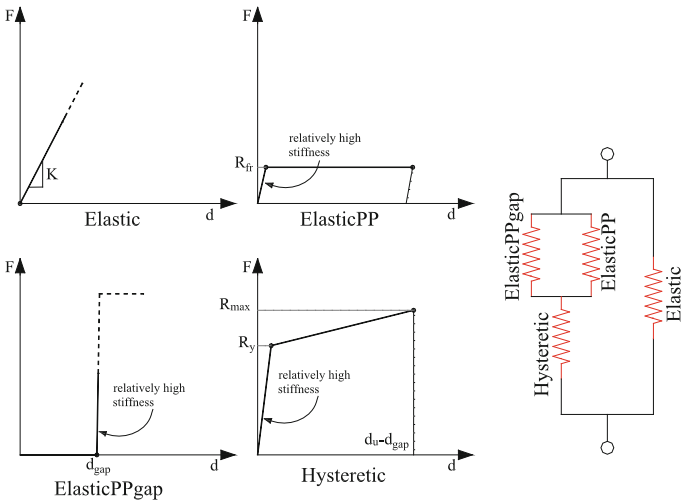

Fig. 5. Materials combination for numerical model of hammer-head strap

These four behaviours should be combined as it is shown in the previous Fig. 5.

The *ElasticPP* behaviour simulates the friction between the hammer-head-strap and the concrete beam due to the tightening torque in the bolt.

The *ElasticPPgap* behaviour is added in parallel to simulate the beginning of stiffness increase that occurs when the head of the strap becomes stuck inside the channel in the panel.

The *Hysteretic* behaviour is added in series to simulate the nonlinear response of the neck of the strap. Finally, the *Elastic* behaviour is added in parallel to limit the rotation due to stiffness activated by force applied perpendicular to the panel.

Hysteretic behaviour model included in OpenSees is determined by five hysteretic parameters: p_x; p_y; α; d_1 and d_2. In order to properly model the response of the hammer-head strap connection, all these parameters should be set, in order, as follow 0.8; 0.4; 0; 0; 0.2.

The main parameters to input for the correct definition of materials that form the connection behaviour are listed in the table below (Table 4).

Table 4. Input parameters for strap behaviour modeling

Strap type	Input parameters					
	K [1/m]	R_{fr} [kN]	d_{gap} [m]	R_y [kN]	R_{max} [kN]	d_u-d_{gap} [m]
TA-210	$1.2 \cdot 10^2$	0.5	0.020	1.44	12	0.085
TA-290	$1.2 \cdot 10^2$	0.5	0.030	1.21	10	0.098

4 Analysis of the Structure with Fixed Panels

4.1 Response of the Structure

In the tests with the panels fixed (V3 and V4) no damage was observed both in the structure and in the panels.

However, during the test V3, for the highest seismic intensity equal to 0.5 g, one of the short hammer-head strap failed at the displacement demand of about 85 mm.

With the developed numerical model, it was possible to simulate in a fairly accurate way the response obtained during the test and the failure of connections. After the failure of the straps, there is a noticeable acceleration increase both in the structure and in the panels, which cannot be correctly approximated by the used numerical model.

The results are illustrated in terms of acceleration of the main structure measured at the slab (Fig. 6), and of acceleration at the top of the panel (Fig. 7).

The results can be also depicted in terms of displacement. In Fig. 8, it can be observed that, after the failure of the short strap in test V3, the numerical response history and the experimental one deviate considerably, which does not happen for the test V4, where the long straps could withstand the seismic intensity of 0.5 g.

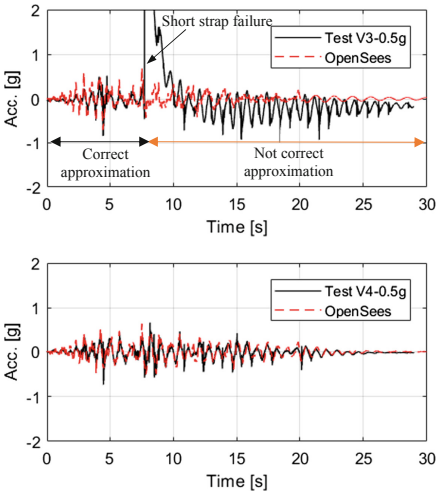

Fig. 6. Slab acceleration for test V3 and V4 at 0.5 g

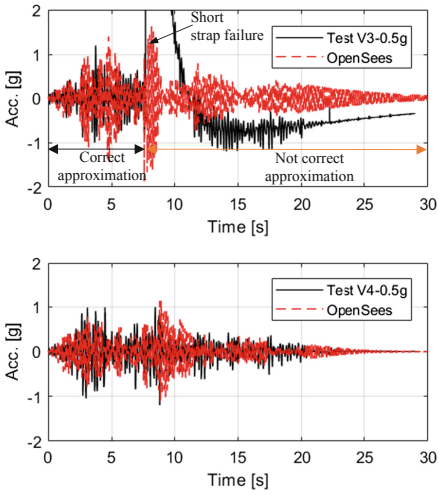

Fig. 7. Panel P1 top acceleration for test V3 and V4 at 0.5 g

In order to correctly match the real response after the connections' failure, the numerical model will be improved.

It could be worthy to show the global hysteretic behaviour of the structure in terms of acceleration by relating the slab's acceleration and displacement (Fig. 9).

4.2 Response of Connection

Since the numerical model approximates quite well the response of the structure and panels both in terms of acceleration and displacement, it is reasonable to suppose that the elasto-plastic model of the connections presented in paragraph 3.5 is plausible. However, in the absence of specific and direct measurements of force and displacement in the connections during the tests, it has not been possible yet to compare the real behaviour with the numerical one, which is reported in Fig. 10 for an input acceleration scaled to 0.5 g.

Figure 10 showed what expressed in subsect. 3.6: the stiffness increases at large displacement due to the impact between strap's head and panel. The forces perpendicular to panels' plane also slightly increased the stiffness of the connection from the very beginning of the response. Further physical considerations can be found in the work of Isaković et al. (unpubl.).

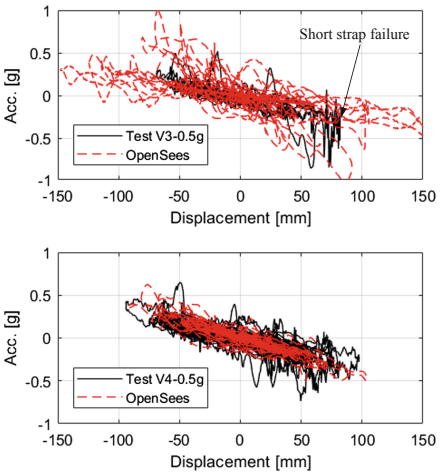

Fig. 9. Acceleration-displacement relationship for test V3 and V4 at 0.5 g

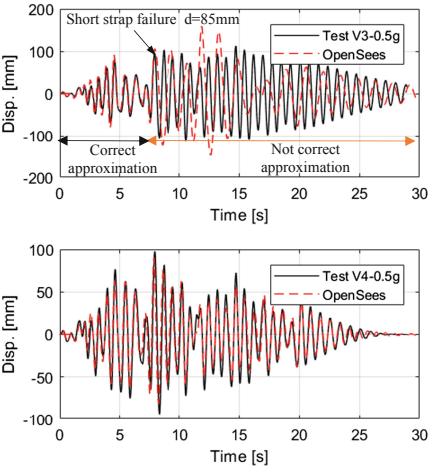

Fig. 8. Slab displacement for test V3 and V4 at 0.5 g

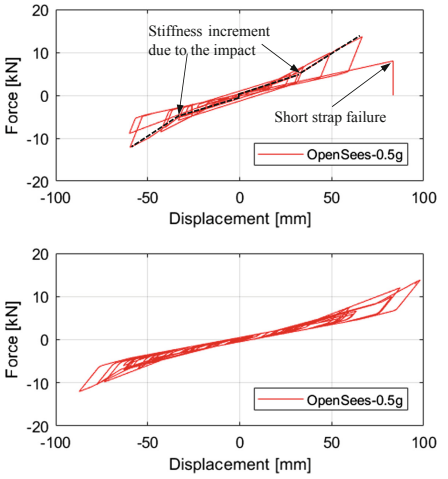

Fig. 10. Connections hysteretic behaviour in the numerical model for test V3 and V4 at 0.5 g

5 Rocking Panels

5.1 Numerical Model

The model is still the matter of study because it is more complex mostly for these two reasons:

1. The panels are uplifting, and this uplift should properly modeled.
2. The top of the panels and the connections moved in horizontal as well as in vertical direction.

During the seismic excitation the following mechanism was observed (Fig. 11):

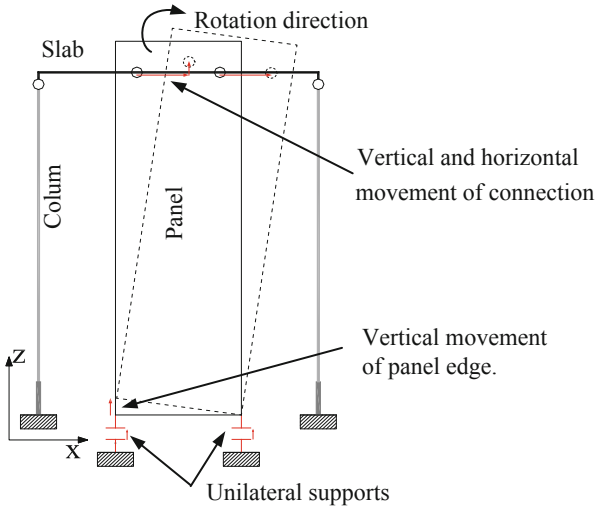

Fig. 11. Framework behaviour of rocking panels

1. As long as the horizontal displacement of the connection was small, and any deformation occurred in the strap, the vertical sliding between the strap head and the channel casted on the panel can freely occur.
2. When the horizontal displacement was widely increased, the strap's head was deformed in the horizontal direction and was stacked inside the channel. The uplift of the panel caused the uplift of the strap.
3. When the panel moved downwards, the connection was pulled down by the panel, and deformed in the vertical direction.

Consequently, while the horizontal behaviour of the straps can be approximated with the one described in paragraph 3.6, the vertical behaviour is more complex and quite difficult to predict. For these reasons, the numerical model needs to be improved in order to correctly match the response obtained during the tests V1 and V2.

6 Conclusions

A full-scale experiment on one storey RC precast structure was recently performed by the University of Ljubljana, in cooperation with IZIIS, Macedonia, using their large shake table. The main purpose was to study the response of precast building with two types of cladding panels: fixed at the base and these which were allowed to rock.

The aim of the study, presented in this paper was to model the experimentally observed response, with special emphasis on the connections between panels and main structure.

In the paper, a numerical model for the typical hammer head strap connections is described. It is based on a previous work performed at the University of Ljubljana. Two important modifications were made:

1. Activation of some stiffness, due to the force applied perpendicular to the plane of panels, was taken into account.
2. An increase of the stiffness in the connections, due to the impact between the panel and the straps, was also considered.

The results provided by the numerical model for the structure with fixed panels agree with the experimental quite well. The only exception is the response after the failure of the straps. The numerical model for rocking panels still have to be improved. The model of the connections should be enhanced to be able to describe the interaction of the straps' vertical and horizontal movement and deformation.

However, this is a challenge that will be addressed in the continuation of this research project.

Acknowledgements. The experimental campaign was funded by Slovenian National Research Agency within the project "Seismic resilience and strengthening of precast industrial buildings with concrete claddings". The authors intend to thank the Kolektor CPG company – construction plant Laže for the tests specimen preparation.

Prof. dr. Matej Fischinger for making available the experimentation data. Finally, the authors are grateful to prof. dr. Golubka Nečevska Cvetanovska, prof. dr. Roberta Apostolska, prof. dr. Lidija Krstevska and prof. dr. Zoran Rakićević, from IZIIS, for their help during the planning of the experiments and their execution.

References

Bournas DA, Negro P, Taucer FF (2014) Performance of industrial buildings during the Emilia earthquakes in Northern Italy and recommendations for their strengthening. Bull Earthq Eng 12(5):2383–2404. https://doi.org/10.1007/s10518-013-9466-z

Filippou FC, Popov EP, Bertero VV (1983) Effects of bond deterioration on hysteretic behavior of reinforced concrete joints. University of California, Earthquake Engineering Research Center. https://books.google.si/books?id=hycIAQAAIAAJ

Isaković T, Zoubek B, Fischinger M (unpublished) Full-scale shake table tests of vertical cladding panels in one-storey RC precast industrial buildings. Ljubljana

Magliulo G, Ercolino M, Petrone C, Coppola O, Manfredi G (2013) The Emilia earthquake: seismic performance of precast reinforced concrete buildings. Earthq Spectra 30(2):891–912. Earthquake Engineering Research Institute. https://doi.org/10.1193/091012EQS285M

Mander BJ, Priestley NMJ, Park R (1988) Theoretical stress-strain model for confined concrete. J Struct Eng 114(8):1804–1826 American Society of Civil Engineers. https://doi.org/10.1061/(ASCE)0733-9445(1988)114:8(1804)

Mazzoni S, Mckenna F, Scott MH, Feneves GL (2009) OpenSees: a framework for earthquake engineering simulation. University of California, Pacific Ea. Berkeley. http://opensees.berkeley.edu/OpenSees/manuals/usermanual/

Neuenhofer A, Filippou FC (1997) Evaluation of nonlinear frame finite-element models. J Struct Eng 123(7):958–966. American Society of Civil Engineers. https://doi.org/10.1061/(ASCE)0733-9445(1997)123:7(958)

Paulay T, Priestley MJN (1992) Seismic design of reinforced concrete and masonry buildings. Wiley Interscience Publication, New York. ISBN 978-0-471-54915-4

Spacone E, Filippou FC, Taucer F (1998) Fibre beam–column model for non-linear analysis of R/C frames: part I. Earthq Eng Struct Dyn 25(7):727–742. Wiley-Blackwell. https://doi.org/10.1002/(SICI)1096-9845(199607)25:7%3C727::AID-EQE577%3E3.0.CO

Takeda T, Sozen MA, Nielsen NN (1970) Reinforced concrete response to simulated earthquakes. American Society of Civil Engineers. https://books.google.si/books?id=-UIwGwAACAAJ

Zoubek B, Fischinger M, Isakovic T (2016) Cyclic response of hammer-head strap cladding-to-structure connections used in RC precast building. Eng Struct 119:135–148

Seismic Strength of One-Story Precast Building Dowel Connections

M. Cimmino[1], G. Magliulo[1,2(✉)], and G. Manfredi[2]

[1] Construction Technologies Institute ITC-CNR, Via Claudio 21, 80125 Naples, Italy
gmagliul@unina.it
[2] Department of Structures for Engineering and Architecture, University of Naples Federico II, Naples, Italy

Abstract. Typical European precast buildings commonly show dowel beam-to-column connections which consist of vertical steel dowels, embedded in the column and passing through or inserted in holes in the beam. These connections can be characterized by two different failure modes depending on the concrete cover/dowel diameter ratio so that the failure mode involves the yielding of the dowel and the crushing of the concrete around the dowel or the concrete cover splitting in the direction of the load or in the orthogonal direction (side splitting). In this paper, beam-to-column dowel connections are designed according to the Italian seismic building code and the Eurocode 8 general principles, for a set of case-study buildings, considering different geometrical layouts for primary structure and different seismic hazard levels. Different connection configurations are also considered and the connection shear strength is estimated taking into account code and literature formulations, in order to assess their seismic performance.

Keywords: Dowel connection · Connection shear strength · Single-story RC precast buildings · Connection seismic failure

1 Introduction

Single-story RC precast buildings are typically adopted in European regions for industrial, commercial, educational and/or sportive uses. This structural typology consists of socket foundations, vertical columns and pinned horizontal beams, covered by roof elements.

Recent earthquakes (Magliulo et al. 2014b; Ercolino et al. 2016; Faggiano et al. 2009) and experimental tests have shown that most of the collapses of industrial single-story RC precast buildings are related to beam-to-column connection and roof-to-beam connection collapses, even though, in some cases, these buildings were designed for seismic loads. For this reason, in the last years, experimental studies have been performed to determine the capacity of the more spread connection types, related numerical models and new types of connections have been developed (Magliulo et al. 2014a, 2015; Zoubek et al. 2015; Magliulo et al. 2017). As a consequence, new design

M. di Prisco and M. Menegotto (Eds.): ICD 2018, LNCE 42, pp. 110–123, 2020.
https://doi.org/10.1007/978-3-030-23748-6_9

formulae for these connections have been provided, which are not yet included in code provisions and spread design guidelines.

This paper investigates the seismic performance of industrial single-story RC precast buildings, designed according to the Italian building code and Eurocode provisions for different seismic hazard levels. In particular, dowel beam-to-column dowel connection seismic capacity is investigated using the recent available formulation in building codes and technical literature and considering all the possible failure modes that can activate for this type of connection, when subjected to cyclic shear loads.

2 Description of the Case Studies

2.1 Design and Geometry of the Primary Structure

The reference structure consists of precast columns fixed at the base with isolated socket foundations (Fig. 1): the sockets are connected in both directions by a concrete gridwork. The columns are connected, by means of dowel connections, to the main precast prestressed beams in the transversal direction (x direction), and by means of bolted connections to the secondary beams, in the longitudinal direction (z direction). The main precast beams show variable cross-section width and depth, with the top sloping at 10%. The longitudinal secondary beams are assumed to have a rectangular cross section. They are also connected to the main beams by bolted steel angles. The roof consists of precast adjacent TT elements. A rigid diaphragm is considered, obtained through a cast in situ concrete slab, 5 cm deep, which connects the ribs.

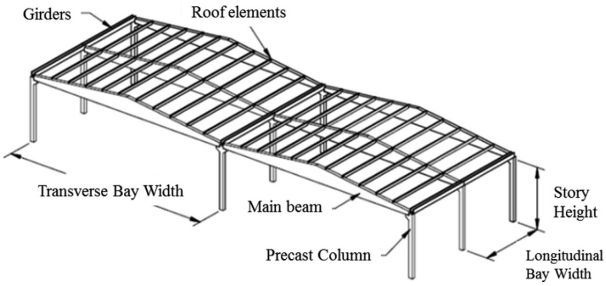

Fig. 1. Structural layout for industrial precast buildings

The cladding system consists of vertical precast panels (specific weight of 4 kN/m^2), connected to the horizontal roof beams (i.e. to the main beams, along the transversal direction, and to the secondary beams, along the longitudinal direction). Assuming industrial use for the building, the presence of a crane is considered: precast corbels in the internal side of the columns support crane runway beams to which the crane is connected. The crane runway beams are considered to be the same for all the case studies, i.e. HEA400 steel beam, assuming that they do not reach the maximum deflection level according to CNR provisions.

The reference buildings have one bay along x direction and four bays along z direction. The span length along x (L_1) and z direction (L_2) are assumed as variables so that two different geometries can be defined. In the following, geometries with L_1 = 15 m, L_2 = 6 m are defined as "short span" (SS), while geometries with L_1 = 20 m, L_2 = 8 m are defined as "long span" (LS). For both geometries, column height is equal to 9 m.

Table 1 shows the adopted materials for structural elements.

Table 1. Adopted materials for structural elements

Element	Concrete	Mild steel	Prestressing steel
Concrete slab	C25/30	B450C	–
Roof element	C45/55	B450C	Seven-wire strands
Precast main beam	C45/55	B450C	Seven-wire strands
Column	C45/55	B450C	

The precast structures are designed according to the Italian building code D.M. 14/01/2008 (2008) (for more details see also Ercolino et al. (2017), which complies with the Eurocodes (CEN 2005). Regarding the seismic forces, according to the Italian building code D.M. 14/01/2008, the seismic action can be evaluated using response spectra, related to the site hazard and the reference limit state. The site hazard is defined by the seismic hazard parameters (ag, F0, Tc*), for damage limit state DLS and life safety limit state (LLS), reported in the Annex B of the Italian building code, depending on the geographical position and on the return periods. Table 2 shows the adopted seismic parameters for the considered four sites, which allow to estimate design loads in order to perform the design procedure against the two limit states.

Table 2. Seismic hazard parameters

Site	Limit state	a_g [g]	F_o [–]	T_c^* [sec]
L'Aquila	DLS	0.104	2.332	0.281
	LLS	0.261	2.364	0.347
Napoli	DLS	0.06	2.335	0.312
	LLS	0.168	2.374	0.338
Roma	DLS	0.055	2.502	0.268
	LLS	0.123	2.633	0.288
Milano	DLS	0.024	2.554	0.191
	LLS	0.05	2.656	0.28

In the following, Tables 3 and 4 show the details of the elements carrying seismic forces, i.e. columns, with particular reference to the base sections.

Table 3. Column design details for SS buildings

Site	Soil type	B_{col} [m]	ρ [%]	Transversal reinforcement
AQ	A	0.75	1.29	3 ϕ10/6.5 cm
NA		0.75	1.29	3 ϕ10/6.5 cm
RM		0.75	1.29	3 ϕ10/6.5 cm
MI		0.75	1.00	5 ϕ10/11 cm
AQ	C	0.75	1.34	4 ϕ10/7 cm
NA		0.75	1.29	3 ϕ10/6.5 cm
RM		0.75	1.29	3 ϕ10/6.5 cm
MI		0.75	1.00	5 ϕ10/11 cm

Table 4. Column design details for LS buildings

Site	Soil type	B_{col} [m]	ρ [%]	Transversal reinforcement
AQ	A	0.85	1.25	4 ϕ10/7.5 cm
NA		0.85	1.25	4 ϕ10/7.5 cm
RM		0.85	1.25	4 ϕ10/7.5 cm
MI		0.85	1.00	3 ϕ10/5.5 cm
AQ	C	0.90	1.71	7 ϕ8/8 cm
NA		0.90	1.09	5 ϕ10/9 cm
RM		0.85	1.25	4 ϕ10/7.5 cm
MI		0.85	1.00	3 ϕ10/5.5 cm

The presented case studies have been investigated in Ercolino et al. (2017) and it has been observed that they show very high safety ratios, with respect to the attainment of the collapse limit state related to the column failure. Table 5 shows structural capacities in terms of lateral displacement, i.e. the roof horizontal displacement which corresponds to a 50% degradation of the base shear on the pushover curves. For this reason, in the following, high attention is paid to the collapse of dowel beam-to-column connections which showed weak performance during recent earthquakes.

2.2 Design and Geometry of the Dowel Connection

Design procedure and construction details for the adopted beam-to-column dowel connections are described in the following.

The considered configuration consists of two vertical threaded bars embedded in the column for a length h_d equal to eight times their diameter, passing through the beam and fixed on its bottom surface thanks to nuts and washers. A neoprene pad (1 cm thick) is placed between beam and column so that the whole beam width can be held and the vertical dowels result to be symmetric with respect to the beam longitudinal axis. The pad depth in the direction of the main beam is dimensioned so that the dowels stay in its middle. The neoprene pad is designed according to CNR10018 (1989).

Table 5. Structural displacement capacity

Site	Structural displacement capacity [m]				
	Soil type	SS		LS	
		X	Z	X	Z
AQ	A	0.871	0.926	0.861	0.928
NA		0.871	0.926	0.861	0.928
RM		0.870	0.926	0.861	0.928
MI		0.831	0.884	0.834	0.899
AQ	C	0.923	0.981	0.920	0.991
NA		0.871	0.927	0.853	0.920
RM		0.871	0.927	0.861	0.928
MI		0.832	0.884	0.834	0.899

The vertical threaded bars are designed according to the capacity design approach, in order to avoid the connection failure before the formation of the plastic hinge in the column base. For this reason, connections are dimensioned for the minimum between: (a) a shear force determined from the seismic analysis, assuming the behavior factor $q = 1$; (b) a shear force determined as the ratio between the column base resisting moment, M_{Rd}, and the column height, multiplied by the factor γ_{Rd}, equal to 1.2 for DCM or to 1.35 for DCH. Then, the maximum between the resulting shear force (seismic force) and the higher shear force for the design combinations at ultimate limit state is assumed as design force (V_{design}).

For each case study, all the beam-to-column dowel connections are designed referring to the maximum value of the design shear forces for all the connections (Table 6).

It is worth noting that for the considered case studies, the connection design always depends on the seismic action, except for very low hazard conditions, i.e. buildings sited in Milan, on soil A, for both SS and LS geometries, where wind actions result to be dominant.

Table 6. Design shear force for beam-to-column dowel connections

Site	Soil type	V_{design} [kN]				
		SS	LS	Soil type	SS	LS
AQ	A	142.00	209.73	C	250.67	315.07
NA		118.55	183.51		141.87	219.33
RM		94.97	145.83		142.00	209.73
MI		78.59	114.00		92.62	142.08

According to CNR10025/84 (1985), the dowel diameter d_b is assumed equal to:

$$d_b = \sqrt{\frac{V_{Ed}}{n \cdot \alpha \cdot \sqrt{f_{yd} \cdot f_{cd}}}} \quad (1)$$

where $n = 2$ is the number of dowels and $\alpha = 1.6$ is a coefficient taking into account the confinement provided by the beam-column mutual pressure. Resistant values for d_b are assumed.

Design strength values for concrete (f_{cd}) and threaded bars (f_{yd}) are reported in Tables 7 and 8.

Table 7. Mechanical properties for concrete C45/55

R_{ck} [MPa]	f_{ck} [MPa]	γ_c [–]	α_{cc} [–]	f_{cd} [MPa]
55	45.65	1.5	0.85	25.87

Table 8. Mechanical properties for threaded bars

Class [–]	f_{yb} [MPa]	γ_s [–]	f_{yd} [MPa]
8.8	649	1.15	564.35

Additional steel stirrups (f_{sk} = 450 MPa, γ_s = 1.15, f_{sd} = 391.3 MPa) are designed to absorb horizontal forces due to the vertical pressure and to the shear force in the connection (V_{design}).

The summary of the beam-to-column dowel connections details are reported in Table 9.

Table 9. Beam-to-column dowel connection details

Site	Soil type	SS		LS	
		D	St	D	St
AQ	A	M22	3 ϕ10	M27	4 ϕ10
NA		M20	3 ϕ10	M27	3 ϕ10
RM		M20	3 ϕ10	M22	3 ϕ10
MI		M18	3 ϕ10	M20	3 ϕ10
AQ	C	M30	5 ϕ10	M33	9 ϕ8
NA		M22	3 ϕ10	M27	4 ϕ10
RM		M22	3 ϕ10	M27	4 ϕ10
MI		M18	3 ϕ10	M22	3 ϕ10

3 Dowel Connection Shear Strength

Considering the designed beam-to-column connections, their shear capacities are evaluated according to the available formulae in codes and technical literature. Mean values for material mechanical properties are adopted (f_c = 59.75 MPa, f_{ctm} = 3.83 MPa, f_y = 816 MPa, f_s = 490.30 MPa). Two possible failure modes are considered: (a) a local failure which involves the vertical dowels, with the formation of plastic hinges, and the crushing of the surrounding concrete. According to Vintzeleou and Tassios (1986), this failure mode can activate for large concrete covers, i.e. higher or equal to 8 times the dowel diameter; (b) a global failure which involves the whole connection zone, with the spalling of the concrete cover in the direction of the shear force (frontal cover) or in the transversal direction (lateral cover). According to Vintzeleou and Tassios (1986), this failure mode can activate for small concrete covers, i.e. lower or equal to 4 times the dowel diameter. In this case, also the contribution of the transversal stirrups is taken into account.

3.1 Local Failure Mode Formulations

The available formulations for connection shear strength calculation, when local failure occurs, do not depend on the considered direction for the acting shear force. They depend on the dowel diameter (resistant value) and on the mechanical properties for concrete and threaded bars (mean values for concrete compressive strength and steel yielding strength). For the selected case studies, they provide the same connection shear strength on both column and beam side.

According to Vintzeleou and Tassios (1986), the connection shear strength under cyclic loads (Eq. (3)) should be assumed equal to the half of the corresponding value under monotonic loads (Eq. (2)).

$$V_{R,mono}^{V\&T} = n \cdot 1.3 \cdot d_b^2 \cdot \sqrt{f_y \cdot f_c} \tag{2}$$

$$V_{R,cycl}^{V\&T} = 0.5 \cdot V_{Rd,cycl}^{V\&T} \tag{3}$$

SAFECAST guidelines (SAFECAST 2012) formula takes into account also additional tensile stresses σ acting on the dowel, introducing the coefficient $\alpha = \sigma / f_y$.

$$V_R^{Safecast} = n \cdot 0.9 \cdot d_b^2 \cdot \sqrt{f_y \cdot f_c \cdot (1 - \alpha^2)} \tag{4}$$

EOTA provisions, for bonded anchors in concrete (TR029 2007; TR045 2013), account for steel failure through Eq. (5), for monotonic loads, and Eq. (6), for cyclic loads, where A_s is the dowel cross section area, α_{gap} = 1.0 in case of no hole clearance between anchor and fixture and α_{seism} = 0.85 is the reduction factor to take into account the influence of large cracks in case of anchor group.

$$V_{R,mono}^{EOTA} = n \cdot 0.5 \cdot A_s \cdot f_u \tag{5}$$

$$V_{R,cycl}^{EOTA} = \alpha_{gap} \cdot \alpha_{seism} \cdot V_{R,mono}^{EOTA} \tag{6}$$

Figure 2 shows the connection shear strength according to CNR 10025/84 (1985) and to Eqs. (2)–(6), for SS (not filled markers) and LS (filled markers) buildings in L'Aquila, soil C, divided by the corresponding design shear force.

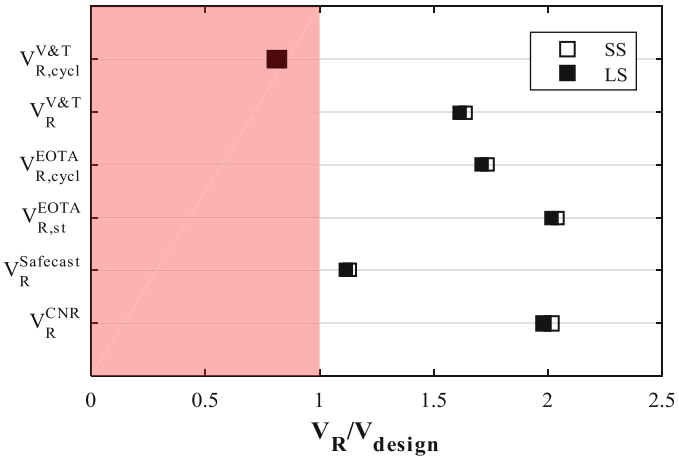

Fig. 2. Connection shear strength for local failure mode, cases AQ soil C, SS and LS

It can be observed that, with exception of Eq. (3), which provides very low and too conservative shear strength values, the selected formulations provide connection shear strength values higher than the design shear force, for SS and LS buildings.

The high connection shear strength values resulting from Eqs. (5) and (6) should not be taken into account because the corresponding failure mode (dowel shear failure) is not very representative for the considered connection typology.

The lowest and most conservative connection shear strength values result from Eq. (4).

These observations are generally applicable to all the considered case studies.

3.2 Global Failure Mode Formulations

The available formulations for connection shear strength calculation, when global failure occurs, depend on the considered direction for the acting shear force and on the considered connection side.

For this reason, using the selected formulations, connection shear strength along x and z direction, on the beam and column sides, for both SS and LS buildings is considered in the following.

Equations (7) and (8) provide shear strength, according to experimental and numerical investigations performed by Vintzeleou and Tassios (1986), when frontal cover spalling or side cover spalling occur, respectively. In these formulations, c represents the concrete cover depth and b_{ct} is the net width of the element.

$$V_R^{V\&T,bott} = 5 \cdot f_{ctm} \cdot c \cdot d_b \cdot \frac{c}{0.66 \cdot c + d_b} \tag{7}$$

$$V_R^{V\&T,side} = 2 \cdot f_{ctm} \cdot b_{ct} \cdot d_b \tag{8}$$

According to SAFECAST guidelines, the connection shear strength (Eq. (9)) also depends on the effective embedment of the dowels (h_d, Eq. (10)), on the presence of edge reinforcement ($\psi_{re} = 1$ is assumed, because there is not specific reinforcement limiting concrete cover splitting) and on the concrete element width b (Eq. (12)).

$$V_R^{Safecast} = 1.4 \cdot k \cdot d_b^{\alpha} \cdot h_d^{\beta} \sqrt{f_c \cdot c^3} \cdot \psi_{re} \tag{9}$$

$$\alpha = 0.1 \cdot (h_d/c)^{0.5} \tag{10}$$

$$\beta = 0.1 \cdot (d_b/c)^{0.2} \tag{11}$$

$$k = b/(3 \cdot c) \leq n \tag{12}$$

TR029 (2007) and TR045 (2013) account for global failure through Eqs. (13) and (14), for monotonic and cyclic loads, respectively. In Eq. (13), k_1 is equal to 2.4 for applications in non-cracked concrete, $A_{c,V}$, $A_{c,V}^0$ and $\psi_{s,V}$ are obtained according to TR029 (2007).

$$V_{R,mono}^{EOTA} = k_1 \cdot d_b^{\alpha} h_d^{\beta} \cdot \sqrt{f_c} \cdot c^{1.5} \cdot \frac{A_{c,V}}{A_{c,V}^0} \cdot \psi_{s,V} \tag{13}$$

$$V_{R,cycl}^{EOTA} = \alpha_{seism} \cdot \alpha_{gap} \cdot V_{R,mono}^{EOTA} \tag{14}$$

When global failure mode is expected, contribution of the transversal stirrups should be taken into account using Eqs. (15) and (16), which result from Zoubek et al. (2015) numerical investigations, where n is the number of effective stirrups, A_s is the area of a stirrup leg, e_1 and e_2 are the distances of the dowels from the two stirrup legs parallel to the shear force, and α is the angle shown in Fig. 3.

$$V_R^{Zoubek} = n \cdot A_s \cdot \frac{f_{sy}}{2} \cdot \left(\frac{e_1 + e_2}{e_1}\right) \quad if \ \tan\alpha \geq 1 \tag{15}$$

$$V_R^{Zoubek} = n \cdot A_s \cdot \frac{f_{sy}}{2} \cdot \left(\frac{e_1 + e_2}{e_1}\right) \cdot \tan\alpha \quad if \ \tan\alpha < 1 \tag{16}$$

Figures 4 and 5 show the connection shear strength values, on both column (circle markers) and beam (triangle markers) side, for SS (not filled markers) and LS (filled markers) buildings in L'Aquila, soil C, along x and z direction, respectively. It can be

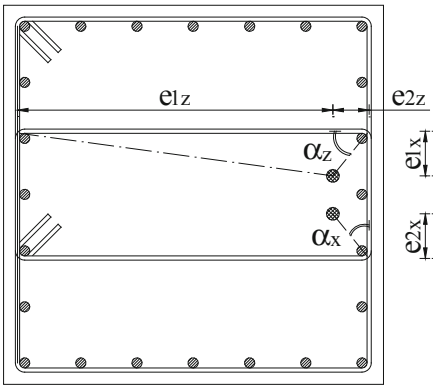

Fig. 3. Layout of the transversal stirrups in the beam-to-column dowel connection

observed that in both the directions and for both the geometries the connections, characterized by a low dowel cover and designed according to Italian practice, are underdesigned, i.e. their strength is lower than the required design strength.

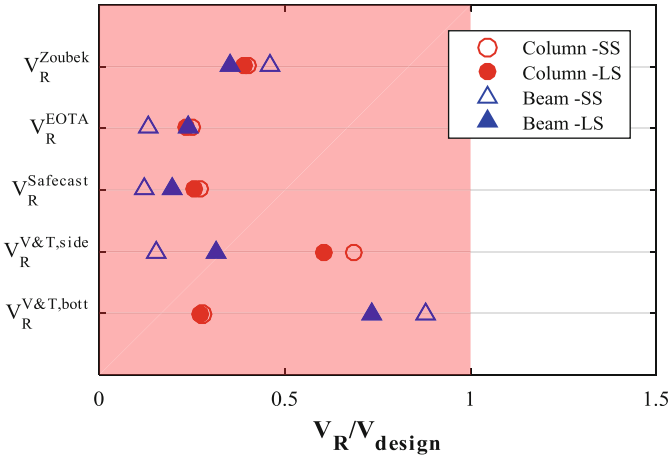

Fig. 4. Connection shear strength for brittle failure mode - x direction, SS and LS buildings, AQ soil C

Moreover, it is worth noting that, for the selected case studies, along both x and z direction, the transversal stirrups placed in the connection region on the beam side are able to offer a shear strength contribution which should be taken into account. On the column side, they result quite effective only along x direction.

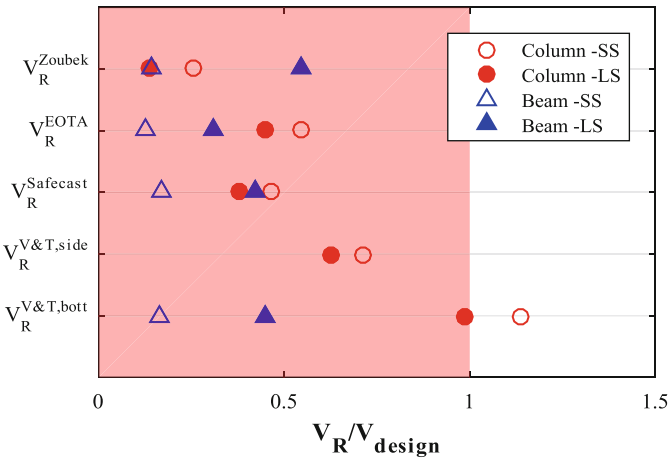

Fig. 5. Connection shear strength for brittle failure mode - z direction, SS and LS buildings, AQ soil C

4 Connection Shear Capacity

Using the presented formulae in Sect. 3, the connection shear capacity, in both the horizontal directions, x and z, is evaluated. In each direction, shear strength in the connection zone is obtained for both beam and column side. On each side, both local and global failure mode is considered, using the formula which returns the minimum shear strength value for each mechanism. Then, on each side, the element shear strength in the connection zone is assumed equal to the minimum shear strength between the two considered failure modes. It is worth noting that for all the considered beam-to-column dowel connections the local failure provides higher shear strength so that the minimum shear strength is always offered by global failure mode formulae and the resulting failure mechanism involves concrete cover splitting. In Tables 10 and 11 failure modes for column ("Col.") and beam ("Beam") side are summarized, along x and z direction, respectively: "C/B" represents the global failure due to frontal concrete cover splitting; "C/S" represents the global failure due to side concrete cover splitting; "Y" correspond to the transversal stirrups yielding.

It can be observed that, along the x direction: for SS buildings, on the column side the transversal reinforcement is almost always not able to offer a significant contribution to the connection shear strength, with a consequent global failure which involves the frontal concrete cover; on the beam side, the transversal reinforcement appears to be more effective and is always able to reach yielding. For LS buildings, the transversal reinforcement is quite effective on both column and beam side and only in few cases global failures with concrete spalling are predicted, involving frontal cover (on the column side) or side cover (beam side).

Along z direction: for both SS and LS buildings, on the column side a global failure mode with side cover spalling is expected for all the considered sites; on the beam side

Table 10. Element and connection failure modes along x direction

Site	Soil type	X Direction			
		SS		LS	
		Col.	Beam	Col.	Beam
AQ	A	C/B	Y	Y	Y
NA		C/B	Y	Y	Y
RM		C/B	Y	Y	C/S
MI		Y	Y	C/B	C/S
AQ	C	Y	Y	Y	Y
NA		C/B	Y	Y	Y
RM		C/B	Y	Y	Y
MI		Y	Y	C/B	C/S

Table 11. Element side failure modes along z direction

Site	Soil type	Z Direction			
		SS		LS	
		Col.	Beam	Col.	Beam
AQ	A	C/S	Y	C/S	Y
NA		C/S	Y	C/S	Y
RM		C/S	Y	C/S	Y
MI		C/S	Y	C/S	Y
AQ	C	C/S	Y	C/S	Y
NA		C/S	Y	C/S	Y
RM		C/S	Y	C/S	Y
MI		C/S	Y	C/S	Y

the transversal reinforcement is still very effective, as along the x direction, much more for LS buildings.

Finally, the connection shear strength is assumed equal to the minimum between shear strength on column and beam side.

When shear force acting along x direction is considered, the connection shear capacity is always limited by the column shear strength, for SS buildings. On the contrary, for LS buildings the connection shear capacity is limited by the beam shear strength, except for Milan where the frontal cover splitting on the column side is critical.

When shear force acting along z direction is considered, the connection shear capacity is always limited by the beam shear strength, for SS buildings. On the contrary, for LS buildings the connection shear capacity is limited by the column shear strength.

5 Conclusions

In this paper seismic strength of dowel beam-to-column connections for one-story RC precast buildings is investigated.

Code and literature based formulae are adopted to estimate the connection shear strength. Since no limitations on the concrete cover depth is required during the connection design procedure, two possible failure modes are considered, on both column and beam side, which account for large or small concrete cover, respectively.

In particular, for large concrete covers, a local failure mode is expected with the vertical dowel yielding. For small concrete covers, a global failure mode is expected with the concrete cover spalling in the frontal or transversal direction with respect to the shear acting force. In this case, also the contribution of the additional transversal stirrups in the connection region is accounted.

It can be observed that the code and literature formulae for global failure always provide very low and unrealistic connection shear strength values which neglect the significant contribution offered by the transversal stirrups placed in the connection region. This contribution particularly increases the connection shear strength when the geometrical connection layout leads to arrange effective transversal reinforcement.

Consequently, it is observed that the connection failure always depends on the concrete cover limited spalling strength and this can lead to an actual connection shear strength lower than the value resulting from the capacity design. This results in the failure of the beam-to-column connection before the formation of the plastic hinge at the column base.

Moreover, considering the failure modes expected on both column and beam sides, it can be concluded that:

- if the failure on the beam side is neglected (e.g. when beam prestressign and effective column top fork are provided), the connection failure on the column side is always related to the concrete cover spalling (frontal cover for acting shear forces in the x direction, side cover for acting shear force in the z direction), except for LS buildings (with large column cross sections) and shear force along x direction. In these cases, effective transversal reinforcement reaches the yielding;
- if the failure on the beam side is also considered (e.g. when beam prestressing and effective column top fork are not provided), this could affect the whole connection failure mode, along x direction (for LS buildings) and along z direction (for SS buildings).

Acknowledgements. This research study has been funded by Italian Department of Civil Protection, in the framework of the national projects DPC-ReLUIS-EUCENTRE RINTC 2016 and DPC-ReLUIS-EUCENTRE RINTC 2017. The contribution of Marianna Ercolino, Roberto Nascimbene and Davide Bellotti for interesting discussions is gratefully acknowledged.

References

CEN (2005) Eurocode 8 - Design of structures for earthquake resistance - EN 1998-1

CNR10018 (1989) Apparecchi di appoggio per le costruzioni. Istruzioni per l'impiego (in Italian)

CNR10025/84 (1985) Istruzioni per il progetto, l'esecuzione ed il controllo delle strutture prefabbricate in conglomerato cementizio e per le strutture construite con sistemi industrializzati (in Italian)

D. M. 14/01/2008. Norme Tecniche per le Costruzioni

Ercolino M, Bellotti D, Magliulo G, Nascimbene R (2017) Vulnerability analysis of industrial RC precast buildings designed according to modern seismic codes. Eng Struct 158:67–78

Ercolino M, Magliulo G, Manfredi G (2016) Failure of a precast RC building due to Emilia-Romagna earthquakes. Eng Struct 118:262–273

Faggiano B, Iervolino I, Magliulo G, Manfredi G, Vanzi I (2009) Post-event analysis of industrial structures behavior during L'Aquila earthquake. Progettazione sismica 3(English Special Edition):203–208

Magliulo G, Ercolino M, Cimmino M, Capozzi V, Manfredi G (2015) Cyclic shear test on a dowel beam-column connection of precast buildings. Earthq Struct 9(3):541–562

Magliulo G, Cimmino M, Ercolino M, Manfredi G (2017) Cyclic shear tests on RC precast beam-to-column connections retrofitted with a three-hinged steel device. Bull Earthq Eng 15 (9):3797–3817

Magliulo G, Ercolino M, Cimmino M, Capozzi V, Manfredi G (2014a) FEM analysis of the strength of RC beam-to-column dowel connections under monotonic actions. Constr Build Mater 69:271–284

Magliulo G, Ercolino M, Petrone C, Coppola O, Manfredi G (2014b) Emilia Earthquake: the seismic performance of precast RC buildings. Earthq Spectra 30(2):891–912

SAFECAST (2012) Design guidelines for connections of precast structures under seismic actions

TR029 (2007) Design of bonded anchors

TR045 (2013) Design of metal anchors for use in concrete under seismic actions

Vintzeleou EN, Tassios TP (1986) Mathematical models for dowel action under monotonic and cyclic conditions. Mag Concr Res 38(134):13–22

Zoubek B, Fischinger M, Isakovic T (2015) Estimation of the cyclic capacity of beam-to-column dowel connections in precast industrial buildings. Bull Earthq Eng 13(7):2145–2168

FE Analysis of the Flexural Behavior of Cementitious Composites Using the Concrete Damage Plasticity Model

F. Aymerich[1], L. Fenu[2(✉)], and G. Loi[1]

[1] Department of Mechanical, Chemical and Materials Engineering, University of Cagliari, Cagliari, Italy
[2] Department of Civil and Environmental Engineering and Architecture, University of Cagliari, Cagliari, Italy
lg.fenu@gmail.com

Abstract. In this study, the structural and fracture behavior of cementitious composite beams subjected to flexural loads is experimentally and numerically investigated. Six series of mortar specimens reinforced with steel mesh layer ware cast and tested in 4–point bending. Configurations with 2, 4 or 6 mesh layers were examined to characterize the flexural response of materials. A 3D FE model was developed in ABAQUS to predict the nonlinear behavior of the beams and to simulate the evolution of fracture patterns under an increasing load. The nonlinear cracking and crushing response of the mortar was implemented by using the Concrete Damage Plasticity model. For the steel reinforcement, an elasto-plastic model with isotropic hardening was adopted. The results of the numerical analysis are discussed. Comparisons between numerical and experimental results highlight a reasonably good agreement both in term of structural response and of damage growth.

Keywords: Ferrocement · Concrete Damaged Plasticity · FE analysis

1 Introduction

Cementitious composites consist of a matrix of cement mortar reinforced with mesh layers of steel wire (American Concrete Institute 1997). Compared with conventional reinforced concrete, it differs by the manner in which reinforcing elements are arranged within the mortar. In particular, mesh diameter and spacing are much smaller than those of the commonly used reinforcement bars. This type of material was initially proposed by Pier Luigi Nervi (1891–1979), a very famous Italian engineer who built many important buildings all over the world using the *ferrocement,* a cementitious composite (that patented in 1943) with fine mortar matrix and several fine mesh layers of steel wire reinforcing the whole composite thickness together with few mesh layers of small diameter steel rebar much more spaced than the wires. In terms of structural response, cementitious composites exhibit high tensile strength to weight ratio and high crack resistant performance. However, its response until failure is very complex, with the interaction between mortar matrix and reinforcement involving phenomena such as inelasticity, cracking and crushing. The complexity of the involved mechanisms is the

M. di Prisco and M. Menegotto (Eds.): ICD 2018, LNCE 42, pp. 124–133, 2020.
https://doi.org/10.1007/978-3-030-23748-6_10

reason why they are so difficult to be captured (Chen 2007). In this study, the structural and fracture behavior of cementitious composite specimens is experimentally and numerically investigated. The numerical simulations were performed using the Concrete Damaged Plasticity (CDP) model. To overcome convergence difficulties, a dynamic explicit approach was adopted. Comparisons between numerical and experimental results highlight the reliability of the developed 3D model.

2 Experiments

2.1 Specimens Geometry

Experimental tests were carried out on six series of mortar specimens, which were reinforced with 2, 4 or 6 mesh layers.

All the beams had a rectangular cross section of 120 mm × 40 mm and were 240 mm long. The distance between the lower mesh layer and the beam bottom surface was 5 mm. Steel reinforcement with square welded mesh was adopted (mesh size = 10 mm, wire diameter 1 mm).

2.2 Experimental Set-up

Specimens were tested under four-points bending. Two vertical loads were applied symmetrically to the mid-span of the beams with a constant bending region of 80 mm. All the specimens were simply supported with a span of 200 mm, while the distance between each load and the end support was 60 mm (Fig. 1). The bending load was applied by means of a test machine with maximum load capacity of 300 kN. The process was split in two stages. Initially, the load was applied in load control with a speed of 0.5 kN/s, until a total external load of 5 kN was reached. Then, the specimens were loaded under displacement control with a speed of 1 mm/min, until failure occurred. Mid-span deflection was measured and recorded by a linear displacement transducer, while damage and crack pattern evolution were monitored with a camera.

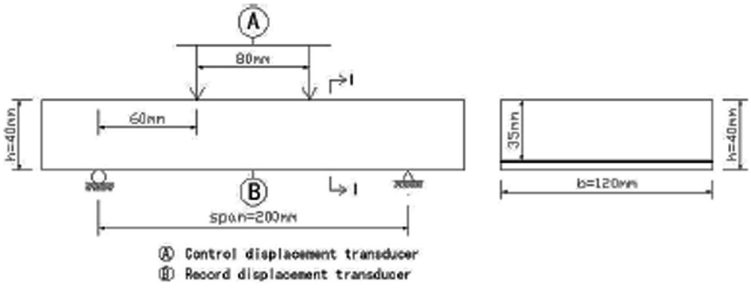

Fig. 1. Experimental test set-up

3 Experimental Results

Planning the experimental tests to characterize the flexural response of the cementitious composite beams, two features were taken into account: the number of steel mesh layers and their orientation. Both of them highly affect the load bearing capacity and the post-peak behavior of the composite beam, as described below.

As shown in Fig. 2, increasing the number of steel mesh layers improves the post-peak bending performance of the cementitious composite beam. In fact, as the volume fraction of steel reinforcement raises, a significant enhancement of both the yielding load and the ultimate displacement was observed.

4 FEM Modeling

4.1 Geometry and Boundary Condition

Due to geometrical and loading symmetry about XY and YZ planes (Fig. 3), it is possible to represent the beam by modeling only one fourth of it, thereby reducing the analysis time. Kinetically, the nodes on the symmetry planes were prevented from displacement along the Z and X direction, respectively. In order to simulate the presence of the roller support, the translations in Y e Z direction of the nodes that identify the bearing line were constrained.

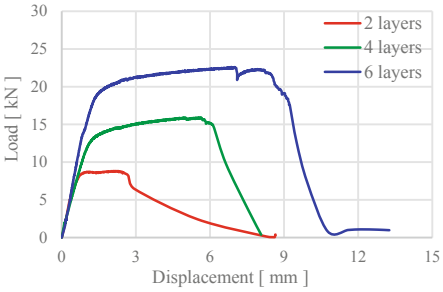

Fig. 2. Load-midspan displacement for different number of steel mesh

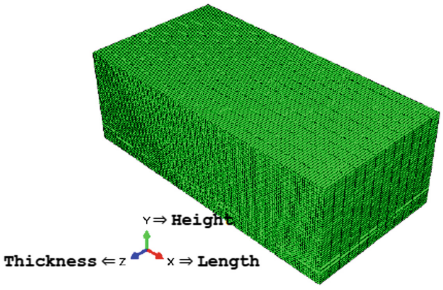

Fig. 3. FEM model of one fourth of the tested specimen

4.2 Elements

Mortar was modeled with 8-node brick elements, whose dimensions were determined by a sensitivity analysis. The full model consists of 57600 nonlinear mortar elements of 1 mm × 1 mm × 2 mm.

Due to their geometry, steel reinforcements were modeled by using 2-node truss elements (T3D2), which can bear only load components along their axis. Their length was equal to the square mesh size of the reinforcement layers.

4.3 Interaction: Embedded Elements

Assuming perfect adhesion between mortar and steel reinforcement, their interaction was modeled by using the embedded element technique. In this way, the mesh layers were embedded within the matrix (host region) at the desired locations (Fig. 4). Their translational degrees of freedom were constrained to be equal to those of the surrounding host elements.

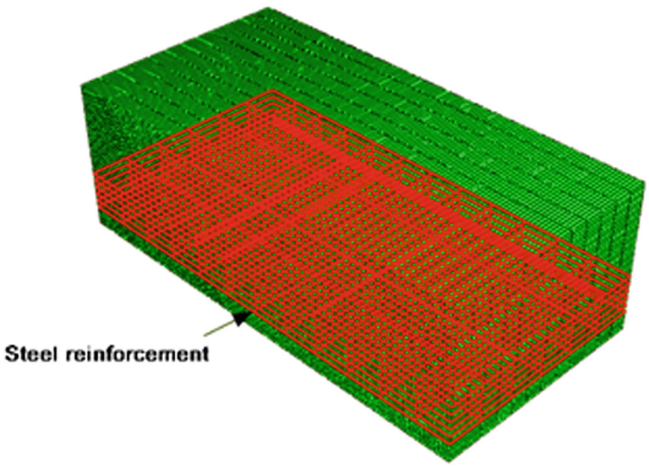

Fig. 4. Reinforcing steel mesh layer modeled as embedded region

4.4 Material Constitutive Laws: Concrete

In order to model the nonlinear response of the mortar, the Concrete Damaged Plasticity (CDP) model was used. The model combines damaged elasticity with isotropic tensile and compressive plasticity. This model assumes that the two main failure mechanisms are tensile cracking and compressive crushing.

In the linear elastic range, mortar response is defined by the Young's modulus E_c and the Poisson's ratio ν_c. A mortar with E_c = 24 GPa and ν_c = 0.2, respectively, was used. Instead, the simulation of the plastic response of the concrete requires the definition of both the damage parameters and the constitutive laws for both tensile and compressive stresses.

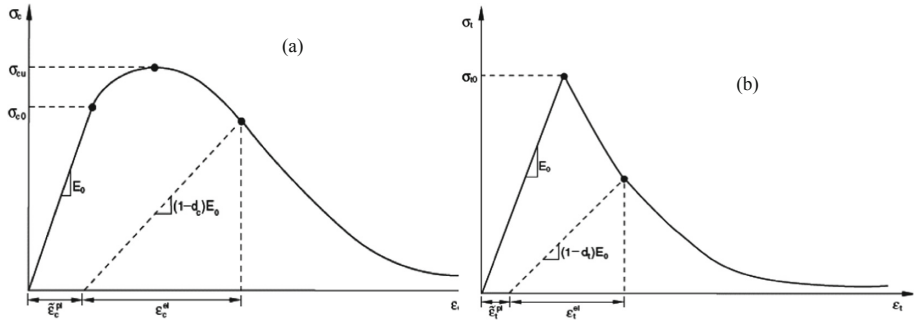

Fig. 5. Behavior of concrete under uniaxial compression (a) and uniaxial tension (b) (Abaqus Analysis User's Manual 2012)

The CDP model makes use of the yield function proposed by Lubliner et al. (1989) and modified by Lee and Fenves (1998) to account for the different response of concrete under tension and compression. Moreover, it assumes a non-associated flow rule, according to Drucker-Prager hyperbolic function. Thus, the implementation of this model requires the definition of five parameters:

- Dilation angle is a measurement of angle between hydrostatic axis and yield function in a meridian plane. The value of 38° was adopted (Abaqus Analysis User's Manual 2012; Jankowiak and Lodugowski 2005; Ren et al. 2015);
- Eccentricity is a small positive constant that defines the rate at which the hyperbole potential function approaches its asymptote. The default value of 0.1 was used (Abaqus Analysis User's Manual 2012; Kmiecik and Kaminski 2011);
- $\sigma_{b0}/\sigma_{c0.}$ is the ratio of mortar strength in the biaxial state to the strength in the uniaxial state. According to the experimental results reported by Kupfer (1973), the ABAQUS User's guide suggests the default value 1.16 (Abaqus Analysis User's Manual 2012);
- K_C can be interpreted as the ratio of the distance between the hydrostatic axis and, respectively, the compressive meridian and the tensile meridian in a deviatoric cross plane. In this paper, the default value 0.667 was assumed (see Abaqus Analysis User's Manual 2012; Kmiecik and Kaminski 2011);
- Viscosity regularization introduces corrections to the constitutive laws to increase the rate of convergence.

Under uniaxial compression (Fig. 5a), the mortar response is linear elastic until the yield stress σ_{c0} is reached. The plastic behavior is characterized by stress hardening followed by strain softening beyond the ultimate stress. However, under uniaxial tension (Fig. 5b), the concrete response follows a linear elastic relationship until the tensile strength is reached. Beyond this limit condition, mortar cracks and its strength suddenly decreases.

The subsequent loss of load capability is modeled by implementing tension stiffening, which allows to simulate the load transfer across cracks caused by steel reinforcement. In order to overcome mesh sensitivity problems due to the absence of reinforcement in significant regions of the model, Hilleborg's fracture energy criterion

(Hilleborg et al. 1976) was adopted. This approach assumes a linear loss of strength after cracking and requires the introduction of only two parameters: tensile strength and fracture energy. The latter is a material property, whose value depends on the aggregate dimensions (Modéer 1979). Compressive and tensile strength of the mortar, whose values were calculated according to Eurocode 2 (2004), were, respectively, f_c = 35.8 MPa and f_t = 2.9 MPa.

Fracture energy was 70 N/m with a corresponding ultimate displacement of 0.05 mm (Fig. 6).

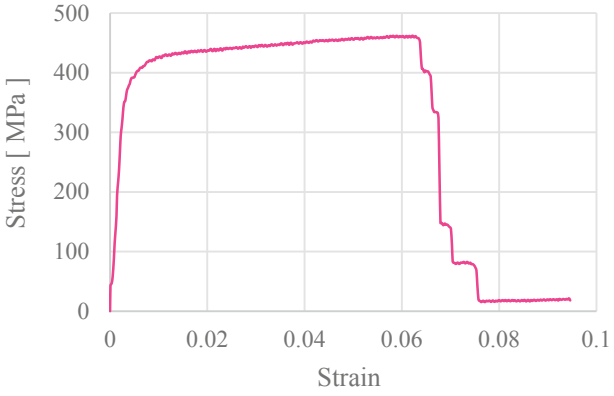

Fig. 6. Stress-Strain curve for reinforcing steel

4.5 Material Constitutive Laws: Steel

Several analysis have been performed, changing different parameters, such as mesh density, element type, material properties, steel mesh layer position and loading velocity. However, only selected results are presented below to highlight the model capability to predict the flexural behavior of a cementitious composite beam.

Figure 7 compares the numerical and experimental load-midspan deflection curves for configurations with 2, 4 or 6 mesh layers, oriented at a 0° angle. The curves report the results obtained for meshes with different element sizes and using elements with reduced integration (C3D8R). The numerical results fit the experimental ones with a very good agreement in the elastic range. When the mortar matrix starts developing plastic deformations, the load sustained by the numerical model is shown to be slightly higher than that obtained experimentally. When the external load approaches the load bearing capacity and high plastic deformations occur, resistance of the composite beam obtained by testing is well estimated by FE analysis, with the strength experimental value only slightly lower than the numerical one.

4.6 Load

The application of a monotonically increasing load was simulated by incrementally increasing the velocity component in Y direction for the nodes that define the contact

line between the upper specimen surface and the loading cylinder of the testing machine. According to a specific temporal function, the velocity was raised until the value of 0.4 m/s was attained. In this way, the total applied load was obtained as the sum of the reaction forces.

5 Results and Discussion

Several analysis have been performed, changing different parameters, such as mesh density, element type, material properties, steel mesh layer position and loading velocity. However, only selected results are presented below to highlight the model capability to predict the flexural behavior of a cementitious composite beam.

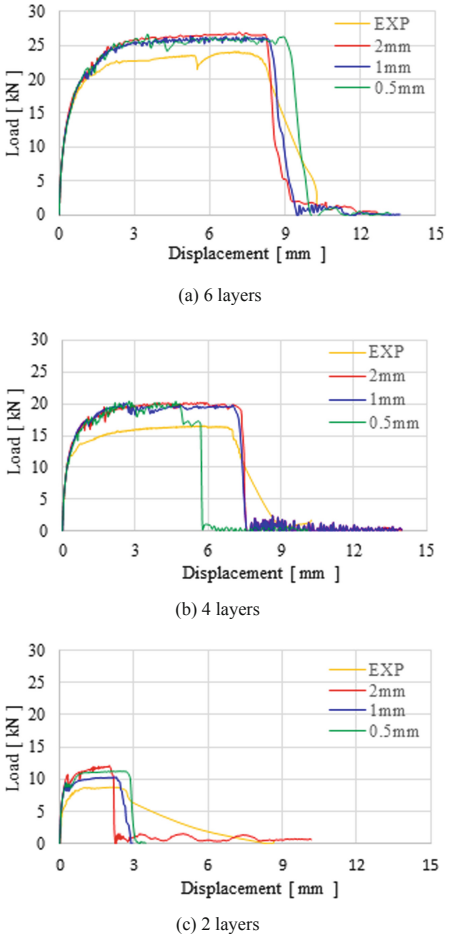

(a) 6 layers

(b) 4 layers

(c) 2 layers

Fig. 7. Load-Midspan deflection for configurations with 0° steel reinforcement orientation

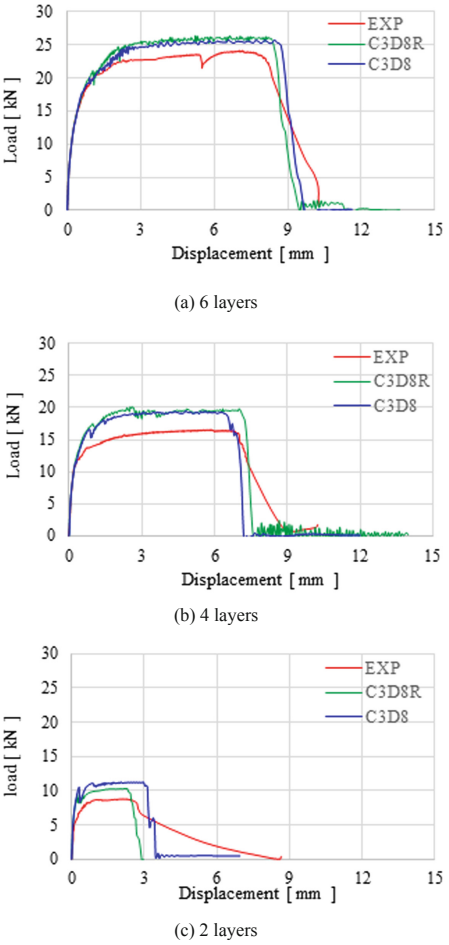

(a) 6 layers

(b) 4 layers

(c) 2 layers

Fig. 8. Load-Midspan deflection for configurations with 0° steel reinforced orientation and different element types

Figure 7 compares the numerical and experimental load-midspan deflection curves for configurations with 2, 4 or 6 mesh layers, oriented at a 0° angle. The curves report the results obtained for meshes with different element sizes and using elements with reduced integration (C3D8R). The numerical results fit the experimental ones with a very good agreement in the elastic range. When the mortar matrix starts developing plastic deformations, the load sustained by the numerical model is shown to be slightly higher than that obtained experimentally. When the external load approaches the load bearing capacity and high plastic deformations occur, resistance of the composite beam obtained by testing is well estimated by FE analysis, with the strength experimental value only slightly lower than the numerical one.

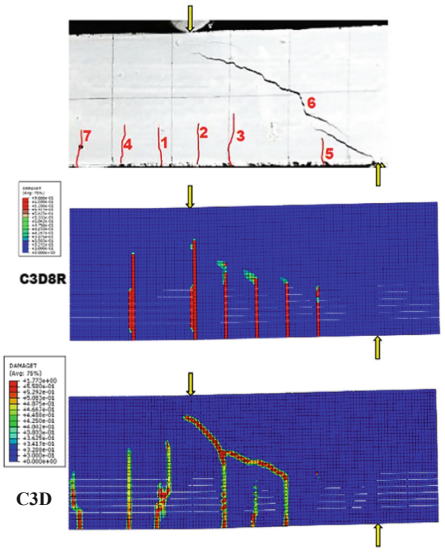

Fig. 9. Comparison of numerical and experimental results: crack patterns for the beam with 6 layers at transition between elastic and plastic range

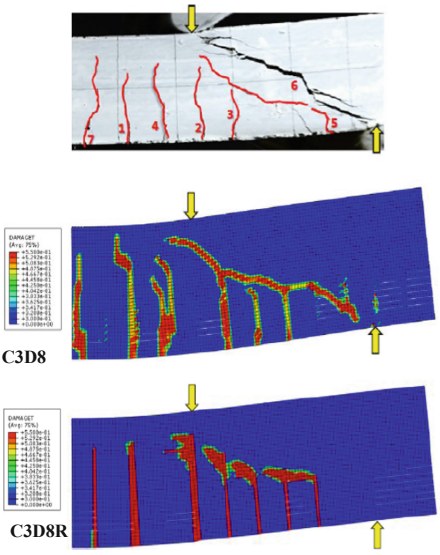

Fig. 10. Comparison of numerical and experimental results: crack patterns for the beam with 6 layers at failure

5.1 Mesh Density

Numerical results do not seem to change significantly as the mesh density increases. In terms of yielding level, the best results are obtained with the 1 mm × 1 mm mesh and the highest percentage error is reached for the 4 steel layers configuration (Fig. 7b).

5.2 Element Type

The effect of the element type on the finite element predictions was investigated with the use of the finer mesh density. The numerical results achieved by using elements with reduced integration (C3D8R, Fig. 8) were compared with those obtained from fully integrated elements (C3D8) in Fig. 8. It is immediately clear that they do not show differences. However, the choice of full integration elements improves the agreement between the numerically predicted and the experimental observed fracture patterns, as visible in Figs. 9 and 10, which compare the crack patterns at two different loading stages for the two element types.

Flexural vertical cracks occur early and, at the transition between elastic and plastic ranges, their growth is followed by the development of a diagonal crack, whose presence can be captured only by using C3D8 element (Figs. 9 and 10). As the inelastic strain increases, cracks propagate until the ultimate state is reached. Even in these conditions, the agreement between the FE analysis and the experimental observations, both in terms of crack location and of crack growth, is significantly better when totally integrated elements are used.

6 Conclusions

In this paper, a nonlinear FE analysis of cementitious composite beams subjected to bending load was performed. In order to simulate the behavior of the mortar matrix, the Concrete Damaged Plasticity was used. By comparison between experimental and numerical results, it was found that the developed model is able to predict the damaged and crack pattern evolution with a reasonable agreement. Also, it was found that the numerical load-displacement trends were very similar to the experimental ones for the whole loading range. Nevertheless the post-peak strength of the numerical model is shown to be always slightly higher than that obtained in the experiments. Therefore, the CDP model can be used to predict the system response even for large plastic deformations until failure.

References

ACI Committee 549 (1997) State of the art report on ferrocement. Manual of Concrete Practice, American Concrete Institute, Detroit, 26

Chen W (2007) Plasticity in reinforced concrete. McGraw Hill, New York

Dassault Systemes Simulias Corp. Providence (2012) ABAQUS analysis user's manual, version 6.12. Rhode Island, USA

European Committee for Standardization. Design of concrete structures – Part 1-1: general rules and rules for buildings EN 1992-1-1. European Committee for Standardization, Brussels

Hilleborg A, Modeer M, Petersson PE (1976) Analysis of crack formation and crack growth in concrete by means of fracture mechanics and finite elements. Cem Concr Res 6:773–782

Jankowiak T, Lodugowski T (2005) Identification of parameters of concrete damage plasticity constitutive model. Found Civ Environ Eng 6:53–69

Kmiecik P, Kaminski M (2011) Modelling of reinforced concrete structures and composite structures with concrete strength degradation taken into consideration. Arch Civ Mech Eng 9(3):623–636

Kupfer HB, Gerstle KH (1973) Behavior of concrete under biaxial stresses. J Eng Mech Div, ASCE 99(EM4):656–666

Lee J, Fenves GL (1998) Plastic – damage model for cyclic loading of concrete structures. J Eng Mech 124(8):892–900

Lubliner L, Oliver J, Oller S, Onate E (1989) A plastic damage model for concrete. Int J Solids Struct 25(3):299–326

Modéer M (1979) A fracture mechanics approach to failure analyses of concrete materials. Doctoral thesis, Delft University of Technology

Nervi P (2010) Costruire correttamente. Hoepli, Milano

Ren W, Sneed LH, Gai Y, Kang X (2015) Test results and nonlinear analysis of RC T-beams strengthened by bonded steel plates. Int J Concr Struct Mater 9(2):133–143

Sümer Y, Aktas M (2015) Defining parameters for concrete damage plasticity model. Chall J Struct Mech 1:149–155

Investigations of Shear Resistance Related to Slab Bridges in Comparison with International Design Standards, Nonlinear FE-Analysis and Results of Full-Scale Test Series

Michaela Kopp(✉), Gerald Köck, and Markus Vill

Department of Civil Engineering, University of Applied Sciences, Vienna, Austria
{michaela.kopp,markus.vill}@fh-campuswien.ac.at

Abstract. This research paper deals with different concrete slab bridges, which were built in the years 1930 to 1990 and should be used in their current mode of operation at least until the end of their expected economic lifetime or even further.

The main target of this research was to display structural reserves of existing slab bridges within the context of the bridge management system nowadays and the differences of the current international standards. To ensure the quality of the results, all investigations are verified by numerical analysis.

Finally the investigations pointed out that 50% of the design value of the reinforcing steel in addition to the concrete contribution according to EC 2 should be used for the verification of existing slab bridges with bent-up bars. Furthermore, with the consideration of these calculative assumptions, the normative safety of bridge structures could be achieved and many bridges are still safe to use in their mode of operation, if the maintenance conditions are adequate.

Keywords: Austrian Federal Railways · Bridge stock · Verification · International design standards · Eurocode 2 · Shear crack · Shear resistance of concrete · Stirrups · Bent-up bars · Longitudinal reinforcement ratio · Dynamic factor · Slenderness

1 Introduction

According to the recalculation of old structures using current standards some bridge structures do not need any strengthening, where as many of them need to be strengthened or completely replaced. Due to the conservative approaches in terms of design, it is not possible to provide documented evidence of conformity for slab bridges

G. Köck—Master Student, 2017.

M. di Prisco and M. Menegotto (Eds.): ICD 2018, LNCE 42, pp. 134–148, 2020.
https://doi.org/10.1007/978-3-030-23748-6_11

of the last century. But for all that, these structures are still in use and do not show many noticeable damages.

According to the recalculation using current standards some bridge structures do not need any strengthening whereas others may need to be strengthened or even completely replaced. In addition to that, the Eurocode 2 prescribes that bent-up bars should cover only fifty percent of the entire shear load and should be fully anchored in the compression zone. Checking the condition of such structures has shown in many cases, during maintenance work that the condition is good and no relating damages were observed. Due to the conservative approaches in terms of design, it is not possible to provide documented evidence of conformity for slab bridges of the last century.

In this way, there is often no option to fulfil the requirements of the current standards for the assessment of the existing bridges, which has to be done, if there is a change due to enlargement of loads. This high level of safety, which happens due to neglected load bearing effects, was investigated for existing concrete slab bridges with bent-up bars. The calculation, respectively the assumptions, was generated referring to the proof of perforation. Contrary to bent-ups in slab bridges, the provision for bent-up bars in the ceiling refers to the thickness of the slab. The results of the numerical simulation and the suggestion in this research paper are to consider fifty percent contribution of the yield strength of the bent-up bars as seen in a verification example in Table 1. This research focused on the differences of the current international standards, therefore 23 existing bridges were analysed given by an example below, Fig. 16. To get realistic results all outcomes are compared to the condition of the real structure and with the outcome of the FE-analysis. The FE-analysis represents the modeling of the complete reinforcement. The different standards are compared to their action relating to key attributes like the slenderness, span width, decade, inclination, longitudinal reinforcement, transverse reinforcement, compressive strength and the yield strength of the reinforcement. The majority of these objects have a span, which does not exceed 8 metres, a slenderness ratio of 15 to 20 and were built in the 1970s. Only 8 of 23 bridges were inclined and most of the structures have a compressive strength of 20 to 30 N/mm^2. To fulfil the load bearing criteria an economical use of reinforcement ratio should guideline the design codes under terms of required but as less as possible [6].

Table 1. Comparison between different design standardizations and the numerical analysis

Bridge	Shear resistance (kN/m)			Shear stress (N/mm^2)	Performance ratio ()	
B05	EC 2	MC 10 LoA II	ATENA 3D	τ_{test}	ATENA/EC 2	ATENA/MC10
	$V_{Rd,c}$		$V_{R,test}$	$V_{R,test}/(bw*z)$		
	374	335	819	1.61	2.17	2.43

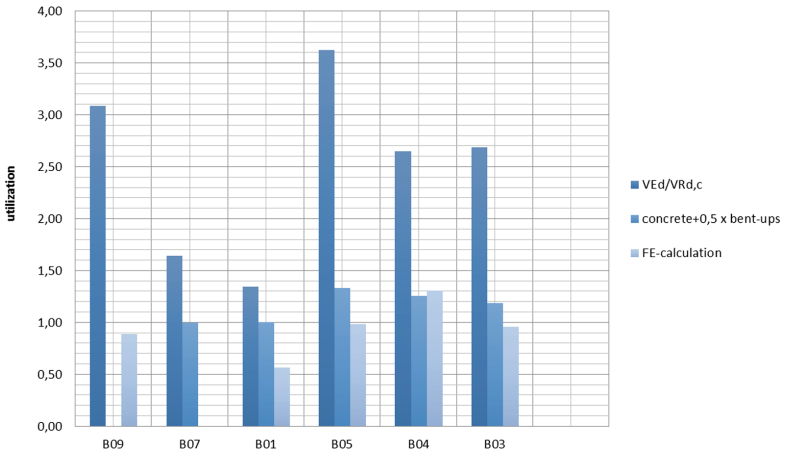

Fig. 1. Overview of the different bridges regarding the FE-modeling, EC2 and the research design proposal.

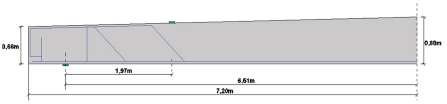

Fig. 2. Dimensions of beam B05.

Fig. 3. Reinforcement of the 2D structural model B05.

2 Shear Load Assessment of Existing Concrete Bridges

2.1 Investigations of Bridge Structures

For the analysis of the ultimate load, a cross-sectional area of the existing reinforcement of the total span was used. The span has a length of 7.2 m, the height of the slab varies between 0.66 m and 0.8 m in the middle of the bridge. The concrete class was C30/37 and the thickness of the concrete cover was about 3 cm. Steel plates were used to induce forces into half of the bridge's structure due to symmetric boundary conditions. The dimensions of the steel plates were about 20 cm in length and 3 cm in thickness and they positioned at the distance of 3.5 times of the effective depth of the section. All results are listed in Table 1. The reinforcement of the beam was calculated to the whole slab. The analysis was separated in two load cases. Load case 1, was the support of the beam with the steel plates and load case 2, was the load which induced the prescribed deformation to press the slab downwards. The load steps with different multiplier were calculated step by step. The first 40 load steps have a coefficient of 1.0, the next 40 steps worked with a coefficient of 0.1 and the next steps were continuously levelled till 120 analysis steps were achieved.

3 Nonlinear Fe-Modeling

3.1 2D-Input Data Bridge 5

In comparison with other bridge structures, B05 pictures the highest shear resistance, as shown in Fig. 4 excepting B09 bridge structure, which was a post-tensioning structure (Fig. 4). The stated reasons therefore are the lean beam and the high graduated shear reinforcement ratio of about $\rho_w = 0.013$. Also, the good concrete quality of C30/37 supports the load-bearing behaviour (Fig. 4).

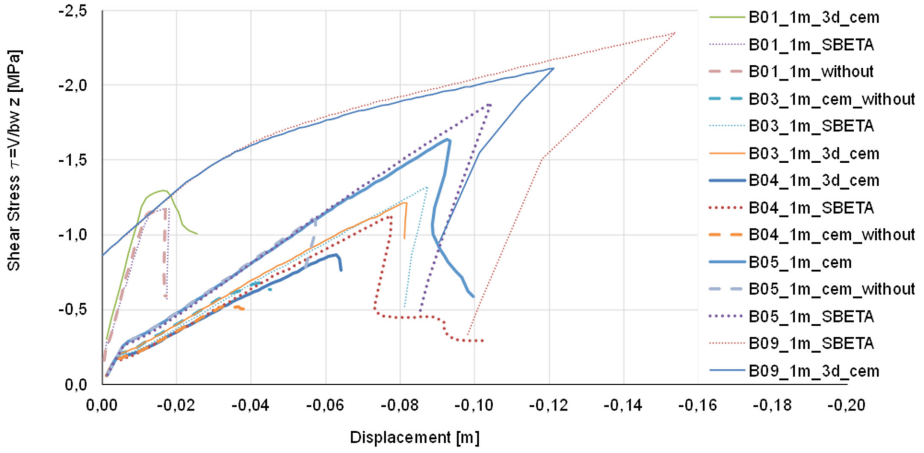

Fig. 4. Overview of the parameter study 2D and 3D.

4 2D-Modeling

4.1 Bridge 5

The nonlinear-finite-element simulation was carried out with the software ATENA. Therefore, different material models were used to calculate the bridge structures. In total five bridge structures, built between the 1940s and the 1990s, were investigated. For the simulation, the SBETA Model, as well as a Fracture Plastic Constitutive Model (CC3DNonLin Cementitious2), was used for analysis of the material model.

4.2 Parameter Study 2D Beam

Figure 5 shows an ultimate load of 819 kN/m which leads to failure at a displacement of 92 mm. After achieving the maximum load, the iterative calculation process is stopped due to discontinuity. Figure 5 significantly marks higher shear resistance of the SBETA material. Furthermore, the chart describes a shear failure, with the big differences due to the shear resistance of structures with and without bent-up bars. The design shear resistance was achieved by the beams without shear reinforcement.

According to EC 2 the shear was about 246 kN/m, which points out existing reserves of the load-bearing behavior in contrast to the FE-model. The FE-Model faced a resistance of about 560 kN/m, this would mean in further consequence, that EC 2 shows additional safety. The simulation of the slab without bent-up bars was limited by an ultimate load of about 550 kN [2].

4.3 Required Characteristic Action of Shear (VEk) Under the Terms of LM71 and Eurocode 1 for Railway Bridges

As Fig. 5 shows, the calculations illustrate ultimate load level of 819 kN/m, whereby the required design load for railways should consider a load level of about 925 kN/m as a result of all load combinations and additional load class factors. This implies that the value of the FE-model overruns the characteristic value of load model 71 according to EC1, which correlates with the other findings of this research.

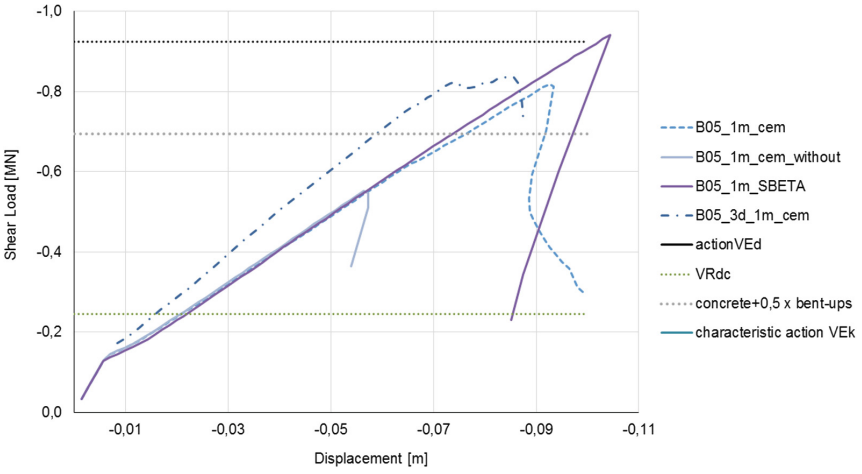

Fig. 5. Depiction of the differences between shear-load displacement course with and without bent-up bars and different material parameters.

The current standards allow taking into account 50% of the shear contribution of the bent-up bars in addition to the shear stirrups. A combination of the contributions of bent-up bars and concrete without shear reinforcement is not allowed in regards with present design standards [1, 2, 8].

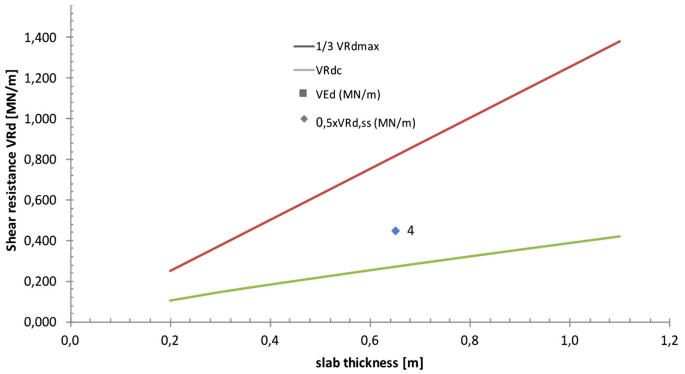

Fig. 6. Comparison of shear resistance in regards to the thickness of structure B05 according to EC 2 and EC1.

4.4 Detailed Results of the 2D Model

At the transition of condition I to condition II the maximum stress of the reinforcement is about 15 N/mm^2 before cracking. This level is reached at load step 5 (Fig. 7).

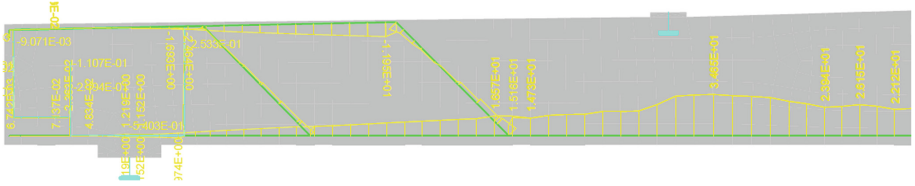

Fig. 7. The progress of steel stress σ_{xx} of B05 at transition of condition I to condition II [stress; sigma xx; [MPa]].

The maximum crack width is about 0.8 mm, which starts at a stress level of σ_T = 2.75 MPa. The simulation shows the starting of concrete cracking at load step 6, which equals a deflection of 1.0 mm (Figs. 8 and 9).

The maximal stress of the reinforcement at the level of V_{Rdc} appropriate to EC 2 faces a force of 374 kN/m, which was achieved at load step 26. This resistance causes a stress of 146 N/mm^2 in the reinforcement. The concrete starts cracking at a stress level of 60 N/mm^2 in the reinforcement, which is set at load step 6. This confirms the assumption that the bent-up bars can only be activated, if there is an increase of the strain in the concrete and a crack crosses the shear reinforcement.

Figure 10 displays the results of the quasi-continuous load, which is about 44% of ultimate load. The chart illustrates the different load levels and points out that there is no exceeding of the ultimate load. The stress in the longitudinal flexure reinforcement has a value of 160 MPa and the stress in the bent-up bars show values of 38 MPa after cracking. The results show that the shear forces are mainly covered by the concrete contribution (Fig. 11).

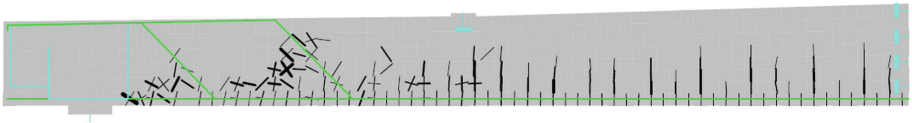

Fig. 8. Crack configuration and crack openings of structure B05 starting with a width of more than 0.1 mm.

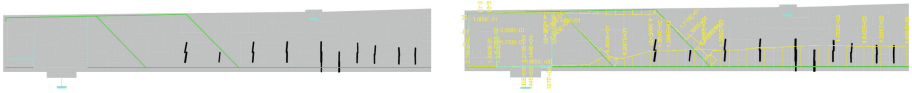

Fig. 9. The progress of steel stress σ_{xx} at the load concrete resistance level V_{Rd} of EC 2 with a flexural crack width starting from 0.1 mm [stress; sigma xx; [MPa]].

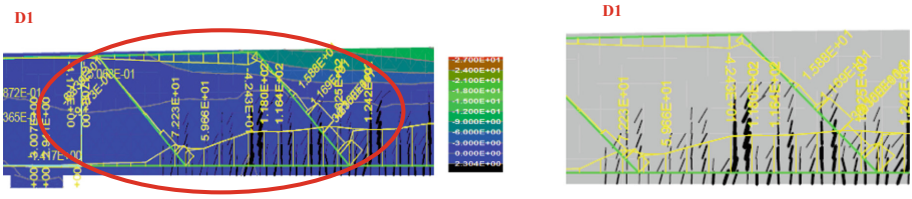

Fig. 10. 2D girder modeling at quasi-continuous load V_{Ek} = 350 kN/m.

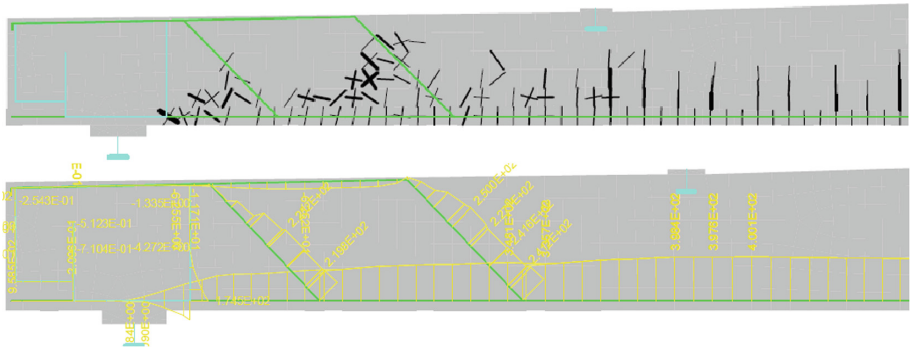

Fig. 11. The progress of steel stress σ_{xx} at ultimate load level [stress; sigma xx; [MPa]].

At ultimate load, which starts at load step 68, the bent-up bars face a shear stress of 250 MPa. Figure 10 shows that the concrete is cracking through the shear reinforcement, which results rising shear stress. In this connection, the shear reinforcement operates at 50% of its capacity (Fig. 11).

The area of stress includes shear stress from τ xy −3.0 MPa to +3.0 MPa as peak values (Fig. 12).

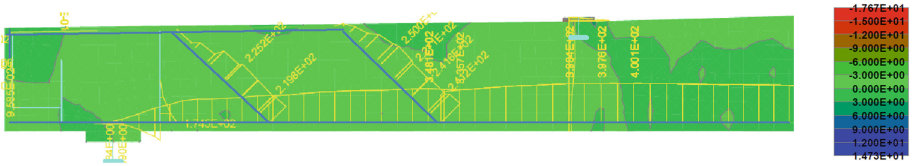

Fig. 12. Progress of stress τ xy at ultimate load [MPa].

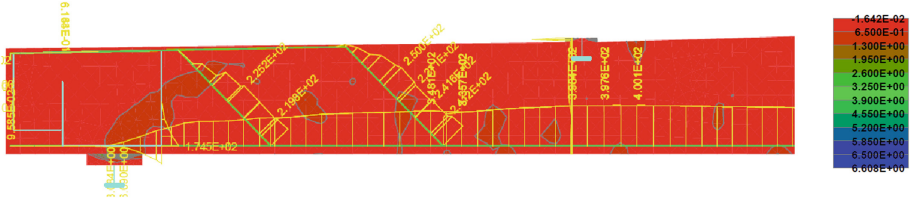

Fig. 13. Principal tensile stresses [MPa] and steel stress.

At load step 68, the maximum stress of reinforcement at ultimate limit state represents 250 N/mm^2 in the bent-ups. At this condition there are cracks perpendicular to the bent-up bars, as seen in Fig. 11, so a higher steel stress yields in the bent-ups. To sum up the FE-modeling confirm previous assumptions of 50% bent-up bar utilization due to perpendicular cracks [2].

5 Comparison of the Different Test Series

Figure 14 displays the shear stress of the different samples as a function of the inner lever arm. The described bridge structure is noted as B05. The approach exemplifies the 2D and 3D analysis picture quite similar results. The overview of Fig. 14 makes clear that the numerical results of this investigation confirm to the results of other researchers. Further, this work deals with the question of a realistic bent-up bar calculation and how it could be represented in an appropriate calculation model for Eurocode 2 or fib Model Code. To adapt the currently valid standards for the assessment of existing structures, continuing test series have to be carried out. These FE-models vary between two different conditions, one condition uses bent-up bars, the other does not have any kind of shear reinforcement, and consequently, there are two kinds of material parameters as mentioned before.

The calculation displays the bridges with shear failure and the bridges with bending failure and it also gives advices for the right use of the different material parameters. Nowadays, the most important design specification insists on the verification of existing bridges and giving a statement about their condition. Through the use of the current valid design standards, it is not possible to get positive, documented evidence of conformity, so this approach uses nonlinear FE-modeling to expose load bearing reserves. To get a good overview, the complementary shear stress of the analyzed slabs is compared with the limits of B2302 and the V_{Ek} values of load model 71. The design

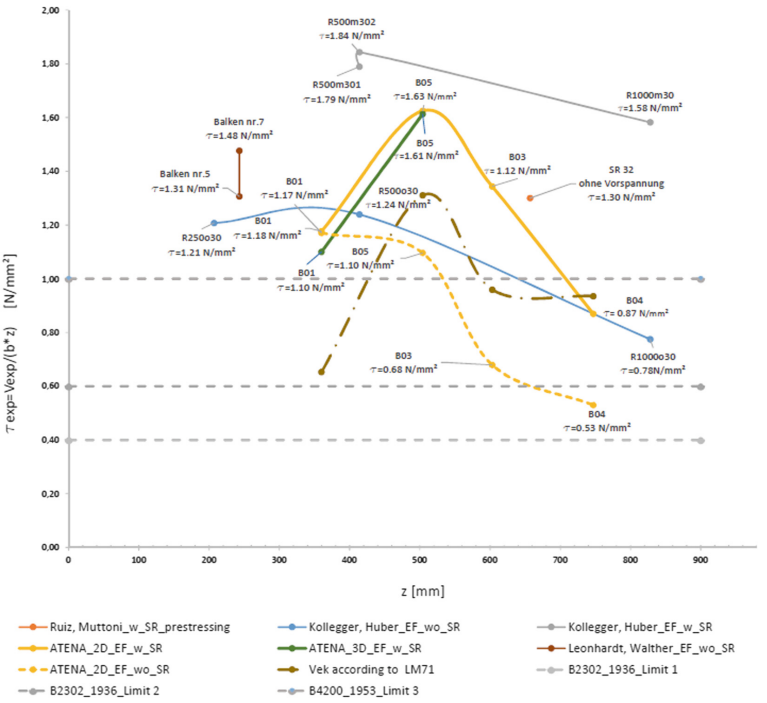

Fig. 14. 2D girder modeling – comparison of shear stress as a function of the inner lever arm.

concept of B2302 from the year 1936 deals with a high level of loads for beams without any shear reinforcement. As opposed to this, one-third of the shear reinforcement is needed compared to current requirements. The analyzed models also contain a pre-stressed concrete bridge, which shows the threefold concrete design ultimate load of EC2 provisions. As a threshold matter, there was no exceedance of the yield strength of bent-up bars during the simulation at ultimate limit state.

Neither there was a total utilization of steel stress. Therefore a specific percentage of the yield strength of bent-up bars in addition to the shear contribution of concrete should be used in the calculative approach. Conformable to the study, the bent-up bars consideration is limited to 50% of the yield strength of steel, because the strain of the shear reinforcement inclination would constitute big cracks, which further results a reduced shear contribution of concrete. According to design standards, the shear resistance of bent-up bars can be considered, if the concrete struts display an underutilization. Furthermore, it is important to mention, that the maximum space between the bent-up bars of the existing bridges exceed the defined design limits in many cases. It becomes apparent, that the contribution of the bent-up bars of beams or slab without required shear reinforcement significantly influences the shear behaviour.

This fact gives reasons for the good condition of the existing bridges, which are not confirmable with the shear design standards nowadays. Therefore, a new simplified verification model for existing bridges is urgently needed, which also involves the continuously rising traffic impact. Last but not least it's important to say, that the analysed bridges last the impact of the actual traffic, because of the present lower traffic loads in comparison to the values of Eurocode 1, which should be mainly used for designing bridges and not for verification.

Finally, it's important to have bridge inspections need to be condensed in terms of time to fulfil the criteria of the bridge management guidelines. In case of doubt, the structure has to be verified by numerical, respectively extended methods [2, 4, 5, 7, 8].

6 Comparison of International Standards

Figure 16 shows the nominal shear resistance of seven different standards as a function of the longitudinal reinforcement ratio. The analysis results same trends due to different concrete strength with similar longitudinal reinforcement ratio. Regarding higher longitudinal reinforcement ratios, different standards do not conform to each other and also the impact of this parameter is not clear at this time.

Figure 15 shows according to the results of 23 bridge structures that stocky respectively compact structures enable the formation of a pressure arch in contrast to slender ones. This causes the distinct increase of the utilization under the terms of rising slenderness.

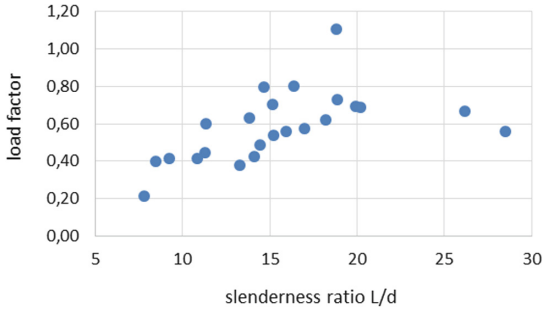

Fig. 15. Analysis of different $M_{Ed}/M_{Rd,c,EC2}$ level due to different l/d values.

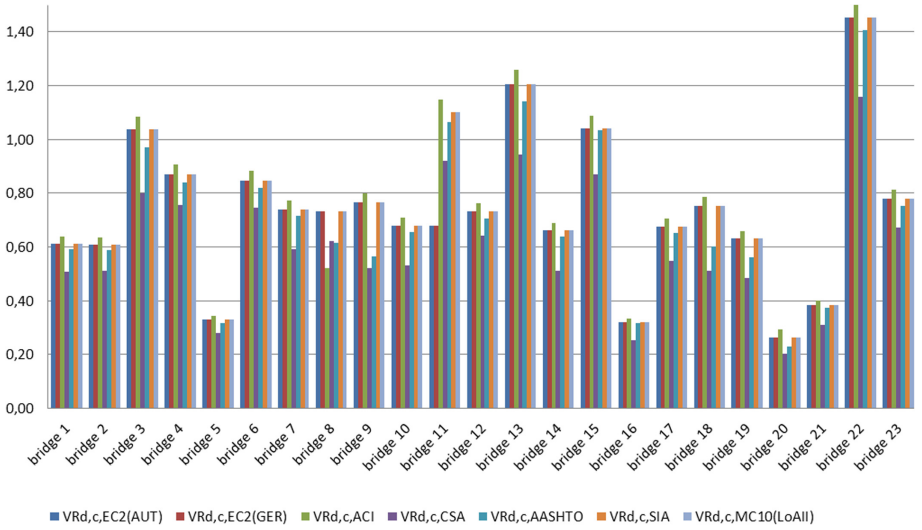

Fig. 16. Comparison of seven international standards.

7 Experimental Outcome

In the following section the outcome of the testing series are compared with regards of their load bearing behaviour. The testing includes set-ups with distributed loads and without shear reinforcement and set-ups with concentrated loads with bent-up bars. The analysis showed that present standards are not able to predict the structural behaviour of set-ups with distributed loads. Concerning this uncertainty in current standards a detailed analysis will not be benefiting. It comes clear that the most influencing parameter, due to the nominal values of shear resistance states the slenderness ratio a/d. Further beams without shear reinforcement and different bent-up bars were tested. Variable parameters of the testing were the location of the bent-ups to the support or other shear bars, the quantity of bent-ups and the impact of a second bent-up row. The following Eq. 1 estimates the influence of bent-up bars, to consider the degree of the shear resistance of bars in addition to the concrete shear resistance.

The following Eq. 1 estimates the influence of bent-up bars, to consider the degree of the shear resistance of bars in addition to the concrete shear resistance.

$$x = \frac{\left(1 - \frac{Vexp}{VRk,c}\right) * VRk,c}{VRk,s} = \frac{Vexp - VRk,\ c}{VRk,\ s} \tag{1}$$

The analysis pointed out that structures with greater spans and slenderness result a diminished bending and shear resistance as seen in Table 2 published as “Load carrying behaviour of beams with bent-up bars as shear reinforcement” in IABSE Symposium Vancouver 2017. The comparison of two objects with similar dimensions displays different behaviours. Reasons are given to the lower steel and concrete

qualities and the use of 90% quantity of steel and the shallow angle of the structure. The shallow angles lead to concentrated loads in general. Another investigated result is given by a higher shear resistance on the basis of an increased level of transversal rebar. In addition to that, the investigations pointed out that the longitudinal reinforcement does not affect the shear resistance. Sherwood points out that the slenderness of a structure seems to be crucial parameter regarding the shear behavior. Further it is important to take into account that the reinforcement strain influences the shear strength distinctively more than the quantity of steel. Along to this there is also a difference to the shear resistance approach of the Model Code and Eurocode. The formula of Eurocode does not include any longitudinal strains of the reinforcement. The existing bridge stock also includes many structures with exceeded spacing between the bent-ups, which are not comprised in any parameter of the formula. According to the outcomes of the testing series of the Technical University of Vienna beams with bents close to supports and only one row of bent- ups show a very low level of the activated shear bars based on a high slenderness and a higher traverse gap. It is mentionable that a bent-up close to the support might not be critical, if there is a second row of bent-ups. The comparison of the different design standards showed that guidelines from 1940 to 1956 display almost a linear graph relating to the dynamic factor in contrast to B4003:1984 and B4003:1994, which display a roughly parabolic graph. Further older standards show quite higher dynamic values for greater spans than 6 m in opposite to standards from nowadays. The research pointed out that loads with shorter span widths follow higher values from load model B4003:1984. This is caused by two concentrated loads, which are not distributed and this valid whether the dynamic factor is considered or not. For greater spans load model SW2 displays the highest values without using any dynamic influences. Based on the proportional approaches of older standards, they still overstep values with dynamic factors. In the analysis no safety factors or prospective load increases were added, but in general older standards and heavy fright models fall below these values. Further it is important to mention, that the load class factor is not multiplied with the freight model. The nominal shear resistance of different standards displays the same calculative approach, if the same longitudinal ratio has been used due to the level of resistance. Another interesting aspect appears by the reason of different longitudinal ratios but the same concrete strength, which follow the same trend mark. The analysis of the test series confirmed that the use of current design methods cannot predict the behaviour of load distribution. Test series on similar specimen and the nonlinear FE-simulation pointed out that bent-ups only got activated, if the old-factor is adequate. This further implies that a higher shear resistance could be achieved, if two rows of bent-ups are arranged. In these cases where only one row of bent-up bars, were disposed, the main shear crack was not crossing the bent-up, which means that this bar was not activated before failure. The investigation also contains analysis of beams without stirrups, therefore bent-up bars were used as shear reinforcement. The load bearing behaviour of these bent-ups were tested regarding to their location and quantity of bent-ups, to analyse the influence of a second row regarding to the shear resistance as seen in Table 2.

Table 2. Experimental outcome due to the testing parameter

Setting	L	d	L/d	s_{ls}/d	s_t/d	rows	V_{exp}	Setting	L	d	L/d	s_{ls}/d	s_t/d	rows	V_{exp}
	[m]	[m]	[-]	[-]	[-]	[-]	[kN]		[m]	[m]	[-]	[-]	[-]	[-]	[kN]
B000-3d	6.5	0.493	13.2			0	251.09	B177z-3d	6.5	0.493	13.2	1.56	0.81	2	425.40
B000-4d	6.5	0.493	13.2			0	226.08	B177-4d	6.5	0.493	13.2	1.56	0.81	1	276.07
B149-3d	6.5	0.493	13.2	0.99	0.81	1	303.83	B249-3d	6.5	0.493	13.2	0.99	0.41	1	450.11
B149-4d	6.5	0.493	13.2	0.99	0.81	1	226.92	B249-4d	6.5	0.493	13.2	0.99	0.41	1	270.74
B149z-3d	6.5	0.493	13.2	0.99	0.81	2	453.33	BzL1-3d	8.5	0.605	14.0	1.16	0.66	1	295.84
B149z-4d	6.5	0.493	13.2	0.99	0.81	2	325.84	BzL1-4d	8.5	0.605	14.0	1.16	0.66	2	255.48
B177-3d	6.5	0.493	13.2	1.56	0.81	1	453.95	BzL2-3d	6.2	0.605	14.0	1.16	0.66	2	339.36
B177z-4d	6.5	0.493	13.2	1.56	0.81	2	324.27	BzL2-4d	8.5	0.605	14.0	1.16	0.66	1	254.82

Along this research work a degree of shear resistance for bars was calculated and compared with the results of the 1992-1-1:2017 readout. The assumptions pointed out, that beams without shear reinforcement have a degree of zero, but beams with a reduced slenderness and an appropriate distance to the support activate the present shear bars. The second row of bent-ups states a security to capture the critical shear crack, which implies the distinctive higher shear reliability in its mode of operation. To sum up it is also benefiting to have a higher value of transversal rebar ratio regarding to the shear resistance. In contrast to that, a higher longitudinal ratio does not generate a better shear behaviour. Test series of full-scale shear investigations on slab bridges, which were carried out by the Technical University of Vienna, displayed that bent-ups only got activated, if the a/d-factor is adequate and a higher reliability of shear can be taken for granted due to the arrangement of two bent-up rows. Along it is important to develop tools or introduce measures for load distribution of concentrated loads to simplify the design process and estimations of the real conditions. Further it is mentionable, that a clear differentiation regarding to highway and railway bridges is needed to prevent unrealistic peak loads. Additional it is useful to take into account that the strain of the longitudinal reinforcement seems to influence the shear strength more than the quantity of rebar. Additional loads are combined with short axle distances, which cannot be distributed to great extent. For the verification process it is necessary to create a simplified model for load distributions and combinatorics of loads. The assessment of these 23 railway objects illustrated that the German draft of the Eurocode 2, the Canadian standard CSA and the Model Code LoA II follow the most conservative results. As a next step the existing bridge stock has to be proven due to the load bearing and the location of the bent-ups. Concluding it is important to take into account that an application of additional load should not be used in general, only if it is necessary, so further specifications have to be done according to the load model [1, 3, 6].

8 Conclusions

Due to the different investigations, results of both models 2D and 3D (not published in this paper) showed free reserves in the load bearing capacity compared to EC 2 and fib Model Code. Referring to the live load trains according to the current ONR 24008, a high level of safety still remains. In accordance with the defined assessment proposal of this paper and in consideration of the ratio of the concrete contribution, a positive verification could be achieved. Many parameters depend on the load capacity of slab bridges, so no general guidance could be listed. Only by taking each parameter such as the aggregate interlock, dowel effective, arch effect and the shear contribution of concrete into account, realistic conditions can be simulated. An established theory in the field of structural engineering makes clear that the aggregate interlocking resistance of the cracked tension zone is considered as an additional shear resistance mechanism. To get an efficient output for slabs with low shear reinforcement, the results were compared to the conservative approach of EC 2 and Model Code 2010. This comparison points out that beams without shear reinforcement do not show any differences between using EC 2 and Model Code for the level of approximation II. The nonlinear finite element

simulation showed that the bent-up bars contribution could be taken into account with 50% of the design value of reinforcing steel in addition to the concrete contribution according to EC 2. The limit of 50% is caused by the limitation of crack pattern, which would further reduce the concrete contribution. The design proposal of this research got also implemented in the ONR 24008 and ÖN B 4008-2. Moreover, it is suggested to have additional bridge inspections to get a reliable projection about the structural behaviour due to present mode of operation. With the help of frequent surveying and inspections of the existing structures, it becomes clear that there is no current demand for strengthening or replacement of many structures. Thus, the engineering standards for the assessment of existing concrete bridge structures have to be adjusted, especially for shear load capacity. Finally, the investigations pointed out that the normative safety of bridge structures could be achieved by considering a reduced resistance of bent-up bars in combination with the load bearing capacity of the concrete contribution. The results of the FE modeling and the comparison of the different test series from different universities and different researchers confirm that the structures are still safe to use for the current load classes, if the maintenance condition of the bridge structure is adequate.

References

1. International Federation for Structural Concrete: fib Model Code for Concrete Structures 2010. Lausanne 2010
2. Kopp M (2016) Numerical modeling and analysis of load bearing capacity of slab bridges with regard to shear resistance. Master thesis, Civil Engineering, University of Applied Sciences, Vienna
3. Köck G (2017) Assessment and analysis of existing concrete slab bridges with respect to their shear force capacity. Master thesis, Civil Engineering, University of Applied Sciences, Vienna
4. Natário F, Ruiz MF, Muttoni A (2014) Shear strength of RC slabs under concentrated loads near clamped linear supports. Eng Struct 76:10–23
5. ÖNORM EN1991-2: Eurocode 1: Einwirkungen auf Tragwerke, Teil 2: Verkehrslasten auf Brücken. Wien 2012
6. ÖNORM EN1992-1-1: Eurocode 2: Bemessung und Konstruktion von Stahlbeton- und Spannbetontragwerken. Wien 2015
7. ÖNORM B2302: 1931 01 01: Eisenbeton; Berechnung und Bemessung von Tragwerken
8. ÖNORM B4008-2: 2017 01 01: Bewertung der Tragfähigkeit bestehender Tragwerke- Teil 2: Brückenbau

Modeling of the Shear Connection Capacity of Hybrid Steel Trussed Composite Beams

M. Latour[1], A. Monaco[2(✉)], and G. Rizzano[1]

[1] Department of Civil Engineering, University of Salerno, Via Ponte Don Melillo, Fisciano, SA, Italy
[2] Department of Architecture and Design, Politecnico di Torino, Viale Mattioli 39, Turin, Italy
alessia.monaco@polito.it

Abstract. Hybrid Steel Trussed Composite Beams represent a technical solution in use in numerous countries since many years. They are able to join the advantages of prefabrication with those of cast in place structures: they are easy to manufacture, fast to realize, monolithic and with no need of formwork. The behavior of these beams has been recently topic of discussion in the scientific community because the knowledge both related to the reinforced concrete structures and that of composite constructions cannot be straightforwardly extended to this typology, which is intermediate between one and another technology. This paper provides a contribution towards a better understanding of the mechanism of transfer in the beam typologies with bottom steel plate. A FE model is set up and, subsequently, a simple design formula for the prediction of the shear capacity of the concrete-steel connection is derived and verified on the results of parametric FE analyses.

Keywords: Hybrid steel trussed composite beams · Push-out tests · FE modelling · Shear capacity

1 Introduction

A hybrid steel-trussed concrete beam (HSTCBs) is a particular type of composite girder which is in use in the Italian and South American construction market since the 70s. Such girders are constituted by a steel truss embedded in a concrete core. The truss is typically composed by a steel plate or by a precast concrete slab working as bottom chord, designed to be the formwork during the concrete cast and the steel reinforcement in the service phase, while welded steel bars are generally used to form the upper chord. Moreover, ribbed or smooth steel bars welded to the plate are used to form the web of the truss. The success of these beams in the construction industry is mainly due to the practical advantages related to the adoption of this beam, such as the partial prefabrication, the easy and fast buildability and the possibility to apply easily HSTCBs to long spans.

After about sixty years from the first applications and from the submission of the initial patents, HSTCBs have been recently under a significant attention of the Italian

M. di Prisco and M. Menegotto (Eds.): ICD 2018, LNCE 42, pp. 149–161, 2020.
https://doi.org/10.1007/978-3-030-23748-6_12

scientific community for the development of specific codes and related guidelines, with a growing debate on some particular issues arising with these beams.

In this framework, about ten years ago, the main companies producing HSTCBs have pushed strongly the inherent research activities, supporting significantly the development of studies in this field. Among the issues faced within this activity, great interest has been paid to the study of the lateral-torsional buckling in the casting phase, the behavior of the welded connections between the elements of the truss, the problems related to the creep, the behavior of beam-to-column joints, the shear resistance and the mechanism of the shear transfer between the bottom chord of the truss and the diagonal (among others Aiello 2008; Izzo et al. 2010; Vincenzi and Savoia 2010; Colajanni et al. 2014, 2015a, b, 2017a, b, 2018; Monaco 2016; Campione et al. 2016; Ballarini et al. 2017). In particular, the mechanism of shear transfer from the bottom chord to the inner concrete core represents one of the main issues to be investigated in order to correctly understand the behavior of these beams both at the serviceability and ultimate limit state conditions.

Owing to the lack of specific code requirements in this regard, recently, new tests have been carried out in Italy, analyzing the mechanism of transfer through the development of specific push-out tests (Aiello 2008; Colajanni et al. 2014) focusing the attention on the role of the main geometrical and mechanical parameters affecting the response of the beam. The authors have performed several tests by varying the following parameters: the type of bars used to form the truss (smooth or ribbed), the concrete and steel quality, the diameter and the slope of the truss diagonal and the depth of the beam.

Also from the modelling standpoint recently, some attempts to provide simplified analytical formulations able to predict the load carrying capacity of the shear connection between the steel plate and the concrete have been made (Colajanni et al. 2015a; Chisari and Amadio 2014).

Nevertheless, despite the significant work already carried out by the scientific community in last few years, there is still a lack of knowledge and, due to the limited number of available numerical and experimental results, new efforts to further investigate the stress transfer mechanism from the steel truss to the concrete of HSTCBs are needed.

Within this framework, the present work deals with the calibration of a 3D Finite Element (FE) model of HSTCBs, which is developed in order to carry out a detailed investigation of the stress transfer mechanism between the steel truss and the concrete core. To this scope, as a first step, the accuracy of the proposed FE model is verified on some of the existing experimental push-out tests (Aiello 2008). Afterwards, the same FE model is used to perform a parametric analysis by generating a number of push-out tests with different geometrical and mechanical characteristics in order to individuate the main parameters affecting the maximum force that can be transferred from the plate to the concrete through the diagonals of the truss. Finally, a design equation able to predict the shear resistance, inspired to models already available in the existing technical literature dealing with the resistance of dowels and piles in cohesive soils, is suggested. The accuracy of the model is verified by means of comparison with the results of push-out tests available in technical literature and with the FE results.

2 FE Model

The FE model has been developed by means of the software Abaqus 6.10 (SIMULIA 2010). In order to investigate in detail the interaction mechanism arising between the steel diagonals of the truss and the concrete core, a 3D FE model has been developed accounting for the actual geometry of the specimens, the material geometrical non-linearity and the interaction stresses arising between the bars and the surrounding concrete.

Concerning the meshing of the beam, the truss has been discretized by means of brick elements adopting a structured meshing technique while the concrete block has been discretized by using linear tetrahedra with free meshing technique that is more effective in cases of complicate geometries (Fig. 1).

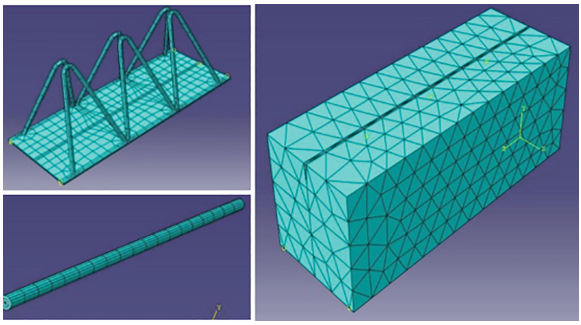

Fig. 1. Adopted meshing techniques.

Materials have been modelled by means of a quadri-linear law for the steel (Faella et al. 2000) and a damaged plasticity model for the compressed concrete (Lubliner et al. 1988).

For the definition of the interaction between the steel rebars and the concrete core, four models have been used. Particularly, two models intend to simulate the case of HSTCB with ribbed steel trusses and the other two models aim to simulate the case of smooth steel diagonals. For Ribbed-Steel-Bar-Models (RSBMs) two approaches have been used: the first one provides a simplified modelling of the concrete-steel interaction by simply tying the nodes of the two surfaces in contact (RSBM-1), the second one provides the insertion of cohesive contact elements between the steel rebar and the surrounding concrete (RSBM-2). RSBM-2 allows a more accurate simulation of the separation phenomena arising during a push-out test; it is characterized by a progressive stiffness degradation of the interface, driven by a damage process. In this model the damage is assumed to start and develop according to the well-known stress-slip relationship by Eligehausen et al. (1983).

Two further models were developed aiming to study the case of HSTCBs with smooth steel trusses (Smooth Steel Bars Models - SSBMs): in the first simplified approach, a frictionless contact between the steel and the concrete has been introduced

(SSBM-1); in the second approach, a cohesive model with damage evolution has been implemented (SSBM-2), using the stress-slip relationship by Verderame et al. (2009).

3 Validation of the FE Model

The accuracy of the FE model has been checked by comparing the numerical slip-load curves versus the corresponding experimental curves of some of the push-out tests carried out by Aiello (2008). The comparison is shown in Figs. 2 and 3 for ribbed and smooth specimens, respectively.

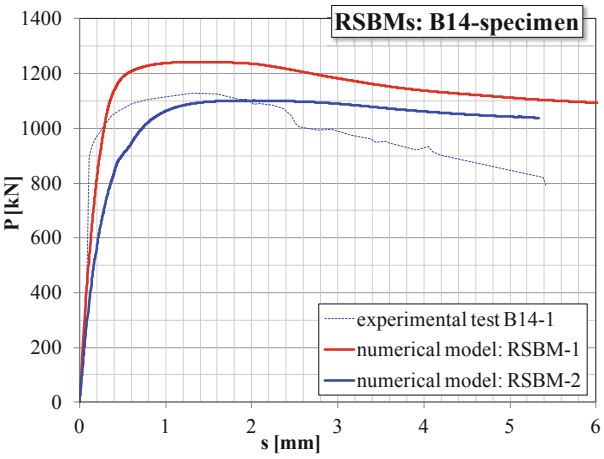

Fig. 2. Comparison between experimental results and RSBMs of B14-specimen.

As expected, RSBMs-1 provides an overestimation of the maximum resistance because of the tie interaction introduced between steel-concrete surfaces. Conversely, the implementation of a cohesive interaction property at the steel-concrete interface in RSBMs-2, due to the more accurate modelling of the traction-separation and bonding phenomena, allows to obtain a more accurate result which fits satisfactorily the experimental slip-load curves. As regards specimens with smooth steel truss, the comparison between experimental and numerical results in Fig. 3 demonstrates that both SSBM-1 and SSBM-2 provide force versus displacement curves very similar, because, in case of bond between smooth steel and concrete, the interface experiences a more contained damage than in case of ribbed steel. Finally, observing the afore-mentioned curves it can be appreciated the different behaviour of HSTCBs concerning with both strength and stiffness, depending on some fundamental parameters such as the diameter of the diagonal bars, steel yielding strength and the constitutive law characterizing all steel surfaces embedded in the concrete core.

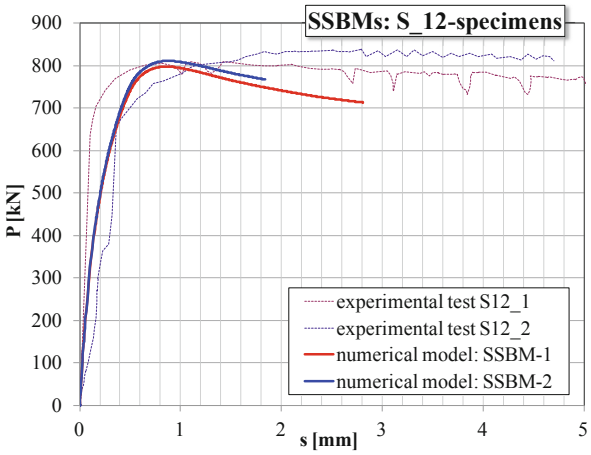

Fig. 3. Comparison between experimental results and SSBMs of S12-specimens.

4 Parametric Analysis

In order to investigate the main parameters influencing the maximum load that can be transferred from the steel plate to the concrete, numerical simulations of push-out tests have been developed. The geometrical and mechanical parameters have been varied starting from the basic geometry of the tests performed by Aiello (2008). The following four parameters have been considered in the analysis: diameter of the diagonal bars, yield stress of the steel, compressive strength of concrete, bars typology (smooth or ribbed).

Thirty-six simulated tests have been generated; in all cases, the bottom steel plate and the rebar constituting the upper chord are assumed to have a yield stress equal to 355 MPa and 450 MPa respectively.

The numerical simulation has been carried out by considering that the rebar composing the upper chord has the same superficial finishing of the bars composing the diagonals of the truss, i.e. all the bars composing the truss are always all ribbed or all smooth. Table 1 reports a synoptic scheme containing the identity tags used to individuate all the considered analyses. In particular, letters A, B and C define the concrete cylindrical compressive strength (32, 25 or 16 MPa); numbers 12 or 14 individuate the diameter of the truss diagonals; numbers 2, 3 or 4 identify the steel yield stress (235, 355, 450 MPa respectively) and, finally, the letter "X" has to be read as "R" in case of ribbed bars or as "S" in case of smooth rebars.

Before generating the thirthy-six analyses, in order to investigate also the influence on the push-out resistance of the thickness of the bottom plate, two models have been generated considering two alternative plates of 10 mm and 6 mm. The comparison of the results (not reported here for brevity) has evidenced a limited influence of this parameter on the strength and a higher influence on the stiffness. In particular, the increase of plate thickness of 4 mm leads to an increase of the resistance and of the initial stiffness of about 1.6% and of 28% respectively. Therefore, assuming that the

Table 1. Identity tags of numerical analyses.

	f_y = 235 [MPa]	f_y = 355 [MPa]	f_y = 450 [MPa]
f_c = 32 [MPa]	A12-2X A14-2X	A12-3X A14-3X	A12-4X A14-4X
f_c = 25 [MPa]	B12-2X B14-2X	B12-3X B14-3X	B12-4X B14-4X
f_c = 16 [MPa]	C12-2X C14-2X	C12-3X C14-3X	C12-4X C14-4X

X = R ribbed steel bars; X = S smooth steel bars

thickness of the bottom plate does not significantly affect the resistance, only the other geometrical and mechanical parameters previously reported have been examined in the parametric analysis. The extensive discussion of the FE parametric results is available in Colajanni et al. (2015a). Table 2 reports the results of the numerical parametric analyses in terms of maximum slip load for each simulation. The values of maximum laod reported are expressed in kN.

Table 2. Numerical peak loads from the parametric FE simulations.

		f_y = 235 [MPa]	f_y = 355 [MPa]	f_y = 450 [MPa]
f_c = 32 [MPa]	*R-12*	592	719	793
	R-14	683	837	939
	S-12	553	657	715
	S-14	662	807	900
f_c = 25 [MPa]	*R-12*	617	735	820
	R-14	669	814	947
	S-12	510	606	663
	S-14	622	765	867
f_c = 16 [MPa]	*R-12*	474	577	645
	R-14	591	726	802
	S-12	441	525	580
	S-14	559	696	782

It is worth noting that the peak force increases less than linearly as far as the concrete strength increases and, in the case of ribbed bars, after a certain value of the concrete resistance, it does not increase anymore. In fact, the simulations do not show a significant increase of the peak load for concrete with resistance higher than 25 MPa. Similarly, the results of the numerical simulations obtained by varying the steel yield stress of the truss diagonals shows the significant influence of the steel yield stress on the ultimate load. The developed analyses have provided preliminary results in order to develop an analytical model able to predict the ultimate shear load of the steel-concrete connection of HSTCBs starting from the geometrical and mechanical properties of the construction details. The formulation of the analytical model is presented in the next section.

5 Analytical Modelling

On the basis of the theoretical studies available dealing with the dowel effect and the resistance of piles in concrete soils (Vintzeleou and Tassios 1986, 1987; Broms 1964), the shear strength of the connection of HSTCBs, that is the ultimate force that can be transferred from the steel plate to the concrete core of the beam through the diagonals of the truss, is herein evaluated. Starting from the mechanisms described in Broms (1964) and Vintzeleou and Tassios (1990), some significant parameters are identified for extending the existing formulations for the prediction of the resistance of steel dowels/piles to the case of inclined steel bars loaded against concrete. Particularly, the effect of the lateral confinement degree of the steel rebar and the length of the plastic hinge arising on the latter are highlighted. Moreover, in contrast to what usually do in the available reference studies, in the present formulation also the influence of the bending moment-axial force interaction in the presence of shear is considered.

In particular, the examined case can be regarded as the case of an inclined dowel surrounded by concrete with different degree of confinement depending on the lateral concrete cover, welded to the steel plate of the beam and linked to the upper longitudinal rebar so that a two-plastic-hinge-mechanism arises with the bending moment associated to the axial force in the presence of shear.

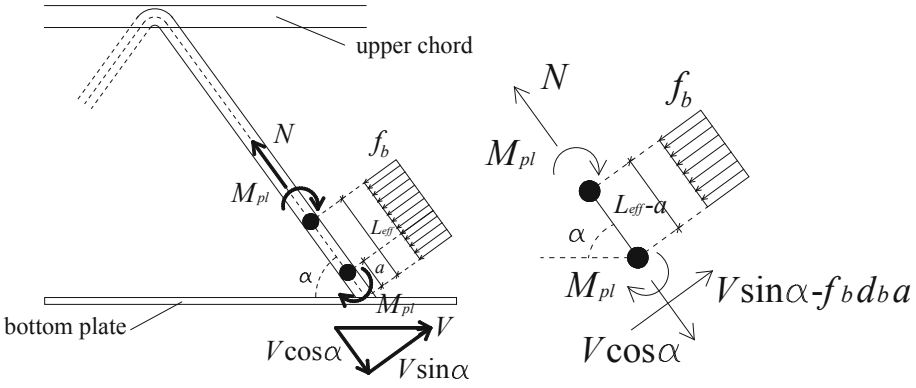

Fig. 4. Mechanical model: scheme of the mechanism and equilibrium of forces.

The mechanism and the main parameters taken into account in the proposed model are schematically represented in Fig. 4. Thus, in the model, the most significant parameters are introduced as explained in the following:

(i) the inclination of the dowels (i.e. the inclination of the diagonals of the truss) is introduced by means of the angle α individuated on the inclined plane of the truss.

The angle α can be easily calculated starting from the geometric dimensions of the truss, according to the following expression:

$$\alpha = \arccos\left(\frac{0.5\,s}{\sqrt{0.25\,s^2 + d^2 + 0.25\,b^2}}\right) \tag{1}$$

in which s is the spacing of the truss and b and d are the width and depth, respectively.

(ii) the bearing stress of concrete $f_b = \psi f_c$, is a function of the lateral concrete covers c_1 and c_2 as defined in the model proposed by Vintzeleou and Tassios (1990). For the examined case, a correction coefficient $\delta = \sqrt{\frac{\psi}{3}}$ varying in the range 0.60–1.30 can be expressed through the following equations:

$$\begin{array}{ll} \delta(I) = 0.6 + \frac{c_1}{d_b}\left(0.027\frac{c_2}{d_b} + 0.10\right) & \text{for } 0 \le \frac{c_1}{d_b} \le 3 \text{ and } 0 \le \frac{c_2}{d_b} \le 5 \\ \delta(II) = 0.9 + 0.08\frac{c_2}{d_b} & \text{for } \frac{c_1}{d_b} \ge 3 \text{ and } 0 \le \frac{c_2}{d_b} \le 5 \\ \delta(III) = 0.6 + 0.233\frac{c_1}{d_b} & \text{for } 0 \le \frac{c_1}{d_b} \le 3 \text{ and } \frac{c_2}{d_b} \ge 5 \\ \delta(IV) = 1.3 & \text{for } \frac{c_1}{d_b} \ge 3 \text{ and } \frac{c_2}{d_b} \ge 5 \end{array} \tag{2}$$

Therefore, the coefficient ψ can be introduced for calculating the plastic bearing stress of concrete assuming $\psi = 5$, when the confinement effect is fully exploited (i.e.$c_1/d_b \ge 3$ and $c_2/d_b \ge 5$), while $\psi = \left(\delta\sqrt{3}\right)^2 \le 5$,when the confinement effect depends on the side concrete cover.

(iii) the boundary condition of the head of the dowel: the dowel is assumed perfectly fixed to the steel plate of the beam so that a mechanism involving two plastic hinges occurs. The plastic hinges are placed at a distance equal to (L_{eff} -a) being L_{eff} the effective length of the diagonal rebar involved in the mechanism and a the length of the plastic hinge next to the steel plate of the beam.

(iv) the bending moment developed in the plastic hinges is the one of the M-N domain according to Millard and Johnson (1984):

$$M_{pl} = \frac{d_b^3}{6} f_y \left(1 - N^2 \Big/ \left(\pi \frac{d_b^2}{4} f_y\right)^2\right) \tag{3}$$

(v) the interaction M-N-V is introduced in the model according to Eurocode 3 rules in which shear is introduced in the given axial force and bending interaction criterion with the reduction of the ultimate strength of steel by means of a coefficient (1-ρ), where $\rho = (2\ V/V_{Ru}\text{-}1)^2$ for $V \ge 0.5V_{Ru}$, being $V_{Ru} = 0.8f_uA_{sw}$ (where f_u is the ultimate strength of the steel bar whose cross section area is A_{sw}).

Considering the scheme reported in Fig. 4 the following equilibrium equations can be written:

$$V\cos\alpha = N \tag{4a}$$

$$V\sin\alpha - f_b \cdot d_b \cdot a = f_b \cdot d_b \cdot \left(L_{eff} - a\right) \tag{4b}$$

$$2M_{pl} + f_b \cdot d_b \cdot 0.5\left(L_{eff} - a\right)^2 = \left(V \sin\alpha - f_b \cdot d_b \cdot a\right)\left(L_{eff} - a\right) \tag{4c}$$

in which the plastic bending moment M_{pl} can be expressed as function of the dowel force V by substituting Eq. (4a) into Eq. (3).

From Eqs. (4a)–(4c), considering that the unknowns of the problem are V, N and L_{eff}, the following expression can be derived:

$$V^2\left(\frac{\sin^2\alpha}{2f_b\,d_b} + \frac{16\cos^2\alpha}{3\,\pi^2 d_b f_y\left(1-\left(\frac{10\,V}{f_u\,\pi\,d_b^2}-1\right)^2\right)}\right) - V\cdot a\cdot\sin\alpha - \left(\frac{d_b^3}{3}f_y\left(1-\left(\frac{10\,V}{f_u\,\pi\,d_b^2}-1\right)^2\right) - \frac{f_b\,d_b\,a^2}{2}\right) = 0 \tag{5}$$

where, as mentioned before, f_b is equal to ψ f_c and the value of the yielding stress of the steel rebar in Eq. (5) is reduced by considering the interaction with the shear force (M-N-V interaction) when applicable, according to Eurocode 3 (CEN 2005a) prescriptions.

Conversely, if the M-N-V interaction is neglected and $a = 0$ is assumed, a simpler closed form for the dowel force V, easily applicable in design practice, can be obtained:

$$V = \frac{d_b^2\sqrt{2f_y f_b}}{\sqrt{3\sin^2\alpha + \frac{32f_b}{\pi^2 f_y}\cos^2\alpha}} \tag{6}$$

Therefore, two significant cases can be finally considered within the proposed formulation, named in the following *model 1* and *model 2*:

- *model 1*, based on the evaluation of the dowel force acting on a single diagonal rebar of the truss of the HSTCB developed by considering the actual plastic hinge length a and by calculating the actual degree of concrete confinement ψ through the coefficient δ expressed in Eq. (2). In this case the calculation of V has to be conducted by solving Eq. (5), that takes into account the M-N-V interaction effects according to Eurocode 3 prescriptions.
- *model 2*, developed by neglecting both the actual M-N-V interaction effects and the plastic hinge length (i.e. assuming a = 0) and by considering the maximum degree of concrete confinement (i.e. assuming $\psi = 5$). In this case the calculation of V can be conducted in the closed form done by Eq. (6).

In the following section, both models are validated against the experimental results of push-out tests by Aiello (2008) and against the results of the FE parametric simulations by Colajanni et al. (2015).

6 Model Validation

The accuracy of the models is verified with experimental data and FE results collected from the technical literature. As already mentioned, the problem of studying the stress transfer mechanism between steel and concrete has been experimentally investigated by means of push-out tests that are inspired to the test procedures specified in Eurocode 4 (CEN 2005b) for classical composite beams. Push-out test results obtained by Aiello (2008) are considered. As regards the FE data, the results of the previous parametric analysis are exploited for the validation (Colajanni et al. 2015a). Particularly, eight experimental results and thirty-six FE simulations are taken into account for the validation of the proposed model.

The proposed analytical formulation has been applied to the reference dataset and the results are reported in Table 3. Both model 1 and model 2 have been considered.

Table 3. Validation of the proposed formulation against experimental and numerical data.

ID	$P_{theo,1}/P_{exp}$	$P_{theo,2}/P_{exp}$
Experimental data (Aiello 2008)		
S12_1	1.00	0.89
S12_2	0.97	0.87
S14_2	0.90	0.84
S14_3	0.88	0.82
S14_4	0.83	0.77
B12_1	0.89	0.83
B12_2	0.88	0.82
B14_1	1.02	0.99
Parametric FE data (Colajanni et al. 2015a)		
A12-2R	1.09	0.94
A12-3R	1.06	0.97
A12-4R	1.03	0.99
A12-2S	1.17	1.01
A12-3S	1.16	1.06
A12-4S	1.14	1.10
A14-2R	1.25	1.11
A14-3R	1.19	1.13
A14-4R	1.14	1.14
A14-2S	1.29	1.14
A14-3S	1.24	1.17
A14-4S	1.19	1.19
B12-2R	0.91	0.81
B12-3R	0.87	0.84
B12-4R	0.83	0.86
B12-2S	1.10	0.98
B12-3S	1.05	1.02
B12-4S	1.03	1.06
B14-2R	1.10	1.01
B14-3R	1.03	1.04

(*continued*)

Table 3. (*continued*)

ID	$P_{theo,1}/P_{exp}$	$P_{theo,2}/P_{exp}$
B14-4R	0.94	1.01
B14-2S	1.19	1.09
B14-3S	1.09	1.10
B14-4S	1.03	1.10
C12-2R	0.87	0.85
C12-3R	0.80	0.87
C12-4R	0.77	0.88
C12-2S	0.94	0.92
C12-3S	0.88	0.95
C12-4S	0.86	0.98
C14-2R	0.91	0.93
C14-3R	0.83	0.94
C14-4R	0.81	0.96
C14-2S	0.97	0.98
C14-3S	0.87	0.98
C14-4S	0.83	0.98
Avg	*1.00*	*0.98*
CVr	*14%*	*11%*

As it can be observed, model 1 provides a quite accurate prediction of the total force attained during the push-out test ($P_{theo,1}$) with a ratio $P_{theo,1}/P_{exp}$ almost equal to one. The associated coefficient of variation CVr is 14%.

In general, if only the M-N-V interaction effects are neglected, the model yields to an average overestimation of the theoretical resistance of the connection. Then, when also the plastic hinge length is neglected as done in model 2, the analytical prediction provides a more conservative result with quite good assessment of the experimental load $P_{theo,2}$ with an extremely contained underestimation of P_{exp} ($P_{theo,1}/P_{exp} = 0.98$) and coefficient of variation equal to 11%. Furthermore, it can be observed that the error in the theoretical prediction due to the assumption of a plastic hinge length equal to zero is then compensated by the simplified hypothesis of the maximum degree of confinement not dependent on the side cover.

In conclusion, even though model 1 proves to be more effective in the prediction of the maximum load in almost all examined cases, the simplified code-compliant model 2 provides a very satisfactory prediction and easy application of the analytical formula by practitioners for design purpose.

7 Conclusions

In this paper the response of hybrid steel trussed composite beams has been investigated. In particular, the mechanism of the shear transfer between the steel plate, representing the bottom chord of the truss, and the inner concrete core, through the diagonals has been analyzed.

In order to assess the local behavior of the beam a FE model in ABAQUS has been developed and validated versus experimental results retrieved from the available technical literature. The FE model has shown to be able to provide accurate results and, therefore, it has been used to generate further cases, useful to analyze the influence of the main parameters affecting the value of the shear capacity.

In order to provide a simple tool for design, new equations have been suggested, providing a mechanical model based on the results of previous studies dealing with the dowel effect and analysis of piles subjected to horizontal forces in cohesive soils. The model has proven to be accurate and easy to be applied by practitioners, even though it relies on strong simplifications.

References

Aiello MA (2008) Analisi sperimentale della connessione acciaio-calcestruzzo nelle travi reticolari miste. In: VII Workshop Italiano sulle Strutture Composte, Benevento, 23–24 Ottobre

Ballarini R, La Mendola L, Le J, Monaco A (2017) Computational study of failure of hybrid steel trussed concrete beams. J Struct Eng ASCE 143(8):13, art. no. 04017060

Broms BB (1964) Lateral resistance of piles in cohesive soils. J Soil Mech Found Div Proc ASCE 90(SM2):27–63

Campione G, Colajanni P, Monaco A (2016) Analytical evaluation of steel-concrete composite trussed beam shear capacity. Mater Struct 49(8):3159–3176

CEN (2005a) Eurocode 3 - EN1993-1-1: Design of steel structures. Part 1-1: General rules and rules for buildings. European Committee for Standardization (CEN), Brussels, Belgium

CEN (2005b) Eurocode 4 — design of composite steel and concrete structures — part 1-1: general rules and rules for buildings

Chisari C, Amadio C (2014) An experimental, numerical and analytical study of hybrid RC-encased steel joist beams subjected to shear. Eng Struct 61(1):84–98

Colajanni P, La Mendola L, Monaco A (2014) Stress transfer mechanisms investigation in hybrid steel trussed-concrete beams by push-out tests. J Constr Steel Res 95:56–70

Colajanni P, La Mendola L, Monaco A (2015a) Stiffness and strength of composite truss beam to R.C. column connection in MRFs. J Constr Steel Res 113:86–100

Colajanni P, La Mendola L, Monaco A (2017a) Experimental investigation on the shear response of precast steel-concrete trussed beams. J Struct Eng ASCE 143(1), art. no. 04016156

Colajanni P, La Mendola L, Monaco A (2018) Stress transfer and failure mechanisms in steel-concrete trussed beams: Experimental investigation on slab-thick and full-thick beams. Constr Build Mater 161(1):267–281

Colajanni P, La Mendola L, Latour M, Monaco A, Rizzano G (2015b) FEM analysis of push-out test response of Hybrid Steel Trussed Concrete Beams (HSTCBs). J Constr Steel Res 111:88–102

Colajanni P, La Mendola L, Latour M, Monaco A, Rizzano G (2017b) Analytical prediction of the shear connection capacity in precast steel-concrete trussed beams. Mater Struct 50(1), art. no. 48

Eligehausen R, Popov EP, Bertero VV (1983) Local bond stress-slip relationships of deformed bars under generalized excitations. Report No. UCB/EERC 83–23. University of California, Berkeley, CA, USA

Faella C, Piluso V, Rizzano G (2000) Structural steel semirigid connections. CRC Press, Boca Raton

Izzo L, Miglioli M, Minelli F, Plizzari G (2010) Qualificazione e progettazione delle travi prefabbricate reticolari miste. 18° Congresso C.T.E., Bologna, 11–13 novembre

Lubliner J, Oliver J, Oller S, Onate E (1988) A plastic damage model for concrete. Int J Solids Struct 25(3):299–326

Millard SG, Johnson RP (1984) Shear transfer across cracks in reinforced concrete due to aggregate interlock and to dowel action. Mag Concr Res 36(126):9–21

Monaco A (2016) Numerical prediction of the shear response of semi-prefabricated steel-concrete trussed beams. Constr Build Mater 124:462–474

SIMULIA (2010) Abaqus 6.10 Theory Manual, Dassault Systèmes Simulia Corp.

Verderame GM, De Carlo G, Ricci P, Fabbrocino G (2009) Cyclic bond behavior of plain bars. Part II: analytical investigation. J Constr Build Mater 23:3512–3522

Vincenzi L, Savoia M (2010) Stabilità di tralicci PREM in prima fase. 18° Congresso C.T.E., Bologna, 11–13 novembre

Vintzeleou EN, Tassios TP (1986) Mathematical models for dowel action under monotonic and cyclic conditions. Mag Concr Res 38(134):12–22

Vintzeleou EN, Tassios TP (1987) Behavior of dowels under cyclic deformation. ACI Struct J 84:18–30

Vintzeleou EN, Tassios TP (1990) Eccentric dowels loaded against core of concrete sections. J Struct Eng 116:10

Applications and Realizations

SEACON and Resilient FRP-RC/PC Solutions: The Halls River Bridge

M. Rossini[1(✉)], T. Cadenazzi[1], S. Nolan[2], and A. Nanni[1]

[1] Department of Civil, Architectural and Environmental Engineering, University of Miami, Coral Gables, FL, USA
mxrl465@miami.edu
[2] Florida Department of Transportation, State Structures Design Office, Tallahassee, FL, USA

Abstract. The SEACON project features the University of Miami (UM), the Florida Department of Transportation (FDOT), along with European partners (Politecnico di Milano) and representative of the industrial sector working toward the development of innovative material solutions to address sustainability and resilience challenges in construction. The project aims to develop sustainable concrete solutions using seawater and chloride-contaminated aggregates. An integral component involves validating Fiber Reinforced Polymers (FRP) and stainless steel (SS) as non-corrosive reinforcement for Reinforced Concrete (RC) and Prestressed Concrete (PC) applications. The Halls River Bridge (HRB) features large-scale implementation of innovative materials. It showcases the SEACON research outcomes and serves as a proof-of-concept for the validation of design philosophies to be included in the new generation of FRP design guidelines. This paper speaks about the issues of design of a non-corrosive FRP-RC/PC structure. HRB is presented as a successful case study.

KEYWORDS: FRP-RC · FRP-PC · Design guidelines · Resilience · Sustainability

1 Research Significance

Corrosion of Mild Carbon Steel (MCS) and High-Strength Carbon Steel (HSCS) reinforcement is a durability concern in aged Reinforced Concrete (RC) and Prestressed Concrete (PC) structures. Extensive development of transportation infrastructure, in combination with aggressive environments, may represents a severe Maintenance, Rehabilitation and Replacement (MRR) liability both in the United States (Nolan and Nanni 2017) and Europe (Bertolini et al. 2005). RC corrosion is ubiquitous, but greatly exacerbated by aggressive sub-tropical environments (Nolan et al. 2018) and exposure to de-icing salt and carbonation in cold-weathered regions (Ahmad 2003).

In the case of transportation infrastructure in coastal areas, the immediate corrosion problems are experienced by bridge substructures, sheet pile bulkheads, pile bent caps, bearing piles, and seawalls (Rossini et al. 2018b). In the State of Florida alone, approximately 3,600 coastal miles are armored with aging sheet piles for an estimated $21B MRR liability (Nolan et al. 2018).

M. di Prisco and M. Menegotto (Eds.): ICD 2018, LNCE 42, pp. 165–180, 2020.
https://doi.org/10.1007/978-3-030-23748-6_13

A traditional solution to address reinforcement corrosion entails designing concrete mixes with limited permeability and superior durability characteristics (Bertolini et al. 2005). This approach lays the durability burden on cement manufacturer and ready-mix producer. Furthermore, it typically involves cement-rich concrete mix-designs. Whereas low-impact cements are being investigated (Bertola et al. 2018), the raising demand for high-quality mixes may exacerbate the environmental impact of the concrete industry (Bertola et al. 2016).

Fiber-Reinforced Polymers (FRP) represent a proven non-corrosive alternative to steel in rehabilitation (Rossini et al. 2018c) and new constructions (Spadea et al. 2018). Commercially available solutions include Glass FRP (GFRP) bars, Carbon FRP (CFRP) strands, and Basalt FRP (BFRP) bars (Ruiz et al. 2018). Deployment of FRP reinforced concrete (FRP-RC) and FRP prestressed concrete (FRP-PC) eliminates the issue of reinforcement corrosion, irrespectively of the concrete mix-design (Bertola et al. 2016).

The SEACON-Infravation project is a research effort jointly funded by the European Commission and government agencies such as the US Federal HighWay Administration (FHWA) and the Italian ANAS. SEACON aims to develop low-impact concrete using seawater, chloride-contaminated cement, and recycled aggregates. Seaconcrete requires coupling with non-corrosive reinforcement. Thus, within SEACON, lays the validation, deployment and support for standardization of FRP, MSS, and HSSS reinforcement.

2 Halls River Bridge

The Halls River Bridge (HRB) is a short-spanned traffic bridge currently under construction in Homosassa, Florida (Fig. 1a). The bridge is part of a replacement project for an existing structure that reached functional deficiency and is aged beyond its service life (Fig. 1b). The new structure comprises five spans for a total length of 56.6 m. It serves as the only passageway over the Halls River for the community of Homosassa Springs. The water way is tidally affected by seawater contamination, particularly during storms, given the proximity to the Gulf of Mexico.

Fig. 1. Halls River Bridge under construction (a) and existing bridge before demolition (b). [Courtesy of Astaldi Construction Corporation]

Given its exposure conditions and structural configuration, the HRB was selected to serve as demonstrator for both the SEACON project and the Florida Department of Transportation (FDOT) Transport Innovation Challenge (TIC). One of the aims of the latter is to leverage the deployment of non-corrosive technologies in transportation infrastructure. Furthermore, the HRB served as test-bed and active laboratory for the development of a new generation of FRP design and construction guidelines. This includes the new edition of the Bridge Design Guide Specifications for GFRP-RC (BDGS-GFRP) (AASHTO 2018). The draft of the AASHTO BDGS-GFRP was developed by a task force lead by the University of Miami (UM) and representatives of State Departments of Transportation (DOTs) and FHWA.

The HRB comprises a number of innovative material and structural solutions targeting a reduced environmental impact and an extended service life of 100+ year (Cadenazzi et al. 2018a). The structure includes CFRP-PC bearing piles, CFRP-PC/GFRP-RC sheet piles, hybrid HSCS-PC/GFRP-RC sheet piles, GFRP-RC pile bent caps and bulkhead caps, a GFRP-RC bridge deck, GFRP-RC traffic railings, GFRP-RC approach slabs and a 20 m long GFRP-RC gravity wall. The original design implemented Hillman Composite Beams (HCB), consisting of a composite GFRP shell encasing a steel-reinforced concrete shallow tied-arch and lightweight filling foam. This complex structural solution was developed under the National Cooperative Highway Research Program's Innovations Deserving Exploratory Analysis (NCHRP-IDEA) program and selected by FDOT for further exploration (Cadenazzi et al. 2018b). An alternative GFRP-RC solution that provides equivalent strength and performance is shown in this study.

In addition to innovative reinforcement solutions, the HRB features deployment of sustainable concrete mixes in the elements of the substructure. Concrete mixed with seawater is used for the bulkhead cap, concrete with Recycled Concrete Aggregates (RCA) and concrete with Recycled Asphalt Pavement (RAP) aggregates is used for the GFRP-RC gravity walls. White cement concrete and another mixture of high-content slag and fly ash are used in the GFRP-RC traffic railings for investigation of enhanced night-time and wet weather visibility. The bulkhead cap includes test-blocks on the water side to be periodically extracted and tested to assess FRP durability in chloride-exposed sea-concrete. The test blocks include GFRP, CFRP, and BFRP bars.

3 Design Consideration

3.1 Guidelines and Design Approach

A number of design and construction guidelines for FRP-RC and FRP-PC exist worldwide. A detailed discussion of CFRP-PC design can be found in Spadea et al. (2018). Principles of GFRP-RC design are discussed by Rossini et al. (2018a).

In general, the brittle nature of FRP is addressed by introducing a specific reduction factor for the flexural strength of the structure (ϕ). The ultimate strength of the material is reduced accounting for the effects of long-term exposure to moisture by introducing an environmental reduction factor (C_E). The jacking stress for prestress is limited to safe values by introducing a jacking reduction factor (C_j). The resistance to sustained

stress is reduced to avoid creep rupture by introducing a creep rupture reduction factor (C_c). The difference in bond performance with respect to steel is accounted for by introducing a bond reduction factor (C_b).

Table 1 summarizes design parameters for CFRP-PC according to a selection of international guidelines. The values used for the HRB design align with the FDOT Structures Manual (FDOT 2018a), Construction Specifications (FDOT 2018b) and Structures Index (FDOT 2016a; FDOT 2016b). Table 2 summarizes design parameters for GFRP-RC according to a selection of international guidelines. The values used for HRB design align with the proposed AASHO BDGS-GFRP (AASHTO 2018).

Table 1. Design parameters for CFRP-PC.

	JCSE	CNR	*fib* MC	ACI 440.4R	FDOT	AASHTO CFRP
	1997	2007	2013	2004	2018	2018[1]
ϕ_t	0.87	0.60	0.80	0.85	0.85[4]	0.75
C_E	1.00	0.90	0.90[2]	0.90[3]	0.90[3]	1.00
C_J	0.80	–	–	0.65	0.70	0.75
C_C	0.70	0.90	0.80	0.60	0.60[4]	0.70
C_b	–	0.59	0.71[2]	–	0.71[3]	–

[1] under consideration.
[2] from *fib* bulletin 40 (*fib* 2007).
[3] from ACI 440.1R (ACI 2015).
[4] from ACI 440.4R (ACI 2004).
[5] from JSCE-CES23 commentary (JSCE 1997)

Table 2. Design parameters for GFRP-RC.

	JCSE	CNR	*fib* MC	ACI 440.1R	FDOT	AASHTO GFRP
	1997	2007	2013	2015	2018	2018[1]
ϕ_t	0.77	0.60	0.80	0.55	0.55[3]	0.55
C_E	1.00	0.70	0.55[2]	0.70	0.70[3]	0.70
C_f	–	–	–	0.20	0.20[3]	0.25
C_C	0.50[5]	0.30	0.30	0.20	0.20[3]	0.30
C_b	0.77	0.59	0.71[2]	0.71	0.71[3]	0.83

[1] under consideration.
[2] from *fib* bulletin 40 (*fib* 2007).
[3] from ACI 440.1R (ACI 2015).
[4] from ACI 440.4R (ACI 2004).
[5] from JSCE-CES23 commentary (JSCE 1997)

In the following, High-Strength Stainless Steel HSSS will be considered for comparison with CFRP in prestress applications. In the United States, the material is not regulated at the federal level, but is included in the FDOT Structures Manual (FDOT 2018a), Construction Specifications (FDOT 2018b), and Structures Index (FDOT 2016a; FDOT 2016b).

Sea-concrete is not regulated at either the State or Federal level. FDOT Construction Specifications (FDOT 2018b) were used where applicable and modified accordingly. RCA and RAP nonstructural concrete mixes are regulated by FDOT Construction Specifications (FDOT 2018b).

3.2 Material Properties

FRP is a brittle composite material, elastic until failure, stronger, but less stiff with respect to Mild Carbon Steel (MCS) and High-Strength Carbon Steel (HSCS). The guaranteed strength of an FRP bar or strand is defined as the experimental average value minus three standard deviation (ACI 2015). The approach is more conservative with respect to the calculation of characteristic strengths for steel reinforcement and concrete, defined as the average minus 1.64 standard deviations under the assumption of normal distribution (CEN 2008). The minimum specified values for strength and stiffness of GFRP bars are defined by ASTM D7957 (ASTM 2017a). CFRP strands and HSSS strands are not regulated at the federal level, but the FDOT Construction Specifications (FDOT 2018b) include minimum specified values for strength and references to applicable acceptance criteria. HSCS strands are regulated by ASTM A416 (ASTM 2017b), whereas MCS bars are regulated by ASTM A615 (ASTM 2016).

Tables 3 and 4 report the experimental and specified properties for the CFRP strands (SML 2017a) and M13 GFRP bars (SML 2017b) deployed in the HRB. Table 5 reports the specified properties of certified HSSS strands (FDOT 2018b). Figure 2 compares the mechanical properties of CFRP, GFRP, HSSS, HSCS, and MCS. HSSS performance is closer to CFRP rather than HSCS. This includes a quasi-brittle behavior with no plastic plateau.

Table 3. Mechanical properties for 15.2 mm CFRP strands.

CFRP 15.2 mm	Stress		ε_f	F_f	E_f	a_f
	/	MPa	%	kN	GPa	mm^2
Mean	f_{fm}	3267	2.08	378	157	115
Guaranteed	f^{*}_{fu}	2990	1.90	346		
Specified	$f^{'}_{fu}$	2336	1.51	270	155	116
Design	f_{fd}	2102	1.36	243		
Jacking	$f_{f,j}$	1471	0.95	170		
Sustained	$f_{f,s}$	1261	0.81	146		

Experimental properties for FRP products lay above the minimum specified values. The general conservativeness in approaching FRP characterization and design is

Table 4. Mechanical properties for M13 GFRP bars.

GFRP M13	Stress		ε_f	F_f	E_f	a_f
	/	MPa	%	kN	GPa	mm^2
Mean	f_{fm}	983	1.57	125	62.7	147
Guaranteed	f^*_{fu}	883	1.41	112		
Specified	f'_{fu}	758	1.69	96	44.8	127
Design	f_{fd}	530	1.18	67		
Jacking	$f_{f,j}$	n.a.	n.a.	n.a.		
Sustained	$f_{f,s}$	160	0.36	20		

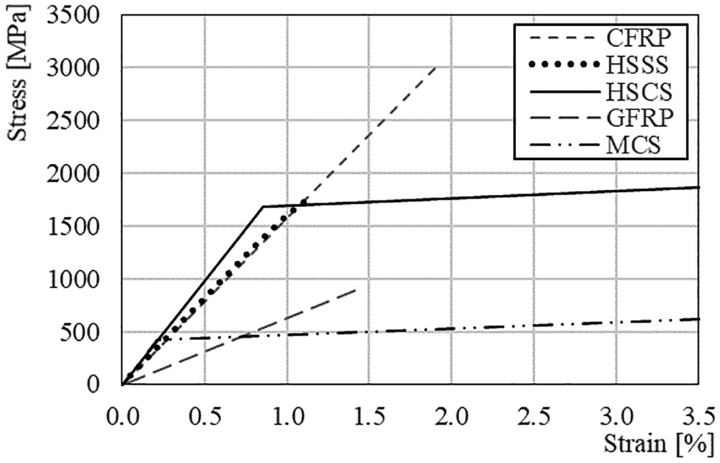

Fig. 2. Mechanical properties of various reinforcement materials.

derived by the historically limited confidence in deploying non-ductile innovative materials with respect to traditional solutions. Rationalization of design requirements is a major area of advancement for FRP-RC/PC. The new generation of design regulations is moving toward relaxing historic overconservative assumptions (Rossini et al. 2018a).

All the prestressed elements of the bridge entail equivalent C40/50 concrete. Bulkhead cap sea-concrete mix is designed for a compressive strength of 38 MPa at 28 days. RCA and RAP concrete are equivalent C16/20 nonstructural mixes.

Table 5. Mechanical properties for 12.7 mm HSSS strands.

HSSS 12.7 mm	Stress		ε_s	F_s	E_s	a_s
	/	MPa	%	kN	GPa	mm^2
Ultimate	f_{su}	1724	1.10	170	162	99
Yielding	f_{sy}	1606	1.00	159		
Jacking	f_{sj}	1293	0.80	128		

4 Structural Members

4.1 CFRP-PC Bearing Piles

The Halls River Bridge comprises a total of 36 CFRP-PC bearing piles, divided over 6 bent caps. The piles are designed according to FDOT Index series 22600 (FDOT 2016a) for a compressive strength of 3254 kN and a flexural strength of 325 kN-m. The cross section is squared with a side of 460 mm (Fig. 3a). Prestress is applied through 12 CFRP strands of 15.2 mm diameter tensioned at 151 kN each. Confinement is provided by a spiral of 5 mm CFRP single wire with a pitch varying from 25 mm to 76 mm to 152 mm as showed in Fig. 3b. Whereas next generation design guidelines suggest concrete clear cover values of 20 mm to 38 mm, the FDOT Structures Manual (FDOT 2018a) imposed a concrete clear cover of 76 mm for compatibility with traditional prestressing patterns. The value coincides with standard practice for steel reinforcement in aggressive subtropical environment.

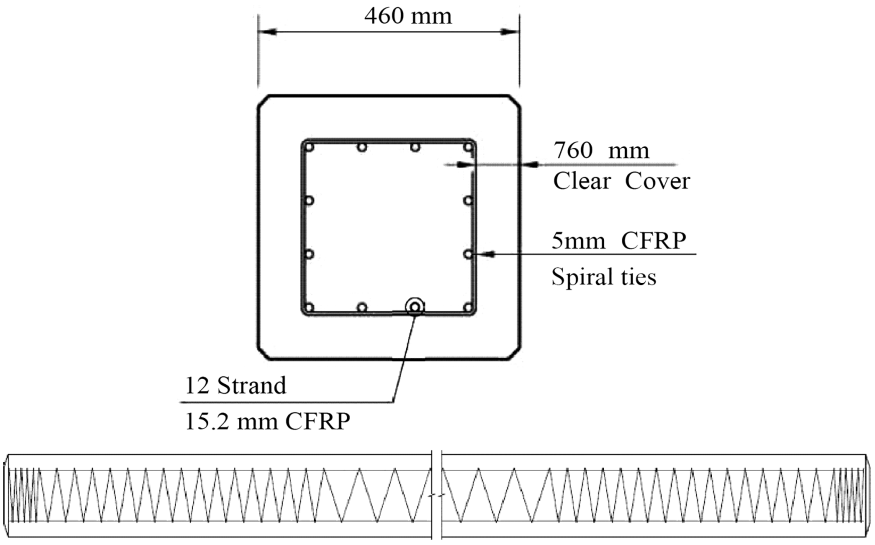

Fig. 3. Bearing pile cross section (a) and lateral view (b).

Table 6 compares three different reinforcement alternatives for the same pile configuration. The cost column reports the strand material cost per linear meter of pile, as estimated by FDOT (2015). P_i is the initial prestress on each strand. ΔP includes the total prestress losses as a percentage of the initial prestress. σ_{∞} is the level of stress in the concrete after losses at t_{∞}. Prestress efficiency (e_p) is computed as the ratio of retained prestress at t_{∞} over the initial prestress. CFRP stands up as the most efficient alternative and is less expensive with respect to HSSS. The higher material cost with respect to HSCS strands is expected to be absorbed over the long term thanks to the superior durability of CFRP (Cadenazzi et al. 2018a).

Table 6. Comparison of different reinforcing material for the same sheet pile configuration.

	Strands	Cost	P_i	ΔP	σ_∞	e_p
	n°	$/m	kN	%	MPa	–
CFRP	**12**	**150**	**151**	**16%**	**7.3**	**0.84**
HSSS	16	210	116	18%	7.2	0.82
HSCS	12	40	156	24%	6.8	0.76

The piles were designed to be driven by impacting hammer to a depth of 19 m, for a total length of 21 m. Unexpected geotechnical conditions forced driving the three piles of one of the intermediate bents to a depth of 46 m requiring splicing of additional segments (Cadenazzi et al. 2018b). MSS M25 bars were used as dowels, whereas CFRP dowels are undergoing validation to be ready for the second construction phase. Figure 4 shows pile driving and splicing.

Fig. 4. Bearing pile driving and splicing operations.

4.2 CFRP-PC/GFRP-RC Sheet Piles

The Halls River Bridge comprises a total of 149 CFRP-PC/GFRP-RC sheet piles located in direct contact with saltwater. Furthermore, a total of 86 Hybrid HSCS-PC/GFRP-RC sheet piles are located in the less exposed portion of the retaining walls. The piles are designed according to FDOT Index 22440 (FDOT 2016b) for a compressive strength of 3904 kN and a flexural strength of 224 kN-m. The cross section is rectangular with a width of 760 mm and a depth of 300 mm. The wall system is modular with male-female connections (Fig. 5a). Prestress is applied through 8 CFRP strands of 15.2 mm diameter tensioned at 170 kN each. Confinement is provided by M13 GFRP ties with a pith varying from 102 mm to 305 mm as showed in Fig. 5b. Concrete clear cover is set to 76 mm.

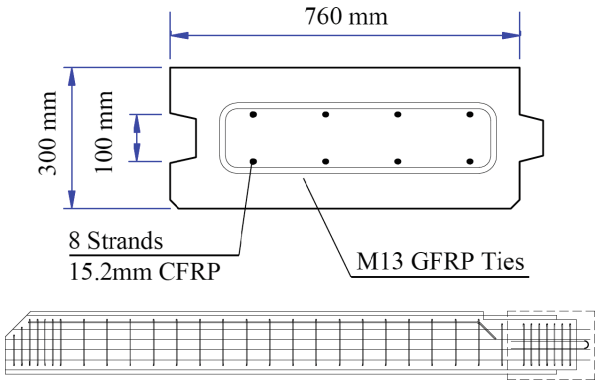

Fig. 5. Sheet pile cross section (a) and lateral view (b).

Table 7 compares three different reinforcement alternatives for the same sheet pile configuration. As discussed for the case of bearing piles, CFRP stands up as the most efficient alternative and is less expensive than HSSS. The higher cost with respect to HSCS is expected to be absorbed thanks to the superior durability of CFRP (Cadenazzi et al. 2018a).

Table 7. Comparison of different reinforcing material for the same sheet pile configuration.

	Strands n°	Cost $/m	P_i kN	ΔP %	σ_∞ MPa	e_p –
CFRP	**8**	**100**	**170**	**11%**	**5.2**	**0.89**
HSSS	14	183	116	16%	5.8	0.84
HSCS	10	33	245	16%	8.8	0.84

The sheet piles were designed for installation by water-jetting to a depth of 8 m for a total length of 9 m in a cantilever configuration. The unexpected presence of a layer of hard limestone reduced the installation depth to approximately 4 m for relevant portions of the wall. To guarantee the required strength and stiffness to the retaining wall, an anchored sheet pile variant was adopted. The sheet piles were cut to length and the cut-off portions were installed as deadmen. The sheet pile bulk head cap was connected to the deadmen through MSS bars mildly tensioned using screw couplers (Cadenazzi 2017). Figure 6 shows the installation of the sheet piles.

4.3 GFRP-RC Pile Bent Caps

The Halls River Bridge comprises 6 GFRP-RC cast-in-place pile bent caps of rectangular cross section having a width of 1.22 m and a depth of 0.91 m (Fig. 7). Each bent cap is under-reinforced with failure controlled by FRP rupture. Design is governed by service considerations, as typical for the case of GFRP-RC. Since the provisions for

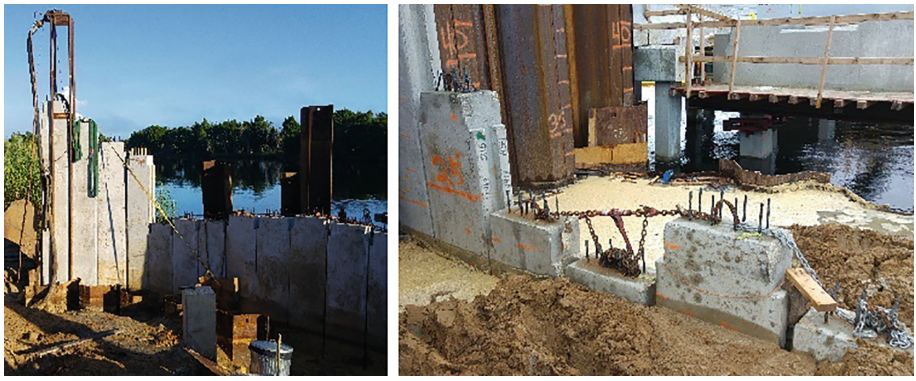

Fig. 6. Sheet piles during installation

Fig. 7. Pile bent cap after demonlding.

this type of element are particularly conservative, new provisions have been proposed for the next generation of design guidelines.

The design of the bent cap of the HRB according to ACI 440.1R (ACI 2015) and the first edition of the AASHTO BDGS-GFRP (AASHTO 2009) is discussed by Rossini et al. (2018a) and requires 16 M25 GFRP bars to resist a factored moment of 575 kN-m. This corresponds to an area of reinforcement 2.7 times the area of steel reinforcement required for an equivalent member. According to the provisions of the second edition of the AASHTO BDGS-GFRP (AASHTO 2018), the bent cap design requires 9 M25 GFRP bars. This corresponds to a reduction of 40% with respect to the first edition.

Figure 8 shows the number of M25 bars required for the bent cap according to the first and second editions of the AASHTO BDGS-GFRP. The quantities are plotted in parametric diagrams as a function of the bond reduction factor ($C_b = 1/k_b$). Further details on the approach adopted can be found in Rossini et al. (2018a). The two diagrams show how a rationalization of the sustained and cyclic demand, along with a slight relaxation of design factors per Table 2, result in a decrease of the amount of reinforcement required. According to the second edition of the AASHTO BDGS-GFRP,

crack width governs over cyclic fatigue, creep rupture, and strength. Further savings are expected to come from improved GFRP bond performance, as expressed by the bond reduction factor ($C_b = 1/k_b$) (see Table 2).

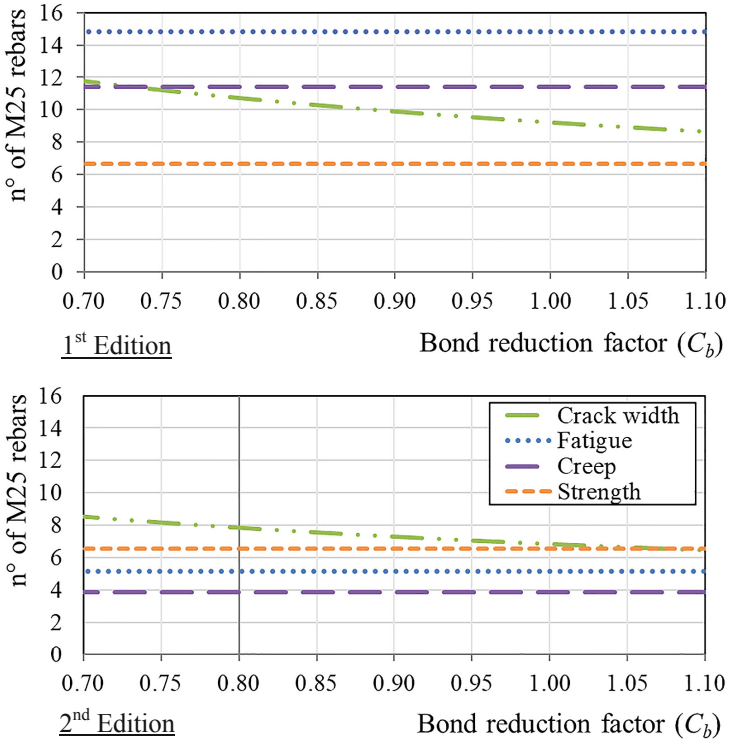

Fig. 8. Required amount of reinforcement for the pile bent cap according to AASHTO BDGS-GFRP.

Table 8 summarizes the various design alternatives for the bent cap, including the selected option and a comparison to an equivalent MCS-RC member. The higher material cost is expected to be absorbed over the long period thanks to the superior durability of GFRP (Cadenazzi et al. 2018a). Challenges and opportunities related to the use of GFRP in the construction of the bent caps are discussed by (Cadenazzi et al. 2018b).

4.4 GFRP-RC Girders

The Halls River Bridge comprises 45 Hillman Composite Beams (HCB) consisting of a composite GFRP shell encasing a steel-reinforced concrete shallow tied-arch and lightweight filling foam (Fig. 9). This complex structural solution is reinforced with 18 galvanized unstressed steel strands of 12.7 mm diameter and connected to the deck

Table 8. Comparison of different reinforcement layout for the same bent cap configuration.

	M25 Bars n°	Cost $/m	GFRP to steel ratio
BDGS-GFRP 1st	16	61	2.7
HRB Design	**12**	**46**	**2.0**
BDGS-GFRP 2nd	9	34	1.5
Mild Carbon Steel	6	20	1.0

through galvanized steel connectors. The composite shell is intended to enhance durability of the RC structural core (Aboelseoud and Myers 2016). Corrosion of the galvanized steel connectors in a more aggressive environment is an unaddressed concern.

Fig. 9. HCB during installation.

An alternative GFRP-RC precast solution is discussed in this section, designed to ensure the same level of strength and performance in addition to validated durability performance (ASTM 2017a). Maintaining the original rectangular section of the HCB with a width of 590 mm and a depth of 530 mm, a total of 18 M25 GFRP bars is sufficient to resist against a factored moment of 1085 kN-m. The girder is connected to the deck through M13 GFRP shear connectors in the shape of closed stirrups spaced 50 to 200 mm. The member complies with the AASHTO BDGS-GFRP 2nd edition (AASHTO 2018), whereas design according to the first edition of the guideline is not permitted. Figure 10 visualizes the level of strains in the member under different loading conditions. Given the conservativeness of the strength reduction factor for FRP-controlled failures (ϕ_f), the strains under Ultimate Load (Ultimate L.) lay below the flexural failure threshold defined as Nominal Resistance (Nominal R.) by a margin of about 50%.

The GFRP-RC precast solution discussed has a total cost estimated at $430 per linear meter per member, corresponding to a portion of the cost of HCB estimated at

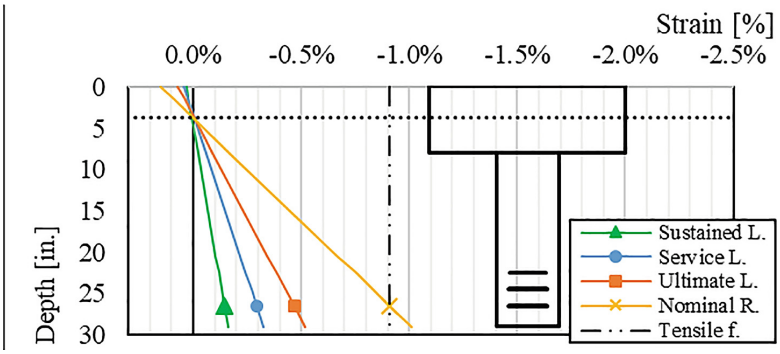

Fig. 10. GFRP-RC girder sectional analysis. Geometry not to scale.

$1580 per linear meter per member (Cadenazzi et al. 2018a). The challenges and opportunities related to HCB installation are discussed by Cadenazzi et al. (2018b).

4.5 GFRP-RC Deck, Slabs, Railings and Bulkhead Caps

The entire structure of the bridge, including secondary element and the entire superstructure, is reinforced with corrosion-resistant and hybrid solutions. The GFRP-RC deck is designed according to the first edition of AASHTO BDGS-GFRP (AASHTO 2009). Decks tend to undergo less corrosion in Florida, not being exposed to deicing agents nor being in contact with seawater. The choice of GFRP for the deck was made for consistency and concept demonstration.

The GFRP-RC railings were designed according to FDOT Index D22420 (FDOT 2017a). Railings design is discussed by Rocchetti et al. (2018).

The GFRP-RC bulkhead cap was design according to FDOT Index 22440 (FDOT 2016b). The GFRP-RC approach slabs were designed according to FDOT Index D22900 (FDOT 2017b). In these cases, corrosion is a major problem given the exposure to saltwater in the tidal zone and soil, respectively.

The 2nd edition of the AASHTO BDGS-GFRP (AASHTO 2018) covers the design of every component of a GFRP-RC bridge, including substructure and continuous railings. The provisions align with FDOT Structures Manual (FDOT 2018a), Construction Specifications (FDOT 2018b), and Structures Index (FDOT 2016a, b, 2017a, b).

5 Summary and Conclusions

In this study, HRB is presented in its role of demonstrator for a series of innovative material and structural solutions part of the SEACON research project and related efforts. Furthermore, HRB served as a proof-of-concept for the development of a new generation of design and construction guidelines for FRP-RC/PC structures.

1. The SEACON research project and its outcomes in terms of development of innovative concrete mixes and validation and deployment of non-corrosive reinforcement have been discussed.
2. The design of CFRP-PC bearing piles, CFRP-PC/GFRP-RC sheet piles, GFRP-RC pile bent caps, and GFRP-RC girders has been presented.
3. CFRP strands proved their superior structural efficiency and appealing economic implications with respect to corrosive (HSCS) and non-corrosive (HSSS) metallic alternatives.
4. The appealing economic implications and validated durability performance of GFRP-RC have been discussed. Costs are in the order of 1/3 with respect to alternative corrosion-resistant solutions (e.g. HCB).
5. The implications of the second edition of the AASHTO BDGS-GFRP on GFRP-RC design have been discussed. This includes both reinforcement savings in the order of 40% with respect to the first edition (e.g. GFRP-RC bent cap) and the possibility to use GFRP reinforcement for new members (e.g. GFRP-RC girders).
6. A comprehensive state-of-the-practice review for FRP design and application in bridges has been provided.

Acknowledgements. The authors gratefully acknowledge the financial support from: (1) "Sustainable concrete using seawater, salt-contaminated aggregates, and non-corrosive reinforcement" Infravation, 31109806.005-SEACON; (2) "I/UCRC Center for the Integration of Composites into Infrastructure (CICI)," NSF, 1439543; (3) Zegna Foundation for supporting the first author's research activity in the field of composite materials for infrastructural applications; and, (4) Florida Department of Transportation (FDOT) for access to the Halls River Bridge design material.

References

AASHTO (2009) LRFD bridge design guide specifications for GFRP-reinforced concrete bridge decks and traffic railings, 1st edn. American Association of State Highway and Transportation Officials, Washington, DC

AASHTO (2018) AASHTO LRFD bridge design guide specifications for GFRP-reinforced concrete, 2nd edn. American Association of State Highway and Transportation Officials, Washington, DC

Aboelseoud MA, Myers JJ (2016) Durability of hybrid composite beam bridges subjected to various environmental conditioning. ASCE J Compos Constr 20(6):04016045(1-13)

ACI Committee 440 (2004) Prestressing concrete structures with FRP tendons. ACI 440.4R-04. American Concrete Institute, Farmington Hills, MI

ACI Committee 440 (2015) Guide for the design and construction of structural concrete reinforced with fiber-reinforced polymers (FRP) bars. ACI 440.1R-15. American Concrete Institute, Farmington Hills, MI

Ahmad S (2003) Reinforcement corrosion in concrete structures, its monitoring and service life Prediction - a review. Cem Concr Compos 25(4–5 SPEC):459–471

ASTM (2016) Standard specification deformed and plain carbon-steel bars for concrete. A615/A615 M-16. ASTM International, West Conshohocken, PA

ASTM (2017) Standard specification for low-relaxation, seven-wire steel strand for prestressed. ASTM A416/A416 M-17. ASTM International, West Conshohocken, PA

ASTM (2017) Standard Specification for solid round glass fiber reinforced polymer bars for concrete reinforcement. ASTM D7957/D7957 M-17. ASTM International, West Conshohocken, PA

Bertola F, Canonico F, Bianchi M, Nanni A (2016) The SEACON project. International Cement Review, June, pp 63–66

Bertola F, Gastaldi D, Canonico F, Paul G (2018) CSA and slag: toward CSA composite binders. In: International workshop on calcium Sulfoaluminate cements, Zurich, CH

Bertolini L, Elsener B, Pedeferri P, Polder RB (2005) Corrosion of steel in concrete: prevention, diagnosis, repair. Wiley-VCH Verlag GmbH & Co. KGaA, Weinheim, DE

Cadenazzi T (2017) Halls river bridge: corrosion-free design with FRP composites. Part 3: contractor perspective. In: The Composites and Advanced Material Expo (CAMX 2017), Orlando, FL

Cadenazzi T, Hunter R, Siddiqui M, Nanni A (2018b) Halls River Bridge project. Composite Manufacturing Magazine

Cadenazzi T, Rossini M, Nolan S, Dotelli G, Arrigoni A, Nanni A (2018a) Resilience and economical sustainability of a frp reinforced concrete bridge in Florida: LCC analysis at the design stage. In: The sixth international symposium on life-cycle civil engineering (IALCCE). Ghent, NE. Accepted

CNR (2007) Guide for the design and construction of concrete structures reinforced with fiber-reinforced polymer bars. CNR-DT 203/2006. National Research Council, Rome, IT

FDOT (2015) Design standards development report for corrosion resistant prestress concrete piles. Florida Department of Transportation, Tallahassee, FL

FDOT (2016a) Square CFRP & HSSS prestressed concrete piles. Index 22600. Florida Department of Transportation, Tallahassee, FL

FDOT (2016b) Precast concrete CFRP/GFRP & HSSS/GFRP sheet pile wall. Index 22440. Florida Department of Transportation, Tallahassee, FL

FDOT (2017a) Traffic railings: 32" F Shape - GFRP reinforced. Index D22420. Florida Department of Transportation, Tallahassee, FL

FDOT (2017b) Approach slabs - GFRP reinforced. Index D22900. Florida Department of Transportation, Tallahassee, FL

FDOT (2018a) Structures manual. Florida Department of Transportation, Tallahassee, FL

FDOT (2018b) Standard specifications for road and bridge construction. Florida Department of Transportation, Tallahassee, FL

fib (2007) FRP reinforcementin RC structures. Bullettin 40. fédération internationale du béton, Lausanne, CH

fib (2013) Model code for concrete structures. MC2010. Wilhelm Ernst & Sohn, Berlin, DE

JSCE (1997) Design guidelines of FRP reinforced concrete building structures. Concrete Engineering Series no. 23. Japan Society of Civil Engineers, Tokyo, JP

Nolan S, Nanni A (2017) Deployment of composite reinforcing - Part 1: Impetus for more widespread application in transportation infrastructure. Concrete International, May, pp 40–46

Nolan S, Rossini M, Nanni A (2018) Seawalls, SEACON and sustainability in the sunshine state. In: Transportation Research Board 97th annual meeting, Washington, DC

Rocchetti P, Claure G, De Caso y Basalo F, Nanni A (2018) Implementation of closed GFRP stirrups in FRP-RC design of traffic barriers. ACI Spec Publ 327:34(1–12)

Rossini M, Bruschi E, Matta F, Poggi C, Nanni A (2018a) Case-specific parametric analysis as research-directing tool for analysis and design of GFRP-RC structures. ACI Spec Publ 327:34 (1–12)

Rossini M, Jalles P, Balconi G, Nanni A (2018b) GFRP strand prototype: experimental investigation and technology readiness. In: 9th international conference on fibre-reinforced polymer (FRP) composites in civil engineering (CICE 2018), Paris, FR

Rossini M, Nanni A, Poggi C (2018c) Quantitative approach to anchoring spikes design in flexural applications. In: 9th international conference on fibre-reinforced polymer (FRP) composites (CICE 2018), Paris, FR

Ruiz Emparanza A, Kampmann R, De Caso Y Basalo F (2018) State-of-the-practice of global manufacturing of FRP rebar and specifications. ACI Spec Publ 327:45(1–14)

SML (2017a) Certified laboratory test report: evaluation of carbon fiber reinforced polymer (CFRP) strands for prestressing per FDOT Dev933. R-5.10_TOK-US_FDOT933.2. Structures and Materials Laboratory, University of Miami, Coral Gables, FL

SML (2017b) Certified laboratory test report: Evaluation of GFRP bars per FDOT Dev932. R-5.10_04-12-17_Dev932_Final. Structures and Materials Laboratory, University of Miami, Coral Gables, FL

Spadea S, Rossini M, Nanni A (2018) Design analysis and experimental behavior of precast double-tee girders with CFRP strands. PCI J 63(1):72–84

Design Recommendations for Foundation Slabs with Punching Shear Reinforcement

E. Camnasio(✉) and J. Bujnak

Peikko Group Corporation, Lahti, Finland
elena.camnasio@peikko.com

Abstract. The structural performance of reinforced concrete foundation slabs or footings supporting isolated columns is often limited by the punching shear capacity in the area around the column. This can be significantly increased by using vertical punching shear reinforcement, which is typically provided under the form of tailor made stirrups or industrially produced double-headed studs. The lack of knowledge about the performance of slabs reinforced with this kind of reinforcement elements, which are not included in current EN 1992-1-1, has been the main motivation behind an experimental research program at the EPFL in Lausanne consisting in full scale laboratory tests of footings reinforced with Peikko PSB® studs. The results of this program have been used to develop design recommendations for slabs reinforced with Peikko PSB® studs that are now implemented in ETA 13/0151. The paper summarizes the main outcomes of the research project and presents practical design recommendations yielding from it.

KEYWORDS: Shear reinforcement · Punching shear strength · Experimental investigation · Design method

1 Introduction

Reinforced concrete foundation slabs are usually used to limit differential subsidence due to a non-uniform load distribution by a better usage of ground load bearing resistance. However, the structural performance of reinforced concrete foundation slabs is often limited by the punching shear capacity in the area around the column. This might occur for compact footings as well, where punching phenomenon depends on column size and member slenderness.

Punching usually occurs so that a concrete cone is separated from the foundation element and bending reinforcement is pulled away from concrete (Fig. 1). Experience shows that failure by punching is particularly dangerous since it is a brittle phenomenon without any previous signs of warning, such as extensive deformation or cracks. Moreover, a slab without vertical reinforcement has only a very limited resistance against punching. This resistance can be enhanced by shear reinforcement in forms of stirrups or double-headed studs.

M. di Prisco and M. Menegotto (Eds.): ICD 2018, LNCE 42, pp. 181–192, 2020.
https://doi.org/10.1007/978-3-030-23748-6_14

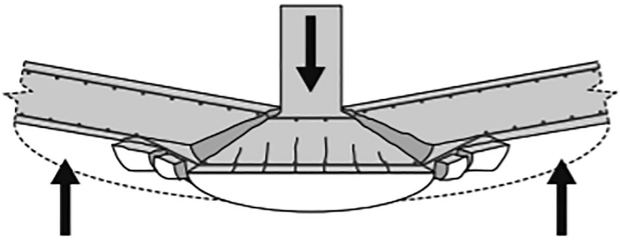

Fig. 1. Failure of a foundation slab by punching.

1.1 Punching Reinforcement with Double-Headed Studs

Double-headed studs have been used in Europe as an efficient system against punching failure of concrete flat slabs over the past 20 years. Such system enables to reach resistance levels that are significantly higher than resistances of slabs reinforced by traditional techniques thanks to better anchorage capacity to concrete.

Double-headed studs are designed to prevent the development of inclined punching cracks by acting as vertical tensile components in a system of strut and ties, as shown in Fig. 2a. Moreover, the ductility of the slab is increased.

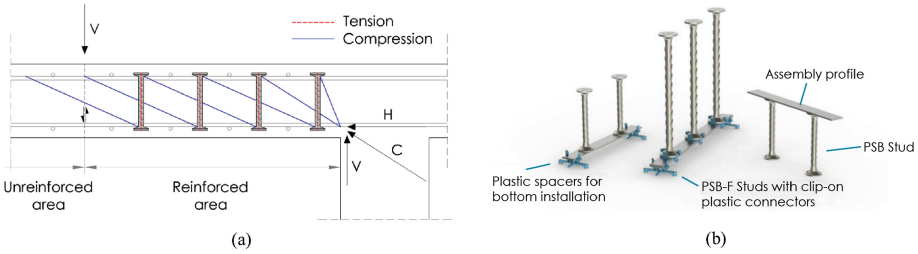

Fig. 2. (a) Forces in a slab with double-headed studs; (b) PSB® reinforcement elements (adapted from Peikko Group 2013).

In particular, Peikko PSB® reinforcement elements (Peikko Group 2013) consist of double-headed studs welded on an assembly profile that has no load bearing function (Fig. 2b). This guarantees the correct spacing and positioning of the studs. Moreover, PSB® studs allow for a faster and more efficient installation from the top or at the bottom of the reinforcing cage of slab or footing, which makes this system preferable to other ones.

2 Design of Punching Reinforcement

Despite being a system that is widely used in the common practice, the design methods for slabs reinforced by double-headed studs are not yet implemented in EN 1992-1-1 (CEN 2014) for reinforced concrete structures.

2.1 Design Recommendations of EN 1992-1-1

In order to design the shear reinforcement, EN 1992-1-1 gives clear provisions to calculate the resistance of the slab without punching reinforcement ($v_{Rd,c}$) and to consider number and diameter of reinforcement links in basic control perimeter and number of perimeters or reinforcement links necessary to activate a sufficient resistance on the outer perimeter ($v_{Rd,out}$). However, there is some ambiguity regarding the verification of the maximum resistance of the slab ($v_{Rd,max}$). Several alternative empirical verifications have been considered during the development of the code (European Concrete Platform 2008). Current version of the Code (CEN 2014) verifies the maximum resistance of the slab as follows:

$$V_{Rd,max} = min\begin{cases} 0.24\left(1 - \frac{f_{ck}}{250}\right) f_{cd} u_0 d \\ 1.5 v_{Rd,c} u_1 d \end{cases} \quad (1)$$

This formula is based on an empirical model that has been widely discussed, which led to modification of main Eurocode over the years and differentiation in national annexes of six Countries (Table 1, Bujnak 2015). In fact, such approach takes into account geometrical and material properties of the concrete slab only, not considering the influence of the anchorage properties of the reinforcement, which might be significant in case of double-headed studs.

Table 1. Maximum resistance of the slab according to Eurocode national annexes.

Germany DIN EN 1992-1-1	$1.4 v_{Rd,c} u_1 d$
Austria Onorm EN 1992-1-1	$\min\begin{cases} 0.24\left(1 - \frac{f_{ck}}{250}\right) f_{cd} u_0 d \\ \kappa v_{Rd,c} u_1 d \end{cases}$ $\kappa = 1.4 \, for \, d \leq 200\text{mm}$ $\kappa = 1.6 \, for \, d \geq 700\text{mm}$
Finland SFS EN 1992-1-1	Refers to former National Standards
Slovakia STN EN 1992-1-1	$\min\begin{cases} 0.24\left(1 - \frac{f_{ck}}{250}\right) f_{cd} u_0 d \\ \kappa v_{Rd,c} u_1 d \end{cases}$ $\kappa = 1.4 \, for \, d \leq 200\text{mm}$ $\kappa = 1.8 \, for \, d \geq 700\text{mm}$
United Kingdom BS EN 1992-1-1	$\min\begin{cases} 0.24\left(1 - \frac{f_{ck}}{250}\right) f_{cd} u_0 d \\ 2.0 v_{Rd,c} u_1 d \end{cases}$
Sweden SIS EN 1992-1-1	$\min\begin{cases} 0.30\left(1 - \frac{f_{ck}}{250}\right) f_{cd} u_0 d \\ 1.6 v_{Rd,c} \frac{u_1}{u_0} u_1 d \end{cases}$

2.2 Design Recommendations of ETA 13/0151

European Technical Assessment 13/0151 (ETA 2018) filled such deficiency of the Code and it currently represents the only official and valid reference for the design of slabs reinforced with studs in Europe. Such document stems from a research program conducted by Peikko during 2012 at the Swiss Federal Institute of Technology (EPFL) in Lausanne. Main reason to initiate the investigations was to assess the real performance of slabs reinforced with PSB® studs by providing experimental evidence (Fig. 3).

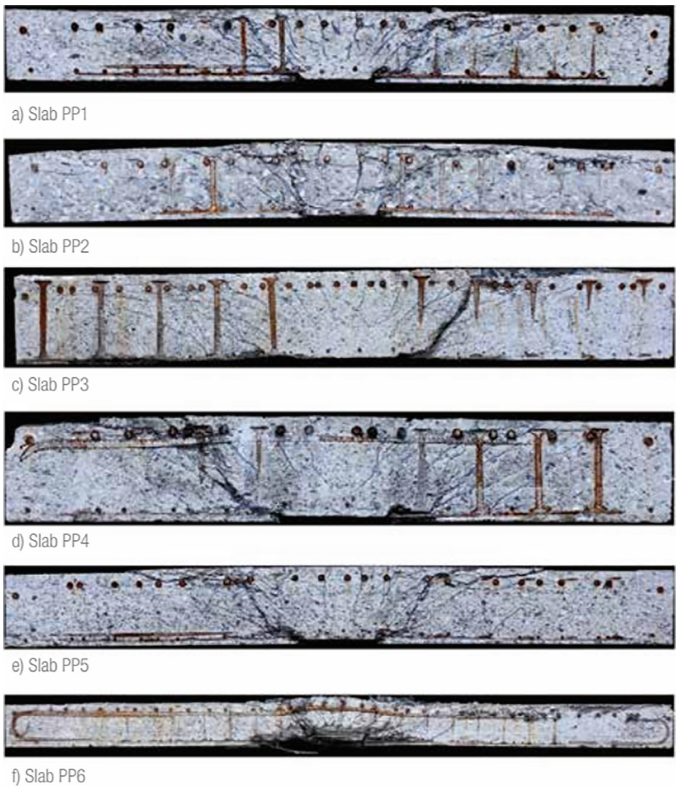

Fig. 3. Saw cut sections of slabs with Peikko PSB® studs after failure (Muttoni and Bujnak 2013).

Several full-scale tests have been performed according to common understanding of assessment procedure (EOTA 2012). More information about the research program can be found in Muttoni and Bujnak (2013). The results of the tests were integrated with the experimental database coming from previous studies (Lips et al. 2012) in order to define the factor k_{max} for calculating the maximum resistance of the slab reinforced by double-headed studs under the following form:

$$V_{Rd,max} = k_{max} V_{Rd,c} \tag{2}$$

It was calculated that a magnification factor k_{max} = 1.96 provides sufficient level of safety, i.e. 5% fractile equal to 1.0, for slabs with a slenderness L/d < 30. For foundation slabs and footings, ETA 13/0151 sets k_{max} = 1.62.

Even though ETA 13/0151 makes partly reference to the design concepts of EN 1992-1-1, the verification of the maximum resistance of the slabs cannot be overlapped to the Eurocode design method. This means that formula (1) cannot be applied in case of double-headed studs, since it is dependent on the type of reinforcement used in the slab. Moreover, combining ETA and Eurocode approaches would lead to unnecessarily conservative design (Bujnak 2015).

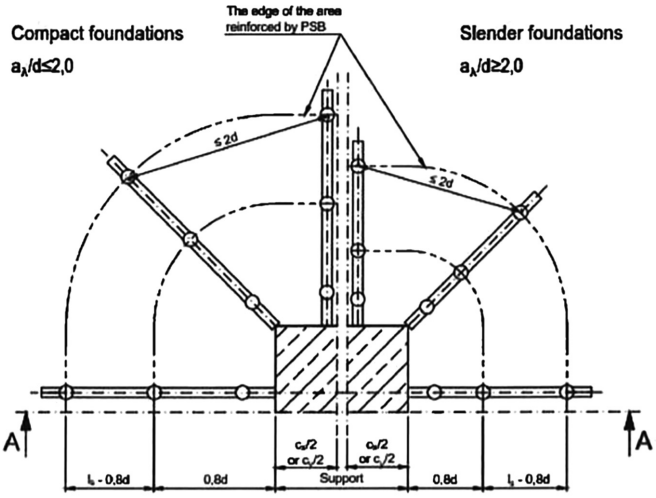

Fig. 4. Maximum allowed spacing of studs in slender and compact footings (ETA 2018).

Besides technical description and performance assessment of the product, ETA 13/0151 gives also provisions regarding both positioning of the studs, which are shown in Fig. 4 for compact and slender footings, and installation conditions.

3 Experimental Program

While the punching strength of slender slabs has been widely investigated, only few tests on reinforced concrete footings have been carried out in the past. An experimental program was therefore carried out at EPFL in Lausanne in order to investigate the performance of compact footings under punching shear (Simões et al. 2016). Main investigation parameters were influence of column size, member slenderness and the presence of compression and shear reinforcement, which was made with Peikko PSB® studs.

3.1 Specimens and Test Setup

Eight full-scale reinforced concrete footings were tested. All the specimens were square with the same height (0.55 m) but different side length (2.12 m or 1.59 m). Square columns had side length of 0.30 mm or 0.45 m to allow variations in shear slenderness. The bottom flexural reinforcement was kept constant for all the specimens (0.75%) while the top compression reinforcement was used only for some specimens. Four specimens had shear reinforcement consisting of 25 mm diameter PSB® studs in radial arrangement along two or three perimeters (Fig. 5a).

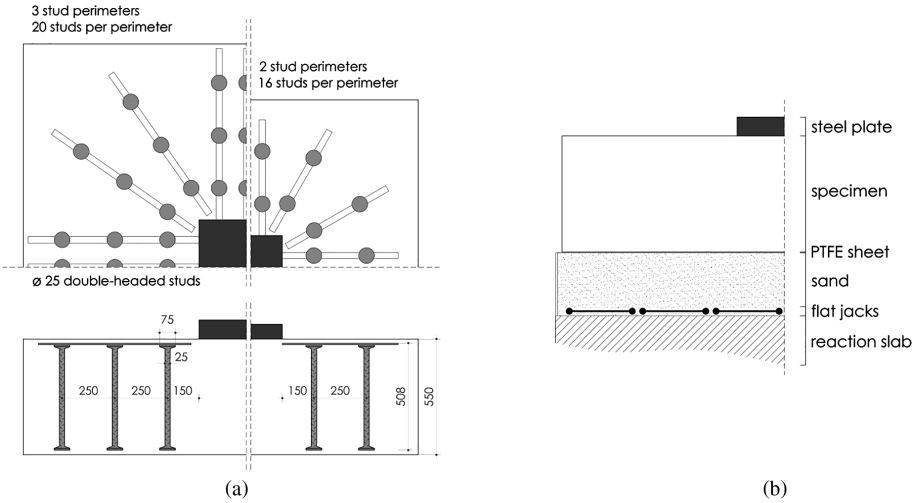

Fig. 5. (a) Layout of shear reinforcement of some of the specimens; (b) Test setup configuration achieving uniform soil pressure (adapted from Simões et al. 2016).

The innovative test setup allowed to apply a uniform pressure below the bottom surface of the footing. This was achieved by the use of flat jacks connected in series that applied a uniform distribution of the load to a layer of sand ~300 mm deep, on which the footing was placed. The friction between sand and concrete was reduced by placing a PTFE sheet and the expansion of the sand under loading was allowed by leaving a gap around the sides of the footing (Fig. 5b).

3.2 Main Results

The specimens with shear reinforcement failed in punching inside the shear reinforced zone by crushing of concrete struts close to the column. The maximum load at failure was greater than that of the corresponding specimens without shear reinforcement of about 30% to almost 60%. This shows that the punching strength of reinforced concrete footings can be significantly increased by the presence of double-headed studs.

The specimens with shear reinforcement presented a more ductile failure, with approximately double outer rotation, as it is assessed by the load-rotation curves. A plateaux of the curves was also observed, which indicates a flexural-shear interaction.

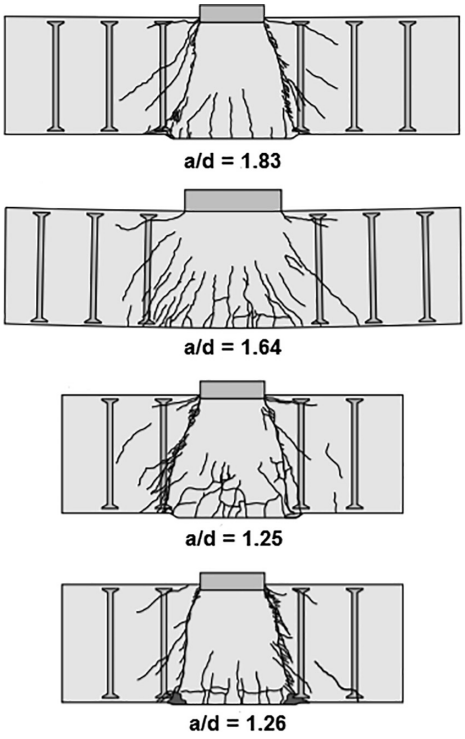

Fig. 6. Schematic representation of the saw cut sections of the shear reinforced specimens (adapted from Simões et al. 2016).

In general, the crushing failure developed along a surface between the edge of the column and the first row perimeter of studs. The inclination of this surface is steeper for more compact footings, as shown in Fig. 6. It means that the effectiveness of this reinforcing system is dependent on the shear slenderness, which determines the location and inclination of concrete struts.

In fact, a lower angle between the concrete struts and the shear reinforcement reduces the effectiveness of the studs, due to the force equilibrium between compressive and normal transverse strains in concrete and tensile strains in the studs. However, the excellent anchorage conditions of PSB® studs enables their full activation upon the onset of transverse strains, thus providing a satisfactory punching strength capacity.

4 Design Example

A design example of a 350 mm thick ground slab loaded by a square column (c = 40 cm) is herein presented. The considered design data are listed in Table 2.

Table 2. Design data.

Concrete grade	C30/37
Concrete cover	$c_u = c_0 = 30$ mm
Diameter of bending reinforcement	$Ø_x = Ø_y = 16$ mm
Spacing of bending reinforcement	$a_{sx} = a_{sy} = 150$ mm
Applied load	$V_{Ed} = 1100$ kN
Position of the column	Internal column
	$\beta = 1.15$

The following geometrical dimensions are calculated:

$$d = \frac{d_x + d_y}{2} = 304\,\text{mm} \tag{3}$$

$$\rho_l = \sqrt{\rho_x \rho_y} = 0.44\% \tag{4}$$

$$u_1 = 2\pi \cdot 2d + 4c = 5420\,\text{mm} \tag{5}$$

$$u_0 = 4c = 1600\,\text{mm} \tag{6}$$

The punching shear resistance $v_{Rd,c}$ and the maximum shear resistance $v_{Rd,max}$ of the slab without punching reinforcement are calculated according to ETA 13/0151 as follows:

$$v_{Rd,c} = \frac{0.18}{\gamma_c} k(\varrho_l f_{ck})^{1/3} = 0.514\,\text{MPa} \tag{7}$$

$$v_{Rd,max} = k_{max} v_{Rd,c} = 0.833\,\text{MPa} \tag{8}$$

where:

$$k = 1 + \sqrt{\frac{200}{d}} \leq 2 \tag{9}$$

It has to be noticed that calculation according to EN 1992-1-1 would underestimate the actual maximum shear resistance of the slab reinforced with PSB® studs ($V_{Rd,max,\text{EN1992-1-1}} = 1271$ kN < $V_{Rd,max,\text{ETA13/0151}} = 1372$ kN).

PSB® reinforcement can be used when the design value of the shear stress verifies the following equation:

$$v_{Rd,c} \leq \frac{\beta V_{Ed}}{u_1 d} = 0.768\,\text{MPa} \leq v_{Rd,max} \tag{10}$$

In this case shear reinforcement made with 12 PSB® rails with 4 diameter 14 studs each is selected, as indicated in Fig. 7. If the design value of the shear stress is lower than the punching shear resistance of the concrete slab, then no PSB® reinforcement is needed. On the other hand, PSB® reinforcement is not usable whether the maximum resistance of the slab is exceeded.

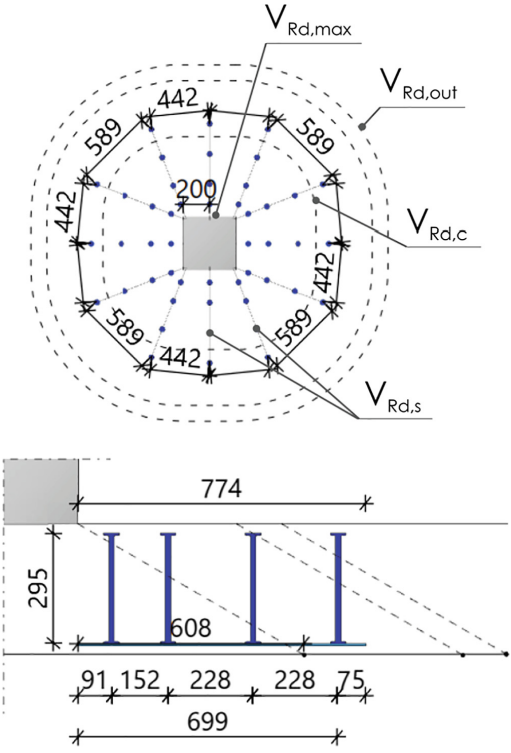

Fig. 7. Selected PSB® reinforcement.

The geometrical constraints regarding the spacing between the studs ($s_0 \leq 0.3d$; $s_0 + s_1 \leq 0.8d$ and $s_2 \leq 0.75d$ Fig. 4) are respected, as well as the minimum number of PSB® studs in one element, the provided length of a single rail ($l_{s,prov} \geq l_{s,req}$) and the required length of outer perimeter ($u_{out,prov} \geq u_{out,req}$):

$$u_{out,req} = \frac{\beta V_{Ed}}{v_{Rd,out} d} = 8095\,\text{mm} \tag{11}$$

$$l_{s,req} = \frac{u_{out,req} - 4c}{2\pi} - 1.5d = 578\,\text{mm} \tag{12}$$

$$n_{req} = \frac{l_{s,req} - (s_0 + s_1)}{s_2} + 1 \cong 4 \tag{13}$$

$$l_{s,prov} = s_0 + s_1 + (n_{prov} - 2)s_2 = 699\,\text{mm} \tag{14}$$

$$u_{out,prov} = 2\pi(l_{s,prov} + 1.5d) + 4\text{c} = 8857\,\text{mm} \tag{15}$$

Final checks refer to resistance of the slab in the outer perimeter and resistance of the studs inside the control perimeter, which have to be greater than the acting shear load:

$$v_{Rd,out} \geq v_{Ed,out} = \frac{\beta V_{Ed}}{u_{out,prov} d} = 0.470\,\text{MPa} \tag{16}$$

$$V_{Rd,s} = A_{sw,0.8d} f_{yd} = 1606\text{kN} \geq V_{Ed} \tag{17}$$

All above calculations and checks can be easily carried out by using the software Peikko Designer® (Peikko Group 2018), which automatically gives optimized solution for stud rails positioning and dimensioning.

5 Conclusions

Double-headed studs are an efficient reinforcement technique to increase the punching shear capacity and ductility of foundation slabs and footings. The PSB® studs manufactured by Peikko Group are currently the only studs on the European market whose performance has been tested in foundation slabs. Consequently, the ETA 13/0151 allows to justify resistances that are about 10% higher than the resistances of foundation slabs or footings reinforced by conventional reinforcement products available on the market.

Acknowledgements. The authors would like to thank EPFL in Lausanne and Professor Muttoni for fruitful cooperation during the experimental program on shear punching reinforcement.

Notation

$A_{sw,0.8d}$	Cross-section of punching reinforcement in a distance between $0.3d$ and $0.8d$ from column face
a/d	Span-to-depth ratio
a_s	Spacing of bending reinforcement
c	Column side
c_0	Bottom concrete cover
c_u	Upper concrete cover
d	Effective depth of the slab
k	Coefficient for size effects

L	Span of the slab
$l_{s,prov}$	Provided length of one element
$l_{s,req}$	Required length of one element
n_{prov}	Provided number of studs in none element
n_{req}	Minimum number of studs in one element
u_0	Column perimeter
u_1	Basic control perimeter
$u_{out,prov}$	Provided control perimeter
$u_{out,req}$	Required control perimeter
f_{ck}	Characteristic concrete strength
f_{cd}	Design concrete strength
f_{yd}	Design steel strength
k_{max}	Magnification factor
s_0	Spacing between column perimeter and first stud
s	Spacing between the studs
s_w	Radial distance of the studs
V_{Ed}	Design shear force
$V_{Rd,s}$	Resistance force of the studs
$V_{Rd,max}$	Maximum resistance force of the slab
$v_{Ed,out}$	Shear stress on the outer perimeter
$v_{Rd,c}$	Resistance of the slab without punching reinforcement
$v_{Rd,out}$	Resistance of the slab on the outer perimeter
$v_{Rd,max}$	Maximum resistance of the slab
β	Load increase factor
γ_c	Concrete safety factor (= 1.5)
ρ_l	Bending reinforcement ratio
Ø	Reinforcement diameter

References

Bujnak J (2015) ETA 13/0151: design of flat slabs with PSB reinforcement elements. Concr Connect 1(2015):19–22

BS (British Standards) (2009) UK national annex to Eurocode 2, EN 1992-1-1/NA:2009. London

CEN (European Committee for Standardization) (2004) Eurocode 2: design of concrete structures. General rules and rules for buildings, EN 1992-1-1:2004. Brussels

CEN (European Committee for Standardization) (2014) Amendement for: design of concrete structures. General rules and rules for buildings, EN 1992-1-1/A1:2014. Brussels

DIN (German Institute for Standardization) (2011) Nationaler Anhang - National festgelegte Parameter - Eurocode 2: Bemessung und Konstruktion von Stahlbeton - und Spannbeton-tragwerken - Teil 1-1: Allgemeine Bemessungsregeln und Regeln für den Hochbau, EN 1992-1-1/NA:2011. Berlin

EOTA (2012) Common understanding of assessment procedure 03.01/05. Double-headed studs for the increase of punching resistance in flat slabs on column, for European technical approval. Brussels

ETA 13/0151 (European Technical Assessment) (2018) Peikko PSB punching reinforcement

European Concrete Platform (2008) ASBL: Eurocode 2 commentary. Brussels

Lips S, Fernández Ruiz M, Muttoni A (2012) Experimental investigation on the punching strength and the deformation capacity of shear-reinforced slabs. ACI Struct J 109(6):889–900

Muttoni A, Bujnak J (2013) Performance of slabs reinforced by Peikko PSB studs demonstrated by full scale tests and validated by ETA approval starting April 2013. Concr Connect 1 (2013):18–23

Onorm (Austrian Standard) (2011) National annex to Eurocode 2 of Austria, B EN 1992-1-1/NA:2011. Vienna

Peikko Group (2013) PSB® Reinforcement against punching failure of slabs. Technical manual

Peikko Group (2018) Peikko Designer® (1.0.2.78). https://www.peikko.com/design-tools/

SIS (Swedish Standards Institute) (2011) National annex to Eurocode 2 of Sweden, EN 1992-1-1/NA:2011. Stockholm

SFS (Finnish Standards Association) (2007) The Finnish national annex to the standard SFS-EN 1992-1-1, EN 1992-1-1/NA:2007. Helsinki

Simões JT, Bujnak J, Fernández Ruiz M, Muttoni A (2016) Punching shear tests on compact footings with uniform soil pressure. Struct Concr 4:603–617

STN (Slovak Technical Standard) (2013) National annex to Eurocode 2 of Slovakia, EN 1992-1-1/NA/Z1:2013. Bratislava

Safety Check Procedures of Fiber Reinforced Concrete Curbs for Bridge Slabs

F. Di Carlo[1(✉)], A. Meda[1], Z. Rinaldi[2], and F. Simonelli[3]

[1] Department of Civil Engineering and Computer Science Engineering (DICII), University of Rome Tor Vergata, via del Politecnico 1, 00133 Rome, Italy
di.carlo@ing.uniroma2.it
[2] Department of Industrial Engineering (DII), University of Rome Tor Vergata, via del Politecnico 1, 00133 Rome, Italy
[3] Mapei S.p.A., via Cafiero 22, 20158 Milan, Italy

Abstract. The construction of new curbs or the replacement of existing ones is usually due to the need of installing safety or anti-noise barriers. Recent studies, developed by the authors and proven by experimental tests, have shown the effectiveness of a new technology, based on the use of high performance fiber reinforced concrete. This technology shows several advantages: a significant reduction in execution time of the curb and of installation of barriers elements, thanks to the rapid achievement of high resistance; lack of interference between barriers anchorages and reinforcement rebars. Aim of the study is the formulation of simplified procedures for the safety check of curb-slab systems, against the action of the vehicle impact, with reference to curbs rebuilding on existing reinforced concrete bridge slabs. Finally, safety check criteria of curbs, characterized by rectangular or L-shaped cross section, are proposed, based on both global and local behaviours.

Keywords: Fiber-reinforced concrete · Curbs · Bridge slabs · Safety check criteria

1 Introduction

The curbs construction for existing bridge slabs represents a worthy issue, recently analysed and studied not only from a static point of view but also regarding economic and technological aspects. The construction of new curbs or the replacement of existing ones is usually due to the need of installing safety or anti-noise barriers. Recent studies, developed by the authors and based on the outcomes of full-scale experimental tests, showed the effectiveness of a new technology based on the use of high performance fiber reinforced concrete (HPFRC), in order to eliminate the traditional steel reinforcement (Devitofranceschi et al. 2014). The use of fiber reinforced concrete (FRC) is growing continuously due to its several advantages, not only in terms of cost reduction, but also in terms of improvement in quality and structural performance (Di Carlo et al. 2016a). The adoption of this technology allows a reduction of the construction time, with the main advantage of limiting traffic interruption. Furthermore, thanks to the high strength of the material in the first few hours after concrete casting, also a reduction of

M. di Prisco and M. Menegotto (Eds.): ICD 2018, LNCE 42, pp. 193–206, 2020.
https://doi.org/10.1007/978-3-030-23748-6_15

the time required for the barriers installation is found. Another advantage, connected to the lack of the traditional reinforcement, consists in avoiding interference between barriers anchorages and reinforcement rebars. Experimental tests performed by the authors at the Laboratory of the University of Rome Tor Vergata showed the effectiveness of this technology and allowed the first installations on the Italian road network.

The possibility of using high performance fiber reinforced concrete (HPFRC) for strengthening of RC structures has been investigated in (Marini and Meda 2009; Martinola et al. 2007, 2010; Meda et al. 2008, 2014; Preti and Meda 2013). The effectiveness of this retrofit technique has been shown in Beschi et al. (2015). Numerical analyses of HPFRC elements can be found in Di Carlo et al. (2016b).

Aim of this work is the formulation of simplified procedures for performing safety checks of the curb-slab system, with reference to the rebuilding of the fiber reinforced concrete curb on an existing traditional reinforced concrete (RC) slab. In particular, reference is made to curbs characterized by rectangular and L-shaped cross section, taking into account mainly the structural effects due to the vehicle impact. Global and local safety checks are accounted for. Furthemore, design rules and criteria of the curb-slab system are proposed.

2 Experimental Tests

The experimental tests on full-scale RC slabs with external HPFRC curbs have been performed at the Laboratory of the University of Rome Tor Vergata (Devitofranceschi et al. 2014). In particular, six 300 mm thick, 2500 mm long and 1250 mm wide slabs have been realized. After the slab casting, two 150 mm long cores with a diameter equal to 120 mm have been realized in the middle point of the contact surface between edge beam and slab, in order to ensure an adequate connection. The fiber reinforced concrete is characterized by a mean compressive strength equal to 102 MPa. Figure 1 shows the details of the test specimens.

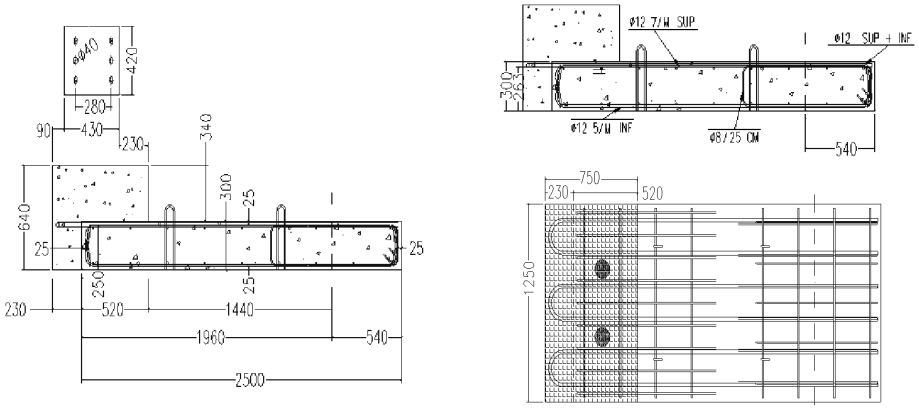

Fig. 1. Details of the test specimens.

The test set-up shown in Fig. 2 reproduces the horizontal action due to the impact of the vehicle on the safety barrier. The slab is constrained with a cantilever scheme by means of two 2000 kN hydraulic jacks. The horizontal force is applied to the vertical element of the safety barrier, at the height of 960 mm from the extrados surface of the curb by means of a hydraulic 4000 kN jack.

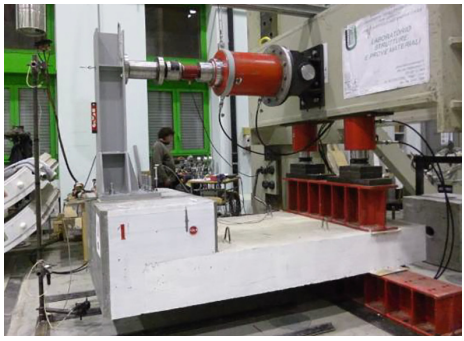

Fig. 2. Test set-up.

The displacements were measured with a system of potentiometric transducers and LVDT devices. Figure 3 shows an example of the obtained results, in terms of horizontal load – drift (displacement of the loading point) diagram.

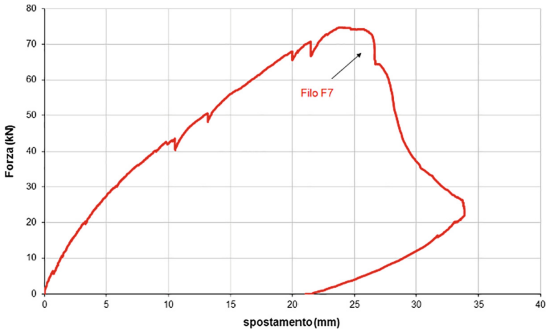

Fig. 3. Load-drift diagram.

All the specimens shown a similar behaviour, in terms of cracking pattern and collapse mechanism. At the cracking load, vertical cracks at the slab extrados and a horizontal crack between curb and slab occurred (Fig. 4).

The cracking pattern at the maximum load was instead characterized by the presence of a crack developing from the upper corner of the concrete slab (Fig. 5).

Fig. 4. First cracking.

Fig. 5. Maximum load.

3 Simplified Safety Check Procedure

This section is devoted to the formulation of simplified procedures for performing safety checks of FRC curbs cast on traditional RC slabs. Reference is made to rectangular and L-shaped curbs (Fig. 6).

The curb is mainly subjected to the effects of the horizontal action due to the impact of the vehicle on the safety barrier (Fig. 7).

3.1 Rectangular Curbs

In case of rectangular curbs, steel connectors have to be placed in order to ensure an adequate connection with the existing slab. The first safety check regards the longitudinal section made up by the FRC curb and the existing RC slab (Fig. 8).

The safety check of the section can be performed by means of bending moment (M) - axial force (N) envelopes, defined by using a stress-block constitutive law for both compressive and tensile branches of FRC material (Model Code 2010), and for the

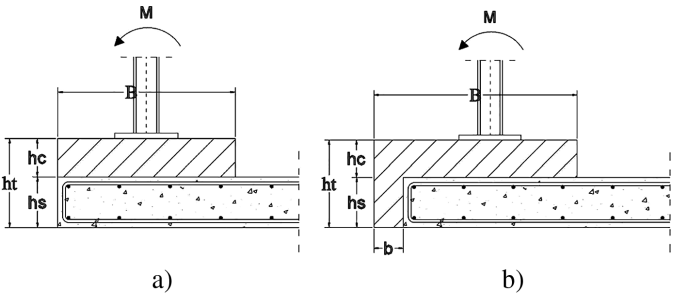

Fig. 6. Curb geometry: (a) rectangular; (b) L-shaped.

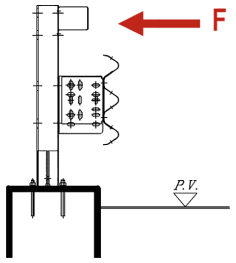

Fig. 7. Actions due to the vehicle impact.

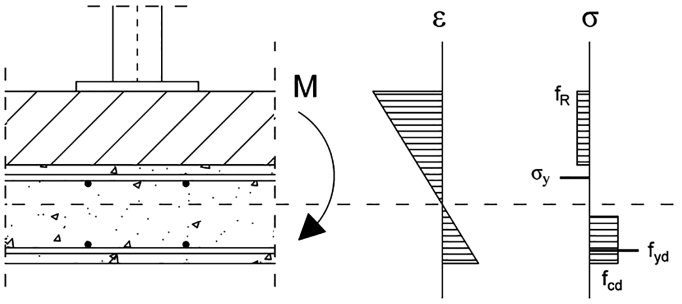

Fig. 8. Longitudinal section.

compressive behaviour of traditional concrete. The design compressive strengths of FRC and traditional RC materials are respectively equal to:

$$f_{cdFRC} = \frac{\alpha_{cc} \cdot f_{ckFRC}}{\gamma_c} \tag{1}$$

$$f_{cd} = \frac{\alpha_{cc} \cdot f_{ck}}{\gamma_c} \tag{2}$$

where f_{ckFRC} and f_{ck} are the characteristic strengths of the two materials, α_{cc} is the long term load coefficient equal to 0.85 and γ_c is the safety factor equal to 1.5. The design tensile strength of FRC is given by (Model Code 2010):

$$f_{Ftud} = \frac{1}{\gamma_f} \cdot \frac{f_{R3k}}{3} \tag{3}$$

where f_{R3k} is the tensile stress corresponding to a crack mouth opening displacement (*CMOD*) equal to 2.5 mm and γ_f is the safety factor equal to 1.5.

An elastic-plastic constitutive law is implemented for the reinforcement rebars.

In case of existing decks, instead of design values, mean strengths of concrete and steel, properly reduced by means of confidence factors, have to be considered.

The ultimate condition consists in the attainment of the ultimate strain of one of the two materials. In particular, the ultimate compressive strain of both FRC and RC materials can be taken equal to 3.5‰. According to Model Code 2010, the ultimate tensile strain ε_{fu} is equal to 2%. It is worth highlighting that it cannot be higher than the value corresponding to a maximum crack width equal to 2.5 mm. In order to define a relationship between strain (ε) and crack opening (w) values, the definition of a characteristic length l_{cs} is required:

$$\varepsilon = \frac{w}{l_{cs}} \tag{4}$$

Which for slab elements, according to Model Code 2010, can be taken equal to the element thickness. Ultimately, it reads:

$$\varepsilon_{ULS} = \min\left(\varepsilon_{fu}, \frac{2.5\,mm}{l_{cs}}\right) \tag{5}$$

An example of bending moment-axial force envelope is shown in Fig. 9.

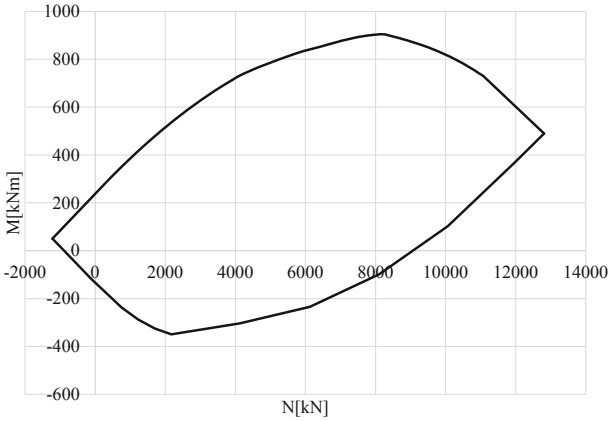

Fig. 9. Example of M-N interaction envelope.

The second safety check refers to the shear strength of the steel connectors between curb and slab (Fig. 10).

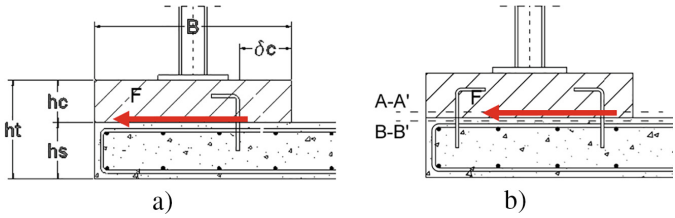

Fig. 10. Connectors: (a) single; (b) couple.

Having fixed the diameter, the number of the connectors or of the couple of connectors to be placed between two vertical elements of the safety barrier is respectively given by:

$$n_{ctot} = \frac{F}{\tau_{con} \cdot A_{1co}} \tag{6}$$

$$n_{ctot} = \frac{F}{2 \cdot \tau_{con} \cdot A_{1co}} \tag{7}$$

where F is the horizontal force due to the vehicle impact, A_{1co} is the area of the single connector and τ_{con} is the tangential strength, defined according to NTC 2008 as:

$$\tau_{con} = \min\left(\frac{0.8 \cdot f_{uk}}{\gamma_v}, \frac{0.29 \cdot f_{ck} \cdot E_c}{\pi} \cdot \frac{4}{\gamma_v}\right) \tag{8}$$

with f_{uk} the characteristic strength of the connector, E_c the Young Modulus of the concrete and γ_v the safety factor equal to 1.25.

The third safety check regards the contact surface between the curb intrados and the slab extrados. In particular, two safety checks have to be performed by considering both FRC and RC sections (Fig. 11).

The bending moment due to the vehicle impact is counteracted by compressive stresses acting in the compressed parts the two considered sections and by tensile stresses of steel connectors and FRC material. Stress-block constitutive laws are used for both compressive and tensile branches of FRC material and for the compressive behaviour of traditional concrete.

The last safety check regards the contact surface between the steel plate of the vertical element of the barrier and the curb extrados. In this case, the steel coach screws counteract the tensile stresses.

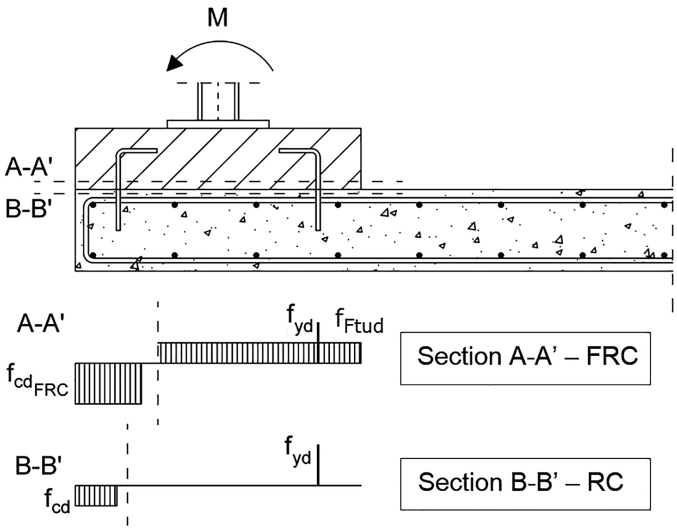

Fig. 11. Contact surface curb-slab.

3.2 L-Shaped Curbs

Similarly to rectangular curbs, the first safety check regards the longitudinal section made up by the FRC curb and the existing RC slab (Fig. 8). The hypotheses regarding the constitutive laws of the involved materials are analogous. The safety check, performed by means of *M-N* interaction envelopes, is the same of the one related to the case of rectangular curb, since the vertical portion of the L-shaped curb does not play a role.

The safety check of the steel connectors placed between curb and slab is substantially analogous to the previous case of rectangular shape. Figure 12 shows the two cases of L-shaped curb with a single steel connector or a couple of connectors.

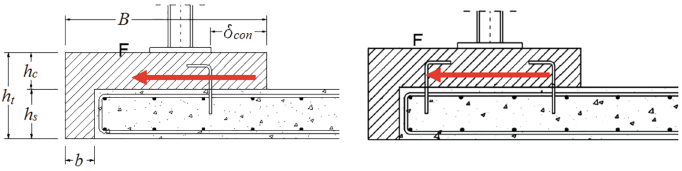

Fig. 12. Connectors: (a) single; (b) couple.

With reference to the safety check regarding the contact surface between curb intrados and slab extrados, two checks have to be performed by considering both FRC and RC sections. The check of the FRC section is similar to the case previously described. Regarding the RC section, it is worth to highlight that, depending on the

position of the neutral axis, the contributions of compressive stresses acting in the FRC and RC portions, have to be considered (Fig. 13).

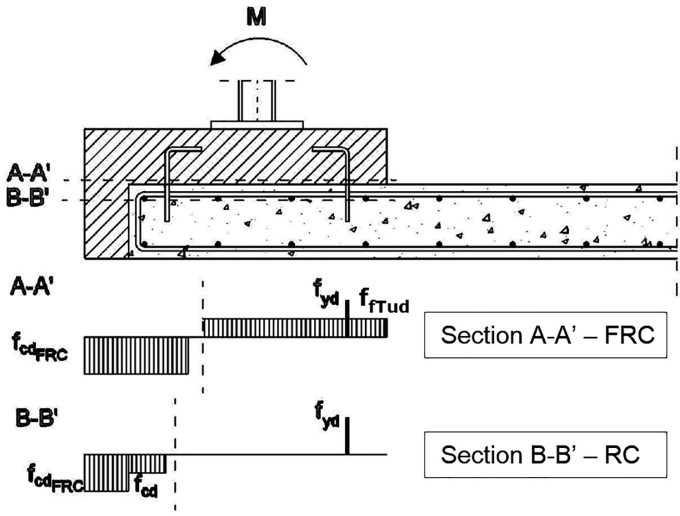

Fig. 13. Contact surface curb-slab.

In a similar way to the case of rectangular curb, the last safety check regards the contact surface between the steel plate of the vertical element of the barrier and the curb extrados.

4 Case Studies

In this section the results of case studies regarding the various curb geometries previously analysed are shown.

4.1 Case Study: Rectangular Curb

The first case study addressed refers to a rectangular curb. The geometrical and mechanical properties are summarized in Tables 1 and 2, respectively.

Figure 14 shows the *M-N* interaction envelope: the safety check results to be satisfied since the loading point, defined by an axial force equal to 100 kN and a bending moment equal to 96 kNm lays within it.

The number of steel connectors to be placed between the vertical elements of the safety barrier is equal to:

$$n_{ctot} = \frac{100kN}{260MPa \cdot 114mm^2} = 3.37 \tag{9}$$

Table 1. Geometrical properties.

Geometrical properties	Value
Depth [mm]	1250
Width [mm]	700
FRC curb thickness [mm]	150
RC slab thickness [mm]	200
Slab longitudinal reinforcement [1/m]	5∅16
Slab concrete cover [mm]	30
Connectors diameter [mm]	12
Distance of the connectors from the curb side [mm]	100
Force due to the vehicle impact [kN]	100
Height of the safety barrier [mm]	960

Table 2. Mechanical properties.

Mechanical properties	Value
Traditional reinforced concrete	
Characteristic compressive strength [MPa]	25
Design compressive strength [MPa]	14.17
Ultimate compressive strain [-]	3.5‰
Fiber reinforced concrete	
Characteristic compressive strength [MPa]	78
Design compressive strength [MPa]	44.2
Ultimate compressive strain [-]	3.5‰
Tensile strength for CMOD = 2.5 mm [MPa]	5.6
Characteristic tensile strength [MPa]	1.87
Design tensile strength [MPa]	1.24
Ultimate tensile strain [-]	2%
Steel reinforcement	
Characteristic tensile strength [MPa]	450
Design tensile strength [MPa]	391
Connectors	
Tangential strength of the connectors [MPa]	262

Referring to the safety check of the contact surface between the curb intrados and the slab extrados, from the side of the curb, the ultimate bending moment results to be equal to 548 kNm, higher than the acting bending moment, equal to 96 kNm. With reference to the side of the existing slab, the safety check is also satisfied, since an ultimate bending moment equal to 98.8 kNm is obtained.

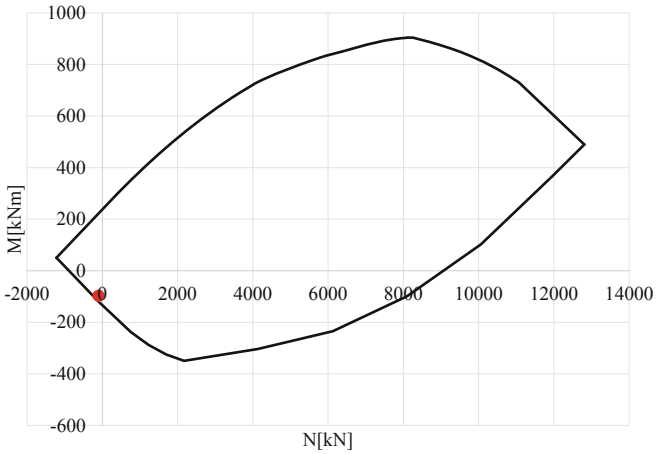

Fig. 14. *M-N* interaction envelope.

4.2 Case Study: L-Shaped Curb

The L-shaped curb analysed in this paragraph is characterized by the geometrical properties shown in Table 1. The width of the element is equal to 700 mm, but it presents a 150 mm wide portion external to the existing slab. The mechanical properties of all materials are shown in Table 2.

Similarly to the previous case, the safety check of the longitudinal section is performed with the *M-N* interaction envelope shown in Fig. 15. The safety check is satisfied, being the loading point contained within the domain.

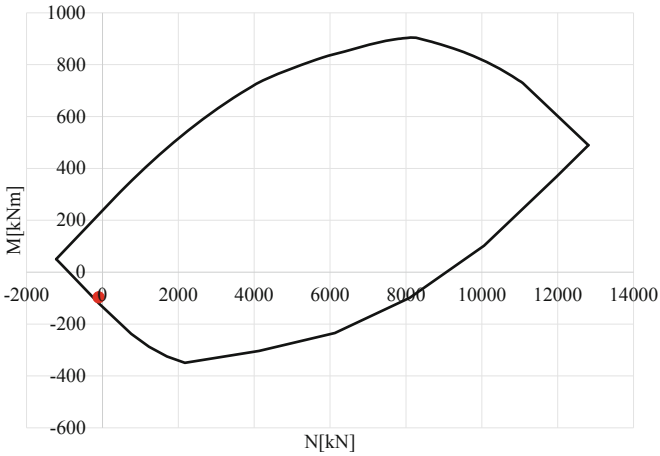

Fig. 15. *M-N* interaction envelope.

Equation 9 gives the number of the steel connectors. Referring to the safety check of the contact surface between curb intrados and slab extrados, from the side of the curb, the ultimate bending moment results to be equal to 547.7 kNm. With reference to the side of the existing slab, an ultimate bending moment equal to 115.7 kNm is obtained. Both safety checks are then satisfied

4.3 Case Study: L-Shaped Curbs with Ineffective Connectors

This section is devoted to the analysis of the outcomes of the experimental tests, discussed in paragraph 2. In order to account for the collapse mode occurred during the experimental tests – consisting in the failure of the two FRC cores - the behaviour of the connection system has been modelled by introducing an equivalent steel reinforcement area, in terms of tensile strength. In particular, an equivalent ∅10 steel connector has been considered. The mean values of concrete and steel strengths are considered.

The analytical collapse condition of the FRC curbs cast on traditional RC slab is due to the attainment of the ultimate bending moment at the contact surface between the curb intrados and the slab extrados, from the side of the existing slab. The maximum numerical horizontal action, due to the impact of the vehicle on the safety barrier, which can be sustained by the curb is equal to 74 kN. The results obtained through the performed experimental tests are in perfect agreement, showing in fact a mean collapse load equal to 71.5 kN (Table 3).

Table 3. Experimental collapse load values.

Curb	Maximum load (kN)
I	75
II	68
III	78
IV	65
V	68
VI	75
Mean value	71.5

Both safety checks of the contact surface between curb intrados and slab extrados, from the side of the curb (ultimate bending moment equal to 798 kNm), and of the longitudinal section are satisfied. Figure 16 shows the bending moment-axial force interaction envelope of the longitudinal section.

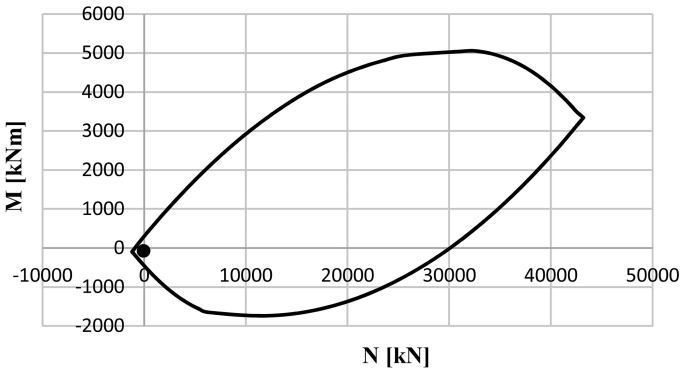

Fig. 16. *M-N* interaction envelope.

5 Conclusions

The use of fiber reinforced concrete (FRC) is growing continuously due to its several advantages, not only in terms of cost reduction, but also in terms of improvement in quality and structural performance. Recently, the interest in using FRC as a substitute of traditional reinforced concrete in curbs construction for existing bridge slabs is rising steadily. Its main advantages consist in a reduction in construction time, limiting traffic interruption, a decrease in time required for barriers installation and an elimination of interferences between barriers anchorages and reinforcement rebars. Full-scale experimental tests, developed by the authors at the Laboratory of the University of Rome "Tor Vergata", have shown the effectiveness of this technology, allowing the first installations on the Italian road network.

For this reason, a formulation of simplified procedures for performing safety checks of the curb-slab system is developed and discussed in this paper. In particular, reference is made to the rebuilding of a FRC curb on an existing RC slab. Rectangular and L-shaped curbs are addressed. Furthermore, the case of curb with ineffective connection systems – e.g. with FRC cores – is dealt with.

References

Beschi C, Riva P, Metelli G, Meda A (2015) HPFRC jacketing of non seismically detailed RC corner joints. J Earthquake Eng 19(1):25–47

Decreto Ministeriale (2008, January 14) Approvazione delle nuove norme tecniche per le costruzioni. Supplemento Ordinario n. 30 alla Gazzetta Ufficiale n. 29 del 4 febbraio 2008

Devitofranceschi A, Luzzo E, Meda A, Rinaldi Z, Simonelli F, Tironi D (2014) Cordoli in calcestruzzo fibrorinforzato in solette da ponte per l'applicazione di barriere antirumore. In: Giornate AICAP 2014, Bergamo, 22–24 Maggio 2014

Di Carlo F, Meda A, Rinaldi Z (2016a) Design procedure for precast fibre-reinforced concrete segments in tunnel lining construction. Struct Concr 17(5):747–759

Di Carlo F, Meda A, Rinaldi Z (2016b) Numerical cyclic behaviour of un-corroded and corroded RC columns reinforced with HPFRC jacket. Compos Struct 163:432–443

fib Model Code for Concrete Structures (2010) Ernst and Sohn, 2013
Marini A, Meda A (2009) Retrofitting of R/C shear walls by means of high performance jackets. Eng Struct 31(12):3059–3064
Martinola G, Meda A, Plizzari GA, Rinaldi Z (2007) An application of high performance fiber reinforced cementitious composites for R/C beams strengthening. In: 6th international conference on fracture mechanics of concrete and concrete structures, FraMCos-6, Catania, 17–22 June 2007, pp 1541–1548
Martinola G, Meda A, Plizzari GA, Rinaldi Z (2010) Strengthening and repair of RC beams with fiber reinforced concrete. Cement Concr Compos 32(9):731–739
Meda A, Mostosi S, Riva P (2014) Shear strengthening of reinforced concrete beam with high-performance fiber-reinforced cementitious composite jacketing. ACI Struct J 111(5):1059–1068
Meda A, Plizzari GA, Rinaldi Z, Martinola G (2008) Strengthening of R/C existing columns with high performance fiber reinforced concrete jacket. In: Proceedings of the 2nd international conference on concrete repair, rehabilitation and retrofitting (ICCRRR08), Cape Town, South Africa, Balkema, CRC Press, 24–26 November 2008
Preti M, Meda A (2013) RC structural wall with unbonded tendons strengthened with high-performance fiber-reinforced concrete. Mater Struct 48(1):249–260

Applications of Non-metallic Concrete Reinforcements

M. Arduini[1] and G. Balconi[2(✉)]

[1] Coforce, Reggio Emilia, Italy
[2] Sireg Geotech, Milan, Italy
g.balconi@sireg.it

Abstract. Initial pilot projects assessing the potential applications of non metallic concrete reinforcements date back to the end of the '90s. In 2001, reinforcements made with Glass Fiber Reinforced Polymers ("GFRP") were used for the first time to realize a tunnel excavation front containing wall. This temporary application was motivated by the easiness of severing the reinforcement directly with the TBM during excavation, a technique (known as Soft-Eye) currently widely used in the field of geotechnics. Today, non-metallic concrete reinforcements for permanent applications are the focus of new interest triggered by the awareness that, due to a number of factors, the effective duration of existing concrete structures does not correspond in most cases to that of design. This paper presents some concrete structures realized in recent years with GFRP reinforcements that guarantee long term behaviour.

Keywords: Fibre-reinforced concrete · Glass Fibre Reinforced Polymers · GFRP · GFRP reinforcements · Permanent concrete reinforcement · Reinforced concrete durability

1 Introduction

The first applications of non metallic cages for concrete reinforcement date back to the end of the '90s. These consisted mainly of pilot or sample projects aiming to show the potential of an innovative technology.

The realization of the first containing wall for a tunnel excavation front reinforced with Glass Fibre Reinforced Polymers ("GFRP") took place in London in 2001. Since then this temporary application, motivated by the easiness of cutting the GFRP cage by the TBM itself during excavation, has rapidly expanded in the field of Geotechnics. Currently, tunnel construction projects worldwide utilize the technique known as Soft-Eye.

Today, non-metallic concrete reinforcements are the focus of interest and attention for a different reason. Awareness of the fact that the effective duration of existing concrete structures do not, in most of the cases, correspond to the theoretical duration of the design project has generated the need to identify efficient alternative solutions. Concerned with guaranteeing compression resistance, Civil Engineers in the past have

M. di Prisco and M. Menegotto (Eds.): ICD 2018, LNCE 42, pp. 207–218, 2020.
https://doi.org/10.1007/978-3-030-23748-6_16

not given sufficient attention to a number of factors affecting the duration of concrete structures, such as concrete's porosity and permeability, electrical potential, proper concrete cover, the quantity and quality of the water effectively present in the concrete cast, among others. In order to avoid repeating the same mistakes done in the past, the use of non-metallic concrete reinforcing cages acquires importance for the design of structures in civil engineering.

The use of non-metallic concrete reinforcements in civil construction remains limited due to the lack of design guidelines and test standardization. As a result, the use of GFRP in construction works is still mainly driven by the need to solve specific challenges, for which the GFRP reinforcements constitute an efficient solution. Some of these cases are hereby presented.

2 Interference with Electric Circuits

2.1 Athens Tram's Track Beds

In the scope of railway infrastructure, devices known as "mass detector circuits" are nowadays one of the methods used for train detection for various safety purposes. These systems operate via an electric oscillating circuit, which indicates a change in frequency when the metal mass of a rail vehicle crosses the mass detector coil. The detectors are casted in the RC track beds.

In order for the steel reinforcement not to interfere with the signals, the section of the track bed containing the detectors must be strengthened with non-metallic reinforcements.

In the case of the Athens Tram, it was absolutely necessary to replace the original project's steel reinforcements with thermally and electrically non-conductive GFRP cages for the installation of mass detectors in some lines during 2017.

Figure 1 shows the non-metallic cage already installed in a section of the track bed. The mass detector device fits perfectly in the internal space of the GFRP cage.

The cages were built with GFRP rebars with diameters of 12, 16 and 20 mm (Glasspree® rods). Stirrups in varied geometries had to be manufactured. For the concrete cast, C45/55 was chosen. The design project for the GFRP reinforcement achieved equivalent design strength in longitudinal and transversal directions, as well as shear contribution, as the original steel design while guaranteeing long term performance. Figure 2 compares a cross section of the original design using steel rods with that of the GFRP equivalent longitudinal reinforcements. Images of the GFRP cages on site are shown in Figs. 3, 4.

Fig. 1. GFRP reinforcements installed in a section of the Athens tram track beds

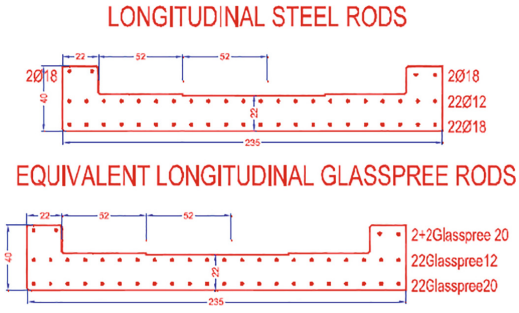

Fig. 2. Cross section of original design with steel rods (top) and of equivalent ultimate limit design (ULS) design with Glasspree rods (bottom)

Fig. 3. GFRP reinforcing cage assembled on the track beds

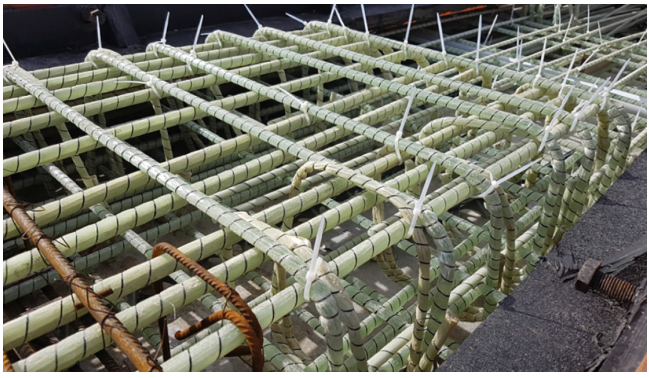

Fig. 4. Detail of GFRP reinforcing cage

3 Aggressive Environments

3.1 Private Swimming Pool

Concrete structures built in humid environments where oxygen and water are present together and in contact with the structure's surface are subject to high deterioration risk. When comparing the comprehensive cost of building and maintaining a concrete structure in such environment over time, the substitution of steel reinforcements with non-corrosive GFRP cages clearly represents a competitive alternative. One example of such structures in risky environments are swimming pools, which contain water and other aggressive substances.

The private swimming pool realized with GFRP reinforcements and concrete (SCC) C35/45 shown in Fig. 5 (model in Fig. 6) was built between 2008 and 2009 in Norway. The construction process using the non-metallic reinforcing cage is the same as with traditional steel reinforcements. The glass fibres in the reinforcements, sensible to alkaline environments, are protected with a polymeric (vinylester) matrix that

Fig. 5. Swiming pool realized with non-metallic reinforcement

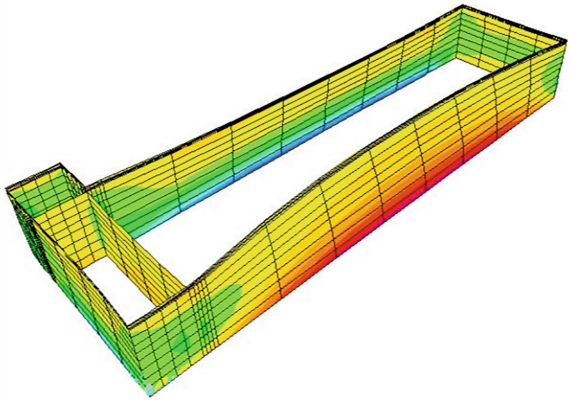

Fig. 6. FEM model

ensures its long term duration. Eliminating the corrosion formation expansive process, the risk of the concrete conglomerate spalling is eliminated Though continuing its carbonation process over time, the reduction in its potential performance is not a risk.

The pool's dimensions where 12,5 m × 3,4 m (see the pool's slab metrics and cage design in Fig. 7). Figure 8 shows a cross section diagram of the GFRP cage. As a whole, the GFRP reinforcing cage was composed of: 3500 m of Glasspree of 12 mm diameter, 800 m of Glasspree stirrups of 8 mm diameter and 2000 m of Glasspree stirrups of 12 mm diameter. Figures 9, 10 show images of the structure under construction.

Using GFRP reinforcements the comprehensive weight of the cage was reduced to 1300 kg, with a reduction in installation costs due to the lightness of the GFRP bars. However the main advantage remains the corrosion-free nature of the GFRP rebars, that enables the construction of the swimming-pool without dealing with protection treatments to the reinforced concrete box against chloride corrosion.

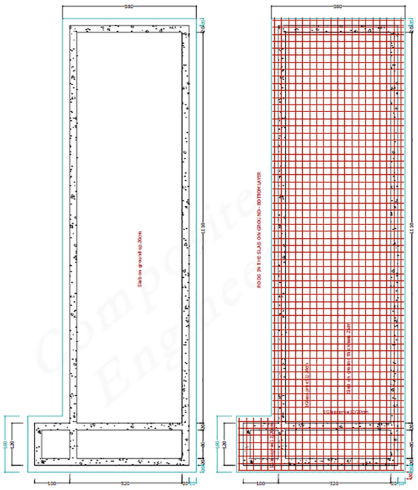

Fig. 7. Design of Glasspree cage for pool's slab

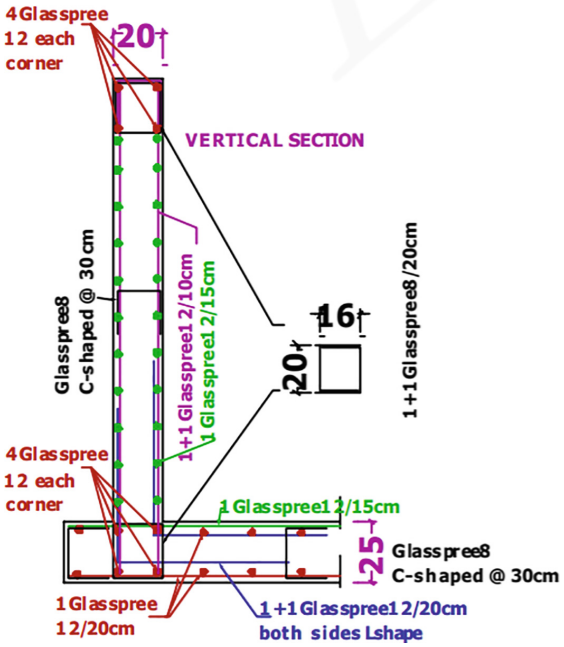

Fig. 8. GFRP cage transversal section detail

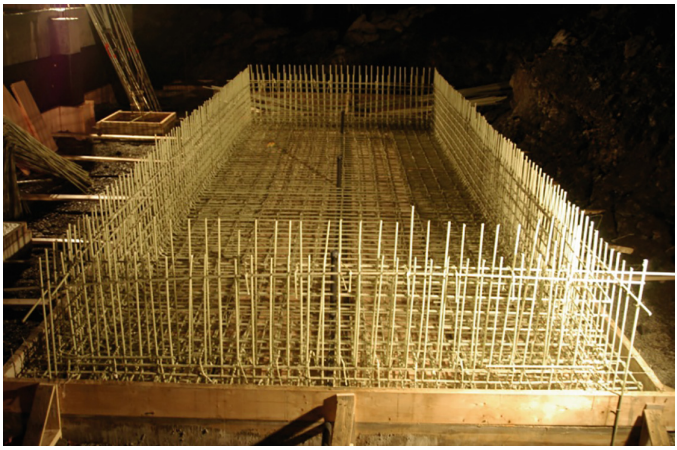

Fig. 9. Pool's GFRP cage

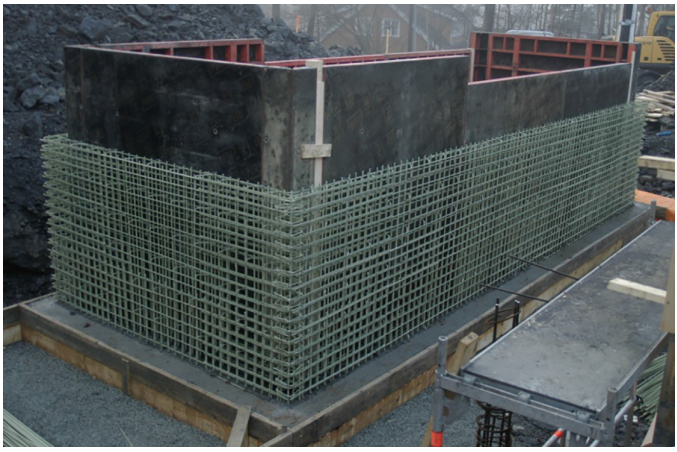

Fig. 10. Pool's side GFRP reinforcements

3.2 Manfredonia's Underwater Harbour Slab

Coastal reinforced concrete structures in contact with sea water are highly vulnerable due to the high levels of chlorides, sulphates, alkaline carbonates, magnesium, and other elements present in the water. The high concentration of chlorides in sea water can significantly deteriorate the reinforcing steel rods, causing a reduction in the sectional area and a detachment of the concrete cover. Salinity, expressed as the number of grams of dissolved salts per litre of water, can reach 35% in Italian marine waters.

For these reasons, permanent non-metallic concrete reinforcements were used in the construction of a submerged concrete slab in 2015 at the Manfredonia port, in the south of Italy. The 40 m long and 6 m wide slab descends from the shoreline down to 5 m under sea level in order to allow for boat docking and storing (Figs. 11, 12). The

structure was designed for supporting the weight of amphibious vehicles hauling up to 60 ton vessels. Concrete had to be casted under salt water.

Partially submerged in salt water and in a shoreline affected by salt corrosion, such structure couldn't be durable if reinforced with steel. In order to make a structure reinforced with steel durable in such environment, expensive protection treatments would have been required, such as anticorrosion coatings, cathodic protection (CP), etc. On the contrary, there are no disadvantages when using GFRP reinforcements. Salt's aggressive action no longer impacts the structure.

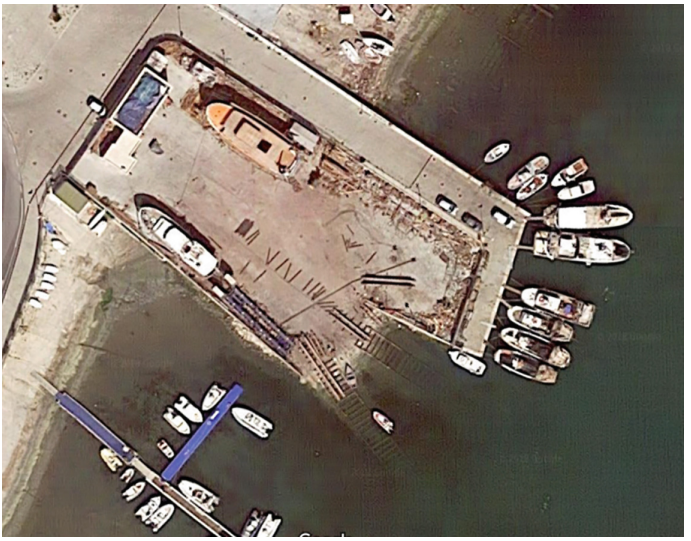

Fig. 11. Aerial view of the Manfredonia Port submerged slab

Fig. 12. GFRP cage installed under sea water. Diver casting concrete on the right side

Fig. 13. Casting of the slab

Moreover, the design process of concrete reinforced structures exposed to an adverse environment usually demands a special prescription: for example, Concrete XS3 class is required due to the presence of sea water chlorides, and consequently an extraordinary concrete cover thickness (45 mm according to EC2) is needed, minimum Rck 45 MPa, etc. Such special requirements are no longer necessary when reinforcing the structure with GFRP rebars. Saving in concrete means saving in CO2 impact.

4 Concrete Structures Close to Railways

4.1 Flooring and Wall Slabs

Corrosion causing stray currents may originate from direct current distribution lines, substations, or street level railway networks, etc., and flow into pipe systems or other steel structures present. Alternating currents may occasionally cause corrosion.

Stray current problems stem from the fundamental design of electrified rail transit systems, whereby current is returned to substations via the running rails. The ground surrounding the rails can be viewed as a parallel conductor to the rails. The magnitude of the stray current flow into the ground conductor will increase as its resistivity decreases. Any metallic structure buried in the ground will tend to "attract" stray currents, as it represents a very low resistance current path.

In order to reduce this "attraction", reinforced concrete structures are designed introducing GFRP rebars in some sections, thus interrupting the continuity in the current path.

Conventionally, protecting steel reinforcements can be achieved by implementing a series of preventive measures during construction. Such measures include the introduction of electrical fields and sacrificial elements.

By replacing steel reinforcements with GFRP rebars all kinds of structures (slabs, walls, sub-structures, etc.) could become electrically not conductive.

Fig. 14. Section of slab reinforced with GFRP cage that splits the steel cage

Fig. 15. GFRP reinforcements in a portion of a concrete wall

Fig. 16. Warehouse slabs reinforced with GFRP near airport

The applications shown in Figs. 14–16 show two concrete flooring slabs and a concrete wall realized between 2014 and 2016 where GFRP rebars were used in specific sections to allow the structure to become electrically non-conductive or to split the continuity of the electric current path.

5 Conclusion

In the last decades, infrastructure designers and owners have understood how a poor durability design affects the usability and value of bridges, railways, costal structures, etc. The concrete repair industry has grown significantly also as consequence of this lack of durability.

As mentioned before, non-metallic concrete reinforcements have attracted the attention of civil engineers in response to the durability issue. As a result, GFRP reinforcements are becoming an alternative solution for the design of concrete structures, particularly for niche and specific applications such as those located in aggressive environments (where chloride and salt water are present) or where corrosion caused by stray currents is a risk. The shared enemy in these cases is the deterioration of the steel reinforcements that reduces the structure's duration.

Though still limited by the lack of industry guidelines and tests (only in 2017 ASTM has published a comprehensive Qualification Matrix for the use of GFRP bars in concrete reinforcing), in the last decade GFRP concrete reinforcements have already been employed in cases where the non-corrosive nature of the material provided an efficient solution to specific challenges faced. In the cases included in this paper, the GFRP bars represent a non-metallic permanent reinforcing solution that does not interfere with electric circuits, is not affected by corrosive elements present in the environment, or provides a mean to reduce the conductivity of stray currents.

In all of these cases, the solution implemented enabled savings in time and costs thanks to the elimination of additional protective treatments. Moreover, the use of non-metallic reinforcements increased the value of the concrete structure: the reduction of repair requirements means longer usability, which in turn decreases the down time of structures and infrastructure and finally minimizes the labour and material required during its design life.

The cases presented provide evidence of the applicability of GFRP reinforcements and open the way for the regulation of its use in the field.

References

American Concrete Institute (2015) Guide for the design and construction of structural concrete reinforced with FRP bars. ACI 440 1R 15

Arduini M, Balconi, G (2017) Special topics in relation to glass fiber cages design. Congrès International del'AFTES, Paris

Arduini M, Corba A et al (2005) Non-metallic reinforcement technique for temporary R/C walls. In: Composites in construction 2005 – third international conference, Lyon, France

ASTM International. Standard specification for solid round glass fiber reinforced polymer bars for concrete reinforcement. ASTM D7957/D7957 M −17

Balconi G, Mandelli C, Natoli E (2014) Glass fiber for underground projects – recent applications. Swiss Tunnel Congress, Luzern. Volume Fachtagung für Untertagbau. ISBN 978-3-033-03920-9

Carvelli W, Fava G, Pisani M (2016) Remarks on bond of GFRP rebars and concrete. Elsevier Online Compos J 93:210–220

Carvelli W, Pisani M, Poggi C (2010) Fatigue behaviour of concrete bridge deck slabs. Elsevier Online Compos J 41:560–567

Carvelli W et al (2009) Anchor system for tension testing of large diameter GFRP bars. J Compos Constr 13:344–349. ASCE/September/October 2009

Consiglio Nazionale delle Ricerche (2006) Recommendations and prejudices in the realm of foundation engineering in Italy: a historical review. In Viggiani C (ed) Geotechnical engineering for the preservation of monuments and historical sites; Proc. Intern. Symp., Napoli, Balkema, Rotterdam, 3–4 October 1996

Consiglio Nazionale delle Ricerche (2006) Guide for the design and construction of concrete structures reinforced with fiber-reinforced polymer bars. CNR-DT 203, 2006

Structures of the Generali Tower in Milano – A Concrete Challenge

Mauro Eugenio Giuliani[1,2(✉)]

[1] Redesco srl Milano, Milan, Italy
me.giuliani@redesco.it
[2] School of Architecture, Urban Planning & Construction Engineering, Politecnico di Milano, Milan, Italy

Abstract. The form of the tower is generated by a variation in the plan of each floor, and by a continuous rotation – greater at the lower levels and decreasing towards the summit – of each storey around the centre. The functionality of the internal spaces demand that the perimeter columns be aligned with the form of the outer shell, thus requiring them to slope, each with a different inclination matching the enveloping curvature. This generates an additional, unusual phenomenon, for the tower equilibrium: the horizontal forces resulting from this angular variation produce a global torque, inducing a warping effect in the core elements. The weight of the building and the vertical loads acting on it generate both vertical and horizontal actions, encircling the core. Choosing concrete as the construction material meant great efficiency but also the need of a complex design in terms of analysis and forecast of non-linear and time dependent effects, geometry control and construction phasing.

Keywords: High rise buildings · Non linear behaviour · High performance concrete · Evolutive analysis · Parametric design

1 Introduction

Citylife spa, a real estate company, launched a large new development in a brownfield in the North-West area of Milano which is composed of many residential and office buildings (http://www.city-life.it/en/), the later ones being constituted of three towers:

- the Allianz, designed by A. Isozaki which has been occupied by the Tenant in December 2017
- the Generali, designed by Z. Hadid, currently being fitted out, that will be in full service in July 2018
- the PWC Tower designed by D. Libeskind already currently under construction, to be completed in 2019.

The three towers are integrated in large green areas, within the residential buildings, designed by the above said architects also, and give the plot a special appeal.

For the Generali tower, with due respect of the functionality and efficiency of the layout and compliance with the other constraints set by the client, the project was addressed by means of an heuristic process, geared towards researching the ideal

M. di Prisco and M. Menegotto (Eds.): ICD 2018, LNCE 42, pp. 219–231, 2020.
https://doi.org/10.1007/978-3-030-23748-6_17

"minimum solution" to a problem with many variables (some fixed, others not), which began with the critical evaluation of the initial architectural concept and continued over the course of its subsequent development (Fig. 1).

Fig. 1. The tower completed

2 The Architectural Form

The form is generated by a variation of each floor plan, and by its rotation around the centre, greater at the lower storeys and decreasing towards the top; because of the functional requirements of the internal spaces, the perimeter columns are aligned with the pattern of the facade, thus requiring them to slope, each with a different inclination

Fig. 2. The concrete structure rising

in order to match the enveloping curvature (Fig. 2); the whole geometry is determined by polynomial functions which define the rotation of the stories around a vertical axis, and the variation of the radii of the curves that define the edges of the floors (Fig. 3).

The tower total height is 185.96 m with an elevation of 170.36 above podium level; a typical floor can be inscribed in a 46.90 by 48.90 rectangle (Fig. 4).

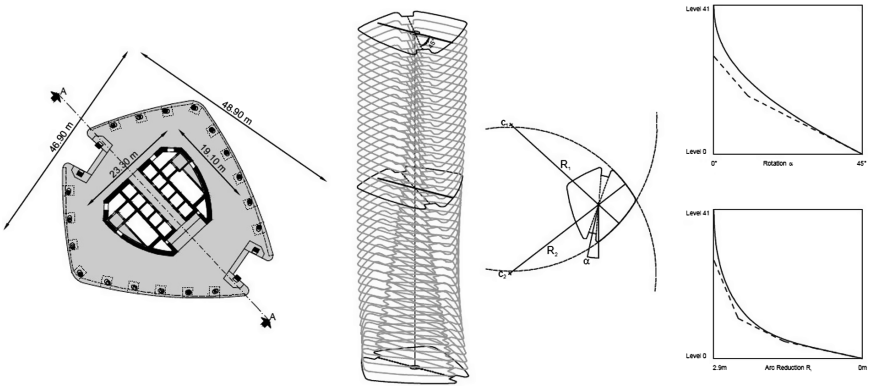

Fig. 3. Parametric definition of the tower's shape

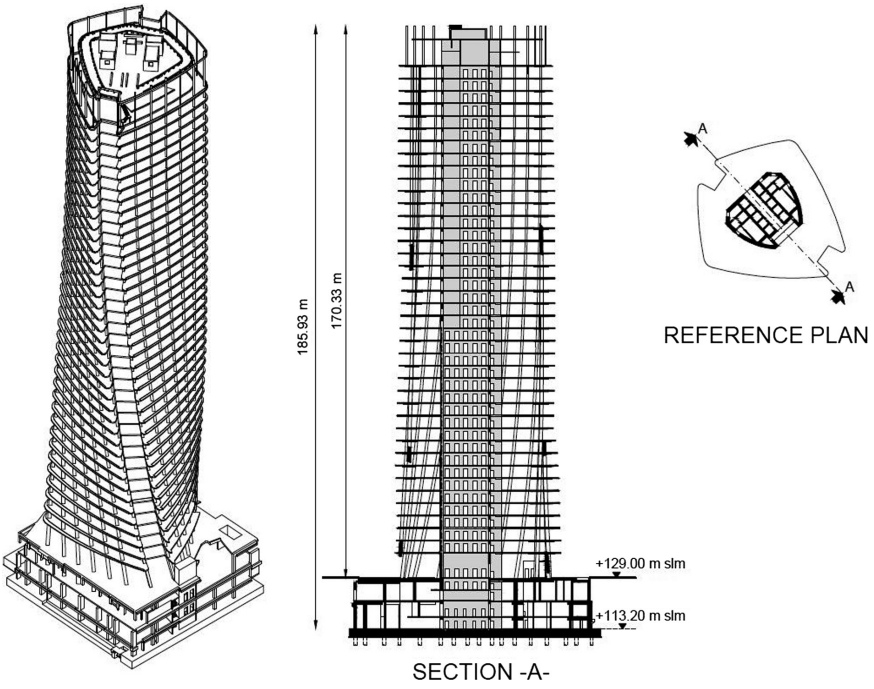

Fig. 4. General shape of the tower structures

3 Sructural Concepts

The most significant features of the structure are summarized in the following:

- the building features a tubular core with dimensions dictated by the architecture on the basis of the requirements for vertical communication;

- the layout of the perimeter columns generates an additional and unusual phenomenon for the tower equilibrium; the orientation change of each axis column at each storey creates horizontal forces necessary for the equilibrium and producing a global warping effect on the core; in other words, the weight of the building generates both vertical and horizontal actions, encircling the core (Fig. 5).

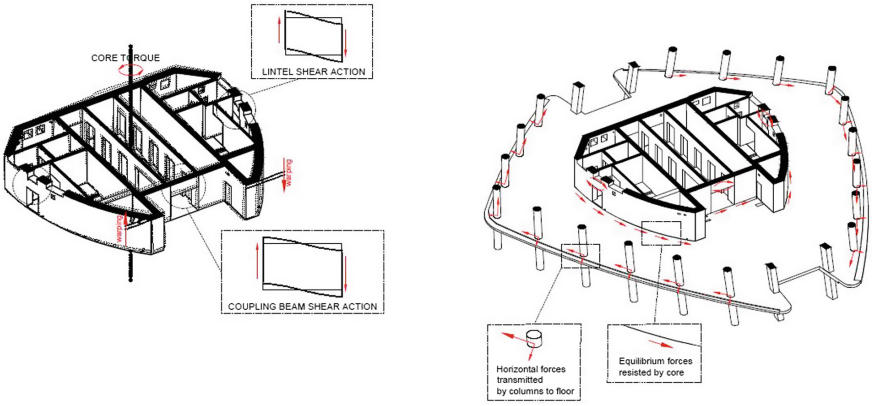

Fig. 5. Torsional effect due to columns layout and distortion in coupling beams and lintels

This conceptually simple functional scheme is effected by integrating and resolving a number of complexities specific to the adopted solution:

- the selection of the reinforced concrete material introduces a high level of non-linearity in the development of the resistant phenomena over time: the material is visco-elastic, and so the deformation and stress evolution during the construction and the subsequent life of the building had to be evaluated by means of iterative, complex analyses and simulations;
- the evaluation of the real stiffness of the parts of the structure, taking account of the effects of cracking, was necessary also;
- because the equilibrium of the structure is based on the interconnection of the core, the columns and the floors, which, at each level, have different relative positions and undergo stress changes during the construction steps, an evolutionary structural analysis had to be implemented;
- the central core includes numerous significant openings towards lift lobbies, fire escapes and services ducts and therefore the ideal torsional resisting scheme is compromised by the interruption of the natural flow of the forces along the walls and therefore the study of specific and unusual structural solutions was mandatory for these positions;
- the extreme compression of the storey heights, yielding a beneficial reduction of the overall height and of the facade surface, without compromising the useable internal surface area, required the reduction of the sections of the door lintels and of the coupling beams between the parts of the core;

- the columns have the greatest inclination on the ground floor while are vertical from foundations to soffit of this storey and this abrupt change in angle, generates horizontal forces equal to the sum of all those generated on the upper floors, but in the opposite direction; the ground floor acts, then, as a strong diaphragm that closes and balances the accumulation of the torsional stress arriving from the part above ground of the tower, driving the stress back to the core;
- floors and columns were resolved with traditional concrete construction solutions.

4 The Structural Elements

4.1 Foundations

A raft with settlement reducing piles was chosen as the most economical and structurally efficient solution. This continuous C32/40 concrete raft, without construction joints, has in plan dimensions of 56.60 m by 54.15 m and a typical constant thickness of 2.50 m; all the 64 piles feature 1.50 m diameter and 36 m length.

4.2 Core

The core is separated into two similar but opposed elements and, because its outer perimeter is open on one side up to the 20th floor (and on both sides from the 20th up), the resistance required the connection of the two halves with beams, to be installed in line with the main outer transversal walls. The stress field acting in the walls, in particular arising from the torsion induced by the inclined columns, creates a distortion of the whole section with the two halves connected (Fig. 5).

It is worth to mention that the state of stress deriving from the vertical loads alone is the predominant one for the beams connecting the core halves and the lintels above the outer walls doors.

4.3 Special Elements of the Core

Up to 20th floor, the beams which couple the two core halves are strong steel elements connected to the walls with post-tensioned bars, while above this level reinforced concrete beams are used.

The lintels in the external walls are made of reinforced concrete with rebar layouts of exceptional geometry, density and diameters.

In both cases, the analysis of the areas where concentrated stresses are introduced into the body of the main walls, constituted one of the most challenging aspects of the project.

Concrete class C 45/55 was specified for the walls, lintels and coupling beams from foundations up to 30th floor and then reduced to C32/40 for the upper levels, but C50/60 was prescribed between ground and second floor.

4.4 Floors

The horizontal floor structures are constituted by solid reinforced-concrete flat slabs with class C32/40; the typical thickness is 32 cm, for spans ranging from around 6 to around 13 m.

The connection between the slabs and the core is ideally hinged, and is designed to allow for the transmission of the in plane stresses, avoiding radial bending moments along the support line while the "annular" form generates non-zero out of plane circumferential actions.

This connection yielded improved structural response and an economy of construction; the main advantages are:

- reduced sensitivity of the floor structures to differential settlement between columns and core;
- constructive simplification of the detail (which can be achieved in general with standard rebar loop boxes or sleeves where necessary);
- separation of the core and the floor construction phases.

Concrete confining rebar were added around the column foot prints for resisting the high local compression stresses.

4.5 Columns

The columns of the external crown of the tower are circular, and the relevant diameter vary from a maximum of 110 cm on the basement floors to a minimum of 50 cm at the summit of the tower, with a scaled variation from one homogenous group of storeys to another.

The rectangular columns of the "cuts" zones of the floors vary from maximum dimensions of 120 by 80 cm on level 0 to a minimum of 75 by 50 cm at the top of the tower.

High resistance and high performance concretes were used for the columns: C60/75 from foundations to soffit of level 21, C50/60 up to the soffit of level 30, C45/55 for the upper levels.

The rebar density is very high, coming close to the limit values specified in the Codes.

4.6 Ground-Floor Slab

This special floor, which serves to "straighten out" the columns, absorbing all of the horizontal forces at the point in which they shift from vertical to inclined, has a thickness of 50 cm, with drop panel areas 90 cm deep adjacent to the core and at the crown of columns; the concrete class is C45/55.

5 Structural Analysis and Verifications in an Evolutive Scenario

Predicting the structural behaviour of each element of the tower, given the specific complexity of the spatial arrangement of the resisting phenomenon, needed to follow a rigorous and sophisticated approach.

The choice of concrete as the structural material has been consciously taken by the Structural Engineer, and led to great advantages in terms of economy, functionality (no drop beams allowed for very compact inter-storey heights while leaving complete freedom to the MEP systems), speed of construction and fire resistance. On the other hand, cracking, shrinkage and creep phenomena introduce a higher level of complexity.

Keeping in mind serviceability needs, one of the most challenging feats has been to exactly fix the limits of deformations that the non-structural elements had to accept: namely the facade – dimension of the stack joints-, the elevator systems and the internal finishing as partition walls, plaster panels etc.

The goal was to give exact values with limited contingency, in order to allow for both economic and aesthetically sound architectural solutions: small stack joints, limited gaps in internal elements etc.

From a modelling/analysis point of view, the approach has been based on a best/worst scenario strategy, aimed to reduce the uncertainty space in the definition of each investigated quantity. Summarizing in the shortest possible way, the following are some of the most significant methods and tools put in place:

- "stiff" models vs "soft" models: results regarding resistance request were obtained by models that incorporated the stiffer configurations, meaning with that concrete and structure/soil interactions were modelled taking into account short term characteristics, reduced cracking and dynamic modulus in seismic and wind response; on the other side, deformation results were obtained with models that took into account greater cracking, long-term characteristics and so on; this led to a complex matrix of analyses configurations amounting to a total of 32 different models, combined then with the relevant load cases and combinations, whose results were used for subsequent verifications of structural elements;
- prior to this, a preliminary assessment of possible areas of cracking and general stress patterns, needed for the evaluation of the modelling parameters, has been carried on;
- evolutionary analyses: in parallel with the elastic/instantaneous analyses, the tower was subject to a series of stage analyses, taking into account the prescribed construction steps and the creep evolution of the concrete; a preliminary simplified study, based on manually-implemented spreadsheet calculations, was carried on in order to validate the subsequent full 3D finite element non-linear step-by-step analyses. In terms of creep laws taken into consideration, a comparison between *CEB-FIP 1990* formulation, *Eurocode* and *FIB Structural Concrete Bulletin 51* and *Constitutive modelling of high strength concrete Bulletin 42* has been carried on, and finally the FIB formulation was used.

- detailed modelling of highly reinforced columns and elements: in all evolutive analyses, it is fundamental to model correctly the build-up of the columns by separating the steel and the concrete as parallel elements; the same applies to other special elements as specific lintels where the effect of important quantities of steel are significantly affecting the long term behaviour;
- reinforcement dimensioning and verification of the core according to a shell-plate model; wall type elements or simple plain stress sections are not reliable nor prone to give optimized rebar layouts in the core walls; we have proven that a plate-shell approach, meaning a verification that combines in-plane and bending stresses is the best method to dimension and verify core walls; the calculations were made by means of in-house software that implements the MUD (Most Unfavourable Direction) method;
- local solid and strut-and-tie models for special elements: stress concentration areas and special elements as coupling beams or the connecting area between ground floor slab and core walls have been studied with the aid of specific continuous modelling and/or strut-and-tie schemes, where local plasticization and step-by-step evolutionary non-linear effects have been introduced if needed.

6 Control and Development of the Structural Form

The structural morphology was developed in successive steps which are summarized in the following:

- parametric modelling phase: on the basis of the principles of the parametric geometry set out by the architect, three-dimensional models were generated to extract the computational models and the first structural geometries.
- 3D-design phase: from the initial phases, the design of the structures was developed by using advanced 3-D design programs, with particular reference to the specific reinforcement zones, where the spatial representation constitutes the only tool that makes it possible to verify real feasibility and the lack of interference in the critical nodes of the structure. These same models were used for extensive structural analysis following a worst/best case scenario philosophy, taking into account all nonlinear effects. Verifications of structural elements was performed by proprietary methods and software, and local detailed solid modelling was used for special elements and critical nodes.
- drafting of the working plans good for tender: the 3-D models were used to create 2-D print-outs; the BIM functions integrated into the model allowed for the exact computation of the rebar and of the volumes and surfaces of the concrete.
- parametric design of reinforcement: the extreme variability of the structural elements (e.g. on every one of the 44 floors there are 22 columns with different inclinations, and floors are different at each level) required the invention of a design method that would allow the direct transfer of the computational and geometric information to the construction drawings, including the exact rebar specification and the associated assembly geometry. This result was achieved through the implementation of appropriate parametric procedures based on spreadsheets and graphic algorithms, right up to the final transfer of the information onto drawings for use on the construction site.

7 Construction

Construction was planned in every detailed in order to achieve a fast and safe erection, getting to a productivity of one floor per week after initial warm-up and tuning of the system and sequences.

- As per design specifications, the foundation was cast without interruptions thus pouring 7660 m^3 of concrete in around 30 h; a special mix was specified for limiting to 70 °C the hydration temperature inside the mass.
- The core was erected in two halves by using a climbing slip form, and keeping the advancing of the core construction up to 3 storeys above the last executed floor.
- The reinforcement of the core was designed and produced as an assembly of pre-fabricated cages to be assembled in a dedicated yard at ground level before hoisting, this reducing to a minimum the manual work of rebar placement on the advancing core.
- Formwork for the floor plates was an industrialized modular panel system (Peri Skydeck) with side transition tailor made areas at both the external and internal edges to allow for the changing of the shape of each floor.
- Columns were cast in steel forms which were anchored to the lower floor with adjustable length struts allowing for the correct positioning in the space of the column top.

8 Monitoring Geometry and Stresses

A complete set of monitoring procedures was established during erection.

The first set of parameters to be monitored are related to geometry, both during construction and after structure completion. The general concept of erection, in terms of compensation of differential column shortening and horizontal movements, was to follow the classical "*up to*" approach: each floor and each column reference points for formwork were set in the theoretical position, which means perfectly according to the general 3D model. This means that:

- vertically, all levels were set at the theoretical value with respect to the upper face of the foundation raft;
- horizontally, all points were set at the theoretical position with respect to the global reference grid.

In this way, all deformations occurred "up to" the day of pouring the concrete of a specific level of the tower were automatically compensated, while all subsequent elastic and non-elastic deformations due to the growth of the structure above and time-dependent effects were not.

Field measurements were put in place and periodically recorded in order to compare the real evolution of the geometry with the calculation results. A combination of traditional topographic readings and laser-scanning systems were used, in order to ensure an adequate level of redundancy in the data acquisition. Main parameters that have been – and still are – recorded are:

- vertical settlement of raft foundation, both centrally and at lateral and intermediate points;
- vertical settlement of slab edges and columns, in a number of points every 5 floors;
- horizontal movements of slab edges and column axis, in a number of points every 5 floors;
- horizontal movements of core walls in 4 points every 5 floors.

In general, comparing results with predicted values showed a very good correspondence with the calculation results was confirmed and no compensation action had to be taken during construction. As an example, the comparison between predicted and registered horizontal movements of column axis at level 20 – after 8 months from casting of the floor - is shown (Fig. 6).

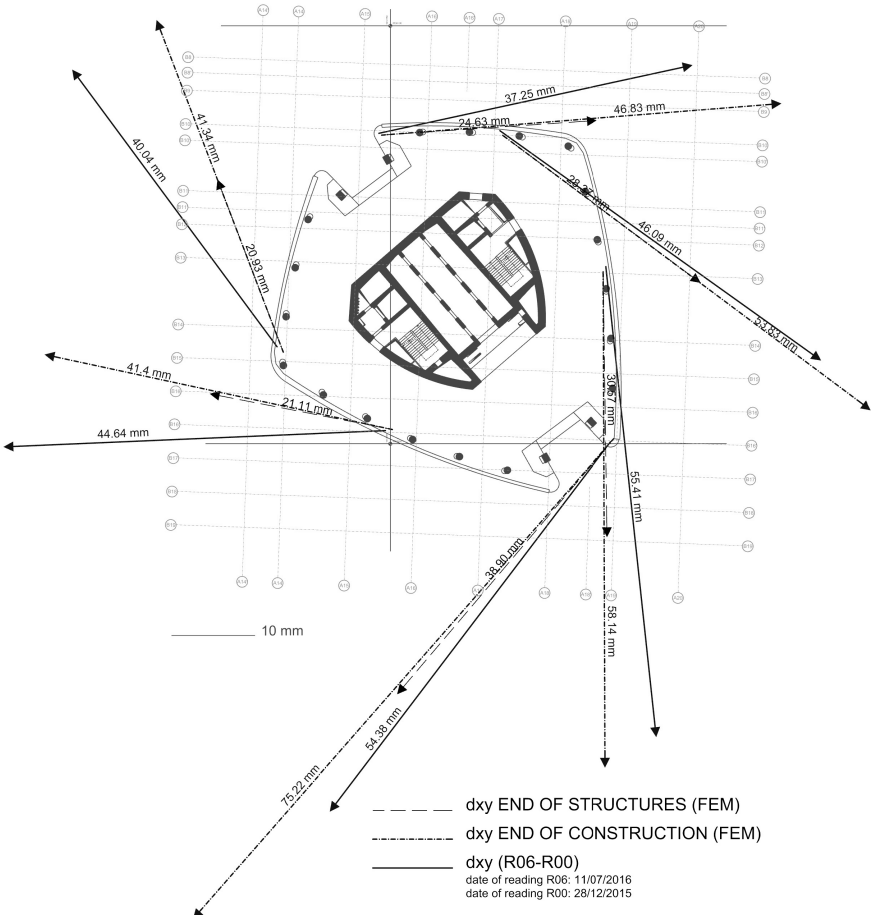

Fig. 6. Recorded vs predicted horizontal movements at level 20, 8 months after casting of the floor

Another set of parameters that has been monitored is related to stresses into structural elements. A mixed system of strain gauges and load cells has been used. In summary, the main quantities that have been monitored were the following:

- stress evolution into pile reinforcement bars;
- pressure at the interface between pile heads and raft;
- pressure at the interface between raft and soil;
- stress evolution into column reinforcement bars.

Also in this case, the correspondence with calculated parameters was extremely good, albeit in some cases the data were lost due to instruments malfunctions.

Finally, dynamic behaviour of the structure, once completed, has been checked in terms of main vibration modes by implementing a recording of acceleration and movements generated by environmental back noise and a subsequent and back-analysis. Main vibrating modes were confirmed both in directions and frequencies, with a 10–15% difference of the latter with respect to the calculated ones – as often is the case, the recorded values showed a slightly stiffer behaviour of the structure.

Table 1. Main data of the construction

Number of floors			44
Height from top of foundation			185,93 m
Inter-storey height			3,84 m
Concrete volume			
Core	Slabs	Columns	Total
19 331 m^3	29 010 m^3	3 055 m^3	51 396 m^3
Rebar weight			
Core	Slabs	Columns	Total
3 806 650 kg	4 551 580 kg	1 330 850 kg	9 689 080 kg

Table 2. Calculated horizontal deflections expressed byb the RSQ of orthogonal components (confirmed at date by surveys)

Time \ Floor	20^{th}	36^{th}	top
End of construction	130 mm	80 mm	10 mm
80 years after	220 mm	175 mm	90 mm
For comparison, max wind induced deflection at top:			
120 mm			

9 Conclusions

From early concept working with the Architect down to detailed design and construction documents, including all rebar lists, as-built details, construction methods and monitoring, the contribution of Structural Engineering to the success of the tower, which is now an icon in Milan's cityscape, has proven fundamental. Concrete as the construction material for high-rise buildings of these dimensions remains the most efficient choice, and can be used also in the frame of non-canonical shapes, provided that a great effort and proficiency is put in place in terms of careful design and specific engineering methods and tools. The responsibility of the Structural Engineer is greater, due to the greater complexity an potential uncertainty of the structural phenomena, but a considerable amount of experience and useful data can be obtained and contributes to the build-up of the common knowledge of Concrete as a material for the present and the future.

10 Credits

Client	City Life spa – Milano
Architect	Zaha Hadid Architects London
Structural Design	M. E. Giuliani Redesco, Milano
Executive Architect:	Planimetro, Milano
Tenant	Generali spa, Trieste
General Contractor and BIM Coordinator	CMB, Carpi

Materials and Investigations

Characterization of Fabric Reinforced Cementitious Matrix (FRCM) Composites for Structural Retrofitting

F. G. Carozzi[1], T. D'Antino[1(✉)], A. Gatti[2], G. Mantegazza[2], and C. Poggi[1]

[1] Department of Architecture, Built environment and Construction engineering ABC, Politecnico di Milano Piazza Leonardo da Vinci 32, 20133 Milan, Italy
tommaso.dantino@polimi.it
[2] Ruredil s.p.a., Via Buozzi,1, 20097 San Donato Milanese, Italy

Abstract. Fabric Reinforced Cementitious Matrix (FRCM) composites are inorganic-matrix innovative materials often particularly suited for strengthening of masonry and concrete structures. These materials are composed of a dry grid of fibers (i.e. an open-mesh textile) embedded in an inorganic-matrix enriched with short fibers. In this paper, some mechanical tests proposed for the mechanical characterization of FRCM composites are presented and discussed. Initially, the mechanical properties of the components (matrix and dry fibers) are described. Then, tensile, debonding, and pull-out test set-ups are presented. Tensile tests are employed to obtain the FRCM stress-strain behavior and identify the main mechanical properties, whereas bond tests (debonding and pull-out) are used to evaluate the failure mode and study the bond behavior of the FRCM composite. The results of some of these experimental tests are necessary to obtain a complete assessment of the FRCM composite in accordance with the current Italian guidelines.

Keywords: Fabric reinforced cementitious matrix · Mechanical characterization · Strengthening

1 Introduction

Fabric Reinforced Cementitious Matrix (FRCM) composites are composite materials composed of an open-mesh dry-fiber textile impregnated with an inorganic matrix. The fibers are disposed in yarns to compose grids with various geometries and weights. The more commonly employed fiber types are carbon, glass, steel, and PBO (polyparaphenylene benzobisoxazole). FRCM composites are particularly indicated for strengthening of masonry members due to their compatibility with the substrate and vapor permeability. In addition, FRCM showed good durability to external agents.

To design an FRCM structural reinforcement, both the mechanical characteristics of the FRCM composite and the bond properties with respect to the specific substrate shall be known. Therefore, each system needs to be tested and assessed by an initial-type testing procedure that should be specified by guidelines or recommendations.

M. di Prisco and M. Menegotto (Eds.): ICD 2018, LNCE 42, pp. 235–247, 2020.
https://doi.org/10.1007/978-3-030-23748-6_18

The mechanical properties may be determined by appropriate experiments on an adequate number of specimens made with the same components and manufacturing techniques. In the literature, several experimental researches are available [Contamine et al. 2011], [Sneed et al. 2015], [Askouni et al. 2017], [Carloni et al. 2017]. The properties of different FRCM composites were deeply investigated and various test set-ups were developed [De Santis et al. 2017]. Several issues were detected, e.g. large variability of the experimental results, influence of the testing set-up, instrumentation, sample preparation, and curing.

The American AC434 [AC434 2011] and the ACI 549 [ACI 549 2013] provide indication the acceptance and design procedures of these materials, respectively. In Italy, a guideline for the initial-type testing of FRCM composites was recently approved. This document describes a series of experimental tests needed to obtain the tensile and bond properties of the FRCM system. In this paper, an overview of different experimental tests performed by the authors on various FRCM systems is described. The results obtained are presented discussing the main information provided by each type of test. Some of these tests are recommended by the recently release Italian guideline on FRCM composites.

2 Mechanical Behavior of FRCM Composites

2.1 Mechanical Behavior in Tension

The typical stress-strain curve of an FRCM sample subjected to tension employing the so-called clamping-grip method [D'Antino and Papanicolaou 2018] was observed to be tri-linear. Details of this test set-up are provided in Sect. 4.1. The first phase represents the uncracked state, where the slope of stress–strain curve is mainly associated with the stiffness of the matrix. The second phase is characterized by the formation of matrix cracks. In this phase, there is a significant decrease of the stiffness and the stress-strain behavior depends on the number of cracks and on the bond between textile and matrix. In some cases, this phase is limited or with a negative slope [Leone et al. 2017]. In the third phase, the matrix is fully cracked and the applied load is mainly borne by the fiber textile. For this reason, the slope of the stress-strain curve should be similar to the elastic modulus of the dry fiber textile.

In Fig. 1, a typical tri-linear stress-strain curve, where the stress is determined dividing the applied load by the cross-sectional area of the fibers, is represented. Points T_1 and T_2 indicate the slope change of the stress–strain curve and represent the end of the first and second phase, respectively. The main parameters provided by the FRCM tensile test using the clamping-grip method are:

- Tensile stresses and strains in the transition point between two subsequent phases (point T_1 and T_2).
- Slope of the stress–strain curve in the three phases, E_1, E_2, and E_3.
- Ultimate tensile stress and strain, σ_u and ε_u, respectively.

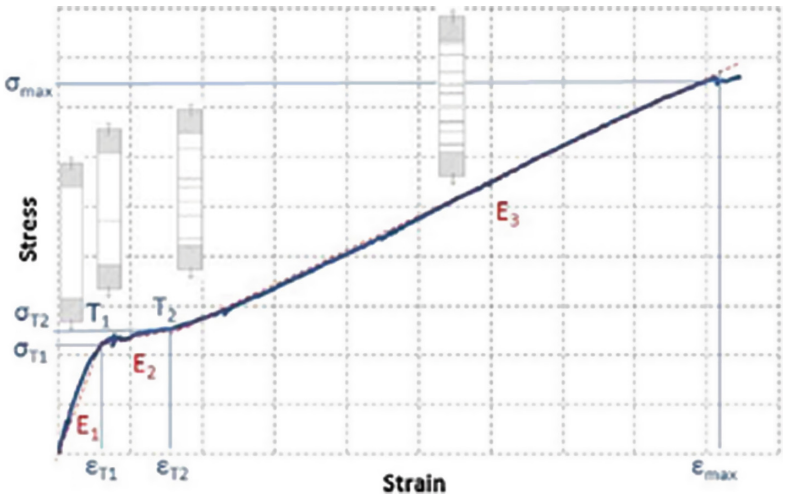

Fig. 1. Typical stress-strain behavior of FRCM in tension [Carozzi and Poggi 2015].

The tensile stress in the first phase can be calculated dividing the applied load by the mortar cross-sectional area to compare the FRCM cracking stress obtained with the tensile strength of the matrix.

2.2 Bond Properties of FRCM Composites

Extensive experimental work was performed to study the bond properties of FRCM composites applied on masonry and concrete substrates [de Felice et al. 2014], [D'Antino et al. 2014], [Carozzi et al. 2017], [Caggegi et al. 2017]. The bond behavior and failure modes observed can be different due to the properties of the mortar, textile geometry, and bond between mortar and textile. A common failure mode when a single layer of textile is employed, is debonding at the matrix-fiber interface with slippage of the textile and, sometimes, mortar cracking. In other cases, a complete detachment of the upper layer of mortar (usually referred to as matrix delamination, [Focacci et al. 2017]) was observed. When the textile presents relatively low mechanical properties (e.g. glass and basalt fibers), failure usually occurs due to textile rupture.

In [D'Antino et al. 2014] and [Carozzi et al. 2016], an idealized stress-slip response associated to matrix-textile debonding, which is represented Fig. 2, was described and discussed. The stress is computed considering the cross-sectional area of the fibers, while the slip between the textile and the substrate is measured. Initially, the applied stress increases linearly up to $\sigma_{A.}$ After that, micro-cracking occurs at the matrix-textile interface and the stress increases non-linearly until the stress value associated with the onset of debonding (σ_{deb}) is reached. For relatively long bonded lengths, the applied stress further increases up to the peak stress, σ^*, due to the presence of friction between fiber filaments and between matrix and fibers. When the fibers are completely debonded from the matrix, the presence of friction is responsible for a residual applied stress, σ_f [D'Antino et al. 2014].

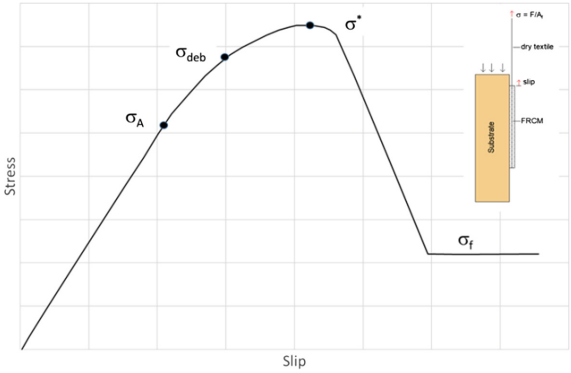

Fig. 2. Idealized stress-slip behavior.

3 Mechanical Characterization of Textile Reinforcement

The textiles used in FRCM materials are open-mesh textiles in which the yarns are composed of a variable number of filaments that could be dry (bare) or impregnated/coated with a polymer matrix. The textiles may present different geometries and weavings. In this paper, certain PBO and carbon (C) fiber textiles are analyzed. The PBO1 textile is an unbalanced grid made of 10 mm and 20 mm spaced yarns, in weft and warp directions, respectively. The cross-sectional area of each yarn in the warp direction is equal to 0.46 mm^2. The PBO2 textile is a balanced fabric made of 12 mm spaced yarns with a cross-sectional area equal to 0.2 mm^2 each. The PBO3 is a unidirectional textile composed of 10 mm spaced yarns with a cross-sectional area of 0.45 mm^2. The carbon textile is a balanced net with yarns spaced at 10 mm on center and a cross-section area of 0.47 mm^2 each.

Tensile tests were performed on dry yarns extracted from the textiles in the warp direction, using a testing machine with a capacity of 2 kN and an extensometer with a gauge length of 25 mm. The experimental results are described in detail in [Carozzi and Poggi 2015] and are briefly recalled in Table 1. The failure mode was characterized by the subsequent rupture of fiber filaments. The values of the elastic modulus present a high variability due to the difficulties in the application of the extensometer and to the particular failure mode.

Table 1. Mechanical properties of dry yarns

Material	Number of tests	Tensile strength		Elastic modulus	
		[MPa]	CoV [%]	[GPa]	CoV [%]
PBO1	7	3845	3.5	215.9	20.8
PBO2	3	3175	2.4	–	–
PBO3	4	3743	9.2	208.1	13.7
Carbon	3	1944	14.9	203.0	9.8

4 Test Methods for the Characterization of FRCM Composites

4.1 Tensile Tests – Test Set-up

The tensile behavior of FRCM samples is influenced by several factors: the test set-up, strain measurement technique, and specimen geometry and fabrication. In the literature, different test set-ups and gripping methods were studied [Contamine et al. 2011], [Zhu et al. 2011], [Hartig et al. 2012], [D'Antino and Papanicolaou 2018]. In [Arboleda et al. 2016] a comparison between two widely diffused test set-ups, namely the clevis-grip and the clamping-grip methods, are analyzed and the mechanical response of the tests is compared. The clamping-grip allows for obtaining the textile tensile rupture, with a trilinear stress-strain curve similar to that depicted in Fig. 1. The use of the clevis-grip method allows for observing the possible slippage between textile and matrix.

The tests described in this paper were performed adopting the clamping-grip method, according to [De Santis et al. 2017]. The two ends of the specimen were fixed into the grips of the testing machine; thus, a compressive stress was applied to the ends of the sample. At these ends, fiber-reinforced tabs were glued to the sample in order to obtain a homogeneous stress distribution and avoid compressive failure of the matrix.

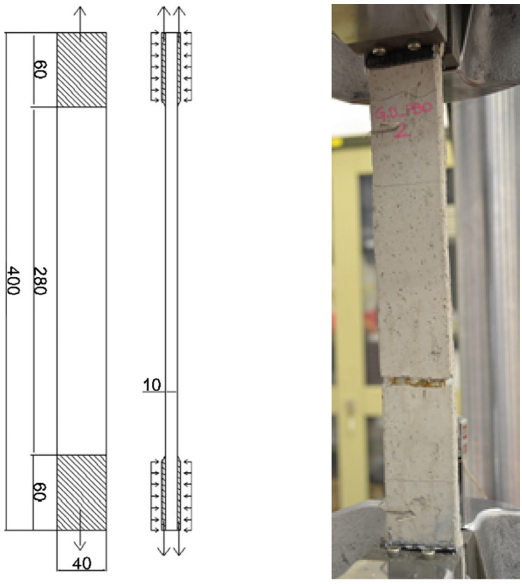

a. b.

Fig. 3. (a) Sketch of the sample and (b) test set-up for tensile tests on FRCM composites [Carozzi and Poggi 2015].

The samples were composed of two layers of mortar (5 + 5 mm) and one layer of textile located between them. The nominal dimensions were 400 × 40 × 10 mm. During the preparation and curing phases, it is important to pay attention to the planarity of the sample and to the possibility that micro-cracks develop due to a non-homogeneous shrinkage.

A testing machine with load capacity of 100 kN was used in displacement control at a rate of 0.1 mm/min in the first phase. After the cracking, the displacement rate was increased to 0.5 mm/min.

An extensometer with a gauge length equal to 200 mm was used to record the strain during the test. In Fig. 3, a sketch of the sample and the test set-up are shown.

4.2 Tensile Tests – Experimental Results

In this section, the results performed on FRCM composites with PBO1 and carbon textiles are reported. In [Carozzi and Poggi 2015] and [Caggegi et al. 2017], a detailed description of tensile tests performed on different types of PBO and carbon FRCM samples is reported, respectively.

For PBO1-FRCM systems, 23 samples were tested, while for C-FRCM 10 samples were tested. In Table 2, the average results and corresponding coefficients of variation obtained are reported. The stress was computed with respect to the fiber cross-sectional area. For PBO1-FRCM samples, the ultimate stress and the slope of the third phase are comparable with the mechanical properties of the dry textile (see Table 1). Moreover, if the mechanical properties of the first phase are computed with respect to the cross-sectional area of the mortar, the stress reached at the end of the first phase is equal to 3.65 MPa and the elastic modulus is 4.84 GPa. These values are comparable to the mechanical properties of the matrix.

Table 2. Experimental results

System		E_1	E_2	E_3	σ_{T1}	σ_{T2}	σ_u
		[GPa]			[MPa]		
PBO1-FRCM	Average	1181	76	216	892	1099	3316
	CoV [%]	19	33	9	15	13	14
C-FRCM	Average	1102	68	186	482	619	1492
	CoV [%]	17	28	22	21	19	19

C-FRCM samples present an average ultimate stress and slope of the third phase lower than the tensile strength and elastic modulus of the dry carbon textile, respectively. This is probably due to slippage phenomena developed between the internal filaments of the yarns. Also for C-FRCM samples, the mechanical properties of the first phase computed with respect to the cross-sectional area of the matrix (stress at first cracking and elastic modulus of 2.02 MPa and 4.96 GPa, respectively) are comparable to the mechanical properties of the mortar.

The stress-strain curves of PBO1-FRCM and C-FRCM samples are reported in Figs. 4 and 5, respectively. The curves resemble the typical tri-linear behavior described in Fig. 1. The results show a large variability, in particular for the stress and strain values reached at the transition points T_1 and T_2. This phenomenon in mainly caused by the non-constant dimensions of the mortar cross-section (the stress are

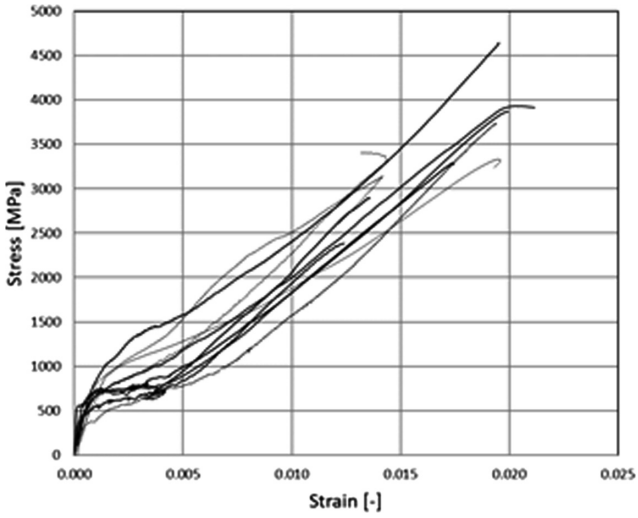

Fig. 4. Stress-strain behavior, PBO1-FRCM samples [Carozzi and Poggi 2015].

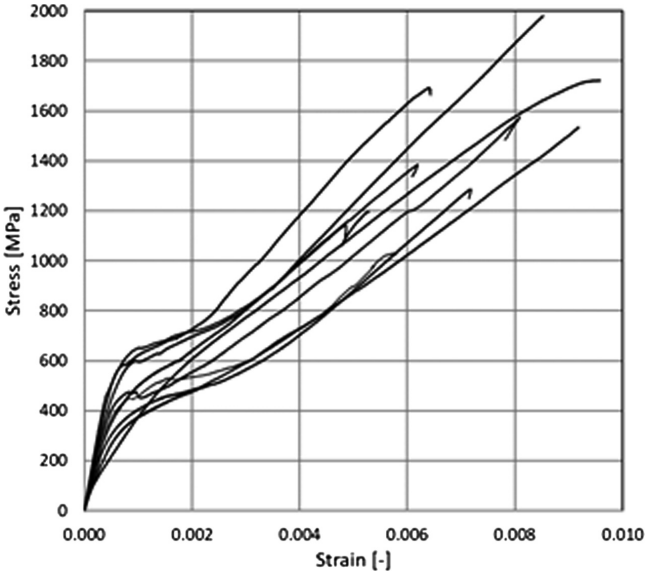

Fig. 5. Stress-strain behavior, C-FRCM samples [Carozzi and Poggi 2015].

computed with respect of the fiber cross-sectional area), non-perfect planarity of the samples or irregular position of the textile in the thickness, and by the presence of mortar micro-cracks invisible to the naked eye.

4.3 Direct-Shear Bond Tests – Test Set-up

Direct-shear bond tests are performed on samples composed by a substrate (masonry or concrete block) onto which the reinforcement, which can have different bonded lengths and widths, is applied. A portion of textile is left bare and at the end of this strip two tabs are applied and inserted into the grips of the testing machine. In the literature, different test set-ups were proposed, mainly single-lap [de Felice et al. 2013] and double-lap [D'Ambrisi et al. 2012].

The tests described in this paper were performed with a single-lap test set-up; the PBO1-FRCM system was applied on concrete blocks whereas the C-FRCM was applied on masonry elements.

The PBO1-FRCM was applied on concrete blocks with dimensions of 125 × 125 × 375 mm. The FRCM composite strips had bonded length and width of 330 mm and 60 mm, respectively. The concrete block was restrained against movement by a steel frame bolted to the testing machine base, whereas the bare textile was pulled. Two LVDTs were applied on the concrete surface close to the edge of the composite bonded region. The LVDTs reacted off of a thin aluminum plate that was attached to a PBO transversal fiber bundle at the loaded end. The test set-up employed is showed in Fig. 6.

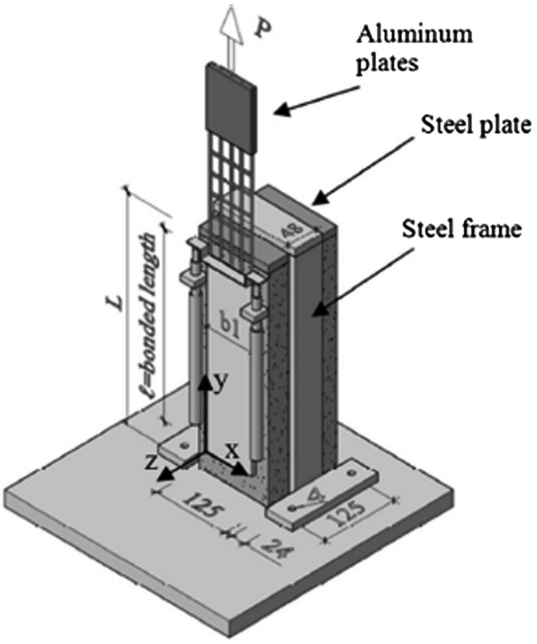

Fig. 6. Direct-shear test: test set-up [D'Antino et al. 2014].

The C-FRCM composite was applied onto a masonry substrate with dimensions of 250 × 120 × 315 mm. The C-FRCM was applied on one of the two largest faces with a bonded length of 260 mm and a bonded width of 100 mm. Two tabs were applied to the free end of the textile and were inserted into bolted steel plates connected with a spherical joint to the testing machine. Two LVDTs were used to measure the slippage between the textile and the substrate.

4.4 Direct Shear Bond Tests – Experimental Results

The results of the tests on PBO1-FRCM samples reported in this paper are part of a wide experimental campaign reported in [D'Antino et al. 2014]. In this section, only tests with a bonded length equal to 330 mm and 450 mm are described.

The failure mode was characterized by slippage at matrix-fiber interface. The average maximum stress obtained by six tests with bonded length equal to 330 mm was 2043 MPa, with a coefficient of variation equal to 6% (Fig. 7).

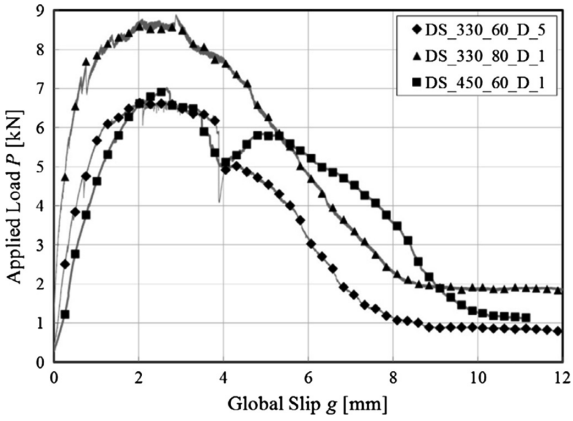

Fig. 7. Applied load-global slip curves for PBO1-FRCM [D'Antino et al. 2014].

In the applied load-global slip curves obtained are reported, where the global slip is the slip measured at the specimen loaded end (i.e. at the end of the bonded length). It is possible to note a first elastic phase, after which the stress increases non-linearly up to the peak load. After the decreasing phase, the applied load becomes constant due to the presence of friction at the matrix-fiber interface.

The results of the tests performed on C-FRCM samples are part of an extensive experimental round-robin test campaign. In this paragraph, the results obtained by the research group of Politecnico di Milano are described [Carozzi et al. 2017]. The failure mode was characterized by textile slippage and rupture of the textile near the loaded end of the bonded area. Five tests were performed: the average maximum stress was equal to 1016 MPa, with a coefficient of variation of 11%. The average slip recorded at the peak load was equal to 0.9 mm. In Fig. 8, the stress-slip curves obtained on the C-FRCM composite are plotted (in red the tests performed by the authors). The behavior is similar to the one described in Fig. 2, even if the friction phase was not observed due to the rupture of the fibers.

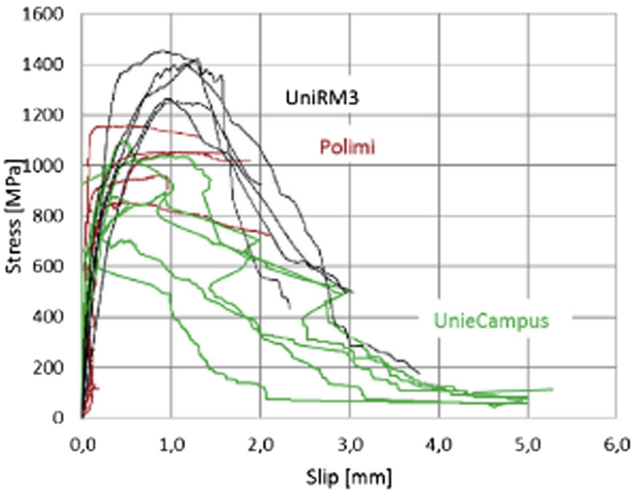

Fig. 8. Stress-slip curves for C-FRCM samples [Carozzi et al. 2017].

4.5 Pull-Out Tests – Test Set-up

Provided that the failure mode obtained by direct-shear tests is debonding at the matrix-fiber interface, the shear tests could be substituted by pull-out tests [D'Antino et al. 2017]. The pull-out test set-up allows for studying the bond properties between textile and matrix. The specimens are light, easy to handle, and could be cast in situ for quality control assessment purposes. The samples presented in this paper were composed of two layers of mortar (330 × 60 × 4 mm each) and one layer of embedded textile. Part of the textile was left bare and two tabs were glued at its end and inserted in the grips of the testing machine. Two metal plate were bonded to the surface of the matrix prism with an epoxy resin and connected with a spherical joint to the testing machine (Fig. 9).

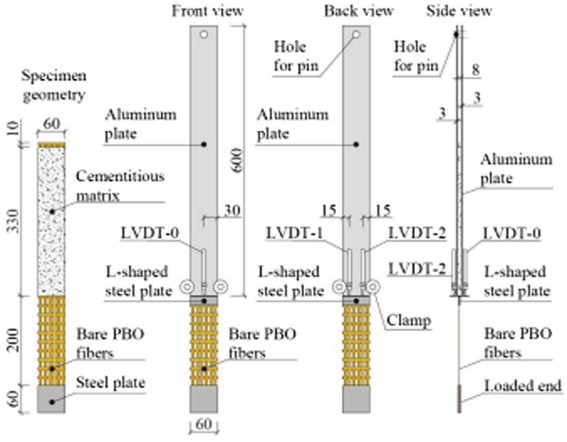

Fig. 9. Pull-out test set-up [D'Antino et al. 2017].

Three LVDTs attached to the aluminum plate were used to measure the slip of the textile with respect to the plates. The tests were performed in displacement control by constantly increasing the slip measured by LVDT-0 (Fig. 9) at a rate of 0.00084 mm/s.

4.6 Pull-Out Tests – Experimental Results

Four tests were performed on PBO1-FRCM samples. The failure mode was characterized by debonding of the textile with a significant slippage (Fig. 10). The maximum stress obtained by 4 specimens was equal to 1642 MPa, with a coefficient of variation (CoV) equal to 5.3%. The slip associated with the peak load was 2.2 mm, with a CoV equal to 9.8%.

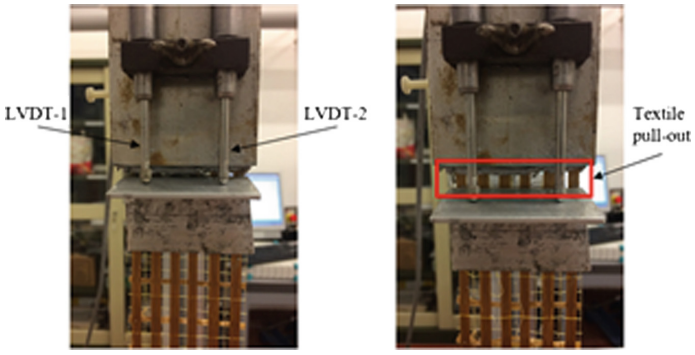

Fig. 10. Pull-out failure mode [D'Antino et al. 2017].

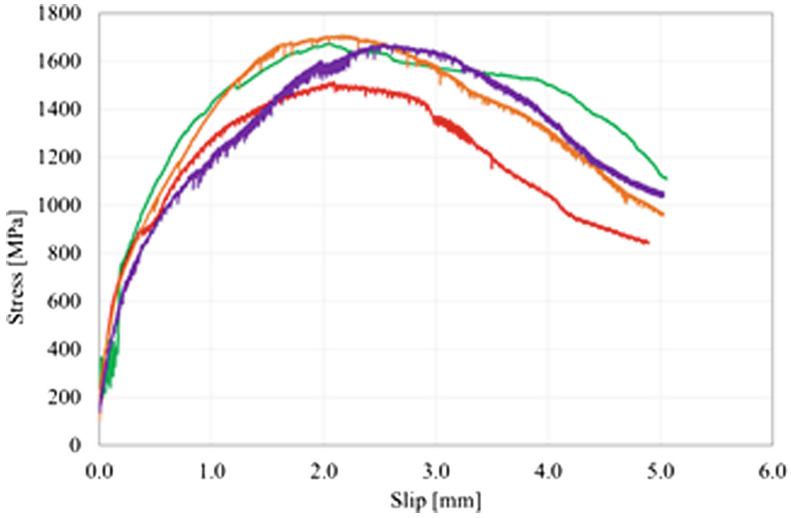

Fig. 11. Stress-slip curves obtained by pull-out tests [D'Antino et al. 2017].

In Fig. 11, the stress-slip curves are reported. The behavior is similar to the idealized response of direct-shear tests (Fig. 2). Moreover, the values of maximum stress and corresponding slip available in the literature [Carloni et al. 2017] are consistent with those obtained by these tests. This test set-up could be a valid alternative to direct-shear test set-ups provided that failure occurs due to matrix-fiber debonding. It presents many advantages, e.g. the rapidity of preparation and the possibility of casting in situ of the specimens for quality assessment control.

5 Conclusions

In this paper, the experimental characterization of various FRCM composites was reported. Both the component materials and the FRCM composites were studied using different mechanical tests. The results of tensile tests on FRCM strips and of bond tests with different set-ups were reported and described.

The choice of the tensile test set-ups has a significant influence on the results obtained. In this paper, the results obtained with the clamping-grip method were described.

The bond properties could be investigated with direct-shear or pull-out tests. Various experimental results of bond tests with the former set-up can be found in the literature on different FRCM composites. The pull-out test set-up, which can easily reproduce the results obtained with direct-shear tests and could be used also for quality control purposes, should be used only provided that failure occurs at the matrix-fiber interface.

To have a complete characterization of an FRCM composite material, the durability of the system should be also investigated. In the literature, only few results are available on this topic. Therefore, further research are needed to clarify the long-term behavior of these promising inorganic-matrix composites.

Acknowledgements. Part of the tests reported in this paper were performed at the Testing Laboratory for Materials, Structures and Constructions of Politecnico di Milano on specimens produced using reinforcing materials and mortars distributed by Ruredil S.p.A. Their financial support is gratefully acknowledged.

References

Arboleda D, Carozzi FG, Nanni A, Poggi C (2016) Testing procedures for the uniaxial tensile characterization of fabric reinforced cementitious matrix composites. J Compos Constr 20 (3):04015063

AC434 (2011) Proposed acceptance criteria for masonry and concrete strengthening using fiber-reinforced cementitious matrix (FRCM) composite system

ACI 549.4R-13 (2013) American Concrete Institute. Guide to design and construction of externally bonded fabric-reinforced cementitious matrix (FRCM) systems for repair and strengthening concrete and masonry structures

Askouni PD, Papanicolaou CG (2017) Experimental investigation of bond between glass textile reinforced mortar overlays and masonry: the effect of bond length. Mater Struct 50(2):164

Caggegi et al (2017) Experimental analysis on tensile and bond properties of PBO and aramid fabric reinforced cementitious matrix for strengthening masonry structures. Compos Part B 127:175–195

Contamine R, Si Larbi A, Hamelin P (2011) Contribution to direct tensile testing of textile reinforced concrete (TRC) composites. Mater Sci Eng A 528(29):8589–8598

Carloni C, Verre S, Sneed L, Ombres L (2017) Loading rate effect on the debonding phenomenon in fiber reinforced cementitious matrix-concrete joints. Compos Part B 108:301–314

Carozzi FG, Colombi P, Fava G, Poggi C (2016) A cohesive interface crack model for the matrix-textile debonding in FRCM composites. Compos Struct 143:230–241

Carozzi FG et al (2017) Experimental investigation of tensile and bond properties of Carbon-FRCM composites for strengthening masonry elements. Compos Part B 128:100–119

Carozzi FG, Poggi C (2015) Mechanical properties and debonding strength of fabric reinforced cementitious matrix (FRCM) systems from masonry strengthening. Compos Part B 70:215–230

Consiglio Superiore dei Lavori Pubblici (CSSPP) (2019) Linea Guida per la identificazione, la qualificazione ed il controllo di accettazione di compositi fibrorinforzati a matrice inorganica (FRCM) da utilizzarsi per il consolidamento strutturale di costruzioni esistenti. Servizio Tecnico Centrale, 43

D'Ambrisi A, Feo L, Focacci F (2012) Experimental analysis on bond between PBO-FRCM strengthening materials and concrete. Compos Part B 44(1):524–532

D'Antino T, Carloni C, Sneed LH, Pellegrino C (2014) Matrix-fiber bond behavior in PBO FRCM composites: a fracture mechanics approach. Eng Fract Mech 117:94–111

D'Antino T, Papanicolaou C (2018) Comparison between different tensile test set-ups for the mechanical characterization of inorganic-matrix composites. Constr Build Mater 171:140–151

de Felice G, De Santis S, Garmendia L, Ghiassi B, Larrinaga P, Lourenco PB, Oliveira DV, Paolacci F, Papanicolaou CG (2013) Mortar-based systems for externally bonded strengthening of masonry. Mater Struct 47(12):2021–2037

De Santis S, Carozzi FG, de Felice G, Poggi C (2017) Test methods for textile reinforced mortar systems. Compos Part B 127:175–195

Focacci F, D'Antino T, Carloni C, Sneed LH, Pellegrino C (2017) An indirect method to calibrate the interfacial cohesive material law for FRCM-concrete joints. Mater Des 128:206–217

Hartig F, Jesse F, Schicktanz K, Haubler-Combe U (2012) Influence of experimental setups on the apparent uniaxial tensile load-bearing capacity of textile reinforced concrete specimens. Mater Struct 45(3):433–446

Leone M et al (2017) Glass fabric reinforced cementitious matrix: tensile properties and bond performance on masonry substrate. Compos Part B 127:196–214

Sneed LH, D'Antino T, Carloni C, Pellegrino C (2015) A comparison of the bond behavior of PBO-FRCM composites determined by double-lap and single-lap shear tests. Cement Concr Compos 64:37–48

Zhu D, Peled A, Zaguri E, Mobasher B (2011) Dynamic tensile testing of fabric-cement composites. Constr Build Mater 25(1):385–395

Structural Behavior of RC Beams with EAF Slag as Recycled Aggregates: Numerical Versus Experimental Findings

D. De Domenico[1(✉)], F. Faleschini[2], C. Pellegrino[2], and G. Ricciardi[1]

[1] Department of Engineering, University of Messina, Messina, Italy
dario.dedomenico@unime.it
[2] Department of Civil, Environmental and Architectural Engineering, University of Padua, Padua, Italy

Abstract. This papers aims at investigating the structural behavior of reinforced concrete (RC) beams with electric arc furnace (EAF) slag as full replacement of coarse natural aggregates. A few real scale EAF RC beams have been experimentally investigated under four-point bending tests in order to analyze their structural behavior in terms of peak load, deflections and crack patterns in comparison with traditional RC beams without recycled aggregates. Then, a numerical investigation has been carried out through two different three-dimensional finite element procedures: the former is a conventional step-by-step incremental analysis based on a nonlinear stress-strain law for concrete in compression and a post-failure response in tension based on a smeared-crack approach; the latter is an iterative, simplified methodology based on the application of the limit analysis theory. Comparison between numerical and experimental results is discussed and the main advantages and drawbacks of the two proposed numerical procedures are outlined.

Keywords: Reinforced concrete · Electric arc furnace (EAF) slag · Recycled concrete · Finite element modelling · Limit analysis

1 Introduction

The use of recycled materials as partial or full replacement of coarse natural aggregates in reinforced concrete (RC) members is particularly appealing because of the resulting economic and sustainability implications. Of particular relevance to this research, encouraging results have been obtained quite recently by using electric arc furnace (EAF) slag as partial or total replacement of natural aggregates in the structural concrete mixes (Manso et al. 2004; Pellegrino and Gaddo 2009; Pellegrino et al. 2013; Arribas et al. 2015; Rondi et al. 2016). The EAF slag is a by-product of steel production in electric arc furnace plants. Considering the high amounts of EAF slag developed in countries like Italy and Spain (around the 30% of the overall European production), investigating alternative uses of these products avoiding their mere landfilling is an important research subject that deserves investigation. To further encourage these investigations, previous studies have demonstrated that the use of EAF as coarse aggregates improves the mechanical properties of concrete, in terms of

M. di Prisco and M. Menegotto (Eds.): ICD 2018, LNCE 42, pp. 248–261, 2020.
https://doi.org/10.1007/978-3-030-23748-6_19

compressive and tensile strength, elastic properties (Faleschini et al. 2017c), and durability. These enhanced mechanical features are not only observed in small scale specimens, but also in applications involving real-scale structural elements like columns (Kim et al. 2013), beams (Pellegrino and Faleschini 2013) as well as beam-column joints (Faleschini et al. 2017a, b).

Along this research line, the present contribution aims to analyze, both from an experimental and numerical point of view, the structural behavior of 8 real-scale RC beams with EAF slag as full replacement of natural aggregates. These beams exhibited either bending or shear failure, and were compared to four reference RC beams with natural aggregates. The experimental results are then numerically simulated with two different finite element (FE) procedures (De Domenico et al. 2018). The first method implies a conventional step-by-step incremental analysis based on a bilinear plasticity model for steel in conjunction with a nonlinear stress-strain law for concrete in compression and a post-failure response in tension based on a smeared-crack approach in order to capture fracture onset and development with increasing load. The second method is an iterative, simplified methodology based on the application of the limit analysis theory, considering a plasticity model for concrete and steel. Despite the different underlying theoretical principles, the same failure surface is adopted for comparative purposes of the two procedures. Comparison between numerical and experimental results is discussed and the main advantages and drawbacks of the two numerical procedures are outlined.

2 Experimental Campaign

2.1 Materials

From a chemical viewpoint, the composition of the EAF slag is: iron oxides (Fe_xO_y) 34%; CaO 28%; SiO_2 17%; Al_2O_3 11%; others (MgO, MnO, Cr_2O_3) 10%. The EAF slag particles utilized in this study were subdivided into three classes, depending on their mean size, cf. Figure 1: class 1E includes particles of [4–8] mm, class 2E comprises [8–16] mm particles, and class 3E [16–22] mm particles. As to the natural aggregates (NAs), class 1 N includes particles of [4–16] mm, 2 N comprises particles of [16–31.5] mm, and class S [0–4] mm.

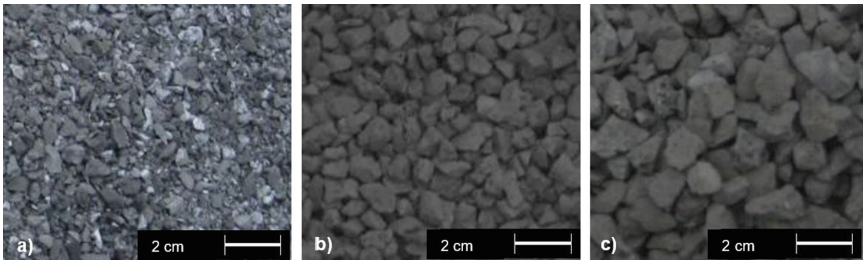

Fig. 1. EAF slag particles with class: (a) 1E; (b) 2E; (c) 3E

The main physical properties of both EAF slag and natural aggregates used in the experimental campaign are listed in Table 1. It is worth noting the high density of the EAF slag in comparison with the natural aggregates, which is due to the contents of metallic iron, iron and manganese oxides.

Table 1. Aggregates physical properties

Aggregate type	Density (kg/m^3)	Absorption (%)	Expansion (%)	Shape
EAF slag 1E	3824	0.69	0.25	angular
EAF slag 2E	3876	0.37	0.35	angular
EAF slag 3E	3900	0.5	0.35	angular
NA 1 N	2724	0.6	–	roundish
NA 2 N	2732	0.8	–	roundish
NA S	2736	1.16	–	roundish

*EAF: electric arc furnace; NA: natural aggregate.

The mix proportions are listed in Table 2. A cement type CEM 42.5 II/A-L 42.5R was used. The apparent specific weight of the cement is 3142 kg/m^3, while the specific surface, evaluated with the Blaine test method, is 4809 cm^2/g. In order to increase the workability while limiting the water/cement ratio, some water-reducing admixture (WRA) and air-entraining admixture (AEA) were employed as reported in Table 2. An S4 consistency class was obtained, with a slump value ranging between 160–210 mm according to the Abrams cone method.

Table 2. Mix proportions (for 1 m^3 of concrete batch)

	Reference concrete	EAF concrete
Cement (kg)	290	310
Water (kg)	159.5	164.3
w/c ratio	0.55	0.53
EAF slag - 1E (kg)	–	869
EAF slag - 2E (kg)	–	722
EAF slag - 3E (kg)	–	450
NA – class 1 N (kg)	597	–
NA – class 2 N (kg)	745	–
NA – class S (kg)	756	617
WRA (kg)	1.16	1.24
AEA (g)	46.4	49.6

Table 3. Mechanical properties of reference and EAF concrete

	Reference concrete	EAF concrete	EAF/reference [%]
Specific weight at 28 days (kg/m^3)	2447	3006	+ 22.8
$f_{c,cube}$ at 7 days (MPa)	27.2	48.8	+ 79.4
$f_{c,cube}$ at 28 days (MPa)	34.5	58.3	+ 68.9
f_c at 28 days (MPa)	28.6	48.4	+ 69.2
f_{ctm} at 28 days (MPa)	3.54	4.38	+ 23.7
E_{cm} at 28 days (GPa)	37.4	40.05	+ 7.1

The relevant mechanical properties are listed in Table 3. It is worth noting the increase of strength values obtained with EAF slag in place of natural aggregates, which is in line with several experimental findings from the literature (Pellegrino and Gaddo 2009; Arribas et al. 2015; Faleschini et al. 2015; Rondi et al. 2016). The strength increase is observed since the early age of maturation, and it is kept during time.

2.2 EAF RC Beams and Testing Set-up

All the twelve RC beams considered in this study have the same geometry, as reported in Fig. 2, namely a span length of 2 m, a cross-section of 185 × 300 mm and effective depth of 270 mm. Stirrups ϕ8/200 mm were adopted. Typical four-point bending tests were conducted.

The mean yield and ultimate strengths of the steel bars adopted for all the beams were 535 MPa and 650 MPa, respectively. In order to capture different failure mechanisms, four different reinforcement arrangements were prepared as sketched in the bottom part of Fig. 2. Beams labelled A1 and A2 failed due to bending, whereas beams B1 and B2 failed due to shear (with and without stirrups). The longitudinal steel reinforcement ratio $\rho = As/(b \cdot d)$ ranged from 0.157% (for A1 beam) to 3.62% (for B2 beam). For each kind of beam, one sample was casted with the reference mixture (with only natural aggregates), and two were casted with the EAF concrete. Therefore, an overall number of 12 beams was considered in this experimental campaign, 8 of which with EAF slag. Ultimate load, ultimate deflection at the mid-span, cracks pattern and width were measured for all the specimens.

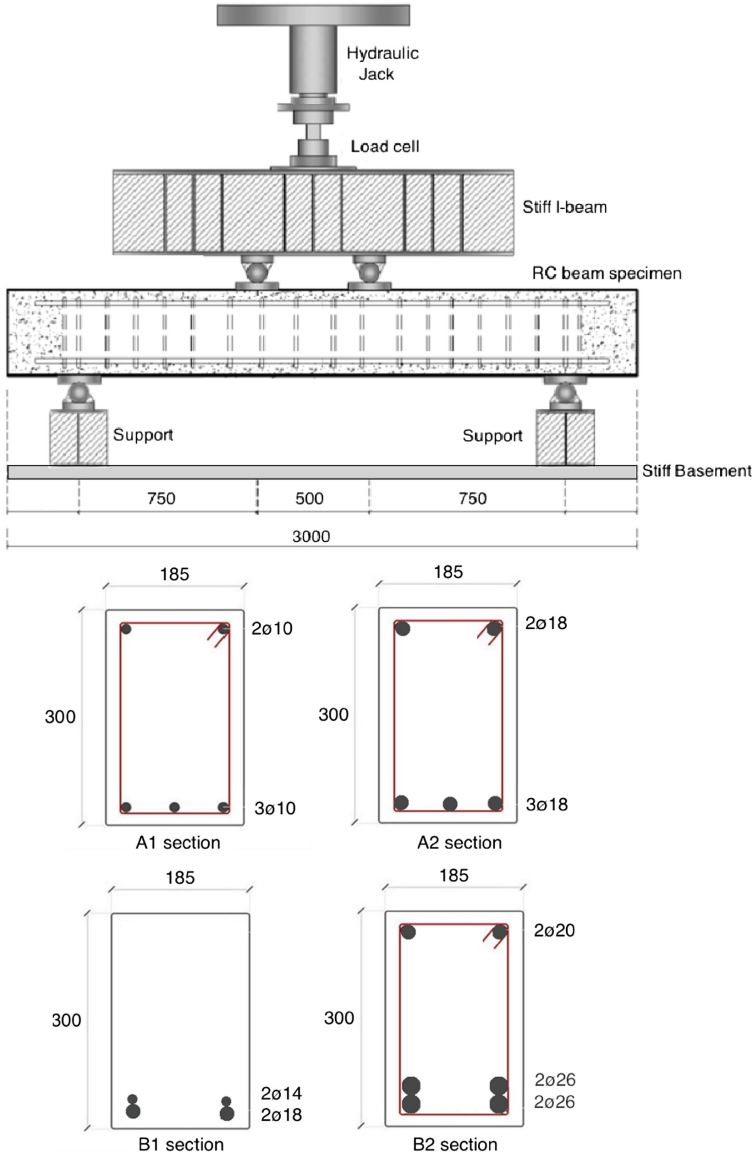

Fig. 2. Test setup and sketch of EAF RC beam cross-sections

3 Incremental Nonlinear Method

The most commonly used numerical approach for simulating the structural behavior of RC elements is to perform incremental nonlinear analyses. Particular attention is to be paid to the constitutive model for concrete and steel. In this research work, the 3D finite element software ADINA has been used (ADINA 2011), and the main constitutive assumptions implemented in this FE code are briefly outlined below.

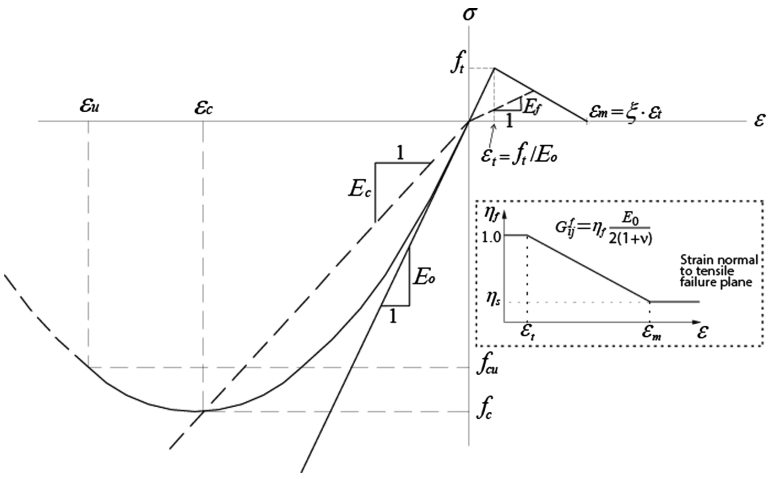

Fig. 3. Uniaxial stress-strain curve of concrete implemented in the ADINA code

In particular, the constitutive model for concrete is based upon the uniaxial stress-strain law depicted in Fig. 3. Three strain phases are incorporated, namely tension, ascending branch of compression and descending branch of compression. The stress-strain curve is linear in tension up to the maximum tensile stress f_t, and nonlinear in compression with a strain softening behavior from compression crushing failure (stress f_c, strain ε_c) up to an ultimate strain ε_u. The post-failure behavior in tension is governed by a smeared-crack model so as to describe the fracture onset and development with increasing load. When the tensile stress in a principal stress direction exceeds the tensile strength, cracking develops and plane stress conditions are assumed at the plane of tensile failure. Shear modulus degradation, fracture energy and tension stiffening are considered in the post-cracking behavior. A failure criterion, derived from the Menétrey-Willam triaxial surface (Menétrey and Willam 1995), is assumed to define the crushing failure in compression as well as the cracking failure in tension.

On the other hand, steel re-bars are governed by a plastic-bilinear material model. The von Mises yield condition with an associated flow rule is adopted, and a bilinear isotropic hardening rule is assumed. The equations of motion of the assembled FE model are integrated via a full Newton iteration method, with the time-step being adjusted depending on whether convergence at the current iteration is met (ADINA 2011).

4 Limit Analysis Procedure

The second numerical procedure adopted in this research work is based on the combination of FE method and limit analysis theory. Details of this numerical procedure, implementation aspects and geometrical interpretation are extensively discussed in (Pisano et al. 2013a, b, c, 2014, 2015; De Domenico et al. 2014a, b; De Domenico 2015; Bouabid et al. 2015).

According to the limit analysis principles, under certain hypotheses the collapse load and failure mechanism of a structure can be determined directly, without resorting to incremental step-by-step analyses. Application of the limit analysis theory to RC elements dates back to the first 60s with the pioneering work by Drucker (Drucker 1961), while more recent formulations can be found in the textbook by Nielsen and Hoang (Nielsen and Hoang 2011). The two fundamental theorems of the limit analysis theory aim to construct a statically and plastically admissible stress field (for the lower bound – static theorem) and a kinematically and plastically admissible collapse mechanism (for the upper bound – kinematic theorem). In this way, the application of the two fundamental limit analysis theorems provides two limit loads, an upper bound and a lower bound, to the actual collapse load.

It is worth noting that plain concrete is not particularly a ductile material, which is an underlying requirement of the limit analysis theory. Nevertheless, the presence of steel re-bars and their confinement action mitigates or reduce strain localization and/or brittle failure mechanisms. Furthermore, it has been found that the use of EAF slag within the cement paste leads to a further reduction of the crack width and to an overall increase of the ductility. As an example, in Fig. 4 the crack width at failure of a conventional concrete beam and of a beam with EAF slag is compared. All these phenomena and circumstances are fully consistent with the applicability of a limit analysis approach.

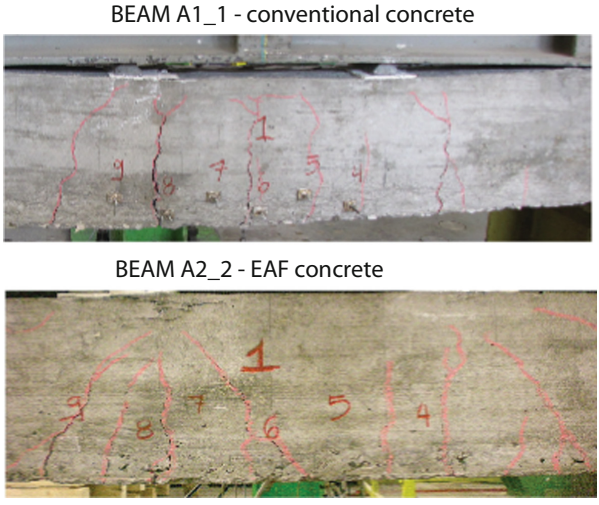

Fig. 4. Crack width at failure of beam with conventional concrete and with EAF concrete

In particular, a nonstandard limit analysis approach is pursued as per Radenkovic's theorems (Lubliner 1990) due to the dilatancy of concrete, which implies a nonassociated flow rule. The application of the two fundamental theorems of limit analysis (kinematic and static) strictly depends on the chosen yield surface. In this research work, the triaxial Menétrey-Willam yield surface (Menétrey and Willam 1995) with

cap in compression illustrated in Fig. 5 has been adopted for EAF concrete. As can be seen, this surface is smooth, has parabolic meridians, which indicates an increase of the material shear capacity with increasing hydrostatic pressure, and deviatoric cross-sections whose shape changes from triangular to circular (bulged) with increasing confining pressure. This surface provides an excellent fit of experimental data (Chen 1982) and has been extensively used in the literature. A cap in compression is incorporated in order to close the surface in the regions of triaxial compressions. The cap surface has been calibrated according to experimental data (Li and Crouch 2010).

The kinematic and static theorems of limit analysis are applied within a so-called modulus variation iterative procedure combined with the FE method. More specifically, the structural model is assumed to have elastic properties that are different from zone to zone. The limit state solution is simulated by carrying out sequences of linear elastic analyses and by systematically adjusting the elastic properties (i.e., the Young's modulus and the Poisson's ratio) of the various elements within the FE model. The rationale underlying the updating of the elastic properties during the iterations is aimed to construct, for the given yield surface of concrete sketched in Fig. 5 and for an assumed von Mises yield surface of steel bars, a statically admissible stress field (for the lower-bound approach of limit analysis) and a kinematically admissible displacement field or collapse mechanism (for the upper-bound approach of limit analysis). More specifically, the kinematic approach aims to construct a plastically admissible

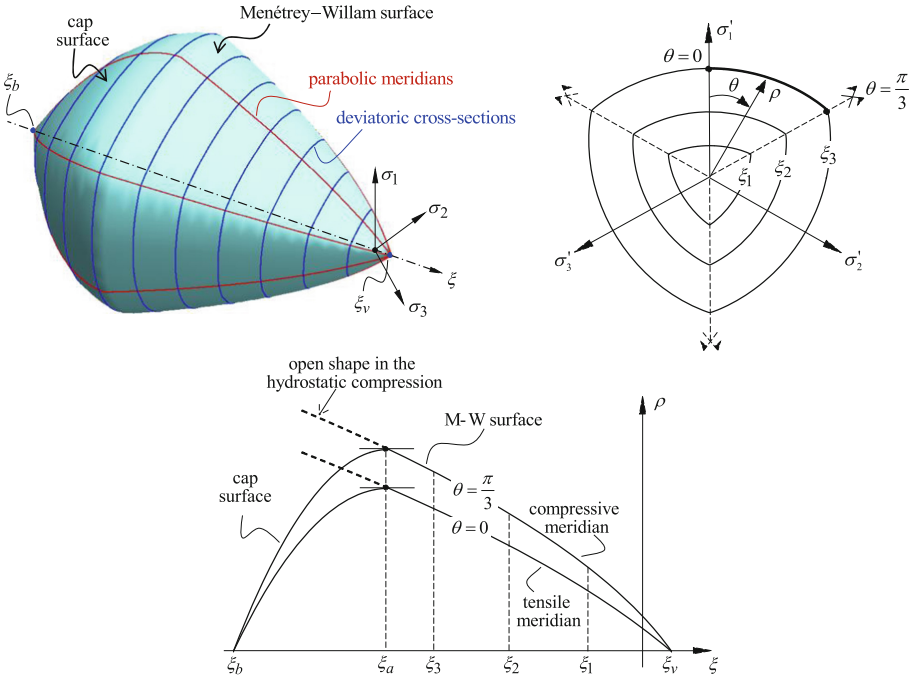

Fig. 5. Menétrey-Willam yield surface with cap in compression, 3D sketch, parabolic meridians and deviatoric cross-sections

strain field by adjusting the elastic properties of the structure so that the elastic strain rate can be interpreted as a strain rate a collapse (i.e., a vector that is normal to the yield surface). On the other hand, the static approach aims to construct a statically admissible stress field all lying within or at the boundary of the yield surface. This implies that the most critical zones (having a stress point outside the yield surface) are weakened by a reduction of the elastic properties so that a stress redistribution takes place in the structure. More details on the algorithms applied in the limit analysis procedure can be found in (De Domenico et al. 2018).

It is worth noting that, according to the proposed limit analysis methodology, both the kinematic and static theorem of limit analysis are simply applied by performing iterative sequences of linear elastic analyses, while accounting for actual plastic behavior for concrete and steel expressed by the assumed yield criteria. This reduces the resulting computational effort, and requires minimal knowledge on the material properties, in particular only the elastic moduli are necessary, which may be an advantage over more sophisticated nonlinear incremental analyses.

5 Numerical Versus Experimental Results

The main results of the experimental campaign carried out are here briefly described. The two numerical procedures outlined in the previous sections are used to simulate the experimental findings in terms of ultimate deflection, peak load and failure mechanism. The FE analyses for both the procedures have been performed using the ADINA code (ADINA 2011). Three-dimensional hexahedral solid elements with 8 nodes per element and $2 \times 2 \times 2$ integration points have been used for the concrete portions of the model, whereas embedded two-node linear truss elements (rebar element types) have been adopted for steel reinforcement, including longitudinal bars and stirrups. No significant slip of the bars were noticed in the experiments, which justifies the simple assumption of perfect bond condition between concrete and steel. After a preliminary mesh sensitivity study, the final FE mesh consists of 1440 solid elements and 320 truss elements. The main mechanical properties used in the FE model are those listed in Table 3; the fracture energy governing the post-failure behavior in tension has been set equal to 80 J/m^2 and 110 J/m^2 for conventional and EAF concrete, respectively (according to experimental data collected in a previous work).

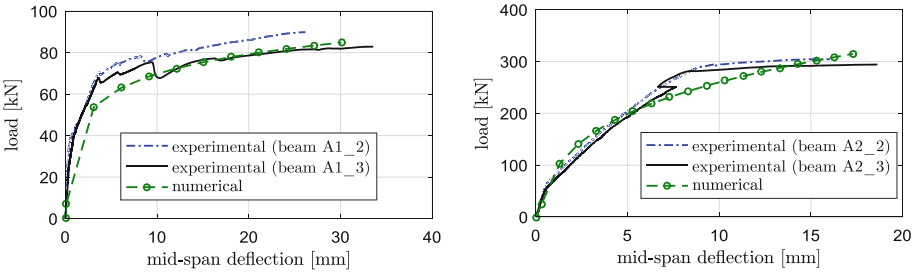

Fig. 6. Load versus mid-span deflection curves for two EAF RC beams failing due to bending

Some emblematic comparisons between experimental and numerical load versus mid-span deflection curves are depicted in Fig. 6. It can be seen that a reasonable agreement is observed in terms of peak load prediction, and mid-span deflection.

Table 4. Peak loads and ultimate deflections, experimental results versus numerical prediction via nonlinear incremental analyses

Beam	Experimental values		Incremental nonlinear analysis	
	P_{EXP} [kN]	d_{EXP} [mm]	P_{NUM} [kN]	d_{NUM} [mm]
A1_1	82.37	36.7	75.61	39.1
A1_2	89.85	26.2	84.39	30.1
A1_3	82.88	33.6	84.39	30.1
A2_1	274.46	15.9	314.34	17.8
A2_2	304.28	16.0	314.51	17.3
A2_3	294.06	18.6	314.51	17.3
B1_1	180.44	8.6	189.54	9.3
B1_2	205.90	5.3	198.75	6.3
B1_3	198.06	7.2	198.75	6.3
B2_1	350.54	9.4	378.13	10.6
B2_2	428.15	9.2	408.52	8.8
B2_3	378.62	8.2	408.52	8.8

Table 5. Peak loads of the RC beams, experimental results versus numerical prediction via limit analysis procedure

Beam	Experimental values	Limit analysis approach	
		Upper bound	Lower bound
	P_{EXP} [kN]	P_{UB} [kN]	P_{LB} [mm]
A1_1	82.37	84.23	78.12
A1_2	89.85	91.62	81.57
A1_3	82.88	91.62	81.57
A2_1	274.46	280.92	265.65
A2_2	304.28	306.04	289.09
A2_3	294.06	306.04	289.09
B1_1	180.44	174.98	167.42
B1_2	205.90	195.77	186.99
B1_3	198.06	195.77	186.99
B2_1	350.54	363.31	344.85
B2_2	428.15	408.29	395.67
B2_3	378.62	408.29	395.67

The values of the peak loads and ultimate deflections for all the tested beams recorded in the experimental campaign and those computed in the nonlinear incremental analysis are listed and compared in Table 4. By inspection of this table, it is noticed that the EAF RC beams behaved better than the conventional RC beams, exhibiting higher peak loads and smaller mid-span deflections at failure. Furthermore, the agreement between experiments and numerical analyses seems to be quite acceptable. It can be noticed that higher mid-span deflections than the experimental ones are predicted in the numerical analyses, especially for conventional RC beams with natural aggregates. The mean error on the peak error is 6.83% and 4.87% for beams failing in bending and in shear, respectively.

In addition to the incremental nonlinear analysis, further numerical simulations have been carried out via the limit analysis procedure described above. This procedure can identify a bounding interval, upper bound – lower bound, within which the collapse load is expected to occur, as reported in Table 5. More precise predictions were obtained for beams failing in bending, and slightly less accurate results were noticed for beams B1 and B2, which instead failed in shear either because of the absence of stirrups, or due to an over-reinforced longitudinal bar arrangement. These results are consistent with the assumptions of the limit analysis theory, which implies a ductile behavior of the structural element, a circumstance that is not really met in the case of beams B1 and B2 (more brittle failure mode). However, a significant saving of computational effort is attained since only linear elastic analyses (with spatially varying elastic properties) are to be performed.

A monotonic convergence of both the kinematic and the static approach of limit analysis during the iterations is achieved after nearly twelve iterations (linear elastic analyses) as documented in Fig. 7.

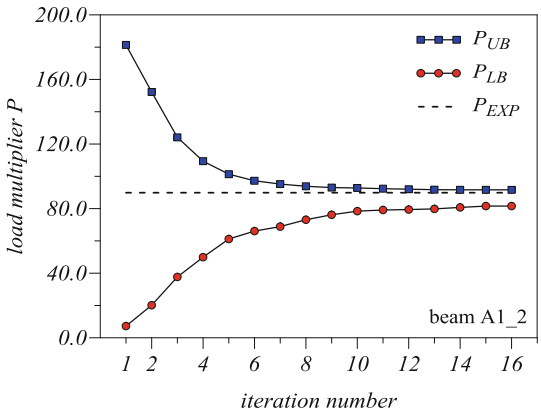

Fig. 7. Iterative values of upper bound and lower bound of the collapse load compared to the experimental peak load

The limit analysis procedure (in the kinematic approach) also provides useful information on the expected collapse mechanism that the RC beam exhibits at failure. As an example, the distribution of the strain rates at collapse of the beam A2_2 as predicted by the FE model in conjunction with the limit analysis procedure is shown in Fig. 8 and compared to the experimental collapse mechanism. The plastic zones observed in the FE model are sufficiently confined and located close to the critical zones identified in the experimental test.

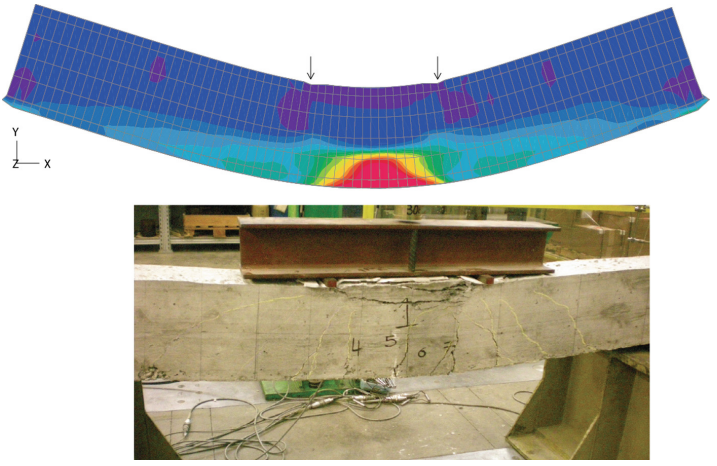

Fig. 8. Numerical (FE method with limit analysis procedure) versus experimental collapse mechanism of beam A2_2

6 Conclusions

The structural behavior of RC beams with EAF slag as full replacement of natural aggregates has been scrutinized from both an experimental and a numerical viewpoint. It has been found that the beams with EAF concrete exhibit higher ultimate flexural and shear strength than the corresponding beams with conventional concrete, reduced crack widths and higher ultimate deflections. Calibrated on the basis of experimentally detected material properties, two numerical procedures have been proposed to simulate the structural behavior of EAF RC beams, namely an incremental nonlinear method and a limit analysis procedure. The former is able to describe the force-displacement curves step-by-step, thereby giving useful indications on the ultimate load and ultimate deflection. On the other hand, a simplified limit analysis procedure has also been pursued, motivated by the enhanced ductility of EAF concrete. This latter procedure is a direct and simpler method of analysis, which provides a bounding interval (upper bound and lower bound) of the collapse load, and some information on the failure mechanism through the observation of the strain rates at collapse. Applications to other structural elements, e.g. slabs, walls and joints, deserve further investigation to extend the knowledge on concrete with EAF slag and to gain more confidence before a practical implementation in civil engineering structure is performed.

References

ADINA R & D, Inc (2011) Theory and modeling guide volume I: ADINA. Report ARD 11–8. Watertown, MA, USA

Arribas I, Santamaria A, Ruiz E, Ortega-Lopez V, Manso JM (2015) Electric arc furnace slag and its use in hydraulic concrete. Constr Build Mater 90:68–79

Bouabid A, De Domenico D, Pisano AA, Limam O (2015) Collapse load of composite laminates: lower bound evaluation by stress field analytical approximation. Compos Part B Eng 75:345–354

Chen WF (1982) Plasticity in reinforced concrete. McGraw–Hill, New York

De Domenico D, Faleschini F, Pellegrino C, Ricciardi G (2018) Structural behavior of RC beams containing EAF slag as recycled aggregate: numerical versus experimental results. Constr Build Mater 171:321–337

De Domenico D, Pisano AA, Fuschi P (2014a) A FE-based limit analysis approach for concrete elements reinforced with FRP bars. Compos Struct 107:594–603

De Domenico D, Fuschi P, Pardo S, Pisano AA (2014b) Strengthening of steel-reinforced concrete structural elements by externally bonded FRP sheets and evaluation of their load carrying capacity. Compos Struct 118:377–384

De Domenico D (2015) RC members strengthened with externally bonded FRP plates: a FE-based limit analysis approach. Compos Part B Eng 71:159–174

Drucker DC (1961) On structural concrete and the theorems of limit analysis. Publ Int Assoc Bridge Struct Eng 21:49–60

Faleschini F, Fernández-Ruíz MA, Zanini MA, Brunelli K, Pellegrino C, Hernández-Montes E (2015) High performance concrete with electric arc furnace slag as aggregate: mechanical and durability properties. Constr Build Mater 101:113–121

Faleschini F, Bragolusi P, Zanini MA, Zampieri P, Pellegrino C (2017a) Experimental and numerical investigation on the cyclic behavior of RC beam column joints with EAF slag concrete. Eng Struct 152:335–347

Faleschini F, Hofer L, Zanini MA, dalla Benetta M, Pellegrino C (2017b) Experimental behavior of beam-column joints made with EAF concrete under cyclic loading. Eng Struct 139:81–95

Faleschini F, Santamaria A, Zanini MA, José JS, Pellegrino C (2017c) Bond between steel reinforcement bars and electric arc furnace slag concrete. Mater Struct 50:170

Kim SW, Kim YS, Lee JM, Kim KH (2013) Structural performance of spirally confined concrete with EAF oxidising slag aggregate. Eur J Environ Civ Eng 17(8):654–674

Li T, Crouch R (2010) A C_2 plasticity model for structural concrete. Comput Struct 88:1322–1332

Lubliner J (1990) Plasticity theory. Macmillan Pub. Co, New York

Manso JM, Gonzalez JJ, Polanco JA (2004) Electric arc furnace slag in concrete. J Mater Civ Eng 16(6):639–645

Menétrey P, Willam KJ (1995) A triaxial failure criterion for concrete and its generalization. ACI Struct J 92:311–318

Nielsen MP, Hoang LC (2011) Limit analysis and concrete plasticity, 3rd edition CRC Press, Taylor & Francis Group, USA

Pellegrino C, Faleschini F (2013) Experimental behavior of reinforced concrete beams with electric arc furnace slag as recycled aggregate. ACI Mater J 110(2):197–205

Pellegrino C, Gaddo V (2009) Mechanical and durability characteristics of concrete containing EAF slag as aggregate. Cement Concr Compos 31(9):663–671

Pellegrino C, Cavagnis P, Faleschini F, Brunelli K (2013) Properties of concretes with black/oxidizing electric arc furnace slag aggregate. Cement Concr Compos 37:232–240

Pisano AA, Fuschi P, De Domenico D (2013a) A kinematic approach for peak load evaluation of concrete elements. Comput Struct 119:125–139

Pisano AA, Fuschi P, De Domenico D (2013b) Peak loads and failure modes of steel-reinforced concrete beams: predictions by limit analysis. Eng Struct 56:477–488

Pisano AA, Fuschi P, De Domenico D (2013c) Failure modes prediction of multi-pin joints FRP laminates by limit analysis. Compos Part B Eng 46:197–206

Pisano AA, Fuschi P, De Domenico D (2014) Limit state evaluation of steel-reinforced concrete elements by von Mises and Menétrey-Willam-type yield criteria. Int J Appl Mech 6 (5):1450058–1. https://doi.org/10.1142/S1758825114500586

Pisano AA, Fuschi P, De Domenico D (2015) Numerical limit analysis of steel-reinforced concrete walls and slabs. Comput Struct 160:42–55

Rondi L, Bregoli G, Sorlini S, Cominoli L, Collivignarelli C, Plizzari G (2016) Concrete with EAF steel slag as aggregate: a comprehensive technical and environmental characterisation. Compos Part B Eng 90:195–202

Experimental Assessment of Bond Characteristics in Reinforced Concrete with Electric Arc Furnace Slag

Flora Faleschini[1(✉)], Amaia Santamaria[2], Mariano Aneglo Zanini[1], and Carlo Pellegrino[1]

[1] Department of Civil, Environmental and Architectural Engineering, University of Padova, Via Marzolo 9, 35131 Padua, Italy
flora.faleschini@dicea.unipd.it
[2] Department of Mining, Metallurgical and Materials Science, University of Basque Country, Alameda de Urquijo s/n, 48013 Bilbao, Spain

Abstract. The anchorage between deformed steel bars embedded in concrete blocks has been studied for many years in literature, thus leading to a well-established knowledge on this topic. However, literature is more limited when novel kind of concretes are used, e.g. recycled concretes or electric arc furnace (EAF) slag concretes. This study deals particularly on EAF concrete, and bond between steel reinforcement was studied experimentally through pull-out tests, according to RILEM recommendations. Six series of samples were used, characterized by different aggregate type and water/cement ratio. Bond-slip relationships were analyzed, and the main bond stress characteristics were obtained. Additionally, experimental results were compared with analytical predictions, obtained with empirical formulations collected from literature. Results indicate that bond strength is enhanced when EAF slag is used as recycled coarse aggregates in relatively high-strength concrete.

Keywords: Bond · Recycled concrete · Pull-out test

1 Introduction

1.1 Concrete with Electric Arc Furnace Slag

The use of manufactured or recycled aggregates for producing novel type of concretes, characterized by few environmental impact and cost, is gaining improved attention in the last years. Particularly, the use of by-products from the metallurgical industry has been found very attractive, as it allows reducing significantly carbon emissions. The so-called electric arc furnace (EAF) slag concrete has the same (or even better) mechanical and durability-related properties than ordinary conglomerates (Pellegrino et al. 2013; Faleschini et al. 2015).

EAF slag particles are heavy-weight manufactured aggregates, similar to dark grey/black stones, with few pores and characterized by high resistance to fragmentation. They are constituted mainly by iron, calcium, silicon and aluminium oxides, with high crystalline nature; when appropriately cured, the risk of potential expansion due to

M. di Prisco and M. Menegotto (Eds.): ICD 2018, LNCE 42, pp. 262–272, 2020.
https://doi.org/10.1007/978-3-030-23748-6_20

free calcium and magnesium hydration is almost null (Manso et al. 2006). Existing studies demonstrated that, when EAF slag fully replaces coarse aggregates in concrete, mechanical properties are typically enhanced, if compared to corresponding conventional mixes (Papayianni and Anastasiou 2010). Such promising results at material scale promoted study development also at structural level, which up to now remains however limited in few applications. Among them, it is worth recalling the good results achieved by Pellegrino and Faleschini (2013) on real scale RC beams subject to gravity loads, who demonstrated an improvement of the ultimate capacity both against flexural and shear failure. Additionally, Faleschini et al. (2017a, 2017b) studied the experimental behaviour of real scale exterior RC beam-column joints subject to lateral load, cyclically applied as a seismic-like action, and demonstrated improvements in the ultimate shear capacity of the panel joint, enhanced dissipation energy and ductility, and similar stiffness decay than in the reference joint.

1.2 Bond Between Steel and Concrete

Bond is one of the most important property of reinforced concrete (RC) structures, and it influences the structural behaviour RC structures in many ways, thanks to the complex interaction between the two materials. Bond resistance is offered by all those mechanisms allowing axial forces transmission from steel reinforcement to the surrounding concrete, which can be identified as chemical adhesion, mechanical interaction and friction. Among these components, it is well-known that mechanical interaction is mainly affecting bond strength for deformed bars.

To evaluate bond resistance between steel and concrete, two test-setups may be used, according to RILEM recommendations: pull-out or beam end test. The former is the most used test, as it allows to draw bond stress-slip curves and estimate the main characteristics of the bond stress–slip evolution, through a simple and cheap method. The main drawback of this method is that it places concrete in compression and bar in tension, a situation which is not common in the practice; as a result, bond strength is generally overestimated. Two failure mode can occur: pullout and splitting, depending on geometrical parameters and confinement. The latter test method is instead much more complex, but it better represents the stress state of real design situation.

The aim of this work is to study bond stress-slip law of EAF slag concrete and compare it with the behavior of conventional concrete. For this scope, an experimental campaign based on pull out tests is performed, which allow to clearly represent the concept of anchoring a bar, through the use of economical specimens, and thus providing a direct bond measure. It is worth recalling that this subject, i.e. bond between steel reinforcement and new cement-based materials, is also a subject of interest of the *fib* TG 2.5 Bond and Material Models.

2 Materials and Methods

2.1 Concretes Mix Design

Six concrete mixes were prepared to manufacture the specimens, varying w/c ratios and aggregates' type. To cast the concretes, an ordinary Portland cement type I 52.5R class was used; water was taken from the urban supply system of the city of Padova, and did not contain any undesirable compounds that could affect the quality of the concretes; a commercial water reducing admixture was used to achieve the desired workability; river sand (0–4 mm) was used as fine natural aggregate (NA) in all the mixes; and lastly, three types of coarse aggregates (4–16 mm) were used (two natural and one manufactured). Natural gravel aggregates type I have roundish shape; the second type of natural aggregates (type II) is crushed natural limestone; lastly, EAF slag was used. It is worth recalling that slag aggregates bulk density is about 3854 kg/m^3, whereas it is 2701 and 2850 kg/m^3 for natural aggregates type I and II, respectively.

Concrete mixture compositions are listed in Table 1. It is worth recalling that two different strength targets were chosen, hence two w/c ratios (0.45 and 0.6) were used, at different cement dosages (300 and 400 kg/m^3), maintaining the same water content in the mix. To achieve the same consistency in the fresh state, an increase in water reducing admixture (WRA) dosage was necessary for mixtures including EAF slag and type II aggregates (i.e., natural crushed limestone). Additionally, a slight variation in mixture proportions was necessary to take into account the different shape of roundish and sharp aggregates.

Table 1. Concrete mix details in (kg/m^3)

	Low strength			High strength		
	I-L	II-L	EAF-L	I-H	II-H	EAF-H
Cement	300	300	300	400	400	400
Water	180	180	180	180	180	180
w/c	0.6	0.6	0.6	0.45	0.45	0.45
NA type I	1039	–	–	987	–	–
NA type II	–	908	–	–	863	–
EAF slag	–	–	1202	–	–	1156
NA sand	851	1064	1082	808	896	991
WRA	0.6	2.1	1.2	2.8	4.0	4.0

2.2 Specimens Preparation and Test Methods

After mixing, Abrams cone test was performed to verify that all the samples achieved the required *S4* consistency class. Then, nine cylindrical specimens with $h \times d = 200 \times 100$ mm were casted per each mix to evaluate compressive, tensile strength and elastic modulus, according to the European standards of the *EN* 12390 series, at 28 days of ageing. Three cubic specimens (with 160 mm side) per each mix were manufactured for pull out tests. All the cylindrical and pull out specimens were demolded after one day; then

they were cured in controlled humidity and temperature conditions ($T = 20 \pm 2$ °C; $RH \geq 95\%$), until time of testing.

Ribbed steel rebars were used for pull-out tests, with a nominal diameter equal to 16 mm, and a nominal tensile strength of 500 MPa. The clear distance between the lugs in the ribbed bars was about 10 mm, measured at the lug mid-height.

Pull-out specimens were casted with the bar horizontal (see Fig. 1). Cubes' side (160 mm) was 10 times the diameter of the bar (16 mm), and the embedded length (80 mm) was 5 times the diameter of the bar, following *RILEM* guidelines (1978). A plastic sleeve was used over half the embedded length to minimize platen restraint effects at the loaded end. Tests were carried out at 28 days of ageing, applying the load in displacement-control mode, to capture the post-peak behavior. The unloaded end slip was measured with a variable differential transducers (*LVDT*), with a precision of 0.001 mm, and records were continuously acquired.

Fig. 1. Pull-out molds and specimens

3 Results

3.1 Concretes Properties

All the concretes produced displayed a good workability, with a measured slump about 200 ± 5 mm, i.e. they belong to S4 consistency class. Fresh density increases when EAF slag aggregate is used; as an example, it increases respectively of +13.6% and +3.8% more than when NA type I and type II are used, respectively, for low strength mixtures.

Concerning compressive strength, for all the concretes produced with the lower strength target, the failure was governed by the cementitious matrix low quality, regardless the aggregates type. As expected, no significant compressive strength differences were displayed among the concrete types. Conversely, for the concretes produced with the higher strength target, significant differences were displayed among the concrete types. Indeed, in this case, coarse aggregate type was significantly influencing the strength. Mix II-H and EAF-H were characterized by a strength gain of +15.3% and +30.7%, if compared to Mix I-H: such enhancement is directly associated to the type of coarse aggregate used, which are crushed in the former cases, and

roundish in the latter. Additionally, in the case of EAF concrete, this strength gain can be acknowledged also to a better quality of the ITZ zone, already observed in other experimental works in literature (Arribas et al. 2015).

Similar for compressive strength, also tensile strength enhancement was observed for concrete mixtures with crushed aggregates. Such improvement attained +32.5% if mixture EAF-H is compared to I-H, whereas it is about +26.3% if mixture II-H is compared to I-H. Less differences are observed for the lo-strength target concretes.

Concerning concrete elastic modulus, EAF concretes have higher values of E due to the nature of the slag itself, made by stiff minerals of iron.

Table 2 summarizes the results discussed above.

Table 2. Properties of the tested concrete

	Low strength			High strength		
	I-L	II-L	EAF-L	I-H	II-H	EAF-H
Slump (cm)	20.5	21.0	19.5	20.5	19.5	20.0
Density (kg/m^3)	2307	2371	2668	2373	2444	2835
f_c (MPa)	32.0	28.8	29.0	38.0	44.6	49.7
f_{ct} (MPa)	2.88	2.70	2.58	3.44	3.94	4.56
E (GPa)	36.3	33.0	39.0	42.7	35.3	45.7

3.2 Bond-Stress Slip Relationships

All the specimens failed for pull-out mode (Fig. 2- left), except for two specimens

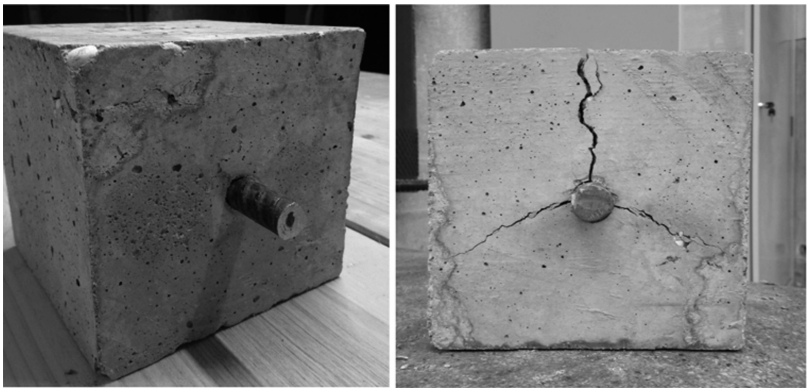

Fig. 2. Left: pull-out failure. Right: splitting failure

made of Mix EAF-H concrete, that failed for splitting (Fig. 2- right).

The global bond stress-slip curves for the low-strength concretes are shown in Fig. 3: for each concrete, one curve only is plotted, being all the other similar.

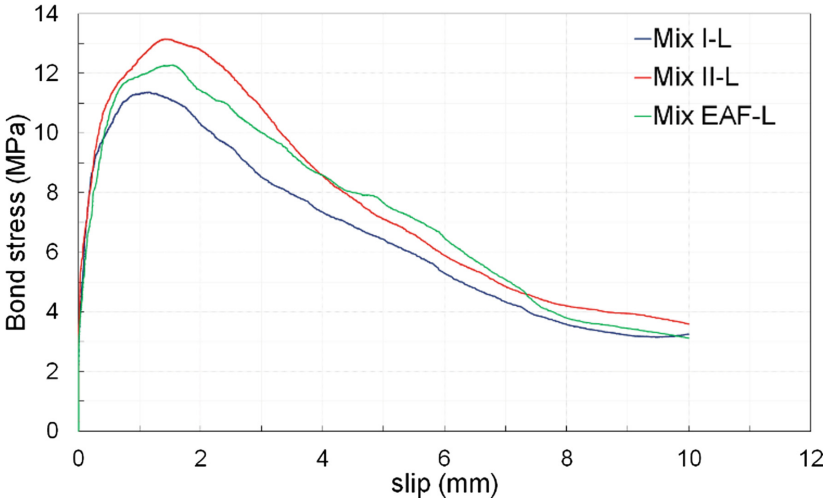

Fig. 3. Bond stress – slip relation, concretes with low strength

A threshold value between 3–4 MPa is observed, before slip evolution, in all the specimens.

Instead, remarkable differences are observed in Fig. 4 for the high-strength target, not only in the ascending branch of the curves, where the rib bearing bond mechanisms seems more pronounced in the EAF-H concrete. Also the frictional mechanism along the new sliding plane originated around the bar shearing off allowed the specimen to attain higher bond values. However, it should be recalled that, in this case, stress-slip curve of only one EAF concrete is shown in the graph, because of two failures reported as per splitting. Even though this difference was exhibited, a similar peak strength was attained by the specimens failing due to splitting (R2 and R3) and pull-out (R1), as it can be seen in Fig. 5.

Concerning instead mix I-H and II-H, the ascending curve and post-peak response are similar, due to the fact that adhesion and friction mechanisms exhibit little dependence on compressive strength; the most significant difference is in the ultimate bond, which is mostly affected by concrete compressive strength.

From pull-out tests, it is possible to obtain the ultimate bond strength τ_U and the characteristic bond strength τ_M. τ_U is defined as the bond stress corresponding to the ultimate load (F_U), whereas τ_M is calculated as the mean value of three bond stresses ($\tau_{0.01}$, $\tau_{0.10}$, $\tau_{1.00}$), corresponding to slip values of s = 0.01, 0.10 and 1.00 mm. The ultimate slip, s_u, which corresponds to the ultimate bond strength, is also measured. Then, normalized bond strength τ_U^* is calculated as the ultimate bond strength divided by the square root of the concrete compressive strength at 28 days. Table 3 lists the main characteristics obtained from the stress-slip curves: the values of τ_U, τ_M, τ_U^*, F_u (peak force) and s_u (slip at the peak force) are reported. It can be observed that for the low-strength target concretes, few differences were displayed among the three mixtures, regarding both τ_U and τ_M values. This result is due to the fact that pull-out failure is mainly governed by concrete compressive strength, which is very similar among

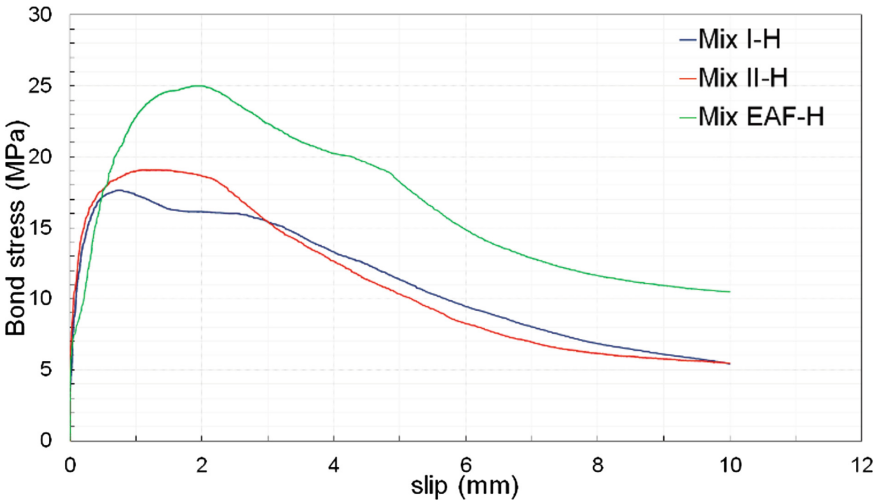

Fig. 4. Bond stress – slip relation, concretes with high strength

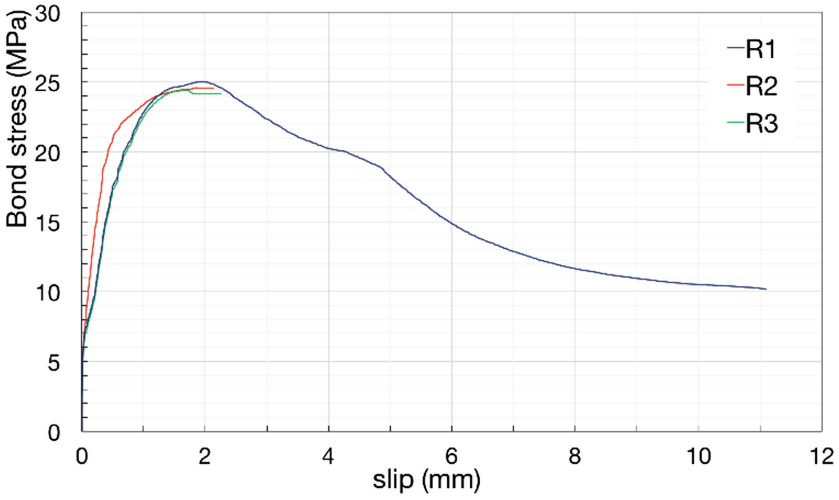

Fig. 5. Bond stress – slip relation, mix EAF-H

such concretes, as a result of the low quality of the cementitious matrix. Indeed, looking also to the standardized bond strength, such value is very similar for the low-strength concretes, regardless the aggregate type used.

For the concretes prepared with a better quality of the cementitious matrix (low w/c and high cement dosage), the increase in bond characteristics is remarkable. Additionally, when crushed aggregates are used, such enhancement is further visible, i.e. for Mix II-H and Mix EAF-H. For the latter concrete, it is worth noting that in two cases (over three) splitting failure mode was observed, as a result of the insufficient

Table 3. Bond characteristics

	Low strength			High strength		
	I-L	II-L	EAF-L	I-H	II-H	EAF-H
τ_M (MPa)	6.08	6.33	6.39	9.94	11.7	12.2
τ_U (MPa)	10.3	12.7	10.8	17.5	19.0	24.7
τ_U^* (MPa)	1.81	2.36	2.0	2.84	2.83	3.51
F_U (kN)	41.3	51.0	43.3	70.4	75.8	99.4
su (mm)	1.14	1.33	1.19	0.84	1.15	1.82

confinement that could not prevent splitting of concrete cover. Comparing the normalized bond strength, a significant increase is also noted for the Mix EAF-H, if compared with the others.

4 Prediction Equations Vs Experimental Results

Idealized stress-slip curves can describe the experimental local behavior (i.e., in case of short embedded length) of bond between concrete and ribbed bars. The *BPE* model, initially proposed by Eligehausen et al. (1983) is currently adopted by the *fib* Model Code 2010 (2013), and it can be used for the evaluation of the bond stress at the correspondent slip value. The parameters for defining the mean bond stress-slip relationship of ribbed bars can be found in Table 6.1-1 of the MC2010. For pull-out failure and "all other bond conditions" (i.e., when the casting position of the bars has an inclination less than 45° to the horizontal, and reinforcement are located up to 250 mm from the bottom or at least 300 mm from the top concrete layer), the value of the ultimate bond resistance is given by the ultimate pull-out strength (Eq. 1):

$$\tau_{u-pull-out} = 1.25 \cdot f_c^{0.5} \tag{1}$$

Instead, for splitting failure, the ultimate bond resistance is given by Eq. 2, in case of no-transverse reinforcement:

$$\tau_{u-split} = 0.7 \cdot 6.5 \cdot \left(\frac{f_{cm}}{25}\right)^{0.25} \cdot \left(\frac{25}{d}\right)^{0.2} \cdot \left[\left(\frac{c_{\min}}{d}\right)^{0.33} \cdot \left(\frac{c_{\max}}{c_{\min}}\right)^{0.1}\right] \tag{2}$$

Many other authors proposed predicting equation for the assessment of the bond strength between concrete and ribbed bars, both for pull-out and splitting failure, in case of monotonic loading. Most of the existing formulations include, as relevant parameter, concrete compressive strength f_c, concrete cover c, steel bar diameter d and the embedment length l_b. Some of them include also the confinement influence, to distinguish between pull-out and splitting failure.

Oragun et al. (1977) proposed an empirical formulation (Eq. 3), based on a nonlinear regression analysis of tests carried out on beam-specimens with unconfined lap splices. The equation was derived using a dataset having mostly *c/d* values less than

2.5; specimens failing due to splitting after steel yielding were not taken into account in the regression. Stresses are expressed in (Psi).

$$\tau_u = [1.22 + 3.23 \cdot (c/d) + 53 \cdot (d/l_b)] \cdot f_c^{0.5} \quad (3)$$

Kemp (1986) proposed a prediction equation (Eq. 4) obtained through a multiple linear regression analysis, derived on a total of 157 stub cantilever specimens. The influence of clear cover, bar spacing, stirrups, and dowel forces were studied on this research. Stresses are expressed in (Psi).

$$\tau_u = 232 + 2.716 \cdot (c/d) \cdot f_c^{0.5} \quad (4)$$

Chapman and Shah (1987) conducted an experimental investigation for the assessment of bond stress at early age of concrete maturation. They developed an empirical formulation based on pull-out specimens (Eq. 5), which is conservative in the prediction of matured concrete specimens, also according to the same authors. They did not distinguish between pull-out, splitting or steel bar yielding failure, and the stresses in the formulation are expressed in (Psi).

$$\tau_u = [3.5 + 3.4 \cdot (c/d) + 57(d/l_b)] \cdot f_c^{0.5} \quad (5)$$

Al-Jahdali et al. (1994) proposed an expression (Eq. 6) for bond strength estimation, with unites expressed in the S.I. system, based on an experimental campaign on 36 pull-out specimens. Also in this case, the authors did not distinguish between the possible failure modes, i.e. splitting, pull-out, tensile concrete fracture and steel yielding.

$$\tau_u = [-0.879 + 0.324 \cdot (c/d) + 5.79(d/l_b)] \cdot f_c^{0.5} \quad (6)$$

Recently Aslani and Nejadi (2012) proposed an empirical formulation (Eq. 7), derived from tests conducted on both pull-out and beam-specimens made with self-compacting concrete, collected in literature. They did not distinguish between possible failure modes, and units are expressed in the S.I. system.

$$\tau_u = [0.672 \cdot (c/d)^{0.6} + 4.8(d/l_b)] \cdot f_c^{0.55} \quad (7)$$

Figure 6 shows the estimated vs. the experimental ultimate bond stress of the specimens analyzed in this work, using the above formula. It is worth recalling that average material properties were used to compute the theoretical predictions, without applying any partial safety factor coefficient. A poor correlation between the experimental results and the theoretical values is obtained using all the provisional formula. It is indeed worth to note that most of these formula "converge" to a range of constant values, because of few influencing parameters (concrete compressive strength, concrete cover and bar diameter), which are also not significantly varying in the present experimental campaign. The only formulation which provided largely unconservative estimates of the ultimate bond strength is Eq. 7, which was derived for SCC concretes,

which exhibited even better bond than ordinary vibrated concretes in some cases in literature.

Concerning the prediction made with *fib* Model Code 2010 formulations, Eq. 1 was applied for specimens failing for pull-out, and Eq. 2 for the ones failing due to splitting. In both cases, they provide highly conservative predictions.

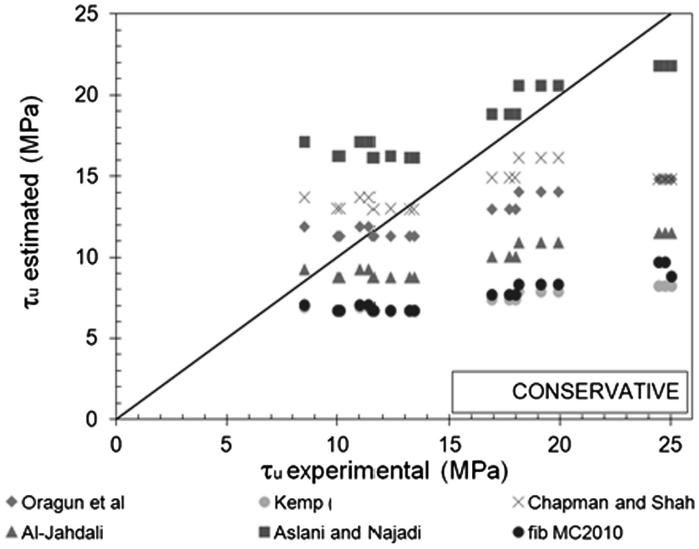

Fig. 6. Estimated vs experimental results

5 Conclusions

This works deals with an important aspect of structural application of electric arc furnace slag in concrete, namely the bond between concrete and steel reinforcement bars. A future development of this research would be the assess of bond characteristics using the beam end test, which provide similar bond conditions to those found in real applications. Results of this experimental work allow to state that bond strength between concrete and ribbed steel bars (mean, ultimate and residual frictional) is higher when crushed aggregates are used, referring to high-strength concrete target. The highest enhancement is observed in specimens with *EAF* slag, with an increase of up to +40% if compared to the conventional concrete. Concerning concretes manufactured with low strength target, few differences are observed among the tested mixtures. The existing predicting equations for ultimate bond strength prediction with ribbed bars are typically conservative for (relatively) high strength concretes, whereas they fit better for low strength concretes. The equations proposed by Kempt and *fib MC2010* are the most conservative ones.

Acknowledgements. This work is supported by the Spanish Ministry MINECO and FEDER Funds for financial support through Project BlueCons: BIA2014-55576-C2-2-R, and by the project funded by the University of Padova PRAT "Sustainable heavy weight concretes for nuclear shielding in strategic facilities". The authors would to express their gratitude to the Vice-Rectorate of Investigation of the University of the Basque Country for grant PIF 2013, the grant for mobility of researchers 2015 and, likewise, to the Basque Government for financial support to Research Group IT781-13. The authors would like also to thank Zerocento S.r.l. for providing the EAF slag, and Italcementi-Heidelberg for providing the cement.

References

Al-Jahdali FA, Wafa FF, Shihata SA (1994) Development length for straight deformed bars in high-strength concrete. ACI Spec Publ 149:507–522

Arribas I, Santamaría A, Ruiz E, Ortega-López V, Manso JM (2015) Electric arc furnace slag and its use in hydraulic concrete. Constr Build Mater 90:68–79

Aslani F, Nejadi S (2012) Bond behavior of reinforcement in conventional and self-compacting concrete. Adv Struct Eng 15(12):2033

Chapman RA, Shah SP (1987) Early-age bond strength in reinforced concrete. ACI Mater J 84(6):501–510

Eligehausen R, Popov EP, Bertero VV (1983) Local bond stress–slip relationships of deformed bars under generalized excitations. University of California, report no. UCB/EERC-83/23

Faleschini F, Bragolusi P, Zanini MA, Zampieri P, Pellegrino C (2017a) Experimental and numerical investigation on the cyclic behavior of RC beam column joints with EAF slag concrete. Eng Struct 152:335–347

Faleschini F, Fernández-Ruíz MA, Zanini MA, Brunelli K, Pellegrino C (2015) High performance concrete with electric arc furnace slag as aggregate: mechanical and durability properties. Constr Build Mater 101:113–121

Faleschini F, Hofer L, Zanini MA, dalla Benetta M, Pellegrino C (2017b) Experimental behavior of beam-column joints made with EAF concrete under cyclic loading. Eng Struct 139:81–95

fib Model Code 2010 (2013) *fib* Model Code for Structures 2010. Ernst and Sohn, Berlin, Germany

Kemp EL (1986) Bond in reinforced concrete: behavior and design criteria. ACI J 83(7):50–57

Manso JM, Polanco JA, Losañez M, González JJ (2006) Durability of concrete made with EAF slag as aggregate. Cement Concr Compos 28:528–534

Oragun CO, Jirsa JO, Breen JE (1977) A reevaluation of test data on development length and splices. ACI J 74(3):114–122

Papayianni I, Anastasiou E (2010) Production of high-strength concrete using high volume of industrial by-products. Constr Build Mater 24:1412–1417

Pellegrino C, Cavagnis P, Faleschini F, Brunelli K (2013) Properties of concretes with black/oxidizing electric arc furnace slag aggregate. Cement Concr Compos 37:232–240

Pellegrino C, Faleschini F (2013) Experimental behavior of reinforced concrete beams with electric arc furnace slag aggregate. ACI Mater. J. 110–2:197–205

RILEM/CEB/FIP (1978) Bond test for reinforcing steel: 2. Pullout Test, Recommendation RC 6

Exterior RC Beam-Column Joints Made with Recycled Concrete: Experimental Behavior Under Lateral Cyclic Reversed Loading

Flora Faleschini[1,2(✉)], Mariano Angelo Zanini[1], Lorenzo Hofer[1], and Carlo Pellegrino[1]

[1] Department of Civil, Environmental and Architectural Engineering, University of Padova, Via Marzolo 9, 35131 Padua, Italy
flora.faleschini@dicea.unipd.it
[2] Department of Industrial Engineering, University of Padova, Via Gradenigo 6, 35131 Padua, Italy

Abstract. The use of recycled materials to cast reinforced concrete structures opens to new frontiers in developing high-performances and sustainable building materials. Recently, the use of electric arc furnace (EAF) slag as artificial aggregate allowed to produce cement-based materials characterized by high mechanical strength and good durability-related properties. However, few tests were carried out in literature dealing with full scale reinforced concrete structural elements. This paper shows the results of the first experimental campaign on two real-scale exterior beam-column joints made with EAF concrete, subject to cyclic lateral load and column axial load, and failing due to shear of the panel joint and yielding of steel bars in the beam. Results are analyzed in terms of hysteretic behavior, dissipated energy, ductility, and local panel joint behavior, and compared with the ones derived for a reference specimen, made with the same concrete mix proportions.

Keywords: Beam-column joints · Cyclic test · Electric arc furnace slag · Reinforced recycled concrete

1 Introduction

Re-utilization of industrial waste in civil works is becoming an intensive business, as it allows achieving several benefits for the environmental safeguard, both in terms of natural resources preservation and waste disposal reduction. In this context, several laboratory and limited in situ researches about electric arc furnace slag (EAF) re-use in cement-bound mixtures have been carried out during the last years. Due to its appearance as gravel, EAF slag has been applied satisfactorily in concrete, allowing to achieve at least the same or even better mechanical properties and durability than ordinary mixtures (Pellegrino et al. 2013; Santamaría et al. 2016). Few tests were also carried in real-scale structures: Pellegrino and Faleschini (2013) investigated the structural behaviour of reinforced concrete (RC) beams under four point bending tests.

M. di Prisco and M. Menegotto (Eds.): ICD 2018, LNCE 42, pp. 273–288, 2020.
https://doi.org/10.1007/978-3-030-23748-6_21

The study evidenced enhanced ultimate flexural and shear capacity for the beams casted with the EAF concrete. Kim et al. (2013) analyzed instead the ductility of spirally confined RC columns made with EAF concrete, also in this case obtaining at least similar or even better performance of the recycled concrete. In view of these results, some constructors have also enhanced the use of this type of slag in real construction works (Arribas et al. 2015), even if applications were limited to lightly-reinforced mass-concrete applications (i.e., foundations) and pre-cast concrete blocks.

The use of such slag is also allowed by the European standard EN 12620 (CEN 2008), which regulates aggregates use in concrete, and it classifies EAF slag as a manufactured aggregate. Some of the key-characteristics of this kind of material can be summarized with the following list: high-strength; high stiffness; high crushing and fragmentation resistance; heavyweight; volumetrically stable when correctly managed and pre-treated.

Hence, this study aims to improve the current knowledge about EAF slag concrete, through the evaluation of the structural behaviour of real-scale RC beam-column joints, tested against seismic-like action. Hence, three specimens were casted, two made with EAF concrete and one with a conventional mixture; the same reinforcement was used for all the specimens. The joints were tested under horizontal reversed cyclic loading, applied in quasi-static conditions. The objective of assessing the effect of using EAF slag on the overall structural behavior of the joints implies the necessity to highlight how concrete resisting mechanisms are influenced by such addition in the concrete mix, when it is used in this kind of structure. Accordingly, joints were designed to achieve the so-called beam-joint ($B + J$) failure, which is mainly governed by concrete properties, and particularly, by its compressive strength, as pointed out by Kim and LaFave (2007).

2 Materials and Methods

2.1 Raw Materials

EAF slag used in this work is produced in Padova, and it complies with the requirements in EN 12620 (2008). It is constituted by hard and dense crushed particles, whose chemical composition is made by a set of iron, calcium and silicon oxides (about 75%), plus minor amount of magnesium, aluminum and manganese oxides. Due to their composition, the average apparent density of the slag is about 3800 kg/m^3. The water absorption is similar to than of natural aggregates, and it is about 0.9%. Slag is used in three sizes: 4–8 mm, 8–12 mm and 8–16 mm. Other than slag, natural aggregates (NA) with siliceous origin were used in two sizes, a 0–4 mm river sand, and a 4–16 mm roundish gravel. The average apparent density of NA is about 2700 kg/m^3, and water absorption is about 1.1%. Cement type CEM II-A/L 42.5R, with high content of clinker and limestone, is used for concrete manufacturing. Additionally, a water-reducing admixture (WRA) was necessary to achieve the desired consistency.

2.2 Concrete Mixtures and Specimens Preparation

Two concrete mixes included EAF slag as coarse aggregate; one mix was casted with natural aggregates only, as a reference. The mixes were prepared using Bolomey aggregates proportioning, fixing water/cement ratio at 0.45, and cement dosage at 400 kg/m^3. Strength target was to achieve at least a cubic compressive strength of 45 MPa after 28 days, under standard curing conditions. Some trial mixtures were performed initially to define the best mix proportions (Faleschini et al. 2015). Lastly, the mixes reported in Table 1 were used to cast the beam-column joints: Mix E1 has the same proportions than the reference (Mix C), except for a slight increase in WRA dosage, necessary to achieve the S4 slump class, and a slight increase in the fines content, necessary to adjust the grading curve. Mix E2 was designed with a lower binder content (320 kg/m^3) than the other two concretes, lower WRA content and higher w/c ratio, aiming at producing a more environmentally sustainable mixture.

Table 1. Concrete mix details in (kg/m^3)

	Mix C	Mix E1	Mix E2
Cement	400	400	320
Water	180	180	180
w/c	0.45	0.45	0.5
NA - coarse	992	–	–
EAF slag	–	1142	1222
NA sand	812	992	1071
WRA	4.00	4.80	3.84

For each mix, about 800 L of concrete were mixed in an experimental plant sited in Calusco d'Adda (BG, Italy) owned by Italcementi-Heidelberg in November 2015, to prepare, other than the beam-column joints, the following specimens: twelve cubic specimens with 10 cm sides, for assessing concrete compressive strength at 1, 7, 28 days (cured under standard conditions) and 120 days (i.e., time of testing, and cured with the joints at T = 20 ± 2 °C and RH = 50 ± 5%); six cylindrical specimens with d = 100 mm and h = 200 mm, for assessing splitting tensile strength and secant elastic modulus, at 28 days.

Concerning casting operations, it is worth recalling that no significant differences between the reference and the EAF slag mixtures were experienced, obtaining in all the cases a fluid concrete consistency, and that no abrasion problems inside the mixer was observed. Figure 1 shows a phase of casting operations, where it is possible to see how EAF concrete well flows inside the formwork, put in horizontal position. Specimens dimension were: (a) beams with cross section 30 × 50 cm, length 250 cm; (b) columns with cross section 30 × 30 cm, and total height 410 cm. The reinforcement was made up of deformed bars of B450C class, characterized by an average f_y = 555 MPa and f_u = 639 MPa, and corresponding strains ε_y = 0.002 and ε_u = 0.104. Figure 2 shows the details of the joints dimension and reinforcement.

Fig. 1. Specimen casting

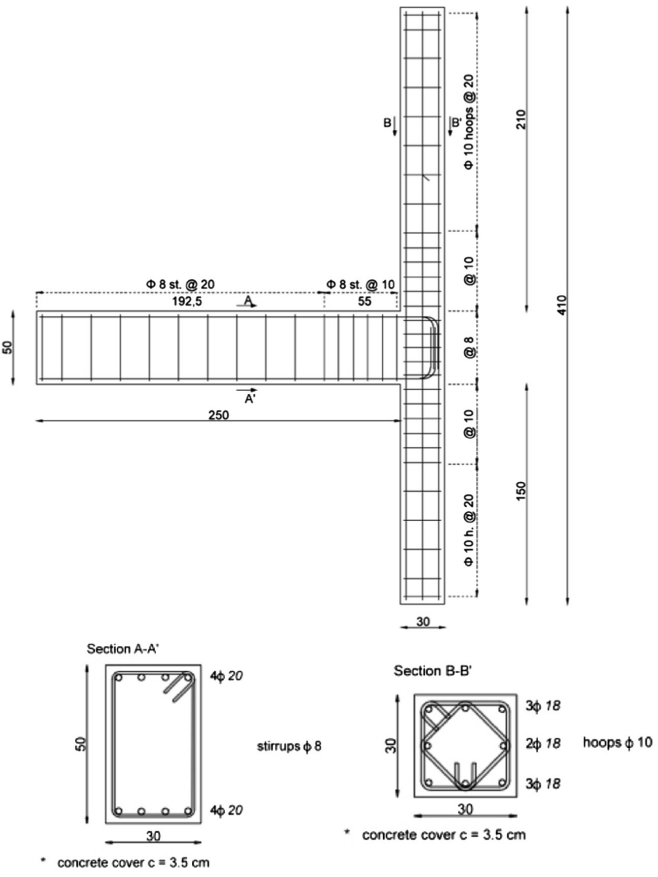

Fig. 2. Reinforcement details (measures are expressed in cm)

Specimens geometry and reinforcement aim to represent one-way exterior joints belonging to the first floor of a multistory RC building, with geometrical characteristics similar to common existing Italian structural types. Requirements related to a low ductility class (*CD B*) were used for joints design at the ultimate limit state (life safety) according to the Italian Building Code (2008), to better highlight the resisting mechanisms of concrete. It is worth noting that low ductility RC structures do not have to follow explicitly capacity design rules, but only adopt prescribed reinforcement details and minimum amount of steel.

2.3 Concrete Properties

All the concretes displayed a good workability, with a measured slump belonging to the S4 slump class, ranging between 19 and 20 cm, evaluated through the Abrams cone method.

Concerning physical and mechanical properties, Table 2 lists the results in terms of density, compressive and tensile strength, and elastic modulus. Results show that EAF concretes display higher specific weight than Mix C one, respectively about +12% and +15% for Mix E1 and E2.

Table 2. Concrete properties

	Mix C	Mix E1	Mix E2
Density (kg/m^3)	2420	2710	2796
$f_{c,cube}$ 1 day (MPa)	17	10	15
$f_{c,cube}$ 7 days (MPa)	44	48	31.7
$f_{c,cube}$ 28 days (MPa)	48.7	60.6	54.9
$f_{c,cube}$ 120 days (MPa)	49	62	55.5
$f_{c,t}$ (MPa)	3.59	4.25	3.45
$E_{c,s}$ (GPa)	32.67	42.55	42.19

The gain in compressive strength (at 28 days) is about +24% and +13% respectively for Mix E1 and E2 at 28 days. Mix E1, which has almost the same materials' proportions that the reference concrete, has a pronounced strength gain, which could be directly related to EAF slag use as coarse aggregate. Mix E2 is also characterized by an improved strength, even though binder content was reduced by 20% and the w/c ratio is increased: this means that such differences are balanced by slag mechanical properties and possibly also by a better quality of the interfacial transition zone (ITZ).

Tensile strength enhancement was also observed for concrete mixtures with EAF slag: Mix E1 displayed an increase of +18%, whereas Mix E2 was characterized by a similar strength than the conventional one (−4%).

Concerning concrete elastic properties, secant elastic modulus of EAF concretes was very similar, and in both the cases it was greater than the one of conventional mixture (+30% and +29% for Mix E1 and E2, respectively).

2.4 Test Setup

After 28 days, the joints were transported from the experimental plant of Calusco d'Adda (BG) to the Laboratory of the Dept. of Civil, Environmental and Architectural Engineering of the University of Padova. The specimens, originally placed horizontal, were then lifted and tested in the typical position, where they are placed in real frame structures. Figure 3 shows the lift operation of one of the joints.

Fig. 3. The RC EAF1 beam-column joint

Figure 4 shows the test set-up used in this work, that aimed to simulate a seismic-like action to the test specimens. A lateral load was applied close to the top of the column, to directly correlate the measured displacements of the joint to the inter-story drift of an entire frame. The position of the load application is chosen in order to obtain at least an inter-story height of 300 cm (in this case 384 cm, governed by laboratory constraints). Lateral load application was reversed cyclic quasi-static, with displacement control, following the ACI 374.1-05 (2014) recommendations. Thirteen successive displacement-controlled cycles were applied, and for each displacement, three fully reversed cycles were applied. Testing continued gradually, increasing until reaching at least a drift ratio equal to 3.5% (θ_{lim}), as stated by the normative. The chosen maximum drift allows to reach a state of near collapse for the tested joints. Load cycles were applied fixing a constant duration, equal to 360 s.

The axial force, which corresponds to the gravity loads induced by the upper floors in the prototype structure, is applied to the column and kept constant and equal to 400 kN for all the testing time. No P-Δ effects were induced, due to the external prestressing system used to apply the axial load in the column.

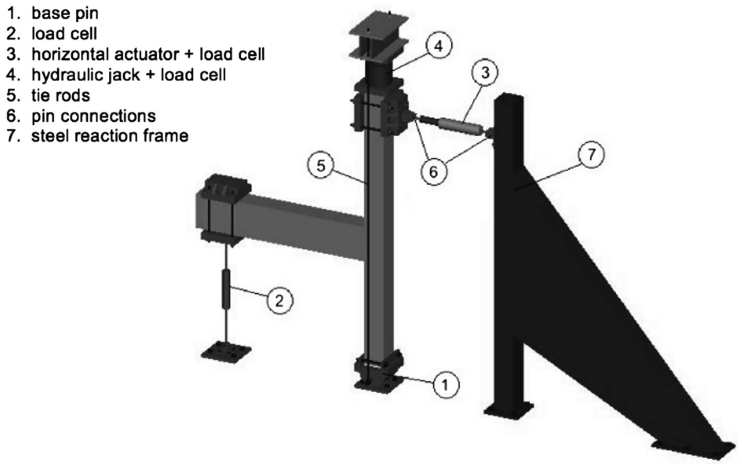

Fig. 4. Test-setup

Joints were instrumented to monitor relevant global displacement, loads, concrete and steel strains. The following instrumentation was used:

- Three load cells were used to measure the applied forces and the reaction at the beam free end (indicated with numbers 2–3–4 in Fig. 4);
- Eight linear potentiometers were applied on the panel joint, four on the beam and four on the columns, close to the intersection to monitor concrete strains (see Fig. 5);

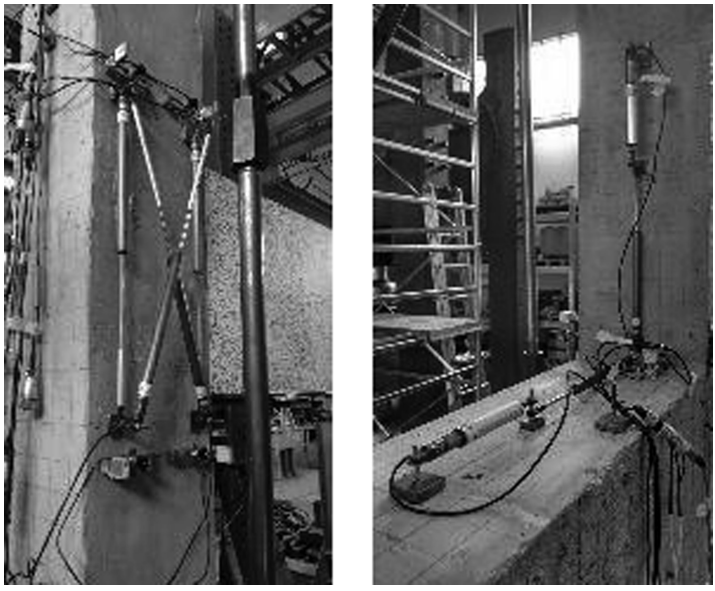

Fig. 5. Linear potentiometers and strain transducers onto the panel joint and applied to the column and beam

- Two wire-transducers were applied respectively to the top of the column and to the beam free end, to evaluate global displacements (close to numbers 2–3–4 in Fig. 4);
- Eight strain transducers were placed on the panel joint surface to monitor concrete strains (see Fig. 5);
- Seventeen strain gages were used to measure steel reinforcement strains: four were placed on the longitudinal beam bars, two on beam stirrups, five on the longitudinal bars of the column, and six on the hoops of the column (see Fig. 6).

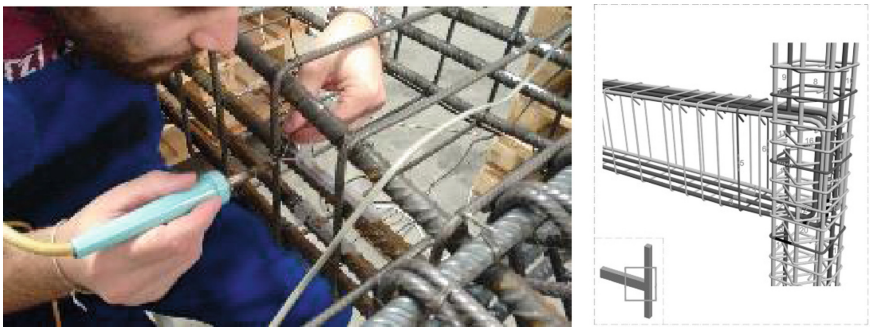

Fig. 6. Strain gages application and disposition

3 Results

3.1 Failure Mode and Cracks Pattern

Joint panel shear failure was induced through testing exterior joints with stiff beams, however this being reached only after steel yielding. During the tests, shear-induced diagonal cracks and concrete cover spalling occurred at the ultimate drift ratio, for all the test specimens tested. Sub-vertical cracks appeared also along the beam, located particularly close to the connection with the column. The failure mechanism is the so-called $B + J$ type, a mixed mechanism in which diagonal cracking in the joint panel was accompanied by flexural damage in the beam. Yielding of steel reinforcement bars in the beam occurred before than the cracking in the panel joint.

In the joint made with Mix C, a large number of cracks were exhibited since the 4th cycle ($\Delta = \pm$ 6 mm, $\theta = 0.15\%$) in the beam, starting from the connection with the column, and then moving to the free-end. Their size continued to grow during the test, whereas their spacing reduced up to 5–7 cm (in the region close to the column) at the end of the load history. The first crack in the panel joint occurred at the 5th cycle ($\Delta = \pm$ 9 mm, $\theta = 0.23\%$); significant cracking however appeared after the 10th cycle ($\Delta = \pm$ 50 mm, $\theta = 1.3\%$), resulting then in concrete spalling at the end of the test. Limited column cracking started around the 10th cycle too, being more pronounced in the upper semi-column than in the lower.

In both the joints made with EAF concrete, no cracks were visible up to the 6th cycle ($\Delta = \pm$13 mm, $\theta = 0.34\%$); first cracking occurred in the beam, also in these

cases starting from column interface and increasing their size and number, during the load cycle, along the element. The first cracks in the panel joint occurred at the 8th cycle ($\Delta = \pm 25$ mm, $\theta = 0.65\%$), being diagonal and starting from the corners between the beam and columns. At the end of the test, many cracks developed in the panel joint of both tested specimens, which displayed also concrete spalling on the external side, opposite to the beam location; limited column cracking started instead around the 10th cycle. Compared to the reference joint, in the panel joint of the specimens made using EAF slag, and particularly in the one made with Mix E1, concrete seemed more integer after the test, displaying a reduced number of cracks; in the column, the cracked region is more confined close to the panel joint.

A map of the damage in the panel joint is displayed in Fig. 7, as a result of an inspection of the ultrasound pulse velocity (UPV) after the end of the test.

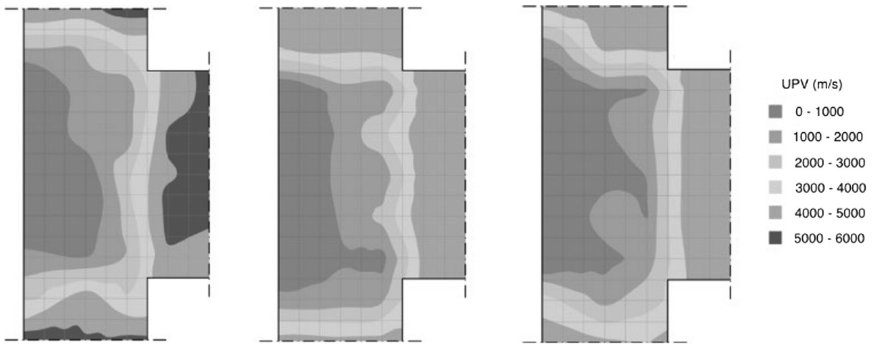

Fig. 7. Damage of the panel joint, respectively for the joints made with mix C, mix E1 and mix E2

3.2 Load-Displacement Response

Figure 8 shows the hysteresis curves of the tested specimens, with also the values of the maximum attained loads in both the loading directions. The maximum drift value reached by all the specimens is about $\theta = 3.9\%$, even larger than the recommended limit of $\theta = 3.5\%$. Curves' shape is similar both in the positive (push condition) and negative (pull) branch, for all the tested specimens. Joints made with EAF slag concrete were characterized by higher ultimate loads, attained at reduced displacement than in the control specimen, only in the right side of the graph. Instead, in the left side, higher ultimate loads are attained at the same displacement cycle than in the reference joint.

The $B + J$ failure mode induced limited deformation capacity of the elements, due to the strength reduction occurred as a consequence of panel joint cracking. At the last applied cycle, all the specimens displayed a strength reduction of about 30% with respect to their maximum load. The enhancement of the maximum load in both EAF slag specimens is about + 7%. Joints made with EAF concretes had a very close experimental behavior, reaching almost the same maximum load and displacement, even though concrete mixtures differ both in w/c ratio and cement dosage.

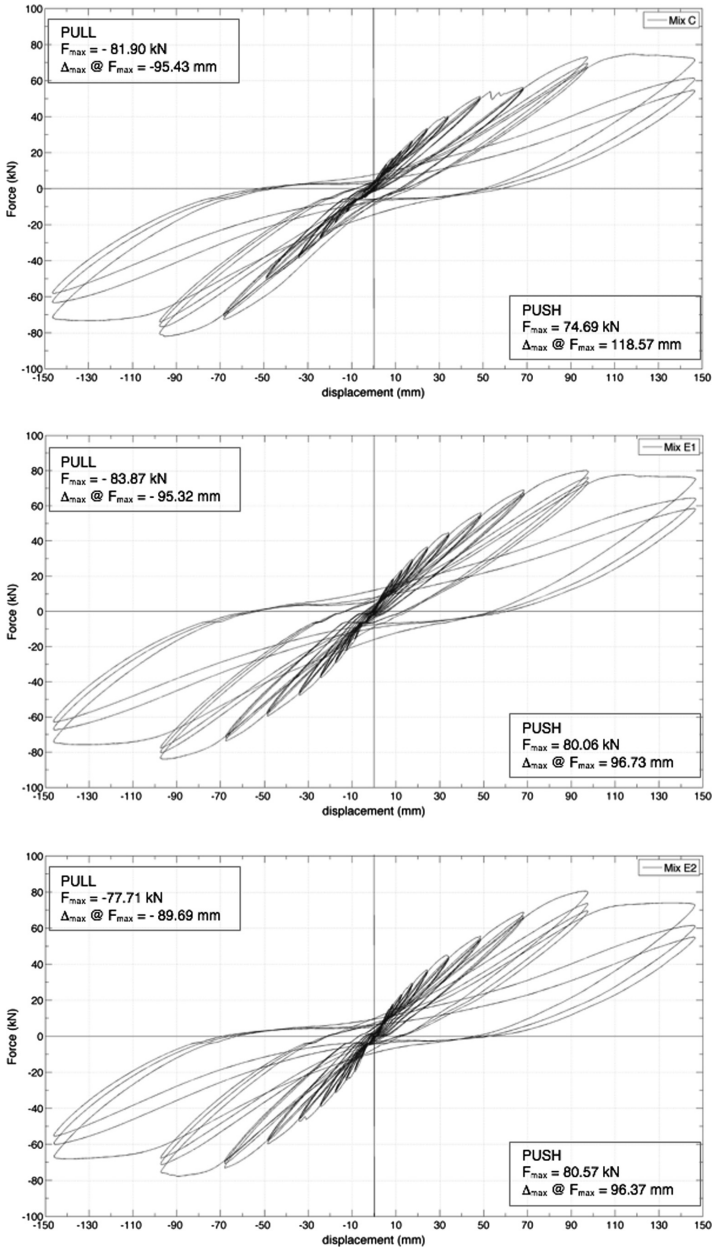

Fig. 8. Lateral load–displacement hysteretic response of the tested specimens

3.3 Stiffness Decay

All the joints displayed a fast stiffness decay, typical of the shear failure mechanism, after reaching the maximum load. Pinching effect is indeed responsible of fast stiffness decay when shear-induced failure is involved in the cyclic behavior of RC beam-column joints, as a consequence of repeated opening and closing of cracks.

Initial stiffness is estimated being about 2.8 kN/mm, 3.25 kN/mm and 3.05 kN/mm respectively for specimens made with Mix C, E1 and E2. After the first applied load cycles, stiffness decay is very similar for all the tested samples, being about −40% at a drift value of $\theta = 0.3\%$. Then decay is more pronounced as drift increases, being between −56 and −59% at $\theta = 1\%$, and at the end of testing it is equal to −87% for all the joints. The initial stiffness difference between the specimens tends to decrease as drift values increase, leading to similar behavior of all the tested specimens after the elastic phase.

3.4 Ductility

Joints ductility can be quantified through a normalized displacement index μ, which is the ratio between the ultimate displacement Δ_u and displacement at the yield point Δ_y. Ultimate displacement is typically assumed at 0.8–0.9 of the peak load (Paulay 1989), whereas yield displacement can be estimated from a bilinear curve, which is interpolating the experimental curve, assuming an equivalent elastic-perfectly plastic response. Here, for the definition of the equivalent response, two criteria have been adopted: the area under the bilinear curve is the same of that under the experimental curve, and the distance between them is minimized. Among all the curves complying with first requirement, the one for which the mean absolute error (MAE) is minimum has been chosen. Additionally, here Δ_u was assumed as the displacement corresponding to the 10% loss of the peak load (0.9 Fmax).

The calculated displacement ductility index $\mu = \Delta_y / \Delta_u$ increases in the specimens made with EAF slag, being 2.58 and 2.71 in Mix E1 and Mix E2; instead its value is 2.37 in Mix C.

3.5 Energy Dissipation

One of the key parameters for analyzing earthquake-resistant structures relates to their ability to dissipate energy during their reversed cyclic loading. Figure 9 shows the cumulated dissipated energy E_d versus drift ratio θ for the tested specimens.

Another parameter that can be used to quantify the dissipated energy is the equivalent viscous damping ratio ξ_{eq}, which at each i-th cycle represents a "normalized" value of E_d, evaluated according to Eq. 1:

$$\zeta_{eq,i} = \frac{1}{2\pi} \cdot \frac{E_{d,i}}{E_i} \tag{1}$$

In the above equation E_i represents the available energy, which is the product of the applied displacement at the top of the column and the corresponding lateral force.

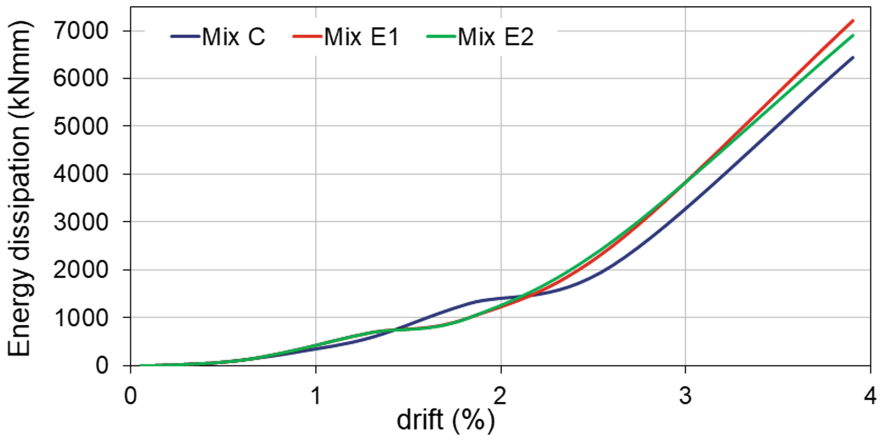

Fig. 9. Cumulated dissipated energy vs. drift

At the end of the test, ξ_{eq} is equal to 19.6%, 21.0%, and 20.6% for the specimens made with Mix C, Mix E1 and Mix E2, respectively.

3.6 Reinforcement Steel Strains

The performance of the local behavior of the joints can been evaluated through the monitoring of strains in steel reinforcement bars. Here, results of longitudinal reinforcement in the beam, close to the panel joint, and transversal bars inside the panel joint are reported. Figure 10 shows the reinforcement bars strain vs. time, for the monitored longitudinal beam bars (bottom reinforcement) and panel joint transverse bars: the horizontal line indicates the value of bars yield stress.

First yielding of longitudinal steel bars in the beam occurred around the 9th and 10th loading cycles in the joint made with Mix C, at about Δ = +44.52 mm (F = 45.91 kN) in the push condition, and at −43.04 mm (F = −53.67 kN) in the pull one. The joint made with Mix E1 displayed the first yielding of steel longitudinal bars in the beam at about Δ = +44.41 mm (F = 53.29 kN) in the push condition, and at −39.39 mm (F = −51.66 kN) in the pull one. Lastly, the same conditions were reached at Δ = +44.89 mm (F = 53.51 kN) in the push loading, and at – 42.79 mm (F = −55.17 kN) in the pull one, for the joint made with Mix E2.

Yielding of transversal reinforcement inside the panel joint was reached at increased values of the applied displacement, around the 10th and 11th loading cycles in the joint made with Mix C and Mix E2, and in the 12th cycle for the joint made with Mix E1. In the conventional specimen, the central stirrup first yielded at Δ = −66.20 mm (F = −71.66 kN), in the pull condition. The second joint made with Mix E1 reached the same condition at Δ = +97.53 mm (F = 79.82 kN), during positive loading, whereas the latter, made with Mix E2, at Δ = −63.62 mm (F = −70.95 kN), during negative loading.

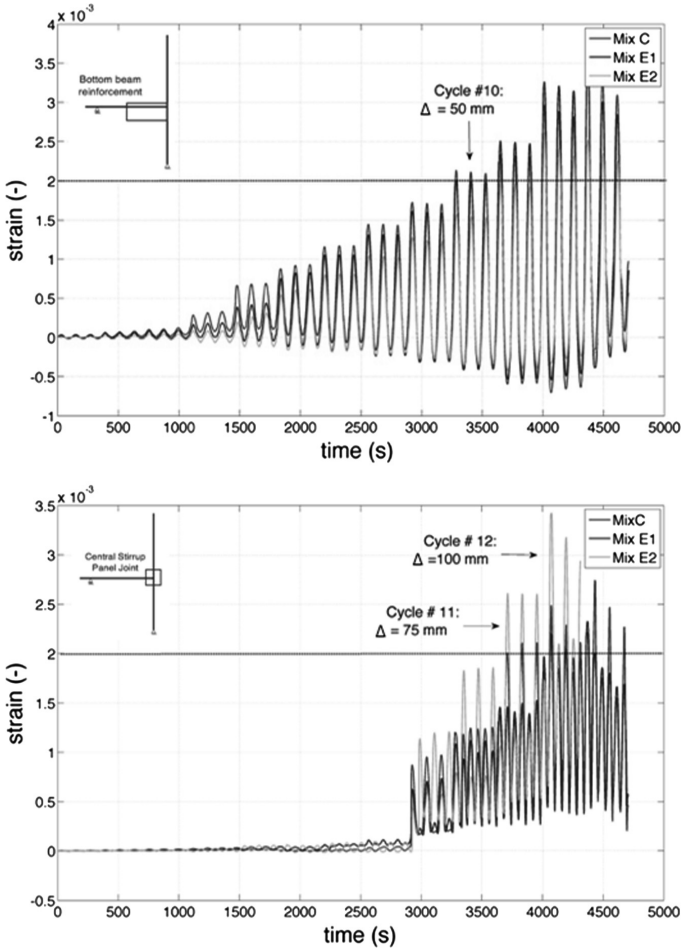

Fig. 10. Steel strain vs. time

3.7 Joint Shear Strain and Stress

Joint shear stress-strain relationship can be also used to assess the experimental local behavior of the tested joints. For the evaluation of joint shear strain, the instrumentation shown in Fig. 5 for concrete strain monitoring in the panel joint has been employed, as done also in other experimental tests carried out by Hassan (2011) and Ricci et al. (2016).

For each joint face, the joint shear strain $\gamma_{s,i}$ (Eq. 2) was evaluated using a certain set of strain measurements: ε_x and ε_z are respectively the translational strains in the horizontal and vertical directions, $\varepsilon_{\theta s}$ is instead the strain in the diagonal direction, defined by an angle θ_s, measured from the horizontal axis. Beam displacement sign convention is maintained for shear strain, i.e. negative joint shear strain corresponds to downward beam displacement.

$$\gamma_{(s,i)} = (\varepsilon_{\theta s} - \varepsilon_x cos^2\theta_s - \varepsilon_z sen^2\theta_s)/(sen\theta_s cos\theta_s) \quad (2)$$

Joint shear stress is obtained as follows: first, joint shear V_{jh} is calculated according to Eq. 3, where T is the tensile force acting in beam longitudinal steel reinforcement, and V_c is the shear force acting in the column:

$$V_{jh} = T - V_c \quad (3)$$

T is calculated starting from the value recorded by the load cell V_b located at the beam free end, through Eq. 4:

$$T = (V_b \cdot L_b) / 0.9\, d \quad (4)$$

where L_b is the beam span, and d is the effective depth of beam section. The joint stress (v_j) is then evaluated as the acting shear force divided per the joint area A_c (Eq. 5):

$$v_j = V_{jh} / A_c \quad (5)$$

Figure 11 shows the stress-strain relationships obtained for the tested joints: the curve of the joint made with Mix C is quite symmetric, whereas the specimens made with Mix E1 and Mix E2 displayed an asymmetric behavior, attaining higher deformation in the negative branch. The peak point in the positive loading curve was reached almost at the same joint strain for all the specimens, whereas in the negative curve joint made with Mix E1 reached the peak point at a slightly higher deformation than other samples. Maximum shear stress in the positive curve is about 8.4 ± 0.02 MPa, whereas in the negative is about 8.25 ± 0.4 MPa. After the peak point, a reduction in joint strength is observed in all the specimens. The obtained local behavior agrees with the global one: joints made with EAF slag attained higher shear stress, not only in the peak values, but particularly in the first loading cycles, where the effects of concrete properties are more relevant.

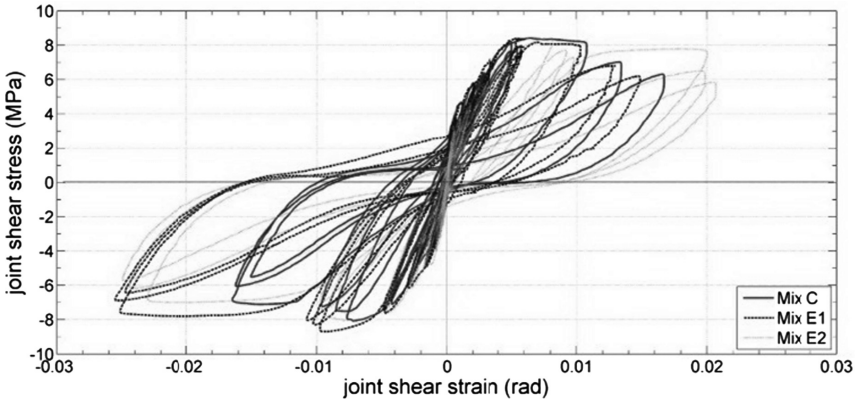

Fig. 11. Joint shear stress vs strain

4 Conclusions

This work summarizes some results of an experimental campaign dealing with the behavior of beam-column joints made with EAF concrete under cyclic loading. To better highlight the influence of EAF slag use as recycled aggregate in concrete mixtures, joints were designed to achieve a beam-joint ($B + J$) failure, induced by shear failure of the panel joint, which is mainly governed by concrete compressive strength, and as a consequence, coarse aggregates properties.

Promising results were achieved, that demonstrated that the use of EAF concrete allows the joints to attain higher loads than the control specimen, even when the mix contains significantly less amount of cement and higher water/cement ratio. Stiffness decay during load history was very similar for all the tested specimens, even if initial secant stiffness is higher in the EAF slag joints than in the control one. The dissipated energy and ductility are very similar for all the specimens: a slight increase is however observed for the joints made with EAF concrete. Concerning panel joint integrity, a reduced cracking pattern was visible, after the test, in the specimen made with E1 concrete.

Acknowledgements. The authors would gratefully acknowledge Heidelberg-Italcementi Group SpA and ZeroCento Srl for supplying raw materials and for their economical support. Additionally, Eng. Pietro Lotti, Tiziano Gheno, Emanuele Mantesso and Paolo Bragolusi are sincerely acknowledged for their help during the experimental campaign.

References

ACI 374.1-05 (2014) Acceptance criteria for moment frames based on structural testing and commentary

Arribas I, Santamaría A, Ruiz E, Ortega-López V, Manso JM (2015) Electric arc furnace slag and its use in hydraulic concrete. Constr Build Mater 90:68–79

CEN (2008) EN 12620 aggregates for concrete. Comité Europeen de Normalisation, Brussels, Belgium

Faleschini F, Fernández-Ruíz MA, Zanini MA, Brunelli K, Pellegrino C (2015) High performance concrete with electric arc furnace slag as aggregate: mechanical and durability properties. Constr Build Mater 101:113–121

Hassan WM (2011) Analytical and experimental assessment of seismic vulnerability of beam–column joints without transverse reinforcement in concrete buildings. PhD dissertation. Berkeley, California, USA

Kim S-W, Kim Y-S, Lee J-M, Kim K-H (2013) Structural performance of spirally confined concrete with EAF oxidising slag aggregate. Eur J Environ Civ Eng 17(8):654–674

Kim J, LaFave JM (2007) Key influence parameters for the joint shear behaviour of reinforced concrete (RC) beam-column connections. Eng Struct 29(10):2523–2539

Italian Building Code (2008) DM 14/01/2008: Norme Tecniche per le Costruzioni

Paulay T (1989) Equilibrium criteria for reinforced concrete beam–column joints. ACI Struct J 86(6):635–643

Pellegrino C, Cavagnis P, Faleschini F, Brunelli K (2013) Properties of concretes with black/oxidizing electric arc furnace slag aggregate. Cement Concr Compos 37:232–240

Pellegrino C, Faleschini F (2013) Experimental behavior of reinforced concrete beams with electric arc furnace slag aggregate. ACI Mater J 110–2:197–205

Ricci P, De Risi MT, Verderame GM, Manfredi G (2016) Experimental tests of unreinforced exterior beam–column joints with plain bars. Eng Struct 118:178–194

Santamaría A, Rojí E, Skaf M, Marcos I, Gonzalez JJ (2016) The use of steelmaking slags and fly ash in structural mortars. Constr Build Mater 106:364–373

Strain Measurement in a Reinforced Concrete Beam Using Embedded Smart Concrete Sensors

A. D'Alessandro(✉), A. Meoni, F. Ubertini, and A. Luigi Materazzi

Department of Civil and Environmental Engineering, University of Perugia, Perugia, Italy
antonella.dalessandro@unipg.it

Abstract. The paper is aimed at investigating the use of embedded smart concrete sensors for monitoring the strain in full-scale reinforced concrete beams. The new sensors are made of the same matrix material of the concrete elements to be monitored and can be easily embedded into structural components before casting, thus achieving a durable and distributed sensing solution for structural health monitoring purposes. The self-monitoring ability is obtained through the dispersion of nano-metric conductive carbon-based fillers which induce new piezoresistive properties. In this study, a set of smart concrete sensors was embedded on top of a simply supported reinforced concrete beam and the dynamic performance of the element was evaluated, by measuring the variation in electrical resistance of the smart concrete sensors and benchmarked against measurements carried out with traditional strain gauges. The results of such comparisons demonstrate that the new sensors are apt for strain monitoring in RC structural components.

Keywords: Reinforced concrete beams · Smart concrete · Structural health monitoring · Strain measurement · Modal identification

1 Introduction

Novel nano- and micro-cementitious materials appear promising in the literature scenario of innovative research programs due to their interesting properties suitable for several applications (Modal et al. 2008; Pisello et al. 2017). In the field of civil engineering several studies concern the enhanced mechanical capabilities they exhibit (Li et al. 2003; Metaxa et al. 2009). Further innovative researches investigate multifunctional applications. Among them, the self-sensing ability appears promising. Such a property allows the development of a self-monitoring system for concrete structures. Indeed, the concrete elements could become strain sensors if doped with piezoresistive particles or instruments with smart cementitious embedded sensors. Such sensors are made with the same matrix material of the structures they are embedded in, thus achieving a durable and distributed sensing solution for structural health monitoring purposes (Coppola et al. 2011; Han et al. 2007). The self-monitoring capability is achieved through the introduction of conductive piezoresistive micro- or nanoparticles into the structural material. The variation of the strain is detected through the

M. di Prisco and M. Menegotto (Eds.): ICD 2018, LNCE 42, pp. 289–300, 2020.
https://doi.org/10.1007/978-3-030-23748-6_22

observation of electrical resistance variation between two embedded electrodes subjected to a stabilized constant tension. The dielectric nature of the matrix material determines a drift of the electrical signal in unloaded conditions, called polarization effect, which can however be reduced through a preliminary application of a constant tension (Cao and Chung 2004). A growing interest in smart cementitious materials has been reported throughout scientific literature (Rainieri et al. 2013; Han et al. 2011; Azhari and Banthia 2012; Camacho-Ballesta et al. 2016) above all about the characterization of their peculiar properties. However few works concerning structural elements made by using these materials are available. The Authors started a research about cementitious materials doped with carbon-based nanometric fillers investigating, in the first step of the work, the self-sensing capabilities of the materials and analyzing the issues related to the fabrication of sensors with suitable characteristics of homogeneity, repeatability and scalability (Materazzi et al. 2013; Ubertini et al. 2016; Downey et al. 2017). After the analysis of the results of the first tests, the Authors investigated the application of the smart sensors with better performances to structural concrete elements (D'Alessandro et al. 2017). The present paper describes the setup and the results of a experimental campaign carried out on a reinforced concrete beam with seven embedded cementitious smart sensors doped with carbon nanotubes (CNTs). With respect to their previous works, the Authors extended the investigation to all the manufactured sensors and to all the embedded sensors, comparing the vibration results to those obtained from different identification approaches. Section 2 reports the characteristics of the materials used for the fabrication of the self-sensing materials, and the description of the experimental setups of the tests. Section 3 describes the electrical and electromechanical tests, while Sect. 4 reports the results. Section 5 comments the experimental campaign and concludes the paper.

2 Materials and Experimental Methods

2.1 Fillers

The fillers used as doping for the cementitious matrix of the sensors were Arkema carbon nanotubes (CNTs). Their carbon content is more than 90% and their apparent density is between 50 and 150 kg/m^3. They are multi-walled with a mean diameter of 5–10 nm and length of 200–500 μm. Their peculiar aspect ratio makes them particularly suitable for electrical applications. Figure 1(a) shows that they appear as a black powder, while Fig. 1(b) is a micrograph of an aqueous suspension of CNTs obtained using a Scanning Electron Microscope (SEM) with a magnification of 100 kX. In the SEM picture the dimensional characteristics of the CNTs are clearly visible. The nanometric dimensions of the fillers and the Van der Waals forces which exist among the nanotubes determine the agglomeration of the particles in normal conditions: an optimized dispersion procedure was developed to achieve a material more homogeneous and isotropic.

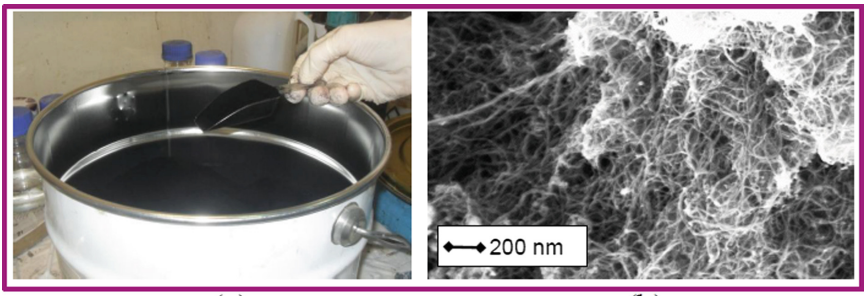

Fig. 1. (a) Appearance of carbon nanotubes; (b) Microscope enlargement of a sample of carbon nanotubes.

2.2 Cement-Matrix Sensors with CNTs

Table 1 shows the components of the cement-based materials doped with CNTs used to prepare the smart sensors. The water/cement ratio was 0.45. The cement was 42.5 pozzolanic. The amount of the CNTs was the 1% of the weight of the cement. The same quantity of a Lignosulfonic acid sodium salt was introduced in the mix design to improve the filler dispersion. Also a 0.5% of plasticizer based on polycarboxylate ether polymers was added to the dough in order to obtain a satisfactory workability.

Table 1. Mix design of cementitious material with carbon nanotubes.

Components (kg/m^3)	Cement-based sensors
Cement	1277
Water	575
CNTs	12.8
Dispersant	12.8
Plasticizer	6.3
w/c ratio	0.45

Figure 2 shows the preparation process of the sensors and of the RC beam. First, the sensors were formed and cured and then they were embedded on the top surface of a RC beam during its molding.

The CNTs were dispersed into the water through the addition of a dispersant and the sonication of the suspension for 30 min (Fig. 2(a)–(b)).

Then the dispersed aqueous suspension, the cement and the plasticized were manually mixed (Fig. 2(c)).

Successively, the dough was poured into oiled molds and four stainless steel nets were embedded symmetrically on the top surface of the samples. The inner nets were placed at a distance of 2 cm, while the outer ones at a mutual distance of 4 cm. The nets consisted of wires with a nominal diameter of 1 mm and placed at a mutual distance of 0.6 mm. Twelve cubes with sides of 51 mm were fabricated.

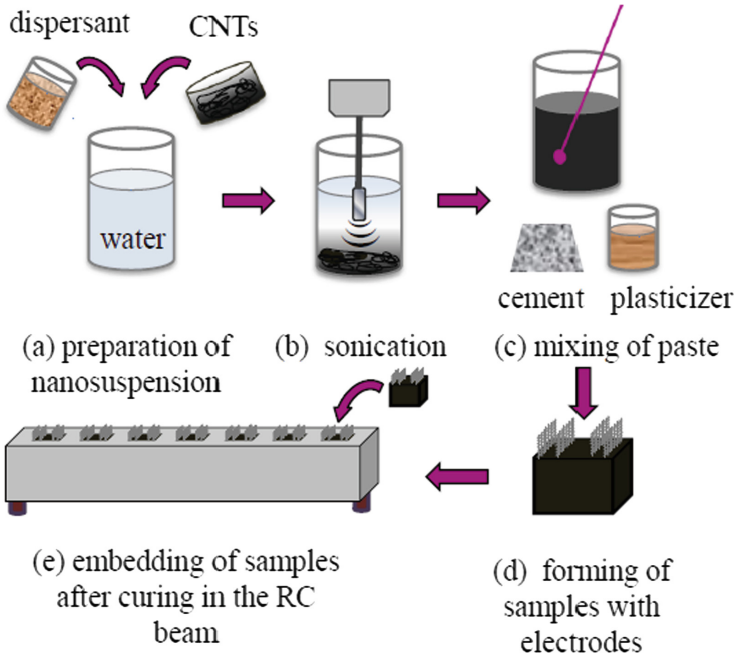

Fig. 2. Preparation process of a reinforced concrete beam with embedded cementitious sensors

The samples were unmolded after 48 h and cured in laboratory conditions for 28 days (Fig. 2(d)). After curing, the samples were instrumented with two strain gauges 2 cm long with a Gauge Factor of 2.1, placed on opposite lateral sides. Then the single sensors were investigated through electrical and electromechanical tests.

2.3 Reinforced Concrete Beam Preparation with Embedded Cementitious Sensors

After the analysis of the electrical characteristics of the samples, seven of them were embedded (instrumented with the strain gauges) on the top surface of a RC beam, during the concrete casting, at a mutual distance of 25 cm. Figure 3 shows the dimensions of the RC beam and the deployment of the cementitious sensors. The beam was manufactured using ordinary concrete with Portland cement and a characteristic strength of 30 MPa. The beam had a square section with sides of 25 cm and length of 220 cm. It was simply supported through two steel plates embedded on the bottom part of the beam, at a distance of 200 cm. The longitudinal reinforcement consisted of 6 steel rebars with a diameter of 8 mm (2 upper and 4 lower) and steel stirrups with diameter of 8 mm placed - in the central part of the beam - at a mutual distance of 160 mm, reduced to 100 mm near the supports. Figure 4 describes the geometry of the cementitious sensors (Fig. 4(a)), their application on the upper surface of the RC beam (Fig. 4(b)) and the appearance of the RC beam with embedded cementitious sensors after curing.

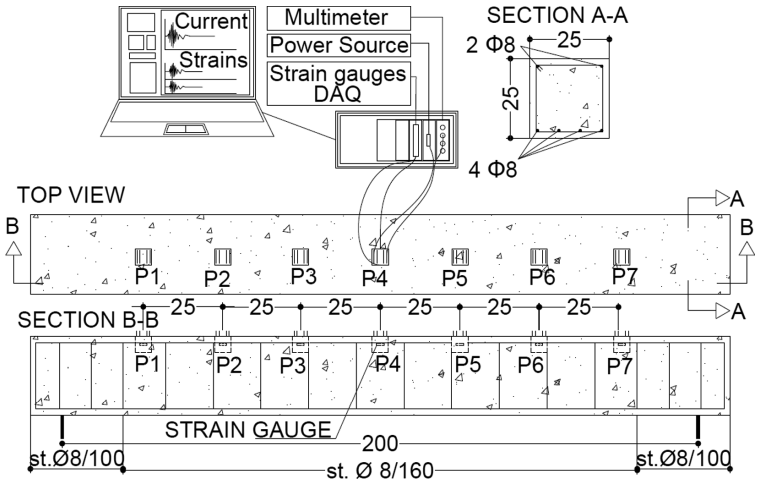

Fig. 3. Experimental setup of the reinforced beam instrumented with embedded sensors (measures in cm).

2.4 Experimental Setup

For the electrical, electromechanical and vibration tests, a stabilized tension was applied to the internal electrodes, placed at a mutual distance of 20 mm, through a PXIe-1073 chassis device with the module 4130. The electrical measurements were carried out using another PXI module, n. 4071. The electrical output of the traditional strain gauges was recorded through PXI device, too. The electrical current of each sensor was measured after 6000 s of application of a tension of 5 V, in order to reduce the polarization effect. The electrical resistance was evaluated through the relation expressed in (1).

$$R(t)\big|_{t=tp} = \frac{V}{I(t)\big|_{t=tp}} \tag{1}$$

where V and $I(t)$ are the applied constant voltage and the measured variation of current intensity over time, respectively, and tp is the polarization time.

The electromechanical tests were carried out using a servo-controlled universal dynamic testing machine, model IPC Global UTM14P (Fig. 5). In order to investigate the sensitivity of the cementitious sensors, both cyclical and sinusoidal loads were centrally applied on the section of the samples. The first were applied with a 1 kN/s speed, up to a load of 2 kN; the second ones had increasing frequencies from 0.25 to 8.0 Hz, with loads between 0.5 and 1.5 kN.

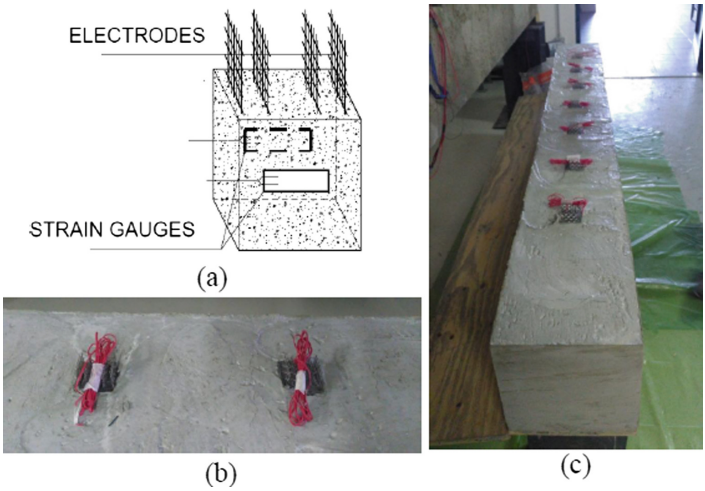

Fig. 4. (a) Sketch of an instrumented sensor; (b) Sensors embedded into the RC beam; (c) RC beam with embedded sensors, after curing.

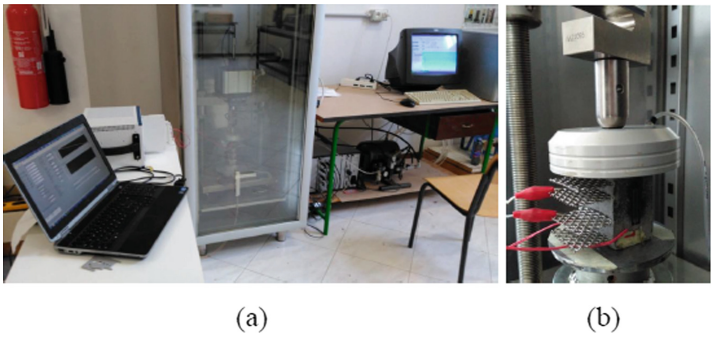

Fig. 5. (a) Experimental setup of the compressive tests on cementitious sensors; (b) detail view of a sensor.

3 Experimental Campaign

The experimental campaign consisted in electrical and electromechanical tests on single nanomodified cementitious sensors, and in vibration tests on the RC structural beam with embedded sensors.

3.1 Electrical and Electromechanical Tests on the Cementitious Sensors

Electrical tests were aimed at investigating the conductive properties of the material and the issues related to the electrical measurements. As mentioned before, DC current produced a drift of the signal. Electromechanical tests, with application of both cyclical

and dynamic loads, permitted to evaluate the sensitivity of each sensor through the achieving of their gauge factors *GF*:

$$GF = -\frac{\Delta R/R_0}{\varepsilon} \tag{2}$$

where ΔR was the incremental variation in electrical resistance, R_0 the unstrained electrical resistance, and ε the measured axial strain, (positive in compression). Figure 6 shows the two different load histories for electromechanical tests on single cementitious sensors.

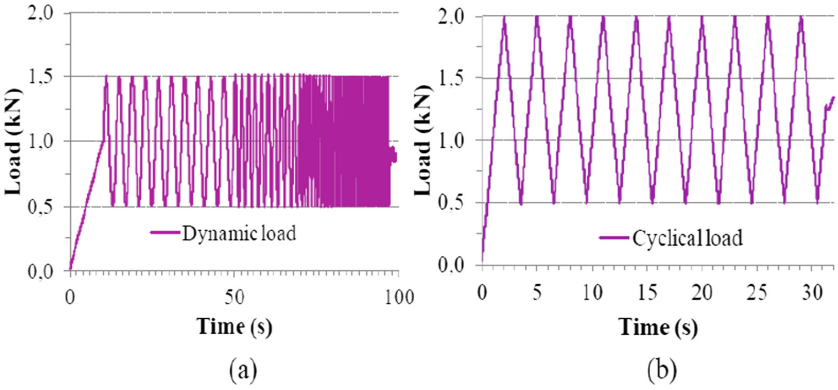

Fig. 6. (a) Cyclical and (b) dynamic loads applied on the single sensors.

3.2 Vibration Tests on the RC Beam with Embedded Cementitious Sensors

Vibration tests were performed after a polarization of thirty minutes, applying random hits in time and space with an instrumented hammer. During the tests, a voltage of 2.5 V was provided to each sensor. The current was recorded with a sampling rate of 1000 Hz. The tests investigated the performance of all the seven sensors embedded into the RC beam, of the strain gauges placed on the sensors and of the piezoelectric accelerometers applied on the extrados of the beam. The data obtained from such tests permitted to evaluate the principal modal frequencies of the structural element. The results of the smart cementitious sensors were compared to the ones obtained through traditional strain gauges, piezoelectric accelerometers and analytical calculation.

4 Results

4.1 Electrical and Electromechanical Tests on the Cementitious Sensors

Figure 7 shows the values of electrical resistance obtained through the electrical tests on the 12 samples. The mean value of such feature was 614.3 Ω while the standard

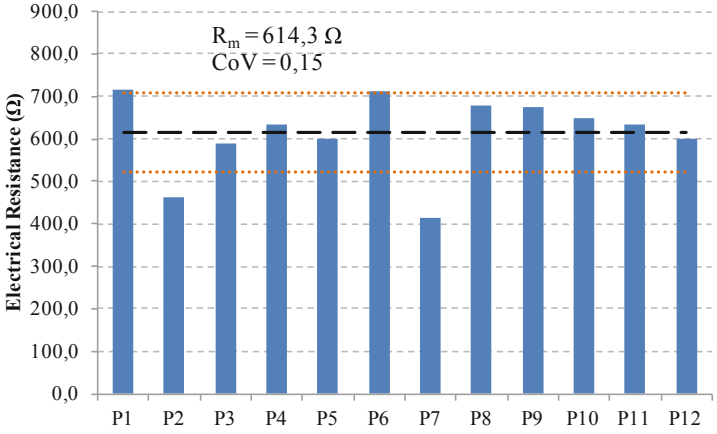

Fig. 7. (a) Variation of electrical resistance of the different cementitious samples with average value and standard deviation.

deviation was 92.7 Ω. The resulting Coefficient of Variation CoV was 0.15. The series of new cementitious sensors demonstrated a reasonable repeatability, whereby the CoV of variation was very similar to that one of concrete-like materials. Table 2 shows the values of GF of all the cementitious samples, obtained with both cyclical and dynamic tests. Their mean value, standard deviation and coefficient of variation are 18.47, 25.22, 1.37 and 25.36, 43.65, 1.72, respectively.

The results demonstrate a higher scatterin of the values of GF with respect to those of the unstrained resistance, thus demonstrating the importance of a specific calibration of the sensors before their embedding into the structural element.

4.2 Vibration Tests on the RC Beam with Embedded Cementitious Sensors

Figure 8 shows examples of time histories of strain and normalized variation of electrical resistance obtained from sensors embedded in different position of the RC beam during vibration tests. Signals have been filtered in order to eliminate the residual drift after the polarization phase. Despite signal noise due to the high sampling frequency used to acquire the data, hammer hits are clearly visible in all the considered outputs. In order to demonstrate the strain sensing capability of the embedded sensors, Fig. 9 reports the comparison between the average strain, acquired by two strain gauges placed on the lateral sides of the sample P4 and the strain computed from the filtered electrical output provided by the sensor, using Eq. (2). By overlapping the signals, a good agreement between acquired and estimated strain can be noted. The spectral analysis carried out on the outputs of the vibration tests allowed to identify the modal frequencies of the beam. Figure 10 reports the PDS of the sensors P3, P4 and P6 and of the corresponding strain gauges. The modal frequencies were compared to the results obtained through the analytical approach and from the traditional strain gauges and accelerometers. Table 3 demonstrates the good agreement of the results.

Table 2. GF of the samples obtained from the measurements during cyclical and dynamic loads.

Type of sample	GF	
Cyclical test	Dynamic test	
P1	25.95	39.94
P2	1.99	3.63
P3	5.43	8.26
P4	22.56	10.73
P5	8.79	13.23
P6	28.38	32.95
P7	1.17	1.10
P8	1.78	1.54
P9	26.40	23.32
P10	1.47	2.24
P11	90.77	158.06
P12	6.94	9.31
Mean value	18.47	25.36
Standard Deviation	25.22	43.65
CoV	1.37	1.72

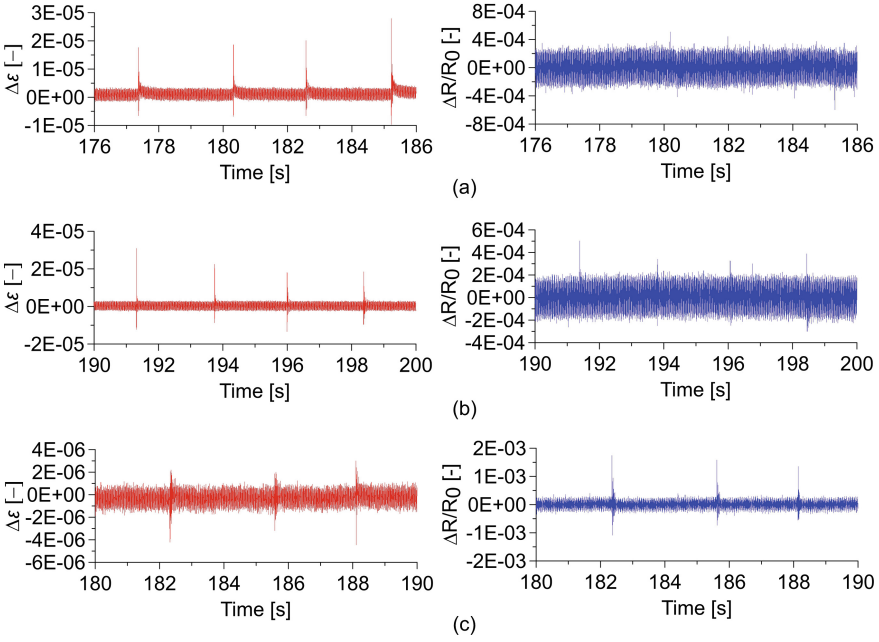

Fig. 8. Examples of time histories of strain and normalized variation of electrical resistance during vibration tests for (a) P3, (b) P4 and (c) P6.

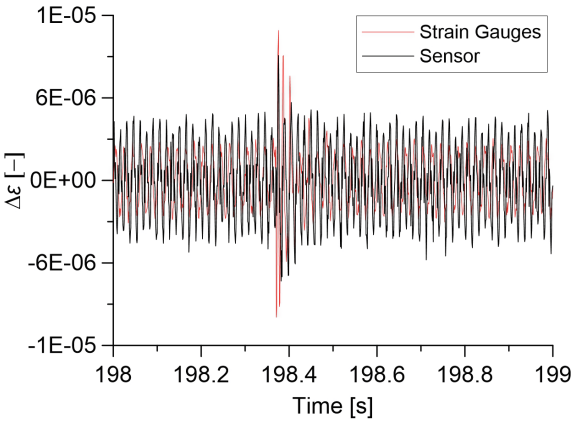

Fig. 9. Time histories of measured average strain from strain gauges and estimated strain from electrical measurements.

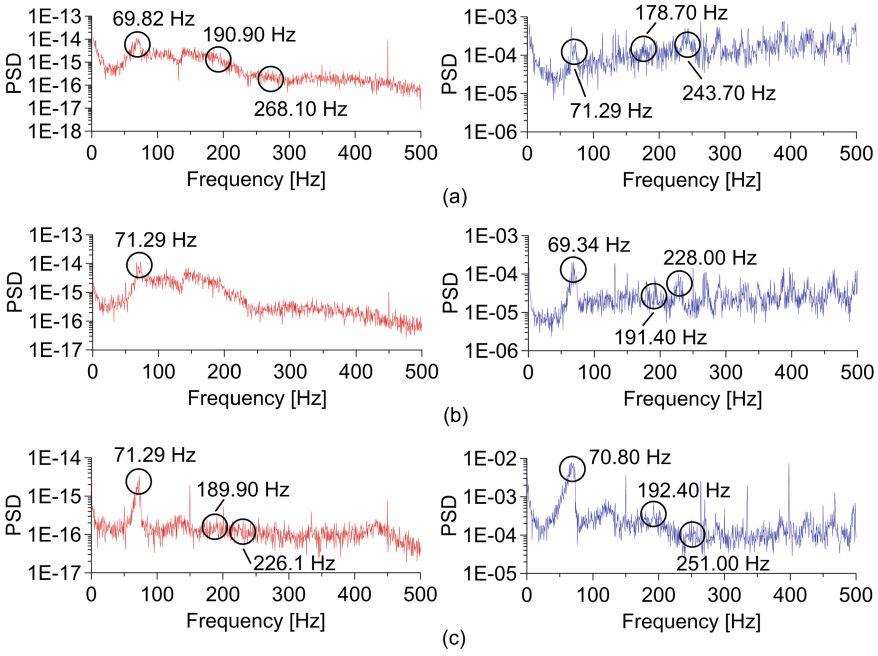

Fig. 10. PSD of strain gauges and smart sensors measurements for (a) P3, (b) P4 and (c) P6.

Table 3. Modal frequencies of the beam evaluate with different methods.

Type of modal analysis	Modal frequencies (Hz)		
	V1	V2	V3
Analytical	69.47		277.80
Smart sensors	70.80	192.40	251.00
Stain gauges	71.29	189.90	226.10
Accelerometers	80.57	186.00	265.60

5 Comments and Conclusions

This research was aimed at investigating the dynamic analysis of a RC beam through novel cement-based CNT-doped embedded sensors, in comparison to traditional ones. The electrical behavior and the sensitivity of the smart sensors were first investigated through electrical and electromechanical tests with cyclical and sinusoidal applied loads. After their characterization, the sensors were embedded at the top of a full-scale RC beam. Vibration tests on the beam showed that the novel sensors were able to identify impulsive loads and to provide dynamic strain measurements permitting the identification of the main modal frequencies of the beam. The agreement of the results with those ones obtained from traditional transducers and from the analytical approach demonstrate that the novel carbon-based cementitious sensors are promising for monitoring full-scale concrete structures through their embedding into structural elements.

Acknowledgements. This project has received funding from the European Union's Framework Programme for Research and Innovation HORIZON 2020 under Grant Agreement No. 765057. The support of the Italian Ministry of Education, University and Research (MIUR) through the funded Project of Relevant National Interest "SMART-BRICK: Novel strain-sensing nanocomposite clay brick enabling self-monitoring masonry structures" is also gratefully acknowledged.

References

Azhari F, Banthia N (2012) Cement-based sensors with carbon fibers and carbon nanotubes for piezoresistive sensing. Cem Concr Comp 34:866–873 (2012)

Camacho-Ballesta C, Zornoza E, Garcés P (2016) Performance of cement-based sensors with CNT for strain sensing. Adv Cem Res 28(4):274–284

Cao J, Chung DDL (2004) Electric polarization and depolarization in cement-based materials, studied by apparent electrical resistance measurement. Cem Concr Res 34:481–485

Coppola L, Buoso A, Corazza F (2011) Electrical properties of carbon nanotubes cement composites for monitoring stress conditions in concrete structures. Appl Mech Mater 82:118–123

D'Alessandro A, Ubertini F, García-Macías E, Castro-Triguero R, Downey A, Laflamme S, Meoni A, Materazzi AL (2017) Static and dynamic strain monitoring of reinforced concrete components through embedded carbon nanotube cement-based sensors. Shock and Vibration, Volume 2017, 3648403, 11 pages

Downey A, D'Alessandro A, Baquera M, García-Macías E, Rolfes D, Ubertini F, Laflamme S, Castro-Triguero R (2017) Damage detection, localization and quantification in conductive smart concrete structures using a resistor mesh model. Eng Struct 148:924–935

Han B, Ou J (2007) Embedded piezoresistive cement-based stress/strain sensors. Sensor Actuat A - Phys 138:294–298

Han B, Yu X, Ou J (2011). Multifunctional and smart nanotube reinforced cement-based materials. In: Gopalakrishnan K, Birgisson B, Taylor P, Attoh-Okine N (eds) Nanotechnology in civil infrastructure. A paradigm shift. Springer, pp 1–48

Li H, Xiao H, Ou J (2003) A study on mechanical and pressure-sensitive properties of cement mortar with nanophase materials. Cem Concr Res 34:435–438

Materazzi AL, Ubertini F, D'Alessandro A (2013) Carbon nanotube cement-based transducers for dynamic sensing of strain. Cem Conc Comp 37:2–11

Metaxa ZS, Konsta-Gdoutos MS, Shah SP (2009) Carbon nanotubes reinforced concrete, ACI Special Publication, 267SP, pp 11–20

Mondal P, Shah SP, Marks LD (2008) Nanoscale characterization of cementitious materials. ACI Mater J 105:174–179

Pisello AL, D'Alessandro A, Sambuco S, Rallini M, Ubertini F, Asdrubali F, Materazzi AL, Cotana F (2017) Multipurpose experimental characterization of smart nanocomposite cement-based materials for thermal-energy efficiency and strain-sensing capability. Sol Energy Mater Sol Cells 161:77–88

Rainieri C, Song Y, Fabbrocino G, Markand JS, Shanov V, (2013) CNT-cement based composites: Fabrication, self-sensing properties and prospective applications to structural health monitoring. In: Proceedings SPIE, fourth international conference on smart materials and nanotechnology in engineering 8793, p 10

Ubertini F, Laflamme S, D'Alessandro A (2016) Smart cement paste with carbon nanotubes. In: Loh KJ, Nagarajaiah S (eds) Innovative developments of advanced multifunctional nanocomposites in civil and structural engineering. Woodhead Publishing, pp 97–120

The Effect of Freeze-Thaw Cycles on the Mechanical Performance of RAC

C. S. Rangel[1], M. Amario[1], M. Pepe[2(✉)], E. Martinelli[2], and R. D. Toledo Filho[1]

[1] Civil Engineering Department, COPPE, Federal University of Rio de Janeiro, Rio de Janeiro, Brazil
[2] Department of Civil Engineering, University of Salerno, Salerno, Italy
mapepe@unisa.it

Abstract. The recycling of Construction and Demolition Waste (CDW) to be used as aggregates for concrete is a potential alternative to minimize the environmental impact. In cold regions, the damage caused to concrete structures by freezing and thawing is a serious problem. This study presents the results of experimental tests aimed at investigating the influence of the use of Recycled Concrete Aggregate (RCA) on concrete submitted to 150 freeze-thaw cycles. Aggregates made from laboratory-produced concrete waste were used in two size fractions (i.e., Coarse 0–4.8 to 9.5 mm and Coarse 1–9.5 to 19 mm). Concrete mixtures of normal strength and high strength were produced with only natural aggregate and mixtures with 100% RCA in each of the size fractions. The mechanical behavior and physical properties were evaluated. The results showed that, for both natural and recycled concretes, the most affected class was the normal strength class.

Keywords: Recycled Concrete Aggregate · Recycled aggregate concrete · Freeze-thaw cycles · Durability · Compressive strength

1 Introduction

Concrete is one of the most widely used construction materials in the world. Its popularity can be explained by its mechanical performance low cost and availability. In fact, several statistics show that the average annual rate of concrete production is around 1 ton per person based on the world population (Medina et al. 2014). On the other hand, every year, with demolition of buildings, millions of tons of waste are produced in the construction industry, which become a significant concern due to its impact on the conservation of natural resources and the preservation of the environment. One of the possibilities explored for the reduction of the environmental impact of concrete industry is represented by the use of recycled aggregates for the partial-to-total replacement of natural aggregates leading to the so-called Recycled Concrete Aggregates (RACs). As a matter of principle, this alternative solution not only reduces the use of natural resources, but also addresses the issue of safe and sustainable disposal of the huge volumes of construction and demolition waste generated around the world.

M. di Prisco and M. Menegotto (Eds.): ICD 2018, LNCE 42, pp. 301–311, 2020.
https://doi.org/10.1007/978-3-030-23748-6_23

It is worth to mention that, due to the intrinsic characteristics of RCAs, i.e., the presence of the Attached Mortar leading to high porosity capacity of the aggregates, the resulting RAC's durability behaviour can be significantly affected (Huda and Alam 2015). In fact, the exposure to extreme temperatures, such as frost conditions, is one of the main causes of deterioration of concrete. The freeze-thaw resistance of concrete is affected by several factors, such as porosity, water content and type of aggregate (Bogas *et al*. 2016). Thus, before any practical applications, the freeze-thaw durability performance of RAC must be evaluated to ensure that it presents required performance even in severe exposure conditions.

Šeps *et al*. (2016) pointed out that the properties of the RACs are affected by the quality of the Recycled Concrete Aggregate (RCA) that depend on the processing (crushing, grading, elimination of impurities, etc.) and properties of the original concrete. In addition, there was a considerable reduction in compressive strength after 50 freeze-thaw cycles in concrete with low cement dosage due to the deterioration of the RCA. Wu *et al*. (2017) have observed that the relative compressive strength (i.e., the ratio between the strengths measured after and before the degradation cycles) of RAC is lower than that of NAC under the same freeze-thaw cycles. By comparing the stress-strain curves after 0 and 125 freeze-thaw cycles, the descending branch of the stress-strain curve of the RAC became more pronounced, which meant that the RAC fragility increased as freeze-thaw cycles were increased. Liu *et al*. (2016) analysed the attached mortar of RCA from different origins. They concluded that there were already some initial cracks in the mortar before the beginning of freeze-thaw cycles, due to shrinkage of the concrete samples and the type of crushing used. The number of initial cracks was higher in the aggregates from low-strength concrete waste. After 150 cycles of freeze-thaw, the number of cracks in adhered mortar from high-strength concrete waste was more than five times the initial value and subsequently increased to six times the initial value, indicating that this sample suffered serious damage. However, the mortar adhered to the aggregate of low-strength concrete waste showed good resistance during the freeze-thaw cycles, with the final crack density being almost similar to the initial one.

The objective of this study is to investigate the influence of freeze-thaw cycles (performed based on ASTM C666 (2008) standard) on the physical and mechanical performance of normal (35 MPa) and high strength (60 MPs) concrete including coarse RCAs.

2 Experimental Investigation

2.1 Materials

This study concentrates the investigation on aggregates and, for this reason, a detailed characterization of their properties was carried out. The natural aggregates used were three:

- a fine fraction, composed of quartz sand, with nominal diameter smaller than 4.75 mm;
- a coarse aggregate (named "Nat-C0"), composed of coarse granite rocks, with nominal diameter between 4.75 mm and 9.5 mm;

– and a coarse aggregate (named "Nat-C1"), also composed of coarse granite rocks, with a nominal diameter between 9.5 mm and 19 mm.

The Recycled Concrete Aggregates (RCAs) were generated from laboratory-produced concrete waste. The original concrete was produced with average compressive strength of 30 MPa at 28 days, a water-to-cement ratio equal to 0.6 and a cement dosage equal to 353 kg/m^3. At 28 days of age, the original concrete was reduced to smaller pieces by the use of a mechanical press, and then a jaw crusher was used to further reduce particle size by crushing process. In the second step, the material was subjected to air drying and separation in an industrial mechanical sieve. The recycled material of nominal diameter between 4.75 mm and 9.5 mm was classified as coarse aggregate 0, "RCA-C0", and the material of nominal diameter between 9.5 mm and 19 mm was classified as coarse aggregate 1, "RCA-C1". In the last step, the homogenization of the recycled aggregates was carried out through the well-known longitudinal blending bed technique, which consists of alternately and in opposite directions spreading the same amount of material along a pile. Figure 1 shows the coarse aggregates used in this study.

The characterization of the aggregates was performed through several tests. Specific gravity and water absorption were performed in the coarse aggregates according to NBR NM 53 (2009), and in the fine aggregate according to NBR NM 52 (2009) and NBR NM 30 (2001), respectively. Table 1 reports the results for the mentioned properties.

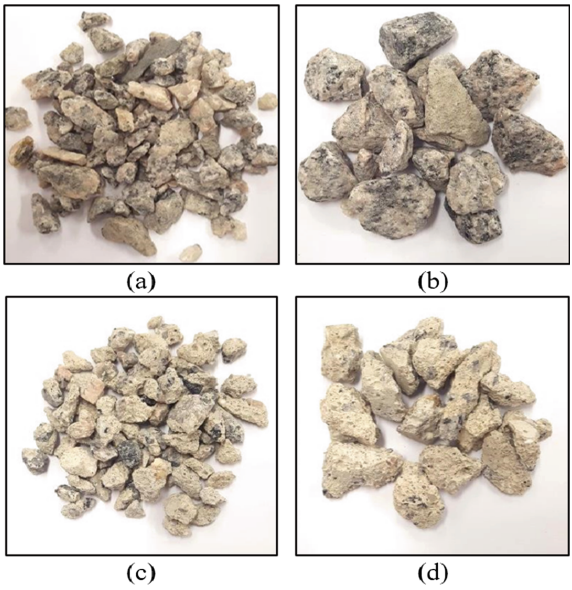

Fig. 1. Coarse aggregates: (a) Nat-C0; (b) Nat-C1; (c) RCA-C0; (d) RCA-C1

Table 1. Properties of the aggregates used in this study

Properties	Sand	Nat-C0	Nat-C1	RCA-C0	RCA-C1
D_{max} (mm)	4.75	9.5	19	9.5	19
SG*(kg/m^3)	2447	2662	2636	2178	2105
Absorption (%)	0.5	1.5	1.3	7.3	8.2

SG*: specific gravity

A high initial strength Portland cement was used, labeled CPV-ARI according to NBR 5733 (1991), characterized by a compressive strength of 40 MPa at 28 days and a specific gravity of 3181 kg/m^3. Finally, a superplasticizer (MC Powerflow 1180), with a solids content of 35% and a specific gravity of 1070 kg/m^3, was used to control the workability.

2.2 Concrete Mixtures Composition

The mix-design of the concrete mixtures was performed according to the Compressive Packing Model (CPM) (de Larrard 1999): the model assumes that the overall compactness achieved by the dry granular skeleton determines the properties of the resulting concrete. BetonLab Pro 3 software was used to optimize the desired properties for concrete through the CPM.

Concrete mixtures were developed for two classes of compressive strengths: normal strength of 35 MPa and high strength of 60 MPa. For each class, three mixtures were designed: a "reference" ordinary concrete with only natural aggregates (0% RCA), a recycled concrete with 100% RCA in the coarse aggregate fraction 0 and a recycled concrete with 100% RCA in the coarse aggregate fraction 1. Table 2 shows the compositions of the six concrete mixtures. The two natural mixtures were named as "CX-Nat", where "X" indicates the strength class (35 and 60). The four RAC mixtures were named "CX-RCA-Y", where "X" indicates the strength class (35 or 60) and "Y" indicates the fraction of coarse RCA that was used (C0 for fraction 0 and C1 for fraction 1). The superplasticizer content was 0.2% and 1.5% of solids in ratio to the cement dosage for the mixtures of 35 MPa and 60 MPa, respectively.

It is worth mentioning that in the recycled concrete mixtures, a conventional mix-design with the simple replacement of natural aggregate for RCA by volume was not performed: the CPM defines the ideal compactness for each mixture, considering the individual properties of each component material, in order to obtain the desired properties (among them, compressive strength of 35 MPa and 60 MPa at 28 days). Regarding how to consider the high absorption of the RCAs, the recycled materials were added in the dry condition to the mixture, and the absorption was considered in the calculation of the compositions by the program. The absorption value of 50% of total absorption obtained experimentally was used. This value is based on the studies developed by Pepe *et al.* (2016) and Amario *et al.* (2017). The authors concluded that the coarse RCAs absorb about 50% of the value of their total absorption during the concrete mixing process, both for fraction 0 and fraction 1.

Table 2. Concrete mixtures compositions

Materials	C1		C0		S	C	W
(kg/m^3)	Nat	RCA	Nat	RCA			
C35-Nat	452	0	457	0	868	325	212
C35-RCA-C0	451	0	0	373	866	338	217
C35-RCA-C1	0	361	456	0	867	336	216
C60-Nat	448	0	452	0	860	448	150
C60-RCA-C0	448	0	0	371	861	458	152
C60-RCA-C1	0	356	450	0	856	461	151

*C1: coarse aggregate fraction 1; C0: coarse aggregate fraction 0; S: sand; C: cement; W: water

2.3 Mixing Procedure

Due to the high water absorption of the RCAs, a specific methodology was adopted for the mixing process: the total water was divided into two equal parts, and the addition of the parts was performed at different times of the mixture.

The mixing procedure was carried out in the following steps: 1 - all the aggregates were mixed for 1 min; 2–50% of the total water was added and the mixing continued for another 1 min; 3 - the cement was added and the constituents were mixed for another 1 min; 4 - the superplasticizer and the second half of the water were added, and all materials were mixed for 8 min.

Cylindrical samples of 75 mm diameter and 150 mm height were cast from all concrete mixtures. The fresh concrete was compacted by the use of a vibrating table in two layers for 30 s each. Samples were demolded after 24 h and cured at 21°C temperature and 100% humidity until the age of testing.

2.4 Test Methods

The procedure to perform the durability tests on concrete subjected to freeze-thaw cycles was based on ASTM C666 (2008). The freeze-thaw cycles in the concretes were started at the age of 28 days. Initially, the specimens were kept immersed in water at 21 °C temperature for 48 h, and then the cycles were started. One cycle consisted in reducing the temperature of the specimens from 4 °C to −18 °C and then reheating to 4 °C again. The total cycle time is 5 h and a total of 150 cycles were performed. The cylindrical specimens were weighed in dry state, before and at the end of the procedure, to follow the mass variation. For all mixtures, non-degraded samples were kept in a moist chamber (21 °C temperature and 100% humidity) as reference, and they were tested at the same age as the degraded samples for comparison purposes.

The slump tests were performed for all mixtures in accordance with NBR NM 67 (1998). The compressive strength tests were performed on cylindrical samples according to NBR 5739 (2007), in Shimadzu 1000 kN mechanical press, at a rate of axial displacement of 0.1 mm/min. Compressive strength tests were performed for all

mixtures for 28 days and were also performed for reference samples (without degradation) and 150 freeze-thaw cycles samples. Tensile splitting tests were performed on all mixtures at 28 days, according to NBR 7222 (2011).

Table 3. Rheological and mechanical properties of concrete mixtures

Mixture	Slump	$f_{c,28}$	$E_{c,28}$	$f_{t,28}$
	mm	MPa	GPa	MPa
C35-Nat	175	34.2 (± 2.4%)	21.3 (± 2.1%)	2.7 (± 1.7%)
C35-RCA-C0	180	35.7 (± 0.8%)	22.1 (± 2.4%)	2.7 (± 3.7%)
C35-RCA-C1	165	35.3 (± 0.9%)	21.2 (± 3.4%)	2.9 (± 5.2%)
C60-Nat	165	60.1 (± 1.5%)	29.1 (± 3.2%)	3.9 (± 3.2%)
C60-RCA-C0	180	60.5 (± 1.1%)	29.8 (± 1.5%)	4.0 (± 3.7%)
C60-RCA-C1	170	61.9 (± 1.3%)	30.1 (± 4.6%)	4.4 (± 3.4%)

3 Results and Analysis

3.1 Properties of RAC at Fresh and Hardened States

Table 3 presents the mean values (and coefficient of variations) of: slump, 28-day compressive strength $f_{c,28}$, strain at maximum stress $\varepsilon_{c,28}$, modulus of elasticity $E_{c,28}$ and 28-day splitting tensile strength $f_{t,28}$.

The slump results show values between 165 mm and 180 mm for all concrete mixtures, which allows a proper moldability of the concrete. Table 3 shows that all the mixtures reached values of compressive strength expected by the mix-design methodology for the age of 28 days. The results of strain at maximum stress and modulus of elasticity have very close values for the natural concrete mixtures and the RACs, in the two strength classes. Thus, it can be stated that, for both normal strength (35 MPa) and high strength (60 MPa) mixtures, the recycled aggregates do not significantly influence the stress-strain curve of the materials (Fig. 2). The results of tensile strength were the similar for natural and recycled concrete for the class of 35 MPa, but for the class of 60 MPa, although similar, it can be identified that the recycled concrete with RCA-C1 showed a slightly higher tensile strength value than the others.

As for the rupture form in the compressive strength test, samples of the normal strength mixtures showed several diagonal thin fissures, maintaining their initial cylindrical appearance, while the high strength samples resulted in explosive rupture when the maximum load was reached, and the samples lost their initial cylindrical appearance. In general, all the considerations mentioned above point out that there were no significant differences in the mechanical behaviour between natural concretes and RACs: this is a consequence of the adopted mix-design methodology, which explicitly considers the specific characteristics of the RCAs and their different properties in comparison to the natural aggregates.

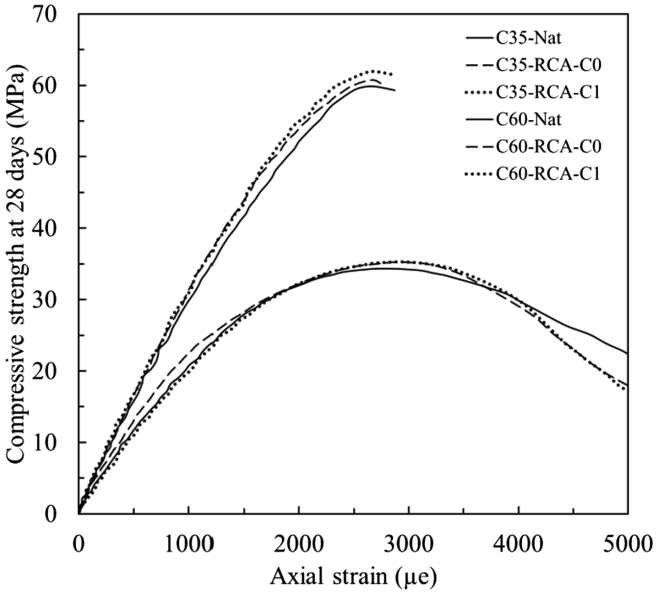

Fig. 2. Typical stress-strain curves of 28-day compressive strength tests

3.2 Mechanical Performance of RAC After Freeze-Thaw Cycles

Table 4 shows the mean values (and coefficient of variations) for reference concrete samples (without degradation, with the same age of the degradation samples) and for concrete samples subjected to the 150 freeze-thaw cycles: compressive strength f_c, strain at maximum stress ε_c, modulus of elasticity E_c and mass loss Δ_{ml} after degradation.

About the compressive strength of the reference samples (Table 4), the increase of time caused an increase in the values when compared to the 28 days samples (Table 3), as expected, due to hydration processes. The same was observed for the modulus of elasticity, which increased with increasing compressive strength in time, indicating a higher stiffness. Analogously, strain at maximum stress decrease when compressive strength increases. This behavior was verified for all mixtures for the two classes.

In general, freezing and thawing damage occurs on the concrete because of its porosity, as it absorbs water and then this water turns to ice at negative temperatures. This phenomenon causes reduction in the mechanical strength, alteration in the internal structure of pores and appearance of cracks in the concrete. When comparing the results of the reference mixtures and the degraded ones (Table 4), the freeze-thaw cycles caused a decrease in the compressive strength in all the mixtures, as expected. Figure 3 shows the percentage of this decrease in compressive strength.

The degradation samples results are optimistic, since the recycled concretes did not necessarily present a higher drop in compressive strength than the natural concretes, which could be expected due to their greater water absorption. It is worth noting that the same behavior occurs for the two strength classes: the higher impact on the

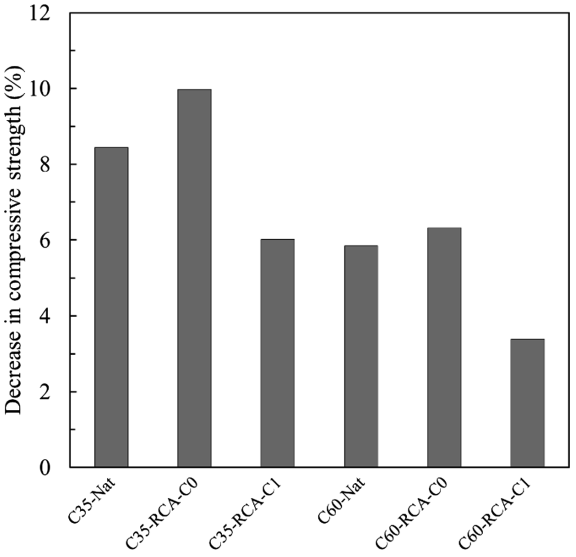

Fig. 3. Percentage of decrease in compressive strength due to freeze-thaw cycles degradation process

compressive strength occurred for the mixtures with the recycled coarse aggregate 0 (RCA-C0); followed by the natural concrete mixtures; and finally the mixtures that showed the lowest strength drop due to degradation processes were the ones with the recycled coarse aggregate 1 (RCA-C1). That is, the RCA with the largest nominal diameter allows a greater temperature variation (associated with a change in the volume of water when it turns into ice), causing less negative impacts on the properties of the corresponding concrete. Moreover, the results highlight that the impact on the strength was higher for the normal strength class than for the high strength class for all the mixtures, which can be explained by the higher water absorption of concretes with lower strength due to their higher porosity.

Regarding the modulus of elasticity, the results show that the freeze-thaw cycles cause a decrease in the stiffness of the concrete for both the normal and high classes, probably due to changes in the internal pore structure due to the repeated temperature variation. Also on the modulus of elasticity, the percentages of decrease compared to the reference values were higher for the normal strength class. The results of strain at maximum stress indicate a higher deformation for the degraded concretes samples, and this behavior is associated with resistance, that is, with the drop in strength there was an increase in the strain value at the peak. Finally, the mass loss results were higher for the class of 35 MPa. In addition, it should be noted that for both classes, the mixtures that suffered the greatest mass loss were those containing RCA-C1. This fact can be related to the better capacity of the concretes produced with this material in terms of durability, as mentioned above. These results highlight that the RCA nominal diameter significantly influences on the mechanical, physical and durability properties of the RACs.

The typical stress-strain curves of concretes that suffered degradation are presented in Fig. 4. In general, it is possible to observe that the typical behavior of the stress-strain

curves was not affected by the freeze-thaw cycles, showing a behavior similar to the curves for 28 days (Fig. 2). The concrete samples rupture also occurred similarly to that observed for 28 days, that is, diagonal cracks in normal strength class samples and explosively for high strength class samples.

Table 4. Mechanical properties of concrete mixtures after freeze-thaw cycles

Mixture	No degradation: reference			Degradation: 150 freeze-thaw cycles			
	$f_{c,ref}$	$\varepsilon_{c,ref}$	$E_{c,ref}$	$f_{c,FT150}$	$\varepsilon_{c,FT150}$	$E_{c,FT150}$	Δml
	MPa	με	GPa	MPa	με	GPa	%
C35-Nat	39.1 (± 3.6%)	2837 (± 4.2%)	23.5 (± 1.3%)	35.8 (± 0.9%)	2920 (± 5.1%)	22.2 (± 0.4%)	1.8
C35-RCA-C0	42.1 (± 4.3%)	2884 (± 4.5%)	24.1 (± 3.1%)	37.9 (± 4.1%)	2953 (± 4.2%)	22.3 (± 3.6%)	1.7
C35-RCA-C1	39.9 (± 2.2%)	2763 (± 3.5%)	23.8 (± 2.2%)	37.5 (± 1.4%)	2992 (± 3.0%)	22.5 (± 1.5%)	2.2
C60-Nat	65.0 (± 1.4%)	2549 (± 4.4%)	32.3 (± 2.8%)	61.2 (± 3.9%)	2580 (± 0.8%)	30.6 (± 3.6%)	1.2
C60-RCA-C0	64.9 (± 4.8%)	2516 (± 4.6%)	33.1 (± 1.5%)	60.8 (± 4.2%)	2681 (± 4.8%)	31.8 (± 2.8%)	1.3
C60-RCA-C1	68.0 (± 1.9%)	2612 (± 4.6%)	32.5 (± 3.1%)	65.7 (± 1.1%)	2662 (± 1.1%)	31.9 (± 1.6%)	1.5

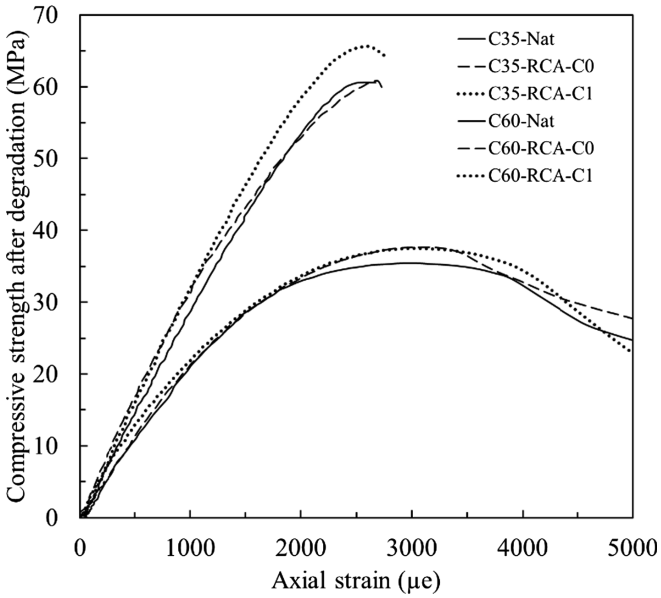

Fig. 4. Typical stress-strain curves of compressive strength tests after degradation process (150 freeze-thaw cycles)

4 Conclusions

This study reported the results of experimental tests performed on natural and recycled concrete from different compressive strength classes. The following comments can be observed:

- Mixtures of normal and high strength concrete can be performed by replacing 100% of natural coarse aggregate by RCAs in the fractions investigated in this study, provided that an appropriate methodology is adopted for the mix-design, taking into account the specific characteristics of the RCAs;
- The well-known Compressive Packing Model (CPM), originally developed for conventional structural concrete, confirms its accuracy and reliability in the case of the RAC mixtures considered in this study;
- There are no quantitatively significant variations for the recycled concrete and the corresponding natural concrete, either in terms of workability in the fresh state, nor in strength and modulus of elasticity in the hardened state at 28 days;
- Regarding the concrete performance after repeated freeze-thaw cycles, there was a decrease in compressive strength and modulus of elasticity in all mixtures. Also, all mixtures suffered mass loss at the end of the cycles;
- The impact of the degradation process on the strength and mass loss was higher for the normal strength class than for the high strength class, which can be explained by the higher water absorption of concrete with lower resistance, due to its higher porosity;
- However, the results are optimistic, since the recycled concretes produced with the RCA larger fraction (RCA-C1) presented a lower percentage decrease in compressive strength than the corresponding natural concretes, clearly showing that the presence of RCA does not cause directly a decrease in the durability of the concrete;
- Coincidentally, the concrete mixtures that suffered the higher mass loss were those containing RCA-C1, and this fact can be related to the higher durability capacity of these concretes;
- These results show that the RCA diameter significantly influences the mechanical, physical and durability properties of the RACs.
- Finally, although a complete replacement of natural aggregates with recycled one was not performed, it is worth mentioning that the encouraging conclusions described above are consequences of the appropriate mix-design methodology adopted for RACs and further experimental studies are required, exploring other RCAs variables to confirm the preliminary results obtained in this study.

Acknowledgements. The study is part of SUPERCONCRETE Project (H2020-MSCA-RISE-2014, n. 645704): the Authors wish to acknowledge the financial contribution of the EU-funded Horizon 2020 Programme. More specifically, it was partly developed during the mobilities of both Prof. Romildo D. Toledo Filho at the University of Salerno (Italy), and Dr. Marco Pepe at the Federal University of Rio de Janeiro (Brazil).

References

Amario M, Rangel CS, Pepe M, Toledo Filho RD (2017) Optimization of normal and high strength recycled aggregate concrete mixtures by using packing model. Cement Concr Compos 84:83–92

ASTM C666 (2008) Resistance of concrete to rapid freezing and thawing. American Society for Testing and Materials

Bogas JA, De Brito J, Ramos D (2016) Freeze–thaw resistance of concrete produced with fine recycled concrete aggregates. J Clean Prod 115:294–306

de Larrard F (1999) Concrete mixture proportioning: a scientific approach. E&FN Spon, London and New York, p 1999

Huda SB, Shahria Alam M (2015) Mechanical and freeze-thaw durability properties of recycled aggregate concrete made with recycled coarse aggregate. J Mater Civ Eng 27(10):04015003

Liu K, Yan J, Hu Q, Sun Y, Zou C (2016) Effects of parent concrete and mixing method on the resistance to freezing and thawing of air-entrained recycled aggregate concrete. Constr Build Mater 106:264–273

Medina C, Zhu W, Howind T, de Rojas MIS, Frías M (2014) Influence of mixed recycled aggregate on the physical–mechanical properties of recycled concrete. J Clean Prod 68:216–225

NBR 5733 (1991) High early strength Portland cement – specification. ABNT

NBR 5739 (2007) Concrete - compression test of cylindric specimens – method of test. ABNT

NBR 7222 (2011) Concrete and mortar – determination of the tension strength by diametrical compression of cylindrical test specimens. ABNT

NBR NM 30 (2001) Fine aggregate - test method for water absorption. ABNT

NBR NM 52 (2009) Fine aggregate - determination of the bulk specific gravity and apparent specific gravity. ABNT

NBR NM 53 (2009) Coarse aggregate - determination of the bulk specific gravity, apparent specific gravity and water absorption. ABNT

NBR NM 67 (1998) Concrete – slump test for determination of the consistency. ABNT

Pepe M, Toledo Filho RD, Koenders EA, Martinelli E (2016) A novel mix design methodology for Recycled aggregate concrete. Constr Build Mater 122:362–372

Šeps K, Fládr J, Broukalová I (2016) Resistance of recycled aggregate concrete to freeze-thaw and deicing salts. Procedia Eng 151:329–336

Wu J, Jing X, Wang Z (2017) Uni-axial compressive stress-strain relation of recycled coarse aggregate concrete after freezing and thawing cycles. Constr Build Mater 134:210–219

Effect of a Crystallizing Admixture on Concrete Properties: Italian Concrete Days

F. Longhi[1(✉)] and F. Surico[2(✉)]

[1] Technical Office Concrete Admixtures, Mapei S.p.A, Milan, Italy
f.longhi@mapei.it
[2] R & D Concrete Admixtures, Mapei S.p.A, Milan, Italy

Abstract. The present work aims at investigating the effect of a crystallizing admixture on concrete properties. Several concrete mixtures, properly prepared with different W/C ratios and different cement contents, have been compared with similar ones containing different dosages of Crystallizing admixture. The crystallizing effect of the product has been assessed and discussed both on fresh and hardened properties of the mixtures studied. Evaluations on setting time and strength development have been done on reference and trial mixes. Specific testing like the evaluation of chloride ion diffusion, accelerated carbonation testing and other tests have been performed to have an overview on all aspects on different levels of permeability. The crystallizing effect has been detected and demonstrated with a Scanning Electron Microscopy (SEM-EDS). The pictures of crystals growing into the capillary voids are intended to demonstrate the blocking effect of the cement matrix through the crystallizing compounds.

Keywords: Crystallizing admixture · Watertight concrete · Durability

1 Introduction

Concrete is roughly made of 75% of aggregates, 15% of cement and around 10% of water. If in 2017 is expected to have a global production of cement around 4,5 billion of tons, a global consumption of 340 billion of aggregates and 3 billion of water will be consumed. A consumption of such a big quantity of raw material should require a more sustainable industrial development.

Many solutions could be taken to reduce the consumption of raw materials in this direction: recycling waste products, increasing the use of supplementary cementitious material, replacing of virgin aggregates with recycled aggregates from demolition of buildings and using non potable or recycled water instead of pure water.

Because of lacking of regulations and laws that facilitate the use of recycled material to boost the passage from a prescriptive specification to a performance-based standard, it is quite difficult to expect a reduction of raw material consumption in the short-term.

An alternative sustainable approach is to improve the durability of concrete in order to reduce maintenance cost, save energy and materials. If we could extend the service life from 50 years to 150 years or more, we could postpone of 100 years the costs connected to the consume of natural resources. The present work wants to investigate if

M. di Prisco and M. Menegotto (Eds.): ICD 2018, LNCE 42, pp. 312–324, 2020.
https://doi.org/10.1007/978-3-030-23748-6_24

it is possible to improve the performance of conventional concrete using an additional crystallizing admixture. The research program has been launched in Australia, in order to get results to be shared in a wider region such as New Zealand, South East Asian and Pacific countries. The tests have been performed at Boral Laboratory, by BCRC Building & Construction, Research & Consulting. Most of the tests has been carried out in laboratories registered with the National Association of Testing Authorities (NATA), but there are several ones for which no laboratory accreditation was available. The final purpose is to evaluate which are the strong points of the use of crystalline product and which concrete properties are improved.

2 Crystalline Admixture

Crystalline waterproofing admixtures consist of active chemicals provided in a carrier of cement and filler. The particular nature of these materials leads to an increase of the density of calcium silicate hydrate, generating pore-blocking deposits and increasing the resistance to water penetration.

With regard to capability of forming crystalline compounds, it is relevant to refer to the ACI 212.3R.10, Report on Chemical Admixture for Concrete.

The chapter of this document regarding the waterproofing admixtures is titled Permeability Reducing Admixtures or PRA's. According to this chapter, there are three classes of admixtures that are playing a role in the reduction of concrete permeability. These admixture classes are:

- Hydrophobic or water-repellent;
- Mineral fillers;
- Crystalline materials.

With regard to the above admixture classes, the ACI 212.3R.10 comments on these classes of admixtures as follows:

- The water-repellent admixture, based mostly on fatty acids, oils or waxes emulsions are effective in "reducing the absorption and ingress of chlorides into concrete, but usually only under non-hydrostatic conditions (PRAN).
- The mineral fillers such as talk, bentonite, lime or alkaline silicates may "shrink the pores of concrete and restrict the water passage". These mineral fillers are also classified as PRAN's and do not fully block all pores;
- Crystalline-based admixtures (PRAH) are hydrophilic, reacting with the cement matrix, forming crystals. These crystals are able to block the pores, improving the "concrete's ability to resist water penetration under pressure". The crystalline-based admixtures are mostly considered suitable in concrete structures with severe waterproofing applications.

The present work aims to investigate the effect of a Crystalline – based permeability reducing admixture The assessment is performed on the properties of fresh and hardened concrete mixture containing the admixture compared to a control mix without crystalline admixture.

3 Compliance Testing Results

3.1 Control Mix Description

The first series of tests aims to define the type of admixture according to the requirement of AS 1478.1. Crystalline admixture is considered a special purpose admixture since its performance attributes are outside of the existing categories which are normally used in concrete. The main purpose of the compliance testing aims to ensure that the product is not detrimental to the concrete. Crystalline admixture could be used to provide specific property to concrete without affecting the setting time of concrete. In accordance to this, specific tests have been carried out to define crystalline admixture as special purpose normal setting admixture (type SN).

The results reported below are the average of two duplicated mixes.

Description of the control mix (Table 1).

Table 1. Description of the control mix

Material	type	Kg/m^3
Cement	Type I	305
Fine sand	Dune	410
Coarse sand	River	440
10 mm	Crushed	280
20 mm aggregates	Crushed	740
Water	Pure	200

The Reference mix was prepared adding 1% by the weight of cement of the crystalline product.

Table 2. Control mix vs test mix

	Control mix	Test mix
Water l/m^3	200	196
Slump	80	85
Air content	1,2%	2,2%
Density	2370	2350
Concrete temperature °C	22.0	22.0
Type of mixer	PAN	PAN
Setting time	Control Mix	Test mix
Initial setting time	4 h 30 min	4 h 45 min
Final setting tine	6 h 15 min	6 h 30 min
Bleeding	Control Mix	Test Mix
Bleeding	3,7%	3,8%

3.2 Fresh Properties

3.3 Comments on Fresh Properties

Slump: Crystalline product complies with the standard requirements of 80 ± 10 mm;

Setting time: crystalline product complies with both initial and final setting as an SN admixture product (special purpose/normal setting) (Table 2);

Water demand: crystalline product required 4 litres less water than control. This is a good outcome, as it may have positive impact on compressive strength and drying shrinkage;

Air content: Crystalline product shows an 1% air content increase compared with control mixes.

Bleeding: The concrete mixes where crystalline product was added, showed a bleeding of 3.8%, that is similar to the bleeding of control mixes

3.4 Hardened Properties

Table 3. Hardened properties

Compressive strength			
Age	Control mix	Test mix	Gain %
3	18,0	21,0	117%
7	25,0	31,0	124%
28	35,0	38,5	110%
Drying shrinkage [με]			
Age	Control mix	Test mix	Gain %
7	180	180	–
14	280	270	3,7%
21	340	330	3,0%
28	390	370	5,4%

3.5 Comments on Hardened Properties

Compressive strength: The compressive strength results for the concrete mixes containing the crystalline product were improved when compared to control concrete. In particular an increase of 17% and 24% of compressive strength has been noted at early ages of 3 and 7 days compared with the control mixes. The increase in compressive strength was 10% at 28 days (Table 3).

AS1478.1 requires that SN admixtures have a compressive strength of minimum 90% of control at the same age of test and that has been achieved at all ages tested to date.

Drying shrinkage: Drying shrinkage shows that concrete with Crystallizing product reaches 10 micro-strain lower when compared to control mix at early age and 20 micro-strain lower when compared at 28 days age.

Crystalline product was found to be compliant with the requirements of AS1478.1:2000 as a type SN admixture. Following to that a second stage of tests was designed and carried out to assess the relevant technical improvements of concrete.

4 Comparison Testing

4.1 Testing Program

The concrete trial mixes program was designed to assess a series of concrete mixes for strength grade 40 MPa. Mixes with maximum sized aggregate of 20 mm, slump of 100 mm and water cement in the range 0,35 to 0,40 were prepared and compared with concretes admixed with a crystallizing product (Tables 4 and 5).

A summary of the mixes prepared with different cementitious compositions are reported below.

A Shrinkage Limited cement was used in combination with fly ash and GGBFS with different proportions. The table also reports the dosage rate of crystalline product.

Table 4. Description of the mixtures

	Cement	Fly ash	GGBFS	Crystalline product
MIX 1	75%	25%	–	
MIX 2	75%	25%	–	1%
MIX 3	50%	30%	20%	–
MIX 4	50%	30%	20%	2%

A water reducing admixture based on lignosulphonate have been used to achieve the slump target.

Table 5. Fresh properties

	MIX n. 1	MIX n. 2	MIX n. 3	MIX n. 4
Material	kg/m^3	kg/m^3	kg/m^3	kg/m^3
Cement	300	300	215	215
Fly Ash	100	100	130	130
GGBFS	–	–	85	85
Crystalline admix.	–	**4,0 (1%)**	–	**8,5 (2%)**
Fine sand	220	220	190	190
Coarse sand	550	550	540	540
10 mm	300	300	300	300

(*continued*)

Table 5. (*continued*)

	MIX n. 1	MIX n. 2	MIX n. 3	MIX n. 4
20 mm	720	720	720	710
Water	198	198	198	198
WR	1,1 (0,28%)	1,1 (0,28%)	1,3 (0,3%)	1,3 (0,3%)
Slump (mm)	**100**	**100**	**95**	**95**
Air (%)	**1,6**	**1,6**	**1,4**	**1,2**
Density (kg/m^3)	2380	2380	2360	2360
Type of mixer	PAN	PAN	PAN	PAN
T °C	25	25	25	25
Bleeding of concrete AS1012	**MIX n. 1**	**MIX n. 2**	**MIX n. 3**	**MIX n. 4**
Bleeding	2,4%	2,2%	2,8%	2,9%

Table 6. Compressive strength

Compressive strength	MIX n. 1	MIX n. 2	MIX n. 3	MIX n. 4
Age	MPa	MPa	MPa	MPa
1 day	12,0	13,5	7,1	9,6
3 days	23,5	25,5	18,5	18,5
7 days	31,5	32,5	30,5	31,5
28 days	45,5	42,5	47,2	48

4.2 Comments on Fresh Properties

Water demand: the addition of crystallizing product has no significant influence on water demand.

Water/Cement ratio: as expected, due to consistent water demand, the addition of the crystalline product has no significant impact on w/c ratio.

Slump: The addition of the crystallizing product has no significant influence on slump.

Air content: The addition of the crystallizing product has no significant impact on air content

Bleeding: Crystallizing product has no significant impact on bleeding.

4.3 Hardened Properties

The strength of concrete specimens was tested according to AS 1012.9

Three concrete drying shrinkage specimens were prepared for each mix according to AS 1012.13 (Table 7)

Table 7. Drying shrinkage

Drying shrinkage (microstrain)	MIX n. 1	MIX n. 2	MIX n. 3	MIX n. 4
7 days	230	240	340	300
14 days	350	360	480	410
21days	420	430	550	470
28 days	460	470	590	510
56 days	560	580	680	600

4.4 Comments on Compressive Strength and Drying Shrinkage

The use of the crystalline product seems to have no effect on compressive strength development.

The drying shrinkage of MIX n. 2 does not show a significant reduction compared to MIX n. 1.

MIX n. 4 shows the lowest shrinkage values probably due to the higher dosage of crystalline product which leads to a reduced capillary porosity.

5 Sorptivity Test

The sorptivity test (RMS B80/B1 exposure) measures the depth of water penetration into test specimens after 7 days of curing in specified environments (wet, plastic bag, wax). Immediately following dry conditioning (21 dd), the specimens shall be put into the water bath for 6 h according to the exposure class. Specimens were broken and six measurements were made for each specimen. The average depth of penetration is calculated and multiplied by 2.

Table 8. Sorptivity results

Test method T362	MIX n. 1	MIX n. 2	MIX n. 3	MIX n. 4
Method 1	Wet curing			
Average sorptivity test	13,5 mm	13,5 mm	14,0 mm	8,5 mm
Method 2	curing with plastic bags			
Average sorptivity test	14,0 mm	17,5 mm	18,5 mm	16,5 mm
Method 3	curing with wax			
Average sorptivity test	15,0 mm	15,5 mm	16,5 mm	15,5 mm

Table 9. B80.7. Durability requirements for concrete

Class of exposure	Min Cem content Kg/m^3	Max W/C	Max. Sorptivity Penetration depth (mm)	
			GP cement	Blend cement
B1	320	0,5	25	25

The testing summary are presented into the Table 6.

Sorptivity tests were performed on 100×100×350 mm prism prepared in accordance with AS1012 part 11 (Table 8).

5.1 Comments on Sorptivity

The following table, from RMS B80/B1, specifies the minimum requirements for durability of concrete with blended cement (Table 9).

All mixes show sorptivity values lower than the maximum values permitted of 25 mm for RMS/B1exposure and 20 mm exposure for blended cement in concretes under all curing conditions.

The concrete with 1% of the crystalline product addition (MIX n. 2) does not show a significant reduction of water penetration depths compared to the control mix.

The concrete with 2% of crystalline product addition (MIX n. 4) shows the greatest reduction for all three curing conditions tested.

Generally the sorptivity results of all mixes with crystallizing product admixture indicate that these mixes have low permeability at early ages under all curing conditions (wet, bagged, waxed). It follows that this lower concrete permeability is likely to result in an improved durability. The sorptivity test provides an early indication of low permeability concrete but specific testing for other durability related properties is also required.

6 Chloride and Sulfate Content

The determination of chloride and sulfate in hardened concrete was performed according to the test procedure described in AS 1012.20.1. The nitric acid extraction method was used and the results are below summarized (Table 10):

Table 10. Chloride and sulfate content

%	MIX N. 1	MIX N. 2	MIX N. 3	MIX N. 4
Chloride as Cl	0,006	0,006	0,008	0,007
Sulfate as SO_3	0,58	0,68	0,46	0,54

6.1 Comments on Chloride and Sulfate Content

All results are very low and the table above reports the contributes of crystalline product on chloride and sulfate content. Crystalline product has no negative impact on chloride and sulfate contents of the concrete mixes tested.

7 Chloride Ion Diffusion Testing

The NT Built 443 method specifies a procedure for the determination of penetration parameters for estimating the resistance against chloride penetration into hardened concrete. The method requires the assessment of chloride content profile in concrete samples after 35 days of immersion in a 16,5% sodium chloride solution. The chloride diffusion coefficient is calculated as per Fick's second law. The initial acid soluble chloride content is determined according to NT BUILD 208.

The following tables report for each sample the D value (best fit diffusion coefficient) the Cs (best fit chloride content at surface) and the Average diffusion coefficient (A) (Table 11).

Table 11. Chloride Ion diffusion Coefficient

MIX N. 1: Control 75% SL + 25% FA			
Samples	1	2	3
D = m^2/s	7,79* 10^{-12}	6,67*10^{-12}	7,55* 10^{-12}
Cs = %	1,000	1,01	1,15
A	7,34* 10^{-12} m^2/s		
MIX N. 2: Control 75% SL + 25% FA with 1% crystallizing product			
Samples	1	2	3
D = m^2/s	4,51* 10^{-12}	4,68* 10^{-12}	4,69* 10^{-12}
Cs = %	1,00	1,15	1,02
A	4,63* 10^{-12} m^2/s		
MIX N. 3: Control 50% SL + 20% GGBFS +30% FA			
Samples	1	2	3
D = m^2/s	3,35 * 10^{-12}	3,75* 10^{-12}	3,13* 10^{-12}
Cs = %	1,30	1,35	1,30
A	3,41* 10^{-12} m^2/s		
MIX N. 4: Control 50% SL + 20% GGBFS +30% FA + 2% crystallizing product			
Samples	1	2	3
D = m^2/s	1,21 * 10^{-12}	1,42* 10^{-12}	9,49* 10^{-13}
Cs = %	1,60	1,29	1,35
A	1,19* 10^{-12} m^2/s		

7.1 Comments on Chloride Ion Diffusion Coefficient

The MIX n. 2 with 1% of crystallizing product shows a significant reduction of 37% in the chloride diffusion coefficient when compared to a control mix number 1 designed with no crystallizing product.

The MIX n. 4 with 50% SL cement, 20% GGBFS, 30% FA and 2% of crystallizing product had the lowest chloride ion diffusion coefficient.

The excellent result represents a significant reduction of 65% in chloride ion diffusion coefficient when compared to control MIX n. 3 without the crystallizing admixture.

8 Early SEM-EDS Assessment

The impact of crystallizing admixture on concrete durability is partially related to the growth of crystals into the pore voids in the cement matrix. The assessment of concrete specimens with a scanning electron microscope (SEM-EDS) provides a tangible evidence that growing of crystals is partially responsible of the permeability reduction.

Since crystallizing product is supposed to have a reactive behavior with the components of the hydration process, a SEM-EDS assessment on two concrete samples was carried out in order to detect the crystals formation and analyze the chemical composition of the crystalline compounds deposited in the gaps of the cement matrix.

SEM-EDS assessment was carried after 8 months on the following concrete mixes:

- MIX n. 1: control mix with 75% SL cement and 25% fly ash;
- MIX n. 2: 75% SL cement, 25% fly ash and 1% crystalline product

Disc specimens with 10 mm diameter were sawn for stripped concrete cylinders and dried at 38 °C for 2 days. Freshly exposed concrete chips were prepared earlier on the day of the measure, in order to avoid carbonation and any other potential deleterious issues related to the concrete surface. The samples to be tested were coated with carbon examined under a Zeiss LS15 SEM images with a Brucker SDD X Flash 5030 detector for elemental composition analyses.

9 Comments on *SEM-EDS* Assessment

The SEM images and EDS spectrum on control mix at an age of 8 months are below reported (Figs. 1 and 2).

The control mix does not show the presence of any crystals in the concrete structure. Some gel-like texture and unreacted spherical particles of fly ash were noted as presented in Fig. 1. The MIX n. 2 with 1% of crystallizing admixture addition exhibits the presence of needle-like crystalline products. The crystals have a short length of approximately 2–5 μm, and appear to partially block the cement matrix voids and pores, as presented in Fig. 2.

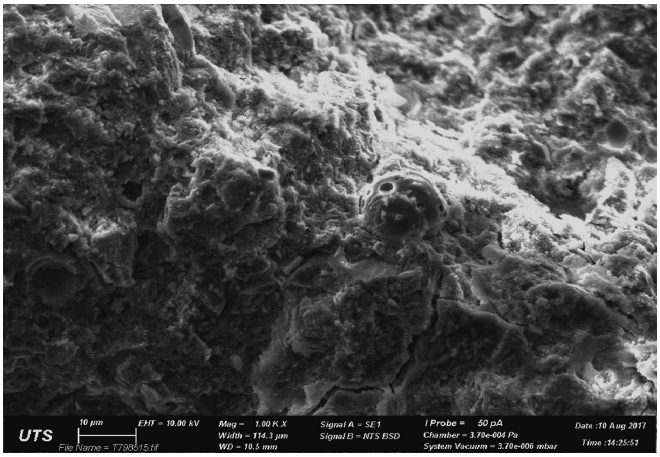

Fig. 1. SEM of control mix @ 1000 magnifications

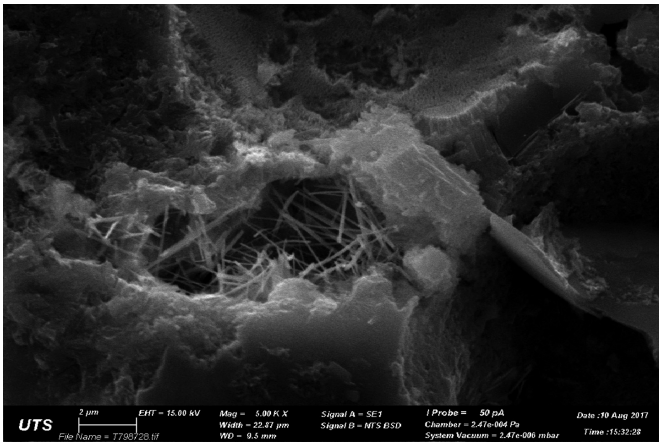

Fig. 2. SEM of Mix N. 2 (@ 5000 magnifications)

The EDS spectrum of the crystals in the concrete samples shown in Fig. 3 has intense peaks of Ca, Si, Al, S and O which are different from ettringite composition with strong peaks for Ca, Al, S and O only. Given the significant presence of Si the needle like crystals are therefore not considered to be pure ettringite although it is likely to be present. Please note that the S is marked as Tl in some of the EDS scans.

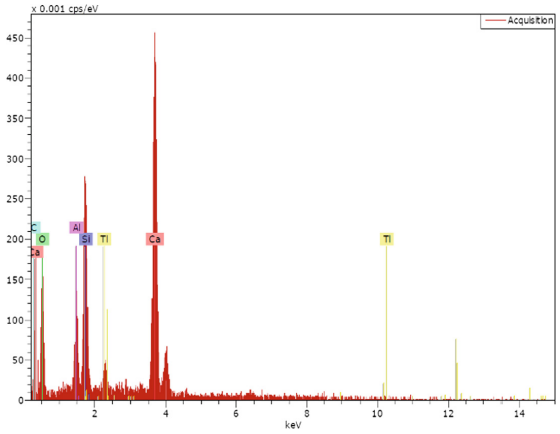

Fig. 3. EDS spectrum of MIX n. 2

10 Conclusions

Compliance assessment for crystalline product has proved that the waterproofing admixture is conforming to a special purpose, normal setting (Type SN) product according to AS 1478:2000.

Further assessments on other concrete mixes showed that crystalline product does not have any significant influence on concrete setting time, slump, water demand, water/cement ratio, air content and bleeding.

The compressive strength at 28 days of admixed concrete have achieved comparable performance of control mixes.

Drying shrinkage of admixed concrete were generally lower or similar to the control. In particular MIX n. 4 has significantly reduced drying shrinkage vs. control mix.

The sorptivity results of all mixes were generally good, providing an early indication of the potential to improve concrete durability due to permeability reduction. All mixes have sorptivity lower than maximum values permitted by RMS/B1.

All the concrete mixes, where the resistance to chloride ion penetration has been assessed, showed a significantly reduced chloride ion diffusion coefficient when compared to control mixes. The results confirm an improved concrete durability for aggressive environments with regard to concrete structures exposed to chloride in marine environments compared with concretes without crystallizing admixtures.

When the crystalline admixture is added, a new crystalline structure already develops at the age of 8 months, partly blocking the voids and pores of the cement matrix mass potentially limiting the water and chloride penetration through pores and capillary channels.

References

1. ACI 212.3R.10 – Report on chemical admixtures for concrete
2. AS 1012.13 – 2015 Methods of testing concrete - determination of the drying shrinkage of concrete for samples prepared in the field or in the laboratory
3. AS 1478.1 – 2000 chemical admixtures for concrete, mortar and grout. Part 1: admixtures for concrete
4. AS 3972 – 2010 General purpose and blended cement
5. NT Built 443 Concrete, hardened: Accelerated chloride penetration
6. Metha, P.K.: Concrete Technology at the crossroads problems and opportunities SP144 ACI, Farmington Hills, Mich
7. Test method T362 Interim test for verification of curing regime – Sorptivity
8. Roads and Maritime Services (RMS) (2012) Guide to QA Specification B80: Concrete Works for Bridges, 2nd edn. Road and Maritime Services, Sydney, NSW

The Effect of Calcium Sulfoaluminate Cement on the Engineering Properties of High Performance Concretes with and Without Fibers

V. Afroughsabet[1], S. Cattaneo[1,3(✉)], G. L. Guerrini[2], and S. Tortelli[2]

[1] Department of Architecture, Built Environment and Construction Engineering, Politecnico di Milano, Milan, Italy
sara.cattaneo@polimi.it
[2] Global Products Innovation Department, Heidelberg Cement Group, Bergamo, Italy
[3] Construction Technologies Institute, Italian National Research Council (ITC-CNR), Viale Lombardia 49, San Giuliano Milanese (MI), Milan, Italy

Abstract. This study investigates the effect of fully replacement of ordinary Portland cement (OPC) with calcium sulfoaluminate cement (CSA) as a sustainable binder in High Performance Concrete (HPC). In addition, the effect of introducing double hooked-end (DHE) steel fibers at fiber volume fraction of 1% was assessed. The mechanical properties of HPC were evaluated and the microstructure of the concretes was studied with scanning electron microscopy (SEM) method. The replacement of OPC with CSA cement results in an improvement in the mechanical properties of HPC particularly at later ages of curing. The addition DHE steel fibers significantly increased the engineering properties of concrete. The bond between cement matrix and steel fibers has been enhanced due to the expansive behavior of CSA cement. The SEM observations also show the significant influence of CSA cement on the microstructure of concrete by formation a rich amount of ettringite that subsequently results in an improvement in the properties of concrete.

Keywords: High performance concrete · Calcium sulfoaluminate cement · Double hooked-end steel fibers · Mechanical properties · SEM observation

1 Introduction

Portland cement concrete is the most widely used human-made material on the planet; about 25 billion metric tons are produced globally each year (Celik et al. 2014a). Nowadays the demand for using high performance concrete (HPC) is widely increased throughout the world (Biolzi et al. 1997). As commonly known, for the production of a HPC matrix, a large amount of binder is normally used. Even though the reasons for concrete's dominance are diverse, the massive production and consumption cycle of concrete have significant environmental impacts, making the concrete industry unsustainable. Currently, Portland cement concrete production accounts for around 7%

M. di Prisco and M. Menegotto (Eds.): ICD 2018, LNCE 42, pp. 325–336, 2020.
https://doi.org/10.1007/978-3-030-23748-6_25

of carbon dioxide (CO_2) emissions annually (Celik et al. 2014b). Most of the emissions are attributable to the production of ordinary Portland cement (OPC) clinker. The current approach to overcome this problem is through the reducing clinker factor, and replacing OPC with supplementary cementitious materials such as fly ash, slag, silica fume and natural pozzolan (Gartner and Hirao 2015). However, due to growing field experience and increasing demand for those materials, there is an essential need to develop concrete made with new generation of cement such as calcium aluminate cements (CAC), calcium sulfoaluminat cement (CSA), alkali-activated binders, and supersulfated cements (Juenger et al. 2011). Recently, CSA cement gained an increased attention due to its lower amount of CO_2 emission as compared to that of the OPC (Gartner 2004). It is reported that the CO_2 emission may reduce up to 35% by replacing OPC with CSA cement (Berger et al. 2013). Additionally, concretes fabricated with CSA cement can result in an increased sulfate resistance, high impermeability and chemical resistance, and low chance for alkali–silica reaction (Tang et al. 2015).

Several benefits of HPC compared to the conventional concretes have significantly increased its use to different structural applications. However, the brittleness of HPC is higher with respect to the normal-strength concrete due to the higher strength, which subsequently increases the vulnerability of HPC to the initiation and propagation of cracks with different sizes in the body of concrete (Savino et al. 2018). The addition of discrete fibers in concrete is recognized as a suitable solution to overcome this weakness and develop materials with enhanced tensile strength, flexural strength, toughness, and thermal shock strength (Sanal et al. 2016; Afroughsabet et al. 2017, 2018; Simões et al. 2017).

This research was aimed to study the effect of CSA cement and DHE steel fibers on the engineering properties of HPC. Compressive strength, splitting tensile strength, flexural strength, modulus of elasticity, and microstructural observation were performed to evaluate the properties of concrete at different curing ages. The findings of this research are highly promising and show that the simultaneous use of CSA cement and DHE steel fibers can significantly increase the engineering properties of HPC.

2 Materials and Methods

To explore the effect of CSA cement and DHE steel fibers on the engineering properties of concrete, four different concrete mixes were developed in this study. The concrete mixes included concretes containing 100% OPC and 100% CSA without and with 1% DHE steel fibers. To assess the effect of curing age on the strength of concrete, the compressive strength tests were conducted at the ages of 1, 7, 28, and 56 days. Additionally, the splitting tensile tests were performed at 7, 28, and 56 days. All the other features of concretes were evaluated at 28 days.

2.1 Materials

The binder materials used in this study were ASTM Type 1 Portland cement, and CSA produced by Italcementi Group. The chemical composition and physical properties of binders were listed in Table 1. Both natural sand, with a 2.9 fineness modulus, and

crushed gravel, with a nominal maximum size of 19 mm, were used as the aggregates at a volume fraction of 50%. The water absorption, specific gravity and other relevant data for the aggregates are given in Table 2. To achieve the desired workability in different concrete mixes, a Driver Care 10 -Sika, was used as a superplasticizer. Additionally, in CSA cement-based concretes, Tartaric acid was used as a retarder to increase the setting time of those mixes. Double hooked-end (DHE) steel fibers with a 60-mm length and an aspect ratio of 65 was employed in this study. The appearance of DHE steel fibers is shown in Fig. 1.

Table 1. Chemical composition and physical properties of binders

Item	Binder (%)	
	ASTM type I	CSA
SiO_2	19.8	7.5
Al_2O_3	4.1	35.0
Fe_2O_3	2.7	1.5
MgO	3.8	–
SO_3	3.4	15.5
Na_2O	0.4	–
K_2O	0.9	–
CaO	61.9	41.0
	Compounds	
C_3S	62.1	–
C_2S	16.7	18.0
C_3A	2.7	–
C_4AF	10.0	–
$C_4A_3\$$	–	60.0
$C_{11}A_7F$	–	4.4
$CaSO_4$	–	9.9
Fluorellestad	–	4.5
Others	8.5	3.2
	Physical properties	
Specific gravity (kg/m^3)	3,170	3,100
Specific surface (m^2/kg)	360	450

2.2 Concrete Mixtures and Mixing Procedure

The water-binder ratio was maintained at 0.35 for all mixtures. A pan mixer was used for the preparation of all the mixes. Prior to adding the raw materials, the surface of the pan mixer was cleaned with a wet towel to avoid the absorption of aggregates moisture by the mixer. The mixing procedure, which was designed by trial, was chosen as follows: Initially, the fine aggregate and cement were mixed for one min. Afterward, approximately half of the water including SP, was introduced into the mixer; the ingredients were further mixed for two minutes. The Saturated Surface Dry

Table 2. Physical properties of the aggregates

Aggregate type	Maximum size aggregate (mm)	Water absorption (%)	Specific gravity	Fineness modulus
Fine aggregate	4.75	1.1	2.65	2.9
Coarse aggregate	19.0	0.96	2.74	–

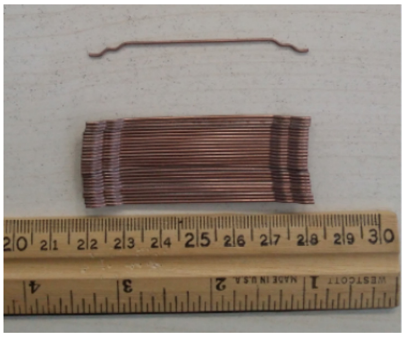

Fig. 1. DHE steel fibers

(SSD) coarse aggregates and remaining mixing water were then introduced, and the mixing was carried on for another 5 min. To fabricate uniform fiber-reinforced concrete, discrete fibers were added gradually to the rotating mixer and were mixed for an additional 5 min to obtain a homogenous concrete mix. Details of mix proportions and the results of a slump test are summarized in Table 3. The content of SP in that table is given as a percentage of the total mass of the binder. To determine the workability of fresh concrete, slump tests were performed as per ASTM C 143 during the preparation of the concrete mixes. The specimens were molded with different dimensions that matched the requirements of their standards test. The samples were covered with a wet plastic sheet to prevent them from dripping water in the first 24 h of curing. Then, the concrete specimens were demolded and immersed in lime-saturated water at 23 °C until reaching their testing ages. For each test, three samples were prepared, and the average value is reported as the final result.

2.3 Testing Methods

Compressive and splitting tensile strength tests were performed using a 3000-kN universal compression machine in accordance with ASTM C39 and ASTM C496, respectively. Cubic specimens with a side 100 mm long were used to determine the compressive strength, whereas cylindrical specimens with diameter of 100 mm and height of 200 mm were used to evaluate the splitting tensile strength of the concrete. The flexural strength tests were carried out as per BS EN 14651 on the prismatic beams with dimensions of 150 × 150 × 600 mm. The modulus of elasticity tests were

Table 3. Mix proportions

Mix no.	Mixture ID	W/B	Water	Binder		Fine agg.	Coarse agg.	Fiber (%)	SP (%)		Slump (cm)
				OPC	CSA						
			(kg/m^3)					DHE	DC10	Tartaric	
1	OPC	0.35	157.5	450	–	905	895	–	1.0	–	21
2	CSA			–	450	901	891	–	1.2	0.2	20
3	OPC-DHE			450	–	892	882	1	1.2	–	21
4	CSA-DHE			–	450	888	878	1	1.4	0.2	19

conducted on the cylindrical specimens with dimensions of 100 × 200 mm as per ASTM C469. To study the microstructure of concrete made with different type of binders, several images were taken from the fracture surface of concrete specimens by using scanning electron microscopy (SEM) method.

3 Results and Discussions

3.1 Consistency

The consistency of the different mixes developed in this study was evaluated by a slump test, and the results are shown in Table 3. The slump values of the concretes varied between 19 and 21 cm.

It was observed that a minimum of 1% superplacticizer was required to adjust the consistency of concrete. As it can be seen, higher content of superplacticizer was used in CSA-based concretes compared to that of the OPC to obtain an almost similar slump value. This can be explained by the fineness of CSA particle size that is lower compared to that of the OPC. Furthermore, the fast rate of CSA cement hydration and its high demand of water to generate ettringite are other reasons that necessitate the addition of higher amount of superplacticizer. The results further indicate that the incorporation of steel fibers had a negative influence on the properties of fresh concrete. The long steel fibers and aggregates interlock in the body of concrete and lead to a reduction in the slump value. To attain the same consistency in the concretes with and without fibers, the content of superplacticizer was slightly increased. Figure 2 shows the appearance of fresh concrete during the slump test for the OPC mix without fibers and CSA cement-based concrete reinforced with 1% DHE steel fibers.

3.2 Compressive Strength

The compressive strength results of different mixes at curing ages of 1, 7, 28, and 56 days are shown in Fig. 3. The compressive strength of CSA cement-based concrete was significantly lower at 1 day compared to that of the concrete manufactured with OPC. This can be explained by the presence of retarder in concrete made with CSA cement that delayed the formation of ettringite and consequently resulted in a reduced

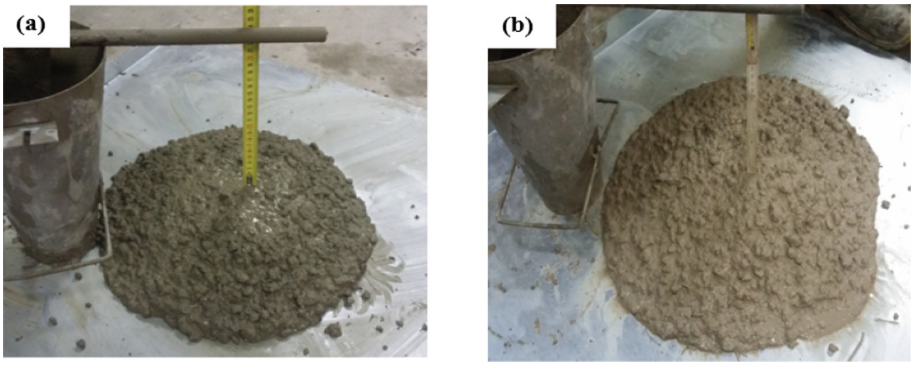

Fig. 2. Slump test

compressive strength. On the other hand, the strength of this concrete mix at 7 days was slightly higher than that of the OPC concrete. It was also observed that the compressive strength of CSA mix was increased by 10% and 12% at 28 days and 56 days, respectively, compared to that of the OPC concrete. The results of fiber-reinforced concrete indicate that the addition of 1% DHE steel fibers in concrete led to an increase in the compressive strength of concrete. For instance, the compressive strength of CSA-DHE1 was increased by 11%, 5%, 5%, and 4% at 1, 7, 28, and 56 days, respectively as compared to the corresponding mix without fiber (i.e. CSA mix). DHE steel fibers, owing to their high elastic modulus and particular shape that restricts the propagation of cracks, alters the tendency of cracks, and subsequently improves the compressive strength of concrete (Afroughsabet et al. 2016).

The results further indicate that the strength evolutions of CSA cement-based concretes is higher compared to those of the OPC mixes. As it can be observed, the 28 and 56 days compressive strength of OPC concrete were 9% and 13% higher than its 7 days strength, while the compressive strength of CSA concrete were 18% and 24% higher than its 7 days strength. The higher rate of strength improvement in CSA concrete compared to that of OPC concrete can be explained by the development of a significant amount of ettringite. The presence of ettringite leads to an enhancement in the microstructure of the concrete that consequently increased the compressive strength of concrete.

3.3 Splitting Tensile Strength

The splitting tensile strength results of different concrete mixes at curing ages of 7, 28, and 56 days are shown in Fig. 4. The results show that the full replacement of OPC with CSA cement resulted in a slight reduction in 7 days tensile strength, while its 28 and 56 days splitting tensile strength were increased compared to those of the OPC. As can be seen in Fig. 4, the splitting tensile strength of CSA concrete was 11% higher at both curing ages of 28 and 56 days compared to those of OPC concrete. The strength reduction at 7 days can be attributed to the presence of retarder that delayed the ettringite formation. However, at later ages of curing, a rich amount of ettringite has

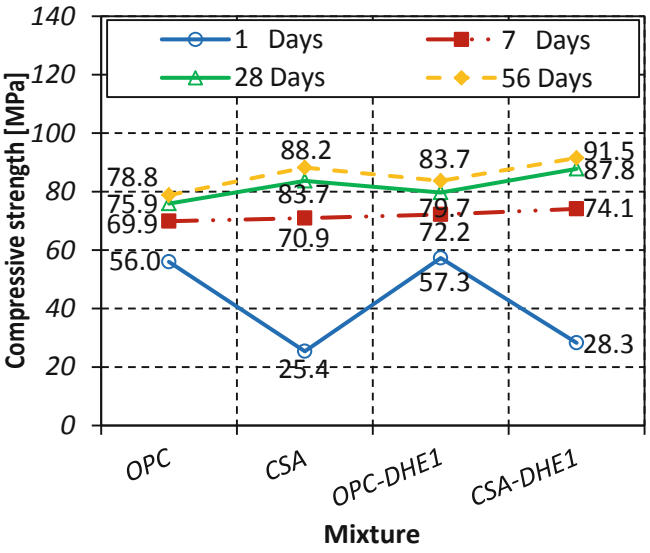

Fig. 3. Compressive strength

been formed as a result of yeelimite hydration, which consequently caused an improvement in the strength of concrete. The results further indicate that introducing 1% DHE steel fibers in concrete significantly increased the splitting tensile strength of concrete. For instance, the splitting tensile strength of OPC-DHE1 was increased by 67%, 70%, and 77% at 7, 28, and 56 days, respectively with respect to the plain OPC mix. These increases for CSA-DHE1 mix were 59%, 76%, and 78%, respectively when compared to the CSA mix. It was observed that the best performing mix was CSA-DHE1 achieved splitting tensile strength of 8.48 MPa at 56 days. This improvement is attributed to the high tensile strength, elastic modulus, and effective anchoring mechanism of DHE steel fibers, which restrained the extension of macro-cracks in concrete.

3.4 Flexural Load-CMOD Curve and Residual Flexural Tensile Strength

The diagram of 28-day Load-CMOD (Crack Mouth Opening Displacement) for different concrete mixes is shown in Fig. 5. The behavior of concretes without fibers was almost linear up to the maximum load, followed by a sharp descending branch up to failure point, then the beam specimens split into two separated parts. The results indicate that the full replacement of OPC with CSA cement resulted in an increase of 20% in the maximum flexural load of concrete. The results of fiber-reinforced concretes illustrate that the addition of fibers remarkably improved the post-cracking behavior of FRC with an extensive cracking process between first crack load and peak load. It was noticed that the addition of 1% DHE steel fibers changed the behavior of concrete and a deflection-hardening performance was occurred in both mixes reinforced with steel fibers. Figure 5 shows that after the appearance of the first crack, the flexural load was gradually reduced. However, the presence of discrete DHE steel fibers in concrete and their

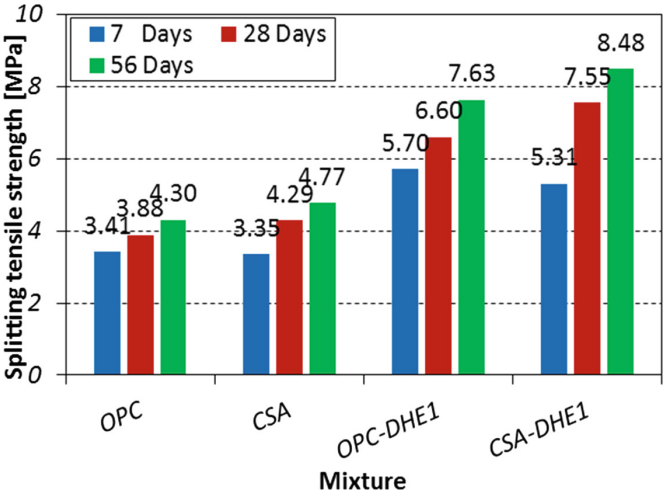

Fig. 4. Splitting tensile strength

ability to carry the load resulted in an increase in the flexural strength after the first crack. The residual flexural tensile strength for different concrete mixes is shown in Fig. 6. The residual flexural strengths corresponding to CMOD at 0.5 mm, 1.5 mm, 2.5 mm, and 3.5 mm are defined as $f_{R,1}$, $f_{R,2}$, $f_{R,3}$, and $f_{R,4}$, respectively.

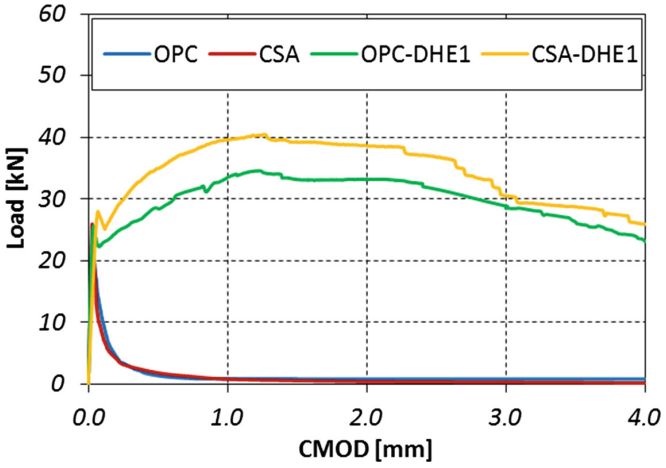

Fig. 5. Flexural load-CMOD curves

The residual flexural strengths in concretes without fibers are very similar and lower than 0.5 MPa. On the other hand, the incorporation of 1% DHE steel fibers in concrete caused a significant enhancement in the residual flexural strength. As can be seen in Fig. 6, the maximum residual flexural strength was attained at CMOD equal to

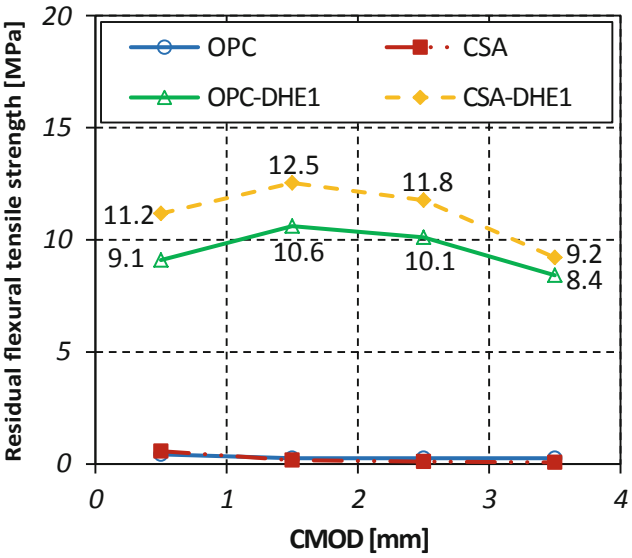

Fig. 6. Residual flexural tensile strength

1.5 mm. The residual flexural strength was reduced due to the extension of macro-cracks and the failure of fiber anchorage or debonding of fibers and the matrix (Wang et al. 2013; Balaguru and Najm 2004).

3.5 Modulus of Elasticity

The 28-days modulus of elasticity of different concrete mixes is shown in Fig. 7. The results indicate that the full replacement of OPC with CSA cement led to an increase in the modulus of elasticity of concrete. The elastic modulus of CSA cement-based concrete was increased by 24% as compared to that of the OPC mix. This increase can be explained by the ability of CSA cement to densify the microstructure of cement matrix and improving the characteristics of ITZ, which those consequently lead to an enhancement in the modulus of elasticity of concrete. The results of FRC indicate that the addition of 1% DHE steel fibers in concrete gradually increased the modulus of elasticity of concrete. This result suggests that introducing steel fibers with elastic modulus higher than that of the cement matrix can result in an improvement in the modulus of elasticity of the concrete.

3.6 SEM Observation

To study the microstructural properties several concretes were fabricated with different binders and the fracture surface was analyzed with the SEM method as shown in Fig. 8. As can be observed, the hydration products of OPC concrete consists of featureless gel of C-S-H, ettringite crystals with needle-like shape, and calcium hydroxide (CH) crystals with plate shape. The results indicate that the content of calcium

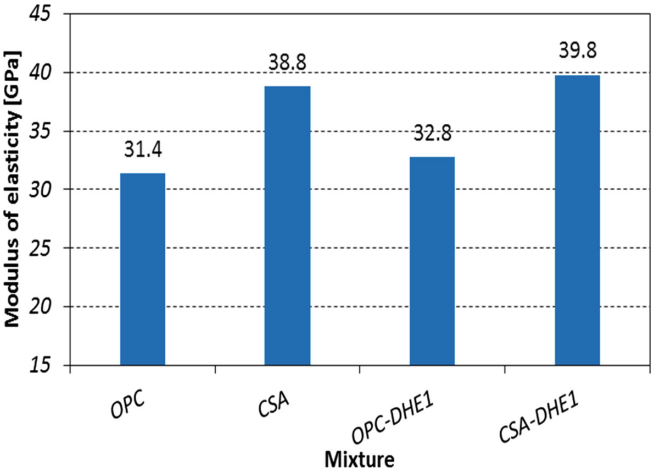

Fig. 7. 28-days modulus of elasticity

hydroxide is relatively higher over that of the ettringite. Additionally, it can be seen that the length of ettringite crystals developed in OPC concrete varied from 1 to 3 μm. Moreover, some pores existed in the surface of cement matrix that can adversely affect the durability properties of concrete. Figure 8(b) shows the hydration products of CSA cement-based concrete, which mainly consist of prismatic ettringite crystals with different sizes. This type of ettringite crystals causes an improvement in the mechanical properties of concrete and also leads to the dimension stability of cement (Arjunan et al. 1999; Mudbhatkal et al. 1986).

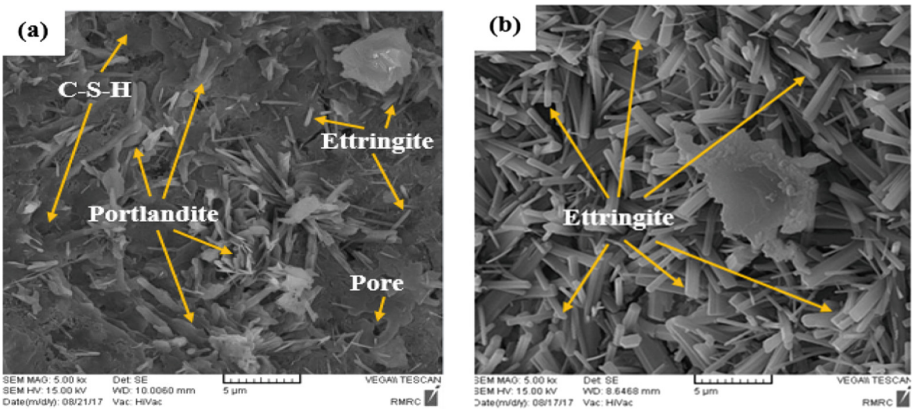

Fig. 8. SEM images: (a) OPC (b) CSA concrete

4 Conclusions

The following conclusions can be drawn from the experimental results:

The slump values of all concretes considered in this study varied from 19 to 21 cm. However, more dosage of superplasticizer was used in CSA cement-based concretes to achieve almost similar consistency to those of the OPC mixes. The addition of steel fibers adversely affects the consistency of concrete.

The full replacement of OPC with CSA cement results in an increase in the mechanical properties of concrete particularly at later ages. This can be attributed to the formation of a rich amount of the ettringite crystals that, due to the interlocking effect, improve the mechanical properties of concrete.

The results also indicate that the strength evolutions of CSA cement-based concretes is higher compared to those of the OPC mixes.

The addition of 1% DHE steel fibers in concrete significantly increases the mechanical properties of concrete specially the splitting tensile and flexural strengths of concrete. For instance, the splitting tensile and flexural strengths of OPC-DHE1 mix at 28 days were increased by 70% and 61% over those of the OPC mix. These increases for CSA-DHE1 mix compared to those of the CSA mix were 76%, and 55%. Moreover, the addition of 1% DHE steel fibers in concrete results in a deflection-hardening behavior.

The SEM results indicate that the hydration products of OPC concrete mix mainly consist of portlandite, while prismatic ettringite crystals are the main products of CSA cement-based concrete.

References

Afroughsabet V, Biolzi L, Ozbakkaloglu T (2016) High-performance fiber-reinforced concrete: a review. J Mater Sci 51(14):6517–6551

Afroughsabet V, Biolzi L, Ozbakkaloglu T (2017) Influence of double hooked-end steel fibers and slag on mechanical and durability properties of high performance recycled aggregate concrete. Compos Struct 181:273–284

Afroughsabet V, Biolzi L, Monteiro PJ (2018) The effect of steel and polypropylene fibers on the chloride diffusivity and drying shrinkage of high-strength concrete. Compos B Eng 139:84–96

Arjunan P, Silsbee MR, Roy DM (1999) Sulfoaluminate-belite cement from low-calcium fly ash and sulfur-rich and other industrial by-products. Cem Concr Res 29(8):1305–1311

ASTM C 39 (2003) Standard test method for compressive strength of cylindrical concrete specimens

ASTM C 143 (2010) Standard test method for slump of hydraulic-cement concrete

ASTM C 469 (2014) Standard test method for static modulus of elasticity and Poisson's ratio of concrete in compression

ASTM C 496 (2011) Standard test method for splitting tensile strength of cylindrical concrete specimen

Balaguru P, Najm H (2004) High-performance fiber-reinforced concrete mixture proportions with high fiber volume fractions. Mater J 101(4):281–286

Berger S, Aouad G, Coumes CCD, Le Bescop P, Damidot D (2013) Leaching of calcium sulfoaluminate cement pastes by water at regulated pH and temperature: experimental investigation and modeling. Cem Concr Res 53:211–220

Biolzi L, Guerrini GL, Rosati G (1997) Overall structural behavior of high strength concrete specimens. Constr Build Mater 11(1):57–63

BSEN 14651 (2007) Test method for metallic fibre concrete-measuring the flexural tensile strength (limit of proportionality (LOP), residual)

Celik K, Meral C, Mancio M, Mehta PK, Monteiro PJM (2014a) A comparative study of self-consolidating concretes incorporating high-volume natural pozzolan or high-volume fly ash. Constr Build Mater 67:14–19

Celik K, Jackson MD, Mancio M, Meral C, Emwas AH, Mehta PK, Monteiro PJM (2014b) High-volume natural volcanic pozzolan and limestone powder as partial replacements for Portland cement in self-compacting and sustainable concrete. Cem Concr Compos 45:136–147

Gartner E (2004) Industrially interesting approaches to "low-CO_2" cements. Cem Concr Res 34 (9):1489–1498

Gartner E, Hirao H (2015) A review of alternative approaches to the reduction of CO_2 emissions associated with the manufacture of the binder phase in concrete. Cem Concr Res 78:126–142

Juenger MCG, Winnefeld F, Provis JL, Ideker JH (2011) Advances in alternative cementitious binders. Cem Concr Res 41(12):1232–1243

Mudbhatkal GA, Parmeswaran PS, Heble AS, Pai BVB, Chatterjee AK (1986) Non-alitic cement from calcium sulphoaluminate clinker-optimisation for high strength and low temperature application. In: U Proceedings of the 8Pth P international congress on the chemistry of cement, pp 364–370

Tang SW, Zhu HG, Li ZJ, Chen E, Shao HY (2015) Hydration stage identification and phase transformation of calcium sulfoaluminate cement at early age. Constr Build Mater 75:11–18

Şanal İ, Özyurt N, Hosseini A (2016) Characterization of hardened state behavior of self compacting fiber-reinforced cementitious composites (SC-FRCC's) with different beam sizes and fiber types. Compos B Eng 105:30–45

Savino V, Lanzoni L, Tarantino AM, Viviani M (2018) Simple and effective models to predict the compressive and tensile strength of HPFRC as the steel fiber content and type changes. Compos B Eng 137:153–162

Simões T, Octávio C, Valença J, Costa H, Dias-da-Costa D, Júlio E (2017) Influence of concrete strength and steel fibre geometry on the fibre/matrix interface. Compos B Eng 122:156–164

Wang JY, Chia KS, Liew JYR, Zhang MH (2013) Flexural performance of fiber-reinforced ultra lightweight cement composites with low fiber content. Cem Concr Compos 43:39–47

Seismic Retrofitting of Masonry with Fabric Reinforced Mortar

S. De Santis[1], G. De Canio[2], G. de Felice[1(✉)], and I. Roselli[2]

[1] Department of Engineering, Roma Tre University, Rome, Italy
gianmarco.defelice@uniroma3.it
[2] SSPT-USER-SITEC Laboratory, ENEA, Rome, Italy

Abstract. Masonry walls are particularly vulnerable against out-of-plane seismic actions. Fabric Reinforced Mortars (FRM) composites, comprising high strength fabrics applied with inorganic matrices, may be used to prevent or delay the onset of collapse mechanisms, and integrated with traditional techniques in compliance with the preservation criteria required for applications to historic structures. This work describes a shake table test carried out on two full-scale wall specimens, one made of two leaves of rubble stones and one of regular tuff blocks. The walls were subjected to out-of-plane vertical bending under seismic base motion. Natural accelerograms were applied in both horizontal and vertical direction with increasing scale factor to collapse. The walls were tested unreinforced, then repaired and strengthened with FRMs, and tested again.

Keywords: Composite materials · Shake table tests · Steel Reinforced Grout (SRG)

1 Introduction

Recent earthquakes have shown the high seismic vulnerability of unreinforced masonry walls against out-of-plane seismic actions. If out-of-plane overturning is prevented by steel tie-bars, collapse may take place by bending, leaf separation or disaggregation, depending upon boundary conditions, wall section morphology and layout of masonry (de Felice et al. 2017). A deep understanding of the out-of-plane seismic response of existing masonry structures and on the most appropriate retrofitting technologies is necessary, in order to ensure an adequate protection of the life and health of people and to safeguard the built heritage in earthquake prone areas. Fabric Reinforced Mortar (FRM) composites, comprising high strength textiles bonded to the structural members by means of an inorganic matrix, can be efficiently used for structural retrofitting. They offer versatility, easy and fast installation, and high mechanical performances with minimum mass increase (e.g., see Ivorra et al. 2017). Furthermore, FRM can be integrated in the plaster layer during the ordinary maintenance works of the façades, as a compatible and sustainable for the seismic protection of the built heritage, which, as an additional advantage, is relatively cost-efficient (indicatively, €80 ÷ 120/m^2).

A number of experimental investigations have been carried out so far on either small-medium scale wall panels under three/four-point bending (Papanicolaou et al. 2008, 2011;

M. di Prisco and M. Menegotto (Eds.): ICD 2018, LNCE 42, pp. 337–346, 2020.
https://doi.org/10.1007/978-3-030-23748-6_26

Valluzzi et al. 2014) or full-scale specimens under bending (Babaeidarabad et al. 2014), compression and bending (Bellini et al. 2018) or earthquake base motion (De Santis et al. 2016). These tests have shown the effectiveness of FRMs for improving the out-of-plane flexural strength of masonry walls. Nevertheless, a deeper knowledge still needs to be gained before they can be confidently used in engineering practice.

This work describes a shake table test carried out on two full-scale wall specimens, one made of two leaves of rubble stones and one of regular tuff blocks, subjected to seismic out-of-plane vertical bending. The walls were tested unreinforced, then repaired and strengthened with FRMs, and tested again. A basalt mesh was applied over the entire surface of the stone wall, while a unidirectional textile of ultra-high tensile strength steel was used on the tuff wall. Both textiles were bonded with a lime based mortar. The response of the specimens before and after retrofitting are compared in terms of acceleration and displacement capacity, failure modes and dynamic properties.

2 Experimental Setup and Input Signals

2.1 Wall Specimens Under Investigation

Two full-scale wall specimens were tested on the shake table, one in rubble stone masonry and one in regular tuff masonry, having 3.48 m height, 1.53 m width and 0.25 m thickness (Fig. 1). The walls were built on a reinforced concrete foundation anchored to the shake table, to make it possible to test them together. The first layer of masonry was partially laid in the foundation to prevent the development of a crack at the masonry-to-concrete interface. The stone wall was built with roughly squared lime stone units arranged in two leaves, partially connected by transversal stones. It had 24.2 kN/m^3 weight density (γ), 14.3 N/mm^2 compressive strength (f_c) and 4522 N/mm^2 Young's modulus (E_c). The tuff wall was built squared blocks in one leaf and had γ = 12.3 kN/m^3, f_c = 5.9 N/mm^2, and E_c = 1575 N/mm^2. On top of each wall, a top beam was built with four layers of clay bricks and an M15 lime-based mortar (γ = 1800 kN/m^3), reinforced with a steel textile in the bed joints to provide tensile and bending strength. Each top beam was connected to the underlying masonry wall with three 600 mm long steel connectors inserted in drilled holes and then injected with a lime-based grout. In order to avoid overturning and induce out-of-plane vertical bending under seismic base motion, the horizontal displacement of the top beams was constrained. On the other hand, their upward displacement and rotations were free, aiming at reproducing the constrain conditions experienced by a perimeter wall at the last floor of a masonry building. Two stiffened steel frames were placed on the shake table near the masonry walls. The frames were connected to each other on top by means of two IPE200 I beams. Eight rubber hollow cylinders were fixed to the beams and put in contrast with the brickwork top beams, two on the front and two on the back, for each specimen. Finally, an additional load of 600 kN was placed on top of each wall (using steel plates) to simulate a light (timber) roof.

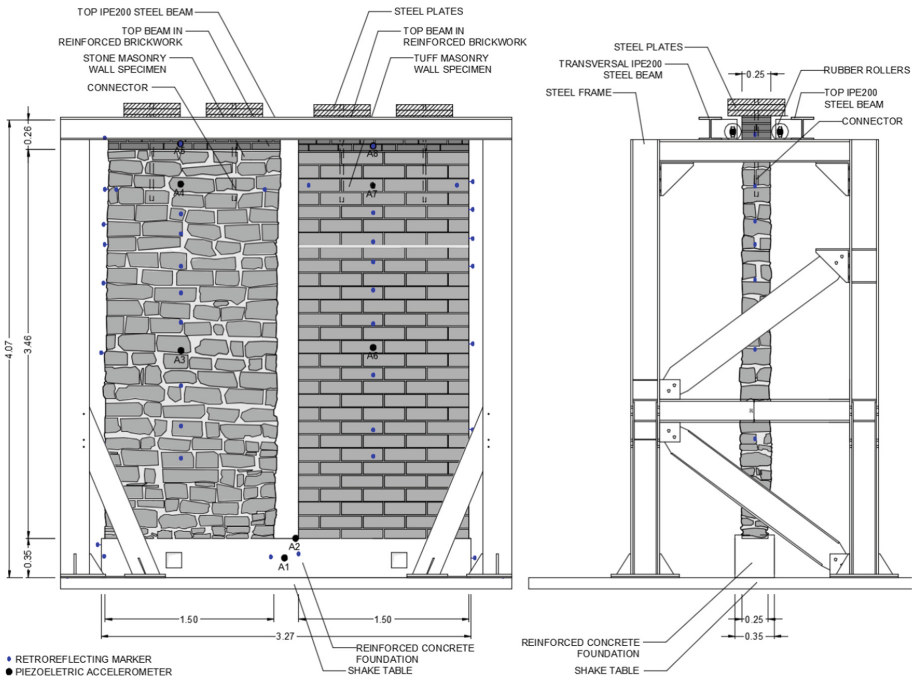

Fig. 1. Experimental setup for shake table tests.

2.2 Input Signals

Five input signals were selected amongst the records of the following severe earthquakes in Italy: 1980 Irpinia 1997 Umbria-Marche 2009 L'Aquila 2012 Emilia, and 2016 Centre Italy. Table 1 lists the signals in the order in which they were applied and includes the date of the event, the name of the record station and the peak ground acceleration (PGA) in horizontal and vertical directions. For the horizontal direction, the orientation (North-South or East-West) is also specified. The chronological order of the inputs was chosen based on the PGA in the horizontal direction to obtain a sequence with increasing intensity. The signals were applied in both horizontal and vertical directions with increasing scale factor (SF) up to the attainment of a severe damage, close to collapse. Random tests under PGA = 0.05 g white noise were carried out after each sequence with the same SF for dynamic identification analyses.

2.3 Instrumentation

Tests were carried out on a 4 m × 4 m shake table with six degrees of freedom and ± 3 g acceleration capacity. Eight piezoelectric accelerometers were installed, two on the reinforced concrete foundation to record the horizontal and the vertical components of the acceleration, and three on each wall specimen, at 1.70 m, 3.18 m and 3.45 m height from the foundation. The accelerometers on the specimens recorded only the horizontal component. Test data were acquired at 100 Hz sampling frequency and

Table 1. Accelerograms selected to perform the shake table tests. Data collected from European Strong Motion Database (ESD). The scale factor of AMT record was corrected in the ESD after the shake table tests and the corrected amplitude is twice as that used in the experimental investigation.

Earthquake		Horizontal comp.		Vertical comp.
Event	Record station	Or.	PGA [g]	PGA [g]
23/11/1980, Irpinia	Bagnoli, BGI	E-W	0.181	0.101
20/05/2012, Emilia	Mirandola, MRN	N-S	0.267	0.303
24/08/2016, Amatrice	Amatrice, AMT	N-S	0.376	0.399
26/09/1997, Umbria-Marche	Nocera Umbra, NCR	N-S	0.492	0.398
06/04/2009, L'Aquila	L'Aquila, AQV	E-W	0.644	0.486

filtered using a third-order baseline correction and a fourth order Butterworth band-pass filter in the 0.35–20 Hz range. A high-resolution 3D motion capture system, named 3DVision (De Canio et al. 2016) was used to measure the spatial displacements of 53 spherical wireless retro-reflecting markers installed on the walls, the foundation, the top beams, and the shake table. Nine near infrared digital camera were used to record the displacements of the markers at 200 Hz frequency. In the analysis of test outcomes discussed in the following sections, accelerations were derived from the accelerometers whereas displacements were obtained from the 3DVision.

3 Tests on the Stone Wall

3.1 Results of the Tests on the Unreinforced Stone Wall

After the first set of tests with SF = 0.25, the mortar joints at 2.40 m height crushed and the wall behaved as a two-block mechanism. The presence of horizontal joints facilitated the development of such horizontal hinge, whereas the crossing units prevented leaf separation. After the test under AQV signal with SF = 0.75 (PGA = 0.48 g), a maximum displacement of 135 mm (backwards) was measured and the wall was considered collapsed, as shown in Fig. 2, having the positive and negative PGA values on the y-axis and the corresponding maximum and minimum displacements on the x-axis. Given the same failure mode, the lower capacity of the stone wall with respect to the tuff wall should be attributed to the higher mass density, which entailed higher inertial forces under the same earthquake base excitation. The frequency of the unreinforced stone wall was 8.5 Hz before the beginning of the test and suddenly decreased to 3.8 Hz after the test with SF = 0.50 (results of the identification analyses after the test with SF = 0.75 were unavailable).

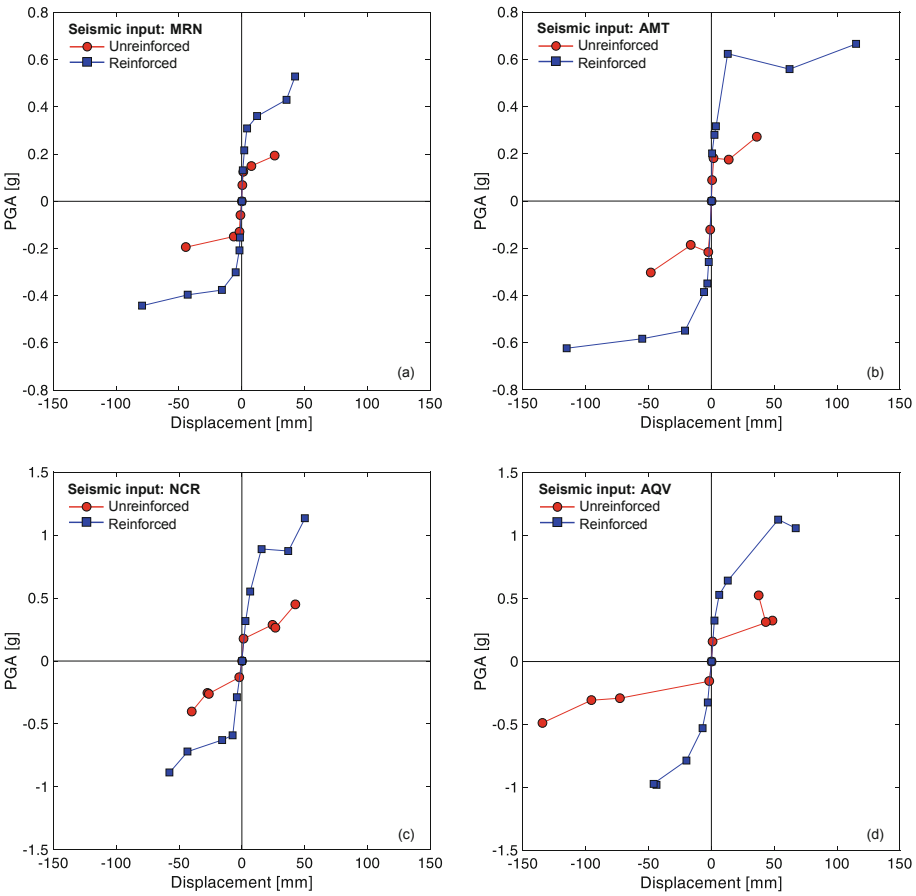

Fig. 2. PGA vs. deflection curves of the stone specimen before and after BFRM retrofitting.

3.2 Retrofitting with Basalt Fabric Reinforced Mortar (BFRM)

After the tests, the stone wall was repaired by repointing the crushed bed joints with lime-based grout and replacing the stones that had fallen down. Then, it was reinforced by applying on both sides a bidirectional balanced basalt fabric with 18 mm × 18 mm grid spacing. The basalt fibre bundles are pre-impregnated to improve adhesion and durability and each roving also includes two stainless steel micro-wires. The basalt mesh has surface mass density $\gamma_f = 400$ g/m^2, design thickness $t_f = 0.064$ mm, tensile strength $f_f = 881$ N/mm^2, tensile modulus of elasticity $E_f = 51.9$ kN/mm^2, and ultimate strain $\varepsilon_f = 1.92\%$. The textile was bonded to the entire surface of the wall, including the top beam, with a lime-based mortar having compressive strength $f_{mc} = 14.5$ N/mm^2, Young's modulus $E_m = 9.6$ kN/mm^2, and tensile strength $f_{mt} = 4.6$ N/mm^2. The overall thickness of the FRM overlay was about 10 mm, even if the unevenness of the substrate entailed a certain local variability. Since the wall had two leaves, transversal connectors (with density of 2/m^2) were also installed with the aim of

preventing leaf separation and improve the substrate-to-FRM bond. The connectors were made by rolling the steel textile used for SRG, inserted in crossing holes drilled in the masonry before the installation of the basalt mesh and injected with lime-based grout at the end of the retrofitting works.

3.3 Results of the Tests on the Stone Wall After Retrofitting

The BFRM reinforcement entailed a gain in seismic capacity of 135% (Fig. 2). A maximum PGA of 1.13 g was recorded during the test with NCR amplified by a SF of 1.75. Collapse occurred during the test with AMT signal and the recorded PGA was, in this case, 0.96 g. The basalt mesh detached locally from the substrate during the set of tests with SF = 1.00; damage progressively developed and, at failure, a large surface of the reinforcement debonded from the masonry (Fig. 3a). Such detachment appeared mainly caused by the crushing of the substrate and the buckling of the FRM overlay, rather than by the shear stresses. The steel connectors not only prevented leaf separation but also ensured an effective load transfer from the wall to the basalt fabric (Fig. 3b), which broke only locally near the edges of the stones. Finally, the frequency of the retrofitted wall was 8 Hz before the beginning of this second session of tests and 3.7 Hz at its end (Fig. 4a).

Fig. 3. Damage pattern on the stone wall retrofitted with BFRM at the end of the shake table tests.

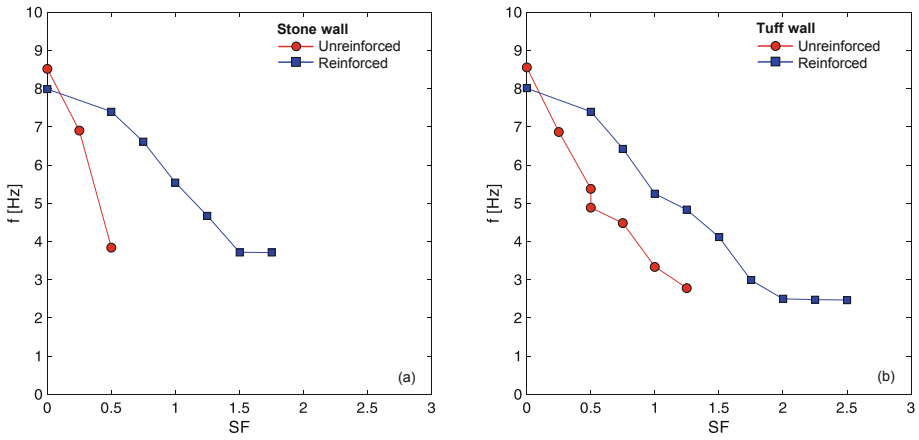

Fig. 4. Frequency vs. scale factor of the tuff wall (a) and of the stone wall, (b) before and after retrofitting.

4 Tests on the Tuff Wall

4.1 Results of the Tests on the Unreinforced Tuff Wall

In total, 31 seismic tests were carried out on the tuff wall with SF from 0.25 to 1.25. The specimen exhibited a nearly elastic behaviour for low intensity inputs, up to the development of a hinge with the crushing of the mortar in the bed joint at 2.70 m height from the foundation, during a test with PGA of 0.31 g. Collapse occurred under AQV signal with SF = 1.25, with a recorded PGA of 0.86 g and a maximum displacement of 112 mm (Fig. 5). The failure mode was characterized by the development of a second hinge, at 3.15 m height. The mortar joints of the hinges crushed but the tuff blocks were not badly cracked. The frequency of the wall (f), derived from the transfer functions of the acceleration time histories recoded under white noise, decreased from 8.5 Hz to 2.8 Hz, as shown in Fig. 3a, in which f is plotted versus the SF of the set of tests preceding the random test.

4.2 Retrofitting with Steel Reinforced Grout (SRG)

After the first test series, the tuff wall was repaired by repointing the crushed bed joints with lime-based grout. Then, it was reinforced with four (two per side) 150 mm strips of Steel Reinforced Grout (SRG) 150 mm spaced. SRG comprised a unidirectional textile made of galvanized Ultra High Tensile Strength Steel (UHTSS) cords 6.35 mm spaced. The textile has $\gamma_f = 670$ g/m^2, $t_f = 0.084$ mm, $f_f = 3191$ N/mm^2, $E_f = 186$ kN/mm^2, and $\varepsilon_f = 2.19\%$. Laboratory bond tests showed that the roughness of the cords and their spacing provide a good interlocking within the mortar and substrate-to-reinforcement load transfer capacity (De Santis et al. 2017). The textile was bonded along the entire height of the wall, including the top beam, with the same lime-based mortar used for BFRM. A first layer of mortar was laid down by hand after having

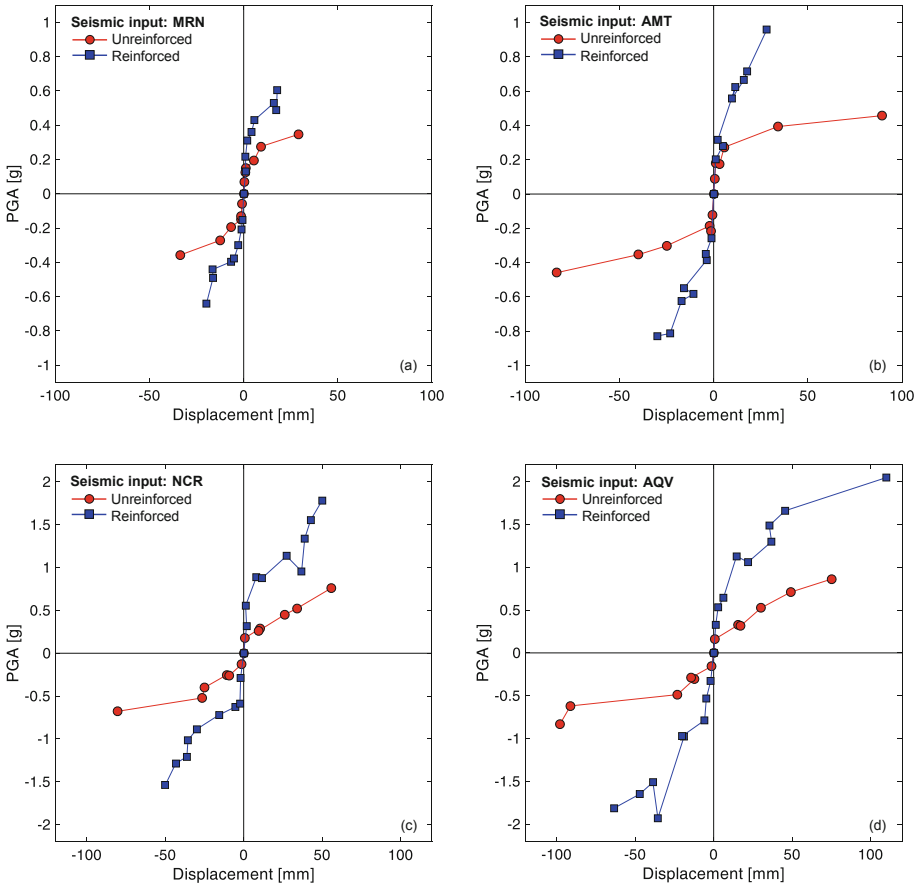

Fig. 5. PGA vs. deflection curves of the tuff specimen before and after SRG retrofitting.

consolidated the substrate with potassium silicate. Then, the steel textile was installed taking care of letting the mortar passing through the voids between the cords. Finally, the second layer of mortar was laid down; the total thickness of the SRG strip was about 10 mm. Each strip was connected to the foundation with a 150 mm long steel connector, made by rolling the textile, inserted in an inclined hole that was eventually injected with a lime-based grout.

4.3 Results of the Tests on the Tuff Wall After Retrofitting

After repair and retrofitting, the specimen was tested again on the shake table, under the same input signals used in the first session. A total of 41 seismic tests were carried out on the strengthened specimen. The SRG reinforcement did not significantly change the initial behaviour of the wall in terms of displacements and stiffness, but limited its out-of-plane deflections under medium-high intensity signals. The out-of-plane seismic capacity of the tuff wall increased to a PGA of 2.05 g (238% that of the unreinforced

wall). Collapse occurred by crushing of the tuff blocks in the same joints where the hinged had formed in the previous tests, without detachment of the SRG strips from the substrate. A slower damage accumulation was observed with respect to the unreinforced specimen, as the frequency of the wall decreased from 8 Hz (very similar to the initial frequency of the unreinforced wall) to 2.5 Hz at the end of the tests (Figs. 4b, 6).

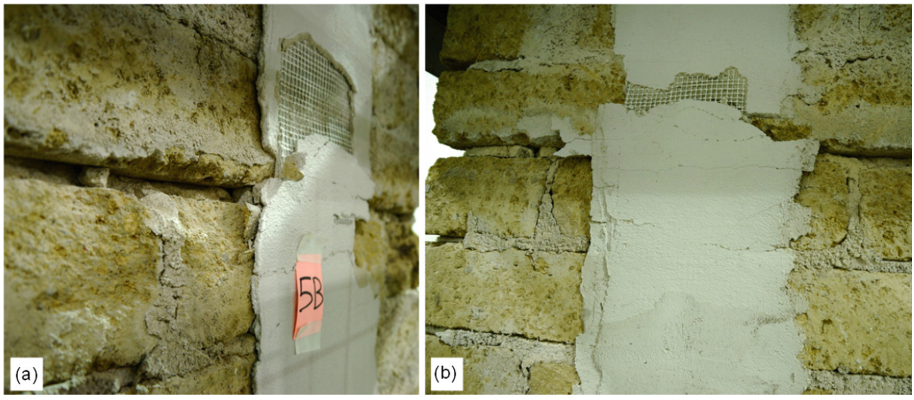

Fig. 6. Damage pattern on the tuff wall retrofitted with SRG at the end of the shake table tests.

5 Conclusions

Externally bonded mortar-based composites proved effective in increasing the seismic out-of-plane bending capacity of masonry walls. A basalt textile reinforced mortar (BFRM) bonded to the entire surface of a stone wall ensured an increase of the strength (135%, 1.13 g vs. 0.48 g) whereas, despite the higher PGA the maximum recorded displacements decreased from 134 mm to 115 mm (−14%). The necessity of reinforcing the wall over its entire surface (in order to prevent disaggregation), required the use of a mesh instead of the unidirectional textile, but this also allowed the application of a relatively weaker material (basalt in place of steel). The transversal connectors resulted essential to avoid leaf separation and improve the load transfer capacity from the masonry to the reinforcement. Steel reinforced grout (SRG) strips enhanced the maximum PGA attained in shake table tests by a full-scale tuff masonry wall by 138% (2.05 g vs. 0.86 g) and its deflection capacity by 12% (110 mm vs. 98 mm). Despite applied in discrete strips, SRG resulted effective thanks to the high tensile strength of the steel cords and the good adhesion with the substrate. BFRM and SRG composites did not change the initial stiffness of the walls, and ensured a lower progressive damage accumulation under increasing intensity of the seismic inputs.

On the one hand, the experimental results obtained in this study cannot be directly extrapolated to other FRM systems, masonry substrates and loading configurations. Other tests could provide important information on the influence of the interaction between orthogonal walls, of openings and of a roof. Other masonry types (e.g., brickwork) and reinforcement materials (e.g., glass) could be investigated to gain a

deeper understanding on this innovative technology. On the other hand, the shake table tests clearly proved the effectiveness of FRM systems for enhancing the out-of-plane seismic capacity of masonry walls, suggesting that composite materials with inorganic matrices can be successfully used to protect the building stock in earthquake prone areas. Based on experimental outcomes, design guidelines should be developed in order for FRM composite materials to be successfully used in the structural rehabilitation and in the protection of architectural heritage.

Acknowledgements. This work was carried out within the Research Projects "Composites with inorganic matrix for sustainable strengthening of architectural heritage" funded by the Italian Ministry for Foreign Affairs (Years 2017–2018, Grant N. PGR00234) and "ReLUIS-DPC 2017", funded by the Italian Department of Civil Protection. Kerakoll SpA provided cofounding and reinforcement materials.

References

Babaeidarabad S, De Caso F, Nanni A (2014) Out-of-plane behavior of URM walls strengthened with fabric-reinforced cementitious matrix composite. J Compos Constr 18(4):04013057

Bellini A, Incerti A, Bovo M, Mazzotti C (2018) Effectiveness of FRCM reinforcement applied to masonry walls subject to axial force and out-of-plane loads evaluated by experimental and numerical studies. Int J Archit Heritage 12(3):376–394

De Canio G, de Felice G, De Santis S, Giocoli A, Mongelli M, Paolacci F, Roselli R (2016) Passive 3D motion optical data in shaking table tests of a SRG-reinforced masonry wall. Earthquakes Struct 10(1):53–71

de Felice G, De Santis S, Lourenço PB, Mendes N (2017) Methods and challenges for the seismic assessment of historic masonry structures. Int J Archit. Heritage 11(1):143–160

De Santis S, Casadei P, De Canio G, de Felice G, Malena M, Mongelli M, Roselli I (2016) Seismic performance of masonry walls retrofitted with steel reinforced grout. Earthquake Eng Struct Dynam 54(2):229–251

De Santis S, Ceroni F, de Felice G, Fagone M, Ghiassi B, Kwiecień A, Lignola GP, Morganti M, Santandrea M, Valluzzi MR, Viskovic A (2017) Round robin test on tensile and bond behaviour of steel reinforced grout systems. Compos B Eng 127:100–120

Ivorra S, Bru D, Galvan A, Silvestri S, Apera C, Foti D (2017) TRM reinforcement of masonry specimens for seismic areas. Int J Saf Secur Eng 7(4):463–474

Papanicolaou CG, Triantafillou TC, Lekka M (2011) Externally bonded grids as strengthening and seismic retrofitting materials of masonry panels. Constr Build Mater 25(2):504–515

Papanicolaou CG, Triantafillou TC, Papathanasiou M, Karlos K (2008) Textile reinforced mortar (TRM) versus FRP as strengthening material of URM walls: out-of-plane cyclic loading. Mater Struct 41(1):143–157

Valluzzi MR, Da Porto F, Garbin E, Panizza M (2014) Out-of-plane behavior of infill masonry panels strengthened with composite materials. Mater Struct 47(12):2131–2145

Bond Behavior of FRCM Composites Applied on Concrete and Masonry

A. Bellini[1(✉)] and C. Mazzotti[2]

[1] CIRI Buildings and Construction, University of Bologna, Bologna, Italy
alessandro.bellini5@unibo.it
[2] Department of Civil, Chemical, Environmental, and Materials Engineering, University of Bologna, Bologna, Italy

Abstract. Fiber Reinforced Cementitious Matrix (FRCM) composite materials have been recently introduced in civil engineering applications for the strengthening of masonry and reinforced concrete elements. The aim of the presented experimental study is to evaluate the bond behavior of carbon and glass FRCM composite materials, in the form of bidirectional grids or unidirectional sheets, applied on different substrates by using a cementitious mortar together with an adhesion promoter. Experimental outcomes obtained on masonry using a cementitious mortar have also been compared with the results coming from the same strengthening systems applied with lime mortar. All specimens were subjected to single-lap shear tests until failure, in order to evaluate failure modes, maximum bond capacity and the whole samples behavior in terms of displacement and strain maps (thanks to Digital Image Correlation technique). Experimental outcomes highlighted the good performance of the strengthening systems tested when applied in combination with the adhesion promoter.

Keywords: FRCM · Bond tests · Concrete · Masonry · Digital Image Correlation

1 Introduction

The use of innovative retrofitting systems has become more and more interesting in the last decades for the strengthening of concrete and masonry structures, typical of Italian and European cultural heritage. The high performance of composites and their low weight, together with some other advantages in terms of easiness and reduced costs of installation in comparison to the traditional strengthening techniques, are pushing the research on this topic. In this framework, Fiber Reinforced Cementitious Matrix (FRCM) composite materials are becoming more and more an attractive solution, relying on several advantages of inorganic matrices in comparison with epoxy resin, such as fire resistance, permeability, better compatibility with the support, reversibility, applicability to wet surfaces.

A great number of studies are currently available on the tensile and bond performance of Fiber Reinforced Polymer (FRP) strengthening systems (Carloni and Subramaniam 2012; Carrara et al. 2013; Mazzotti et al. 2015a, b; de Felice et al. 2016;

M. di Prisco and M. Menegotto (Eds.): ICD 2018, LNCE 42, pp. 347–359, 2020.
https://doi.org/10.1007/978-3-030-23748-6_27

Kwiecień et al. 2016; Sassoni et al. 2017, 2018), but only a limited number of researchers have investigated the tensile and bond behavior of FRCMs (D'Ambrisi et al. 2013; de Felice et al. 2014; Carozzi et al. 2017; De Santis et al. 2017; Leone et al. 2017; Lignola et al. 2017).

In this framework, the presented experimental work is aimed at improving the knowledge about the performance of FRCM retrofitting systems applied on concrete and masonry substrates, investigating in particular their behavior in terms of adhesion between matrix and substrate. To this purpose, after a proper material characterization, single-lap shear tests were carried out on samples, evaluating the effects of surface preparation and of an adhesion promoter on carbon and glass fibers strengthening systems. Bidirectional grids and unidirectional sheets were both applied by using a cementitious mortar, evaluating also the possible performance of a NHL one in combination with the same adhesion promoter. An advanced optical technique (Digital Image Correlation) was used in order to investigate displacements and strain patterns on the surface of the specimens tested. This method allowed to properly analyze the identified failure modes obtaining, for each sample, load-elongation curves, strain profiles along the specimen centerline and complete 3D deformation maps.

2 Materials, Test Set-Up and Instrumentations

2.1 Experimental Program, Materials Properties and Samples Preparation

In order to investigate the bond behavior of carbon and glass FRCM composites applied on concrete and masonry substrates, two different types of samples were prepared. For bond tests on concrete, prisms with dimensions of 150 × 200 × 600 mm^3 (see Fig. 1a) were used; FRCM reinforcements were applied without a particular surface preparation, but only after brushing, cleaning and wetting the surface. Mechanical characterization of concrete was performed by means of compression tests on standard cubes, obtaining a mean compressive strength of 37.23 MPa.

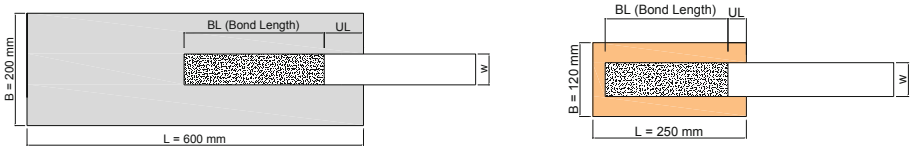

Fig. 1. Geometry of the samples tested: (a) concrete prisms; (b) clay bricks.

As for masonry substrate, single-lap shear tests were carried out on bricks reinforced with GFRCM and CFRCM composites, choosing a new clay brick characterized by mean dimensions ($L \times B \times h$, see Fig. 1b) of about 250 × 120 × 60 mm^3. In this case, specimens were tested after applying FRCM strengthening systems on bricks

without surface preparation and after treating them with a sandblasting process, with the aim of improving surface roughness and then comparing the results in terms of failure modes and maximum bond capacity. In more detail, the sandblasting process on clay bricks was performed by using quartz sand with a particle size between 0.4 and 0.9 mm and a pressure of 700 kPa. Mechanical properties of bricks were evaluated by means of compression and three-point bending tests, obtaining, respectively, a mean compressive strength of 32.90 MPa and a mean flexural strength of 7.14 MPa.

All the samples were strengthened by using carbon or glass fibers applied together with a cementitious (CM) matrix or a natural hydraulic lime (NHL) mortar with the addition, in most cases, of an adhesion promoter. The experimental program is summarized in Table 1 and described, in more detail, in Table 2, where a univocal sample code is used for identifying the samples: the first letter indicates the substrate (C for concrete, B for brick) with an additional letter (S), when present, for identifying the performed sandblasting process; the second group of characters identifies the reinforcement type (C1-C5 for carbon or G for glass); the letter P (if present) indicates the use of an adhesion promoter and is followed by a third group of letters related to the type of mortar used: cementitious (CM) or lime based (NHL). Mechanical characterization of mortars was performed by means of three point bending tests on standard prisms first and then compressive tests on the two remaining broken parts (UNI EN 1015-11:2007). According to the characterization tests, CM matrix exhibited a mean flexural tensile strength of 7.03 MPa and a mean compressive strength of 30.78 MPa, whereas NHL fiber-reinforced mortar showed values, respectively, of 3.76 MPa and 11.17 MPa.

Table 1. Experimental plan.

Substrate	Mortar type	Number of tests	
		Carbon fiber	Glass fiber
Concrete	Cementitious (CM)	6	1
Masonry	Cementitious (CM)	11	4
Masonry	Lime based (NHL)	6	6

Three different types of carbon fibers were used for the strengthening systems:

- the first type (C1) is based on a bidirectional grid with a density of 170 g/m^2, an equivalent dry fiber thickness of 0.047 mm and a strand spacing of 9 mm. Maximum tensile strength and elastic modulus (for the use of the grid within FRCM strengthening systems) are, respectively, 2300 MPa and 220 GPa;
- the second carbon fiber type (C2) is a unidirectional sheet with a density of 160 g/m^2, an equivalent dry fiber thickness of 0.088 and a maximum tensile strength (determined through tensile tests on FRCM coupons) of 1800 MPa;
- the third type (C3) is a unidirectional sheet characterized by a different density in comparison with C2 (300 g/m^2) and with an equivalent dry fiber thickness of 0.167 mm. For this third type of carbon reinforcement, maximum tensile strength (for its use within CM matrix) is 1650 MPa.

Table 2. Experimental results: failure modes and maximum bond capacity.

Substrate	Sample type	Failure mode	Failure load [kN]	Mean [kN]	$\sigma_{f,\ mean}$ [MPa]
Concrete	C_C1P_CM	A	5.75	5.35	2108
		A	4.94		
	C_GP_CM	A	2.62	2.62	910
	C_C4P_CM	B	9.71	9.12	650
		B	8.53		
	C_C4_CM	C	5.90	5.90	421
	C_C5P_CM	D	14.31	14.31	617
Masonry	B_C1P_CM	B	2.96	3.32	1308
		B	3.69		
	B_GP_CM	B*	2.74	2.74	951
	BS_C1P_CM	A	5.60	5.77	2273
		A	5.95		
	BS_C1_CM	E	2.42	2.42	954
	BS_GP_CM	A	2.50	2.79	969
		A	3.07		
	BS_G_CM	E	0.82	0.82	285
	BS_C2P_CM	F	3.41	3.60	744
		F	3.80		
	BS_C2_CM	E	1.16	1.16	240
	BS_C3P_CM	F	3.93	3.67	400
		F	3.42		
	BS_C3_CM	E	1.09	1.09	119
	BS_C1P_NHL	A	4.58	4.19	1651
		F	3.50		
		F*	4.57		
		F*	3.51		
		F*	3.63		
		F*	5.34		
	BS_GP_NHL	A	2.53	2.75	955
		A	2.67		
		A	2.80		
		A	2.77		
		A	2.79		
		A	2.94		

Samples reinforced with C4 and C5 strengthening systems were characterized instead, by the presence of two and three plies of carbon fibers, respectively: the first ply is, for both of them, realized with C2 type reinforcement with an addition of one (or two) plies of C3 type carbon fiber. All the reinforcement layers were applied in combination with an adhesion promoter.

The bidirectional glass fiber grid used (G) is characterized by a density of 300 g/m^2, a strand spacing of 12 mm and an equivalent dry fiber thickness of 0.060 mm; tensile tests on FRCM coupons revealed, for this fourth class of strengthening systems, a maximum tensile strength of 1100 MPa and an elastic modulus of 65 GPa.

The adhesion promoter, used to improve the adhesion between fibers and CM or NHL matrix, is a two-component, water-based product, consisting of two resins supported on an inorganic, microcrystalline, thixotropic matrix, characterized by a flexural strength of 5 MPa, an elastic modulus of 4.5 GPa and by an ultimate deformation of 1.2%.

All the samples were prepared following the same procedure: delimitation of the bond area, wetting of the surface, application of a first (3 mm) layer of mortar, of the adhesion promoter (if present), placing of the reinforcement layer, then application of the adhesion promoter again and, finally, of the upper layer of mortar (3 mm). All thicknesses were controlled by making use of appropriate spacers. The adopted bond length (*BL* in Fig. 1) was 250 mm for concrete samples and 200 mm for all the masonry specimens. An unbonded length *UL* of 70 and 30 mm (for concrete and brick specimens, respectively) was left, starting from the front side of the sample, in order to minimize boundary effects. The adopted reinforcement width *w* (see Fig. 1) was 55 mm for all the samples reinforced with carbon fibers and 50 mm for G type bidirectional glass grid. All the unbonded part of the strengthening systems tested was made with the same materials and the same geometry already described.

2.2 Experimental Set-Up

The purposely designed single-lap set-up used for performing bond tests on the specimens is shown in Fig. 2 and described in detail in (Mazzotti et al. 2015a).

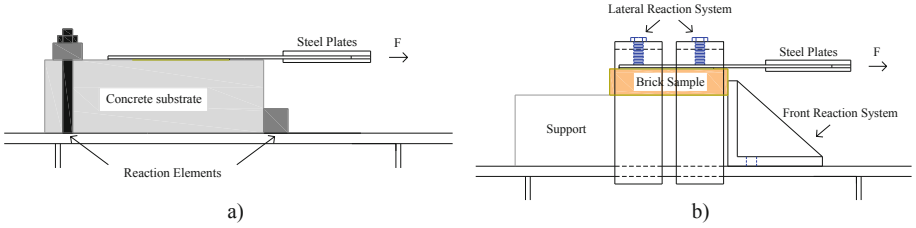

Fig. 2. Experimental set-up used for bond tests: (a) concrete substrate; (b) clay brick substrate.

The experimental set-up is composed of a rigid horizontal frame, with front and rear (for concrete) or lateral (for masonry) steel reaction elements positioned to prevent horizontal and vertical displacements of the samples (see Fig. 2a and b, respectively).

The loaded end of the reinforcement was clamped between two steel plates by using glue and bolts. The traction force was applied by means of an electromechanical actuator, capable of allowing rotations around the vertical axis thanks to an hinge placed between the movable head of the machine and the sample steel plates.

Bond tests were performed under displacement control at a rate of 0.15 mm/min, by using a displacement transducer (LVDT) to control the displacement of the reinforcement free end. The applied traction force was recorded by means of a class 0.5 load cell with a maximum capacity of 100 kN.

The elongation of the sample within the bonded area and the strain distribution were evaluated not by using traditional techniques, but applying the innovative Digital Image Correlation (DIC) technique. As already discussed in (Bellini and Mazzotti 2016), this non-contact full-field optical method, based on high resolution digital cameras, proved to be very useful and reliable for evaluating surface deformations of the matrix, for measuring elongation within the bonded area and for calculating slip between fibers and matrix, allowing to obtain complete 3D displacement and strain maps. Results coming from post-processing DIC data, accordingly, allowed for a proper description and analysis of the identified failure modes. Further details on the required specimens preparation and on the application of this technique can be found in (Mazzotti et al. 2015b).

3 Experimental Results

3.1 Failure Modes and Maximum Bond Capacity

Figure 3 shows the different failure modes observed during bond tests on concrete substrate, identified with a letter (A–D). The same classification is used in Table 2, where failure modes and maximum bond capacity are reported for all the samples subjected to single-lap shear tests, together with the average failure load and the average stress $\sigma_{f,\ mean}$ (referred to the area of dry fibers) for samples of the same type.

Failure mode A (see Fig. 3a) identifies the tensile rupture of the reinforcement outside of the bonded area and is typical of specimens with a good adhesion between matrix and substrate (samples reinforced with bidirectional carbon or glass grids placed within a cementitious mortar and with the addition of an adhesion promoter).

When shifting from bidirectional grids to unidirectional sheets with an increasing number of reinforcement plies, different failure modes could be expected: in fact, C_C4P_CM samples (see Fig. 3b and Table 2) showed a complete debonding of the FRCM composite from the substrate (Failure mode B), whereas in C_C5P_CM specimen a mixed mode (Failure mode D, see Fig. 3d), characterized by the debonding of the strengthening system together with an internal delamination, occurred. The beneficial effect of the adhesion promoter can be highlighted if C_C4P_CM and C_C4_CM specimens are compared: in fact, without the adhesion promoter, a considerably lower maximum bond capacity and a different failure mode, characterized by fibers slippage within the matrix (Failure mode C) can be expected (see Fig. 3c and Table 2). It should be noted that, analyzing the maximum loads, an increasing in fibers area, in presence of the adhesion promoter, leads to an increasing in the maximum bond capacity but also to different failure modes (debonding or internal delamination).

Figure 4 shows instead the typical failure modes revealed by bond tests performed on brick specimens, with the same classification used in Table 2.

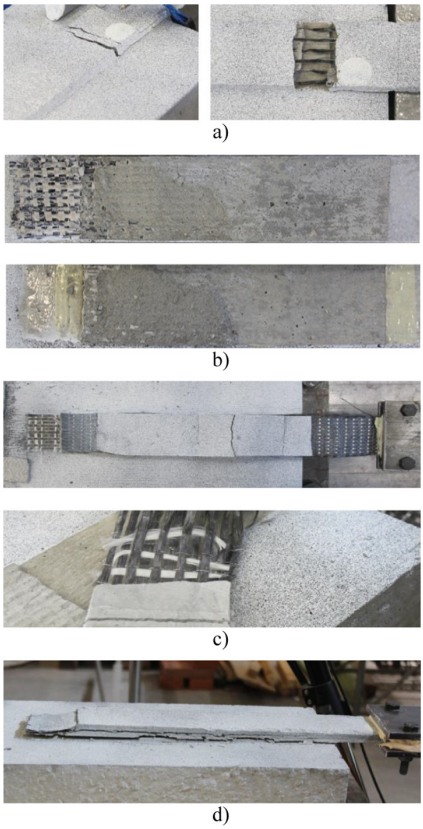

Fig. 3. Bond tests on concrete: identified failure modes: (a) fiber rupture; (b) debonding; (c) fiber slippage; (d) debonding with delamination.

Failure mode A (see Fig. 4a) identifies, as for concrete samples, the fiber rupture outside of the bonded area, occurring when the maximum tensile strength of the strengthening system is reached. Failure mode B (see Fig. 4b), characterized by the complete debonding of the FRCM strengthening system from the substrate, was observed only in clay bricks without surface preparation and proved to be, in the case of bricks, typical of specimens with a poor adhesion between matrix and support. Failure mode B* occurred only in one case (B_GP_CM sample), with fiber tensile failure near the steel plates, used for applying the traction force to the specimen, before a complete debonding.

After treating the bricks with a sandblasting process (passing from B to BS substrate in Table 2), debonding was no more observed, whereas different failure modes occurred. In fact, the improved adhesion between matrix and substrate increased the maximum bond capacity of samples reinforced with bidirectional carbon and glass grids (C1P and GP type) up to the maximum tensile strength of glass and carbon fibers (failure mode A), except for specimens prepared without the adhesion promoter, which

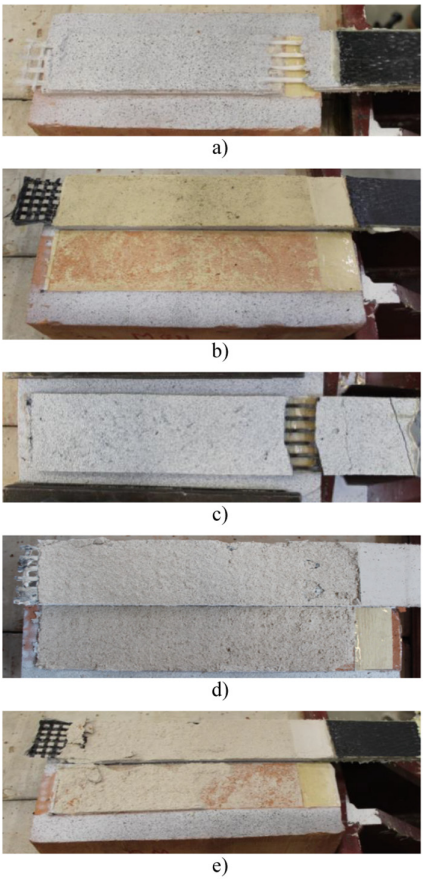

Fig. 4. Bond tests on clay bricks: failure modes: (a) fiber rupture; (b) debonding; (c) fiber slippage; (d) delamination; (e) delamination at different levels.

manifested a remarkable slippage between fibers and matrix (Failure mode E, see Fig. 4c). Accordingly, failure loads were found to be considerably higher after surface treatment with sandblasting, but, again, fibers slippage in the specimens without adhesion promoter (see Fig. 4c) led to very low maximum forces and to a progressive damaging of the fibers. After testing the positive effect of sandblasting on samples prepared with CM mortar, all the following samples were prepared by using this surface treatment.

Samples strengthened with unidirectional sheets (C2 and C3 type) showed instead a different failure mode (F) characterized by the delamination of the reinforcement within the lower mortar layer (see Fig. 4d). Without the adhesion promoter, the already described Failure mode E was found to be still present. If maximum loads are compared, specimens with the adhesion promoter showed performance about three times higher.

After passing from the cementitious matrix to a NHL mortar with significantly lower mechanical properties, samples strengthened with glass fibers showed the same failure mode (A) and proved to be able to reach a very similar maximum bond capacity (with an average value of 2.75 kN instead of 2.79 kN). This result highlights the positive effect of a NHL mortar with relatively high mechanical properties in combination with the adhesion promoter. Samples strengthened with a bidirectional carbon grid (C1 type) showed instead more complex failure modes, occurring at lower average maximum loads (if CM and NHL matrices are compared). In more detail, Failure mode A (tensile rupture of the fibers outside of the bonded area) was observed only in one sample, whereas the most common failure mode was Failure mode F*, quite similar to Failure mode F, but with delamination occurring within the lower mortar layer at different levels (see Fig. 4e).

3.2 Load-Slip Curves, Deformation Profiles and Maps

Examples of force-elongation curves, typical strain profiles along the specimen centerline and strain maps are here reported. The presented experimental results have been obtained by post-processing DIC data, starting from the images captured during bond tests. In more detail, this technique allowed to obtain both the elongation within the bonded area and the strain profiles along the specimen centerline (inside the bond length), together with complete 3D strain maps (Mazzotti et al. 2015b). Some common bond behaviors of the specimens tested are reported in Figs. 5 and 6. Figure 5 shows the typical behavior of samples which manifested failure mode A: the two force-elongation curves are obtained by considering (curve A) or not considering (curve B) the crack at the beginning of the bond length, showing that fiber rupture generally occurred way before a complete debonding or delamination of the reinforcement, considering the very limited elongation recorded. This behavior is confirmed by the analysis of the corresponding strain profiles, reported here for some significant load levels (see Fig. 7), which highlight that deformation is limited, in this case, only to the first portion of the bonded area. This particular behavior suggests that, since debonding or delamination was not properly started yet, without fiber tensile rupture (so using, for example, higher strength fibers or increasing fibers area) the maximum debonding force would have been certainly higher.

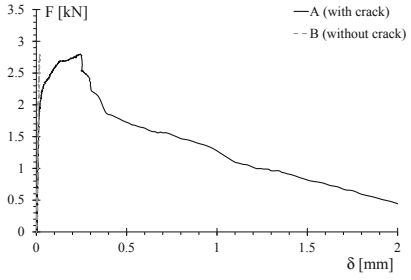

Fig. 5. Typical behavior of samples showing failure mode A: example of a load-elongation curve.

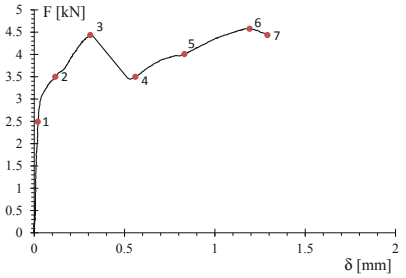

Fig. 6. Typical behavior of specimens showing failure mode B, F and F*: load-elongation curve.

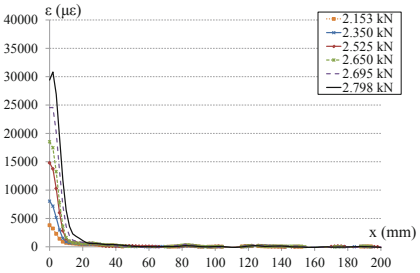

Fig. 7. Failure mode A: strain profiles example.

Figure 6 shows instead the typical behavior of samples characterized by failure modes B, F and F*. The force-elongation curve exhibited an almost linear initial branch up to the onset of debonding or delamination process, followed by a typical non-linear behavior, with a force variable until failure (Bellini and Mazzotti 2016).

An example of typical strain profiles along the specimen centerline obtained for this type of failure modes, corresponding to the points indicated in the force-elongation curve reported in Fig. 6, is shown in Fig. 8. It should be noted that, in comparison to other experimental campaigns concerning bond tests carried out on FRPs applied on brick or masonry prisms (Mazzotti et al. 2015a, b; de Felice et al. 2016), strain profiles appear here much more irregular and characterized by remarkable deformation peaks, showing a different evolution of the debonding or delamination process. A proper analysis of this phenomenon was possible thanks to the images captured during bond tests by using DIC technique, comparing the obtained strain maps with the original pictures. An example of the comparison between the deformation maps obtained by post-processing DIC data and the original raw images is shown in Fig. 9, where a clear correspondence between deformation peaks and cracks appearing in the matrix during the delamination process can be found.

In order to study other possible improvements on CM or NHL matrices and to analyze the effect of mortar joints on the bond behavior of FRCM strengthening systems, which was found to be significant in some experimental studies concerning FRPs (Mazzotti et al. 2015a, b; de Felice et al. 2016; Sassoni et al. 2018), other bond

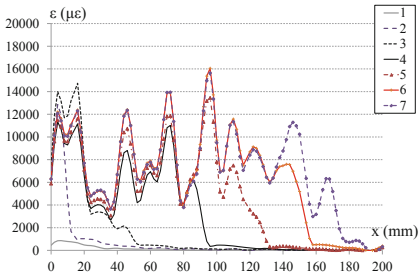

Fig. 8. Failure modes B, F, F*: strain profiles example.

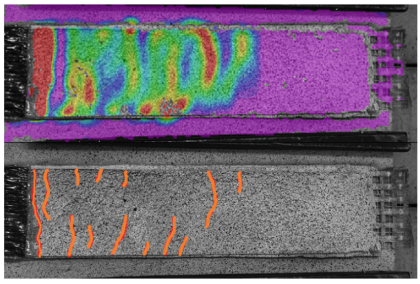

Fig. 9. Example of strain map (thanks to DIC technique) and corresponding cracks in the matrix identified during the delamination process.

tests on CFRCM and GFRCM composites applied on masonry substrates are currently in progress.

4 Conclusions

Results of single-lap shear tests carried out on FRCM composites applied on concrete and masonry substrate are presented and discussed in this paper. FRCM strengthening systems were based on bi-directional carbon and glass grids or unidirectional sheets applied with cementitious or NHL mortars. DIC technique was used with the aim of performing an advanced analysis on the surface of the samples tested, obtaining complete displacement and strain profiles. Crack pattern and failure modes of GFRCM and CFRCM strengthening systems were carefully analyzed, discussing in detail some typical bond behaviors in terms of force elongation curves and strain maps.

Bond tests performed on concrete revealed tensile failure of the fiber as the most common failure mode for bidirectional grids and debonding at the substrate interface with cases of internal delamination for unidirectional carbon sheets applied using two or three plies. The use of an adhesion promoter allowed to obtain sensibly higher maximum loads. Single lap shear tests carried out on bricks by using a cementitious or a NHL lime mortar showed some interesting results: the need of a proper surface preparation for bricks with a smooth surface, the beneficial effect of the adhesion

promoter in changing the failure mode and increasing the maximum loads and, finally, the influence of the mechanical properties of the matrix, in particular when high strength fibers are used.

Tests carried out on FRCMs applied with cementitious mortar allowed to analyze a large variety of failure modes, also dependent on the properties of the fibers used: tensile failure of the composite grid was the most common failure mode for bidirectional grids, whereas delamination within the lower mortar layer was present on samples reinforced with unidirectional carbon sheets. Finally, slippage of the textile within the matrix, occurring at lower load levels, was the typical failure mode revealed in samples without the presence of the adhesion promoter. The substitution of the cementitious mortar with a NHL one showed essentially the occurrence of two main failure modes, primarily dependent on the reinforcement grid type and on its relative strength: fibers tensile failure or matrix delamination. In fact, results were very similar in samples reinforced with low strength (glass) grids, where the same failure mode and almost equal maximum forces were achieved, but significantly changed in the case of carbon fibers, where matrix delamination at lower load levels occurred.

Experimental outcomes show that CFRCM and GFRCM strengthening systems are able to achieve good performance if used in combination with an adhesion promoter, after a proper surface preparation of the support. Cementitious mortars are preferable in terms of pure performance when coupled with high strength fibers, whereas NHL matrices can be considered a good alternative for other low-strength fiber types, such as, for example, glass fibers.

Acknowledgements. The financial support of (Italian) Department of Civil Protection (ReLUIS 2018 Grant – Innovative Materials) is gratefully acknowledged. The authors would like also to thank Ardea Progetti e Sistemi S.r.l. for providing materials and for the kind cooperation.

References

Bellini A, Mazzotti C (2016) Bond behavior and tensile properties of FRCM composites applied on masonry panels. In: Proceedings of SAHC 2016, Leuven, Belgium, 13–15 September 2016, pp 322–239

Carloni C, Subramaniam KV (2012) FRP-masonry debonding: numerical and experimental study of the role of mortar joints. J Compos Constr 16(5):581–589

Carozzi FG, Bellini A, D'Antino T, de Felice G, Focacci F, Hojdys L, Laghi L, Lanoye E, Micelli F, Panizza M, Poggi C (2017) Experimental investigation of tensile and bond properties of carbon-FRCM composites for strengthening masonry elements. Compos B 128:100–119

Carrara P, Ferretti D, Freddi F (2013) Debonding behavior of ancient masonry elements strengthened with CFRP sheets. Compos B 45(1):800–810

D'Ambrisi A, Leo L, Focacci F (2013) Experimental and analytical investigation on bond between carbon-FRCM materials and masonry. Compos B 46:15–20

de Felice G, De Santis S, Garmendia L, Ghiassi B, Larringa P, Lourenço PB, Oliveira DV, Paolacci F, Papanicolau CG (2014) Mortar-based systems for externally bonded strengthening of masonry. Mater Struct 47(12):2021–2037

de Felice G, Aiello MA, Bellini A, Ceroni F, De Santis S, Garbin E, Leone M, Lignola GP, Malena M, Mazzotti C, Panizza M, Valluzzi MR (2016) Experimental characterization of composite-to-brick masonry shear bond. Mater Struct 49(7):2581–2596

De Santis S, Ceroni F, de Felice G, Fagone M, Ghiassi B, Kwiecień A, Lignola GP, Morganti M, Santandrea M, Valluzzi M, Viskovic A (2017) Round robin test on tensile and bond behaviour of steel reinforced grout systems. Compos B 127:100–120

Kwiecień A, de Felice G, Oliveira DV, Zając B, Bellini A, De Santis S, Ghiassi B, Lignola GP, Lourenço PB, Mazzotti C, Prota A (2016) Repair of composite-to-masonry bond using flexible matrix. Mater Struct 49(7):2563–2580

Leone M, Aiello MA, Balsamo A, Carozzi FG, Ceroni F, Corradi M, Gams M, Garbin E, Gattesco N, Krajewski P, Mazzotti C, Oliveira D, Papanicolaou C, Ranocchiai G, Roscini F, Saenger D (2017) Glass fabric reinforced cementitious matrix: tensile properties and bond performance on masonry substrate. Compos B 127:196–214

Lignola GP, Caggegi C, Ceroni F, De Santis S, Krajewski P, Lourenço PB, Morganti M, Papanicolaou C, Pellegrino C, Prota A, Zuccarino L (2017) Performance assessment of Basalt FRCM for retrofit applications on masonry. Compos B 128:1–18

Mazzotti C, Ferracuti B, Bellini A (2015a) Experimental bond tests on masonry panels strengthened by FRP. Compos B 80:223–237

Mazzotti C, Ferracuti B, Bellini A (2015b) Experimental study on masonry elements strengthened by GFRP: the role of inclination between mortar joints and GFRP sheets. Key Eng Mater 624:559–566

Sassoni E, Andreotti S, Bellini A, Mazzanti B, Bignozzi MC, Mazzotti C, Franzoni E (2017) Influence of mechanical properties, anisotropy, surface roughness and porosity of brick on FRP debonding force. Compos B 108:257–269

Sassoni E, Sarti V, Bellini A, Mazzotti C, Franzoni E (2018) The role of mortar joints in FRP debonding from masonry. Compos B 135:166–174

Confinement of Concrete with FRCM Materials

Ciro Faella, Annalisa Napoli(✉), and Roberto Realfonzo

Department of Civil Engineering, University of Salerno, Fisciano, SA, Italy
annapoli@unisa.it

Abstract. Fabric-reinforced cementitious matrix (FRCM) composites have recently enter the market as a promising, sustainable, and durable solution for the external strengthening of RC and masonry structural members. In this paper, an analytical study on the confinement of concrete with FRCM materials is presented. To this purpose, a wide database including results of compression tests performed on more than 250 concrete cylinders externally wrapped with FRCM was collected from the literature, firstly to perform an overall analysis of the efficiency of the FRCM confinement by varying some of the relevant parameters, such as: type of fiber (glass, carbon, steel, PBO or basalt) and geometry of the mesh, number of layers, composition of the inorganic matrix and compressive strength of the unconfined concrete. Then, preliminary relationships for estimating the compression strength of FRCM confined concrete were developed through best-fit techniques.

Keywords: Fabric-reinforced cementitious matrix (FRCM) composites · Concrete confinement · Predictive models

1 Introduction and Background

In existing framed buildings, the external confinement of reinforced concrete (RC) columns with Fiber Reinforced Polymers (FRPs) has met a large consensus at both the academic and industrial levels, as they represent today a competitive alternative to traditional materials.

The key benefits of FRP materials include their light weight, high strength and stiffness, resistance to corrosion, and ease of application; drawbacks, however, cannot be ignored, as they include moderate matrix heat and fire resistance, low glass transition temperature, difficulty of application at low temperatures, impossibility of application on wet surfaces, and lack of vapor permeability.

In order to overcome some of the disadvantages related to the epoxy resin, composite materials employing inorganic matrices, mainly made of cement-based mortars, have recently been proposed as a promising, sustainable, and durable alternative to FRPs. These composites are usually termed Fabric-Reinforced Cementitious Matrix (FRCM) composites, although several other names are used in the literature based on the types of matrix, application, and substrate to strengthen, concrete or masonry (D'Ambrisi et al. 2013).

M. di Prisco and M. Menegotto (Eds.): ICD 2018, LNCE 42, pp. 360–371, 2020.
https://doi.org/10.1007/978-3-030-23748-6_28

The most commonly-used fibers in FRCM composites are made of basalt (B), carbon (C), alkali-resistant (AR) glass (G), poliparafenilenbenzobisoxazole (PBO) and steel (S); the latter ones are actually composed of ultra-high tensile strength steel (UHTSS) micro-wires, which are twisted around each other to form cords or ropes with a micro-fine brass or galvanized coating.

The fibers are typically arranged in bundles and their configuration can be modified from unidirectional to bidirectional textile weaves or fabrics in an attempt to improve bond properties. The spacing among the bundles facilitates the impregnation of each bundle and assures matrix continuity among internal and external matrix layers.

The available experimental and theoretical results on the effectiveness of FRCM systems for strengthening applications to RC members are rather limited if compared to FRPs. Only in the last decade the scientific community and the construction industry have shown a keen interest, and recently a state-of-the-art report has been authored by Carloni et al. (2016). A first attempt towards a design approach for FRCM systems was made in 2013 with the publication of ACI 549.4R (2013), in which all commonly-used fibers were included, i.e., AR glass, carbon, basalt and PBO, except steel fibers and pre-impregnated fabrics.

Experimental studies show that the mechanical behavior of FRPs and FRCMs is significantly different under tensile loading (Ascione et al. 2015), since the strength of FRCM systems is strongly affected by the type and size of the adopted fibers, by the mesh layout and by the properties of the matrix. The FRP systems are typically characterized by a linear elastic constitutive law up to failure, and assuming perfect bond between fibers and matrix is commonly accepted. Conversely, FRCM systems show a bit more complex tensile stress-strain (σ–ε) behavior which can be approximately simplified by the trilinear curve shown in Fig. 1a. This curve consists of three branches which correspond to three different stages of cracking, i.e., (I) uncracked stage, (II) crack development, and (III) cracked stage.

The first stage of the curve reproduces the tensile behavior of the uncracked specimen, with stiffness E_1. The first crack conventionally identifies the transition to stage II where cracking evolution forces stress transfer from the matrix to the reinforcing fibers, with some debonding at the fiber-matrix interface. In the third branch, characterized by the slope E_3 which almost coincides with the elastic modulus of the dry fabric (E_f), the load is mainly resisted by the fibers and the crisis is caused by a progressive rupture of the roving fiber filaments and by the debonding at fiber-matrix interface.

As for composite specimens subjected to tensile loading, even concrete columns confined with FRP and FRCM systems show a significantly different behavior in compression as illustrated in Fig. 1b, where the qualitative trend of axial stress-strain curves for unconfined, FRCM confined and FRP confined specimens is reported.

In the case of FRP-confined specimens, when the lateral confining pressure exerted by the external jacket (f_l) exceeds 7% of the compressive strength of the unconfined concrete (f_{c0}), the stress-strain curve is typically monotonically ascending up to the brittle failure of the FRP system - see curve *b* in Fig. 1b. Conversely, only in the less frequent case of "unsufficiently" FRP confined specimens ($f_l/f_{c0} < 7\%$), the curve shows a post-peak softening branch (see curve *b′* in Fig. 1b) and the maximum strength (f_{cc}) is achieved before the FRP rupture (Lam and Teng 2003).

The stress-strain behavior of FRCM-confined specimens is affected by many factors depending on both the type of FRCM system and the wet lay-up installation procedure. A key factor influencing the stress-strain response is the cracking of the mortar, often occurring prematurely (when its mechanical properties are very poor) and generally responsible for the post-peak softening (curve type *a* in Fig. 1b).

The behavior past matrix cracking is controlled by the bond between the fibers and the matrix. In particular, if bond strength at the fibers-matrix interface is very low, the stress may be suddenly transferred to the fibers, which may bear unevenly-distributed tensile stresses and may lead to a premature failure of the FRCM system at a load level significantly lower than the mesh tensile strength (Bournas et al. 2007). Conversely, if a high-performance matrix is used and matrix-fiber bond is effective, the stresses are gradually transferred to the fiber mesh while cracking evolves up to the failure of the mortar; in this case, the constitutive law of the FRCM system is comparable with that of the FRP, and an ascending stress-strain curve of type *a′* in Fig. 1b is obtained (Tore et al. 2015; Ates et al. 2017).

Furthermore, concerning the FRCM installation procedure, it should be noted that the wet lay-up procedure generally does not guarantee a perfect alignment and uniform arrangement of the fiber filaments inside each fiber bundle. Consequently, the distribution of the stresses inside the fiber bundles is not uniform and debonding may occur at the fiber/matrix interface.

Based on the above considerations, developing reliable predictive models for the compressive strength and ultimate strain of FRCM-confined concrete is no easy task since these models should account for all the mentioned physical and behavioral aspects, and their greater or lesser influence depends on the specific FRCM system selected for the confinement system.

Some formulations have been recently developed by Ombres and Mazzuca (2017) and Cascardi et al. (2017) by analyzing a quite large number of experimental results collected in a database. In particular, the study by Cascardi et al. (2017) is a first attempt to include into the analytical model the influence that matrix properties have on the compressive strength of FRCM-confined concrete.

The study presented in this paper aims to increase the current knowledge by developing new predictive models for the strength of concrete confined with different

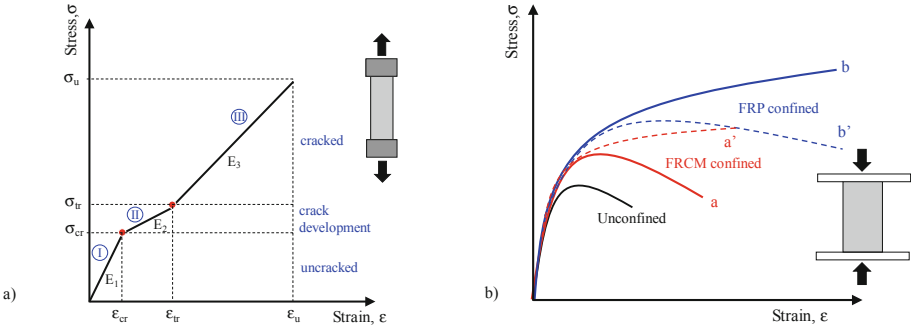

Fig. 1. Typical stress-strain behavior of FRCM systems under tensile loading (a), and typical stress-strain behaviour of concrete confined with FRP/FRCM in compression (b)

FRCM systems. An updated database including more than 250 concrete cylinders externally wrapped with FRCM systems was got from the literature. The proposed models were developed through best-fit techniques applied to the experimental data and comparisons were made with some relationships available in the literature and/or guidelines concerning FRP systems.

2 The Database

The results of 255 compression tests performed on plain concrete cylinders differently confined with FRCM systems were collected from the scientific literature. Among the specimens, 44 were confined with B-FRCM, 43 with C-FRCM, 53 with G-FRCM, 35 with PBO-FRCM and 80 with S-FRCM systems (see Fig. 2a).

The specimens had diameter to-height (H/D) ratio comprised between 2 and 3, and were manufactured with concrete mixtures characterized by an average value of the cylindrical compressive strength (f_{c0}) in the range 15–38 MPa.

In addition to the different nature of fibers used to confine the concrete, both unidirectional (UD) and bidirectional (BD) fabrics were used. Several fiber amounts were adopted in the manufacture of the fabrics in order to have various dry textile's equivalent thicknesses (t_f).

Different types of inorganic matrices were used to impregnate the fabric (from pozzolanic to hydraulic matrices) characterized by a great variability in terms of mechanical properties (for instance, the mortar has a compressive strength $f_{m,c}$ comprised between 2.60–67.00 MPa).

In all cases, the concrete cylinders were wrapped with fabric meshes along the hoop direction of the fibers, by considering a number of layers (n_f) ranging from 1 to 6; the angle of inclination of the fibers with respect to the longitudinal axis (θ) of the specimen was 90°, except in some specimens wrapped with PBO-FRCM systems where the inclination was 30° and 45°.

As mentioned earlier, the compressive behavior of FRCM-confined specimens is significantly influenced by the cracking of the inorganic matrix which may lead to two main failure modes of the external jacket, depending on cracking severity: *(a)* tensile failure in the hoop direction (JF) and, *(b)* debonding (D). In most cases, mortar cracking was observed with the opening of vertical cracks in the overlapping zones, their more or less slow and symmetric propagation along the jacketed cylinder surface. Of course, the greater or lesser width of these cracks has an effect on the slip activated at the fiber-matrix interface, so that either a debonding-induced failure within the matrix or a jacket failure occurs. To this purpose, Figs. 2b and c show the percentage distribution of the number of specimens belonging to each FRCM system failed by jacket failure and debonding, respectively. However, it is worth noting that a mixed mode failure was observed in some specimens confined with two high density S-FRCM layers (=4.72 cords/cm), something that may be attributed to the large stiffness of the textile (i.e., debonding of the outer layer and rupture of the inner layer); this mixed failure mode was attributed to debonding.

Finally, one may note that, as explained in a previous investigation carried out by Realfonzo and Napoli (2011), the analytical study presented in the next section was

performed by considering a smaller database, where all the experimental data and results were collected in 111 homogeneous dataset. Each set represents a group of *N* experimental tests characterized by uniformity in terms of: *(a)* specimen size (D, H); *(b)* compressive strength of the unconfined concrete (f_{c0}), *(c)* geometry (UD/BD, density, t_f, n_f, θ), and mechanical properties of the dry fabric, i.e., elastic modulus (E_f), ultimate tensile strength ($f_{f,u}$) and corresponding strain ($\varepsilon_{f,u}$), *(d)* mechanical properties of the inorganic matrix (when available), i.e., flexural strength ($f_{m,b}$), modulus of elasticity (E_m) and $f_{m,c}$ (already defined earlier), and *(d)* observed failure mode (JF/D).

The experimental results attributed to each dataset represent, therefore, the average values obtained for the collected *N* tests. In particular, the test results under consideration include: the peak compressive strength of the FRCM confined concrete (f_{cc}) and the strain efficiency factor of the FRCM system (k_ε) defined, similarly to FRPs, as the ratio between the ultimate hoop strain reached in the FRCM jacket ($\varepsilon_{j,u}$) and the ultimate strain found from flat coupon tensile tests ($\varepsilon_{f,u}$).

The resulting database is reported in Table 1 where each line stands for a dataset including a number of homogenous tests ranging from 1 to 6.

For each FRCM confining system, Table 2 summarizes the number *N* of specimens collected from the literature and their classification within the two typologies of failure mode; the remaining columns 4 to 8 of Table 2 provide the corresponding information in terms of datasets on both numeric and percentage (%) bases. The highest percentage was always computed in the case of JF mode, even though non negligible % values of debonding failure were obtained in the case of G-FRCM and S-FRCM systems.

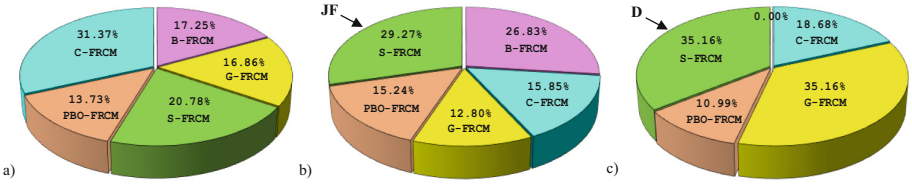

Fig. 2. Percentage distribution of specimens within each FRCM system based on: (a) total number of specimens; (b) jacket failure; (c) debonding failure

3 Strength-Predictive Models

Based on the database in Table 1, preliminary models for predicting the strength of FRCM-confined concrete with circular cross-section, f_{cc}, were developed through a best-fit analysis. As a first attempt, the models were formulated in a non-dimensional form by means of the following equation specified for circular sections:

$$\bar{f}_{cc} = \frac{f_{cc}}{f_{c0}} = 1 + \alpha \cdot \bar{f}_l^{\beta} \tag{1}$$

which is the same generally accepted for the case of FRP systems. Of course, based on the earlier considerations on the role of inorganic matrices, the application of Eq. (1) to

Table 1. FRCM confined concrete specimens.

System	Source	Specimen label	N	Geometry		Matrix's properties			Fabric mesh's properties						Jacket		Results			
				D	H/D	$f_{m,c}$	$f_{m,b}$	E_m	*type*	*density*	t_f	f_{fu}	E_f	ε_{fu}	n_f	θ	f_{c0}	f_{cc}	k_ε	FM
				[mm]	[-]	[MPa]	[MPa]	[GPa]	[-]	[g/m^2]	[mm]	[MPa]	[GPa]	[%]	[-]	[°]	[MPa]	[MPa]	[-]	
B-FRCM	[1]	S4-S6	2	150	2.0	30.00	9.00	–	BD*	126	0.046	1814	91.10	2.0	1	90	15.52	21.11	0.20	JF
		S5-S7	2	150	2.0										2			22.66	0.35	JF
		S14-S15-S18-S19	4	150	2.0				BD**						1		17.83	24.12	0.22	JF
		S16-S17-S20-S21	4	150	2.0										2			27.55	0.30	JF
	[2]	M1-1,..6	6	150	2.0	31.50	4.10	–	BD	236	0.086	894	52.00	2.2	1	90	21.80	26.20	–	JF
		M2-1,..6	6	150	2.0										2			27.21	–	JF
		C1-1,..6	6	150	2.0	22.40	4.70	–							1			28.67	–	JF
		C2-1,..6	6	150	2.0										2			28.78	–	JF
	[3]	B-CM-1	4	150	2.0	82.00	–	–	UD	220	0.200	2800	93.00	2.8	1	90	27.30	32.00	–	JF
		B-CM-2	4	150	2.0										2			35.00	–	JF
C-FRCM	[4]	A_MI2	3	150	2.0	8.56	3.30	–	BD	168	0.047	3350	225.00	1.49	2	90	15.24	20.77	–	*D*
		A_MII2	3	150	2.0	30.61	4.20	–							2			23.88	–	JF
		A_MI3	3	150	2.0	8.56	3.30	–							3			26.50	–	*D*
		A_MII3	3	150	2.0	30.61	4.20	–							3			27.00	–	JF
		B_MII2	3	150	2.0	30.61	4.20	–							2		21.81	27.36	–	JF
		B_MII3	3	150	2.0	30.61	4.20	–							3			32.44	–	JF
	[5]	SERIES C	2	150	2.0	67.00	–	–	BD	111	–	1032	222.98	0.46	2	90	26.00	39.00	–	*D*
		SERIES D	2	150	2.0					324	–	–	204.00	–	3			57.00	–	*D*
	[6]	CF2M-a	1	200	3.0	31.17	9.50	>15.00	BD	168	0.047	4800	240.00	2.0	2	90	16.80	20.83	–	JF
		CF2M-b	1	200	3.0										2		16.08	20.58	–	JF
		CF3M-a	1	200	3.0										3		16.80	23.69	–	JF
		CF3M-b	1	200	3.0										3		16.08	23.96	–	JF
	[3]	C-CM-1	4	150	2.0	82.00	–	–	UD	245	0.168	3900	330.00	1.80	1	90	27.30	35.00	–	*D*
		C-CM-2	4	150	2.0										2			42.00	–	JF
	[7]	C1-gro2-Y-a,b	2	150	2.0	–	–	–	UD	300	0.167	4093	244.00	1.72	1	90	34.62	43.82	–	JF
		C1-gro3-Y-a,b	2	150	2.0										1			43.04	–	JF
		C2-gro3-Y-a,b	2	150	2.0										2			57.60	–	JF
	[8]	CCML1D0-1,..3	3	150	2.0	25.00	–	–	BD	170	0.047	4700	240.00	1.80	1	90	36.80	38.80	–	*D*
G-FRCM	[1]	S3	1	150	2.0	30.00	9.00	–	BD	225	0.043	1440	72.00	2.00	2	90	17.83	15.52	22.35	0.44	JF
		S10,..S12	3	150	2.0										1			20.03	0.22	JF
		S13	1	150	2.0										2			23.00	0.36	JF
	[9]	FABcrete	4	150	2.0	56.26	6.25	–	BD***	225	–	45[1]	–	>3.00	–	–	38.41	41.28	–	*D*
	[5]	SERIE B	2	150	2.0	67.00	–	–	BD	167[2]		1231	74.45	1.65	6	90	26.00	35.00	–	*D*
	[10]	LDG-A-1, A-2	2	152	2.0	2.49	0.20	–	UD	525	0.217	3240	72.40	4.50	2	90	20.40	26.85	–	*D*
		LDG-H-1, H-2	2	152	2.0	31.10	1.36	–							2			30.00	–	*D*
		HDG-A-1, A-2	2	152	2.0	2.49	0.20	–		915	0.378	3240	72.40	4.50	2			24.50	–	*D*
		HDG-H-1, H-2	2	152	2.0	31.10	1.36	–							2			30.00	–	*D*
		1B-1,…3	3	152	2.0	31.10	1.36	–		596	0.246	3399	76.90	4.40	1		21.70	26.30	0.08	*D*
		2B-1,…6	6	152	2.0										2			35.52	0.11	*D*
		2U-1,…6[4]	6	152	2.0										2			33.93	0.08	*D*
		4B-1,…3	3	152	2.0										4			47.90	0.22	*D*
	[11]	CSW	1	150	2.0	–	–	–	BD	610	0.600	4200	75.00	5.60	1	90	24.41	33.60	–	JF
		CDW	1	150	2.0										2			51.16	–	JF
	[3]	G-CM-1	4	150	2.0	82.00	–	–	UD	192	0.220	2100	71.00	2.60	1	90	27.30	31.00	–	JF
		G-CM-2	4	150	2.0										2			33.00	–	JF
	[7]	G1-gro3-N-a,b	2	150	2.0	–	–	–	UD	450	0.177	1500	72.00	2.00	1	90	34.62	36.81	–	JF
		G1-gro3-Y-a,b	2	150	2.0										1			42.31	–	JF
		G2-gro3-Y-a,b	2	150	2.0										2			50.12	–	JF
PBO-FRCM	[6]	CA1,..3-2L	3	154	2.2	≥ 15.00	≥ 2.00	≥ 6.10	BD	88	0.045	5800	270.00	2.15	2	90	24.20	31.23	0.43	JF
		CA4, 6-3L	3	154	2.2										3			36.57	0.51	JF
		CB2,4,6-2L	3	200	1.7										2		24.40	31.17	0.72	JF
		CB1,5-3L	2	200	1.7										3			33.55	0.81	JF
	[12]	20M1_1,2	2	113	2.7	29.0	3.50	6.00	BD	88	0.045	5800	270.00	2.15	1	90	22.60	32.57	0.34	*D*
		20M2_1,2	2	113	2.7										2			42.69	0.34	*D*
		20M3_1,2	2	113	2.7										3			56.93	0.34	*D*
	[13]	CRP1-I	1	152	1.9	30.40	–	6.10	BD	–	0.0455	5800	270.00	2.00	1	90	15.40	24.69	0.42	JF
		CRP2-I	1	152	1.9										2	90		35.00	0.47	JF
		CRP3-I	1	152	1.9										3	90		41.45	0.52	JF
		CRP4-I	1	152	1.9										4	90		49.24	0.41	JF
		CRP5-I	1	152	1.9										1	45		16.19	0.40	JF
		CRP6-I	1	152	1.9										2	45		16.98	0.40	JF
		CRP7-I	1	152	1.9										3	45		17.40	0.50	JF
		CRP8-I	1	152	1.9										2	30		17.45	0.64	JF
		CRP9-I	1	152	1.9										3	30		21.69	0.50	JF
		CRP1-II	1	153	1.9										1	90		43.55	0.30	*D*
		CRP2-II	1	153	1.9										2	90		47.00	0.52	*D*
		CRP3-II	1	153	1.9										3	90		56.60	0.53	*D*
		CRP4-II	1	153	1.9										4	90		56.23	0.83	*D*
		CRP5-II	1	152	1.9										1	45	29.26	31.68	0.34	JF
		CRP6-II	1	152	1.9										2	45		33.79	0.51	JF
		CRP7-II	1	152	1.9										3	45		35.72	0.56	JF
		CRP8-II	1	152	1.9										2	30		35.42	0.52	JF
		CRP9-II	1	152	1.9										3	30		39.52	0.49	JF

(*continued*)

Table 1. (*continued*)

System	Source	Specimen label	N	Geometry		Matrix's properties			Fabric mesh's properties						Jacket		Results			
				D	H/D	$f_{m,c}$	$f_{m,b}$	E_m	type	density	t_f	$f_{f,u}$	E_f	$\varepsilon_{f,u}$	n_f	θ	f_{c0}	f_{cc}	k_e	FM
				[mm]	[-]	[MPa]	[MPa]	[GPa]	[-]	[g/m^2]	[mm]	[MPa]	[GPa]	[%]	[-]	[°]	[MPa]	[MPa]	[-]	
S-FRCM	[14]	A3 x 2h1_1,2	2	150	2.0	22.10	6.78	8.03	UD	9.06[2]	0.562	2187	109.35	2.00	1	90	15.12	22.26	–	*D*
		A3 x 2m1_1,2	2	150	2.0					2.00[3]	0.124	2187	109.35	2.00	1			24.70	–	JF
		A3 x 2m1_3	1	150	2.0					2.00[3]	0.124	2187	109.35	2.00	1			27.58	–	*D*
		A3 x 2l1_1,..3	3	150	2.0					1.00[3]	0.062	2187	109.35	2.00	1			22.80	–	JF
		A12 x h1_1,2	2	150	2.0					9.06[2]	0.562	1870	116.88	1.60	1			25.29	–	*D*
		A12 x m1_1,3	2	150	2.0					2.00[3]	0.124	1870	116.88	1.60	1			26.23	–	*D*
		A12 x m1_2	1	150	2.0					2.00[3]	0.124	1870	116.88	1.60	1			27.46	–	JF
		A12 x l1_1,3	3	150	2.0					1.00[3]	0.062	1870	116.88	1.60	1			22.55	–	JF
		B3 x 2m2_1,..3	3	150	2.0					2.00[3]	0.124	2187	109.35	2.00	1		26.20	36.07	–	*D*
		B3 x 2l2_1,2	2	150	2.0					1.00[3]	0.062	2187	109.35	2.00	1			35.97	–	*D*
		B3 x 2l2_3	1	150	2.0					1.00[3]	0.062	2187	109.35	2.00	1			35.84	–	JF
		B12 x m2_1,..3	3	150	2.0					2.00[3]	0.124	1870	116.88	1.60	1			40.42	–	*D*
		B12 x l2_1,3	2	150	2.0					1.00[3]	0.062	1870	116.88	1.60	1			35.36	–	JF
		B12 x l2_2	1	150	2.0					1.00[3]	0.062	1870	116.88	1.60	1			37.90	–	*D*
	[15]	A1#1	1	150	2.0	22.10	6.78	8.03	UD	1.00[2]	0.062	2014	110.00	1.90	1	90	23.14	28.75	–	JF
		A2#1-1,2	2	150	2.0					1.00[2]	0.062	2480	120.00	2.10	1			32.30	–	JF
		A2#2-1,..3	3	150	2.0					1.00[3]	0.062	2480	120.00	2.10	2			38.56	–	JF
		A3#1	1	150	2.0	4.06	1.00	10.35		1.00[2]	0.062	2014	110.00	1.90	1			29.80	–	JF
		A4#1-1,2	2	150	2.0					1.00[2]	0.062	2480	120.00	2.10	1			30.12	–	JF
		A4#2-1,..3	3	150	2.0					1.00[3]	0.062	2480	120.00	2.10	2			34.02	–	JF
		A5#1	1	150	2.0	20.10	4.24	18.63		1.00[2]	0.062	2014	110.00	1.90	1			33.07	–	JF
		A6#1-1,2	2	150	2.0					1.00[2]	0.062	2480	120.00	2.10	1			32.15	–	JF
		A6#2-1,..3	3	150	2.0					1.00[3]	0.062	2480	120.00	2.10	2			38.02	–	JF
		B1#1	1	150	2.0	22.10	6.78	8.03		1.00[2]	0.062	2014	110.00	1.90	1			30.45	–	JF
		B3#1	1	150	2.0	4.06	1.00	10.35		1.00[2]	0.062	2014	110.00	1.90	1		16.61	26.64	–	JF
		B5#2	1	150	2.0	20.10	4.24	18.63		1.00[2]	0.062	2014	110.00	1.90	1			28.32	–	JF
		C7#1-1,..3	3	150	2.0	55.00	10.00	25.00		1.57[3]	0.084	2800	190.00	1.50	1			31.36	–	*D*
		C8#1-1,2	2	150	2.0					1.57[3]	0.084	2800	190.00	1.50	1		20.73	34.10	–	JF
		C7/8#2-1,2	4	150	2.0					1.57[3]	0.084	2800	190.00	1.50	2			42.43	–	JF
		D8#1-1	1	150	2.0					1.57[3]	0.084	2800	190.00	1.50	1			27.53	–	JF
		D8#1-2,3	2	150	2.0					1.57[3]	0.084	2800	190.00	1.50	1			27.75	–	*JF-D*
		D7#2-1,..3	3	150	2.0					1.57[3]	0.084	2800	190.00	1.50	2		18.27	36.44	–	JF
		D9#1-1	3	150	2.0					4.72[3]	0.254	2800	190.00	1.50	1			40.64	–	*D*
		D10#2-1,2	2	150	2.0					4.72[3]	0.254	2800	190.00	1.50	2			53.53	–	*JF-D*
		E8#1-1,2	2	150	2.0					4.72[3]	0.254	2800	190.00	1.50	1		29.98	40.51	–	JF
		E7#2-1,..3	3	150	2.0					4.72[3]	0.254	2800	190.00	1.50	2			45.21	–	JF
		E9#1-1,..3	3	150	2.0					4.72[3]	0.254	2800	190.00	1.50	1			45.87	–	*D*
		E10#2-1,..3	3	150	2.0					4.72[3]	0.254	2800	190.00	1.50	2			64.19	–	*JF-D*

Notes: * preimpregnated with resin; ** preimpregnated with latex; *** mesh coated with "modified acrylic polymer"; [1] elastic modulus expressed in [kN/m] (per unit width); [2] weight without coating; [3] density expressed in [cord/cm]; [4] jacket applied onto a wax-based bond breaker to facilitate removal, aiming at ensuring reversibility. *Sources:* [1] Di Ludovico et al. (2010); [2] García et al. (2010); [3] Sadrmomtazi et al. (2016); [4] Triantafillou et al. (2006); [5] Ortlepp et al. (2011); [6] Colajanni et al. (2014); [7] Zeng et al. (2017); [8] Gonzalez-Libreros et al. (2018); [9] Gopinath et al. (2011), [10] De Caso y Basalo et al. (2012); [11] Bhuvaneshwari et al. (2014); [12] Trapko (2013); [13] Ombres (2014); [14] Thermou et al. (2016); [15] Thermou and Hajirasouliha (2018).

FRCM systems is an important simplification to describe the real behavior. On the other hand, as long as the mechanical properties of the inorganic matrices are not – or not fully - documented in the literature, the above-mentioned approximation is necessary, because of the extreme variability of the mechanical properties of the inorganic matrices.

Table 2. Distribution of specimens and dataset based on the FRCM system and failure mode.

FRCM system	N. specimens			n. datasets			% datasets	
	All	JF	D	All	JF	D	JF	D
B-FRCM	44	44	–	10	10	–	100%	–
C-FRCM	43	26	17	18	12	6	67%	33%
G-FRCM	53	21	32	20	10	10	50%	50%
PBO-FRCM	35	25	10	25	18	7	72%	28%
S-FRCM	80	48	32	38	24	14	63%	37%
All	255	164	91	111	74	37	–	–

In Eq. (1), α and β are two unknown parameters to be calibrated through best-fit techniques aimed at minimizing the difference between the predicted and the experimental values of the strength, whereas $\bar{f}_l$ is the normalized confining pressure exerted by the FRCM jacket, expressed by:

$$\bar{f}_l = \frac{f_l}{f_{c0}} = k_\alpha \cdot \frac{2 \cdot t_f \cdot n_f \cdot E_f}{D} \cdot \left(k_\varepsilon \cdot \varepsilon_{f,u}\right) \tag{2}$$

In Eq. (2), k_α is the coefficient accounting for the fiber inclination, equal to 1 in the case of θ = 90°, which is given by (DT200 R1 2013):

$$k_\alpha = \frac{1}{1 + [tan(90^\circ - \theta)]^2} \tag{3}$$

Table 3. Best-fit analyses: results.

FRCM system	N	n	k_ε	Model	α	β	$(Err)_m$
B-FRCM	36	8	1.00	1	3.19	1.00	6.98%
				2	–	–	–
C-FRCM	22	11	1.00	1	1.16	1.00	6.36%
				2	1.16	1.00	6.36%
G-FRCM	15	7	1.00	1	2.24	1.00	8.46%
				2	–	–	–
PBO-FRCM	22	15	1.00	1	1.02	1.00	8.81%
				2	1.02	1.00	8.81%
S-FRCM	40	21	1.00	1	3.28	1.00	9.50%
				2	1.33	0.51	7.90%
PBO&C-FRCM	44	26	1.00	1	1.15	1.00	6.98%
				2	1.00	0.87	6.90%
			0.49	1	2.36	1.00	6.98%
				2	1.86	0.87	6.90%
B&S-FRCM	76	29	1.00	1	3.28	1.00	7.74%
				2	1.34	0.51	6.25%

Table 3 reports the results of the best-fit analyses performed to find the values of the parameters α and β which minimize the mean error $(E_{rr})_m$ between the experimental data $\bar{f}_{cc}^{exp}$ and the theoretical one $\bar{f}_{cc}^{th}$. The error minimization on the considered *n* datasets has been performed by applying the mean absolute percentage error (MAPE) method, expressed by:

$$(E_{rr})_m = \frac{\sum_{i=1}^{n} |E_i|}{n} \quad \text{with } E_i = \frac{\left(\bar{f}_{cc,i}^{exp} - \bar{f}_{cc,i}^{th}\right)}{\bar{f}_{cc,i}^{exp}} \cdot 100 \tag{4}$$

The analyses were carried out separately on the datasets included in "JF" failure mode and on those grouped in "D" failure mode. For the sake of brevity, the results in Table 3 exclusively refer to the analyses performed for the "JF" case. One should also note that, for each FRCM system, the number *n* does not always coincide with that indicated in Table 2 for the "JF" case since some datasets were excluded in the analyses due to the lack of proper information or uncertainty in the available tests.

The best-fit analyses were first performed on datasets belonging to the single type of FRCM system; then, only in the cases where the values of α and β found for a given system were similar to those computed for another one, the analyses were performed again and extended to datasets belonging to both systems; this is the case of PBO and C-FRCM systems, and B & S-FRCM systems. Furthermore, the analyses were generally performed by considering the following cases: *(a)* $\alpha \neq 1$ & $\beta = 1$ (Model 1, i.e., linear model), *(b)* $\alpha \neq 1$ & $\beta \neq 1$ (Model 2, i.e., nonlinear model). Due to the lack of a sufficient amount of information for the strain efficient factor, the analyses were always performed by considering $k_\varepsilon = 1$. An exception is represented by the PBO-FRCM, for which an average value equal to 0.49 was found from the available datasets and was used in the best-fit analyses performed in combination with the C-FRCM system.

Figures 3a–f show the comparison between the best-fit models found for FRCM systems and the experimental data (with $\bar{f}_l$ values calculated by applying Eq. 2). For the C-FRCM (Fig. 3b), G-FRCM (Fig. 3c) and S-FRCM (Fig. 3e) systems, the formulations proposed by DT-200 R1 (2013), Realfonzo and Napoli (2011), Napoli and Realfonzo (2016) for the corresponding C/G-FRP and S-FRP systems are also plotted for comparison. Finally, Figs. 4a and b show the comparison between the experimental $(\bar{f}_l; \bar{f}_{cc})$ points and the corresponding predictive models obtained by considering: *(a)* PBO-FRCM and C-FRCM systems together (Fig. 4a), and *(b)* B-FRCM and S-FRCM systems together (Fig. 4b).

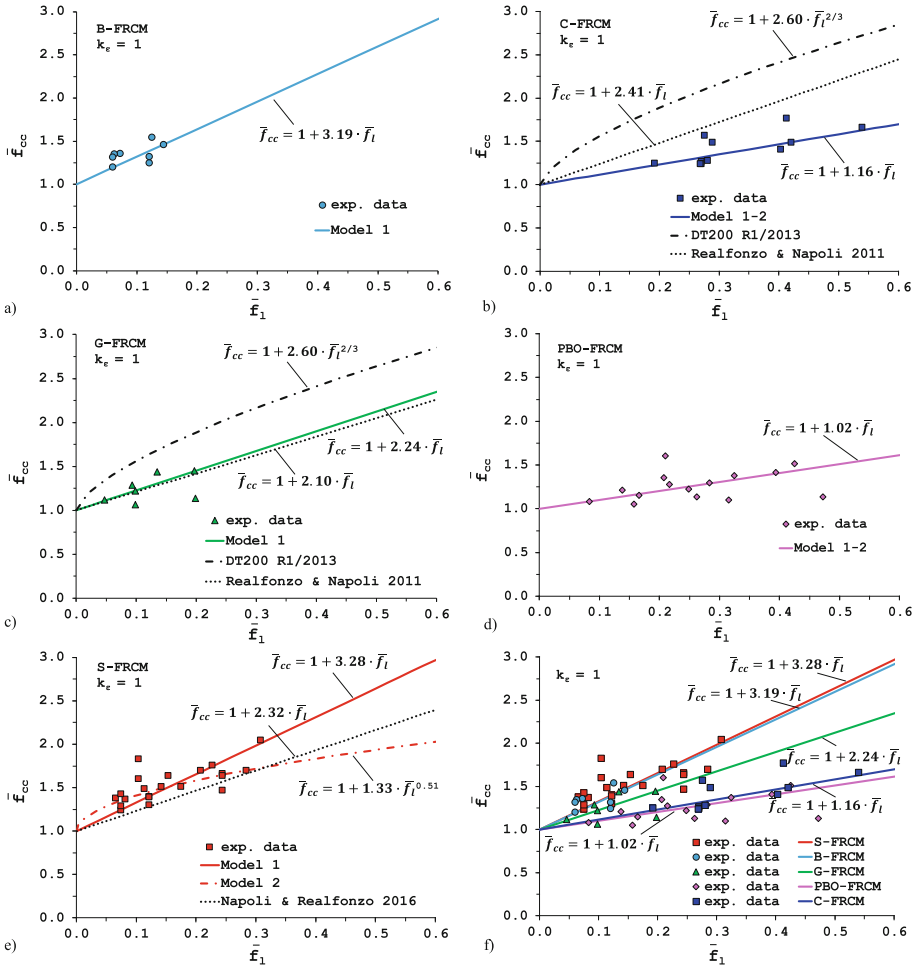

Fig. 3. Predictive models for B-FRCM (a), C-FRCM (b), G-FRCM (c), PBO-FRCM (d), S-FRCM (e) systems, and comparison among all linear models (f)

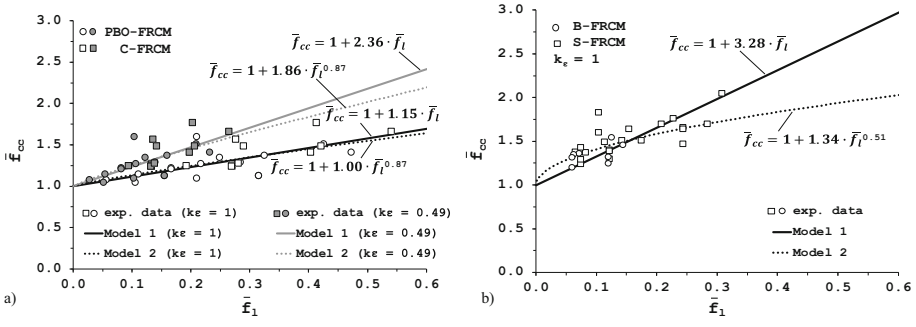

Fig. 4. Predictive models for: PBO-FRCM & C-FRCM systems (a), B-FRCM & S-FRCM systems (b)

4 Conclusions

In this paper, an extended database including 255 compression tests performed on concrete cylinders externally wrapped with FRCM systems is presented. The collected results were used to develop preliminary models for predicting the compressive strength of FRCM-confined concrete. These models were calibrated by applying best-fit techniques to the experimental results which were separately treated for each FRCM system. Since the formulations found for PBO-FRCM and C-FRCM systems were very similar, a unique best-fit model was then developed by considering these two systems together. The same was done for B-FRCM and S-FRCM systems, given the similarity of the found relationships.

References

American Concrete Institute (ACI) (2013) Guide to Design and Construction of Externally Bonded Fabric-Reinforced Cementitious Matrix (FRCM) Systems for Repair and Strengthening Concrete and Masonry Structures. ACI 549.4R-13, Farmington Hills

Ascione L, de Felice G, De Santis S (2015) A qualification method for externally bonded Fibre Reinforced Cementitious Matrix (FRCM) strengthening systems. Compos Part B Eng 78:497–506

Ates AO, Tore E, Khoshkholghi S, Ilki A (2017) Sprayed textile reinforced GFRC for retrofitting of sub-standard non-circular concrete columns. In: Proceedings of the 16th world conference on earthquake engineering, 16WCEE, Santiago, Chile

Bhuvaneshwari P, Saravana Raja Mohan K, Kirthiga R (2014) Stress strain behaviour of concrete element retrofitted using organic and inorganic binders. Asian J Appl Sci 7(4):215–223

Bournas DA, Lontou PV, Papanicolaou CG, Triantafillou TC (2007) Textile reinforced mortar versus fiber-reinforced polymer confinement in reinforced concrete columns. ACI Struct J 104 (6):740–748

Carloni C, Bournas DA, Carozzi FC, D'Antino T, Fava G, et al (2016) Fiber reinforced composites with cementitious (inorganic) matrix. In: Pellegrino C, Sena-Cruz J (eds) Design procedures for the use of composites in strengthening of reinforced concrete structures. State-of-the-Art Report of the RILEM Technical Committee 234-DUC. Springer, pp 349–392

Cascardi A, Longo F, Micelli F, Aiello MA (2017) Compressive strength of confined column with Fiber Reinforced Mortar (FRM): new design-oriented-models. Constr Build Mater 156:387–401

Colajanni P, Fossetti M, Macaluso G (2014) Effects of confinement level, cross-section shape and corner radius on the cyclic behavior of CFRCM confined concrete columns. Constr Build Mater 55:379–389

D'Ambrisi A, Feo L, Focacci F (2013) Experimental and analytical investigation on bond between carbon-FRCM materials and masonry. Compos Part B Eng 46:15–20

De Caso y Basalo FJ, Matta F, Nanni A (2012) Fiber reinforced cement-based composite system for concrete confinement. Constr Build Mater 32:55–65

Di Ludovico M, Prota A, Manfredi G (2010) Structural upgrade using basalt fibers for concrete confinement. J Compos Constr 14(5):541–552

García D, Alonso P, San-José JT, Garmendia L, Perlot C (2010) Confinement of medium strength concrete cylinders with basalt textile reinforced mortar. In: Proceedings of the 13th international congress on polymers in concrete, ICPIC 2010, Madeira, Portugal

Gonzalez-Libreros J, Sabau C, Sneed LH, Sas G, Pellegrino C (2018) Effect of confinement with FRCM composites on damaged concrete cylinders. RILEM Bookseries, vol 15, pp 770–777

Gopinath S, Iyer NR, Gettu R, Palani GS, Ramachandra Murthy A (2011) Confinement effect of glass fabrics bonded with cementitious and organic binders. Procedia Eng 14:535–542

Italian National Research Council (CNR) (2013) Guide for the design and construction of externally bonded FRP systems for strengthening existing structures. CNR-DT200 R1, Rome

Lam L, Teng JG (2003) Design-oriented stress–strain model for FRP-confined concrete. Constr Build Mater 17(6–7):471–489

Napoli A, Realfonzo R (2016) Compressive behavior of concrete confined by SRP wraps. Constr Build Mater 127:993–1008

Ombres L (2014) Concrete confinement with a cement based high strength composite material. Compos Struct 109:294–304

Ombres L, Mazzuca S (2017) Confined concrete elements with cement-based composites: confinement effectiveness and prediction models. J Compos Constr 21(3):1–15

Ortlepp R, Lorenz A, Curbach M (2011) Geometry effects onto the load bearing capacity of column heads strengthened with TRC. In: Proceedings of fib symposium, Prague, Czech Republic

Realfonzo R, Napoli A (2011) Concrete confined by FRP systems: confinement efficiency and design strength models. Compos Part B Eng 42(4):736–755

Sadrmomtazi A, Khabaznia M, Tahmouresi B (2016) Effect of organic and inorganic matrix on the behavior of FRP-wrapped concrete cylinders. J Rehabil Civ Eng 4(2):52–66

Thermou GE, Katakalos K, Manos G (2016) Influence of the cross section shape on the behavior of SRG-confined prismatic concrete specimens. Mater Struct 49:869–887

Thermou GE, Hajirasouliha I (2018) Compressive behaviour of concrete columns confined with steel-reinforced grout jackets. Compos Part B Eng 138:222–231

Tore E, Comert M, Demir C, Ilki A, Marasli M (2015) Seismic retrofit of columns using basalt mesh reinforced sprayed GRC jacket. In: Proceedings of the 17th international congress of the GRCA, Radison Blu, Dubai

Trapko T (2013) Fibre reinforced cementitious matrix confined concrete elements. Mater Des 44:382–391

Triantafillou TC, Papanicolaou CG, Zissimopoulos P, Laourdekis T (2006) Concrete confinement with textile-reinforced mortar jackets. ACI Struct J 103(1):28–37

Zeng L, Li LJ, Liu F (2017) Experimental study on fibre-reinforced cementitious matrix confined concrete columns under axial compression. Kem Ind 66(3–4):165–172

Explosive Spalling in R/C Structures Exposed to Fire: Key Aspects in Experimental Testing

Francesco Lo Monte[1(✉)], Roberto Felicetti[1], Alberto Meda[2], and Anna Bortolussi[3]

[1] Politecnico di Milano, Milan, Italy
francesco.lo@polimi.it
[2] Università degli Studi di Roma Tor Vergata, Rome, Italy
[3] Bekaert Maccaferri Underground Solutions, Aalst, Erembodegem, Belgium

Abstract. Explosive spalling in R/C members exposed to fire consists in the violent expulsion of the hottest layers of concrete, due to the combination of compressive stress and vapour pressure, with the consequent reduction of the bearing cross-section and of the structural fire resistance. Experimental tests aimed at assessing concrete spalling sensitivity can be performed at different scales, namely small, intermediate and real scale, with increasing time and cost of testing. The correct level of investigation must be defined as the right compromise between efficiency and representativeness of the real case. Starting from the comparison among different test setups at different scales, the main parameters to be considered in planning the experimental investigations will be described. On the other hand, with regards to the definition of the mix design, it will be shown how the use of different types of fibre can bring remarkable benefits against spalling.

Keywords: Explosive spalling · Fibre · Fire · Experimental testing · Pore pressure · Thermal stress

1 Introduction

1.1 Explosive Spalling in R/C Structures

Explosive spalling in Reinforced Concrete (R/C) members exposed to fire consists in the violent expulsion of the hottest layers of concrete, due to the combination of compressive stress and vapour pressure in the pores. The main consequences are the reduction of the bearing cross-section and the direct exposure of the reinforcing bars to the flames, both aspects dramatically speeding up the decay of fire resistance.

When the structural behaviour is at issue, the two-fold effect brought in by heating must be carefully tackled, namely the decay of concrete mechanical properties and the incidence of indirect actions due to thermal dilation.

The severity of the fire impact in turn depends on duration and maximum temperature of the fire scenario, which are governed by different factors as fire load, ventilation, geometry of the compartment, fire protection systems. It is worth noting

M. di Prisco and M. Menegotto (Eds.): ICD 2018, LNCE 42, pp. 372–384, 2020.
https://doi.org/10.1007/978-3-030-23748-6_29

that, very high temperatures can be reached in extreme cases, even higher than 1000 °C in case of the most severe scenarios in tunnels.

Spalling has a relevant impact also for the retrofitting phase after the fire. In this regard, fire spalling substantially increases the overall damage to the structures, directly influencing the extent of retrofitting interventions, and then time and cost of their execution. This is, for instance, a key point in tunnels, since the costs connected to traffic disruption must be considered.

Avoiding spalling in such kind of structures generally brings great advantages in these regards, and such result can be achieved with the choice of the right concrete mix in the design phase.

Spalling phenomenon is influenced by both material factors, such as moisture content, porosity, tensile strength and fibre content, and structural factors, namely heating rate, external loads and restraints. The interaction of so many aspects makes rather difficult to predict concrete sensitivity to spalling.

Despite of the complexity of the mechanisms behind spalling, it is generally agreed that the two triggering actors are stress induced by thermal gradients and external loads, on the one hand, and pore pressure rise caused by water vaporization, on the other hand.

Thermal gradients induced by heating introduce compressive stress in the hot layers and tensile stress in the inner core (Fig. 1a). The increase of compression next to the exposed face favours the formation of cracks parallel to the isothermal surfaces with the consequent decrease of the local mechanical stability. Concrete cracking is also fostered by other meso-scale aspects, as for instance aggregate-cement paste kinematic incompatibility, release of absorbed and chemically bound water and cement dehydration (Fu and Li 2010). Furthermore, the rise of pressure in concrete pores takes place (Fig. 1a) due to the vaporization process and to the dilation of liquid water (if saturation occurs). Due to the low porosity and high heat-sensitivity, High-Performance Concrete (HPC) is generally more prone to spalling than Normal-Strength Concrete (NSC), since much higher values of pore pressure can develop in the former (Kalifa et al. 2000; Khoury 2000).

Many research studies in the literature report the addition of polypropylene fibre as the most effective way to reduce concrete spalling sensitivity. Even rather limited amounts of polypropylene fibre (1–2 kg/m^3) are sufficient to effectively reduce the probability of spalling, thanks to the further porosity introduced by fibre melting and subsequent cement paste micro-cracking (Khoury 2008; Pistol et al. 2014; Rossino et al. 2013, 2015).

The interconnection between stress and pore pressure makes necessary investigations involving both aspects, under the same conditions imposed by the normal service of the structure. In the literature, either numerical and experimental studies can be found.

Numerical models have been developed to simulate fire spalling and several approaches based on different simplifying assumptions have been proposed (Gawin et al. 2011). In these models, however, calibration is rather tricky. In particular, a critical point is represented by the mechanical response of the material to pore pressure, for which very few experimental evidences are so far available in the literature (Felicetti et al. 2017).

This makes experimental testing the most reliable way for spalling sensitivity assessment of concrete mixes. However, it is important to underline that no standardized test has been defined yet. The technical committee RILEM 256 SPF (Spalling of concrete due to fire: testing and modelling) has been launched some years ago, aimed at developing common reference guidelines. Within this context, the present paper will try to give an overview about spalling sensitivity assessment via experimental testing, in terms of setup and possible results.

With reference to such aspects, it is emphasized how experimental tests can be carried out at different scales, namely small, intermediate and real scale, with increasing costs and time burden of testing. Hence, the correct level of investigation must be defined as the right compromise between efficiency and representativeness of the actual case. The main parameters to be considered in planning the experimental investigations will be described and, afterwards, the comparison among tests carried out on the same concretes at different scales will be reported.

With regards to the definition of the mix design, the remarkable benefit brought in by the use of polymeric fibre will be also briefly shown.

1.2 Experimental Assessment of Explosive Spalling

Experimental investigations on concrete sensitivity to explosive spalling can be performed on small-, medium- or full-scale tests, either on loaded or unloaded specimens (Krzemieńa and Hager 2015).

In small-scale investigations, temperature and/or pressure are usually monitored in unloaded prismatic specimens made of plain or fibre-reinforced concretes (Kalifa et al. 2000; Lo Monte and Gambarova 2015; Mindeguia et al. 2010; Felicetti et al. 2017). In other small-scale tests, specimens have been loaded via actuators, a steel casing or a ring restraining thermal dilation, or by means of a steel ring loaded by hydraulic jacks (Miah et al. 2016; Hertz and Sørensen 2005; Ozawa et al. 2018; Connolly 1995). The common evidence is that spalling hardly occurs in unloaded and unrestrained small specimens exposed just on one side. More critical – but not well controlled – conditions develop when small samples (cylinders, cubes) are heated in a furnace, due to radial and circumferential cracking induced by thermal gradients involving the whole perimeter.

In medium-scale tests, loaded or unloaded slabs or prismatic specimens are generally heated on one side. External compression (generally uniaxial) can be applied via restraining frames, post-tensioning systems and flat or pancake jacks (Connolly 1995; Heel and Kusterle 2004; Sjöström et al. 2012; Boström et al. 2007; Jansson and Boström 2008; Carré et al. 2013; Rickard et al. 2016; Lo Monte and Felicetti 2017). The general conclusion is that specimens loaded during heating are far more prone to spalling than unloaded ones, and that biaxial compression is a more severe condition than uniaxial loading (Miah et al. 2016).

Finally, full-scale investigations consist in testing structural members or substructures under restraining and loading conditions representative of the real ones. This experimental level is, obviously, the most representative of the structural behaviour.

However, full-scale testing is costly and time demanding, hence unsuitable for a first categorization of several concrete mixes. Furthermore, results are very specific and not directly generalizable.

In this context, three different test setups have been compared for the evaluation of spalling sensitivity and the results are briefly discussed in order to detect possible common triggering factors. Before presenting the results, different possible setups for intermediate scale investigations are discussed so to highlight the main influencing parameters.

2 Intermediate Scale Tests

Intermediate scale tests are generally performed on concrete specimens heated on one side only. The term "intermediate" refers to the size of concrete specimen, which is in between the usual sample size for material properties characterization (cube, cylinder) and for full-scale testing.

As regards the definition of test duration, it should be kept in mind that, for loaded samples, collapse may be reached already within 30 min of heating, and the first hour generally provides the most significant results. When comparing different concrete mixes or different load levels, it is strongly recommended to use the same fire duration for all tests, in order to make directly comparable the different spalling depths.

Two different typologies of test can be performed: *Passive-Restraint* and *Active-Restraint* tests.

In the former case, the load generally changes during heating because of the thermo-mechanical effects on both the specimen and the restraining system. In the latter case, load can be properly measured and also modulated during heating. Uniaxial or biaxial in-plane load can be applied in both kinds of test.

2.1 Passive-Restraint Test

In Passive-Restraint tests, compression is induced by simply restraining the thermal dilation of the specimen. This can be provided via pre-tensioned or post-tensioned tendons, concrete itself in massive samples, steel belts or restraining frames (Fig. 2).

Since confinement is strictly connected to thermal stress (which in turns depends on thermal dilation and elastic modulus), when comparing different mixes, it should be considered that load may differ among the different mixes. Furthermore, the load in the specimen cannot be adjusted during the test.

In the ideal case of a slab uniformly heated on one face, in which the isothermal planes are parallel to the heated-side, compression is induced in the hot layers and tension in the inner core. For bending equilibrium, compression is induced also at the cold side (σ_{th} in Fig. 1a). The magnitude of such stresses depends on specimen thickness, thermal dilation and elastic modulus of concrete and, obviously, on thermal field.

Increasing the thickness of the specimen, the confinement provided by the inner core becomes more effective, increasing the compression in the hot layers. The slab, in fact, tends to undergo sagging due to the dilation of the hot layer and this curvature is partially prevented by the flexural stiffness of the specimen.

Moving from the ideal case to the actual testing conditions, another aspect which must be considered is the disturbance induced by the rim, namely the peripheral part of the slab.

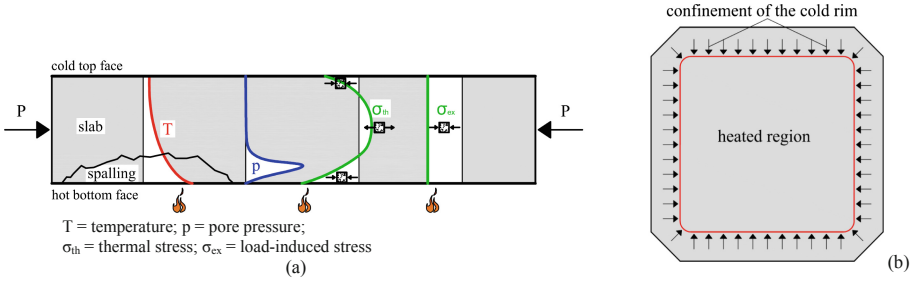

Fig. 1. Concrete slab heated at the bottom: (a) thermal, pore pressure and stress profiles within the slab thickness and (b) plan view of the slab showing the confinement provided by the cold concrete rim.

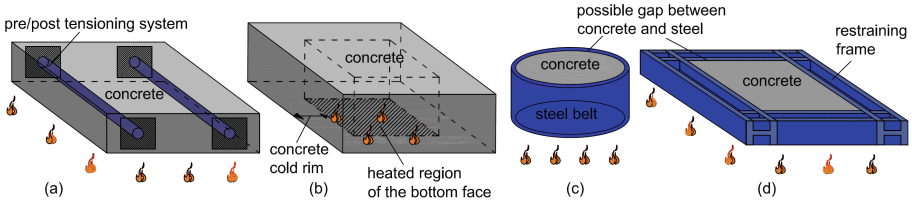

Fig. 2. Passive Restraint test confining systems: (a) post-tensioning, (b) concrete cold rim, (c) steel belt and (d) steel frame.

This may be not directly heated, thus providing a further confinement to the heated region of the specimen (Fig. 1b). Moreover, edge shear deformation due to thermal gradients and load diffusion from any restraint system make the rim not representative of the designed testing condition, to the point that no spalling generally occurs in this region.

In the case of post-/pre-tensioning tendons (Fig. 2a), the initial compression applied to concrete is known. On the contrary, during heating, thermal dilation of the specimen induces an elongation of tendons which increases their tensile load, thus increasing compression in concrete. When concrete stiffness significantly decreases due to temperature rise, the tensile action in tendons and, consequently compression in concrete, starts decreasing. Finally, when the temperature in the tendons is high enough, the decay of steel elastic modulus can even make nil pre-/post-tensioning effect.

The initial increase of tension in tendons is also strictly connected to the thickness of the specimen. In very thick specimens, in fact, the average axial thermal dilation becomes negligible (since, hot layer is just a small portion of the whole slab) and the variation of elongation in tendons is strongly limited. This behaviour can be extended to any kind of passive restraint (cold rim, steel belt or steel restraining frame).

When using pre-tensioning (or post-tensioning, if active control is not adopted) the tensile load in the tendons during the test cannot be controlled. It can be possibly monitored with load cells at the anchors in case of unbonded tendons. However, if temperature and strain in tendons are monitored, the applied load can be assessed (even though with some approximations due to creep strain and elastic modulus decay in hot steel). This approach, however, brings in the difficulty of measuring tendon strain at high temperature.

Confinement can be provided also by means of the cold concrete rim (Fig. 2b), which tends to restrain the thermal dilation of the whole specimen, thus introducing compression in all the thickness. On the other hand, circumferential tensile stress is induced in the cold concrete rim, this leading to cracking and consequently smoothing down the confining effect. In this case, a direct control of the compression introduced in the specimen is not possible.

If a steel belt or a restraining frame is used, compression in concrete is induced in a way similar to that discussed for cold concrete rim. Steel, however, can apply a more effective confinement thanks to its good tensile behaviour. When using circular concrete slabs (Fig. 2c), the steel belt is subjected to pure tension and can be very effective in applying the in-plane compression in concrete.

For a rectangular concrete slab, a rectangular steel frame can be theoretically used (Fig. 2d). In such case, however, steel frame restrains concrete thermal dilation thanks to its flexural stiffness, that, however, is much lower than the in-plane stiffness of concrete. This is the reason why such confinement is expected to be significant just at the corners (Fig. 3a). Confinement by means of steel belt or restraining frame is nil before heating (no compression in concrete) and increases in time, with a behaviour similar to what explained for post-tensioning systems.

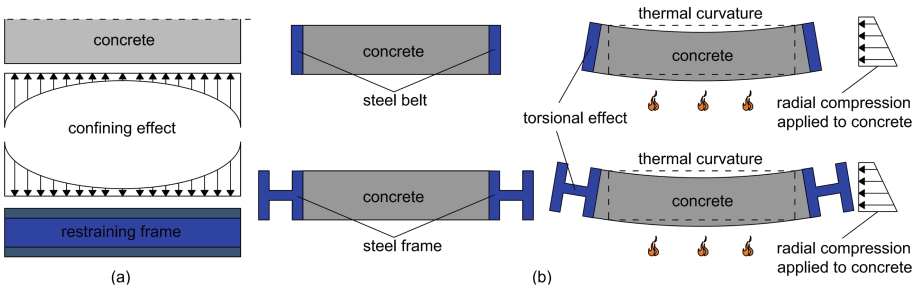

Fig. 3. Distribution of confining stress provided by a restraining frame along a slab side (a), torsional effect on steel belt and restraining frame, and in-plane compression applied to concrete (b).

It is worth noting that when concrete is cast directly in the restraining system, shrinkage during hardening and curing can introduce a gap between the two materials, thus reducing the initial restraining effect during the test.

The rotation of slab edges due to thermal curvature introduces a non-uniform tension in steel belt and bending/torsion on the restraining frame (Fig. 3b). If strain and temperature at different height are monitored in steel, the final circumferential tension can be computed. When the flexural/torsional behaviour of steel restraining frame is hard to be monitored, different load cells can be placed between the frame and the concrete specimen.

2.2 Active-Restraint Test

In Active-Restraint test, concrete specimens are loaded via hydraulic pancake or flat jacks (Fig. 4).

When comparing different mixes, Active-Restraint tests guarantee to apply the same load to the specimens. The external load, in fact, is defined a priori and it can be kept constant in time or varied according to a particular law during heating. Attention should be also paid to the effect of the cold concrete rim, which induces parasitic confinement effects. To limit this constraint, radial slits can be cut so to break the mechanical continuity.

Load is applied via jacks restrained by a system whose stiffness must be properly designed. For restraining the hydraulic jacks, a steel frame, bars or tendons can be used (Fig. 4). The use of spherical heads is important in order to determine the application point and to be able to adapt to the specimen deformation during heating. Flat jacks should be carefully used so to take into account possible boundary effects of the pressurized metal sheet leading to a non-uniform application of the load to concrete.

Uniaxial or biaxial loading can be introduced. It is worth noting that the two loading conditions can lead to different results in terms of spalling severity, since biaxial load induces higher spalling amounts (Miah et al. 2016).

2.3 Heating Rate

For both Passive and Active Restraint tests, the adoption of a particular heating rate represents an important feature of the experimental procedure.

Heating rate (together with specimen geometry and confining/loading system) has a direct influence on spalling risk and progression. It influences the maximum temperature reached and, even more important, thermal gradients, which in turn govern thermal stress magnitude and thermal curvature. Both these quantities define the stress state in concrete, which is a key factor in triggering spalling.

3 Experimental Campaign

With the aim to give an idea about the range of experimental results' scattering ensuing from different test setups, the outcome of a broad experimental campaign is presented in the following (Lo Monte et al. 2017; Lo Monte et al. 2019). In order to characterize

spalling sensitivity of a set of concrete mixes, in fact, three testing procedures have been adopted:

- *hot spot test*: plain concrete cubes of 1 m-side exposed to a localized flame,
- *biaxial loading test*: unreinforced slabs exposed to standard fire at the intrados under in-plane compression,
- *full-scale test*: tunnel lining segment subjected to the design service loads and exposed to fire.

The three setups need an increasing effort in terms of time and cost, because of the different scale of testing. The first two methods are examples of Passive and Active Restraint tests.

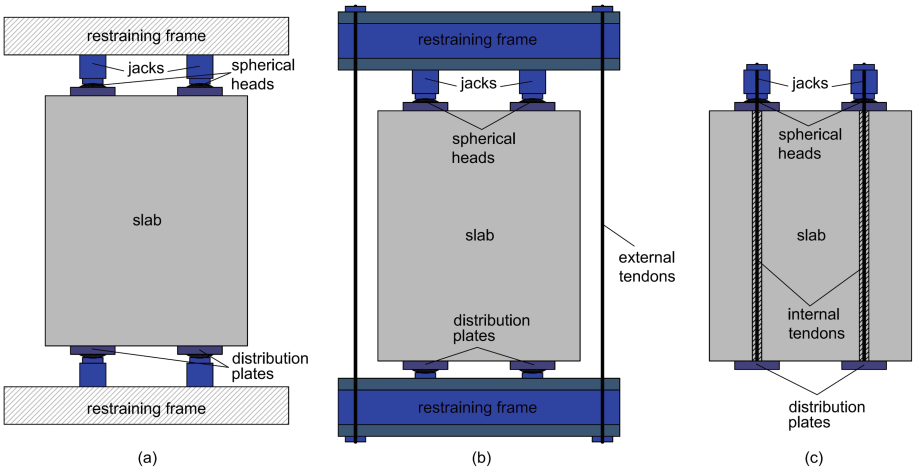

Fig. 4. Active Restraint test: (a, b) hydraulic jacks and (c) actively controlled post-tensioning tendons.

3.1 Hot Spot Test

The test is based on unreinforced concrete cubes with 1 m-side exposed to a 250 mm-diameter hot spot on one face (Fig. 5a). The temperature, monitored by means of a small plate thermometer, reaches instantly 800 °C and then is kept constant. Just the final spalling depth is measured, though onset time and progress of the phenomenon can be surveyed by video recording. Since no external load is applied, stress ensues just from thermal gradients. Confinement is provided by concrete itself, the test being performed on massive samples.

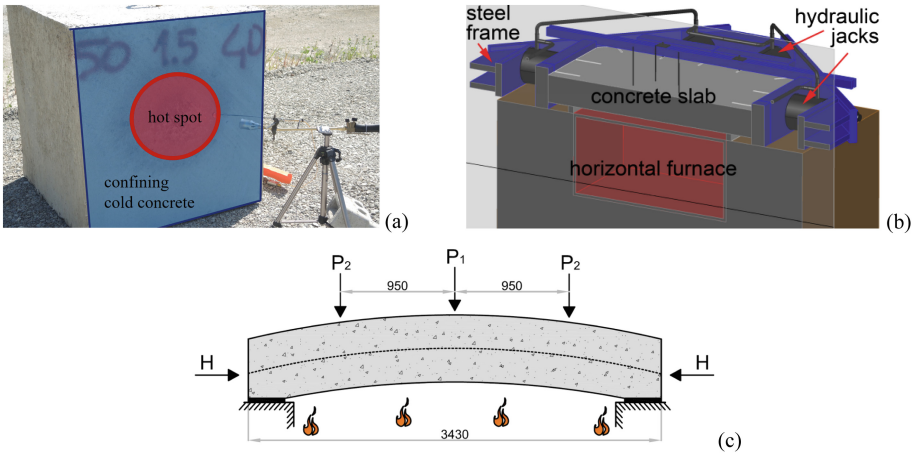

Fig. 5. (a) **Hot spot test**: concrete cube exposed to a jet flame; (b) **Biaxial loading test**: section of concrete slab within the loading system placed over the horizontal furnace; (c) **Full-scale test**: scheme of loading and heating of a tunnel lining segment.

3.2 Biaxial Loading Test

This setup allows to perform hot tests on biaxial loaded slabs under strictly controlled boundary conditions (Lo Monte and Felicetti 2017).

Specimens consist in unreinforced concrete slabs with a thickness of 100 mm and in-plane dimensions of 800 × 800 mm. The intrados is exposed to the standard fire by means of a horizontal furnace powered by an actively controlled propane burner (Fig. 5b). Biaxial in-plane compression can be applied via eight hydraulic jacks. Biaxial membrane loading is implemented in order to emphasize the effect of compression.

3.3 Full-Scale Test

As a final reference case, one full scale test has been performed at the Leipzig Institute for Materials Research and Testing – MFPA. A tunnel lining segment is loaded vertically in three points and horizontally at the abutments by means of hydraulic jacks, as reported in Fig. 5c. Just the bottom face is heated according to the RWS (Rijkswaterstaat) fire curve. Displacements at the actuators and temperature in the thickness are monitored throughout the test. Due to high time and costs required, such experimental procedure has been performed just for the final validation of the reference plain concrete.

3.4 Experimental Results

The 3 tests have been performed on two very similar concretes with a cylindrical compressive strength in the range 45–50 MPa, with different amounts of polypropylene and steel fibres, for a total of 8 mixes.

Hot spot test was adopted for investigating all the concretes, while biaxial loading test for just 6 of them (since 1.5 kg/m^3 of polypropylene fibre proved to be enough to prevent spalling). On the contrary, full scale test was performed on the reference plain mix only (see Table 1).

Table 1. Summary of test results.

	Mix	45_Plain	45_1.5	45_2.0	45_1.5_4D	50_Plain	50_1.5	50_2.0	50_1.5_4D
	pp fibre [kg/m^3]	0	1.5	2	1.5	0	1.5	2	1.5
	steel fibre [-]	N	N	N	Y	N	N	N	Y
hot spot test	fire duration [min]	15	30	15	15	15	30	15	15
	spalling initiation [min]	1	-	-	-	0.75	-	-	-
	max spall. depth [mm]	100	-	-	-	120	-	-	-
biaxial loading test	fire duration [min]	30	60		60	30	60		60
	spalling initiation [min]	17	-		-	15	-		-
	avg spall. depth [mm]	55	-		-	62	-		-
full-scale test	fire duration [min]	120							
	spalling initiation [min]	3							
	avg spall. depth [mm]	154							

In biaxial loading test, the external constant compression was set to 10 MPa, while in real scale test, load was applied according to Fig. 5c with P_1 = 593 kN, P_2 = 297 kN and H = 5300 kN (= average compression of 5.3 MPa).

As reported in Table 1, spalling was observed only in the two plain mixes, 45_Plain/50_Plain with final spalling depths of 100/120 mm in hot spot test, 55/62 mm in biaxial loading test and 154/- mm in full-scale test.

3.5 Discussion

Aimed at understanding the different results collected from the three test setups, numerical analyses have been performed to compute thermal field and stress state in the specimens in a significant time range including spalling time onset (Lo Monte et al. 2017; Lo Monte et al. 2019). This is instrumental to detect possible common triggering conditions.

It is worth noting that the qualitative results of the test setups (especially hot spot and biaxial loading tests) provide consistent information about polypropylene fibre effectiveness in preventing spalling.

Numerical simulations clearly show that temperature evolution is rather different among the test setups because of the different fire curves. Spalling, however, takes place when the temperature at the heated face is within a small range (300–350 °C).

As regards the stress distributions, numerical analyses highlighted several aspects:

1. For both hot spot and biaxial loading tests, the stresses in directions x and y in the plane parallel to the heated face are almost the same due to the double symmetry of both heating and loading.
2. In full-scale test, the stress along the axis of the tunnel lining segment comes from the interaction between thermal gradients and external loads, while in the other direction is caused by thermal gradients only.

3. The stress normal to the exposed face is negligible in biaxial loading and full-scale tests, since heating flux is essentially unidimensional, while tension arise in the hot spot test.
4. Tension is never attained in biaxial loading test, thanks to the external compression.
5. At the onset of spalling, the maximum compression at the hot face is within a rather small range of values among the different setups, namely between 17 (biaxial loading test) and 23 MPa (hot spot test), even though they are reached for different fire durations (1, 3, 15 min for hot spot, full-scale and biaxial loading tests, respectively).

Compressive stress in the order of 20 MPa is expected to be enough for triggering spalling thanks to the contribution of pore pressure when polypropylene fibre is not present (usually in the range of 0.5–2.5 MPa). In all the specimens, orthogonal cracking occurs deeper than the hygrally-active region (namely, where pore pressure develops; Lo Monte and Felicetti 2017), thus favouring pressure build-up in the pores.

4 Conclusions

In the present paper, the main critical aspects concerning the experimental assessment of concrete sensitivity to fire spalling are described, discussing several possible test setups. Afterwards, the results of three different types of test are presented.

As regards the experimental campaign herein reported, firstly a very easy test setup has been adopted testing unreinforced concrete cubes heated by direct flame in a small area (25 cm in diameter). In the second phase, concrete slabs have been tested under biaxial in-plane compression while subjected to standard fire at the intrados. For the final validation, a full-scale test on a concrete tunnel lining segment has been carried out on the reference plain mix only.

Spalling was observed just in mixes without polypropylene fibre, and spalling time onset and final depth resulted rather different among the testing procedures, due to the variation of specimen geometry, external load, boundary conditions and fire exposure.

In order to read such outcome, numerical simulations have been worked out to evaluate both thermal field and stress state in the specimens during heating. It is worth noting as numerical results showed that at spalling onset time, temperature at the hot face was in the small range 300–350 °C for all the specimens, thermal range for which sizable pore pressure can be reached. On the other hand, at the same instant, the maximum compression at the hot face was in between 17 and 23 MPa (even though such stresses have been reached for rather different fire durations depending on the test procedure).

The tensile stress induced by pore pressure, together with tension caused by thermal gradients and meso-scale effects, is expected to lead to an apparent decrease of compressive strength sufficient to instate the conditions for spalling initiation.

In conclusion, even though experimental procedures and final results are different in terms of spalling onset time and final depth, common triggering conditions can be detected. Such differences, however, can be explained only once the effects of specimen geometry, loading and heating conditions are carefully analysed.

Acknowledgements. The Authors are grateful to Leipzig Institute for Materials Research and Testing – MFPA for providing the results regarding the full-scale test on the tunnel lining segment.

References

Boström L, Wickström U, Adl-Zarrabi B (2007) Effect of specimen size and loading conditions on spalling of concrete. Fire Mater 31:173–186

Carré H, Pimienta P, La Borderie C, Pereira F, Mindeguia JC (2013) Effect of compressive loading on the risk of spalling. In: Proceedings of the 3rd international workshop on concrete spalling due to fire exposure, Paris, France, 25–27 September 2013, p 01007

Connolly R (1995) The spalling of concrete in fires. PhD thesis, The University of Aston in Birmingham

Felicetti R, Lo Monte F, Pimienta P (2017) A new test method to study the influence of pore pressure on fracture behaviour of concrete during heating. Cem Concr Res 94:13–23

Fu Y, Li L (2010) Study on mechanism of thermal spalling in concrete exposed to elevated temperatures. Mater Struct 44:361–376

Gawin D, Pesavento P, Schrefler BA (2011) What physical phenomena can be neglected when modelling concrete at high temperature? a comparative study. Part 2: comparison between models. Int J Solids Struct 48:1945–1961

Heel A, Kusterle W (2004) Die Brandbeständigkeit von Faser-, Stahl- und Spannbeton [Fire resistance of fiber-reinforced, reinforced, and prestressed concrete] (in German). Tech. Rep. 544, Bundesministerium für Verkehr, Innovation und Technologie, Vienna

Hertz K, Sørensen L (2005) Test method for spalling of fire exposed concrete. Fire Saf J 40:466–476

Jansson R, Boström L (2008) Spalling of concrete exposed to fire. SP Technical Research Institute of Sweden, Borås

Kalifa P, Menneteau FD, Quenard D (2000) Spalling and pore pressure in HPC at high temperatures. Cem Concr Res 30:1915–1927

Khoury AG (2000) Effect of fire on concrete and concrete structures. Prog Struc Eng Mater 2:429–447

Khoury GA (2008) Polypropylene Fibres in Heated Concrete. Part 2: pressure relief mechanisms and modelling criteria. Mag Concr Res 60(3):189–204

Krzemieńa K, Hager I (2015) Assessment of concrete susceptibility to fire spalling: a report on the state-of-the-art in testing procedures. Procedia Eng 108:285–292

Lo Monte F, Gambarova PG (2015) Corner spalling and tension stiffening in heat-damaged R/C members: a preliminary investigation. Mater Struct 48:3657–3673

Lo Monte F, Felicetti R (2017) Heated slabs under biaxial compressive loading: a test set-up for the assessment of concrete sensitivity to spalling. Mater Struct 50:192

Lo Monte F, Felicetti R, Meda A, Bortolussi A (2017) Influence of the test method in the assessment of concrete sensitivity to explosive spalling. In: Proceedings of the 5th international workshop on "concrete spalling due to fire exposure", Boras, Sweden, 12–13 October 2017

Lo Monte F, Felicetti R, Meda A, Bortolussi A (2019) Assessment of concrete sensitivity to fire spalling: a multi-scale experimental approach. Constr Build Mater 212:476–485

Miah MJ, Lo Monte F, Felicetti R, Carré H, Pimienta P, Borderie CL (2016) Fire spalling behaviour of concrete: role of mechanical loading (uniaxial and biaxial) and cement type. Key Eng Mater 711:549–555

Mindeguia JC, Pimienta P, Noumowé A, Kanema M (2010) Temperature, pore pressure and mass variation of concrete subjected to high temperature – experimental and numerical discussion on spalling risk. Cem Conc Res 40:477–487

Ozawa M, Tanibe T, Kamata R, Uchida Y, Rokugo K, Parajuli SS (2018) Behavior of ring-restrained high-performance concrete under extreme heating and development of screening test. Constr Build Mater 162:215–228

Pistol K, Weise F, Meng B, Diederichs U (2014) Polypropylene fibres and micro cracking in fire ex-posed concrete. Adv Mater Res 897:284–289

Rickard I, Bisby L, Deeny S, Maluk C (2016) Predictive testing for heat induced spalling of concrete tunnels - the influence of mechanical loading. In: Proceedings of the 9th international conference "structures in fire 2016 – SIF'16", Princeton, USA, 8–10 June 2016, pp 217–224

Rossino C, Lo Monte F, Cangiano S, Felicetti R, Gambarova PG (2013) Concrete spalling sensitivity versus microstructure: preliminary results on the effect of polypropylene fibers. In: Proceedings of 3rd international workshop "concrete spalling due to fire exposure", Paris, France, 25–27 September 2013

Rossino C, Lo Monte F, Cangiano S, Felicetti R, Gambarova PG (2015) HPC subjected to high temperature: a study on intrinsic and mechanical damage. Key Eng Mater 629–630:239–244, https://doi.org/10.4028/www.scientific.net/KEM.629-630.239

Sjöström J, Lange D, Jansson R, Boström L (2012) Directional dependence of deflections and damages during fire tests of post-tensioned concrete slabs. In: Proceedings of 7th international conference structures in fire (SIF'12), Zurich, Switzerland, 6–8 June 2012

A Sensor for Embedded Stress Measure of Concrete: Testing and Material Heterogeneity Issues

C. Anerdi, D. Gino, M. Malavisi, and G. Bertagnoli(✉)

Department of Structural, Building and Geotechnical Engineering, Politecnico di Torino, Turin, Italy
gabriele.bertagnoli@polito.it

Abstract. Concrete is well known to be a heterogeneous material that is usually considered homogeneous only referring to a scale of several centimetres. This characteristic makes measuring stresses inside concrete a particularly difficult task. Strains can be measured using several well-known devices. Nevertheless, it is almost impossible to derive a correct estimation of the stress within a concrete structure starting from strain measures as the modulus of elasticity is variable and unknown and creep strains superimpose elastic ones. A preliminary experimental campaign performed to test a stress sensor with the dimensions of a coin to be embedded in concrete is described in the present paper. The effects external applied load are measured comparing the results of short-term loading test performed directly on the sensor and on concrete specimens

Keywords: Concrete · Structural health monitoring · Material heterogeneity · Sensor

1 Introduction: State of the Art

A common technical problem related to the analysis of structures is the monitoring of stresses that are present within the materials.

Measuring the stress within a solid mass is nontrivial and it is usually achieved by measuring deformation parameters on the external surface of the structure, or directly inside it. The stress can then be estimated by knowing of the constitutive law of the material.

This estimation can be simple and reliable for linear elastic materials like steel, whose mechanic characteristics are constant in time and space within the structure.

Elastic parameters of many metals are also known with a great degree of precision and with little statistical scattering.

Much more difficult task is the evaluation of a stress within a structure whose material characteristics are neither uniform in space nor constant over time.

Further difficulties add up if the material is also viscoelastic like concrete, as creep strains are generated under permanent loads and/or stresses are variating in time as a function of creep.

M. di Prisco and M. Menegotto (Eds.): ICD 2018, LNCE 42, pp. 385–399, 2020.
https://doi.org/10.1007/978-3-030-23748-6_30

The most frequently used devices to measure forces or deformations inside concrete structures are: flat jacks, deformeters, and concrete stress meters.

1.1 Flat Jacks

Flat jacks consist on a plane welded metallic reservoir, with two openings for the fluid input and output, which are inflated with oil through a pressurization system. The flat jacks have, typically, a wide and thin shape and are commonly used only for isolated measurements (Gregorczyk and Lourenço 2000).

Flat-jack testing method originates from the field of rock mechanics but, due to his slightly destructive impact, has been considered since the beginning suitable to evaluate the mechanical parameters of the masonry/concrete structures (Binda and Tiraboschi 1999; Fedele and Maier 2007).

Continuous long time measures are possible but quite a complicate hydraulic system has to be installed. They must be inserted in special cavities made within the structure and, once the investigation is completed, they can be removed re-filling the cavity with mortar in order to reduce the damage of the structure. This technique has been widely applied but considered quite invasive. The distance between two referring points above and below the cut is measured before realizing the demolition. The cavity is then cut in the structure causing the referring points to get closer. The jack is inserted. The original stress, orthogonal to the jack faces, is obtained by recording the fluid pressure that is needed to obtain the original distance between the referring points.

This technical solution has many disadvantages:

- Demolition required to obtain the jack housings.
- Dimensions of the jack may be too invasive for a small structure.
- Long human work is needed: installation, measure, installation removal and restoration of damage.
- It is almost non suitable for a continuous monitoring. In fact, since the fluid pressure should also be kept constant over time with extremely low tolerance, the hydraulic connection system is often not compatible with permanent applications.

1.2 Deformeters

The deformeters are devices that measure distance variation between two points constituting the measure base. Such devices can be mechanical (Morice and Base 1953), electromechanical, electrical, inductive and/or magnetic, optical (Ansari 1993; Leite and Corthesy 2001) or laser (Ko and Ni 2005). The measurement base is generally positioned on the external faces of the structure to be monitored and can have a base length between a few millimetres and tens of centimetres.

These devices, according to the realization technology, can measure different parameters: rotation of a gear system, variations in electrical resistance, magnetic field, wavelength of a light source, of electrical capacity of a condenser. All the measures are then brought back to the relative displacement between the two points of the measure base (Neild et al. 2005). The mean strain can therefore be obtained dividing the relative displacement by the length of the base. The stress in the direction of the base length can then be calculated if the constitutive law of the material is known.

These technical solutions have two disadvantages:

- The mechanical characteristics of concrete and mortars, such as the constitutive law, are not constant in space or time and are not generally known with precision a priori.
- Cement conglomerates have a viscoelastic nature that induces a strain increment over time under constant load that can be bigger than two time the elastic one.

1.3 Concrete Stress Meters

A new solution for the measure of stress in concrete structures is a device called "concrete stressmeter" (Carlson and Pirtz 1952). It can be fixed to the reinforcement cage before the casting. This instrument is made of a load cell, in series with a cylinder of concrete. The concrete inside the cylinder should have the same properties of the surrounding one. The lateral surface of the cylinder is de-bonded from the structure by means of a smooth-walled, porous plastic tube. This casing allows the exchange of temperature and humidity along the lateral surface to homogenize the hardening processes between the concrete inside the instrument and outside it, but doesn't allow the transfer of mechanical stresses. The stresses can be transmitted only through the base of the cylinder, where the load cell is placed and through the top of it (Kurata et al. 2009). An example of this product is the Geokon Concrete Stressmeter.

This solution has the following disadvantages:

- It is a voluminous survey system, which therefore needs sufficiently large structures to accommodate it, being applicable only to castings of large dimensions in which the introduction of the device does not generate significant changes in the structural behavior.
- The device should be fixed to the reinforcement cage during the casting phases, and must be placed immediately before the casting and filled with the same material of the casting, thus interfering heavily with the operations of the building site.
- Because of the dimensions of the container, designed to contain the aggregates, the measurement obtained is not punctual information, but an average over the length of 600 mm.

2 A NEW Stress Sensor for Concrete

2.1 Development of a Stress Sensor for Concrete

The first studies for a concrete stress sensor started in October 2015 and led to the patent written by Bertagnoli G. (2016). These studies were then developed and industrialized in collaboration with ST Microelectronics leading to a second patent (Abbasi et al. 2017). The first prototypes of the device were available in spring 2016 when started a testing campaign that is continuing nowadays.

The sensor is a ceramic disc, as shown in Fig. 1, with the dimensions of a coin. Several versions of it have been developed since the spring 2016 as described in the following paragraph.

The aim of this paper is to present the results of a testing campaign and to discuss the possibility of measuring stresses inside concrete, with a small and easy to set up sensor.

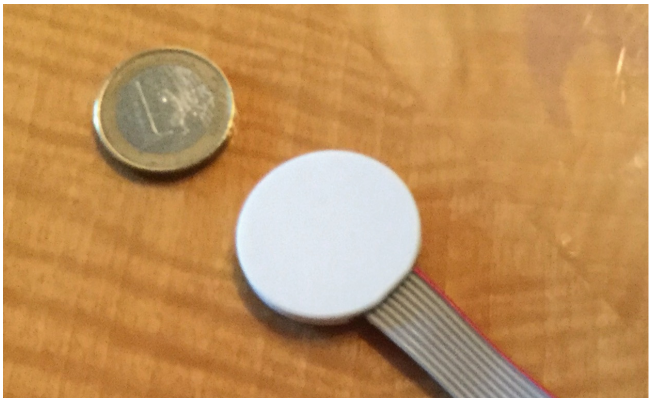

Fig. 1. Ceramic stress sensor

Grounding on the studies done by Bertagnoli G. (2016) and (Abbasi et al. 2017), it is theoretically possible to measure stresses within a continuous homogeneous viscoelastic material by embedding a sensor developed for the purpose.

This work is focused on the evaluation of the uncertainties related to this measure due to:

- the way the stress is applied to the sensor (i.e. boundary conditions);
- the range of the mechanical properties of concrete (Young modulus, Poisson coefficient, cracking, etc.…);
- the heterogeneity of concrete (presence of aggregates and paste, air bubbles, etc.);
- the rheological properties of concrete (creep and shrinkage) and their uncertainty (dependence on w/c ratio, ambient humidity, hydraulic radius);

Several mechanical tests have been carried out, both on the sensor alone and on the sensor embed- ded in concrete specimens.

Long term monitoring has also been performed on concrete specimens to evaluate the effect of shrinkage and creep on the measure of the sensor but will be presented in different document.

3 The Experimental Campaign

3.1 Sensor Versions and Number of Load Tests

Since the beginning of the testing campaign, four different versions of the sensor have been developed by the factory.

Tenths of sensors were tested during the campaign to characterize the production; many of them failed the test because of electrical, mechanical or chemical failures.

At the end, 50 sensors, tested in 189 tests, gave positive results and have been inserted in the database presented in this paper.

The description of sensor version, the number of sensor tested and the number of load test done for each version are given in the Table 1.

3.2 Short Term Load Test Description

The sensor has been tested by applying a compressive stress under different boundary conditions. The type of load test is described in Table 2 (Figs. 2–6).

Table 1. Sensor version.

Version	Tested Spec.	No. of tests	Sensor description
V1.0	11	70	Round 30 mm diameter
V1.1	18	49	Round 30 mm diameter
V1.3	6	19	Round 25 mm diameter
V1.4	15	51	Candy 25 mm diameter

Table 2. Load test boundary conditions.

Test	Description
Steel	The sensor is loaded by direct contact with the steel plates of the bench press
Kapton	A layer of 0.10 mm of Kapton is interposed between sensor and the steel plates of the bench press
RUB	The sensor is loaded interposing two discs of rubber of 2 mm thickness between the bench press and the sensor faces
HYD	The sensor is loaded inside a hydrostatic chamber filled with oil and loaded by a bench press
CUBE	The sensor is placed in the midpoint of a concrete cube 15 × 15 × 15 cm side with sensor faces parallel to cube faces
Φ15 × 30	The sensor is placed in the midpoint of a concrete cylinder with diameter of 15 cm and height of 30 cm with sensor faces parallel to the circular faces of the cylinder
10 × 10 × 40	The sensor is placed in the midpoint of a concrete prism with squared base of 10 × 10 cm and depth of 40 cm with sensor faces parallel to the squared faces of the prism
15 × 15 × 60	The sensor is placed in the midpoint of a concrete prism with squared base of 15 × 15 cm and length of 60 cm with sensor faces parallel to the squared faces of the prism
16 × 16 × 64	Like 15 × 15 × 60 but with slightly bigger dimensions

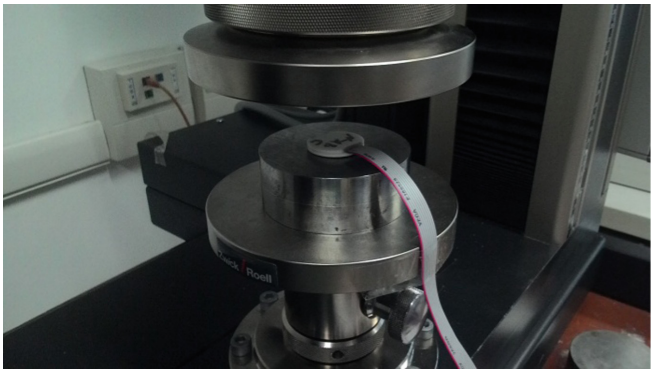

Fig. 2. Load test "Steel" with direct contact between sensor and bench press

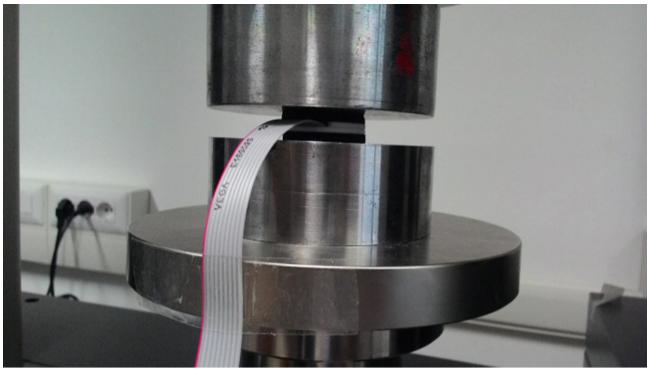

Fig. 3. Load test "RUB" with 2 mm rubber discs between sensor and bench press

Fig. 4. Hydrostatic load cell for "HYD" test

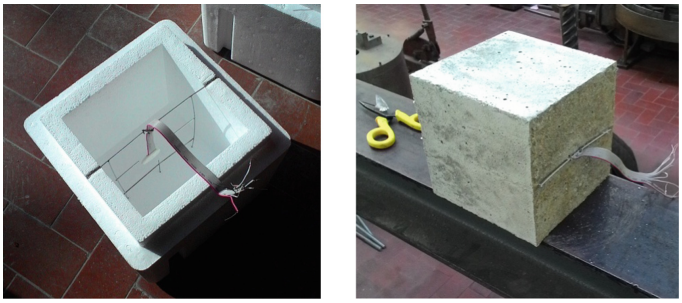

Fig. 5. Typical specimen for load test "CUBE"

Fig. 6. Test on 16 × 16 × 64 cm column

3.3 Long Term Test Description

Long term tests are aimed at measuring the effect of creep and shrinkage on sensor response.

Two kinds of test have been performed: 30 specimens have been measured periodically over a period of 450 days without any load applied, to assess the effect of

shrinkage and the reliability of the instruments; two specimens have been loaded with constant load for 300 days and measured periodically to assess creep effect. The results of this campaign will be presented in another paper.

3.4 Concrete Batches

Eight concrete batches have been realized between May 2016 and November 2017; mean cubic concrete strength of each batch was variable between 22 and 45 MPa.

Table 3. Concrete batches.

Batch	R_{cm} [MPa]	Sensor ID	STT [Y/N]	LTT [Y/N]	Specim.
04/05/16	22	610-13	Y	Y	CUBE
		610-16	Y	Y	CUBE
20/05/16	29	610-15	Y	Y	CUBE
		610-18	Y	Y	CUBE
03/06/16	28	620-12	Y	Y	CUBE
		620-14	N	Y	CUBE
08/11/16	38	630-09	Y	Y	$\phi 15 \times 30$
		630-11	Y	Y	$10 \times 10 \times 40$
		630-25	Y	Y	CUBE
		630-26	Y	Y	$10 \times 10 \times 40$
24/11/16	36	646-02	N	Y	$\phi 15 \times 30$
		646-12	Y	Y	CUBE
		646-13	N	Y	CUBE
		646-14	N	Y	CUBE
		646-15	Y	Y	$16 \times 16 \times 64$
		646-18	N	Y	CUBE
		646-24	N	Y	CUBE
		646-28	N	Y	$\phi 15 \times 30$
		646-30	Y	Y	$16 \times 16 \times 64$
		646-33	Y	Y	CUBE
		646-A01	Y	Y	CUBE
		646-A04	Y	Y	CUBE
		646-A15	Y	Y	CUBE
06/12/16	45	630-01	Y	Y	$10 \times 10 \times 40$
		630-02	Y	Y	$10 \times 10 \times 40$
		646-A17	Y	Y	$16 \times 16 \times 64$
		646-A19	Y	Y	$16 \times 16 \times 64$
		646-A48	Y	Y	CUBE
28/04/17	34	706-09	Y	Y	$16 \times 16 \times 64$
		706-10	Y	Y	$16 \times 16 \times 64$
		706-27	Y	Y	$16 \times 16 \times 64$
		706-33	Y	Y	$16 \times 16 \times 64$
10/11/17	40	706-158	Y	N	$15 \times 15 \times 60$
8		33	26	32	TOT.

Thirty-three sensors have been embedded inside concrete specimens: 26 of them have been tested in Short Term Tests (STT) and 32 in Long Term Tests (LTT). Details are shown in Table 3.

4 Results of Short Term Tests

4.1 Steel, Kapton and Rubber Tests

The first tests were carried out on small size bench presses by applying the load through direct contact between steel clamps and sensors surfaces.

These tests were almost unsuccessful due to the high number of sensors that broke during the test. The main reason of the failures was the impossibility to ensure a regular contact between sensors and clamp surfaces. The sensors are made of a ceramic material, which is stronger and stiffer than ordinary steel, perfectly elastic until failure, but brittle. Both the bench press clamps and the sensors surfaces are plain, parallel and smooth with a tolerance of about 0.05 mm (on the sensor diameter). This tolerance can generate high contact stresses and therefore break the sensor.

A second bias of these tests is the difficulty in controlling perfect bond between sensor and press surfaces. The clamp is much bigger than the sensor itself (see Fig. 2) therefore is subjected to a non-uniform state of stress that leads to a radial deformation, which is different from the sensor's one. Moreover, Poisson coefficient of steel is different from ceramic one (0.30 for steel 0.22 for ceramic).

Such conditions generate friction stresses that should be transmitted between steel and ceramic in addition to normal ones. Such tangential stresses can generate confinement or stretching inside the sensor's body. Finite element simulations confirmed confinement stresses for the tested geometries.

The friction coefficient between steel clamps and ceramic is very small, between 0.05 and 0.2 (Shibata et al. 2014) being both surfaces very smooth.

Such low friction may not be sufficient to ensure perfect bond during the test, therefore slip may occur between sensor and clamp, generating hysteresis in the test output and invalidating it.

The first attempt to overcome the non-uniform contact between steel and ceramic was the introduction of two 0.05 mm Kapton films (0.1 mm total thickness above and below) between the steel clamps and the sensor. This solution granted a better vertical contact but the problem of radial slip and therefore, presence of hysteresis in the test, was still present. A great number of Kapton test presenting big hysteresis has therefore been disregarded.

The friction coefficient between steel and Kapton is not provided by the producer in material datasheet but it is estimated to be around 0.50 according to literature (Samyn et al. 2005).

Better results have been obtained by the interposition of a 1.50 mm sheet of rubber between sensor and clamps. Sensor response remained linear and the hysteretic behaviour disappeared. Almost all tests done with rubber provided an output that could be analysed.

Four sensors (610-01, 610-03, 610-04, 620-13) have been tested under Steel, Kapton and Rubber conditions, all belonging to the 1.0 version. The sensitivities of the sensors measured in μV/(V·MPa) are shown in Table 4.

Table 4. Steel, Capton and Rubber tests output.

Sensor	610-01	610-03	610-04	620-13
Steel*	−95.4	−81.2	−99.5	
		−93.4		
		−87.1		
Steel**		−122.6		−126.9
Kapton	−104*	−133*	−129**	
	−131**	−130*		
		−146**		
Rubber	−162	−161	−157	−122
				−128
				−145

* *1st bench press*
** *2nd bench press*

The average sensitivity obtained with the first bench press is −91 with a c.o.v. of 5.5%. A mean sensitivity of −125 resulted from changing of bench press and clamps. These outcomes demonstrates the difficulty in achieving stable predictable results using direct contact with steel.

The results of the tests done with Kapton film are more homogeneous but the difference between using the 1st and the 2nd bench press is still clear.

Kapton tests provide a higher sensitivity than Steel ones. In fact, the effect of confinement, due to steel clamps, is probably smaller than in case of direct contact with steel. Average sensitivity obtained with Kapton is −123 with a c.o.v. of 10% (1st and 2nd test machine together).

Rubber tests resulted to be the most reliable, giving a stable output. Average sensitivity obtained with RUB is −150 with a c.o.v. of 11% (1st and 2nd test machine together).

The authors consider the sensitivity obtained in RUB test to be very close to the one corresponding to nil lateral restraint and pure uniaxial behaviour as the thickness of the rubber layer is similar to the thickness of the sensor, and the Young modulus of rubber is 3 orders of magnitude smaller than the one of the sensor.

RUB test has then been chosen to characterize the production and will be taken as comparison for tests within concrete in the following paragraphs.

4.2 Concrete Cubes and Cylinders Φ15 × 30 cm

Cubic 15 cm side specimens has been the first choice to test sensors inside concrete due to the high availability of moulds and to the small dimensions of the specimens.

This choice resulted not to be wise in terms of load test results, as the cubic specimens were too short and the sensors too close to the steel clamps of the press.

Therefore it suffers from being inside a discontinuity zone. Non uniform contact between cube side and steel clamp, confinement provided by steel clamps, generate within the cube a stress field whose lines are not parallel and therefore a very high scattering in the response of the sensors.

A total of 67 tests have been done on 11 sensors: the number of tested sensors, their version, and the number of tests per each sensor are resumed in Table 5. The mean sensitivities in μV/(V·MPa) and the coefficient of variation of the distribution is also presented in Table 5.

Table 5. Cube tests.

Version	1.0	1.1	1.3	1.4
Sensors	5	1	2	3
Tests	17 + 4 + 12	3	3 + 1	6 + 3 + 3
	+12 + 4			
Mean sens.	−79	−45	−20	−20
c.o.v.	26%	19%	20%	21%

Three sensors of series 1.0 were tested (17, 12 and 12 times) at different times from casting and have shown a common behaviour. The sensitivity increases after casting, reaches a peak value between 40 and 60 days from casting and then comes back to values comparable to the initial ones. This phenomenon is evidenced in Fig. 7.

The same behaviour shown in Fig. 7 for CUBE tests has been seen in other tests on column specimens and presented in the following paragraphs.

Sensor 630-09 (belonging to version 1.1) has been cast inside a concrete cylinder Φ15 × 30 cm and tested three times obtaining sensitivities of −69.3, −74.7, −91.2 μV/(V·MPa) respectively at 22, 22 and 154 days from casting.

Because of the high dispersion of the CUBE results and the lack of sensitivity respect to rubber tests, CUBE and Φ15 × 30 cm test setups have been abandoned preferring to test specimens with higher slenderness ratios, which will be presented in the following paragraphs.

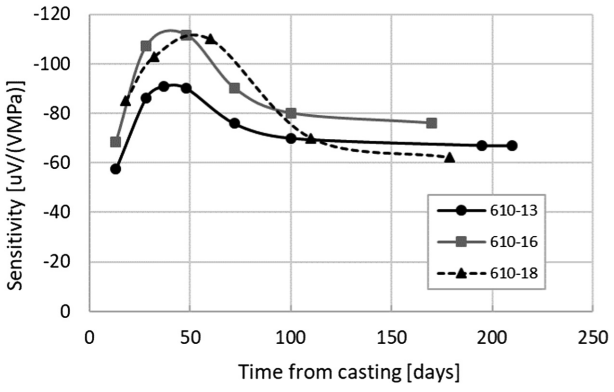

Fig. 7. Sensitivity variation during hardening.

4.3 10 × 10 × 40 cm Columns

Four sensors (630-01, 630-02, 630-11, 630-26) have been tested firstly directly in the bench press by means of a RUB test and then have been placed into 10 × 10 × 40 cm columns. They all belong to the version 1.1.

All sensors were alimented at 10 V and loaded up to 10 MPa both when tested RUB and inside concrete. The tests on the columns have been done at different concrete ages (expressed in days) and showed the sensitivities expressed in μV/(V·MPa) in Table 6.

Table 6. 10 × 10 × 40 cm columns tests output.

Test	630-01	630-02	Test	630-11	630-26
R_{cm}	45	45		38	38
RUB	−122	−123	RUB	−118	−115
125d	−130	−113	22d	−81	−112
125d	−128	−108	22d	−90	nt*
420d	−110	−94	150d	−110	−123
420d	−111	−94	448d	−95	−104
			448d	−96	−105
			448d	nt*	−105

* *not tested*

Each sensor showed linear output with increasing load, nil hysteresis and good repeatability. Different sensitivity has been seen between sensors and at different concrete ages for each sensor. The average sensitivity measured in RUB tests is −119 with 3.5 μV/(V·MPa) standard deviation, whereas in concrete the same values are respectively −106 and 10.8 μV/(V·MPa).

It can be concluded that 2.9% c.o.v. has been found in RUB tests, whereas 18.5% is found inside concrete as it could be logically expected; moreover sensitivity inside concrete is about 11% lower than in RUB test.

4.4 Results of 16 × 16 × 64 cm Columns

Eight sensors (646-15, 646-30, 646-A17, 646-A19, 706-09, 706-10, 706-27, 706-33) have been tested inside 16 × 16 × 64 cm columns and some of them were firstly tested directly in the bench press by means of a RUB test. They belong to the 1.3 and 1.4 version. The concrete used for Sensors 630-01 and 02 was R_{cm} = 45 MPa, whereas the one used for sensors 630-11 and 26 was R_{cm} = 38 MPa.

All sensors were alimented at 10 V and loaded up to 10 MPa both when tested RUB and inside concrete. The tests on the columns have been done at several different concrete ages (expressed in days) and showed the sensitivities expressed in μV/(V·MPa) in Table 7.

Each sensor showed linear output with increasing load, nil hysteresis and good repeatability. At different concrete ages each sensor showed different sensitivity.

The average sensitivity measured in RUB tests was −102 with 6.3 μV/(V·MPa) standard deviation, whereas in concrete the same values were respectively −98 and 18.1 μV/(V·MPa).

Table 7. 16 × 16 × 64 cm columns tests output.

Test	646-15	646-30	Test	646-A17	646-A19
R_{cm}	36	36		45	45
RUB	nt*	nt*	RUB	−101	−95
130d	−125	−101	118d	−88	−103
130d	−128	−93	118d	−94	−105
173d	nt*	−95	118d	−94	nt*
433d	−134	−92	160d	−98	nt*
433d	−119	−89	421d	−74	−102
			421d	−74	−103
Test	706-09	706-33	Test	706-10	706-27
R_{cm}	34	34		34	34
RUB	−106	nt*	RUB	−110	−97
13d	−125	−101	133d	−109	−80
13d	−77	−66	133d	−111	−81

* *not tested*

Only one sensor was tested in a 15 × 15 × 60 cm column (706-158). Concrete strength was R_{cm} = 40 MPa and the tests were done at a concrete age of 81 days showing respectively −102, −102 and −100 μV/(V·MPa) sensitivity. Considering sensor family, 706, and column dimension, this test can be grouped with 16 × 16 × 64 ones.

It can be concluded that 6.2% c.o.v. has been found in RUB tests, whereas 16.4% is found inside concrete as it could be logically expected; moreover sensitivity inside concrete (−98.2) is about 3.7% lower than in RUB test (−102).

4.5 Results of Hydrostatic Tests

Since the beginning of the experimental campaign, the necessity of testing the sensors in an environment where the interfaces used to apply the load were irrelevant with respect to the response was clear to the authors. Therefore, the testing equipment, called Hydrostatic chamber, was designed and developed for the purpose.

Because of the design, realization and testing phase, this equipment became available only at the end of the research period described in this paper.

Four sensors (646-19, 706-86, 706-105, 706-111) have been tested in hydrostatic conditions, twice each, for a total of 8 tests. Series 646 sensor belongs to the version 1.3 whereas 706 belong to the version 1.4.

The sensors were alimented at 10 V, loaded up to 10 MPa. All of them showed the sensitivities expressed in μV/(V·MPa) in Table 8.

Table 8. Hydrostatic tests output.

646-19	706-86	706-105	706-111
−89.3	−95.7	−81.8	−84.4
−89.1	−95.5	−81.8	−84.9

Each sensor showed linear output with increasing load, nil hysteresis and excellent repeatability, but different sensitivity has been noticed between sensors. Average sensitivity of −87.8 μV/(V·MPa) with 6.9% c.o.v. has been measured.

Hydrostatic tests equipment was able to generate stable and repeatable output in the sensors that nevertheless were suffering from quite high production scattering.

The average sensitivity measured in Hydrostatic conditions can be compared to the one obtained in paragraph 4.4 as the sensor series are the same: −98.2 with 16.4% c.o.v. in concrete columns, against −87.8 with 6.9% c.o.v. in oil. This result confirms that, apart from the big scattering, the sensor is able to read the same pressure both if it is applied in hydrostatic conditions inside a fluid and inside a solid, heterogeneous material like concrete.

5 Conclusions

The first part of an experimental campaign dedicated to testing a new stress sensor to be embedded in concrete is presented in this paper.

The sensor is a small ceramic device, with the dimension of a coin, which is designed to be inserted in concrete structures before casting and should provide long term monitoring of stresses. The sensor should be completely passive (without moving parts or fluids inside) and low energy consuming.

According to the designers' intentions, the sensor should provide a measure of the stress (force) applied to its round surfaces regardless of the boundary conditions, i.e. lateral confinement.

Such device should be able to measure pressure both when submerged in a liquid, when it is directly loaded by a machine on its surfaces and when it lies within the stress field inside a concrete structure.

All these conditions have been tested and the results are presented.

The device proved to be able to satisfy the design requests, fair accordance between different loading conditions has been found.

Some testing solutions, like direct steel contact, Kapton contact and cubic concrete specimens have been abandoned as they were ineffective to test the device. Hydrostatic loading equipment demonstrated excellent performance in terms of accuracy and repeatability.

High scattering due to production problems (the device is still a prototype) have been found. Even higher scattering, due to concrete heterogeneity, has been measured.

Long term tests to measure the response of the sensor to rheological properties of concrete are now necessary to complete the study and will be presented in a new paper.

Acknowledgements. The authors would like to acknowledge Safecertifiedstructures Technology s.r.l, STMicroelectronics s.r.l. and Microtel s.r.l. for the collaboration and support during testing.

References

Abbasi M, Bertagnoli G, Caltabiano D, Guidetti E (inventors) ST Microelectronics s.r.l. (Assegnee) Sensore di sforzo per monitoraggio dello stato di salute di strutture fabbricate quali costruzioni, edifici, infrastrutture e simili. Italy Patent Request 102017000044301 20-04-2017

Ansari F (1993) Applications of fiber optic sensors in engineering mechanics. ASCE, Reston, Va

Bertagnoli G (inventor) Safecertifiedstructures Technology s.r.l. (Assegnee), Metodo e dispositivo di indagineper la misurazione di tensioni in una struttura di agglomerate. Italy Patent Request 102016000037314, 12-04-2016

Binda L, Tiraboschi C (1999) Flat-jack test as a slightly destructive technique for the diagnosis of brick and stone masonry structures. Int J Restor Build Monum (Int. Zeitschrift fur Bauinstandsetzen und Baudenkmalpflege) 31:449–472

Carlson RW, Pirtz D (1952) Development of a device for the direct measurement of compressive stress. J Am Concr Inst 49(11):201–215

Fedele R, Maier G (2007) Flat-jack tests and inverse analysis for the identification of stress states and elastic properties in concrete dams. Meccanica 5:387–402

Gregorczyk P, Lourenço PB (2000) A review on flat-jack testing. Engenharia Civil UM 9:39–50

Ko JM, Ni YQ (2005) Technology developments in structural health monitoring of large-scale bridges. Eng Struct 27:1715–1725

Kurata Y, Shionaga R, Takase K, Shimomura T (2009) Study on measurement of concrete stress in structural members by effective stress meter. Creep, Shrinkage Durab Mech Concr Concr 1:293–297

Leite MH, Corthésy R (2001) Stress measurement in concrete structures with modified doorstopper technique. ACI Struct J 29(5):619–628

Morice PB, Base G (1953) The design and use of a demountable mechanical strain gauge for concrete structures. Mag Concr Res 5–13:37–42

Neild SA, Williams MS, McFadden D (2005) Development of a vibrating wire strain gauge for measuring small strains in concrete beams. Strain 41:3–9

Samyn P, Quintelier J, Schoukens G, De Baets P (2005) Sliding properties of polyimide against various steel and DLC-coated counterfaces. In Ivkovic B (ed.), Proceedings of BALKANTRIB 05, pp 506–515

Shibata K, Yamaguchi T, Hokkirigawa K (2014) Tribological behaviour of RH ceramics made from rice husk sliding against stainless steel, alumina, silicon carbide, and silicon nitride. Tribol Int 73:187–194

Slab STRESS – Seismic Testing of a R/C Flat Slab Structure

D. Coronelli(✉) and P. Bamonte

Department of Civil and Environmental Engineering,
Politecnico di Milano, Milan, Italy
dario.coronelli@polimi.it

Abstract. A research entitled Slab STRESS - Slab STructuralRESponse for European Seismic Design, within the European project SERA - H2020-INFRAIA-2016-1, is currently in progress to study the response of flat slab floors under combined gravity and lateral loads. The project is being carried out by a group of European institutions, led by the Politecnico di Milano together with EPFL Lausanne, UNOVA Lisbon and UTCB Bucharest. A real scale flat slab building will be tested at the JRC ELSA reaction wall facility in Ispra (IT). The Seismic European Code ENV 1998 for does not cover flat slab buildings, that are intensively used because of the reduction in construction costs and time, the simplicity of the geometry and possibility to increase available volumes. The paper describes the research objectives, the specimen and features of the testing program.

Keywords: Flat slabs · Seismic response · Testing · Punching

1 Introduction

The Seismic European Code for reinforced concrete buildings does not cover flat slabs, that have been and are intensively used because of the cutting of construction costs and time, the simplicity of the geometry and increased available architectural space.

Code and research developments have been proposed in the European seismic research community (Spence et al. 2007; Pinto et al. 2007). On the basis of Eurocode 8, flat slabs cannot be considered to contribute to the primary seismic resistant system and can be designed as secondary systems supporting gravity loads at the design deformations, due to their compatibility with the primary system (Fardis 2009). Particular care is needed for the punching shear capacity of slab-column connections (Coronelli 2010; Drakatos et al. 2017).

Limited knowledge about the stiffness and non-linear deformations of flat slabs leads to difficulties in design of these systems; in the structural analysis process very high internal forces and moments are calculated, different from the behaviour shown in tests. As a consequence the reinforcement design becomes complicated and uneconomical (Coronelli and Martinelli 2017).

In the program entitled "Slab STRESS" (Slab STructural RESponse for Seismic design in Europe), flat slab floors in a real scale flat slab building will be tested for seismic and cyclic loading at the reaction wall facility of the JRC – ELSA. The research is developed within the European project SERA - H2020-INFRAIA-2016-1, carried

M. di Prisco and M. Menegotto (Eds.): ICD 2018, LNCE 42, pp. 400–409, 2020.
https://doi.org/10.1007/978-3-030-23748-6_31

out by a group of European institutions, led by the Politecnico di Milano together with EPFL Lausanne, UNOVA Lisbon and UTCB Bucharest.

Pseudodynamic testing (Pinto et al. 2004) will be carried out for the seismic loading using nonlinear substructuring to model the primary seismic resistant walls.

The testing of floors will complement and complete the knowledge of previous experiments carried out on isolated slab-column connections, giving information about the stiffness and deformation capacity of these structural systems.

The results will provide the basis for a design procedure based on deformation capacity assessment. Defining the conditions for the flat slab system supporting the gravity loads in correspondence to the design deformation demand, will result in a design proposal for the European seismic code EC8.

2 Test Concept and Design

The research focuses on flat slabs designed as secondary systems with primary energy dissipating system. The chosen primary system are ductile reinforced concrete walls. As the research is focused on flat slab behaviour, taking advantage of the pseudodynamic testing technique (Pinto et al. 2004), the primary part is not in the physical system during the test but is modelled numerically (Fig. 1).

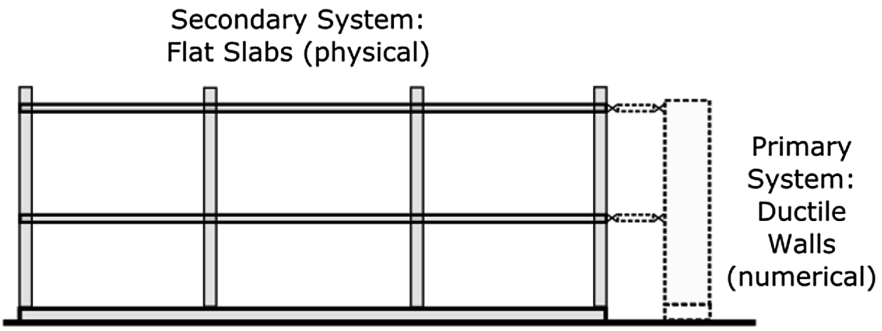

Fig. 1. Test concept.

The approach of ENV 1998 for primary seismic resistant and secondary parts of the structure has been used. The structure has been designed considering the primary dissipative effect of ductile shear walls. Flat slabs bear gravity loads at the seismic lateral ultimate displacement without being part of the seismic resistant ductile system; ENV 1992 is used for their design. The design follows these steps:

(a) The stiffness of the walls is chosen greater than 85% of the total stiffness. The walls are designed for the internal forces obtained with the behaviour factor $q = 4$ for this type of structure, considering the stiffness reduction due to cracking and neglecting the secondary system lateral stiffness contribution. Also displacements of the structure are obtained from this analysis.

(b) The ultimate drift (DR_u) displacements are obtained multiplying by q the displacements of point (a).

(c) The flat slabs are designed taking into consideration test results on slab-column connections (Fig. 2a) for the ultimate drift DR_u in relation to the gravity shear ratio between the shear effect of the gravity load V_g (self weight and added gravity loads) and the punching capacity of the slab V_o (ACI ASCE Committee 421 2007). On the basis of a design formulation proposed by ACI318 (Fig. 2b), if the gravity shear ratio between the shear effect V_u of the seismic combination and the punching capacity of the slab V_o is limited to 0.4, the ultimate drift capacity will be greater than 1.5%. Hence the capacity to bear the gravitational load effects up to the ultimate design drift is guaranteed imposing $V_u/V_o < 0.4$, if the ultimate drift based on the displacements of point (b) is smaller than 1.5% (Fig. 2b).

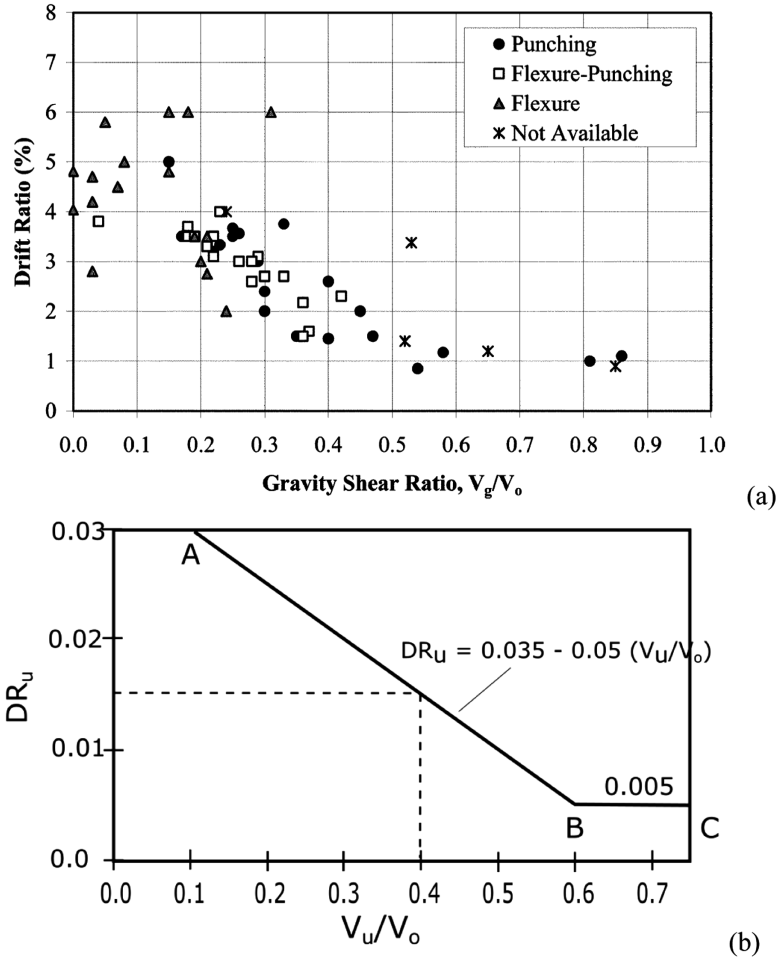

Fig. 2. Ultimate drift capacity (ACI ASCE Committee 421 2007): (a) test results; (b) ACI318 equation.

(d) The slab longitudinal reinforcement design is carried out considering the seismic combination effects, imposing the drift related to displacements obtained at point (a).
(e) The punching shear verifications are carried out with provisions of ENV1992 for eccentric shear (considering $e = M_{Ed}/V_{Ed}$).

The formulation proposed by ACI318 is used,; the outcomes of the test results hopefully will provide a basis of a formulation for the European code.

3 Specimen Description

Taking advantage of the JRC ELSA Reaction wall facility, a flat slab structural system will be tested. On the basis of the test concept explained in the Sect. 2.

The structure is made of two flat slab floors supported on R/C columns. Each floor has 3 bays in the longitudinal direction and two bays in the transverse direction, and the spans are 5 m and 4.5 m (Fig. 3).

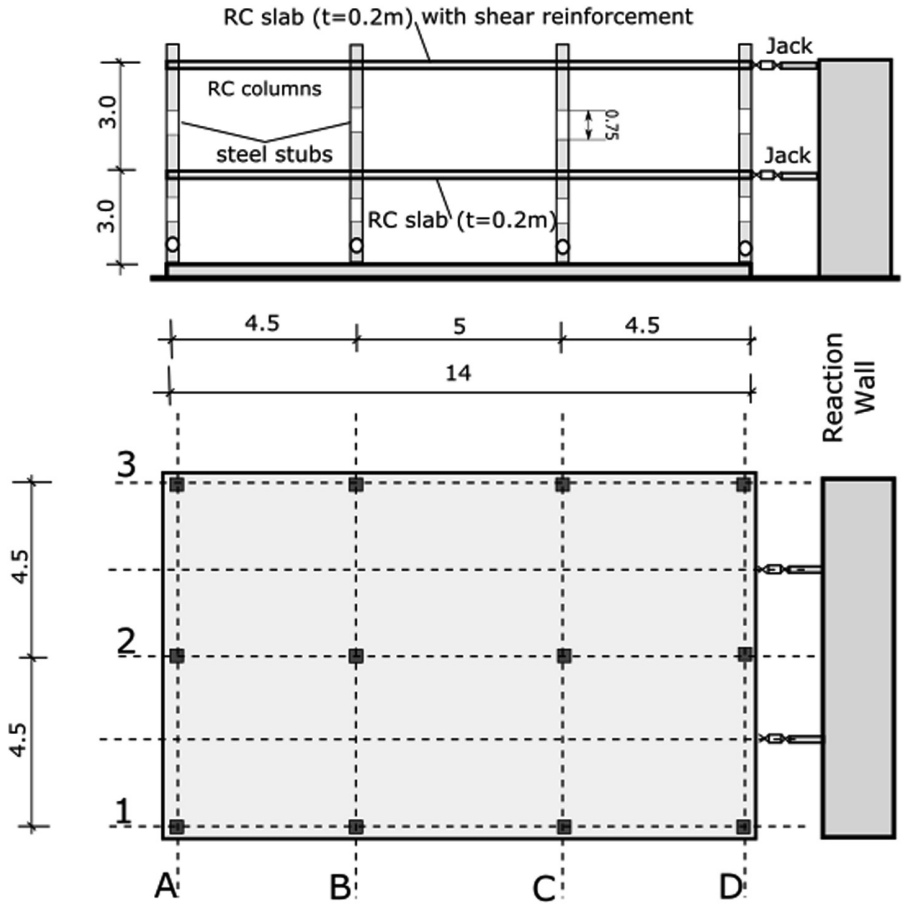

Fig. 3. Specimen dimensions.

The specimen will be built outside the laboratory, and then moved inside in the testing position. A limitation on the transverse spans was imposed by the size of the laboratory doors. Nevertheless the size achieved is that of a real scale building, with span to depth ratios along the orthogonal sides equal to 22.5 and 25.

The floor is made of a reinforced concrete slab without voids, with thickness 20 cm. This dimension in most tests for the seismic response of flat slab floors and column-slab connections was smaller than this, with typical dimensions between 10 cm and 15 cm.

The column height is 3 m from the top of the foundation or floor, to the top of the floor above. The columns have a central steel portion for the measurement of internal forces (Fig. 3, see Sect. 4). According to the definition of a secondary system, the columns are not designed to develop inelastic deformations in the response for seismic loading.

The mass for each slab floor is 63 tons without added gravity loads and 108 tons with added loads. The design was based on uniform distributed load of 3 KN/m^2 for non-structural gravity loads and 2 KN/m^2 for the live loads.

The foundations consist of a reinforced concrete beam grid, providing a fixed base to the specimen and designed to enable moving the specimen inside/outside the lab.

The materials are normal strength concrete C30/37 and steel S450 Class C.

4 Loading Phases and Structural Scheme

The loading program comprises two types of loading, and related to this different constraints at the base of the building.

The first test A is for seismic loading and the base of the columns is a fixed constraint; the flat slab system is connected to the primary walls, modeled numerically (Pinto et al. 2004), limiting the drift to a design value.

The second phase B is cyclic loading of the flat slab frame to failure. The floors will be tested for gravity and lateral cyclic loading of increasing amplitude to near-failure conditions at high drifts.

(A) Seismic loading

Seismic loading will be simulated using the pseudo-dynamic technique with non-linear substructuring (Pinto et al. 2004) for two levels of seismic motion (service Test A.1 and ultimate state Test A.2). Gravity loading will be self-weight and supplementary weight supported on the slabs equivalent to 3.6 KN/m^2 ($3 + 2 \times 0.3 = 3.6$ KN/m^2).

(B) Cyclic loading

The floors will be then tested for gravity and lateral cyclic loading of increasing amplitude to near-failure conditions.

The reinforcement designed for the test A building configuration at the base of the columns will yield forming a plastic hinge at the base with limited moment (see Fig. 3b), reducing the moments in the columns in correspondence of high drifts. Currently also the possibility of modifying the constraints at the base is at study.

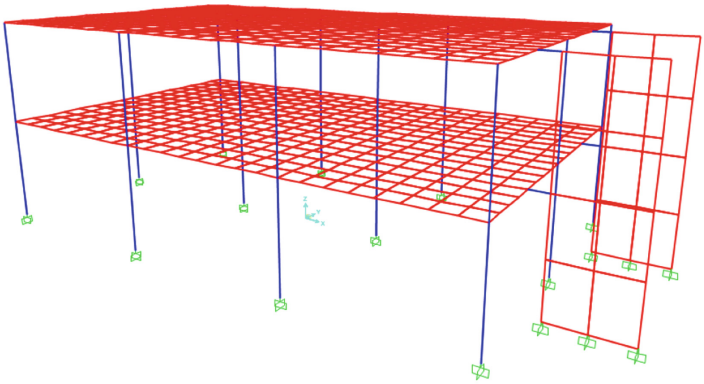

(a) Structural scheme for seismic loading

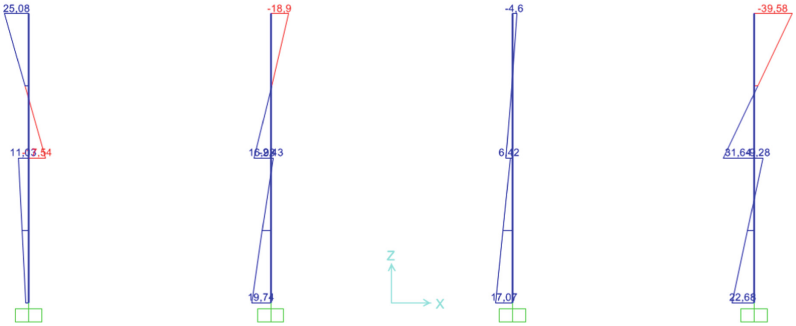

(b) Moments (KNm) for gravity and equivalent static lateral load (maximum value 39.6 KNm)

Fig. 4. Scheme for seismic loading Test A

The loading scheme is based on imposing the same interstorey drift at both floors. A numerical model is shown in Fig. 4, assuming a hinge at the base.

Upper bounds are 1000 KN for the maximum lateral force for each floor and approximately 20 cm maximum stroke maximum values (3% drift).

Lateral actions will be imposed by displacement controlled jacks connected to reinforcement bars anchored within the slab, along the centerline between lateral and interior frames.

Cyclic loading will be carried out to failure with damage progressively spreading and redistribution of internal forces from the first connections reaching ultimate conditions to the less damaged parts of the system, to develop the whole nonlinear response of the floor (Fig. 5).

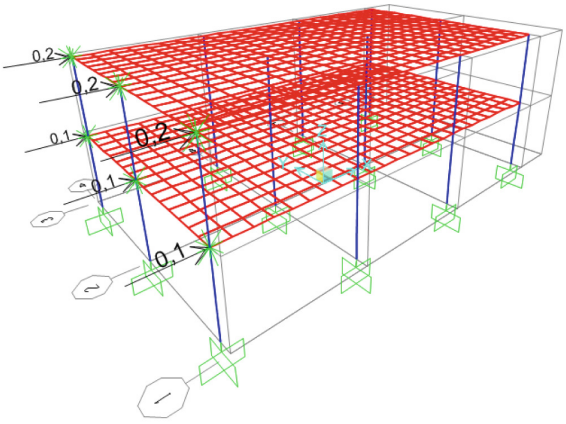

(a) Building and maximum Imposed drifts (m)

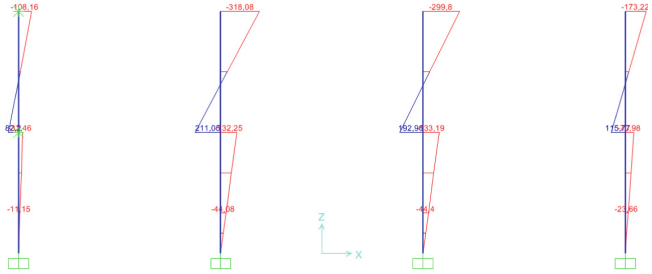

(b) Moments (KNm) at maximum drifts (max. 318 KNm)

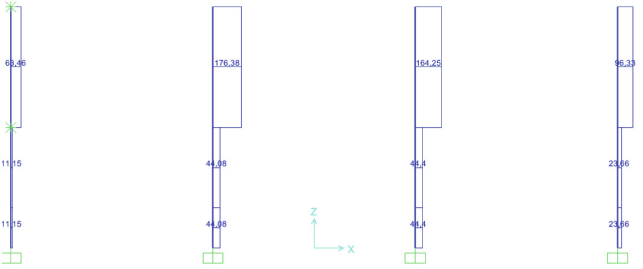

(c) Shear forces (KN) at maximum drift (max. 176 KN).

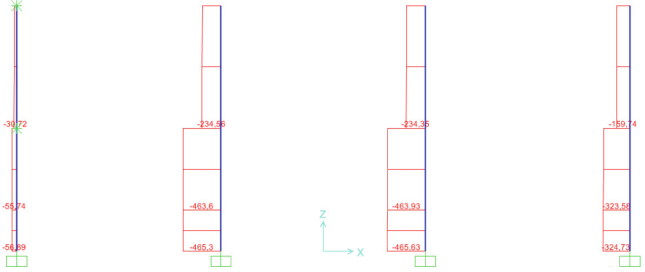

(d) Axial force (KN) at maximum drifts (max. 465 KN).

Fig. 5. Scheme for cyclic loading Test B

5 Measurements

The global building response is measured by the ultimate lateral drift capacity of the floors using displacement transducers. Storey forces will be measured by the jacks load cells providing floor shears.

The connection behavior will be studied measuring the moment-rotation diagrams. Column and slab rotation will be measured by inclinometers on the columns and transducers measuring slab-column relative displacements. The moment must be determined by column internal forces. To this purpose steel stubs will be inserted in the central part of the columns (Fig. 3) with strain gages glued in order to measure moment, axial force and shear.

The possibility to report the cracking above and below the slab using photogrammetry is currently at study.

6 Objectives and Expected Outcome

The research has two main aims: (1) studying the seismic response of a flat slab building validating the design approach presented in section and (2) testing the ultimate drift capacity and punching behaviour of slab column-connections in the floors for alternate actions.

The first aim is the focus of the seismic Test A. The response of the structure will validate the design procedure outlined in Sect. 2. Theoretical analyses following this approach show that the first floor slab can be designed without transverse reinforcement; different approaches imposing the displacement level reached for the ULS design action within the elastic structural analysis result in high internal forces requiring heavier longitudinal reinforcement and transverse reinforcement in the slabs.

The possibility to use the proposed design approach has been explored by Coronelli and Martinelli (2017) in the analysis of real building configurations with wall primary systems.

The prediction of the expected response is currently being tackled following the grid model approach formulated by Coronelli (2010) and applied to slab floors under gravity and lateral actions by Coronelli and Corti (2014).

The real scale of the structure testing is important because no study considered such thickness of the slab within a whole building structure. Moreover the pseudo-dynamic technique will test the effective seismic response of a system with primary and secondary parts. The aim is to show that the secondary flat slabs can follow the displacements of the primary system with limited damage, hence maintaining the structural performance needed for the gravity loads.

The second aim will be investigated in Test B. Studies on the cyclic response of slab-column connections have been carried out mainly on isolated connections, without the boundary conditions of a real floor. Moreover the size-effect can be studied using a real-size slab. Cyclic loading was used by groups in the research team to test individual connections (Almeida et al. 2016; Coronelli et al. 2015; Drakatos et al. 2016). This type of loading is hence selected for the floors in the final tests, in order to compare the connection behaviour for two different types of tests (isolated slab-column connection and complete floor system).

7 Conclusions

Flat slab structures are widely used, although their design is not covered by the European code for reinforced concrete design in seismic zones. The paper has described the preparation of a research program, currently in progress, with the objective to provide the basis for this needed development of the codes.

The main aims of the research are to investigate (1) the seismic design of these structures as secondary parts with ductile primary seismic resistant walls; (2) the response up to punching failure for high lateral drift of the flat slab-column system.

The tests have been designed and will be carried out collaborating with the JRC at Ispra laboratory research team, taking advantage of the reaction wall in the ELSA lab and the pseudodynamic testing technique.

The results will provide the basis for a design procedure based on deformation capacity assessment. Some indications proposed by ACI318 have been adapted to design the specimen; the outcomes of the test results in the Slab STRESS program hopefully will provide a basis of a formulation for the European code.

Defining the conditions for the flat slab system supporting the gravity loads in correspondence to the design deformation demand, will result in a design proposal for the European seismic code EC8.

Acknowledgements. The paper describes the preparation of the program entitled "Slab STRESS" (Slab STructural RESponse for Seismic design in Europe). The research is developed within the European project SERA - H2020-INFRAIA-2016-1, carried out by a group of European institutions, led by the Politecnico di Milano (lead user D. Coronelli) together with EPFL Lausanne (Prof. A. Muttoni), UNOVA Lisbon (Prof. A.M. Ramos) and UTCB Bucharest (Prof. R. Pascu) in collaboration with the JRC – ELSA laboratory in Ispra (IT).

The Authors wish to acknowledge the collaboration of Prof. L. Martinelli and Dr. F. Foti (DICA, Politecnico di Milano) in the program.

References

ACI-ASCE Committee 421 (2015) ACI 421.3R-15 guide to design of reinforced two-way slab systems. Reported by Joint ACI-ASCE Committee 421

Almeida A, Inàcio M, Lúcio V, Pinho Ramos A (2016) Punching behaviour of RC flat slabs under reversed horizontal cyclic loading. Eng Struct 117:204–219

Coronelli D (2010) Grid model for flat-slab structures. ACI Struct J 107(6):645–653

Coronelli D, Corti G (2014) Nonlinear static analysis of flat slab floors with grid model. ACI Struct J 111(2):343–352

Coronelli D, Martinelli L, Foti F (2015) Solai alleggeriti in calcestruzzo armato soggetti ad azioni gravitazionali e Sismiche. Dario Flaccovio Editore srl, 248 pp, ISBN 9788857904702 (English Translation available online)

Coronelli D, Martinelli L (2017) La progettazione sismica dei sistemi a piastra in calcestruzzo armato. Pàtron Editore Bologna, 115 p

Drakatos I, Muttoni A, Beyer K (2016) Internal slab-column connections under monotonic and cyclic imposed rotations. Eng Struct 123:501–516

Drakatos I, Muttoni A, Beyer K (2017) Mechanical model for drift-induced punching of slab-column connections without transverse reinforcement. Am Concr Inst Struct J 115:463–474

Fardis MN (2009) Seismic design, assessment and retrofitting of concrete buildings based on EN-Eurocode 8. Springer, London

Pinto A, Taucer F, Dimova S (2007) Pre-normative research needs to achieve improved design guidelines for seismic protection in the EU. JRC EUR 22858 EN 2007, 34 p

Pinto AV, Pegon P, Magonette G, Tsionis G (2004) Pseudo-dynamic testing of bridges using non-linear substructuring. Earthq Eng Struct Dyn 33:1125–1146

Spence R, Lopes M, Bisch P, Plumier A, Dolce M (2007) Earthquake risk reduction in the European Union. Proposal for a European earthquake risk reduction programme – a discussion document. European Association for Earthquake Engineering, following Lisbon Workshop 2005

Reinforcement of RC Beams by Means of Mortar Liner. Experiments and Design Rules

Marco Arduini[1(✉)], Marco Lenotti[2], and Andrea Nicoletti[2]

[1] FRC Lab, Milan, Italy
marco.arduini@basf.com
[2] BASF CC Italia Spa, Treviso, Italy

Abstract. It is commonly believed that the restoring of degraded reinforced concrete beams does not require particular precautions to ensure perfect adherence. In fact a number of researchers (e.g. Perez, Morency & Bissonnette in Concrete Repair, Rehabilitation and Retrofitting II - 2009) have shown that without adequate preparation of the substrate and without mortars with valuable characteristics it is possible neither to re-establish the original resistant capacity nor to reproduce the same stiffness of the original intact beam. Furthermore, due to the deterioration phenomena of the reinforcements, it is often necessary to intervene not only for the purposes of restoration but also for insertion of new resistant reinforcement in the same restoration. The design for this intervention is implemented assuming the perfect adherence and cross-section remain plane but these assumptions are not always achieved, with the result that the "restored" element has a greater deformability and/or a reduced resistance with respect to expectations. The document CNR DT 200-2013 has established a series of "poles" for calculation of the reinforcement of "glued" systems on healthy reinforced concrete elements, but has neglected to address the aspects related to "restoration" (which, however, are very common for this reinforcement technique) and to consider the aspects related to the transfer of stresses to the substrate-restoration interface. The absence of such control entails the risk of using a reinforcement adhering to a restoration with high properties, but which then delaminates it from the substrate earlier than expected. To understand these aspects, a substantial series of experimental data is presented in this document, processed at the BASF CC - Treviso test laboratory, on approximately forty reinforced concrete beams where the need for restoration/reinforcement by scarification and restoration of the concrete cover was simulated with mortars of different rheology and mechanical strength, with the addition of carbon FRP rods inserted in the repair mortar. The tests are then compared with the calculation regulations provided for in the current legislation in order to validate a specific calculation software that guarantees an adequate safety factor against failure.

Keywords: Fields applications and case studies · Experimental study · FRP internal reinforcement · Bond and interfacial stresses · CFRP reinforced beams

M. di Prisco and M. Menegotto (Eds.): ICD 2018, LNCE 42, pp. 410–420, 2020.
https://doi.org/10.1007/978-3-030-23748-6_32

1 Introduction

The studies concerning concrete with diffused reinforcement started in the 1970s Initially attention focused on the use of short steel fibres of various configurations and form ratio. The aim was to introduce an "isotropic" traction resistance in concrete to avoid the use of reinforcements.

Standard concrete has low elasto-fragile tensile strength, because the fragile behaviour its tensile strength cannot be take into account in the design. Adding special short fibers in the matrix can improve the tensile strength and modify the tensile behaviour in an elasto-hardening law. According to CEB FIP Model Code 2010, this type of concrete can support tensile action. Two families of commercial products have thus appeared in the civil sector: High Performance Fibre Reinforced Concrete e Ultra High Performance Fibre Reinforced Concrete.

Compared to traditional concretes, these two families have the following advantages:

(A) elasto-softening or elasto-hardening tensile behaviour (see Fig. 1)
(B) reduction of resistant sections and consequent saving of mass
(C) high energy dissipation
(D) cracking states containment: greater durability

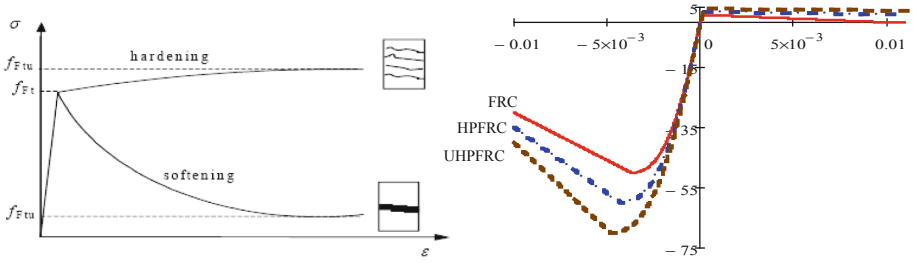

Fig. 1. Tension behaviour of the HPFRC and UHPFRC concretes and the constitutive law of repair mortars addressed in this work

The CNR DT 206 document provides design criteria to create new structures with HPFRC or UHPFRC and more recently the CEB-FIP Model Code 2010 has involved a more organic document where, in addition to traditional reinforced concrete, criteria are provided for the design of new buildings with these materials.

In the restoration sector a detailed design guidelines CNR DT200, together with specific national certification of the production, has completely defined how to reinforce an existing concrete beam, without any cover degradation, attaching a thin layer of FRP material.

When concrete cover need repair a third material is introduced between FRP and concrete: the repair mortar, this new thick interface between FRP and concrete need to

guarantee perfect adhesion to the support and modify the interface shear stress distribution.

Assuming still valid the theory of delamination, provided by CNR, to this case, is a dangerous operation because the adhesion of a polymeric system is not the same as an inorganic system, and the failure mechanism can shift form FRP delamination to repair mortar delamination.

The result could be a real failure load lower than expected. Again in the context of the repair of existing structures, we find ourselves with the difficulty of having to proceed with a very large concrete reinforcement. Could this thickness to be reported already be a reinforcement? If it were a UHPFRC concrete, could it provide sufficient tensile strength to the design's objectives without having to resort to further aid from reinforcements, pre-compression, FRP bonding?

To seek answers to the afore-mentioned questions, experimental results are identified in this document obtained from concrete beam tests which, with different surface preparation methods, are restored with HPFRC cementitious mortars. Three commercial products are analysed that are identified with the abbreviations:

- FRC: shrink-compensated restoration mortar, sprayable, with elasto-softening behaviour: Master Emaco S499 FR
- HPFRC: shrink-compensated restoration mortar, bondable, with elasto-hardening behaviour: Master Emaco S444 FR
- UHPFRC: shrink-compensated restoration mortar, bondable, with very rapid hardening with elasto-hardening behaviour: Master Emaco T1400 FR

2 Experimental Program

Figure 2 shows the dimensions and the type of specimens created. The concrete specimens have the same compressive strength, see Table 1, to simulate the need for restoration. Four ways to prepare the substrate were explored:

- hydro-scarification for 2 cm, obtaining a rough and healthy substrate ±5 mm
- sandblasting the substrate to open the pores and then drilling the substrate for preparation of reinforcements
- grouting of six L-shaped 8 mm rebars for a depth of 40 mm with Masterflow 960 (cementitious grout) spaced 10 cm and hole f12 mm
- creation of holes of 30 mm diameter and 30 mm depth with 10 cm pitch. The holes are filled only by casting motor or spray mortar, a technique suitable only for falling from above
- 300 bar wash on which MP AP4000 adhesion activator is spread

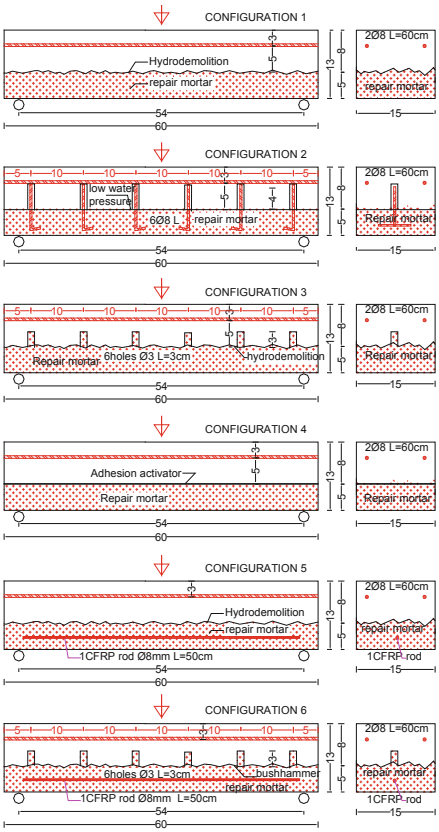

Fig. 2. Scheme of samples tested, dim.in cm

Fig. 3. Substrate preparation techniques

The repair mixes have been poured from top to bottom and then the beams are turned upside down before testing, Fig. 3 shows the surface preparation phase before the mortar application.

The mechanical properties of the reinforcing mortars and the carbon bars used are shown in Tables 1 and 2.

After approximately 2 months from casting of the restoration mortars the 3-point bending test was carried out monotonically at constant speed of 0.2 mm/min.

The load-midspan deflection are shown in Figs. 4, 5 and 6 respectively for samples reinforced with 3 cm of mortar S499, 3 cm of mortar S444 and 3 cm of mortar T1400.

Table 1. Mortar, concrete and CFRP rod mechanical properties

	Diameter mm	Compressive cylinder strength MPa	Flexural index f_{R1k} MPa	Flexural index f_{R3k} MPa	Mean tensile strength f_{tm} MPa	Elastic modulus E
Concrete	NA	33	0	0	NA	30*
FRC (Memaco S499FR)	NA	55	3.5	1.5	NA	28*
HSFRC (Memaco S444FR)	NA	55	6.8	7.4	NA	29*
FHSFRC (MEmaco T1400FR)	NA	55	11.0	9.4	NA	29*
CFRP rod	8	NA	NA	NA	1800	160**

Notes: * in compression
** in tension between 0.1 and 0.5 ftm

Table 2. Experimental results

Contr.	Conf.	Sample	Fmax	Deflect at Fmax	Energy*	F at 7 mm	Failure mode
	Type		kN	Mm	kN*mm	kN	
S499	1	A	16.5	3.4	100.5	13.8	Tension
S499	1	B	17.0	2.2	87.0	14.2**	Tension
S499	2	A	18.5	1.0	88.6	12.7	Tension
S499	2	B	16.3	0.9	89.9	13.3	Tension
S499	3	A	15.8	0.7	80.2	14.0**	Tension
S499	3	B	14.9	3.9	92.2	13.6	Tension
S499	4	A	16.2	4.6	101.3	15.7	Tension
S499	4	B	19.5	1.0	91.8	13.8	Tension
S499	5	A	37.8	4.4	195.4	23.8	Tension
S499	5	B	36.1	4.2	188.3	24.9	Tension
S499	6	A	35.7	3.2	148.0	14.0	Tension
S499	6	B	37.5	3.9	208.8	37.2	Tension
S444	1	A	30.4	2.7	132.7	19.5**	Tension
S444	1	B	27.7	2.2	117.7	17.5	Tension
S444	2	A	22.3	3.2	112.4	18.7**	Tension
S444	2	B	23.0	1.1	109.1	17.2**	Tension
S444	3	A	23.6	2.7	130.5	16.9	Tension
S444	3	B	27.9	3.4	142.1	17.8	Tension
S444	4	A	20.1	1.1	102.2	13.9	Tension
S444	4	B	25.1	2.1	132.0	16.7	Tension
S444	5	A	47.8	5.3	249.3	45.9	Tension
S444	5	B	48.0	4.1	246.7	40.7	Tension

(*continued*)

Table 2. (*continued*)

Contr.	Conf.	Sample	Fmax	Deflect at Fmax	Energy*	F at 7 mm	Failure mode
	Type		kN	Mm	kN*mm	kN	
S444	6	A	42.7	3.5	186.7	20.8	Tension
S444	6	B	41.4	3.7	227.7	37.1	Tension
T1400	1	A	27.7	2.9	143.3	18.5	Tension
T1400	1	B	25.6	2.5	141.4	18.2	Tension
T1400	2	A	23.0	1.2	127.0	17.8	Tension
T1400	2	B	22.4	1.0	132.9	18.1	Tension
T1400	3	A	29.8	3.2	158.0	21.8	Tension
T1400	3	B	28.9	2.6	158.8	21.9	Tension
T1400	4	A	27.9	2.1	151.1	19.8	Tension
T1400	4	B	18.9	1.2	108.4	16.2	Tension
T1400	5	A	53.0	4.1	281.2	50.2	Crushing
T1400	5	B	47.6	8.5	230.7	47.3	Crushing
T1400	6	A	41.8	4.5	224.8	36.5	Tension
T1400	6	B	39.9	4.9	220.7	35.1	Tension

Notes: * Area subtended by the diagram F-f up to the value of 7 mm of arrow
** Area subtended by the F-f diagram up to 6 mm of arrow

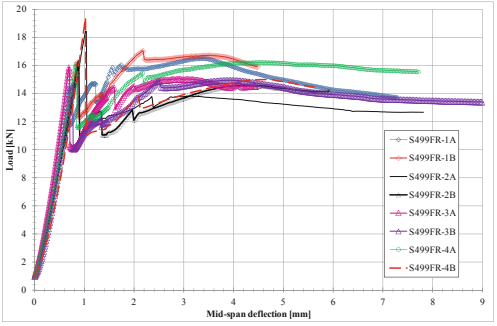

Fig. 4. Load – mid-span deflection for samples reinforced with S499 mortar only

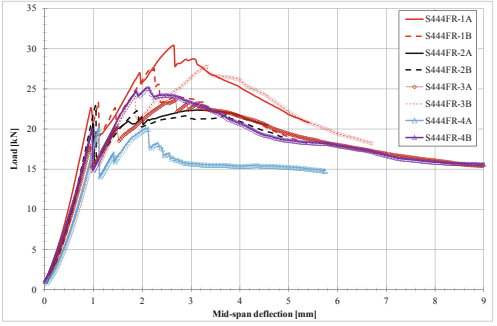

Fig. 5. Load-mid span deflection for samples reinforced with S444 mortar only

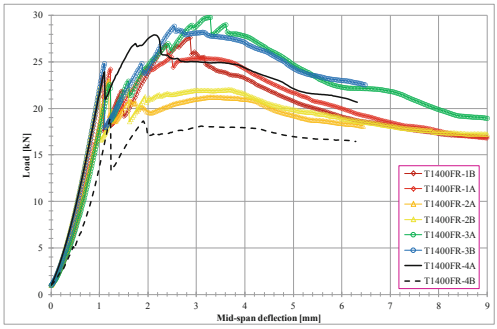

Fig. 6. Load-mid span deflection for samples reinforced with T1400 mortar only

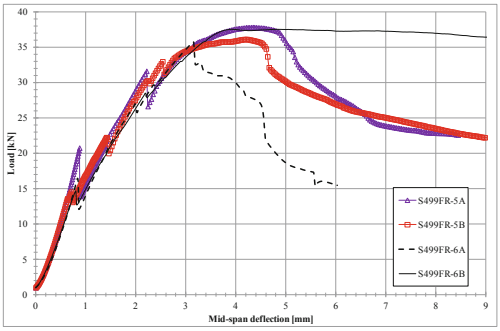

Fig. 7. Load-mid span deflection for samples reinforced with S499 mortar + CFRP rod

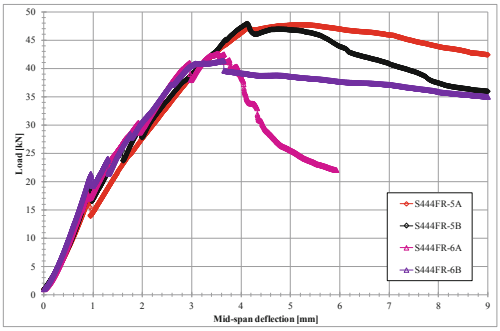

Fig. 8. Load mid span deflection for samples reinforced with S444 mortar + CFRP rod

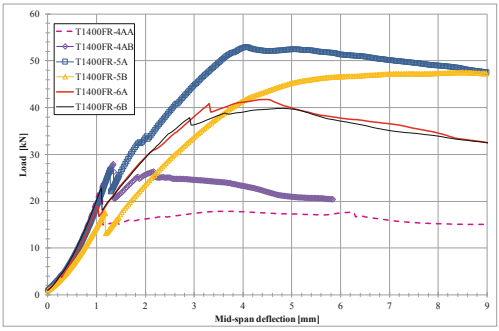

Fig. 9. Load-mid spa deflection for samples reinforced with T1400 mortar + CFRP rod

Similarly, are offered in Figs. 7, 8 and 9 the behaviour of the reinforced samples both with 3 cm mortar plus a piece of carbon bar (introduced at 1.5 cm distance from the bottom face during the application of the repair mortar).

The maximum load reached, the corresponding vertical displacement, the detected failure mode and the load at 6 mm vertical displacement are shown in Table 1.

3 Analysis of the Results

Firstly it is necessary to point out that the method of preparing the substrate considerably impacts on the performance of the system. Reasoning on the mean values obtained, it can be stated that:

- as the "ductility" of the mortar increases, the preparation of the substrate with root holes proves to be advantageous as it allows the obtaining of a higher maximum load and a higher energy expenditure (Fig. 10)
- for mortars with less ductility the adhesion activator is a better compromise for the performance both in terms of maximum load and energy. Slightly lower performance is offered by the hydro-demolition
- in the case of mortar with added reinforcement, the hydro-scarification preparation, instead, provides values that are much better than the root holes

Secondly, it must be pointed out that the contribution of the fibre-reinforced mortar provides a sensitive contribution to the absorption of the tensile stresses. This translates into a post-peak tail that allows maintaining of an almost horizontal load level together with a development of an extensive crack pattern.

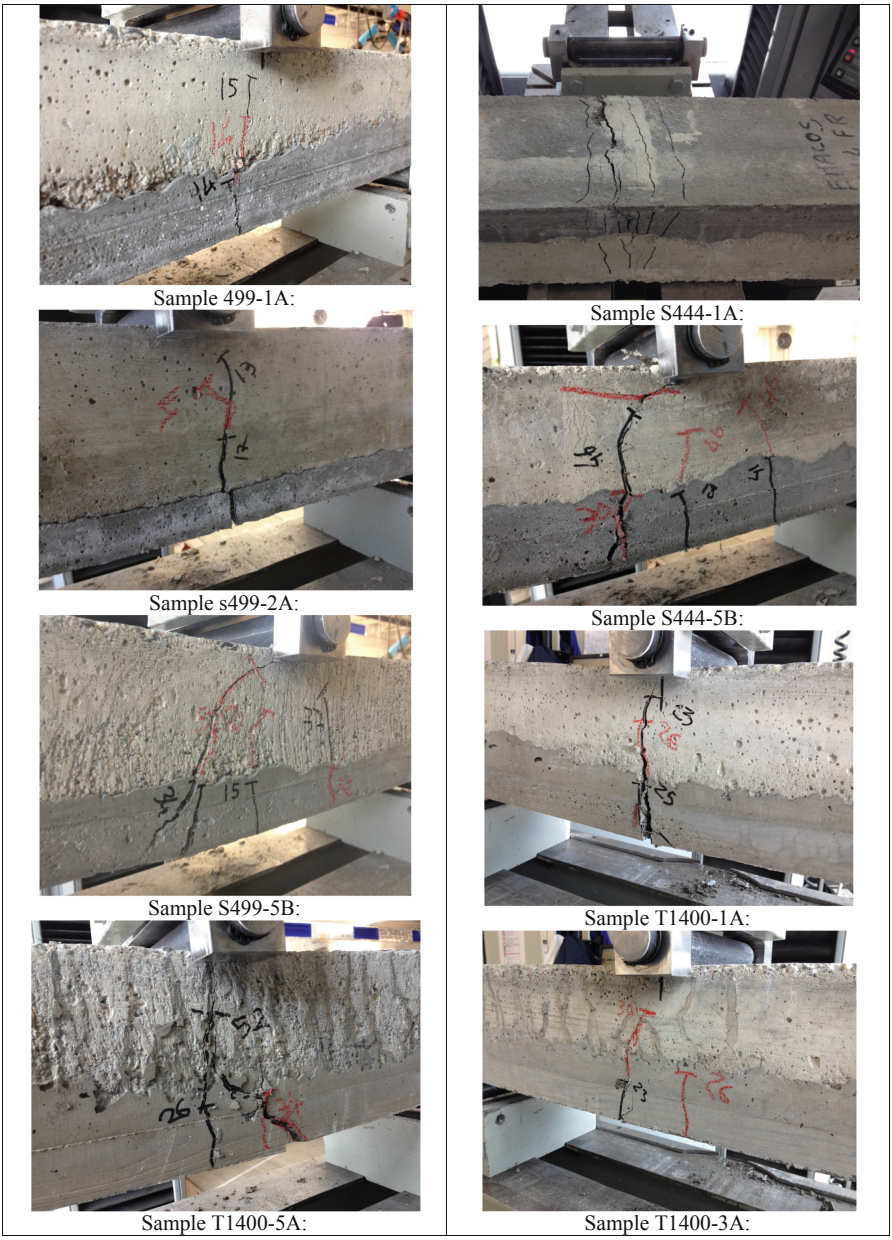

Fig. 10. Cracking state of the samples at the end of the test

4 Model Comparison

It is interesting to compare the experimental results obtained with the theoretical bending behaviour of these 5 schemes:

- a 15 × 13 cm beam (C33 class) reinforced with one CFRP rod only, placed at 1.5 cm distance from bottom face
- a sandwich beam obtained with perfect adhesion of 15 × 8 cm top concrete layer (C33class) and 15 × 5 cm of bottom FRC skin having elasto-softening behaviour in tension as reported in Fig. 1
- a sandwich beam obtained with perfect adhesion of 15 × 8 cm top concrete layer (C33class) and 15 × 5 cm of bottom UHPFRC skin having elasto-plastic behaviour in tension as reported in Fig. 1
- a sandwich beam obtained with perfect adhesion of 15 × 8 cm top concrete layer (C33class) and 15 × 5 cm of bottom FRC skin having elasto-softening behaviour in tension as reported in Fig. 1 + one CFRP rod inside
- a sandwich beam obtained with perfect adhesion of 15 × 8 cm top concrete layer (C33class) and 15 × 5 cm of bottom UHPFRC skin having elasto-plastic behaviour in tension as reported in Fig. 1 + one CFRP rod inside.

Table 3 shows the theoretical maximum load due to the numerical model compared to the mean value of Fmax obtained from experimental results. The comparison between Fu and Fmax shows clearly that CFRP rod slips from mortar at a certain stress action. Applying the delamination limitation due to CNRDT200 (Eq. 4.6) to the CFRP rod inside the repair mortar (using for the thickness t the following ratio: t = Rod area/sample width = 50/150 = 0.33 mm) we obtain: $f_{fdd,2}$ = 821 MPa. With this limitation the last column of Table 3 reports the design ultimate capacity F_{ud} according to CNR DT 200.

The delamination limitation is absolutely necessary to guarantee a minimum safety factor in the design.

Table 3. Comparison between experimental results and design guideline

Contr.	Conf.	Fu	Fmax	F_{ud}
	Type	kN	kN	kN
S499	1	12.5	16.7	12.5
S499	2	12.5	17.4	12.5
S499	3	12.5	15.3	12.5
S499	4	12.5	17.8	12.5
S499	5	58.7	36.9	37.7
S499	6	58.7	36.6	37.7
S444	1	19.4	29.0	19.4
S444	2	19.4	22.6	19.4
S444	3	19.4	25.7	19.4

(*continued*)

Table 3. (*continued*)

Contr.	Conf.	Fu	Fmax	F_{ud}
S444	4	19.4	22.6	19.4
S444	5	69.6	47.9	44.4
S444	6	69.6	42.0	44.4
T1400	1	26.7	26.6	26.7
T1400	2	26.7	22.7	26.7
T1400	3	26.7	29.3	26.7
T1400	4	26.7	23.4	26.7
T1400	5	74.1	50.3	52.3
T1400	6	74.1	40.8	52.3

5 Conclusions

In this paper many experimental results are presented to demonstrate that concrete repair and concrete repair + reinforcement cannot reach expected results if adhesion between repair mortar and concrete support is not perfect. Comparison is offered between 4 methods to promote the adhesion and three types of repair mortar with different behaviour in tension. Results shown that it is possible to reinforce concrete elements by means of special high strength fiber reinforced mortar (HPFRC) as well as adding carbon fiber rods. Some comparison with the Italian design code CNR DT 200 is also presented in order to verify the safety factor of the design.

References

Li VC, Wang S, Wu C (2001) Tensile strain-hardening behaviour of polyvinyl alcohol engineered cementitious composite (PVA-ECC). ACI Mater J 98(6):483–492

Naaman AE, Chao S (2011) Bond behaviour of reinforcing bars in tensile strain- hardening fibre-reinforced cement composites. ACI Struct J 106, 897

Perez F, Morency M, Bissonnette B (2009) Concrete repair, rehabilitation and retrofitting II

Saleem U et al (2011) Ultra-high-performance concrete bridge deck reinforced with high-strength steel. ACI Struct J

Bond Mechanisms Between Steel Bars and Lightweight Rubberized Concrete from Waste Tyres

F. Tondolo[1], M. Leone[2], A. P. Fantilli[1], and M. A. Aiello[2(✉)]

[1] DISEG Department of Structural, Geotechnical and Building Engineering, Politecnico di Torino, Turin, Italy
[2] Department of Engineering for Innovation, University of Salento, Lecce, Italy
antonietta.aiello@unisalento.it

Abstract. It is well known that the concrete industry has a strong environmental impact on our planet. First, there are the huge volumes of material needed to produce the billions of tons of concrete worldwide each year. Then there are the CO2 emissions caused during the production of Portland cement. Together with the energy requirements, water and aggregates consumption and generation of construction and demolition waste, appears evident as the concrete is not particularly environmentally friendly or compatible with the demands of sustainable development.

In this context large number of papers focused on new concrete materials that would be more suitable with environmental point of view. Among these materials, one of the most discussed is rubberized concrete. Rubberized concrete is obtained by incorporating rubber particles, obtained from recycled end of life tyres, as a replacement for mineral aggregates.

Keywords: Bond · FRP rebars · Rubber · Concrete · Waste tyres

1 Introduction

The reuse of rubber from waste tyres as aggregates in concrete is gaining an increasing attention within the scientific community. Possible applications of rubberized concrete structures in civil engineering are: structures in which no high mechanical performances, especially compressive strength, are required; members subjected to high deformations (like zone of bridge piers in contact with the deck); paving slabs or jersey barriers where vibration damping or impact resistance are required.

At the date, different research programs have been carried out on waste tyres replacing natural aggregates in concrete; the rubberized concrete mixtures generally showed lower unit weight compared to plain concrete and satisfactory workability. On the other hand, the mechanical properties of rubberized concrete had a significant reduction mainly when replacing coarse aggregate rather than fine aggregate, while an increased ductility and an improved post peak behavior have been registered under tensile stresses. Besides short term mechanical properties also the effects of rubber on

M. di Prisco and M. Menegotto (Eds.): ICD 2018, LNCE 42, pp. 421–431, 2020.
https://doi.org/10.1007/978-3-030-23748-6_33

concrete durability and on concrete physical properties, as thermal and acoustic, have been addressed.

Within this context an experimental investigation has been planned aiming to deepen the knowledge of the concrete including rubber from waste tyres with a particular focus to the bond behavior when steel reinforced rubberized concrete is utilized. In particular the use of rubber particles as concrete aggregates is addressed in order to develop a lightweight construction materials but with structural purposes. At this scope different concrete mixes, containing fixed amounts of rubber particles as partial replacement of natural sand, were characterized at fresh and hardened stages. In addition, plain concrete was also tested as reference mix.

The possible use of the defined structural rubberized concrete involves the need to analyse the bond between concrete and steel rebars. As well known the bond is a fundamental property for reinforced concrete members since it affects both service and ultimate conditions. The mechanism of crisis by ends pullout or splitting should be taken into account at the ultimate conditions, while the cracking evolution and the consequent degree of damage, deformability and durability under service conditions are correlated to the interface behavior between steel and concrete.

In this context, in order to give a contribution to development in the utilization of rubber in concrete for structural members, the mechanical properties of concrete obtained by a partial substitution of natural aggregate with different volume percentage of waste tyre rubber particles, are investigated. In particular, the experimental research consists in the study of fresh and hardened proprieties of both an ordinary control concrete mixture and four rubberized concrete mixtures.

In addition, pullout tests between steel reinforcement bars and rubberized concrete were performed varying the rubber content and the bar diameter.

2 Materials

The experimental investigation was carried out on five concrete mixtures: a control mixture of ordinary concrete and four rubberized concrete mixtures. Rubberized concrete mixtures were obtained by replacing increasing percentages of natural aggregates with an equivalent volume of rubber particles having the same dimensions. The types of natural aggregates utilized are the following: aggregate 1 (gravel), nominal size between 3 mm and 8 mm; aggregate 2 (fine sand), nominal size between 0 mm and 2 mm; aggregate 3 (river sand), nominal size between 0 mm and 5 mm (Fig. 1).

The quantities of these three aggregates were determined by the mix optimization. First of all it was necessary to define the particle size distributions of the three aggregates by an electromechanical sieve shaker, following EN 9331:2012. In order to maintain the shape of the curve of the natural aggregates found with the Fuller mix optimization, the replacement of the aggregates with rubber particles was made keeping the same size. Exanimating the sieve analysis comparison between natural aggregates and crumb rubber it was observed that the distribution of rubber was similar to that of the Aggregate 3 (05), namely the river sand (Fig. 2).

In particular, the two curves intersected in a range included between 1,0 mm and 4,0 mm grains dimension. Therefore, replacement between rubber particles and natural

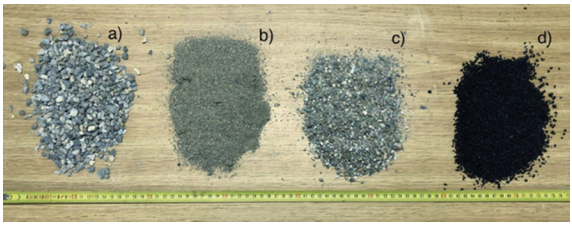

Fig. 1. Used aggregates: (a) gravel (b) fine sand (c) river sand (d) rubber

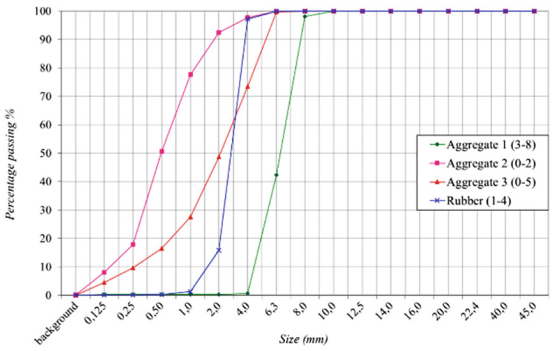

Fig. 2. Sieve analysis comparison between natural aggregates and waste rubber aggregate

aggregates was made with the fractions 2,0 mm and 4,0 mm and 1,0 mm and 2,0 mm. The four rubberized concrete mixtures were obtained by substituting these fractions of Aggregate 3 in percentages of 25%, 50%, 75% and 100% with an equal fraction in volume of crumb rubber.

The components for each concrete mixture are reported in Table 1.

Table 1. Mixdesign

Materials	Dosage (45 L mix)
Cement (CEM II/A – 42,5R)	15,3 kg
Water	7,65 l (w/c = 0,5)
Additive	0,23 kg (1,5% c.w.)
Aggregate 1 (38)	18,1 kg
Aggregate 2 (02)	20,2 kg

As rubber replacement interested only the two fractions of 12 mm and 24 mm of Aggregate 3, it was necessary to separate them. In this phase it was used an electromechanical sieve shaker, both river sand and crumb rubber were sieved in order to obtain fractions 12 mm and 24 mm and make the substitutions. Quantities of 12 mm

and 24 mm fractions of Aggregate 3 and crumb rubber involved in the substitution are showed in Table 2. In the same table the mixtures are labelled by the symbol RuC followed by a number that indicates the replacement amount.

Table 2. Amount of replaced rubber

Concrete mixtures	Fractions [mm]	Aggregate 3 [kg]		Crumb rubber [kg]
		Total	To be replaced	
RuC_25	1–2	36,6	9,1	2,8
	2–4	41,4	10,3	3,2
RuC_50	1–2	36,7	18,3	5,7
	2–4	41,8	20,9	6,5
RuC_75	1–2	37,0	27,8	8,7
	2–4	40,7	30,5	9,5
RuC_100	1–2	36,7	36,7	11,5
	2–4	41,5	41,5	13,0

In the following section the experimental characterization at the hardening and fresch state is discussed referring to concrete mixtures: RuC_0, RuC_25 and RuC_50.

2.1 Proprieties at the Fresh State

In order to evaluate the influence of waste tyre rubber particles on workability of fresh rubberized concrete, when replacing mineral aggregate, slump test were performed according to UNI EN 123502 (2001). The results furnish for all tested mixes a S1 class consistency (UNI EN 2061 2001), thus it is evident that the workability of fresh concrete is not changed by the partial substitution of Aggregate 3 with crumb rubber. This means that rubberized concrete can be mixed, cast and vibrated using equipment and procedures adopted for conventional concrete. Moreover these results are similar to that one obtained by Aiello and Leuzzi (2010).

Density measures showed in Table 3 were obtained by weigthing the cylindrical specimens before compressive strength and splitting tensile tests.

Table 3. Density of ordinary concrete and rubberized concrete mixtures

Concrete mixture	Unit weight [kg/m^3]	Decrease
RuC_0	2330	
RuC_25	2303	1,2%
RuC_50	2244	3,7%

Comparing the density obtained for the two mixtures of rubberized concrete and for the measurements obtained for the reference concrete RuC_0, a decrease in unit weight can be noted. In particular, RuC_25 showed a density decay of 1,2% and RuC_50

showed a density decay of 3,7%. As expected, because of the low density of rubber, a gradual decay of the concrete density was observed with increasing the percentage of mineral aggregate replaced. These results are in agreement with those reported in previous researches concerning the density of concrete prepared with waste tyre rubber aggregates (Khatib and Bayomy 1999; Topçu 1995; Benazzouk et al. 2008).

2.2 Proprieties at the Hardening State

Compressive test includes two different phases: in the first phase the modulus of elasticity was determined according to UNI EN 1239013 (2013); then the compressive strength was evaluated ($f_{c,average}$), according to UNI EN 123903 (2003). In addition splitting tensile strength ($f_{ct,average}$), according to UNI EN 123906 (2010), and flexural strength ($f_{ct,L,average}$), according to UNI EN 1239005, were determined. In all cases, at least five specimens were realized and tested. In the Table 4 the average experimental results are summarized together with the coefficient of variation within the brackets.

Table 4. Mechanical proprieties

Concrete mixture	$f_{c,average}$ [MPa]	$f_{ct,average}$ [MPa]	$f_{ct,L,average}$ [MPa]
RuC_0	30,0 (4,7%)	2,3 (30%)	4,7 (6,8%)
RuC_25	30,9 (25,3%)	2,7 (16%)	3,6 (5,8%)
RuC_50	30,3 (6,0%)	2,1 (38%)	3,7 (6,3%)

In the Fig. 3 the stress strain behavior of the specimens subjected to compression load is drawn.

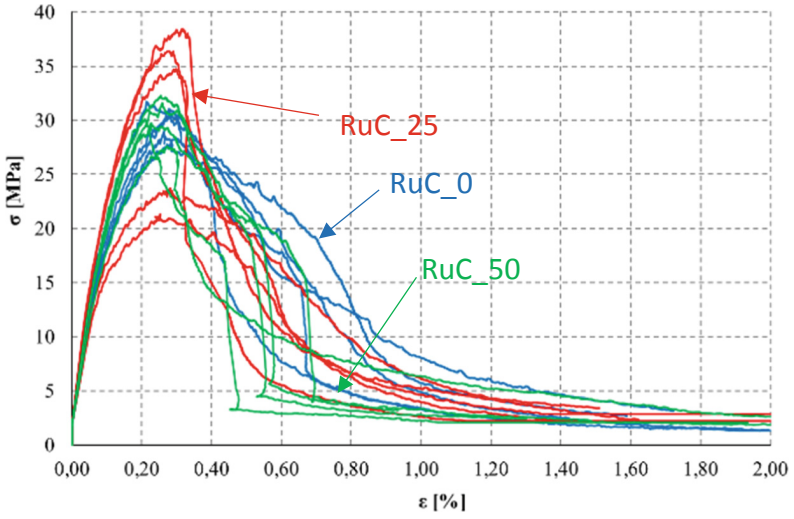

Fig. 3. Compression test: stress strain behavior

From compression strength tests it comes out that no substantial differences occurred between stress strain response of ordinary concrete and that of rubberized concrete.

In fact, all the three mixtures exhibited the same compressive strength and very similar modulus of elasticity values. The Fig. 3 show, also, that the softening behaviour seems not influenced by the rubber replacement. Again, this homogeneity in results between ordinary and rubberized concrete with rubber replacement up to 12% by total aggregates volume is mainly due to the specific kind of substitution made involving reduced size of rubber particles used (from 1 mm to a maximum of 4 mm). In fact, several authors found out that the addition of coarse rubber chips in concrete reduced the compressive strength more than the inclusion of fine crumb rubber (Topçu 1995; Khatib and Bayomy 1999; Eldin and Senouci 1993; Aiello and Leuzzi 2010).

Moreover, the percentages of substitution played an important role. In this case the substitution ratios were 6% and 12% by total aggregate volume and a negligible variation of the compressive strength was registered. On the other hand, for example, Bompa et al. (2017) tested three rubberized concrete mixes with 20%, 40% and 60% rubber replacement by volume of mineral aggregates and obtained a compressive strength reduction of 35%, 68% and 76%, respectively. A detailed analysis of an experimental database was made in Bompa et al. (2017), where the ratio between the average compressive strength of several rubberized concrete mixtures and that of the reference concrete mix is reported. Based on this analysis, Bompa et al. (2017) proposed relationships to estimate the compressive strength of rubberized concrete materials as a function of its volumetric rubber ratio. In Fig. 4 it is reported the compressive strength degradation curve as a function of rubber ratio, in case of fine aggregates replacement. In the same Figure the compressive strength results obtained in this study are added (red markers) as well as those found in literature (black markers). It can be noted that results of this experimental research are not well predicted by the curve proposed by Bompa et al.

As in case of compression strength, also values of tensile strength are quite constant for the three mixtures tested. This means that also tensile strength is substantially not influenced by the rubber content and size utilized in this study. Other authors that focused their studies on tensile strength of rubberized concrete observed a decrease by increasing the rubber content. Ganjian et al. (2009) reported that the reduction in tensile strength with 7,5% replacement of chipped rubber (maximum size about 10 mm) in place of mineral aggregates was 44% and 24% for the rubberized concrete mixture obtained with ground rubber (maximum size 1,2 mm). This confirms again that reduction is higher when using coarse rubber particles.

Results of three points bending tests show that flexural strength of rubberized concrete is lower than flexural strength or ordinary Portland concrete. In fact, maximum loads reached by rubberized concrete specimens were 20% lower than that of control concrete mixture. Considering the behavior observed in compression and splitting tensile tests, in which the three mixtures exhibited similar response, the most important factor in reducing flexural strength could be the lack of good bonding between rubber particles and cement paste. Flexural strength of rubberized concrete was analyzed also by Aiello and Leuzzi (2010). In that experimental research, a larger reduction of flexural strength was observed when the coarse aggregate rather than fine

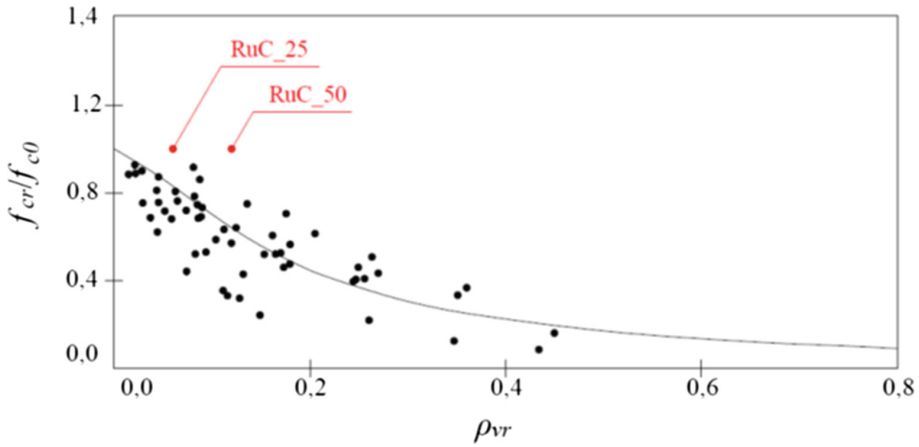

Fig. 4. Compressive strength degradation curve Bompa et al. (2017) plus results obtained in this experimental campaign

aggregate was substituted by rubber particles. Rubberized concrete mixtures prepared with 50% and 75% by volume of coarse aggregate replacement, both presented a decrease in flexural strength, referred to the control mixture, of about 28%. Whereas mixtures obtained with 50% and 75% by volume of fine aggregate substitution, showed a decay of about 5,8% and 7,3% with respect to the control mixture, respectively. Similar results were obtained also by Toutanji (1996).

3 Bond Test

Pullout tests were carried out in order to analyze the bond slip behavior of the specimens at different percentage of rubber replacement. Three concrete mixtures were tested: the control mixture and the rubberized concrete mixtures RuC_25 and RuC_50.

Six cubic pullout specimens were prepared for each rubberized concrete mixture: three of them were 120 mm side with 12 mm embedded deformed bar and the other three were 160 mm side with 16 mm embedded deformed bar. Both 12 mm and 16 mm reinforcement bars were about 600 mm length and made of a grade B450C steel. Each bar was prepared in order to have an un-bonded zone inside the cubic specimen. This un-bonded zone had to be half of the total embedded length and it was realized by applying a plastic sheet on the steel.

The specimens were tested under displacement control, with a rate equal to 0,2 mm/min. The relative displacement between the steel and concrete was measured up to bond failure by means of an LVDT positioned on the unloaded end of the reinforcing bar. Therefore, the parameters measured were the slip between the deformed bar and the concrete sample and the applied force F, as shown in Fig. 5.

The experimental results in terms of average maximum bond strength are reported in Table 5 while the bond stress versus slip curve for all specmens are drawn in the Fig. 6. Taking into account the short bond length, a uniform bond stress distribution

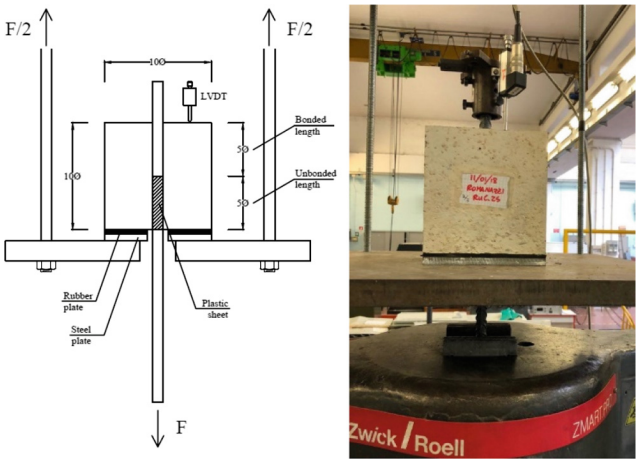

Fig. 5. Pullout test configuration

along the embedded length of the bar was assumed. Consequently, the maximum bond stress values (τmax) were calculated on the basis of the maximum measured applied load (Fmax), according to:

Table 5. Bond test results

Concrete mixture	Bar diameter [mm]	$\tau_{max,\ average}$ [MPa]
RuC_0	12	18,8
RuC_25	12	19,2
RuC_50	12	19,0
RuC_0	16	17,7
RuC_25	16	19,2
RuC_50	16	17,7

$$\tau max = Fmax / \pi \phi L \quad (1)$$

where: ϕ is the nominal diameter of the embedded bar; L is the real embedded length of the steel bar (5ϕ).

From a direct comparison among control concrete and rubberized concrete mixtures it comes out that bond-slip behavior is very similar for all the three mixtures. In fact, not only the average maximum bond stress τmax remains quite constant (Table 5) despite increasing the quantity of rubber in concrete, but also the post-peak τs regime remains unchanged (Fig. 6). This trend is confirmed also by the results available in literature Bompa and Elghazouli (2017).

In addition, no significant differences are found by changing the bar diameter: both samples embedding 12 mm and 16 mm bars shows a maximum bond stress close to

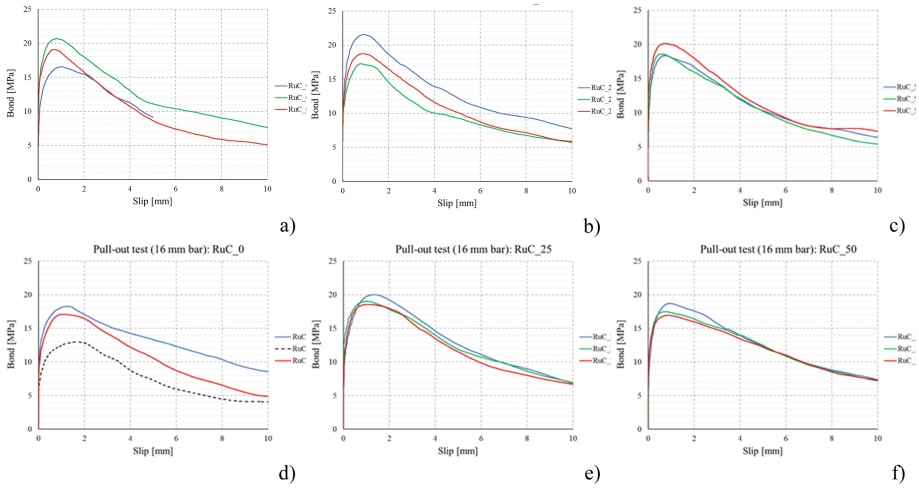

Fig. 6. Bond stress versus slip curves: (a) ϕ = 12 mm/RuC_O; (b) ϕ = 12 mm/RuC_25; (c) ϕ = 12 mm/RuC_50; (d) ϕ = 16 mm/RuC_O; (e) ϕ = 16 mm/RuC_25; (f) ϕ = 16 mm/RuC_50/

18 MPa. During pullout test on control concrete mixture, the specimen RuC_0_16_2 exhibited a behavior that was very different from the others of the same category (Fig. 5d) for unforeseen problem during the test procedure. For this reason, it was decided to consider this result unacceptable and to not include it in determination of τmax average value. All tested specimen developed a pullout failure.

In the Fig. 7 the photos of the tested specimens are reported.

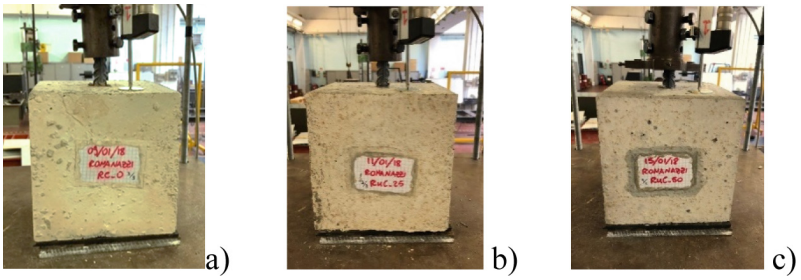

Fig. 7. Specimens after failure: (a) RuC_0_mix; (b) RuC_25 mix; (c) RuC_50 mix/Campioni dopo la crisi: (a) RuC_0_mix; (b) RuC_25 mix; (c) RuC_50 mix

4 Conclusions

The experimental research presented in this work examined the mechanical properties of concrete materials incorporating rubber particles, obtained from recycled tyres, as a replacement for mineral aggregates. The evaluation of the main mechanical properties

has been focused for three different concrete mixtures: an ordinary Portland control mixture, used as reference in results analysis, and two rubberized concrete mixtures obtained by replacing 6% and 12% by aggregates volume with crumb rubber. The mechanical properties that have been investigated were compressive strength, modulus of elasticity, tensile strength, flexural strength and bond between rubberized concrete and steel rebars.

Most of previous available studies has reported an important decrease in mechanical properties of concrete due to the addition of rubber particles ù. In this work a different result has been found, due to the low ratios of rubber replacement in place of mineral aggregates, the mix design procedure and the specific substitution made, namely reduced size of rubber aggregates in place of fine aggregates; in particular all the mechanical properties analysed didn't show substantial variation comparing rubberized and ordinary concrete.

In fact, the compression and tensile strength remained almost constant increasing the rubber substitution. Moreover the bond performance between steel rebars and concrete, in terms of bond strength and bond stress-slip law, remained almost unchanged varying both bar size and concrete type.

These first results suggest that rubberized concrete with substitution up to 12% by total aggregates volume can be used in structural applications. However, further experimental investigations are needed for reliable validation. Moreover, mechanical properties of rubberized concrete mixtures with substitution percentages higher than 12% should be tested to identify the maximum replacement ratio allowed to guarantee concrete structural performances recommended by standards.

References

UNI EN 123502 (2001) Testing fresh concrete: Slump test

UNI EN 2061 (2001) Calcestruzzo, Specificazione, prestazione, produzione e conformità

Aiello MA, Leuzzi F (2010) Waste tyre rubberized concrete: properties at fresh and hardened state. Waste Manage. Elsevier Ltd 30(8–9):1696–1704. https://doi.org/10.1016/j.wasman.2010.02.005

Khatib ZK, Bayomy FM (1999) Rubberized Portland cement concrete. J Mater Civ Eng 11 (3):206–213. https://doi.org/10.1061/(asce)08991561(1999)11:3(206)

Topçu IB (1995) The properties of rubberized concretes. Cem Concr Res 25(2):304–310. https://doi.org/10.1016/00088846(95)000143

Benazzouk A et al (2008) Thermal conductivity of cement composites containing rubber waste particles: Experimental study and modelling. Constr Build Mater 22(4):573–579. https://doi.org/10.1016/j.conbuildmat.2006.11.011

UNI EN 1239013 (2013) Determination of secant modulus of elasticity in compression

UNI EN 123903 (2003) Prova sul calcestruzzo indurito Resistenza alla compressione dei provini

UNI EN 123906 (2010) Splitting tensile strength

Eldin NN, Senouci A (1993) RubberTire particles as concrete aggregate. J Mater Civ Eng 5 (4):478–496

Bompa DV et al (2017) Experimental assessment and constitutive modelling of rubberised concrete materials. Constr Build Mater 137:246–260. https://doi.org/10.1016/j.conbuildmat.2017.01.086

Ganjian E, Khorami M, Maghsoudi AA (2009) Scraptyrerubber replacement for aggregate and filler in concrete. Constr Build Mater. Elsevier Ltd 23(5):1828–1836. https://doi.org/10.1016/j.conbuildmat.2008.09.020

Toutanji HA (1996) The use of rubber tire particles in concrete to replace mineral aggregates. Cement Concr Compos 18(2):135–139. https://doi.org/10.1016/09589465(95)000100

Bompa DV, Elghazouli AY (2017) Bondslip response of deformed bars in rubberised concrete. Constr Build Mater. Elsevier Ltd 154:884–898. https://doi.org/10.1016/j.conbuildmat.2017.08.016

AASHTO Design Specifications for GFRP-RC Bridges: 2nd Edition

M. Rossini[1(✉)], F. Matta[2], S. Nolan[3], W. Potter[3], and A. Nanni[1]

[1] Department of Civil, Architectural and Environmental Engineering, University of Miami, Coral Gables, FL, USA
mxrl465@miami.edu
[2] Department of Civil and Environmental Engineering, University of South Carolina, Columbia, SC, USA
[3] State Structures Design Office, Florida Department of Transportation, Tallahassee, FL, USA

Abstract. The development of a comprehensive bridge design national standard is paramount to allow for a wider and safe deployment of Glass Fiber Reinforced Polymer (GFRP) Reinforced Concrete (RC) in the transportation infrastructure. To respond to this demand, a task force of researchers, practitioners, and transportation officials lead by the University of Miami (UM), the University of South Carolina (USC), and the Florida Department of Transportation (FDOT), has developed a draft of the second edition of the Bridge Design Guide Specifications for GFRP-RC (BDGS-GFRP), now under consideration by the American Association of State Highway and Transportation Officials (AASHTO) committee T6. This paper deals with the salient contents of the document, with specific emphasis on the design of flexural members. Compared to the first edition, changes were proposed to reflect the state-of-the-art from archival literature and harmonize the design philosophy with that of other authoritative national and international standards.

Keywords: GFRP-RC · Design · Guidelines · Bridges · Infrastructures

1 Introduction

Fiber Reinforced Polymers (FRP) bars and strands are a viable corrosion-resistant solution for Reinforced Concrete (RC) and prestressed concrete (PC) in applications were corrosion of Mild Carbon Steel (MCS) and High Strength Carbon Steel (HSCS) represents a durability and safety concern (Spadea et al. 2018). In particular, the application of Glass FRP (GFRP) bars is spreading, with a number of bridges built worldwide over the last 40 years (Bakis et al. 2002; Gooranorimi and Nanni 2017). GFRP technology is tailored for application in aggressive environments. These include: coastal areas in sub-tropical environments (Nolan et al. 2018), cold weathered regions where de-icing salts are used and freeze-thaw cycles occur (Ahmad 2003), urban and industrial areas where concrete is prone to carbonation and exposed to wet-dry cycles (Nanni et al. 2014), geotechnical applications where reinforcement is exposed to moist and contaminated soil (Mohamed and Benmokrane 2014), and applications were the

M. di Prisco and M. Menegotto (Eds.): ICD 2018, LNCE 42, pp. 432–444, 2020.
https://doi.org/10.1007/978-3-030-23748-6_34

presence of stray currents may trigger corrosion in steel reinforcement (Spagnuolo et al. 2018).

Design principles for GFRP-RC are well established (Rossini et al. 2018a) and the technology is commercially available and spreading (Ruiz et al. 2018). Guidelines and regulations have been published in North America, Europe, Russia, and China (Rossini et al. 2018b). In the United States, design principles for GFRP-RC are detailed in guidelines issued by the American Concrete Institute (ACI 2015). The deployment of GFRP-RC in buildings is regulated by the International Code Council (ICC) that maintains an Acceptance Criteria (AC) for GFRP bars (ICC 2016). The deployment of GFRP-RC in infrastructural elements is regulated by the American Association of State Highway and Transportation Officials (AASHTO). AASHTO maintains a specific document that, in its first edition, only covers the design of GFRP-RC bridge decks and open-post railings (AASHTO 2009). ASTM recently published standard specifications for GFRP bars (ASTM 2017). The document does not hold binding status by itself, but it does once referenced in national design and construction codes and standards. The document is expected to relieve the need to include a chapter covering material specifications in design guidelines as it was done in the past. In Canada, the use of GFRP bars in buildings is covered by the guidelines issued by the Canadian Standardization Association (CSA 2012). GFRP-RC deployment in infrastructures is regulated by the Canadian Highway Bridge Design Code (CHBDC) issued by CSA (2014). In Europe, guidelines for GFRP-RC design are published by the International Concrete Federation (*fib* 2007). *fib* also includes GFRP-RC in its Model Code (*fib* 2013). In Italy, guidelines for GFRP-RC design are published by the National Research Council (CNR 2007). In Russia, the deployment of GFRP in buildings is regulated by a specific addendum to the national building code (Minstroy 2018). The approach of the Russian building code is compatible with the one of the Eurocodes that, however, do not include GFRP-RC (CEN 2005a). In China, the deployment of GFRP-RC in infrastructures is regulated by national guidelines (SAC 2010).

The first generation of design guidelines and standards was issued in the late 90s and early 2000s. It succeeded in addressing the behavior of GFRP-RC structures, and the differences with respect to conventional steel RC members (Nanni 1999). However, the limited experimental database available at that time called for the introduction of relatively severe safety factors (Jawaheri and Nanni 2013).

The second generation of GFRP-RC design guidelines represents the recent state-of-the-practice. It expanded and refined the documents from the first-generation. However, little was done to address the issues that prevented one from taking full advantage of the efficiency and economical appeal of GFRP bars (Rossini et al. 2018a).

The third generation of design guidelines is currently under development and publication. It includes the 2nd edition of the AASHTO Bridge Design Guide Specifications for GFRP-RC Bridges (BDGS-GFRP) (AASHTO 2018), the first edition of the ACI Building Code Provisions for Concrete Reinforced with GFRP Bars (currently under development), and an update of the CSA Canadian Highway Bridge Design Code (CHBDC) (scheduled for development).

2 Research Significance

A draft of the second edition of AASHTO BDGS-GFRP (AASHTO 2018) was developed by a task force of researchers, practitioners, and transportation officials led by the University of Miami (UM), the University of South Carolina (USC), and the Florida Department of Transportation (FDOT). Objectives included: updating the provisions to include state-of-the-art archival literature; making the provisions more rational and address the issues preventing one from taking full advantage of the mechanical and economic appeal of GFRP bars; making the design approach consistent with the AASHTO Bridge Design Specifications for traditional construction materials (BDS); and, harmonize the design philosophy with that of other authoritative national and international standards.

3 Guidelines Integration

Consistency and clarity in standards and guidelines are paramount to allow for safe and efficient design of structural members. At the same time, standardization is crucial to leverage deployment of innovative technologies in civil engineering. Nevertheless, GFRP-RC design guidelines typically exist as separate documents with respect to MCS-RC counterparts (AASHTO 2009, 2017), or as addenda to national and local design codes (CSA 2014). Furthermore, overlapping exists, and FRP-RC/PC design guidelines have different approaches one with respect to the other and with respect to design guidelines for traditional structural materials (Rossini et al. 2018b). Differences include: the definition of the material properties to be used for design purposes; the structure of the design equations; and, the value and definition of the design parameters to be used in these equations.

The ideal setting to leverage wider deployment of GFRP-RC in substantial applications entails embedding GFRP bars as an alternative reinforcement solution in a comprehensive standard (Nolan and Nanni 2017). The approach can be expanded to include other materials, as well as PC applications (Rossini et al. 2018b).

4 Design Approach

Rossini et al. (2018b) outlined a unified design approach to FRP-RC/PC. The approach was validated on an FRP-RC/PC pedestrian bridge reinforced with Glass FRP bars, Basalt FRP bars, and Carbon FRP strands. The approach served as a framework for developing the draft of the second edition of AASHTO BDGS-GFRP and is summarized in the following with specific reference to the case of GFRP-RC.

Any mechanical problem can be defined as a system of equilibrium, compatibility and constitutive equations. Structural theories introduce assumptions to simplify the mathematical formulation of common mechanical problems, like the beam model. Classical Euler-Bernoulli assumptions hold valid in GFRP-RC bended elements, and sectional analysis can be carried out. Rigorously, the only difference with respect to MCS-RC is in the constitutive law used to model the reinforcing bars. Similarly to the

design of MCS-RC, limitations in the exploitability of the materials, amount of reinforcement, and maximum strains and deflection are introduced to ensure structural assumptions are met and the desired level of safety and reliability is provided.

4.1 Material Properties

GFRP is a brittle composite material, elastic until failure, stronger, but less stiff with respect to MCS. The guaranteed strength (f^*_{fu}) of a GFRP bar is defined as the experimental average value minus three standard deviation (ACI 2015), corresponding to the 99.9th strength percentile. The definition is reported in Eq. 1 for clarity. The approach is more conservative with respect to the calculation of characteristic strengths for steel reinforcement and concrete, traditionally defined as the average value minus 1.64 standard deviation – 95th strength percentile – under the assumption of normal distribution (CEN 2005a).

$$f^*_{fu} = f_{fm} - 3\sigma_f \tag{1}$$

The strength of commercially available GFRP bars can vary from product to product at varying fiber content and manufacturing techniques (Emparanza et al. 2017). At the time of design, the bar manufacturer is typically not defined. Thus, the minimum guaranteed strength required for certification per ASTM D7957 (ASTM 2017) is taken as the specified tensile strength for design purposes in spite of an experimental value. The specified strength (f'_{fu}) is always less than or equal than the guaranteed experimental strength (f^*_{fu}) of the specific batch of bars that will be deployed in construction, as shown in Eq. 2.

$$f'_{fu} \leq f^*_{fu} \tag{2}$$

Tracing a straight line to limit the exploitability of different products and material systems may slow down the growth of the GFRP industry. Nevertheless, the need for standardization is paramount. A possible solution may lay in the definition of different strength grades, as traditionally done for MCS bars (ASTM 2016), steel profiles (AISC 2017; CEN 2005b), and concrete (FDOT 2018; CEN 2005a).

FRP composites are known to experience strength degradation following long-term exposure to the environment (ACI 2015; *fib* 2007). To account for the phenomenon, the design strength (f_{fd}) of the material is defined per Eq. 3 including an environmental reduction factor (C_E). The approach is in line with the principles of ACI (2015).

$$f_{fd} = C_E f'_{fu} \tag{3}$$

The design strength of the material is the reference value for design calculations, both at the ultimate limit state (ULS) and service limit state (SLS). Furthermore, the strength of FRP under sustained load is reduced to avoid creep rupture (ACI 2015; *fib* 2007). Resorting to the nomenclature suggested by Rossini et al. (2018a), a creep rupture reduction factor (C_c) is applied to the design strength in order to define the

design strength against creep rupture under sustained load ($f_{f,c}$) as in Eq. 4. Similarly, a fatigue reduction factor (C_f) is applied to the design strength in order to define the design strength under cyclic loading ($f_{f,f}$) as in Eq. 5.

$$f_{f,c} = C_c f_{fd} = C_E C_c f'_{fu} \tag{4}$$

$$f_{f,f} = C_f f_{fd} = C_E C_f f'_{fu} \tag{5}$$

The brittle nature of FRP reinforcement implies the possibility to either have over-reinforced flexural members that may fail because of concrete collapse in the compression zone, or under-reinforced flexural members that may fail because of reinforcement rupture in the tension zone (ACI 2015). The two failure modes are characterized by two different strength reduction factors – ϕ_c and ϕ_t respectively – defined to guarantee the same level of safety in the two cases. A flexural member can also undergo shear failure. In this case the strength reduction factor ϕ_s is aligned to values prescribed for MCS-RC in ACI (2014).

GFRP bars lack the plastic plafond typical of MCS bars. Thus, GFRP-RC flexural members do not feature ductile behavior at failure. Nevertheless, GFRP bars reach strain levels higher than the 0.005 ductility threshold set for MCS in ACI (2014). Thus, GFRP-RC flexural members feature a pseudo-ductile behavior comparable to what is required of MCS-RC to foresee upcoming failure. Figure 1a compares the mechanical behavior of GFRP and MCS bars M13. Figure 1b compares the flexural strength reduction factor proposed for GFRP bars to traditional values used for MCS (AASHTO 2017). The strength reduction factors are plotted as a function of the strain reached by the reinforcement at sectional failure. The diagram is adapted from AASHTO (2017).

The different bond characteristics of GFRP bars with respect to steel reinforcement is accounted for introducing a bond reduction factor (C_b). The parameter is defined in Eq. 6 as the inverse of the bond reduction coefficient (k_b) as defined in ACI 440.1R (ACI 2015). By this definition, the bond reduction factor increases at increasing performances, consistently with the other design factors. Better bond performances enhance crack control and reduce crack width at equal load level (ACI 2015).

$$C_b = 1/k_b \tag{6}$$

4.2 Design Factors

Table 1 provides a summary of design factors as reported by international design guidelines, along with the values adopted in the second edition of AASHTO BDGS-GFRP. The flexural strength reduction factor for compression-controlled failures (ϕ_c) is raised from 0.65 to 0.75 (+15%) with respect to the first edition of AASHTO BDGS-GFRP (AASHTO 2009). The value is in line with findings of Jawaheri & Nanni (2013). The creep rupture reduction factor (C_c) is raised from 0.20 to 0.30 (+50%) with respect to the first edition of AASHTO BDGS-GFRP. The value is more reflective of the performances of ASTM-compliant GFRP bars, and about 50% of the experimental findings of Perigny et al. (2012), Sayed-Ahmed et al. (2017), and Keller et al. (2017).

Similarly, the fatigue reduction factor (C_f) is raised to 0.25 (+25%) for alignment with international standards (CNR 2007; *fib* 2013; CSA 2014). The bond reduction factor (C_b) is raised from 0.71 to 0.83 (+17%). The value is reflective of the good bond performances of GFRP bars (Gooranorimi et al. 2018) and is more conservative with respect to international guidelines (CSA 2014).

Table 1. Design parameters for GFRP-RC

	CNR	*fib*	CSA	ACI	AASHTO	
	2007	2013	2014	2015	2009	2018
ϕ_c	0.67	0.67	0.75	0.65	0.65	**0.75**
ϕ_t	0.60	0.80	0.55	0.55	0.55	**0.55**
ϕ_s	-	-	-	0.75	0.75	**0.75**
C_E	0.70	0.55[(1)]	1.00	0.70	0.70	**0.70**
C_c	0.30	0.30	0.25	0.20	0.20	**0.30**
C_f	0.30	0.50	0.25	0.20	0.20	**0.25**
C_b	0.59	0.71[(1)]	1.00	0.71	0.71	**0.83**

[1]from *fib* bulletin 40 (*fib* 2007).

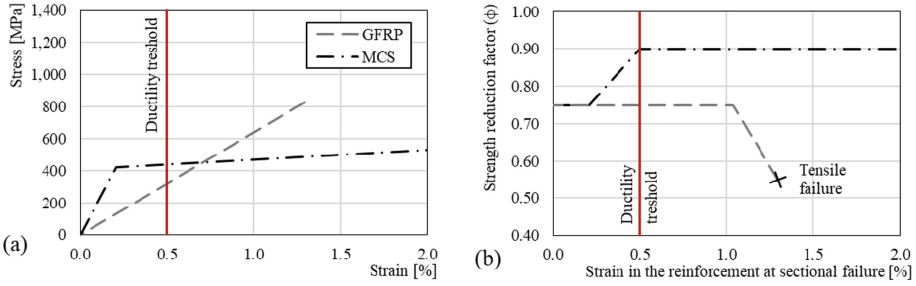

Fig. 1. Mechanical properties (a) and flexural strength reduction factors (b) for M25 bars made with GFRP and MCS.

4.3 Limit States

As for the case of MCS-RC, a GFRP-RC flexural member must be designed against a number of Ultimate Limit States (ULSs) and Service Limit States (SLSs). ULSs include compression failure of the concrete or tension failure of the GFRP bars under factored load. Furthermore, GFRP bars can experience creep rupture under sustained load, and fatigue rupture under cyclic load. These conditions are verified under service loads but represent ULSs in the sense that failure to comply may result in the catastrophic collapse of the member. SLSs include a limit on deflection (L/800 for vehicular bridges), a limit on crack width (0.7 mm), and a limit on concrete stresses under sustained load (0.45 f_c'). The relatively low stiffness of GFRP bars may result in SLSs governing the design.

According to ACI (2015) the creep rupture limit state must be verified under sustained load. The AASHTO BDS for traditional construction materials lacks the explicit definition of a sustained service load. Thus, the first edition of the AASHTO BDGS-GFRP considered the entire amount of service load as sustained. The assumption is overconservative and not aligned with international bridge design guidelines (CEN 2005a). In the second edition of AASHTO BDGS-GFRP the sustained portion of the service load is set equal to the dead load (DL) plus 20% of the live load (LL) as shown in Eq. 7. The approach is in line with ACI (2015) and more conservative with respect to international guidelines that only consider DL as sustained (CEN 2005a; CNR 2007).

$$Sustained\ Load = DL + 0.20\,LL \tag{7}$$

According to ACI (2015) the fatigue rupture limit state must be verified under the sum of the sustained load plus the maximum load experience in a fatigue cycle. In translating this provision to AASHTO language, the total fatigue load is defined as the sum of the Dead Load (DL) plus the factored transient loads defined per AASHTO (2017) Fatigue load combination Fatigue I (F1). The fatigue load combination is reported in Eq. 8. The issue of load combinations for creep rupture and cyclic fatigue is also discussed by Rossini et al. (2018a).

$$Fatigue\ Load = DL + F1 \tag{8}$$

4.4 Philosophy and Applicability

The RC and PC design section of the AASHTO BDS has recently underwent a major update (Montgomery et al. 2017). The second edition of the AASHTO BDGS-GFRP is compatible with the most recent edition of the AASHTO BDS (AASHTO 2017). The GFRP counterpart reflects the structure and organization of the main document and minimizes the differences in design equations to ease application by practitioners. Differences are limited to adjusting design parameters and material properties to account for the different behavior of GFRP bars with respect to MCS. Furthermore, the second edition of the AASHTO BDGS-GFRP is meant for application along with the material specifications published by ASTM (2017). This sets the first example for the next generation of integrated GFRP-RC design, construction, and material guidelines to be consistently developed without overlapping.

The major limitation of the first edition of the AASHTO BDGS-GFRP (AASHTO 2009) laid in the limited field of application as it only covered bridge decks and open-post railings. The second edition of the AASHTO BDGS-GFRP covers all the members that compose a RC bridge. This includes decks, girders, bent caps, bulkhead caps, bearing piles, sheet piles, gravity walls, open-post railings, continuous railings, and approach slabs. It is the first regulation to cover GFRP-RC substructure, and is the most

complete guideline for GFRP-RC design. Its provisions have been developed and tested on a number of structures currently built or under construction. This includes the Innovation Bridge discussed by Rossini et al. (2018b), and the Halls River Bridge discussed by Rossini et al. (2018a).

5 Parametric Analysis

In developing the draft for the second edition of the AASHTO BDGS-GFRP, parametric analysis was used as a tool to quantify the effect of the proposed variation in the design parameters. In the following, a selection of the results of the parametric analysis is discussed. The methodology adopted will be briefly summarized. For more details, reference is made to Rossini et al. (2018a).

The study focuses on the GFRP-RC pile cap of the Halls River Bridge currently under construction in Homosassa, FL (Rossini et al. 2018a) (Fig. 2). The element is deemed representative of large under-reinforced GFRP-RC members acting as pile caps in short-spanned traffic bridges. Given their exposure condition and proximity to water surfaces, these members represent typical applications for GFRP-RC and are of particular interest for FDOT.

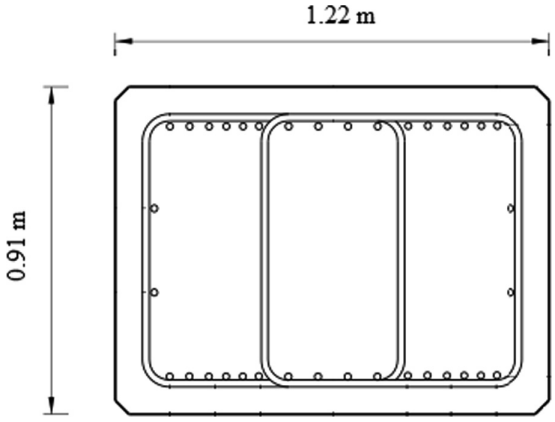

Fig. 2. Transversal section of the pile cap of the Halls River Bridge.

Each parametric curve is constructed by calculating the minimum number of M25 GFRP bars that satisfies the specific design requirement: moment capacity, minimum reinforcement, creep rupture, fatigue, and crack width limits. The design for positive moment capacity based on ACI (2015) and AASHTO (2009) resulted in 16 M25 bars with a guaranteed strength of 550 MPa and an elastic modulus of 45 GPa, for a total area of 8084 mm^2 to resist a factored moment demand of 575 kN-m. The design for positive moment capacity based on the second edition of AASHTO BDGS-GFRP resulted in 9 M25 bars, for a total area of 4547 mm^2. This corresponds to a reduction of 40% with respect to the first edition (Rossini et al. 2018b).

Figure 3 shows the influence of the variation of a selection of parameters on the required amount of reinforcement. The design demand is represented in terms of required number of longitudinal M25 bars. For each diagram, design equations are plotted as a function of the selected range. The remaining parameters are set constant and equal to values recommended in the first and second edition of the AASHTO BDGS-GFRP respectively. The results presented in Fig. 3 are case-dependent, but the trend of the curves is indicative in general.

Comparing Fig. 3a and Fig. 3b shows how the rationalization of the sustained and cyclic load demand discussed in Sect. 4.3 reduces the influence of the cyclic fatigue and creep rupture requirements from governing to negligible. Relaxation of the creep rupture reduction factor (C_c) from 0.20 to 0.30, and the fatigue reduction factor (C_f) from 0.20 to 0.25 contributes to this outcome, but the effect is limited as shown in Fig. 3b.

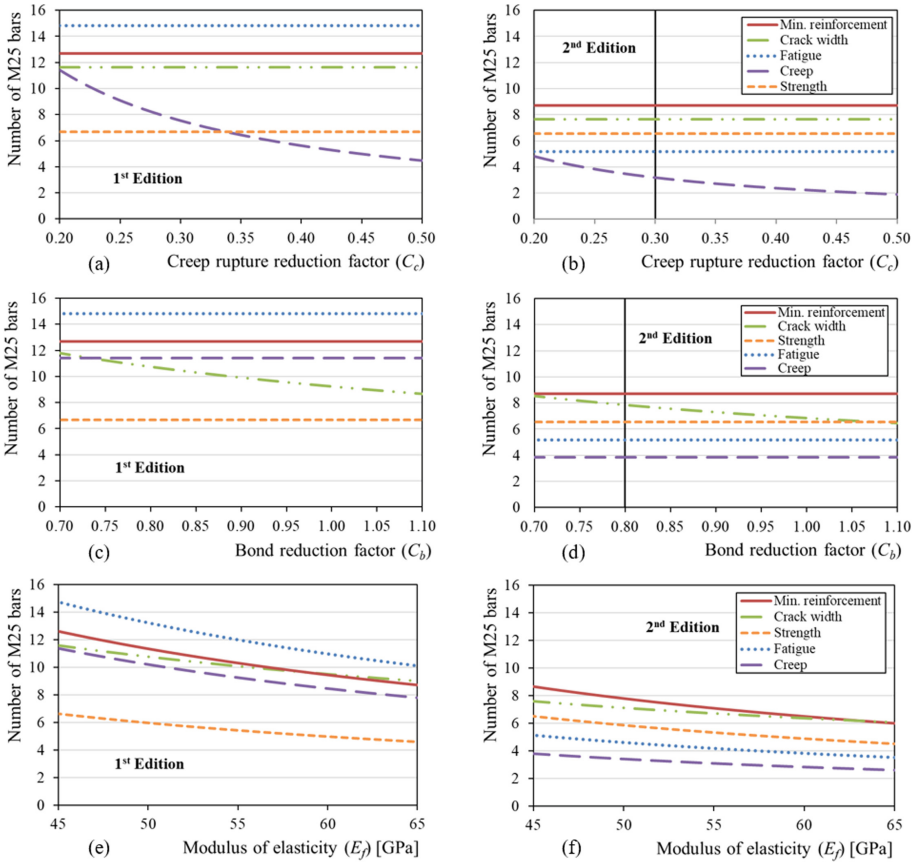

Fig. 3. Required number of M25 bars as a function of the variation of the design parameters using the equations of AASHTO BDGS-GFRP 1st edition (left) and AASHTO BDGS-GFRP 2nd edition (right).

Experimental results suggest that further margin for improvement exists, but additional research is required. The prioritization of research into creep rupture and cyclic fatigue endurance limits is suggested by the limited database available and by mechanical considerations discussed by Rossini et al. (2018a).

The crack width requirement governs over the strength requirement as show in Fig. 3c and Fig. 3d. A relaxation of the bond reduction factor (C_b) from 0.71 to 0.83, along with a relaxation of the crack width limit (w) from 0.5 mm to 0.7 mm, and a relaxation of the minimum concrete clear cover (c_c) from 51 mm to 38 mm, reduces the required amount of reinforcement to fulfill SLSs by about 30%.

The design of large section MCS-RC members is typically governed by minimum reinforcement considerations. This is not the case for GFRP-RC members designed according to the first edition of AASHTO BDGS-GFRP. Conversely, the minimum reinforcement requirement governs the design of GFRP-RC large section members according to the draft of the second edition of AASHTO BDGS-GFRP. This follows the rationalization of the sustained and cyclic load demand discussed in Sect. 4.3. Furthermore, the minimum reinforcement requirement has been aligned to the formulation adopted in AASHTO BDS (2017). This approach ensures a minimum level of strength and ductility to the system as a function of the mechanical properties of the reinforcement, and offsets overconservativeness in some cases. Details are discussed by Rossini et al. (2018a, b).

Figure 3e and Fig. 3f show how improving the stiffness (E_f) – and therefore the strength (f^*_{fu}) – of GFRP bars amplifies the benefits of the proposed refinements in design limits. However, the increment in the elastic modulus should not come from a mere increase of the effective cross-sectional area compared to the nominal design area, but rather a combination of increased fiber ratio, improved material properties, and superior manufacturing quality control.

An improved quality control of the product may help refining most of the design parameters discussed but needs to be reflected in more performing material specifications (ASTM 2017) before designers can take full advantage of it.

6 Conclusions

In this study the salient contents of the draft of the second editions of the AASHTO BDGS-GFRP are discussed along with the conceptual framework functional to the development of the document. Specific emphasis is devoted to flexural members. The differences with respect to the first edition are quantified resorting to parametric analysis.

The second edition of AASHTO BDGS-GFRP (AASHTO 2018) aims to provide a rational and consistent framework for the design of GFRP-RC bridge structures. This is expected to raise awareness and leverage wider deployment of non-corrosive reinforcement solutions in infrastructures. Furthermore, the definition of a consistent regulatory framework is expected to help define and prioritize Research and Development (R&D) areas – at the academic, private, and regulatory level – to make the technology more efficient, economical and environmentally appealing (Rossini et al. 2018a). Specific features of the document include:

1. Design parameters and procedures have been updated to reflect advancements in the state-of-the-art. This includes refinement of the strength reduction factor for compression-controlled failures (ϕ_c); refinement of the creep rupture reduction factor (C_c), fatigue reduction factor (C_f), and bond reduction factor (C_b).
2. Design demands and limit states have been made more rational and consistent with national and international guidelines (CEN 2005a; CNR 2007; ACI 2015; AASHTO 2017). This offsets overconservativeness in creep rupture and cyclic fatigue demands.
3. Design equations have been updated to align the document to the most recent edition of the AASHTO Bridge Design Specifications (AASHTO 2017). This creates a familiar environment for the practitioners approaching GFRP-RC for the first time and resolve some inconsistencies.
4. The document is expanded to include all the reinforced concrete components of a bridge structure. The first edition only included bridge decks and open-post railings. It is the first guideline to include provisions for GFRP-RC substructures.
5. The document is structured to automatically benefit from any refinement in material specifications issued by ASTM (2017). This would not be the case if an additional material specification chapter was to be introduced as done in the first edition.

Acknowledgements. The authors gratefully acknowledge the financial support from: (1) "Sustainable concrete using seawater, salt-contaminated aggregates, and non-corrosive reinforcement" Infravation, 31109806.005-SEACON; (2) "I/UCRC Center for the Integration of Composites into Infrastructure (CICI)," NSF, 1439543; (3) Zegna Foundation for supporting the first author's research activity in the field of composite materials for infrastructural applications; and, (4) Florida Department of Transportation (FDOT) for access to the Halls River Bridge design material.

References

AASHTO (2009) AASHTO LRFD bridge design guide specifications for GFRP-reinforced concrete bridge decks and traffic railings, 1st edn. American Association of State Highway and Transportation Officials, Washington, DC

AASHTO (2017) AASHTO LRFD bridge design specifications, 8th edn. American Association of State Highway and Transportation Officials, Washington, DC

AASHTO (2018) AASHTO LRFD bridge design guide specifications for GFRP-reinforced concrete, 2nd edn. American Association of State Highway and Transportation Officials, Washington, DC

ACI (2014) Building code requirements for structural concrete. ACI 318-14. American Concrete Institute, Farmington Hills, MI

ACI (2015) Guide for the design and construction of structural concrete reinforced with fiber-reinforced polymers (FRP) bars. ACI 440.1R-15. American Concrete Institute, Farmington Hills, MI

Ahmad S (2003) Reinforcement corrosion in concrete structures, its monitoring and service life prediction - a review. Cement Concr Compos 25(4–5 SPEC):459–471

AISC (2017) Steel construction manual, 15th edn. American Institute of Steel Construction, Chicago, IL

ASTM (2016) Standard specification for deformed and plain carbon-steel bars for concrete. A615/A615 M-16. ASTM International, West Conshohocken, PA

ASTM (2017) Standard specification for solid round glass fiber reinforced polymer bars for concrete reinforcement. ASTM D7957/D7957 M-17. ASTM International, West Conshohocken, PA

Bakis CE, Bank LC, Brown VL, Cosenza E, Davalos JF, Lesko JJ, Machida A, Rizkalla SH, Triantafillou TC (2002) Fiber-reinforced polymer composites for construction: state-of-the-art review. ASCE J Compos Constr 6(2):73–87

CEN (2005a) Eurocode 2: design of concrete structures. part 1-1: general rules and rules for buildings. EN 1992-1-1. European Committee for Standardization, Brussels

CEN (2005b) Eurocode 3: design of steel structures. part 1-1: general rules and rules for buildings. EN 1993-1-1. European Committee for Standardization, Brussels

CNR (2007) Guide for the design and construction of concrete structures reinforced with fiber-reinforced polymer bars. CNR-DT 203/2006. National Research Council, Rome, IT

CSA (2012) Design and construction of building components with fibre-reinforced polymers. S806-17. CSA Group, Toronto, ON

CSA (2014) Canadian highway bridge design code (CAN/CSA S6-14). Canadian Standards Association, Mississauga, Ontario, Canada

FDOT (2018) Standard specifications for road and bridge construction. Florida Department of Transportation, Tallahassee, FL

fib (2007) FRP reinforcement in RC structures. Bullettin 40. Lausanne, CH, fédération internationale du béton

fib (2013) fib model code for concrete structures 2010. Wilhelm Ernst & Sohn, Berlin, DE

Gooranorimi O, Nanni A (2017) GFRP reinforcement in concrete after 15 years of service. J Compos Constr 21(5):04017024(1–9)

Gooranorimi O, Claure G, Suaris W, Nanni A (2018) Bond-slip effect in flexural behavior of GFRP RC slabs. Compos Struct 193:80–86

ICC (2016) Acceptance criteria for fiber-reinforced polymer (FRP) bars for internal reinforcement of concrete members. AC 454. International Code Council Evaluation Service (ICC ES), Brea, CA

Jawaheri HZ, Nanni A (2013) Reliability analysis of concrete beams internally reinforced with fiber-reinforced polymer bars. ACI Struct J 110:1023–1031

Keller ML, Shultz-Cornelius M, Pahn M (2017) Synergistic effects of alkaline environment on the behavior of GFRP bars under sustained load. In: 5th International conference on: durability of fiber reinforced polymer (FRP) composites for construction and rehabilitation of structures (CDCC-17). Sherbrooke, QC, pp 95–102

Minstroy (2018) Concrete structures reinforced with fibre-reinforced polymer bars, design rules. 295.1325800.2017. Ministry of Construction Industry, Housing and Utilities Sector, Moscow, RU

Mohamed HM, Benmokrane B (2014) Design and performance of reinforced concrete water chlorination tank totally reinforced with GFRP bars: case study. ASCE J Compos Constr18 (1):05013001-(1–11)

Montgomery KR, Bhide S, Freeby G (2017) The AASHTO LRFD bridge design specifications: section 5 reorganization. Aspire, the Concrete Bridge Magazine, Winter, pp 72–73

Nanni A (1999) Composites: coming on strong. Concr Constr 44:120

Nanni A, De Luca A, Jawahei Zadeh H (2014) Reinforced concrete with FRP bars. CRC Press Taylor & Francis Group, Boca Raton, FL

Nolan S, Nanni A (2017) Deployment of composite reinforcing - part 1: impetus for more widespread application in transportation infrastructure. Concrete International, May, pp 40–46

Nolan S, Rossini M, Nanni A (2018) Seawalls, SEACON and sustainability in the sunshine state. In: Transportation research board 97th annual meeting. Washington, DC

Perigny P, Robert M, Benmokrane B (2012) Creep rupture strength of V-Rod #3 GFRP reinforcing bars. University of Sherbrooke, Sherbrooke, QC

Rossini M, Bruschi E, Matta F, Poggi C, Nanni A (2018a) Case-specific parametric analysis as research-directing tool for analysis and design of GFRP-RC structures. ACI Spec Publ 327:34 (1–12)

Rossini M, Spadea S, Nanni A (2018b) Pedestrian bridge as clarifying example of FRP-RC/PC design. ACI Spring Convention. Salt Lake City, UT: American Concrete Institute (ACI)

Ruiz Emparanza A, Kampmann R, De Caso Y Basalo F (2018) State-of-the-practice of global manufacturing of FRP rebar and specifications. ACI Spec Pub 327:45(1–14)

Emparanza AR, Kampmann R, y Basalo FDC (2017) State-of-the-practice of global manufacturing of FRP rebar and specifications. In: The 13th international symposium on fiber-reinforced polymer reinforcement for concrete structures, American Concrete Institute, Anaheim, CA

SAC (2010) Technical code for infrastructure application of FRP composites. GB 50608-2010. Standardization Administration of China, Beijing, CN

Sayed-Ahmed M, Hajimiragha B, Hajimiragha B, Mohamed K, Benmokrane B (2017) Creep rupture and creep behaviour of newly third generation GFRP bars subjected to sustain loads. In: Fifth international conference on durability of FRP composites (CDCC 2017). Sherbrooke, QC

Spadea S, Rossini M, Nanni A (2018) Design analysis and experimental behavior of precast double-tee girders with CFRP strands. PCI J 63(1):72–84

Spagnuolo S, Meda A, Rinaldi Z, Nanni A (2018) Curvilinear GFRP bars for tunnel segments applications. Compos B 141:137–147

SRG for Strengthening Reinforced Concrete: From Laboratory to Field Applications

P. Casadei[1(✉)] and P. Girardello[2]

[1] Product Manager of the Strengthening Division, Kerakoll Spa, Sassuolomodena, Italy
paolo.casadei@kerakoll.com
[2] Product Specialist of the Strengthening Division, Kerakoll Spa, Sassuolo, Modena, Italy

Abstract. Fiber-Reinforced Cementitious Matrix (FRCM) composites are becoming a wide-spread technology for the rehabilitation and strengthening of reinforced concrete structures due to some advantages that allow them to be a suitable alternative to Fiber-Reinforced Polymer (FRP) composites. In this work, a new family of FRCM composites system made of ultra-high strength steel cords installed with inorganic mortars named Steel Reinforced Grout (SRG) is presented. This paper briefly introduces to the main properties and mechanical characteristics of SRGs, and introduces a case study on a reinforced concrete structures demonstrating the effectiveness of this strengthening solution

Keywords: SRG · UHTSS steel fibers · Reinforced concrete · Strengthening · Seismic retrofit

1 Introduction

Recent seismic events in Italy, starting from the earthquake of L'Aquila in 2009, then the Emilia earthquake in 2012 and the most recent ones happened this summer and few months ago in central Italy have shown the vulnerability of reinforced concrete (RC) structures. Most of the existing building inventory in Europe was designed according to building codes and guidelines that did not take into account seismic loads and when eventually they did, the knowledge towards seismic loads showed how existing codes were still too conservative. If in addition to such considerations, we take into account that most of existing structures have not undertaken any major refurbishment since they were built, we immediately realize in what danger we live every day when we happen to go to an hospital, our kids go to school or simply we go home, and spend time with our loved ones. Till 20 years ago, and in many cases still today, engineers and architects, when intervening on existing structures, were forced to interrupt the use of a structure because available technologies were very invasive and most important among all, were forcing to long times of construction connected to the large use of reinforced concrete, heavy steel plate bonding and section enlargement, the only technologies available to improve the structural performance of any type of building. Composite materials, made of very strong fibers immersed in an epoxy matrix knowns as Fiber Reinforced Polymer (FRP), entered the construction industry in the

M. di Prisco and M. Menegotto (Eds.): ICD 2018, LNCE 42, pp. 445–457, 2020.
https://doi.org/10.1007/978-3-030-23748-6_35

late 80's, and showed rapidly their great performance thanks to their excellent strength to weight ratio and relatively ease and rapid installation times compared to the above well-established techniques. Over the years FRP have met an increasing consensus at both the academic and industrial levels. In civil engineering, the application of these composites, mainly employing carbon or glass fibers, has emerged as a competitive alternative to traditional techniques, and their success it's witnessed by the adoption of specific design guidelines in Europe, USA and Japan. The growing interest towards the development of new effective and cost efficient solutions has recently led to the development of innovative techniques that make use of other materials in lieu of carbon or glass. Among them, composites made with steel textiles have emerged as one of the most promising ones. These systems consist of Ultra-High Tensile Strength Steel (UHTSS) galvanized micro wires twisted in cords, assembled parallel to each other to form unidirectional fabrics. Originally developed for the reinforcement of automobile tyres, they have been first proposed for civil engineering applications in 2002 to strengthen RC beams in bending (Casadei et al. 2005). Like FRPs, steel textiles can be externally bonded to the substrate via wet lay-up, by using either epoxy resin, obtaining a composite known as Steel Reinforced Polymer (SRP). Alternatively, they can be impregnated with an inorganic matrix to yield SRG (Steel Reinforced Grout).

In recent years, innovative materials were developed in order to find a suitable alternative to traditional fiber reinforced polymer (FRP) composites. Steel reinforced polymer (SRP) and steel reinforced grout (SRG) polymers attracted the attention of the scientific community due to the employment of low-cost high-strength steel fibers as an alternative to traditional carbon, glass, or aramid fibers. SRP and SRG systems consist of high-strength steel fibers embedded in a thermosetting epoxy matrix or inorganic mortar matrix, respectively. The available literature is mainly focused on the study of SRP systems, and a large number of experimental works were performed to investigate the bond performances of SRP to a concrete substrate (Santandrea et al. 2016; Napoli et al. 2016), the confinement of concrete members (El-Hacha and Mashrik 2012), and the behavior of RC beams strengthened with SRP composites to increase the flexural performance (Wobbe et al. 2004; Casadei et al. 2005; Pecce et al. 2006). Since SRG systems are able to overcome some drawbacks related to SRP composites, offering several advantages such as higher vapour permeability and resistance to high temperatures without compromising bond with the substrate and overall performance of the composite system, they recently captured the interest of the scientific community.

In the past 10 years this new family of composite materials has shown the be effective, durable and more cost efficient respect to the most known FRPs, making it the best available solution, not only to strengthen and repair existing structures, but also to improve their seismic performance. SRG are making structures able to better withstand any sort of dynamic loads, rather simplifying the job site and transforming FRP's technology, so far available only for experienced and special workers, to be used also from traditional contractors. The paper describes the use of both strengthening techniques through case studies.

2 Material Properties

2.1 UHTSS Galvanized Steel Fiber Sheet

The SRGs composites consist of steel fibers embedded in an inorganic mortar matrix. The steel fibers (cords) are in the form of a unidirectional sheet made of ultra-high tensile galvanized twisted steel filaments (UHTSS) held together by a glass fiber micro-mesh (Fig. 1). Each micro-cord is comprised of five filaments. Three out of the five filaments are straight, and the remaining two filaments are wrapped around the other three with a high torque angle. The cross-sectional area of the cord is 0.538 mm^2. The elastic modulus, the tensile strength, and the ultimate strain of the fibers are equal to 190 GPa, 3000 MPa and 2%, respectively. Filaments and cords are manufactured according to ISO 17832 standard which describes manufacturing techniques and reference parameters.

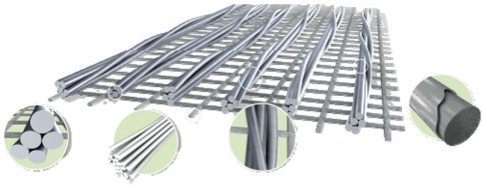

Fig. 1. UHTSS galvanized steel fiber sheet.

The twisting of the filaments allows some mechanical interlock between the cords and the matrix, and may induce an overall ductile behavior upon stretching as a consequence of the unwinding of the three twisted cords around the two linear ones, and yielding in the upper part of the curve as reported in **Error! Reference source not found**. The cords are galvanized making the material free of any corrosion and suitable for different kind of environmental exposure depending on the matrix chosen (Fig. 2).

Zinc coating is governed by EN 10244-2 and typical mass of zinc is greater than 15.97 g/m^2. In Fig. 3 is reported a SEM image of the filament magnified 40× times to determine thickness as well as mineralogy of the zinc coating for quality control purposes. Current standards require that the SRG system shall resist till 3000 h under complete immersion in ocean water as per ASTM D 1141-98 and ASTM C 581-03.

Steel fiber sheets are available in four different densities based upon the spacing with the cords (Fig. 4).

Lower densities, 1.57 and 3.14 cords per cm, are the one suitable for mineral matrices while higher densities, 4.72 and 7.09 cords per cm, can be installed only with epoxy matrices (Kerakoll S.p.a. 2016). SRG presents several advantages respect to traditional FRP composites systems: being made of high strength steel cords, makes them have a considerable shear strength when cords are subjected to stresses perpendicular to their development, not present in other types of fiber. This property makes them particularly attractive for column wrapping and also for easily realizing mechanical anchors/spikes, pro-hibitive with typical FRP strengthening solutions. Simply cutting the mesh on which cords are glued, allows to directly anchor the end of an SRG strip.

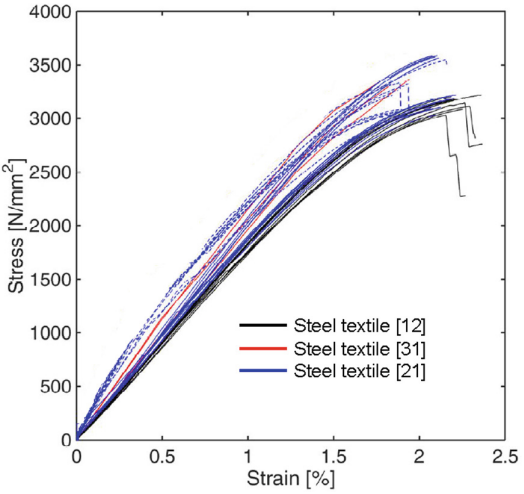

Fig. 2. Stress-strain tensile response curves of dry textile.

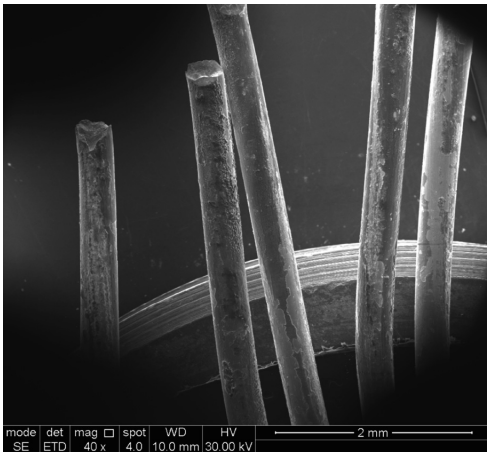

Fig. 3. SEM image of the single filament

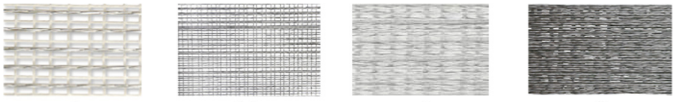

Fig. 4. Four different densities of steel fiber, cords per cm: (a) 1.57, (b) 3.14, (c) 4.72 and (d) 7.09

2.2 Inorganic and Epoxy Matrix

The choice of the matrix is based upon the type of substrate where bonding the composite material. A inorganic mortar matrix (GeoLite) is chosen for the strengthening of RC elements. This matrix forms a monolithic conglomerate that will surround, protect and strengthen RC works without the need to apply several layers (Kerakoll S. p.a. 2016). The even greater result is that such matrix can be also used for general purpose applications on RC elements, so making this new technology even more appealing thanks to the great reduction in material costs as well as ease of application so avoiding the need of specialty contractors to do the job. As already mentioned before, for higher densities of the steel fiber sheet, an epoxy matrix (Geolite Gel) has to be used.

Table 1 reports typical mechanical properties of the matrices.

Table 1. Mechanical properties of the matrices

Material	Compressive strength	Flexural tensile strength	Modulus of elasticity	Adhesive bond
	MPa	MPa	MPa	MPa
GeoLite	55	10	25000	2
GeoLite Gel	75	30	5300	4

3 Structural Behaviour and Research Studies on SRG

Several research studies have been carried out on SRG systems in the last fifteen years. Fundamental mechanical properties (tensile behavior), durability and shear bond performance on concrete substrates have been investigated through tests on small-scale specimens. Medium/large-scale tests have been per-formed on structural members to study the effectiveness of SRP and SRG for strengthening RC beams in bending and shear, confining of RC columns, beam column joint. Fiber sheets with different densities were considered in these tests, and are referred to as low density (LD), medium-low density (MLD), medium density (MD), and high density (HD) of steel fibers. The fiber density is equal to 0.157 cords/mm, 0.236 cords/mm, 0.314 cords/mm, and 0.472 cords/mm for LD, MLD, MD, and HD fiber sheets, respectively. The equivalent thickness of the fibers is equal to 0.084 mm, 0.126 mm, 0.169 mm and 0.254 mm for LD, MLD, MD, and HD fiber sheets, respectively.

3.1 Small Scale Specimens

The SRG-to-substrate bond performance is of primary importance for the effectiveness of externally bonded reinforcements. The bond performances of SRG composites bonded to a concrete substrate were studied by Santandrea et al. (2016) using a single-lap shear test set-up. A number of experimental tests were carried out on concrete prisms specimens having the same nominal dimensions equal to 150 mm (width)

150 mm (depth) × 600 mm (length). Concrete prisms were strengthened applying an SRG strip to the substrate with single-lap schemes, using three different densities of the fiber sheets (LD, MLD, and MD) embedded in the inorganic mortar. The direct shear test set-up was adopted in order to reproduce a Mode II loading condition. The bonded area started approximately 35 mm far from the top edge of the specimen in order to avoid spalling of the concrete prism. For all tests, the bonded width was equal to 50 mm while the bonded length varied from 200 mm to 450 mm. The classical push pull configuration was adopted, where the steel fibers were pulled, while the concrete prisms were restrained by a steel framework. Direct single-lap shear tests were conducted in displacement control. Figure 5 shows a bi-dimensional sketch of the test set-up. Test results are reported in Table 2 that provides for each specimen the geometrical characteristic of the reinforcement, the density of the fiber sheets, and the failure mode. The stress-global slip response of specimens strengthened with LD steel fibers is characterized by an initial linear portion, followed by a non-linear branch before the peak load of 3074 MPa is reached. The failure is characterized by the rupture of the steel fibers (FR) that reach their tensile strength, while the stress-global slip response shows an always-increasing behavior up to the peak load. The stress-global slip responses of specimens strengthened with MLD and MD steel fibers show a plateau after the non-linear branch of the stress-global slip response. The failure mode for these specimens is the delamination (MR) of the external layer of matrix from the internal one. It can be observed that for specimens strengthened with LD steel fibers a bonded length equal or longer than 200 mm is enough to reach the maximum capacity of the strengthening system that coincides with the rupture of the fibers. The increase in the density steel fibers causes a change in the failure mode and a decrease in the peak stress reached by the fibers at failure. Specimens strengthened with MLD steel fibers reached an average peak stress equal to 1807 MPa, while specimens strengthened with MD steel fibers reached an average peak stress equal to 941 MPa.

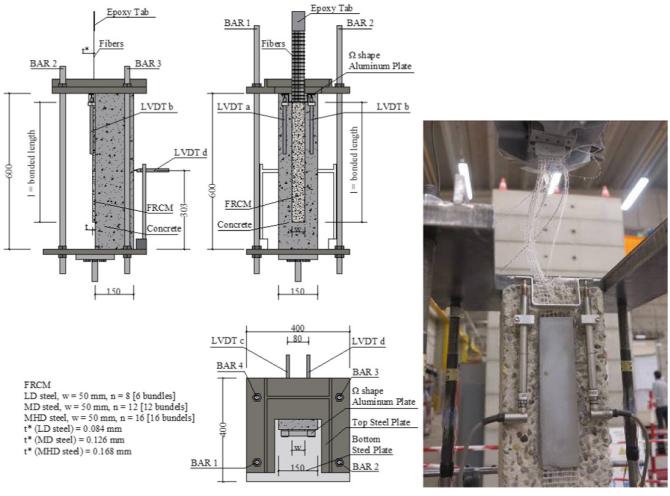

Fig. 5. Single-lap shear test.

Table 2. Bond test results

Density of steel fibers	Number of specimens	Bonded length mm	Bonded width mm	Failure mode
LD	3	200	50	FR
MLD	3	450	50	MR
MD	4	450	50	MR

3.2 Concrete Medium-Large Scale Specimens

The experimental results on reinforced concrete strengthening with SRG on beams (four-point bending test) and beam-column joints (cyclic tests) have allowed verifying the good performance exhibited by SRG systems which have shown strength increases comparable to those obtained from companion specimens strengthened with SRP. The flexural behavior of RC members was investigated by Napoli and Realfonzo (2015) carrying out four-point bending tests (Fig. 6) on RC beams externally strengthened with SRG composites, employing 1 or 2 layers of LD and HD fiber sheets. The ratio among the height and the width of the beam cross-section ranged between 0.50 and 1.50. The geometrical ratio of external reinforcement, ρ_f was scattered and varied from 0.021% to 0.127%, while the external/internal tensile reinforcement ratio, η, varied from 4.28% to 25.89%. The specimens had a value of the equivalent reinforcement ratio, ρ_{eq}, within the range 0.51–0.70%. The effectiveness of SRG composites for the flexural strengthening of RC beams was investigated by comparing the experimental load-deflection response of the strengthened beams with the response of the control beams, mainly in terms of peak load, stiffness, and deflection capacity. The main test results are presented in Table 3 that reports the information about the strengthened beams, together with the height, h, and width, b, of the cross-section, the net span, L, the number of composite layers, n_f, the percentage increase of the peak load, IF, and the failure mode. The load-carrying capacity of the strengthened beams was always higher than the load-carrying capacity of control specimens. The strengthened beams had a slightly larger initial stiffness and post-cracking stiffness when compared with control beams. For all strengthened beams, the debonding of the composite or the rupture of the fibers was associated with a rapid reduction in the applied load and, after that point, the load response continued following the load response of the unstrengthened beam. The failure mode for the beam strengthened with one layer of LD fiber sheets was the rupture of the fibers (FR), while for beams strengthened with 2 layers of LD fiber sheets or with 1 or 2 layers of HD fiber sheets the failure always occurred at the fiber-matrix interface (ID) with the detachment of the external layer of matrix from the internal layer. Both for LD and HD fiber sheets, the increase of the number of layers corresponded to an increase of the load-carrying capacity. Specimens strengthened with HD fiber sheets showed higher values of the load-carrying capacity when compared with beams with LD fiber sheets (Table 3).

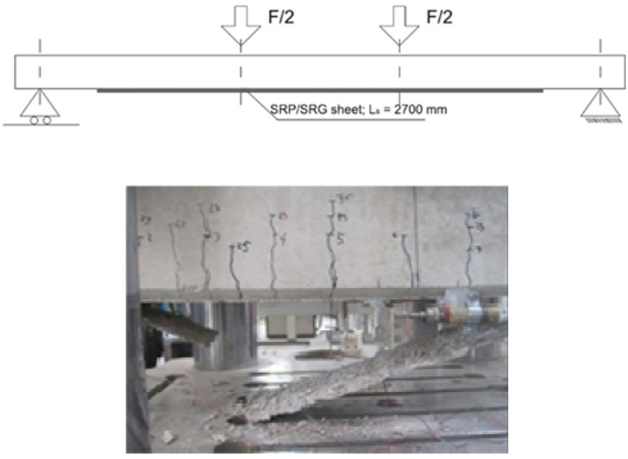

Fig. 6. (a) Sketch of the four-point bending set-up; (b) Failure mode FR.

Table 3. Four-points bending test results

Density of fibers	b mm	h mm	L mm	ρ_f	n_f	IF %	Failure mode
LD	400	200	3.4	0.021	1	36.8	FR
LD	400	200	3.4	0.042	2	51.9	ID
HD	400	200	3.4	0.064	1	53.8	ID
HD	400	200	3.4	0.064	1	55.3	ID
HD	400	200	3.4	0.064	1	42.1	ID
HD	400	200	3.4	0.127	2	93.6	ID
HD	203	305	2.438	0.063	1	11.1	ID
HD	203	305	2.438	0.063	1	11.2	ID

The most significant results was provided by tests conducted on beam-column joints, since the ultimate performance at failure of the strengthening system, showed not only a great increment in load but most of all a significant increase in ductility without sudden rupture of the composite SRG system like commonly experienced with CFRP-GFRP wrapping. The cyclic response of RC beam-column joints strengthened with SRG systems was investigated by De Vita et al. (2017). Seven specimens, designed to be representative of existing beam-column subassemblies with inadequate seismic details and made of medium-low concrete compressive strength, were tested. Specimens were comprised of 2000 mm long columns with 300 mm × 300 mm cross-section, and 1700 mm long beams with 300 mm × 400 mm cross-section. The presence of secondary beams, providing a confining action to the joint, was simulated by 300 mm long members with 300 mm × 300 mm cross-section. Columns were longitudinally reinforced by using 8 Ø14 deformed steel rebars whereas the main beams with 8 Ø20 in both members, the transverse reinforcement consisted of Ø8 steel stirrups, 100 mm spaced. The secondary beams were reinforced with 4 Ø20 crossing

the joint zone. Out of seven, one joint was unstrengthened and used as control specimen, while the others were strengthened with SRG systems. SRG systems employed HD fiber sheets. Two strengthening layouts were studied, which differed for the arrangement of fiber sheets on the joint panel (named "cross" or "diagonal" layout) as showed in Table 4. During the test, the column was mounted horizontally and subjected to a constant axial load of 295 kN. The horizontal force was cyclically applied in displacement control to the main beam. Figure 7 depicts the typical cyclic behavior of the SRG-strengthened specimens. The main test results are presented in Table 4 that shows information about the strengthening layout, the peak lateral forces applied to the beam in the two directions of loading and corresponding displacements and the beam displacements exhibited at the conventional collapse ($\Delta_{85\ \%}$). SRG strengthened specimens generally provided a good performance with respect to the unstrengthened member, with a less degrading post-peak behavior (mainly when the "cross" pattern is employed). The full exploitation of the external strengthening was limited by the slip of the main beam's longitudinal reinforcement (Table 5)

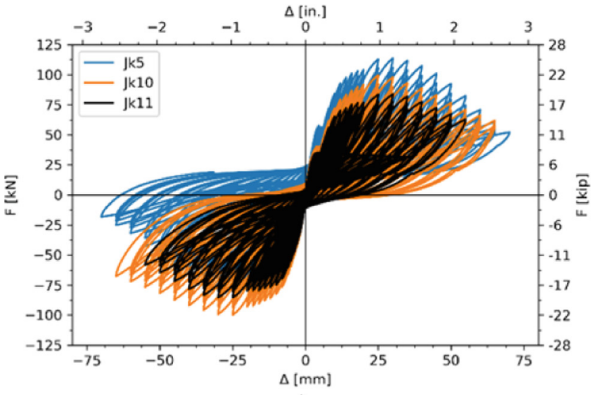

a)

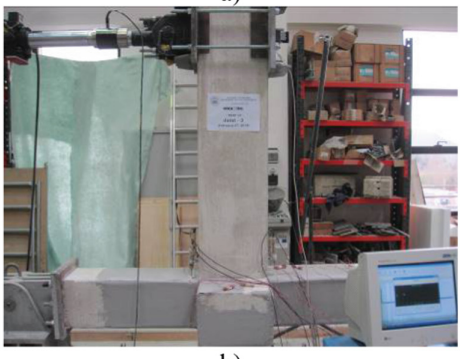

b)

Fig. 7. Cyclic tests on beam-column joints: (a) Load-displacement cyclic curves; (b) Test set-up.

Table 4. Beam-column joints results.

Layout	F^+max	F^-max	Δ^+	Δ^-	$\Delta^+_{85\%}$	$\Delta^-_{85\%}$
	kN	kN	mm	mm	mm	mm
–	84.8	−84.3	31.4	−23.6	46.2	−44.28
+	88.1	−80.1	26.5	−23.4	39.3	−43.8
x	114.6	−78.6	31.1	−23.9	47.5	−41.0
+	153.7	−82.3	36.5	−28.4	53.5	−47.2
+	100.5	−98.8	26.2	−23.7	43.7	−47.1
+	98.1	−86.1	30.9	−29.0	50.6	−53.3
+	99.1	−76.3	26.4	−28.5	57.1	−60.1

4 Case Study

The following case study represents, among many, a typical SRG applications on seismic upgrade and strengthening on a reinforced concrete structure performed in Italy. The reinforced concrete structure presented in this work, is an example of renovation of industrial facilities where structural members, floor systems and columns, where highly damaged and mainly needed to restore their initial performance. In this case study, higher compatibility with substrates, vapor permeability, ease and speed of installation associated with lower cost of intervention without compromising structural performance so far guaranteed by epoxy matrices, made SRG the only possible solution to be adopted by engineers and appreciated by contractors and owners.

4.1 Ex Multedo Foundry, Industrial Facilities - Genova

It was one of the last abandoned industrial buildings in the west part of Genova. Designed in 1917 by Adolfo Ravinetti, the Multedo foundry was originally articulated in three volumes covering an area of about 13'000 square meters. In the first post-war new buildings were added until reached a total of 25'000 square meters. Close in the 60s, since 2009 present an environmental restraint (Fig. 8). The structural restoration project started in the 2015 following the necessity to give new birth to the structure to

Fig. 8. Ex Multedo foundry.

Table 5. Summary of experimental test results

RC beams (four-point bending test)	From 37% to 97% (SRG) From 27% to 106% (SRP)
RC beam-column joints (cyclic test)	From 4% to 81% (SRG)
Note: % increase with respect to un-strengthened specimen	

become a commercial mall, and regarded the RC columns and the deteriorated RC floors in the office building. A linear finite element model was developed to study the behavior of the structure and the outcome of the analysis was compared with limitations given in relevant standards. Based on this analysis the most suitable retrofitting techniques was selected for the construction. It was adopted a SRG technology realized with different density of ultra-high tensile galvanized steel filaments (UHTSS) and a

Fig. 9. Flexural strengthening of beams and slabs.

inorganic matrix to repair and strengthen all structural elements. The great advantage of implementing SRG systems respect to traditional FRPs was due to the high thickness of repair mortar needed to first restore section geometry. The SRG confinement of columns, by means of wrapping, generated an increase of ultimate capacity and deformation for members under concentric or slightly eccentric axial loads; ductility and flexural capacity under combined bending and axial load, was provided when SRG sheets were installed also along the longitudinal axis of the member. On the structural floors, flexural strengthening was necessary on the small beams subjected to bending moment larger than the corresponding actual flexural capacity. Flexural strengthening with SRG materials were applied to the tension side of the member to be strengthened with one or more layers of SRG sheets (Fig. 9).

5 Conclusions

Since the use of UHTSS galvanized steel fiber sheets in civil engineering was proposed in 2004, a number of research studies have been carried out to investigate their mechanical properties and their effectiveness as externally bonded reinforcements for structures. SRGs offer ease and rapidity of installation, short curing durations and versatility. The comprehensive and systematic review of the experimental investigations and case histories carried out so far, on RC structural members retrofitted with SRG, demonstrates the effectiveness, cost efficiency and reliability of this solution for improving the load-carrying capacity of structures (which may be required to comply with increased load demand), safeguarding against deterioration and exceptional loads, and enhancing their resilience to natural hazards, such as earthquakes. Single-lap shear tests showed that using LD fiber sheets the rupture of the fibers is reached, while using MLD, MD and HD fiber sheets the failure consisted in the debonding at the matrix-fiber interface. Confinement tests showed that SRG jackets provide an increase of the maximum load with respect to control specimen and that sharp corners are not detrimental when steel fibers are employed. The load-carrying capacity of beams strengthened with SRG was always higher than the one of control beams. The increase of the number of SRG layers corresponded to an increase of the load-carrying capacity. Beams strengthened with HD fiber sheets showed higher values of the load-carrying capacity when compared with beams with LD fiber sheets. Cyclic tests on RC beam-column joints showed that specimens strengthened with SRG systems have a less degrading post-peak behavior. Tensile tests on SRG coupons showed the classical three linear behaviour. Therefore, research outcomes indicate that SRG can be included with full rights amongst the composite reinforcements with inorganic matrix for the externally bonded retrofitting of structures and that existing design tools can be suc-cessfully used by practitioners for the strengthening design.

Acknowledgements. The authors would like to thank all university, professor, licensed architects, engineers and specialty contractors who have tested, designed and installed the strengthening solutions presented this paper.

References

Casadei P, Nanni A, Alkhrdaji T, Thomas J (2005) Performance of double-t prestressed concrete beams strengthened with steel reinforced polymer. Adv Struct Eng 8(4):427–442

De Vita A, Faella C, Napoli A, Realfonzo R (2017) Cyclic response of R/C beam-column joints strengthened with steel FRP/FRCM composite materials. In: Proceedings of the XVII Convegno ANIDIS - L'Ingegneria Sismica in Italia. Pistoia, pp 17–21

El-Hacha R, Mashrik MA (2012) Effect of SFRP confinement on circular and square concrete columns. Eng Struct 36:379–393

Kerakoll S.p.A.: www.kerakoll.com. Accessed Feb 2016

Napoli A, Realfonzo R (2015) Reinforced concrete beams strengthened with SRP/SRG systems: experimental investigation. Const Build Mat 93:654–677

Napoli A, de Felice G, De Santis S, Realfonzo R (2016) Bond behaviour of steel reinforced polymer strengthening systems. Compos Struct 152:499–515

Pecce M, Ceroni F, Prota A, Manfredi G (2006) Response prediction of R/C beams externally bonded with steel reinforced polymers. J Compos Constr 103(2):195–203

Santandrea M, Imohamed IAO, Jahangir H, Carloni C, Mazzotti C, De Miranda S, Ubertini F, Casadei P (2016) An investigation of the debonding mechanism in steel FRP- and FRCM-concrete joints. In: 4th Workshop on the new boundaries of structural concrete. pp 289–298

Wobbe E, Silva P, Barton BL, Dharani LR, Birman V, Nanni A, Alkhrdaji T, Thomas J, Tunis G (2004) Flexural capacity of RC beams externally bonded with SRP and SRG. In: Proceedings of society for the advancement of material and process engineering 2004 symposium

Technology and Construction Techniques

GFRP Reinforcement for Segmental Linings of Mechanized Tunnels

A. Meda[1], M. Moja[2], E. M. Pizzarotti[2(✉)], and G. Vago[3]

[1] University of Rome Tor Vergata, Rome, Italy
[2] Pro Iter Srl, Milan, Italy
enrico.pizzarotti@proiter.it
[3] ATP Compositi S.r.l, Angri, Italy

Abstract. The use of Glass Fibre Reinforced Polymer (GFRP) reinforcements is gradually spreading to replace or to integrate the traditional steel rebar for tunnels excavated with shielded TBMs and lined with precast segmental lining. The complete replacement of the steel rebar with GFRP is particularly used for segments that should be demolished after their installation, for example for cross-passages or niches realization. GFRP reinforcement cages placed on segments' edges can play an important role to limit the number of cracks and local breakages caused by impacts and unforeseen load conditions, mainly before and during the lining installation. The analyses' results on a 3D model, which allowed to consider the contribution of such reinforcements both during the lining erection and the service, show that they can increase the lining strength. Moreover, GFRP perimetric cages can be coupled with steel fibre reinforcement (SFRC) to increase the overall flexural and local resistance of segments. Examples of dimensioning and results of laboratory tests carried out to show the GFRP reinforcement effectiveness are reported.

Keywords: Glass Fibre Reinforced Polymer (GFRP) · Steel fibre reinforcement (SFRC) · Segments · Laboratory tests

1 Introduction

Using the GFRP rebar instead of the traditional steel one for precast segmental lining of TBM tunnels could be worth in the following cases:

- Portions of tunnel to be demolished: the easier demolition, combined with the high mechanical strength, represents an important property of the GFRP reinforcement. There are several examples of GFRP application in linings to be totally or partially demolished, e.g. realization of niches or lateral cross-passages, as for "soft-eye" solutions for TBM breakthrough diaphragms.
- Durability increase: the life-time of underground works is nowadays pushed to more than 100 years, up to 200. The application of GFRP reinforcements, resistant to the most corrosive environments, could offer a valid alternative to steel, the latter requiring very thick concrete protection in corrosive environments, penalizing the structural resistance especially in case of segment's thin thicknesses.

M. di Prisco and M. Menegotto (Eds.): ICD 2018, LNCE 42, pp. 461–473, 2020.
https://doi.org/10.1007/978-3-030-23748-6_36

- Electrical insulation: the dielectric resistance, typical of GFRP products, represents a valid and interesting solution for segmental reinforcement, especially in railway tunnels in urban areas, where the countermeasures normally adopted are often not completely safe in terms of electrical insulation and cathodic protection. Moreover, traditional solutions are expensive and difficult to maintain; an effective interruption of the conductivity of the segments reinforced with steel (dielectric joint) can be obtained by placing at regular intervals rings reinforced entirely with GFRP.

GFRP reinforcements are particularly recommended for sewer tunnels realization. In these cases, the reinforcements corrosion issue has to be considered also at intrados. When the traditional steel reinforcement is adopted, a special coating protection or a stainless-steel reinforcement is often used to cope with the chemical corrosion and durability problems respect to the internal liquids and to external environment. These two solutions are both extremely expensive. A GFRP reinforcement, being resistant to corrosion, would be technically and economically convenient.

The GFRP reinforcement can also be used to integrate the steel rebar cage and increase the resistance of lining parts subjected to shocks or stress concentrations, at corners and edges. These areas, due to the high concrete cover and to the steel rebar bending, are characterized by a non-well reinforced concrete thickness and, consequently, they are more exposed to cracking and local damaging (Fig. 1).

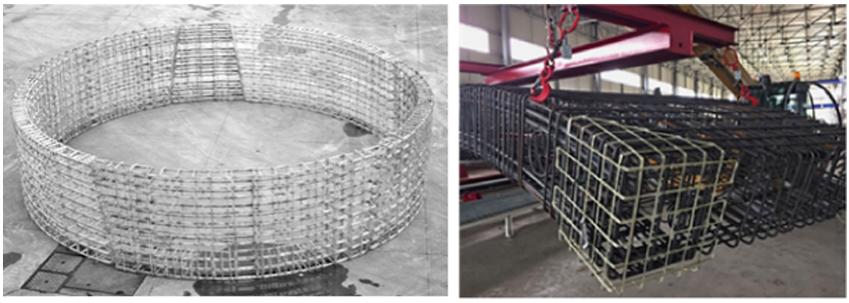

Fig. 1. Full GFRP reinforcement and GFRP edge reinforcement.

Last but not least, the coupling of perimetric GFRP cages with steel fiber reinforced concrete (SFRC) is proving to be extremely effective, since the GFRP rebar can take charge of local concentrated stresses (for example due to thrust jack forces or geometric defects) and fibers of diffuses stresses (given by service loads' axial forces and bending moments).

In this paper, the update of studies and tests (performed by Prof. A. Meda and Prof. Z. Rinaldi at TERC - Tunnelling Engineering Research Centre – University of Rome Tor Vergata) on GFRP reinforcements are presented compared to what has already been reported in Meda, Moja, Pizzarotti, Vago (2017).

Fig. 2. Perimetric GFRP reinforcement cage.

2 Design of GFRP Reinforcements Replacing or Integrating the Ordinary Steel Cage

The design of GFRP reinforced segments can be carried out by means of bending moment - axial force envelopes (M-N). For M-N envelopes definition, different guidelines can be followed (ACI 2006; CNR-DT 203 2007; Fib Bulletin 40 2007).

Regarding the concrete behaviour, the design is the same as ordinary steel reinforced concrete while the GFRP rebar behaviour differs significantly from the steel one. The GFRP rebar shows a linear-elastic behaviour up to failure. Following CNR-DT 203 2007, limits in terms of both strength and deformation should be imposed:

$$f_f = E_f \varepsilon$$

$$f_{fd} = \eta_a \eta_l \frac{f_{fk}}{\gamma_f}$$

$$\varepsilon_{fd} = 0.9 \eta_a \frac{\varepsilon_{fk}}{\gamma_f}$$

where f_{fd} e ε_{fd} are the design strength and ultimate deformation respectively; E_f is the average Young's modulus; η_a, η_l e γ_f are the environmental reduction factors ($\eta_a = 0.7$ for wet environment and $\eta_a = 0.8$ for dry environment), the long-term loading coefficient ($\eta_l = 1$ for provisional structures) and the partial safety factor for GFRP ($\gamma_f = 1.5$). Furthermore, no resistance of GFRP rebar in compression is considered.

Figure 3 show the results of a case study of the drawing of N-M envelopes for a GFRP reinforced segment with 12ϕ12 mm at the extrados and 12ϕ14 mm at the intrados.

The segments edges can often be subjected to cracking and/or breakages caused by collisions during transportation, handling and overturning, or by stress concentration during the thrust phase of the TBM, or even during service.

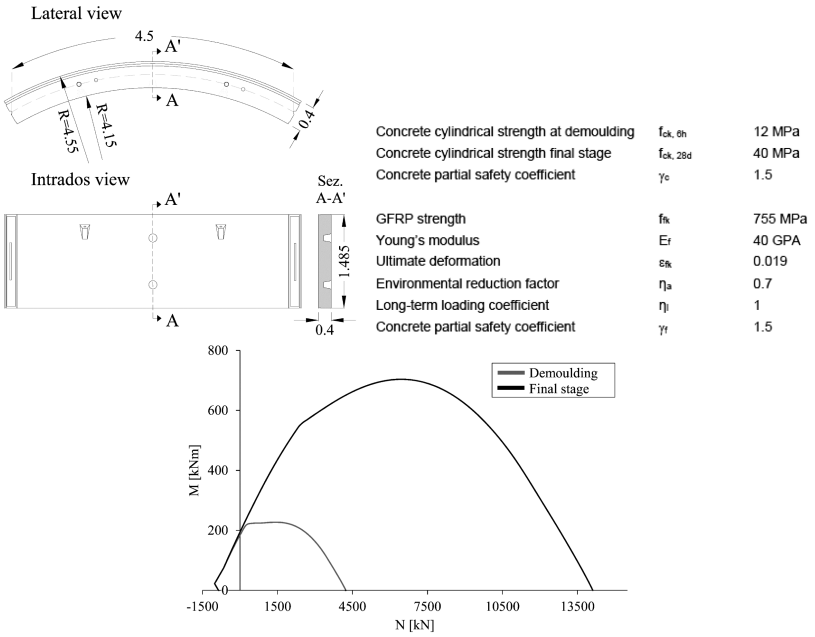

Fig. 3. Segment geometry and M-N envelopes at demoulding and at final stage.

The concrete compressive stresses and the resulting tensile stresses must be verified according to UNI EN 1992-1-1 (2005), DAUB (2013), Leonardt (1986) or by numerical methods. Knowing the distribution of tensile loads in the section, minimum reinforcement is defined taking into account the steel or the GFRP reinforcements strength properties. In any case, it is important to observe that the GFRP reinforcements can be positioned at a much lower distance from the segments' external surface than the steel ones. This leads to a drastic reduction of the cracks opening that, as well known, decreases with decreasing of concrete covers, and ensures an increase of the structure life.

3 Tests on Full GFRP Reinforced Segments

Full scale tests on GFRP reinforced segments have been performed. Two segments were tested under bending: one reinforced with steel rebar and the other with GFRP rebar. The geometry of the segment is illustrated in Fig. 3. More details of the full-scale tests can be found in Caratelli et al. (2016).

Figure 4 summarizes the results in terms of load versus deformation at mid-span curves. To verify the design method above proposed, the experimental results were compared with the M-N envelopes defined adopting the average strength of the materials. Figure 5 shows the obtained results.

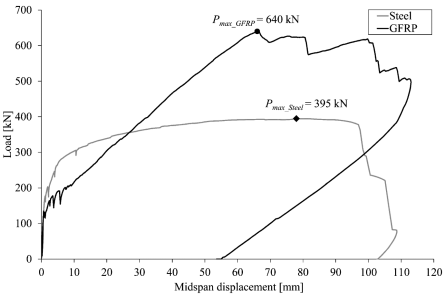

Fig. 4. Bending test results.

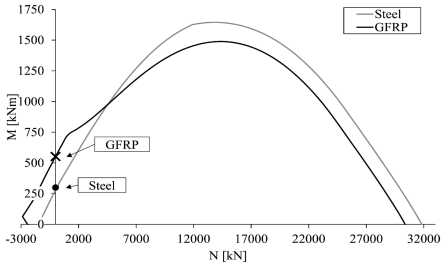

Fig. 5. Comparison between experimental result and analytical evaluation.

4 Flexural Tests on SFRC Segments and SFRC + Perimetric GFRP Cage

Flexural tests were performed on two different precast tunnel segments (thickness = 300 mm, Width = 1400 mm, External Diameter = 6400 mm): one with only SRFC reinforcement (40 kg/m^3 Dramix 4D 80/60BG L = 60 mm) and one also with a perimetric GFRP cage (Fig. 2). The average compressive strength of the concrete was 62.35 MPa; the tensile behaviour of SFRC was characterized through bending tests according to EN 14651 (Fig. 6).

Fig. 6. Bending test set-up and results

The bending tests were performed as illustrated in Fig. 7 in displacement control. During the test, the following measures were continuously registered: the load F, the midspan displacement, the crack opening at midspan (Fig. 8). Furthemore, the crack pattern was recorded at different steps with the help of a grid plotted on the intrados surface.

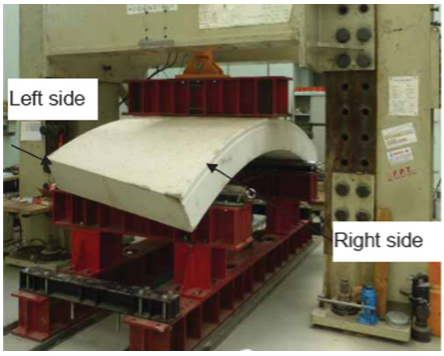

Fig. 7. Segment under bending test

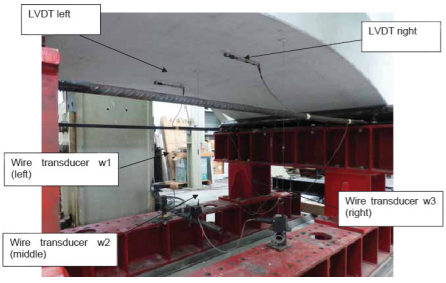

Fig. 8. Bending test instrumentation.

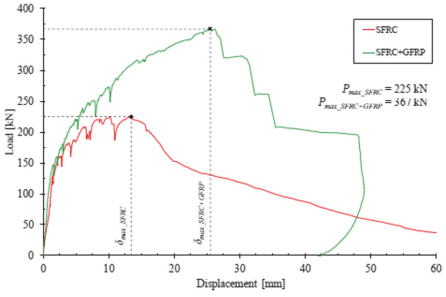

Fig. 9. Bending test: average displacement vs load: comparison between SFRC and SFRC + GFRP segments.

Table 1. Maximum crack widths (n/a = not available).

Loading							
Load [kn]	125	160	180	210	222	250	270
Crack n.	Crack width [mm]						
SFRC	<0.05	0.25	0.35	0.60	1.00	n/a**	n/a**
SFRC+FGR	<0.05	0.10	0.15	n/a*	0.35	0.45	0.70

The behavior of the segments SFRC and SFRC + GFRP are compared in Fig. 9 (average displacement vs load). In Table 1 the maximum crack widths at different load steps are compared.

The presence of the perimetric GFRP cage increases the maximum load from 225 kN up to 367 kN (63%) and reduces the crack width of more than 50%.

5 Concentrated Longitudinal Load Tests on SFRC Segments and SFRC + Perimetric GFRP Cage

The tests were performed on the same segments and with the same reinforcements described in the previous chapter, by applying three uniform concentrated loads up to 2670 kN by successive steps on the transversal face of the segment by adopting the same steel plates of the TBM (Fig. 10).

The SFRC and the SFRC + GFRP final crack patterns are shown in Figs. 11 and 12. In Table 2 the maximum crack widths are compared. The presence of the perimetric GFRP reduces the crack width of more than 33%.

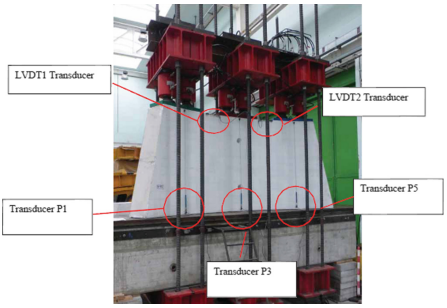

Fig. 10. Set up for concentred longitudinal load test.

On a damaged SFRC + GFRP segment already subjected to a test described above (crack pattern Fig. 12), a non-uniform support was also considered, since a gap of 5 mm was introduced (Fig. 13) on one side of the segment (surface not in contact for

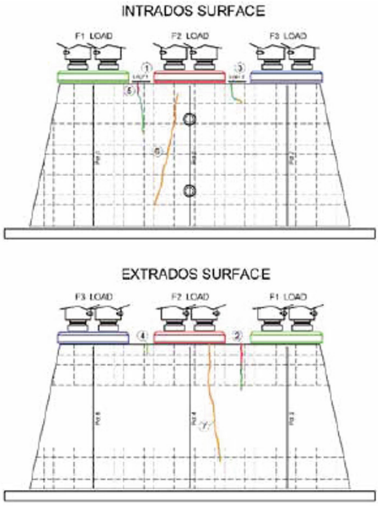

Fig. 11. SFRC – Crack pattern.

about one third of its length). In Fig. 14 the crack pattern at a load of 2260 kN for each steel plate is shown (note that from the load of 1250 kN the gap is closed and the segment gets in touch with the support). In this case, the maximum crack width is about 5 times the case with uniform support.

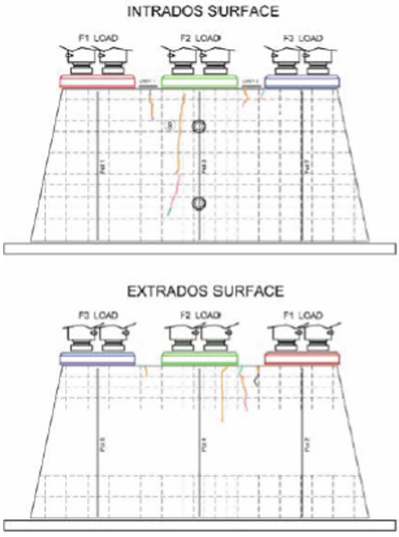

Fig. 12. SFRC + GFRP – Crack pattern.

Table 2. Maximum crack widths.

Load [Kn]				Unload [Kn]
	1st Crack	Service load	Unblocking thrust*	
Reinforcement	1250	1580	2670	0
	Maximum crack width [mm]			
SERC	0.05	0.10	0.40	0.15
SERC + GFRP	<0.05	0.05	0.25	0.10

Note: *For metro tunnel, TBM pushing capacity coincides with unblocking thrust

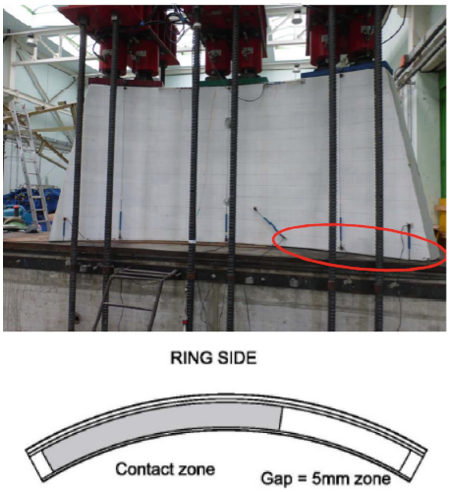

Fig. 13. Concentrated longitudinal load test with gap.

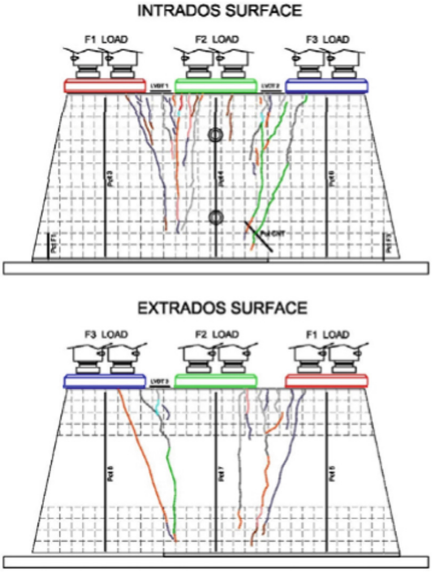

Fig. 14. SFRC + GFRP crack pattern. Load 2260 kN.

6 Lab tests and Models on GFRP Integrative Edges' Reinforcements

Test on GFRP integrative edges' reinforcement have been performed in two different configurations (Figs. 15 and 16). In both test's configuration, two or more blocks were tested: one reinforced only with steel rebar and the others also with GFRP integrative cage.

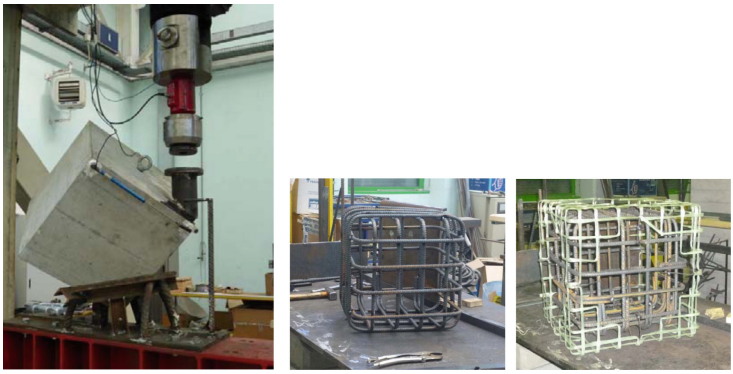

Fig. 15. Lab test (Configuration 1) and block's reinforcement cage.

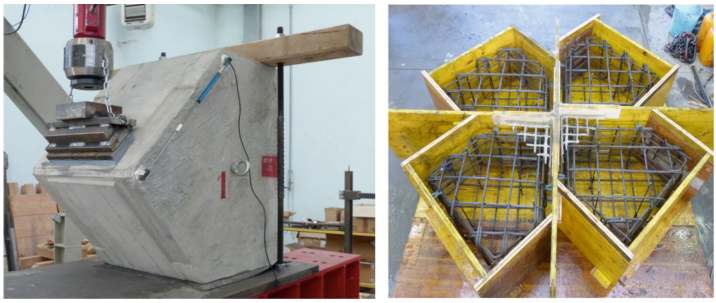

Fig. 16. Lab test (Configuration 2) and block's reinforcement cage.

Figures 17 and 18 summarize the results in terms of load versus deformation (S-RC = block reinforced with steel cage; G-RC = block reinforced with GFRP integrative cage).

The influence of GFRP reinforcement in the edges on the ultimate load of the lining has been also evaluated by 3D models schematizing multiple rings (Moja and Pizzarotti 2016). The longitudinal joints between segments are modelled by means of elastic-plastic springs reacting only under compression, while the transverse joints by means of "beam" type elements having the connectors' and concrete's stiffness (Fig. 19).

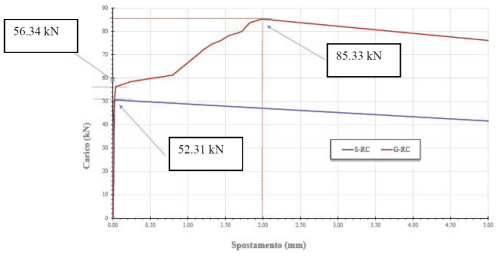

Fig. 17. Configuration 1 – Load displacement results.

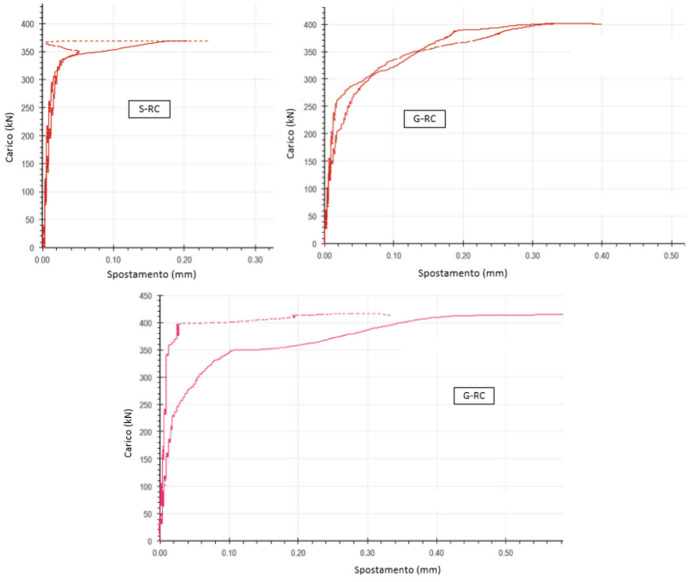

Fig. 18. Configuration 2 – Load displacement results.

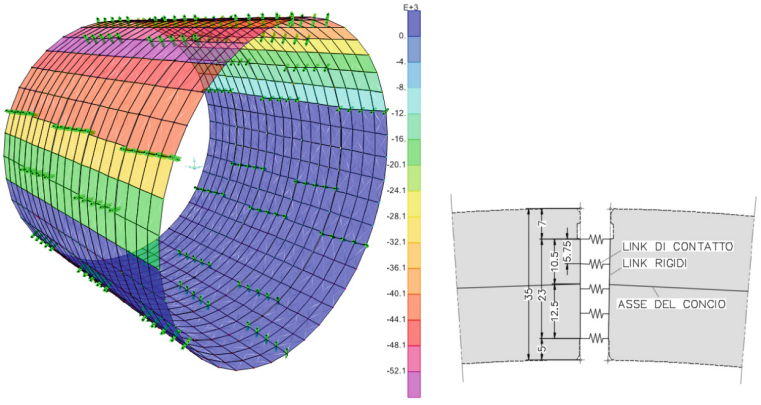

Fig. 19. FEA model scheme - Asymmetric load and longitudinal joints scheme

The models have been loaded with an almost uniform load schematizing the backfill pressure with an asymmetric load (Fig. 17) with variable entity to analyse the behaviour of the system and to define the limit load of the lining. Analyses have shown a concentration of loads at the segments edges with consequent breakage of the first link of the system right at the edge. A significant increase of the asymmetric limit load of the lining is noticed in case of GFRP reinforcement extended to the entire perimeter of the segment and not only at the corner.

Moreover, GFRP reinforcements produce beneficial effects in case of incorrect installation of the segments. If the contact between two segments is limited to only one corner - case that, though not desirable, may happen during the installation of the segments - the asymmetric limit load rises proportionally with respect to the "stress-strain" law assigned to the links that schematizes the joint, deducted from the laboratory tests previously illustrated.

It has also been demonstrated, at least for the hypothesized load conditions, that in presence of an asymmetric load not uniformly distributed along the tunnel axis, the reinforcement of the corners can be beneficial if extended to the total perimeter of the segment (Fig. 20).

Fig. 20. GFRP reinforcement extended to the total perimeter of the segment

7 Conclusion

The tests illustrated in this paper have shown the positive effects that a GFRP rebars cage can have on the behavior of a segment. The advantages are evident both in replacement of the steel cage and as an integration of it along the perimeter of the segment.

As indicated in the conclusion of the report 16 of ITA Working group 2, it has to be emphasized that localized stresses are better resisted by localized reinforcement while diffused stresses are better resisted by spread reinforcement. Therefore, from the static point of view, it's possible to conclude that the better solution to increase the overall flexural and local resistance of the segments could be the adoption of a spreaded reinforcement (SFRC) coupled with a rebars perimetric cage. Accordingly, it's important to note that the effectiveness of the perimetric cage of rebars is inversely proportional to its concrete cover. In this context, the use of GFRP rebars cages allows

to minimize the concrete cover respect the steel ones, maximizing the benefits for the structure.

References

ACI (2006) ACI 440.1R-06. Guide for the design and construction of concrete reinforced with FRP bars. ACI Committee 440, American Concrete Institute

ITA Working Group 2 Research: Report 16: twenty years of FRC tunnel segments practice

Caratelli A et al (2016) Precast tunnel segments with GFRP reinforcement. Tunn Undergr Space Technol 60:10–20

CNR DT 203 (2007) Guide for the design and construction of concrete structures reinforced with fiber-reinforced polymer bars. CNR Italian National Research Council

Fib Bulletin 40 (2007) FRP reinforcement in RC structures Fédération Internationale du Béton (fib). Lausanne, Switzerland

Moja M, Pizzarotti EM (2016) Scavo di gallerie con TBM scudate – Rivestimenti in anelli di conci prefabbricati in c.a. Giornata AICAP - Congresso CTE "Evoluzione e sostenibilità delle strutture in calcestruzzo", Roma, 27 October 2016

DAUB (2013) Recommendations for the design, production and installation of segmental rings. Deutscher Ausschuss für unterirdisches Bauen e. V. (DAUB) - German Tunnelling Committee (ITA-AITES)

UNI EN 1992-1-1 (2005) Eurocode 2 - design of concrete structures – part 1-1. General rules and rules for buildings

Meda A, Moja M, Pizzarotti EM, Vago G (2017) Armature en barre en fibre de verre pour voussoirs de revêtement des tunnels mécanisés. In: AFTES 15° Congrès International. Paris, 13–16 November 2017

On-Site Demonstration Project of Reinforced Concrete with Seawater

F. Bertola[1(✉)], F. Canonico[1], E. Redaelli[2], M. Carsana[2], M. Gastaldi[2], F. Lollini[2], F. Torabian Isfahani[2], and A. Nanni[3]

[1] Buzzi Unicem, Casale Monferrato, Italy
fbertola@buzziunicem.it
[2] Department of Chemistry Materials and Chemical Engineering "Giulio Natta", Politecnico Di Milano, Milan, Italy
[3] Department of Civil Architectural and Environmental Engineering, University of Miami, Miami, FL, USA

Abstract. Chloride-contamination of reinforced concrete (RC) structures, whether arising from the use of chloride-contaminated raw materials or from exposure to aggressive environments, results in corrosion of traditional steel reinforcement. For this reason, design standards worldwide limit the use of chloride-contaminated materials in cement and concrete production, without considering the related advantages in saving natural resources. The SEACON project aims at demonstrating the safe utilization of seawater and salt-contaminated aggregates for sustainable concrete production when combined with corrosion resistant reinforcement. For this purpose, a demonstration was built and exposed to an aggressive environment, with the aim of proving the feasibility of using such different technology to produce RC, and collecting data to evaluate durability aspects.

This paper shows the results achieved through laboratory investigations and the preliminary results of the on-site monitoring, with particular reference to the materials characterization.

Keywords: Concrete · Chloride · Corrosion-resistant reinforcement · Sustainability · Durability

1 Introduction

In October 2015, an international consortium of several industrial partners and academic institutions, led by the University of Miami, launched a two and a half-year project known as "Sustainable Concrete Using Seawater, Salt-contaminated Aggregates, and Non-corrosive Reinforcement", or SEACON (http://seacon.um-sml.com/), funded by the European "Infravation" research program.

The goal of SEACON is to advance the concrete industry by developing a less expensive, more durable, and more sustainable product, and reducing consumption of natural resources, replacing them with chloride-contaminated alternatives used in combination with corrosion-resistant reinforcement. This new approach will also

M. di Prisco and M. Menegotto (Eds.): ICD 2018, LNCE 42, pp. 474–486, 2020.
https://doi.org/10.1007/978-3-030-23748-6_37

extend the durability of the elements, even in harsh environmental conditions. The three targets of this research program are to:

- confirm, through experiments, that the presence of chlorides is not harmful to the properties of concrete (Bertola et al. 2017);
- verify, through laboratory investigations, the suitability of alternative reinforcements to traditional steel, such as GFRP and stainless steel, demonstrating the success of this technology by building two full-scale prototypes, both Italian and American (Rossini et al. 2008), and creating national and international user manuals or guidelines;
- verify impacts and costs of the implementation of SEACON technology through LCC and LCA (Iannicelli Zubiani et al. 2017; Redaelli et al. 2019).

At the end of 2016, the first prototype was built; the model, which consists of a culvert for discharging water from the nearby highway, should verify the effects that chlorides, which are present in the raw materials and also arrive in run-off water from the de-icing salts used on the road surface, have on the various types of structural reinforcement considered in the project.

This paper presents the activities related to the SEACON demonstration project: the preliminary laboratory activities performed, the different phases of construction, and the first values collected through on-site monitoring.

2 Materials and Mix Design

2.1 Materials

All the raw materials needed for the experimental investigation were selected and characterized.

As a binder, a limestone Portland cement (LPC), CEM II/A-LL 42.5R, was used, adding 30 kg/m^3 of fly ash to improve the density of the matrix, and thereby the durability of the whole system.

Natural aggregates were used; two siliceous sands (0–2 and 0–4 mm) and a gravel (4–12.5 mm) from the concrete batching plant (PC) were employed. In addition, a recycled asphalt pavement (RAP) aggregate was investigated in order to use it as partial substitution of natural aggregates. Water absorptions (a_w) and densities (d) measured, according to UNI EN 1097-6, of all the aggregates used are shown in Table 1.

Table 1. Physical tests on aggregates

Type of aggregate	a_w	d
	%	kg/m^3
Sand 0–5 mm	1.0	2650
Gravel 5–7 mm	0.84	2660
Gravel 8–15 mm	0.83	2660
RAP	0.3	2375

Fresh water and natural seawater, collected from the Mediterranean Sea near Cogoleto (GE, Italy), were used. Table 2 reports the elements contained in the waters, measured through ICP-OES, and the chloride content determined through titration, according to Mohr (Chloride in water) with $AgNO_3$.

Table 2. Analysis of fresh water and seawater through ICP-OES and titration (n.a. = not available)

Concentration	Fresh water	Seawater
	mg/l	mg/l
Al	<0.10	0.19
Ca	103	483
Fe	<0.10	<0.10
K	2.6	377
Mg	14	1455
Na	20	11766
S	12	1037
P	<0.10	<0.10
Li	n.a.	0.22
Si	8.9	0.68
Cl^-	71	20898

2.2 Mix Design

Three mix-designs were optimized through preparatory laboratory tests; a traditional concrete (Reference concrete), a concrete made with seawater as mixing water (SEACON concrete), and a concrete with RAP as partial substitution of coarse aggregates (RAP concrete) were designed, based on the best rheology achievable, in order to reach a desired compressive strength (40 MPa at 28 days of curing) and consistency class (S4 class, according to UNI EN 206 Standard - slump between 160 and 200 mm). A specific superplasticizer was selected, and a set retarding agent was used to compensate the known accelerating effect of chlorides (Ghorab et al. 1989). In Table 3, the mixture proportions for the three types of concrete are presented.

3 Demonstrator Activities

3.1 Construction Details

Considering that the final aim was to prove constructability and durability of a structure made with chloride-contaminated concretes combined with non-corrosive reinforcement, the demonstration project was a drainage culvert. To worsen the environmental conditions, the culvert was built along a motorway on which de-icing salts are used during winter; in this way, the concrete is periodically contaminated by chlorides coming from the run-off waters.

Table 3. Concrete recipes

Mix design	u.m.	Reference	SEACON	RAP
LPC	kg/m^3	335	335	335
Fly ash	kg/m^3	30	30	30
Sand 0–5 mm	kg/m^3	800	800	766
Gravel 5–7 mm	kg/m^3	365	365	246
Gravel 8–15 mm	kg/m^3	630	630	526
RAP	kg/m^3	-	-	226
Superplasticizer	kg/m^3	2.19	2.19	2.19
Retarding agent	kg/m^3	-	0.76	-
Water	l/m^3	175	-	175
Seawater	l/m^3	-	175	-

The project site is located along motorway A1 in Pontenure, Piacenza, in the asphalt plant of Pavimental, the infrastructure owner which collaborates in the SEACON project.

The culvert is 30 m-long, and was divided into six segments in which different concretes and types of reinforcements were used (Fig. 1). In particular, segment *A* was built as reference with Reference concrete and carbon steel reinforcements, segments *B*, *C*, *D* and *E* with SEACON concrete and all the different types of reinforcement considered: carbon steel, stainless-steel type 304 (austenic), stainless-steel type 23–04 (duplex), and GFRP, respectively. Finally, segment *F* was cast with RAP concrete, combined with carbon steel reinforcement.

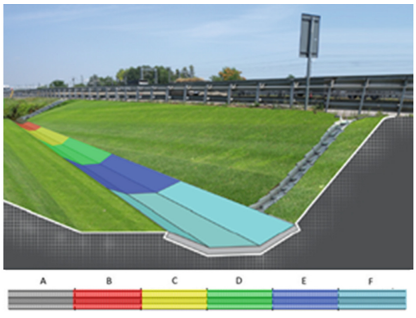

Fig. 1. Scheme of the culvert (courtesy of Pavimental)

Both stainless-steel and GFRP reinforcements were supplied by partners of the SEACON project, respectively by Acciaierie Valbruna and ATP.

The geometry of the cross section is reported in Fig. 2. The three different types of concrete were used for the slab. The side walls were constructed in a single common casting of Reference concrete (indicated as *LE* concrete below), without any kind of reinforcement.

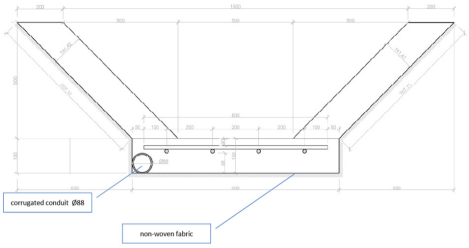

Fig. 2. Cross section geometry (courtesy of Pavimental)

In every segment, reinforcing bars of 16 mm of diameter were organized in the form of mesh with spacing of 200 mm. The different types present in the different segments were not laid in contact between each other.

In segment *B* (SEACON concrete + carbon steel), in addition to the reinforcing mesh, an activated titanium mesh was incorporated in the concrete to allow electrochemical measurements. It was placed below the reinforcement, but not in contact with it.

In each segment, two reference electrodes and a probe for the measurement of the conductance were positioned, except in segment *E*, with GFRP reinforcement, where only the probe and a reference electrode were used.

3.2 Construction Phases

The construction of the concrete culvert was completed in different major stages: excavation and preparation of the site, concrete placement of the side walls (with Reference concrete and no reinforcement), positioning of reinforcements, Fig. 3, and monitoring systems, and concrete placement of the slab, divided into six segments and created using the three different concretes, according to the recipes reported in Table 3.

Fig. 3. Installation of the reinforcement meshes

The concretes were produced in a concrete batching plant of Unical, about 10 km from the casting site.

During the cast of the slab, some tests were performed in order to control the quality of the concretes produced. The slump test was performed first in the concrete batching plant ($Slump_{t0}$) and then repeated at the casting site ($Slump_{cs}$) to check the workability maintenance. Other parameters were determined, including, in particular, air content (A_c), effective water content (w_e), and fresh density (d_F), shown in Table 4.

Table 4. Data measured on-site during the casting

On-site data	u.m.	Reference	SEACON	RAP
$Slump_{t0}$	mm	230	220	220
$Slump_{cs}$	mm	210	180	n.a.
A_c	%	2.5	2.8	2.8
w_e	l/m^3	178	176	173
d_F	kg/m^3	2320	2340	2330

In analyzing the measured values, it is possible to conclude that Reference concrete shows a higher slump value and a lower slump loss, due to the higher water content and the absence of chlorides in the mixture. The slump loss for SEACON concrete was higher compared to Reference, due to the accelerating effect of chlorides. RAP concrete showed a quite high slump value, despite the lower addition of water in the mixture.

The concretes were cast through the use of a pump, shown in Fig. 4.

Fig. 4. Concrete casting

3.3 Complementary Laboratory Tests

During the placement, some cubic specimens were cast on-site with vibration for further analysis in the laboratory. Concrete properties related to the hardened density (d_H) and the compressive strength (S_c) were measured (see Table 5).

Figure 5 shows the strength developments of the three preliminary laboratory concretes in comparison to the cast-in-place samples. Only in the case of Reference concrete, there is a strong difference between the laboratory and the on-site concretes with regard to the medium and long term results (90 day). This is due to a slightly higher water content of the on-site cast concrete confirmed from the greater slump

Table 5. Hardened density and compressive strength measured on the on-site samples

Concrete	Reference		SEACON		RAP	
Time	d_H	S_c	d_H	S_c	d_H	S_c
d	kg/m^3	MPa	kg/m^3	MPa	kg/m^3	MPa
1	2253	19.6	2403	21.1	2351	17.2
7	2370	36.7	2384	40.1	2366	28.6
28	2372	39.0	2380	48.6	2336	36.3
90	2370	40.4	2397	57.8	2339	34.0
120	2381	47.0	2389	57.5	2372	34.5

value obtained and from the higher amount of effective water measured. The best result, instead, was presented by SEACON concrete, that shows very similar results in the two cases.

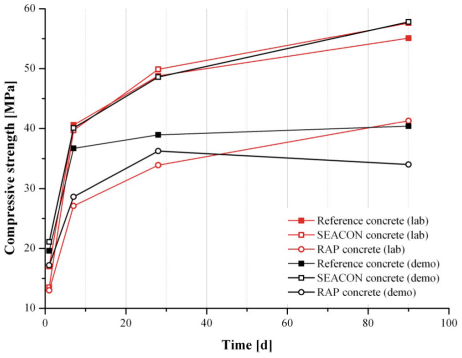

Fig. 5. Strength developments of concretes produced through preliminary laboratory investigations in comparison to on-site concretes

It is important to point out that the strength development for SEACON concrete up to 28 days is higher compared to Reference concrete, and that RAP concrete shows a lower strength development compared to the others.

In addition, the samples collected from the cast were analyzed to determine the initial chloride content. SEACON concrete had initially shown a chloride content equal to 0.16% (referred to concrete mass), in accordance with what was expected.

3.4 Post-construction Inspection and Testing

Both non-destructive and destructive measurements were performed on the demonstration. As non-destructive, the potential mapping of reinforced potential and concrete resistivity and the measurement of concrete cover were performed (Redaelli et al. 2018). With regard to destructive measurements, after 1 year from the cast, the coring of concrete specimens was performed in order to determine the compressive strength,

analyze the chloride content, perform RCM tests, and measure the electrical resistivity and the water absorption. This paper focuses on the destructive activities performed.

While trying to disturb the structure as little as possible, and to avoid the reinforcement, coring activities were performed after one year from the cast, considering the collection of cylinders with 50 or 100 mm-diameters. Overall, 19 cylinders were collected: 9 of 100 mm-diameter, and 10 of 50 mm-diameter: one each of the two types for every segment of the slab, except in the case of GFRP reinforcement, plus three of each type (indicated as *LE* coring samples) on the unreinforced side wall nearby the two gutters, shown in Fig. 6. The carbonation of concrete was measured by spraying phenolphthalein pH indicator inside the holes of the cores. The carbonation depth was nil in all cases. At the end of the coring activities, the resulting holes were closed using a shrinkage-compensating mortar, in order to avoid a preferential route for the entrance of chloride and other aggressive agents.

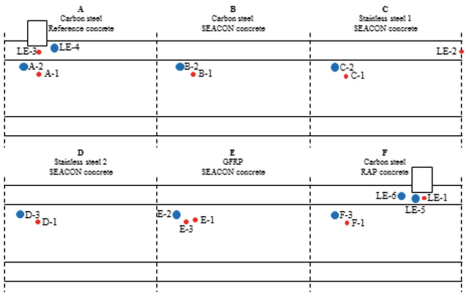

Fig. 6. Scheme of the coring samples: 50 mm-diameter samples in red and 100 mm-diameter samples in blue

Table 6 shows the calculated densities (d_c) and the compressive strength values (S_c) obtained on the coring samples. A decreased strength can be observed for all the concretes comparing these values with those obtained in the lab. This is due to the 1-year environmental exposure and to the coring disturbance; even in this case, SEACON was the highest performing concrete, the one which shows the highest strength.

The results of chloride profile analyses on core samples are presented in another paper (Redaelli et al. 2018): the chloride content at the depth of the reinforcement (i.e. about 30 mm) was the same as the initial chloride content, which was 0.01% with respect to concrete mass for Reference concrete and 0.11% with respect to concrete mass for SEACON concrete. In the case of RAP concrete, a slight increase of chloride content was observed (values of 0.03% with respect to concrete mass were obtained), and this is likely due to a release of chlorides from the RAP aggregate, rather than to the penetration from the outside.

After measuring the chloride profiles, 50 mm cores were further cut to obtain small cylindrical specimens (with approximate height of 60 mm) which were used to measure humidity content and electrical resistivity in different conditions of exposure. The specimens were initially dried at 105 °C, then immersed in deionized water until saturation, and finally exposed to an environment with 80% R.H. and 20 °C. During all

Table 6. Calculated density and compressive strength measured on coring samples

Coring values	d_c	S_c
	kg/m^3	MPa
A-2	2294	40.0
B-2	2329	48.4
C-2	2383	47.0
D-3	2331	46.1
E-3	2347	46.6
F-3	2317	41.0
LE-5	2353	42.0
LE-6	2307	30.7

conditions, the mass (M, in g) and the conductance (C, in μS) were measured, and converted to humidity content (H, in % mass) and resistivity (ρ, in Ω m), respectively, through Eqs. (1) and (2):

$$H = 100 \cdot \left(M - M_{dry}\right)/M_{dry} \quad (1)$$

$$\rho = 10^{-3} \cdot S/(C \cdot h) \quad (2)$$

where M_{dry} is the dry mass, S is the section of the specimen (in mm^2), and h is its height (in mm).

Figure 7 shows the trend of humidity content of the specimens taken from the segments (those taken from lateral walls are not reported) during the various exposure conditions. Initially, all the cores were characterized by a humidity content around 6%; this value is not fully representative of the actual conditions of humidity inside the culvert, due to coring and cutting operations. The water absorption (i.e. the humidity content in saturated condition) was between 6.6% and 7.10% for all specimens. During exposure to 80% R.H. the specimens progressively dried, until values of humidity content between 4% and 5% were reached (the lower values were obtained on initially chloride-free concretes, i.e. *A* and *F*, while the higher values were obtained on SEACON concrete, i.e. *B-E*).

Figure 8 shows the evolution of the corresponding values of concrete resistivity, in the same exposure conditions. Initial values were between 180 and 260 Ω·m. During drying, very high values (>100000 Ω·m, not shown in the Figure) were obtained. In saturated conditions, all values were very close, approximately 120 Ω·m, and finally, after exposure to 80% R.H., all specimens made with SEACON concrete had values around 480 Ω·m, while Reference concrete and RAP concrete showed higher values, of 700 and 800 Ω·m respectively. This data is not in agreement with the results obtained from monitoring concrete resistivity on site, which showed higher values of electrical resistivity in chloride-free concrete compared to SEACON concrete (Redaelli et al. 2018). Further tests will be carried out to better explain these results.

Figure 9 plots the concrete resistivity versus the humidity content for all concrete specimens in all exposure conditions (except drying at 105 °C). An overall linear trend

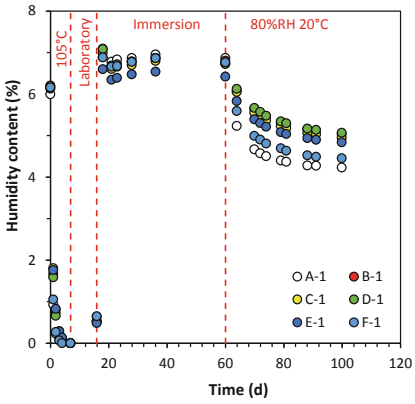

Fig. 7. Evolution of humidity content of concrete specimens during drying, saturation and exposure to 80% R.H.

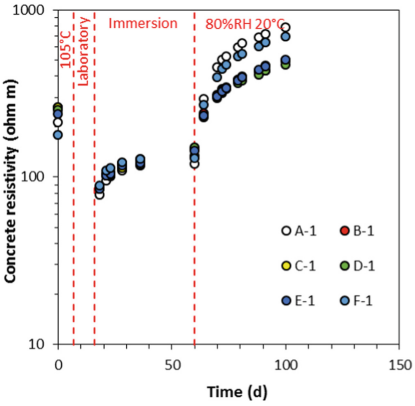

Fig. 8. Evolution of electrical resistivity of concrete specimens during drying, saturation and exposure to 80% R.H.

emerged (with resistivity in logarithmic scale), and no clear difference was observed between chloride-free and SEACON concrete. Hence, for the specimens considered, the concrete resistivity appeared to be mainly affected by the humidity content, rather than the concrete composition.

An RCM (rapid chloride migration) test was performed on one specimen per each type of concrete. The test followed the procedure reported in NT BUILD 492 (1999), and is based on the forced penetration of chloride in concrete through the application of an external current. The test allows for the estimation of the resistance of concrete to chloride penetration expressed as a coefficient of diffusion D_{RCM}. The specimens were obtained by cutting cores with diameter of 100 mm (*A*-2, *D*-3 and *F*-3) with height of 50 mm before compression test. Values of D_{RCM} of $8.2 \cdot 10^{-12}$, $4.4 \cdot 10^{-12}$ and $7 \cdot 10^{-12}$ m^2/s were obtained on Reference, SEACON, and RAP concrete, respectively. These values will be

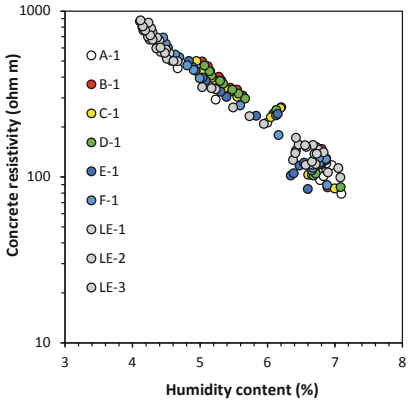

Fig. 9. Electrical resistivity as a function of humidity content of concrete specimens of various compositions in different conditions of exposure

considered as an initial reference value for future evaluation of the service life of the culvert, and will be compared with the chloride profiles that will be obtained in the future.

Table 7 summarizes the results obtained from the physio-chemical and durability characterization of the concretes; in particular, the water absorption (a_w) and the open porosity (P_o), calculated as the ratio between the volume of water absorbed in saturated conditions and the volume of the specimen, density (d), resistivity (ρ) and D_{RCM} are reported. For SEACON concrete and lateral walls concrete, average values of different specimens were considered. Overall, no substantial differences emerged between the different concretes considered that are characterized by very similar values of porosity and resistivity, in spite of the different compositions and mechanical properties.

Table 7. Summary of physio-chemical and durability parameters

	u.m.	Reference	SEACON	RAP	LE
a_w	%	6.87	6.7	6.78	6.6
P_o	%	14.8	14.6	14.5	14.4
d	sat., kg/m^3	2305	2321	2287	2311
ρ	sat., Ω·m	110	118	122	147
D_{RCM}	10^{-12} m^2/s	8.2	4.4	7	-

Since the aim of the demo project is the evaluation of the long-term durability behavior of concrete mixed with seawater, the results of this initial characterization will serve as a reference for future tests, and also as a complement to the monitoring of corrosion conditions of the reinforcement.

4 Conclusions

The SEACON project intended to demonstrate the feasibility of concretes made with seawater and salt-contaminated aggregates, combined with non-corrosive reinforcement, for the production of durable and economical structures.

This paper focuses on the demonstration activities, including the preliminary laboratory study, the construction operations, and the initial results of the monitoring, performed in Italy.

The main goal of this work is the understanding of the effect of chloride-contaminated components (seawater and RAP aggregate) on concrete, in term of fresh, hardened and durability properties. The results obtained can be summarized as follows:

- the use of seawater to produce concretes makes necessary the study of a dedicated mix-design, including the addition of a specific superplasticizer and a retarding agent to counteract the accelerating effect of chloride and maintain the workability;
- the comparison between laboratory results and on-site activities results proves the feasibility in the use of seawater as mixing water;
- successful results have been obtained using RAP aggregates in partial substitution of natural gravel (no retarding agent due to the low content of chlorides);
- the physio-chemical and durability characterizations allowed achievement of parameters that are representative of initial conditions of the concrete. No substantial differences of such parameters emerged for the concrete mixtures with different compositions;
- the results showed that chloride penetration was negligible during the first year of exposure, and the chloride content at the depth of the rebar was the same as the initial level (except for RAP concrete, where a slight increase was observed);
- estimated open porosity was around 14–15% for all specimens, in spite of the different mechanical properties;
- the electrical resistivity in saturated conditions was 110–120 Ω·m for Reference, SEACON and RAP concrete.

Acknowledgements. The project was made possible with the financial support of the ERA-NET Plus Infravation Program, and the contribution of the members of the SEACON project.

The authors also acknowledge Pavimental for allowing the demo construction inside one of their plants, and for their help during the construction activities.

Any opinions, findings and conclusions or recommendations expressed in this paper are those of the authors, and do not necessary reflect the views of the sponsor.

References

Bertola F, Canonico F, Gastaldi D, Nanni A (2017) SEACON project: sustainable concrete using seawater, salt-contaminated aggregates, and non-corrosive reinforcement. In: RILEM proceedings PRO 107; proceeding of XIV DBMC – 14th international conference on durability of building materials and components. Ghent University, Belgium, 29–31 May 2017

Rossini M, Cadenazzi T, Nolan S, Nanni A (2008) SEACON and resilient FRP-RC/PC solutions: the halls river bridge. Submitted to Italian Concrete Days, Giornate aicap 2018, Congresso CTE, 13–15 June 2018

Iannicelli Zubiani EM, Giani MI, Gallo Stampino P, Dotelli G, Nanni A, Life cycle-assessment of reinforced concrete units. In: RILEM proceedings PRO 107; proceeding of XIV DBMC – 14th international conference on durability of building materials and components, Ghent University, Belgium, 29–31 May 2017

Ghorab HY et al (1989) Effect of mixing and curing waters on the behavior of cement pastes and concrete, part-I, macrostructure of cement paste. Cem Concr Res 19:868–878

Redaelli E, Carsana M, Lollini F, Gastaldi M, Torabian Isfahani F (2018) Sustainable concrete with seawater and corrosion resistant reinforcement: results of monitoring of corrosion behaviour. In: Basheer PAM (ed) Proceedings of the Sixth International Conference on Durability of Concrete Structures, Leeds, 18–20 July. Whittles Publishing Ltd., pp 382–389

Redaelli E, Arrigoni A, Carsana M, Dotelli G, Gastaldi M, Lollini F, Bertola F, Canonico F, Nanni A (2019) Culvert prototype made with seawater concrete: materials characterization, monitoring and environmental impact. Adv Civ Eng Mater 8(2). https://doi.org/10.1520/ACEM20180114

NT BUILD 492 (1999) Concrete, mortar and cement-based repair materials: chloride migration coefficient from non-steady-state migration experiments

Precast Segments with Sulphoaluminate Cement and GFRP Reinforcement

M. Bianchi[1(✉)], F. Canonico[1], A. Meda[2], S. Spagnuolo[2], and A. Giamundo[3]

[1] Buzzi Unicem SpA, Casale Monferrato, AL, Italy
mabianchi@buzziunicem.it
[2] Department of Civil Engineering and Computer Science, University of Rome 'Tor Vergata', Via del Politecnico 1, 00133 Rome, Italy
[3] ATP s.r.l, Via Casa Pagano, 3, 84012 Angri, SA, Italy

Abstract. During tunnel excavation by means of a tunnel boring machine (TBM), the lining consists of precast structural elements, placed by the TBM during the excavation process and used as support elements during the advancing phase. The use of concrete based on sulphoaluminate binders allows the production of the elements to be speeded up, a reduction in the number of segments stacked waiting for the required strengths to be achieved and provides a more eco-sustainable process avoiding the use of steam curing. In order to verify the feasibility of the proposed solution, two full-scale tests (bending test and TBM jacks thrust test) on metro tunnel precast segments were carried out. The internal reinforcement consisted of a next-gen Glass Fibre Reinforced Polymer (GFRP) cage. The use of GFRP reinforcement, to replace traditional steel, in tunnel segments provides several advantages mainly related to durability aspects or when the use of a provisional lining is foreseen.

Keywords: Concrete · Sulphoaluminate cement · CSA · GFRP bars · Precast tunnel segments

1 Introduction

Tunnel construction using a mechanized excavation technique by means of a Tunnel Boring Machine (TBM) has been widely used, especially over the last thirty years, allowing for the construction of underground structures. Furthermore, this technique appears to be more effective in urban environments where the excavation has a greater impact, mainly on the surrounding structures.

The production of the precast tunnel segments, which form the final lining, is generally carried out in prefabrication plants, often located some distance from the location where they are installed.

Based on this consideration, it is necessary to take into account the amount of formwork, curing time and storage areas, ensuring a sufficient amount of segments are available to meet demand due to the possible unforeseen acceleration of the excavation speed.

M. di Prisco and M. Menegotto (Eds.): ICD 2018, LNCE 42, pp. 487–502, 2020.
https://doi.org/10.1007/978-3-030-23748-6_38

The formwork opening to remove superficial flaws, the subsequent steam curing of the concrete segments (generally 5–6 h until the concrete strength, f_{ck}, equal to 12÷15 MPa useful for demoulding is reached), are critical operating steps with high environmental and economic impacts.

Once the segments are demoulded, they are stored until the required strength is reached. From that moment, the segments can be installed and will be able to counteract the TBM thrust during the excavation advancement, without suffering structural damage.

To speed up the production process, to reduce the number of segments stored waiting for the required strength to be reached and to obtain sustainable processes without steam curing of the concrete, a new sulphoaluminate cement-based concrete has been developed, able to reach high mechanical performance in a short time.

Sulphoaluminate cements (CSA) are innovative hydraulic binders obtained by grinding clinker, cooked to 1300 °C, which is based on raw materials such as limestone, bauxite and gypsum (in approximately equal proportions). These clinker can be used with the addition of appropriate quantities of gypsum or anhydrite, or can be mixed with Portland cement. Based on these combinations, it is possible, to quickly achieve high mechanical strengths by maintaining very low hygrometric retreats of the concrete.

Buzzi Unicem SpA received the CE marking for its sulphoaluminate binders line, named Buzzi Unicem Next, also paving the way for the use of these binders in the structural field.

A different hydration process compared to the common Portland cements characterizes Sulfoaluminate binders. The hydration of Portland cement is dominated by the reaction of tricalcium silicate (C_3S - Alite) which, in its reaction with water, develops calcium silicate hydrates and calcium hydroxide. The ettringite is the main hydration product of the Sulphoaluminated cements (Bullard et al. 2011).

The pH generated by means of sulphoaluminate cement hydration is higher than 12. Although lower than that of Portland cements (pH > 13), it is sufficient to passivate the reinforcement. However, this characteristic can be exploited to effectively combine these binders with fiberglass reinforcements that are able to resist low-pH values (Bertolini et al. 2015a, b).

The use of fiberglass reinforcing bars, combined with this new concrete, has been investigated.

The use of fiberglass re-bars (Glass Fiber Reinforced Polymer – GFRP), as reinforcement in concrete structures, is an innovative solution that can be used as an alternative to common steel reinforcing bars, especially in conditions where high resistance to environmental attack is required (Almusallam and Al-Salloum 2006; Chen et al. 2007; Benmokrane et al. 2002; Gooranorimi and Nanni 2017). In fact, compared to traditional steel reinforcement bars, fiberglass reinforcements are not affected by corrosion problems, and have high tensile strength and lower weight (Micelli and Nanni 2004; Chen et al. 2007; Nanni 1993; Alsayed et al. 2000). The material is also non-conductive and non-magnetic (Almusallam and Al-Salloum 2006).

The use of fiberglass reinforcements leads to different advantages such as an increase in durability, the absence of corrosion, the possibility to create dielectric joints

and the reduction of concrete cover, limiting cracking problems during transitional phases until the final installation of the lining (Spagnuolo et al. 2017).

In light of the advantages of using this new technology in underground structural fields, over the last few years, experimental campaigns have been carried out both for the characterization of the physical-mechanical properties, and the durability of fiberglass reinforcement with curvilinear axis (Spagnuolo et al. 2018).

Furthermore, several full-scale tests on typical precast segments for different tunnel linings (hydraulic, metro and highway tunnel geometries) were carried out to demonstrate the validity of this new reinforcement to replace traditional steel re-bars (Spagnuolo et al. 2014; Caratelli et al. 2016, 2017).

1.1 Aim of the Research

The object of the research was focused on the characterization of an innovative concrete based on sulphoaluminate cement, testing its chemical and mechanical properties on an industrial scale for the production of precast tunnel segments. Based on the results obtained on fresh concrete, two full-scale metro tunnel precast segments were cast and tested. The segments were reinforced with GFRP re-bars.

Two different full-scale tests (bending test and point load test) were carried out to verify and validate the structural capacity and materials effectiveness, respectively.

2 Experimental Campaign

2.1 Materials and Test Methods

For concrete packaging, a sulphoaluminate cement-based binder, CE marked (Next binder - SL05) was used, dosed at 380 kg/m^3.

The aggregates, used in the mix design, were of calcareous origin originating from the UNICAL concrete mixing plant in Santa Lucia (Rome). The aggregates consisted of the following particle size fractions: 0–4 mm sand, 8–15 mm gravel, 15–25 mm crushed stone.

The fluidifying additive used was Sika CC39/P22.

The concrete mix was carried out by means of a concrete mixer at a room temperature of 20 °C. Tests were also carried out at an external temperature of 30 °C to evaluate the workability time and the strength development at higher temperatures, respectively.

Concrete properties such as consistency class (in accordance with Standard UNI EN 12350-2), maintenance, density (in accordance with Standard UNI EN 12350-6), compressive cubic strength (by means of 150×150×150 mm samples aged at 20 °C and 95% RH, in accordance with Standard UNI EN 12390-3) were defined. The compressive cubic strength evaluation was carried out at 3–4–5–6–24 h, 7 and 28 days, respectively.

The precast segments were cast by means of a truck mixer, by using the same aggregates and mix design (Fig. 1). For the cast, a concrete volume equal to 4 m^3 was mixed.

Both precast segments were reinforced with GFRP re-bars. Each rebar consisted of boron-free E-CR fiberglass 4800tex and matrix thermoset vinyl ester resin-based.

The fiber volume fraction was equal to 60%, for which unidirectional tensile strength and tensile Young's modulus were 1200 MPa and 48 GPa, respectively.

Concrete shrinkage was measured, over time, by means of deformeter EDU by Huggenberger AG (Fig. 2a).

The measurement was carried out by means of two steel plates, drowned or glued to the concrete, fixed at a distance equal to 250 mm (Fig. 2b). The instrument resolution was equal to 0.001 mm with ±0.005 mm accuracy. An Invar reference bar was used as auto-zero comparator. The main advantage, of using a deformeter, consisted s of concrete shrinkage measurements that can be carried out starting a few hours after the casting, directly on the structure.

The experimental campaign on the structural elements was performed by carrying out full-scale tests to simulate the most severe conditions to which the tunnel lining, made by mechanized excavation, would be subjected to during the transitional and serviceability phases.

The two tests were :

- Three points bending test, in order to understand the segment behaviour during the transitional phases (which range from demoulding to installation by means of TBM erector) and to evaluate the maximum bending capacity at the ultimate limit state;
- Point load test to simulate jack thrust exercises by the TBM on the segment during the excavation phase and its progress.

Fig. 1. GFRP reinforcement detail and concrete cast

Fig. 2a. Shrinkage measuring instrument (deformeter)

Fig. 2b. Shrinkage measurement

2.2 Test Results

Table 1 shows the results of the tests carried out on the concrete, depending on the temperature.

Table 1. Properties of the mix design, prepared with superplastizicer CC39T22 at different temperatures

Mix design	Unit	20 °C	30 °C	Ref.
Binder (NextSL05)	kg/m^3	380		380
CEM IV/A(PV) 42.5 N	kg/m^3	380		380
Sand	kg/m^3	892		892
Rubble	kg/m^3	445		445
Gravel	kg/m^3	503		503
Additive CC39/P22	%	0.7		0.7
Water	l/m^3	160		160
Volumetric data				
Yield	%	99.8	100.6	101
Actual water	l/m^3	162	159	161
Air content	%	2	1.9	2.0
Density	kg/m^3	2384	2382	2395

(*continued*)

Table 1. (*continued*)

Mix design	Unit	20 °C	30 °C	Ref.
*Workability loss**				
t_0	mm	195	200	200
t_{30}	mm	190	160	200
t_{60}	mm	180	–	190
*Compressive strength***				
3 h	MPa	3.7	10.0	–
4 h	MPa	10.0	16.1	–
5 h	MPa	15.4	18.0	–
6 h	MPa	18.2	20.3	–
24 h	MPa	39.9	44.2	–
7 days	MPa	54.6	51.9	41.9
28 days	MPa	66.7	64.4	52.6

Note:
*t_0 refers to time zero; t_{30} refers to 30 min after casting; and t_{60} refers to 60 min after casting.
**Compressive strength refers to cubic strength R_{cm}.

2.3 Shrinkage

Graph 1 shows the results of the concrete shrinkage. The shrinkage test was carried out taking into account the same mix design, water content and binder dosage. CEM IV/A (PV) 42.5 N SR pozzolanic cement, normally adopted to cast tunnel segments, was used as the reference binder.

Concrete shrinkage measurement was carried out starting from 2.5 h for the Next-SL05 mix and 7 h for the reference mix after the concrete casting, respectively.

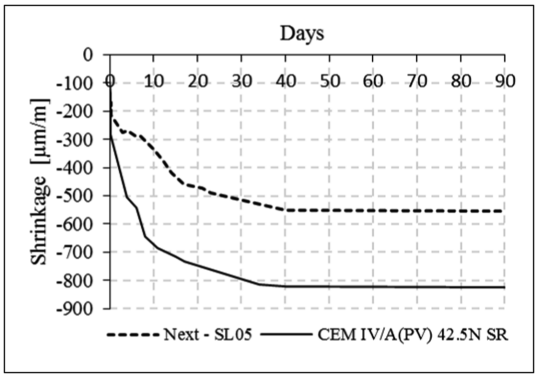

Graph 1. Shrinkage evolution

2.4 Full-Scale Tests

For the full-scale application two metro tunnel segments were cast. Each precast segment was 300 mm in thickness, with 5800 mm internal diameter and 1420 mm in depth (Fig. 3).

The reinforcement consisted of a GFRP cage for which composite re-bars were designed in order to optimize the length of each closed-loop ring (Fig. 4). The optimization allowed the achievement of both performance aspects that segments would need to ensure during the serviceability phase, and technical aspects due to mechanical components located on the structural elements such as cups, connectors, etc.

Each segment consisted of 12 equivalent Ø13 mm base closed-loop rings (longitudinal direction), each of which in turn, contained superimposed rings (A, B and C types) of different length, according to layout as shown in Fig. 4.

The equivalent area of each GFRP ring was equal to 43.9 mm^2.

The cage, in transverse direction, was confined by means of 16 equivalent Ø8 mm GFRP closed-loop stirrups.

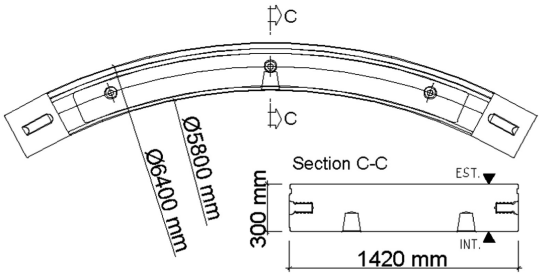

Fig. 3. Segment geometry.

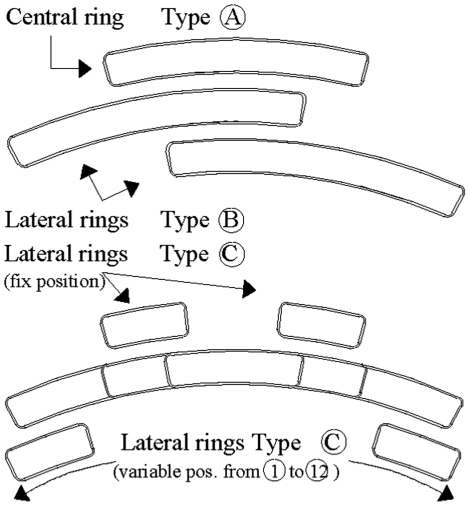

Fig. 4. GFRP reinforcement details

2.5 Three Points Bending Test

A full-scale bending test was carried out in displacement control, according to the testing set-up shown in Fig. 5. The segment was placed on two cylindrical supports with a wheelbase of 2 m. Load was applied by means of a electromechanical jack with a load cell of 1000 kN and 0.2% accuracy, by imposing 10 μm/sec running speed. Load, in turn, was distributed, by means of a frame system, along the segment mid-span on the extrados surface (Fig. 5a).

During the test, in addition to applied load, displacements and crack widths, at the mid-span of intrados surface, were recorded by means of three wire transducers and two Linear Variable Differential Transformers (LVDTs), respectively (Fig. 5b). Increasing the load, new cracks developed, whose width was recorded by means of a crack width ruler.

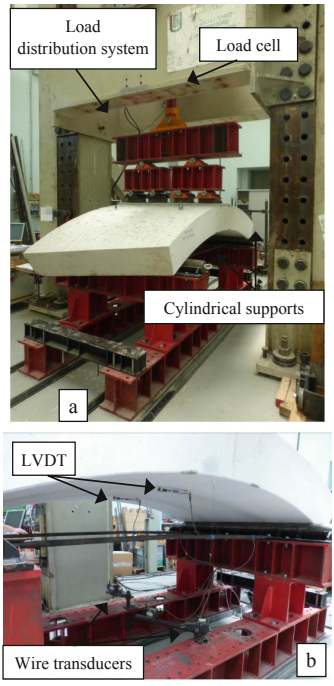

Fig. 5. Testing set-up. Bending test: (a) Load system; (b) Instrumentation

2.6 Point Load Test (TBM)

A point load test, simulating TBM thrust exerted on segments (previously installed on the back of the TBM shield) during its progress, was carried out applying the load according to the testing set-up shown in Fig. 6.

The load, during testing, was applied on each steel pad according to TBM geometry and configuration by means of two 2000 kN hydraulic jacks (max 4,000 kN per steel pad). The testing set-up, for the configuration shown in Fig. 6, was able to provide a maximum load of 12,000 kN (1200 Tons). The segment was placed on a correctly designed reinforced concrete (RC) beam.

As shown in Fig. 6, besides the load, vertical displacements below the thrust steel pads and crack widths between the same were recorded by means of potentiometers (two for each steel pad – intrados/extrados) and two Linear Variable Differential Transformers (LVDTs), respectively. In addition to data acquisition, increasing the load step by step, crack patterns were mapped out. For each significant crack, its width was measured by means of a crack width ruler.

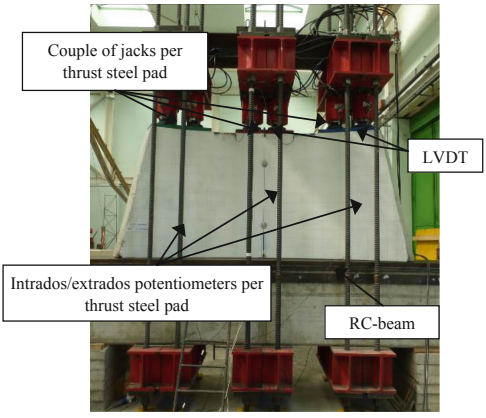

Fig. 6. Testing set-up: point load test (TBM)

3 Results

3.1 Concrete

Based on the results obtained, CSA binders can be used for concrete packaging as can be done with the common Portland cements with the advantage of being able to reduce the binder content (from 400 kg/m^3 to 380 kg/m^3) and to avoid steam curing of the segment to speed up the demoulding process.

CSA cements have a reduced working time compared to pozzolanic cements used for this application, but it is sufficient to be used for the casting of precast elements. The workability time can be modulated depending on the casting temperatures and needs with the addition of retardant additives.

A concrete mix based on Next-SL05 sulphoaluminate binder allows for a compressive strength higher than 15 MPa to be achieved as early as 5 h after casting with a workability time of 90 min at 20 °C.

The influence of temperature considerably modifies the workability time (40 min at 30 °C compared to 90 min at 20 °C), however leaving time for the concrete to be cast in prefabrication. Useful demoulding strengths were already achieved three hours after casting.

The development of a high strength, in the early hours, avoids the thermal cycle of steam curing, making the precast segment production process easier both from an operational point of view and from a logistics point of view of the plant realization.

The results of shrinkage show how mix design based on sulphoaluminate cement is characterized by a shrinkage lower than that obtained with pozzolanic cement, −550 μm/m and −820 μm/m, respectively.

3.2 Three Points Bending Test

A full-scale bending test was carried out 26 h and 40 min after segment casting, for which the average compressive strength (R_{cm}) achieved was equal to 41 MPa.

The first crack (red line in Fig. 7) occurred at a load level of 130 kN with a maximum crack width equal to 0.30 mm. Increasing the load, several cracks developed both on the intrados and lateral surfaces of the segment. Figure 7 shows the crack pattern at the end of the test.

The maximum load achieved was 380 kN with a displacement equal to 38 mm at the mid-span of the segment intrados surface, as shown in the Graph 2 where the load versus average displacement curve is plotted.

Table 2 shows, for each load step, the width of the different crack formed step-by-step.

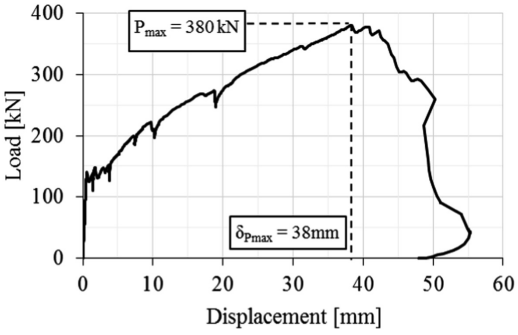

Graph 2. Bending test: load-displacement. curve

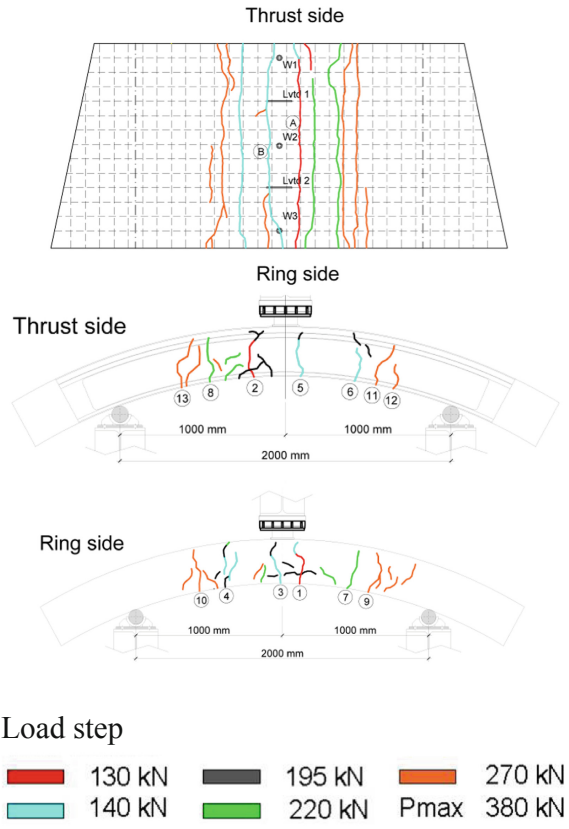

Fig. 7. Bending test: final crack pattern

3.3 Point Load Test (TBM)

A full-scale point load test was carried out 30 h and 30 min after segment casting.

The test was carried out according to two loading/unloading cycles with 250 kN increasing steps. The cycles were :

- Cycle I: 0-1580 kN (TBM service load);
- Cycle II: 0-2670 kN (Unblocking thrust/TBM pushing capacity).

Graph 3 shows the results in terms of load versus vertical displacement (average displacement of intrados/extrados wire transducers) below each steel thrust pad. Maximum compressive displacement was equal to 0.39 mm.

The first crack occurred at a load level of 750 kN (for each steel pad) with maximum crack width less than 0.05 mm between green/red steel pads at the thrust side surface. As the load was increased, several cracks occurred, as shown in Fig. 8. With reference to two maximum imposed load levels (1580 kN for service load and 2670 kN for unblocking thrust load), the maximum crack width was equal to 0.50 mm and 0.80 mm, respectively.

Table 2 Crack widths

	Load level				
Load [kN]	130 kN	140 kN	195 kN	220 kN	270 kN
Crack color					
Crack n.					
1	0.25÷0.30	0.40÷0.45	1.00÷1.20	1.50	2.00÷2.50
2	0.25	0.35	0.90	1.50	2.00
3	-	0.35	1.00	1.25	2.50
4	-	0.30	0.45	0.35	0.40
5	-	0.45	1.25	1.50	2.50
6	-	0.15	0.45	0.70	1.00
7	-	-	-	0.30	0.30
8	-	-	-	0.15	0.35
9	-	-	-	-	0.70
10	-	-	-	-	0.70
11	-	-	-	-	0.60
12	-	-	-	-	0.20
13	-	-	-	-	0.40

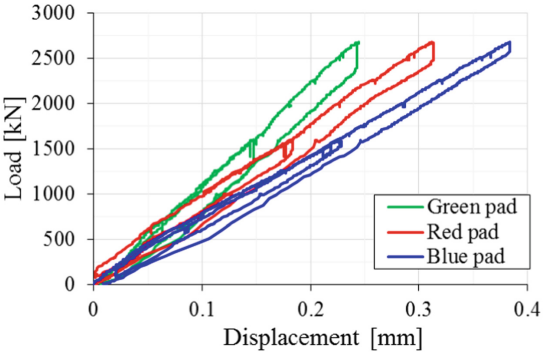

Graph 3. Point load test (TBM): Load-Displacement curve

At the end of the test, when the unload occurred, the maximum residual crack width was equal to 0.15 mm. Tables 3 and 4 show, for the two loading/unloading cycles, the crack widths measured.

Table 3 Crack's width (Cycle I: service load)

Phase	Cycle I (Service)					
	Loading				Unloading	
Load [kN]	750	1000	1250	1580	1000	100
Crack color						

Crack n.	Crack width [mm]					
1	<0.05	0.10	0.30	0.50	0.40	0.15
2	-	0.05	0.20	0.40	0.30	0.15
3	-	0.05	0.30	0.40	0.40	0.15
4	-	-	-	0.05	0.05	Closed
5	-	-	-	-	-	-
6	-	-	-	-	-	-

Table 4 Crack widths (Cycle II: TBM pushing capacity)

Phase	Cycle II (TBM pushing capacity)								
	Loading						Unloading		
Load [kN]	1580	1750	2000	2250	2500	2670	1580	0	0 after 5'
Crack color									

Crack n.	Crack width								
1	0.40	0.45	0.50	0.60	0.70	0.80	0.80	0.25	0.15
2	0.35÷0.40	0.35	0.45	0.45÷0.50	0.50	0.60	0.50	0.20	0.15
3	0.40	0.40	0.50	0.60	0.70	0.80	0.80	0.20	0.15
4	0.05	0.10	0.10÷0.15	0.15	0.20	0.25	0.15	0.05	0.05
5	-	-	0.10	0.15	0.20	0.20	0.10	0.05	0.05
6	-	-	-	-	0.10	0.15	0.10	<0.05	<0.05

3.4 GFRP Reinforcement

The performance of GFRP reinforcement was in line with the values already observed in other experimental situations, both in terms of maximum load achieved (bending test) and in relation to the crack width. With reference to the maximum crack width (cracking load and unloading for bending test and point load test, respectively), these values are within the ranges provided by Regulations and Codes.

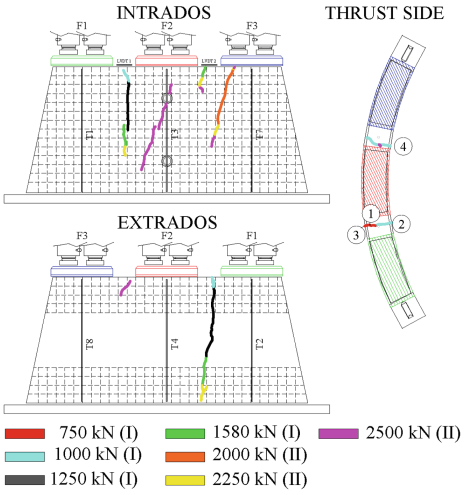

Fig. 8. Point load test (TBM): final crack pattern

4 Conclusions

In the paper, the results of the experimental full-scale tests on metro tunnel segments consisting of sulphoaluminate concrete reinforced with GFRP reinforcement are presented and discussed. Both bending test and three points load test, simulating the TBM thrust, were carried out. Based on the results obtained with experimental full-scale tests, developed by University of Rome Tor Vergata – Tunnelling Engineering Research Centre (TERC), the following aspects can be remarked upon:

- Based on several full-scale tests carried out over the last few years, the obtained results show, once again, the effectiveness of the proposed reinforcement with GFRP bars for tunnel lining. The new GFRP reinforcement optimization has allowed the resolution of the problem of crack width containment due to the low bond strength of the GFRP rebars in both cases: bending actions under service load and during the excavation under TBM thrust.
- The combination of concrete based on sulphoaluminate and GFRP reinforcement represents a synergistic solution which may lead to a new way forward to problems and challenges, such as: the speeding up of production, the reduction of the number of segments stacked waiting for the required strengths to be achieved, and the achievement of a more eco-sustainable process, avoiding steam curing. Finally, the reduction of stacking space could allow for on-site prefabrication.

Acknowledgments. The authors gratefully acknowledge (1) BUZZI UNICEM S.p.A. and (2) ATP S.r.l. for funding the research program; (3) Tunneling Engineering Research Centre (TERC) for the support provided to full-scale tests.

References

Bullard JW, Jennings HM, Livingston RA, Nonat A, Scherer GW, Schweitzer GS, Scrivener KL, Thomas JJ (2011) Mechanism of cement hydration. Cem Concr Res 41(12):1208–1223

Bertolini L, Canonico F, Buzzi L, Carsana M, Bertola F (2015a) Steel corrosion behaviour in real-size concrete elements prepared with sulpho-aluminate cements. 19° IBAUSIL 16–18 septembre 2015 Weimar

Almusallam TH, Al-Salloum YA (2006) Durability of GFRP rebars in concrete beams under sustained loads at severe environments. J Compos Mater 40(7):623–637

Chen Y, Davalos JF, Kim H-Y (2007) Accelerated aging tests for evaluations of durability performance of FRP reinforcing bars for concrete structures. Compos Struct 78(March): 101–111

Benmokrane B, Wang P, Ton-That TM, Rahman H, Robert JF (2002) Durability of glass fiber reinforced polymer reinforcing bars in concrete environment. J Compos Constr 6(3):143–153

Gooranorimi O, Nanni A (2017) GFRP reinforcement in concrete after 15 years of service. J Compos Constr 21(5, October)

Micelli F, Nanni A (2004) Durability of FRP rods for concrete structures. Constr Build Mater 18 (7, September):491–503

Nanni A (ed) (1993) Fiber-Reinforced-Plastic (GFRP) reinforcement for concrete structures: properties and applications, vol 42. Elsevier Science, Developments in Civil Engineering, Amsterdam, p 450

Alsayed SH, Al-Salloum YA, Almusallam TH (2000) Performance of glass fiber reinforced plastic bars as a reinforcing material for concrete structures. Compos Part B: Eng 31(6–7):555–567

Spagnuolo S, Meda A, Rinaldi Z, Nanni A (2017) Precast concrete tunnel segments with GFRP reinforcement. ASCE J Compos Constr 21(5):04017020

Spagnuolo S, Meda A, Rinaldi Z, Nanni A (2018) Curvilinear GFRP bars for tunnel segments applications. Compos B 141(2018):137–147

Spagnuolo S, Meda A, Rinaldi Z (2014) Fiber glass reinforcement in tunneling applications. In: Proceedings of The 10th fib international PhD symposium in civil engineering, pp. 85–90, Québec, Canada, 21–23 July 2014

Caratelli A, Meda A, Rinaldi Z, Spagnuolo S (2016) Precast tunnel segments with GFRP reinforcement. Tunn Undergr Space Technol 60(November):10–20

Caratelli A, Meda A, Rinaldi Z, Spagnuolo S, Maddaluno G (2017) Optimization of GFRP reinforcement in precast segments for metro tunnel lining. Compos Struct 181(2017):336–346

Gastaldi D, Canonico F, Capelli L, Boccaleri E, Milanesio M, Palin L, Croce G, Marone F, Mader K, Stampanoni M (2012) In situ tomographic investigation on the early hydration behaviors of cementing systems. Constr Build Mater 29:284–290

Irico S, Gastaldi D, Canonico F, Magnacca G (2013) Investigation of the microstructural evolution of calcium sulfoaluminate cements by thermoporometry. Cem Concr Res 53:239–247

Paul G, Boccaleri E, Buzzi L, Canonico F, Gastaldi D (2015) Friedel's salt formation in sulfoaluminate cements: a combined XRD and 27Al MAS NMR study. Cem Concr Res 67:93–102

Gastaldi D, Paul G, Marchese L, Irico S, Boccaleri E, Mutke S, Buzzi L, Canonico F (2016) Hydration products in sulfoaluminate cements: evaluation of amorphous phases by XRD/solid-state NMR. Cem Concr Res 90:162–173 (in press)

Winnefeld F, Lothenbach B (2010) Hydration of calcium sulfoaluminate cements – Experimental findings and thermodynamic modeling. Cem Concr Res 40:1239–1247

Aranda MAG, de La Torre AG (2013) Sulfoaluminate cement. In: Pachego-Torgal F, Jalali S, Labrincha J, John VM (eds) Eco-efficient concrete. Woodhead Publishing, Cambridge, p 488

Bernardo G, Telesca A, Valenti GL (2006) A porosimetric study of calcium sulfoaluminate cement pastes cured at early ages. Cem Concr Res 36:1042–1047

Canonico F, Buzzi L, Schäffel P (2012) Durability properties of concrete based on industrial calcium sulfoaluminate cement. In: International congress on the durability of concrete, p. A2-2, Trondheim, Norway

Bertolini L, Bianchi M, Buzzi L, Canonico F, Capelli L (2015) Corrosion behaviour of steel embedded in calcium sulfoaluminate-cement concrete. In: International congress on the chemistry of cement, Beijing, China

Canonico F, Bertola F, Bertolini L, Buzzi L, Carsana M (2015) Steel corrosion behaviour in real-size concrete elements prepared with sulpho-aluminate cements. In: Ibausil, Weimar Germany, HV 13-B A

New Punching Shear Reinforcement System for Footings and Ground Slabs

M. Ricker[1], D. Kueres[2], F. Häusler[3], D. Carminati[4(✉)], and J. Hegger[2]

[1] Department of Civil Engineering, Hochschule Biberach University of Applied Sciences, Biberach, Germany
[2] Institute of Structural Concrete, RWTH Aachen University, Aachen, Germany
[3] HALFEN GmbH, Langenfeld, Germany
[4] HALFEN S.r.l., Bergamo, Italy
diego.carminati@halfen.it

Abstract. Punching shear tests on footings indicated that the inclination of compression struts is much steeper compared to flat slabs. The resulting steeper inclination of shear cracks leads to the assumption that vertically arranged punching shear reinforcement elements are less efficient in footings than in flat slabs. On that basis, a new punching shear reinforcement element with inclined bars was developed. At RWTH Aachen University, 14 punching shear tests on reinforced concrete footings including the new punching shear reinforcement elements were conducted. The test specimens partly failed inside the shear-reinforced zone and at maximum load level. In spite of a reduction of total steel cross sectional area, the test specimens with the new punching shear elements showed a significant increase in punching shear capacity (40–50%) compared to previous test series. The new punching shear reinforcement system allows for a significant reduction of footing's dimensions.

Keywords: Footings · Maximum punching shear capacity · Punching shear · Punching shear reinforcement · Shear span-depth ratio

1 Introduction

The punching shear behaviour of reinforced concrete footings without punching shear reinforcement has been investigated extensively by various researchers in the past (Talbot 1913; Richart 1948; Dieterle and Steinle 1981; Dieterle and Rostásy 1987; Hallgren et al. 1998; Hegger et al. 2006, 2007b, 2009; Siburg and Hegger 2014). According to these investigations, punching shear resistance mainly depends on the flexural reinforcement ratio, concrete compressive strength, and footing dimensions (e.g. effective depth, shear span-depth ratio, size effects), which is in line with previous investigations on flat slabs. However, due to more compact dimensions and soil-structure interaction, footings and ground slabs achieve significantly higher punching shear capacities than flat slabs (Hegger et al. 2006; Hegger et al. 2007b; Hegger et al. 2009; Siburg and Hegger 2014).

M. di Prisco and M. Menegotto (Eds.): ICD 2018, LNCE 42, pp. 503–514, 2020.
https://doi.org/10.1007/978-3-030-23748-6_39

Fewer experimental investigations have been conducted on reinforced concrete footings with punching shear reinforcement (Hegger et al. 2009; Siburg and Hegger 2014). The test results indicate that vertical punching shear reinforcement elements like stirrups (Beutel and Hegger 2002; Fernandez Ruiz and Muttoni 2009; Hegger et al. 2007a) and studs (Andrä 1981; Mokthar et al. 1985; Ricker and Häusler 2014; Ferreira et al. 2014) are less efficient in footings than in flat slabs. Due to the steeper inclination of shear cracks in footings, a higher efficiency of inclined punching shear reinforcement elements (e.g. inclined shearband reinforcement (Pilakoutas and Li 2003), lattice girders (Park et al. 2007), bent-up bars (Einpaul et al. 2016)) can be assumed. A punching test on a reinforced concrete footing with bent-down bars seems to confirm this assumption (Dieterle and Rostásy 1987).

Based on the results of previous test series (Dieterle and Rostásy 1987; Hegger et al. 2006, 2007b, 2009; Siburg and Hegger 2014), a new punching shear reinforcement system with inclined bars was developed. In a first test series (Kueres et al. 2017), the punching shear behaviour of footings with the new punching shear reinforcement element and a failure inside the shear-reinforced zone was investigated. Based on the results of the first test series, the maximum punching shear capacity of footings with the new punching shear reinforcement element was investigated in a second experimental campaign. A series of seven punching tests on reinforced concrete footings was conducted. All test specimens were provided with the new punching shear reinforcement.

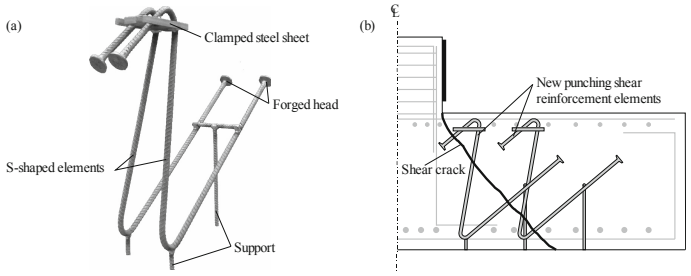

Fig. 1. New Punching shear reinforcement element

2 New Punching Shear Reinforcement Elements

The new punching shear reinforcement elements (Fig. 1 (a)) have an optimized form, which allows the shear crack widths to be efficiently controlled. Due to the inclination of the different sections, the S-shaped elements cross the shear cracks several times (Fig. 1 (b)). The rigid anchorage of the S-shaped elements by means of forged heads, as well as the effective upper anchorage, consisting of a clamped steel sheet, also contributes to the increased failure loads of the test specimens. Another advantage of the upper anchorage element is that no expensive welding is necessary. The mandrel diameter chosen for the new punching shear reinforcement is smaller than allowable according to DIN EN 1992-1-1 (2011) due to space reasons. It was shown by photomicrographs of the hooked bars that the reduced mandrel diameter does not lead to an

increased number of micro-cracks. The full-scale tests of the previous test series (Kueres et al. 2017) confirmed the assumption that the increased concrete pressure due to the small mandrel diameter does not cause premature concrete failure adjacent to the looped anchorage elements.

3 Experimental Campaign

3.1 General

To investigate the punching shear behaviour of column bases with the new punching shear reinforcement system and to evaluate its efficiency, a total of 14 punching shear tests on reinforced concrete footings with uniform soil pressure were conducted. In a first experimental campaign, seven tests (diameter of punching shear reinforcement: $\varnothing_w$ = 10 mm and $\varnothing_w$ = 12 mm) were performed to investigate the punching shear behaviour of footings with the new punching shear reinforcement and a failure inside the shear-reinforced zone. The tests were planned considering the results of former test series on footings without and with stirrups as punching shear reinforcement (Hegger et al. 2009; Siburg and Hegger 2014). Based on the first experimental campaign, a second experimental campaign (seven tests, $\varnothing_w$ = 14 mm) was conducted to investigate the maximum punching shear capacity of footings with the new punching shear reinforcement. The main parameters investigated in both experimental campaigns were the concrete compressive strength, the shear span-depth ratio, the column perimeter-depth ratio, the amount and layout of punching shear reinforcement. In the first experimental campaign, the effect of a longitudinal reinforcement in the compression zone (top reinforcement) was additionally investigated.

3.2 Materials

For all test specimens, commercial ready mixed concrete was used. The concrete mixture was designed to produce a 28-day target cylinder strength of $f_{c,cyl}$ = 25 MPa and $f_{c,cyl}$ = 55 MPa, respectively. For the lower concrete strength, ordinary CEM II 42.5 R Portland cement and a water-cement-ratio (w/c) of 0.65 to 0.73 was used, resulting in a slump of approximately 480 mm. For the concrete with higher strength, ordinary CEM I 52.5 R Portland cement and a water-cement-ratio (w/c) of 0.40 to 0.43 was used, resulting in a slump of approximately 470 mm. The maximum coarse aggregate size was 16 mm for both mixtures. To prevent premature failure, high-strength concrete with concrete compressive strengths between $f_{c,cyl}$ = 111.3 MPa and 122.2 MPa was used for the column stubs. Additionally, the column stubs were strengthened with a steel collar made of 10 mm steel plates.

For all test specimens, the flexural reinforcement consisted of high-grade steel St 900/1100 with yield strengths varying from f_y = 996 MPa to 1044 MPa, a tensile strength of approximately f_t = 1177 MPa, and a Young's modulus of approximately E_s = 194,300 MPa. The high-grade steel was used to prevent a premature flexural failure. The new punching shear reinforcement elements were produced of steel B500 B, with measured yield strengths varying from f_y = 553 MPa to 585 MPa, tensile

Table 1. Test parameters

Specimen	h	d	c	b	$u_{0/d}$	$a_{\lambda/d}$	$f_{c,cyl}$	∅	f_y	ρ_l	top rft	$\varnothing_w$	f_{yw}	Lay--out	V_{flex}	V_{test}
–	mm	mm	mm	mm	–	–	Mpa	mm	Mpa	%	–	mm	Mpa	–	KN	KN
Experimental campaign I																
DF_N1	450	399	200	1800	2.01	2.01	22.5	20	1044	0.79	yes	12	585	II	9862	4082
DF_N2	450	394	200	1800	2.03	2.03	22.6	20	1044	0.79	no	12	585	II	9872	4054
DF_N3	450	394	200	1800	2.03	2.03	20.5	20	1034	0.79	yes	10	547	II	9566	4544
DF_N4	450	394	300	1900	3.05	2.03	20.4	20	1034	0.83	yes	10	547	II	11,297	5045
DF_N5	450	396	300	1900	3.03	2.02	25.2	20	1034	0.83	yes	10	552	IIb	11,905	5937
DF_N6	450	397	400	2000	4.03	2.02	21.2	20	1037	0.86	yes	10	552	II	13,285	6515
DF_N7	450	396	300	1300	3.03	1.26	22.8	20	1037	0.85	yes	10	552	I	14,557	6573
Experimental campaign II																
DF_N8	450	397	300	1300	3.02	1.26	23.0	20	996	0.79	yes	14	553	I	14,020	7743
DF_N0 N	450	396	300	1900	3.03	2.02	22.4	20	1034	0.83	yes	14	569	II	11,437	6380
DF_N9	450	397	300	2700	3.02	3.02	25.1	20	996	0.81	yes	14	553	III	9928	5629
DF_N11	450	397	300	1900	3.02	2.02	53.8	20	996	0.83	yes	14	553	II	12,731	9831
DF_N12	450	397	300	2700	3.02	3.02	51.3	20	996	0.81	yes	14	553	III	10,977	7850
DF_N13	450	395	400	2000	4.05	2.03	22.8	20	996	0.86	yes	14	553	II	12,945	7416
DF_N14	450	396	600	2200	6.06	2.02	21.7	20	996	0.86	yes	14	553	II	15,713	8692

h: slab thickness; d: effective depth; c: square column dimension; b: square footing dimension; u_0/d: specific column perimeter; a_λ/d: shear span-depth ratio; $f_{c,cyl}$: concrete compressive strength; ∅: diameter of longitudinal reinforcement; f_y: yield strength of longitudinal reinforcement; ρ_l: longitudinal reinforcement ratio; $\varnothing_w$: diameter of shear reinforcement; f_{yw}: yield strength of shear reinforcement; layout: layout of punching shear reinforcement; V_{flex}: shear force that produces flexural failure according to yield-line theory; V_{test}: ultimate failure load.

strengths in a range of f_t = 631 MPa and 646 MPa, and a Young's modulus between E_s = 199,100 MPa and 199,800 MPa. Table 1 summarises the properties of the materials used.

3.3 Test Specimens

The test series of the experimental campaign I consisted of seven reinforced concrete footings with side dimensions of 1300, 1800, 1900, and 2000 mm in square. The seven test specimens of the experimental campaign II had side dimensions of 1300, 1900, 2000, 2200, and 2700 mm in square. All specimens had a slab thickness of 450 mm. The square column stubs had side dimensions of 200, 300, and 400 mm (campaign I) and 300, 400, and 600 mm (campaign II) and were cast monolithically at the centre of the footing. The distance between the outer compression fibre and the centroid of the tension reinforcement (effective depth) was approximately d = 400 mm for all specimens, resulting in shear span-depth ratios between a_λ/d = 1.25 and 2.00 (with a_λ being the distance from the column face to the edge of the footing) for campaign I and between a_λ/d = 1.25 and 3.00 for campaign II. The specific column perimeter was in the range of u_0/d = 2.0 and 4.0 (campaign I) and u_0/d = 3.00 and 6.00 (campaign II). In both test series, the flexural reinforcement ratio varied between ρ_l = 0.79% and 0.86%. In the first experimental campaign, the diameter of the inclined bars of the punching shear reinforcement elements was either $\varnothing_w$ = 10 mm or 12 mm. In the second experimental campaign, the diameter of the inclined bars was 14 mm for all specimens. The different layouts of punching shear reinforcement investigated are shown exemplarily in Fig. 3 for test specimens DF_N0 N (Layout II) and DF_N9 (Layout III). Layout II consisted of eight punching shear reinforcement elements in the first row and eight elements in the second row. In the slender specimens (DF_N9 and DF_N12, a_λ/d = 3.00), a third row, consisting of eight punching shear reinforcement elements, was installed. Specimen DF_N8 (Layout I) was tested with a shear span-depth ratio a_λ/d = 1.25. Hence, only one row of punching shear reinforcement could be installed due to space limitations.

3.4 Test Setup and Measurements

The punching shear tests were conducted in accordance with former tests on reinforced concrete footings without and with punching shear reinforcement (Siburg and Hegger 2014). The specimens were tested upside down with the base area on top and loaded by a uniform surface load. The uniform soil pressure was simulated by means of 25 load application points. The load was applied depending on the expected failure load by either 13 hydraulic jacks (12 hydraulic jacks + 1 hydraulic jack with a piston area of half the size), which transferred their load through cross beams, or 25 hydraulic jacks (Fig. 2). All hydraulic jacks were linked to a common manifold and applied the same load independent of the displacement. In order to avoid any formation of membrane forces in the specimens, polytetrafluoroethylene-coated (PTFE) sliding and deformation bearings with dimensions of 140 × 140 mm were placed between the specimens and the cross beams or hydraulic jacks, respectively.

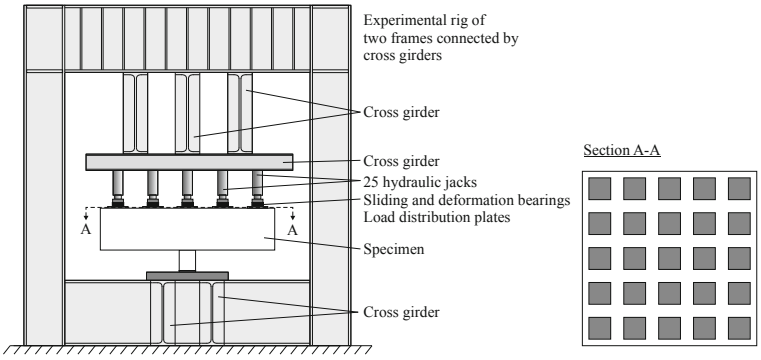

Fig. 2. Test setup

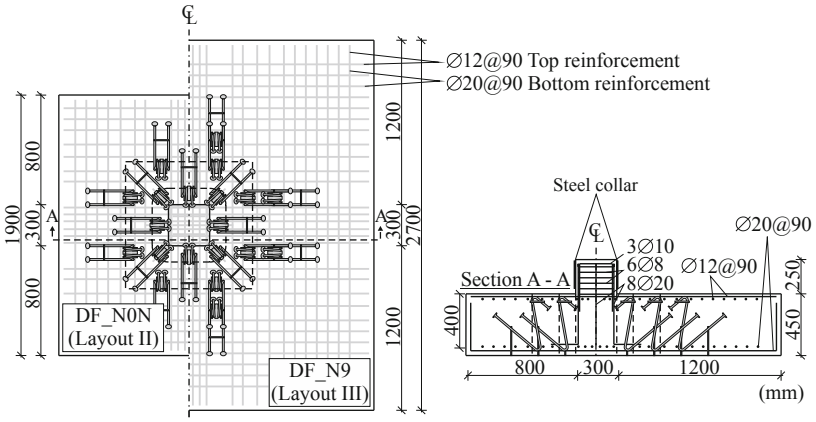

Fig. 3. Layout of flexural reinforcement and punching shear reinforcement for specimens DF_N0 N (Layout II) and DF_N9 (Layout III)

During testing, the vertical displacement of the test specimens was recorded at the corners of the column stub and at the footing's corners using linear variable differential transformers (LVDTs). To investigate the development of the inner shear cracks, the increase in the slab thickness was measured at several points and the penetration of the column into the slab was monitored. Strain gages were used to measure the strains in the flexural reinforcement at six locations and at several points in the punching shear reinforcement elements. To obtain the average strain at the bar's centre of gravity, two strain gages were attached to opposite side faces of the reinforcing bars at each measuring point. The concrete strains were recorded at four locations on the compression face of the footing near the column.

3.5 Test Procedure

The load was applied load controlled in increments of 200 kN (campaign I) or 400 kN (campaign II), respectively. To simulate lifetime loading, the load was cycled ten times between a calculated service load $V_{service}$ and half its value. For the specimens DF_N1, DF_N2, and DF_N3 (campaign I), the service load was 1200 kN corresponding to 40% of the predicted punching shear capacity of an identical footing without punching shear reinforcement according to DIN EN 1992-1-1 (2011) and DIN EN 1992-1-1/NA (2013). For the other specimens of the first experimental campaign, the service load was increased to 1400 kN. For the specimens of the second experimental campaign the service load was defined as the predicted failure load of an identical footing without punching shear reinforcement according to DIN EN 1992-1-1 (2011) and DIN EN 1992-1-1/NA (2013). After the load cycles, the specimens were continuously loaded until failure took place.

4 Experimental Results

4.1 Failure Characteristic

All tests failed in punching of the footing. The failure loads V_{test} are listed in Table 1. Before the failure occurred, increasing slab thickness, increasing strains in the punching shear reinforcement and penetration of the column stub into the slab were observed. The comparison with the flexural capacities of the footings V_{flex} according to yield-line theory (Gesund 1983) in Table 1 reveals the fact that the flexural capacities were not reached and hence confirms that failure occurred due to punching. Strain measurements verify this observation.

4.2 Cracking Characteristics

After testing, saw-cuts of the specimens were used to examine the inner shear crack patterns. In this context, Fig. 4 shows typical crack patterns of specimens with the new punching shear reinforcement and different punching failure modes.

All crack patterns showed finely distributed shear cracks crossing the punching shear reinforcement at several locations. Strain measurements confirmed that the punching shear reinforcement was activated. The saw-cuts of the specimens with a punching failure inside the shear-reinforced zone (e.g. DF_N5, campaign I, Fig. 4a) showed many inclined shear cracks, especially between the first and second row of punching shear reinforcement. In contrast, the footings with a punching failure on the level of the maximum punching shear capacity (e.g. DF_N0 N, campaign II, Fig. 4b) showed a steep failure crack, which developed between the column face and the lower bend of the punching shear reinforcement elements in the first row. In the slender specimens with shear span-depth ratios $a_\lambda/d = 3.00$ (e.g. DF_N9, campaign II, Fig. 4c) the failure crack developed from the third row of punching shear reinforcement, which indicates a failure outside the shear-reinforced zone.

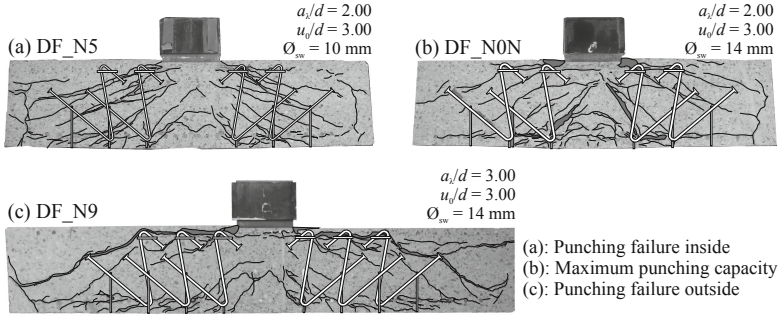

Fig. 4. Saw-cut of different specimens: Punching shear failure inside the shear-reinforced zone (a), punching shear failure at maximum load level (b), and punching shear failure outside the shear-reinforced zone (c).

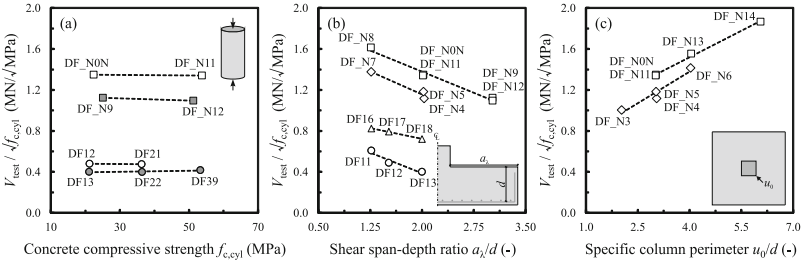

Fig. 5. Effects of concrete compressive strength $f_{c,cyl}$ (a), shear span-depth ratio a_λ/d (b), and specific column perimeter u_0/d (c) on punching shear strength of reinforced concrete footings.

5 Discussion of Experimental Results

5.1 Influence of Concrete Compressive Strength

The influence of the concrete compressive strength on the punching shear capacity of flat slabs was investigated by various researchers in the past (Elstner and Hognestad 1956; Regan 1986; Gardner 1990; Hallgren and Kinnunen 1996; Ramdane 1996). As a result of these investigations, different punching shear design provisions (e.g. ACI 318-14, *fib* Model Code 2010) account for this influence by the square root of the concrete compressive strength $\sqrt{(f_{c,cyl})}$. The influence of the concrete compressive strength on the punching shear capacity of footings without punching shear reinforcement was investigated in two test series (Hegger et al. 2009; Siburg and Hegger 2014). In this context, Fig. 5a shows the normalised failure loads $V_{test}/\sqrt{(f_{c,cyl})}$ for specimens DF12 (Hegger et al. 2009) and DF21 (Hegger et al. 2009) (a_λ/d = 1.50), as well as for specimens DF13 (Hegger et al. 2009), DF22 (Hegger et al. 2009), and DF39 (Siburg and Hegger 2014) (a_λ/d = 2.00). Regardless of the shear span-depth ratio, the tests

show no trend with increasing concrete compressive strength, which confirms the approach of $\sqrt{(f_{c,cyl})}$ for the presented footings.

To verify this effect for footings with the new punching shear reinforcement elements, specimens DF_N0 N and DF_N11 (a_λ/d = 2.00), as well as DF_N9 and DF_N12 (a_λ/d = 3.00), can be considered (Fig. 5a). As already observed for footings without punching shear reinforcement, the approach of the square root of the concrete compressive strength allows for a realistic description of the punching shear capacity of footings with the new punching shear reinforcement elements.

5.2 Influence of Shear Span-Depth Ration

In previous test series (e.g. Hegger et al. 2006, 2007b, 2009; Siburg and Hegger 2014), the effect of the shear span-depth ratio a_λ/d on the punching shear resistance of footings without and with stirrups as shear reinforcement was investigated. Figure 5b shows the normalised failure loads $V_{test}/\sqrt{(f_{c,cyl})}$ for specimens DF11 (a_λ/d = 1.25), DF12 (a_λ/d = 1.50), and DF13 (a_λ/d = 2.00) without punching shear reinforcement as well as specimens DF16 (a_λ/d = 1.25), DF17 (a_λ/d = 1.50), and DF18 (a_λ/d = 2.00) with stirrups as punching shear reinforcement. The shear-reinforced specimens failed at maximum load level, which was indicated by the measured steel strains far below the corresponding yield strain (Hegger et al. 2009). The tests indicate that the punching shear resistance decreases with increasing shear span-depth ratio. This influence is less pronounced for footings with stirrups as punching shear reinforcement than for footings without punching shear reinforcement. Thus, the efficiency of stirrups decreases with decreasing shear span-depth ratio.

To verify this effect for the footings with the new punching shear reinforcement elements, specimens DF_N7 (a_λ/d = 1.25), DF_N4 (a_λ/d = 2.00), and DF_N5 (a_λ/d = 2.00), with a failure inside the shear-reinforced zone (campaign I), as well as specimens DF_N8 (a_λ/d = 1.25), DF_N0 N (a_λ/d = 2.00), DF_N11 (a_λ/d = 2.00), DF_N9 (a_λ/d = 3.00), and DF_N12 (a_λ/d = 3.00) of the second experimental campaign can be considered (Fig. 5b). All these specimens were tested with a column perimeter-depth ratio u_0/d = 3.00. In contrast to the test results of the previous test series (Hegger et al. 2009), a similar correlation between punching shear resistance and shear span-depth ratio as for footings without punching shear reinforcement can be observed regardless of the failure mode. Hence, the efficiency of the new punching shear reinforcement with inclined bars seems not to be affected by the shear span-depth ratio.

5.3 Influence of Column Perimeter-Depth Ratio

Previous experimental investigations on the punching shear behaviour of flat slabs showed a strong correlation between the punching shear resistance and the column perimeter-depth ratio u_0/d (e.g. Regan 1986, 2004). For small ratios u_0/d, the punching shear resistance decreases, which is for example taken into account in the code provisions of DIN EN 1992-1-1 (2011) and DIN EN 1992-1-1/NA (2013) or a new uniform design method for punching shear in flat slabs and column bases (Kueres et al. 2017).

A verification of this effect for footings by means of the results of the previous test series (Hegger et al. 2006, 2007b, 2009; Siburg and Hegger 2014) on footings without and with stirrups as punching shear reinforcement is not possible, since the tests were conducted with a uniform u_0/d-ratio of 2.0.

Figure 5c shows the normalized failure loads $V_{test}/\sqrt{(f_{c,cyl})}$ for specimens DF_N3 (u_0/d = 2.00), DF_N4 (u_0/d = 3.00), DF_N5 (u_0/d = 3.00), and DF_N6 (u_0/d = 4.00), with a failure inside the shear-reinforced zone (campaign I), as well as for specimens DF_N0 N (u_0/d = 3.00), DF_N11 (u_0/d = 3.00), DF_N13 (u_0/d = 4.00), and DF_N14 (u_0/d = 6.00) of the second experimental campaign. Regardless of the failure mode, the tests indicate an increasing punching shear resistance with increasing column perimeter-depth ratio.

6 Conclusions

The results of the experimental investigations on reinforced concrete footings with the new punching shear reinforcement system allow the following conclusions to be drawn:

- The new punching shear reinforcement elements with inclined bars significantly increase the punching shear capacity of reinforced concrete footings. The high efficiency of the new punching shear reinforcement is also evident for footings with higher concrete compressive strength.
- Due to the rigid anchorage and the optimized geometry of the new reinforcement elements, the punching shear capacity of reinforced concrete footings can be considerably increased compared to similar footings with stirrups.
- Many code provisions account for the influence of the concrete compressive strength on the punching shear capacity by the square root of the concrete compressive strength. This approach could be verified by the tests on reinforced concrete footings with the new punching shear reinforcement element.
- While punching shear tests on reinforced concrete footings with stirrups indicate a reduced efficiency of the shear reinforcement with decreasing shear span-depth ratio, the efficiency of the new punching shear reinforcement elements seems not to be affected by the shear span-depth ratio.
- Regardless of the failure mode, the conducted tests on reinforced concrete footings with the new punching shear reinforcement indicate an increasing punching shear resistance with increasing column perimeter-depth ratio.
- The new punching shear reinforcement system allows for a significant reduction of footing's dimensions. Another advantage could be the reduction of minimum reinforcement in ground slabs due to reduced slab thicknesses.

Acknowledgements. The investigations presented were supported by Deutsche Forschungsgemeinschaft (German Research Foundation, DFG-GZ HE 2637/21-1) and the authors wish to express their sincere gratitude.

References

ACI Committee 318 (2014). Building code requirements for structural concrete (ACI 318-14) and commentary (ACI 318R-14). American Concrete Institute, Farmington Hills, MI

Andrä HP (1981) Zum Tragverhalten von Flachdecken mit Dübelleisten-Bewehrung im Auflagerbereich. Beton- und Stahlbetonbau 76(3):53–57 (Part 1), 76(4):100–104 (Part 2)

Beutel R, Hegger J (2002) The effect of anchorage on the effectiveness of the shear reinforcement in the punching zone. Cement Concr Compos 24(6):539–549

Dieterle H, Rostásy FS (1987) Tragverhalten quadratischer Einzelfundamente aus Stahlbeton. Deutscher Ausschuss für Stahlbeton, Heft, p 387

Dieterle H, Steinle A (1981) Blockfundamente für Stahlbetonfertigstützen. Deutscher Ausschuss für Stahlbeton, Heft, p 326

DIN EN 1992-1-1:2011-01. Eurocode 2: Bemessung und Konstruktion von Stahlbeton- und Spannbetontragwerken – Teil 1-1: Allgemeine Bemessungsregeln und Regeln für den Hochbau. Deutsche Fassung EN 1992-1-1:2004 + AC:2010

DIN EN 1992-1-1/NA:2013-04. Nationaler Anhang – National festgelegte Parameter – Eurocode 2: Bemessung und Konstruktion von Stahlbeton- und Spannbetontragwerken – Teil 1-1: Allgemeine Bemessungsregeln und Regeln für den Hochbau. Deutsche Fassung EN 1992-1-1/NA: 2013-04

Einpaul J, Brantschen F, Fernández Ruiz M, Muttoni A (2016) Performance of punching shear reinforcement under gravity loading: influence of type and detailing. ACI Struct J 113 (4):827–838

Elstner RC, Hognestad E (1956) Shearing strength of reinforced concrete slabs. J Am Concr Inst 28(1):29–58

Fernandez Ruiz M, Muttoni A (2009) Applications of critical shear crack theory to punching of reinforced concrete slabs with transverse reinforcement. ACI Struct J 106(4):485–494

Ferreira MP, Melo GS, Regan PE, Vollum RL (2014) Punching of reinforced concrete flat slabs with double-headed shear reinforcement. ACI Struct J 111(2):363–374

fib (Fédération international du béton) (2013). *fib* model code for concrete structures 2010. Ernst & Sohn, Berlin

Gardner NJ (1990) Relationship of the punching shear capacity of reinforced concrete slabs with concrete strength. ACI Struct J 87(1):66–71

Gesund H (1983) Flexural limit analysis of concentrically loaded column footings. ACI J Proc 80 (3):223–228

Hallgren M, Kinnunen S (1996) Increase of punching shear capacity by using high strength concrete. In: Proceedings of 4th international symposium on utilization of high-strength/high-performance concrete, Paris

Hallgren M, Kinnunnen S, Nylander B (1998) Punching shear tests on column footings. Nord Concr Res 21(3):1–22

Hegger J, Häusler F, Ricker M (2007a) Zur maximalen Durchstanztragfähigkeit von Flachdecken. Beton- und Stahlbetonbau 102(11):770–777

Hegger J, Ricker M, Sherif AG (2009) Punching strength of reinforced concrete footings. ACI Struct J 106(5):706–716

Hegger J, Ricker M, Ulke B, Ziegler M (2007b) Investigations on the punching shear behaviour of reinforced concrete footings. Eng Struct 29(9):2233–2241

Hegger J, Sherif AG, Ricker M (2006) Experimental investigations on punching behavior of reinforced concrete footings. ACI Struct J 103(4):604–613

Kueres D, Siburg C, Herbrand M, Classen M, Hegger J (2017a) Uniform design method for punching shear in flat slabs and column bases. Eng Struct 136:149–164

Kueres D, Ricker M, Hegger J (2017b) Improved shear reinforcement for footings—punching strength inside shear-reinforced zone. ACI Struct J 114(6):1445–1456

Mokthar AS, Ghali A, Dilger W (1985) Stud shear reinforcement for flat concrete plates. ACI J Proc 82(5):676–683

Park H-G, Ahn K-S, Choi K-K, Chung L (2007) Lattice shear reinforcement for slab-column connections. ACI Struct J 104(3):294–303

Pilakoutas K, Li X (2003) Alternative shear reinforcement for reinforced concrete flat slabs. J Struct Eng 129(9):1164–1172

Ramdane KE (1996) Punching shear of high performance concrete slabs. In: Proceedings of 4th international symposium on utilization of high-strength/high-performance concrete, Paris

Regan PE (1986) Symmetric punching of reinforced concrete slabs. Mag Concr Res 38 (136):115–128

Regan PE (2004) Punching of slabs under highly concentrated loads. Struct Build 157(2):165–171

Richart F (1948) Reinforced concrete wall and column footings. J Am Concr Inst 20(2):97–127 (Part 1), 20(3):237–261 (Part 2)

Ricker M, Häusler F (2014) European punching design provisions for double-headed studs. Struct Build 167(SB8):495–506

Siburg C (2014) Zur einheitlichen Bemessung gegen Durchstanzen in Flachdecken und Fundamenten. PhD thesis, RWTH Aachen University, Institute of Structural Concrete

Siburg C, Hegger J (2014) Experimental investigations on the punching behaviour of reinforced concrete footings with structural dimensions. Struct Concr 15(3):331–339

Talbot AN (1913) Reinforced concrete wall footings and column footings. Publications of the Engineering Experiment Station, Bulletin No, p 67

Integral Bridges: A Construction Method to Minimize Maintenance Problems

Achille Devitofranceschi[1(✉)] and Elisa Paolieri[2]

[1] Anas SpA, Rome, Italy
a.devitofranceschi@stradeanas.it
[2] Florence, Italy

Abstract. In traditional bridges, expansion joints and supports are installed to facilitate relative displacements and prevent the occurrence of stresses induced by thermal variations. However, such devices can cause maintenance problems. On the other hand, integral bridges are structures without joints and supports where abutments, piers and deck are connected monolithically producing a complex structural and geotechnical interaction. Integral construction thus eliminates maintenance works related to the presence of connection devices. However many countries have imposed restrictive limits on the length of these structures, and this paper aims to identify the maximum length of integral bridges, in relation to the particular boundary conditions considered in the case study. The authors present a study on soil-structure interaction concerning both backfill and foundation soil, and carry out the design of some structural elements of a reinforced and prestressed concrete integral bridge, paying attention to guarantee the necessary flexibility to the structure.

Keywords: Integral bridge · Soil-structure interaction · Maintenance · Thermal variation · Expansion joint · Support · Reinforced concrete · Prestressed concrete

1 Introduction

1.1 Integral Bridges

Traditionally, between superstructure and abutments of conventional bridges, expansion joints and sup-ports are installed to facilitate relative displacements and prevent the occurrence of stresses caused by thermal variations. However such components can cause maintenance problems.

It has been observed (Wallbank 1989) that deicing salts (normally used for roads maintenance in winter season) are the most important source of damage: they penetrate through the joints of the bridge deck and reach the substructures. This process causes corrosion of joints and supports located on abutments and between adjacent spans, becoming essential in defining costs of maintenance in conventional road bridges.

The full version of this article is a publication by aicap (Associazione Italiana Calcestruzzo Armato e Precompresso, www.associazioneaicap.com) entitled *Design of long integral road bridges*.

M. di Prisco and M. Menegotto (Eds.): ICD 2018, LNCE 42, pp. 515–529, 2020.
https://doi.org/10.1007/978-3-030-23748-6_40

Therefore, considering problems associated with expansion joints and supports in traditional bridges, the idea of physically connecting superstructure and substructure to create what is commonly called *integral bridge* is becoming increasingly popular. This concept avoids all the problems associated with connecting and supporting devices because it considers a structure with one or more spans without expansion joints or supports: piers, deck and abutments are connected monolithically to create a complex structural and geotechnical interaction.

However, due to the connection between superstructure and substructure, abutments are forced to move away from the embankment when the temperature decreases and the deck contracts (that is in winter), and to move towards the embankment when the temperature increases and the deck expands (that is in summer). Consequently, the backfill soil behind abutment is subject to cyclic loads induced by temperature variations, which can produce very high earth pressures.

1.2 Advantages and Disadvantages

Expansion joints and supports are expensive to buy, install, maintain and repair, and cause premature damage to the structures. For these reasons, integral bridges are the subject of multiple research and attract the interest of many engineers.

Below are the advantages and disadvantages of integral bridges compared to traditional bridges with expansion joints and supports:

Advantages:

- Significant reduction in maintenance costs by eliminating joints and supports;
- Lower construction costs;
- Elimination of vehicle jumps, previously caused by expansion joints, for vehicles accessing or leaving the bridge. This leads to an improvement in user comfort and to a reduction in noise emitted.

Disadvantages:

- Complexity of design due to the nature of the structure, which obligates the designer to study constraint states that may arise during the life of the bridge;
- Insufficient knowledge of the interaction between soil and structure;
- Lack of codes concerning integral bridges; consequently in many countries engineers refer to general design criteria or foreign standards.

Therefore it is essential to understand the behaviour of integral bridges, and then to propose technical solutions making them even more competitive than traditional bridges.

2 Analysis of Problems

2.1 Soil-Structure Interaction

The interaction between soil and structure involves both geotechnical and structural areas of interest; for this reason, it must be studied through a numerical model in which soil and structure are both present and can act simultaneously.

According to research carried out by the Transport and Road Research Laboratory (England et al. 2000), the nature and magnitude of cyclic displacements imposed on abutments and backfill soil are dependent not only on the environmental temperature but also on the type of construction of the bridge deck. A concrete deck has daily, seasonal and annual variations of temperature minor than a composite deck. Different types of bridge deck will thus produce different patterns of cyclic wall rotations and cyclic soil displacements at abutments, from a mixture of daily and seasonal temperature fluctuations (England et al. 2000).

Therefore, in the specific case of integral bridges, it is more appropriate to adopt a concrete deck in order to minimize earth pressures acting on abutments due to cyclic thermal movements of the superstructure.

Integral bridges are structures without expansion joints and supports that behave as a single structural element. In summer the expansion of the superstructure causes the horizontal translation and the rotation of the abutment towards the embankment. The increase of the earth pressure in summer corresponds to a decrease in winter, when superstructure contracts.

The fundamental problem of this complex mechanism between abutment and backfill soil lies in the fact that the maximum summer earth pressure does not remain constant, but tends to grow with the repeated seasonal expansion and contraction of the superstructure. During winter contraction of the superstructure, a portion of soil slides down towards the abutment; then, when air temperature grows and superstructure extends, that portion of soil does not return to its original position but opposes the displacement of the abutment. Consequently, over the years, a growing earth pressure develops behind abutments. Furthermore, as a result of this settlement, a void develops under the road pavement near the abutment.

In conclusion, the soil-structure interaction problem for integral bridges includes both the progressive increase in summer earth pressure and the settlement of soil behind abutments.

A purely structural solution can be the reduction of the height of each abutment: the bank pad abutment (Design Manual for Roads and Bridges 2003) represents a final support for the bridge that moves horizontally during thermal expansion and contraction of the deck. It acts as a shallow foundation for the last span and as a short retaining wall for the embankment.

On the other hand, if a full height abutment is adopted, it is recommended to use a compressible inclusion between abutment and backfill soil. Subjected to a certain stress, the inclusion has greater deformations than the other materials present, and this results in a localized stress reduction.

A compressible inclusion is very effective in reducing the earth pressure increase during summer, but it can not control the soil settlement behind abutments. In fact,

when the superstructure contracts causing abutments to move away from the embankment, inclusion can not support the soil, which collapses towards the abutment.

There are two possible solutions to try to solve both problems (Fig. 1).

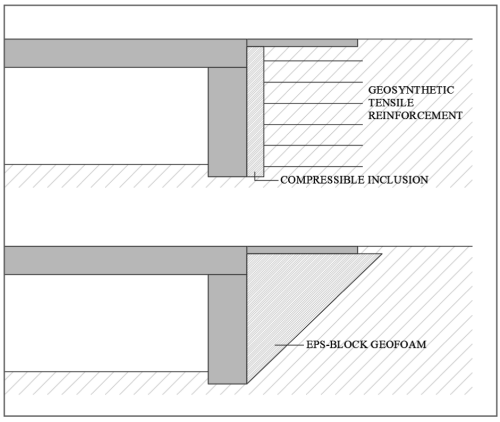

Fig. 1. Solutions for reducing earth pressure and controlling the settlement behind abutments.

In the first solution the ground is stabilised by a geosynthetic tensile reinforcement, while the second one involves the use of a wedge-shaped expanded polystyrene block. Choosing one of the two solutions presented should be based on both technical and economic considerations. The first solution is generally cheaper, while the second one is more expensive but recommended in sites characterized by soft and compressible soils (Horvath 2000).

The bridge studied is supported by full height abutments, then compressible inclusions and geosynthetic tensile reinforcement are included in constructive details. However, in structure modelling, the presence of compressible inclusions and geogrids behind abutments is not considered as their benefit is not quantifiable.

2.2 Transition Zone

In integral bridges, the interaction between transition slab and soil supporting it must also be considered.

Transition slabs provide a gradual transition from the embankment to the bridge and back, and allow to overcome possible settlements of the backfill soil behind abutments. To avoid water infiltration due to expansion joints, transition slabs are directly connected to the ends of integral bridges. They are subject to thermal movements of the superstructure, then the design of such elements must be carried out carefully.

Designers have to pay attention to how longitudinal movements are transmitted to the soil: they can study the geometry of the slab to guarantee a correct stress distribution avoiding excessive settlements, or they can adopt systems that allow to release

transition slab from soil. Therefore, two different types of transition slab can be considered:

(1) *Embedded transition slab*:

It is connected to the abutment using a concrete hinge, then it moves with the abutment during thermal movements of the deck.

A study on the transition slab geometry (Dreier et al. 2011) shows that, increasing the depth of the transition slab's end, designers can minimize the settlement, limit the size of surface discontinuities and improve users' comfort. This can be achieved by increasing both the slope and the total length of the transition slab. For the slope, the authors recommend values between 5 and 20%; the minimum value is required to have a gradual transition from the embankment to the bridge, while the maximum value is used to prevent slides in the soil above the slab.

In this first type of transition slab, longitudinal movements of the deck are transferred to the abutment, then to the slab, and finally to the soil (maximum soil stresses occur near the end of the transition slab). Therefore bridge movements are distributed along the entire length of the transition slab avoiding possible dips and bumps in road pavement (Fig. 2).

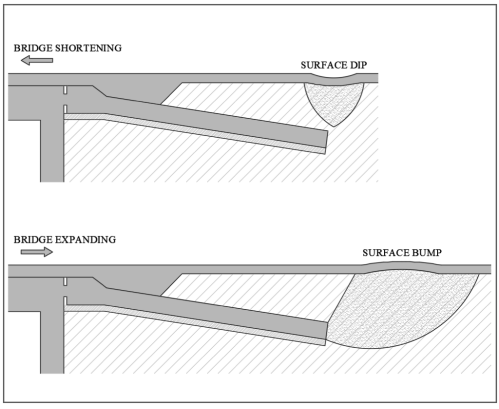

Fig. 2. Potential deformations of pavement: dip due to bridge shortening, and bump due to bridge expansion.

The top surface of the transition slab must be sufficiently rough to prevent sliding between the above soil and the slab itself, otherwise a crack develops at the connection between the superstructure and the slab when the bridge contracts. Therefore, during bridge shortening, cracks develop near the end of the transition slab, making it unlikely that water will reach the structural elements.

(2) *Transition slab with plinth foundation*:

As the previous type of transition slab, it is connected to the abutment using a concrete hinge, then it moves with the abutment when thermal movements occur. It is

horizontal, and it is supported by the abutment (on the bridge side) and by a plinth foundation (on the embankment side). The plinth is positioned beyond the limit of the wedge obtained considering the active earth pressure condition.

In this second type of transition slab, longitudinal movements of the deck are absorbed by the joint installed at plinth foundation (however, water does not have direct access to structural elements of the bridge). The system that allows the sliding of the transition slab on the plinth is composed of an half steel bar with large diameter, two steel plates (one anchored to transition slab, and the other one to the plinth), and anchorages (Nelson type).

3 Description of the Bridge

The integral bridge studied is 620 m long and has 20 spans of 31 m. It is made of reinforced and prestressed concrete, and the deck is integral with substructure both at abutments and piers.

The bridge deck (Fig. 3) has a total width of 12 m. It is supported by 4 prestressed girders with V-section that are 30 m long. The structural slab has a constant thickness of 0.27 m and the transverse slope is created using a layer of asphalt concrete binder with variable thickness.

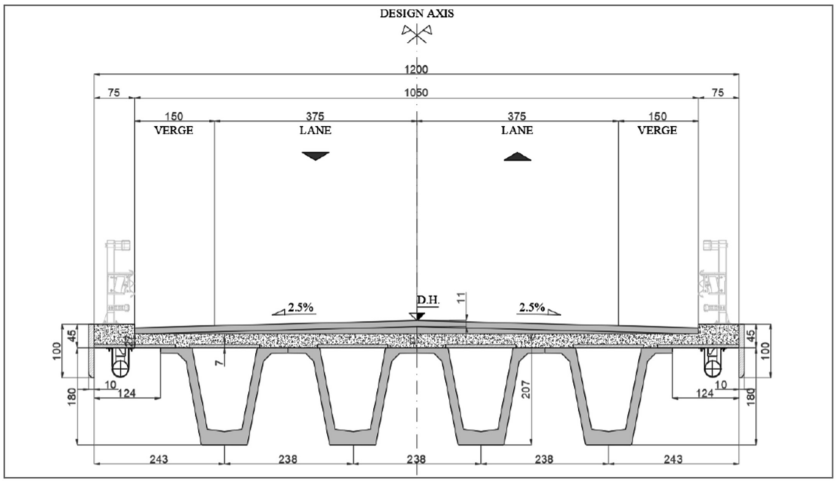

Fig. 3. Bridge deck: cross section at mid span.

Girders are produced in a plant and then moved on construction site. Structural slab and connection zones between deck and substructure are cast in place after the positioning of girders on piers and abutments. The deck is supported by 19 piers and 2 abutments. Piers have different heights, from a minimum of 6.15 m to a maximum of 18.5 m. Both abutments "A" and "B" are full-height frame abutments (Design Manual for Roads and Bridges 2003) and are 9.2 m high.

Abutments and piers are founded on a single row of piles in order to guarantee the necessary flexibility to the whole structure. As a matter of fact, in integral bridges it is more appropriate to adopt foundations that are flexible in the longitudinal direction, because they reduce constraint imposed to thermal movements.

Figures 4–6 show the geometry of abutments, piers and their foundations, while Fig. 7 shows the transition zone behind abutments.

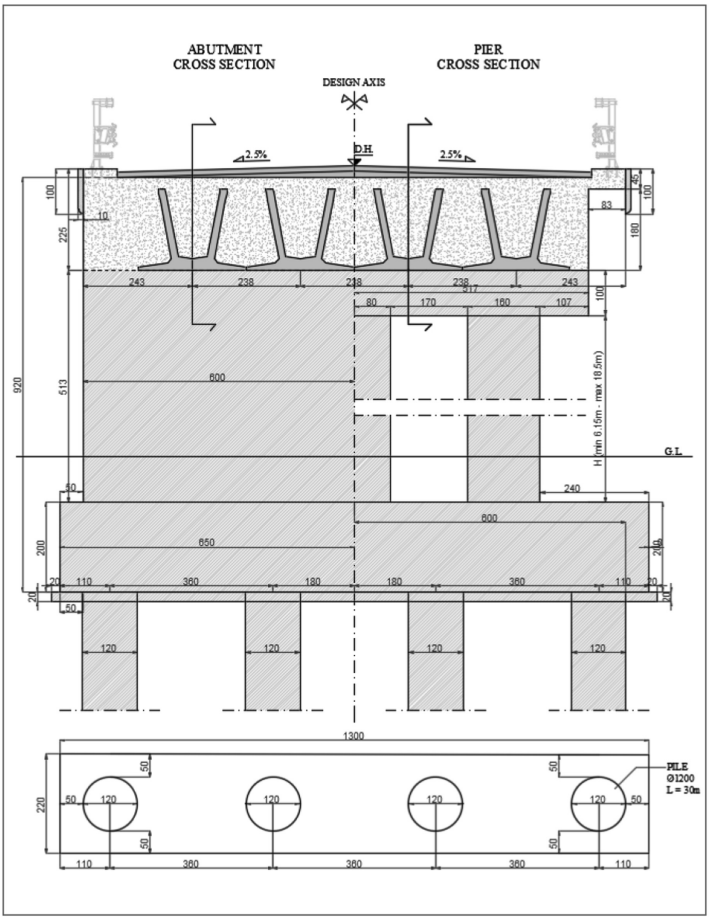

Fig. 4. Abutments/piers: cross section.

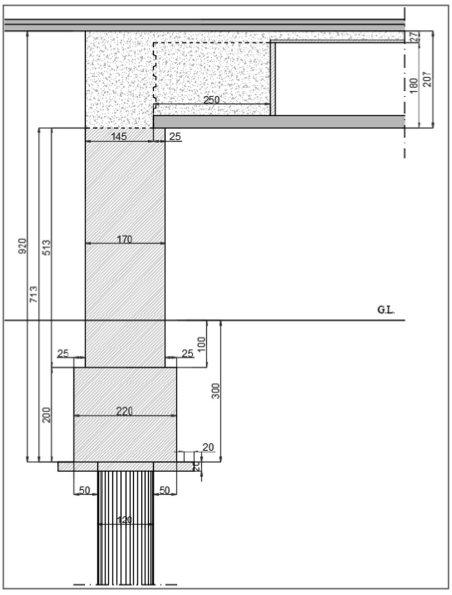

Fig. 5. Abutments: longitudinal section.

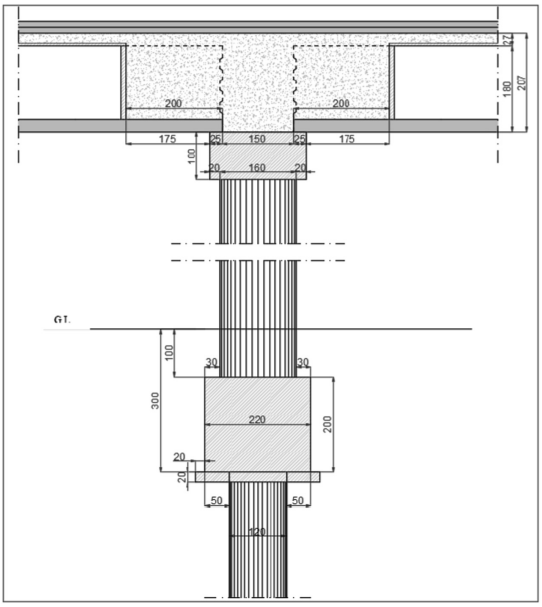

Fig. 6. Piers: longitudinal section.

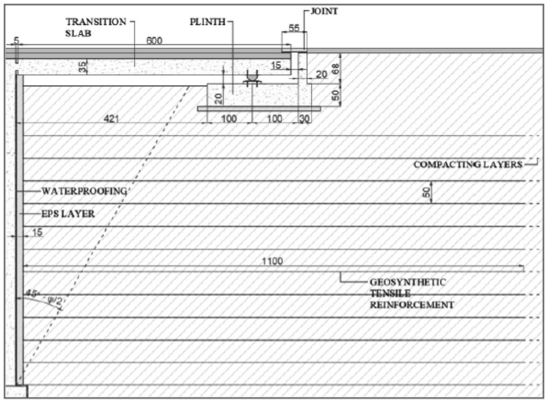

Fig. 7. Transition zone behind abutments: EPS layer (compressible inclusion) and geosynthetic tensile reinforcement adopted to reduce localized stresses and soil settlements respectively.

4 Materials

Materials used are: concrete C50/60 for girders, concrete C32/40 for abutments, piers, foundations and structural slab, steel B450C for passive reinforcement, strands for girders, and DYWIDAG plain bars 32WS for transverse reinforcement at nodes.

5 Load Analysis

Loads included in the model are:

- Permanent actions: structural and non-structural permanent loads, at rest earth pressure (distribution of pressure that increases linearly with depth, $\varphi' = 35°$, $K_0 = 0.43$);
- Impressed deformations: creep and shrinkage (automatically taken into account by MIDAS Civil), thermal actions ($\Delta T_{N,con} = 23$ °C, $\Delta T_{N,exp} = 29$ °C, $\Delta T_{M,heat} = \Delta T_{M,cool} = 7$ °C), active earth pressure (distribution of pressure that increases linearly with depth, $\varphi' = 35°$, $K_A = 0.25$), passive earth pressure (automatically introduced in the numerical model by MIDAS Civil using non-linear springs behind abutments; furthermore the program consider the soil ratcheting through the cycle factor f_{cyc}), differential settlements;
- Live loads (according to italian NTC 2008);
- Wind load (wind pressure p = 1.82 kN/m^2);
- Seismic load: horizontal and vertical components (values in Table 1), and spatial variability of seismic action (maximum displacements at abutments, while at the base of the piers displacements vary linearly between abutment A and abutment B; two scenarios are considered: central fixed point with displacements directed towards abutments, and central fixed point with displacements directed towards the centre of the bridge).

Table 1. Values used for design response spectra.

	a_g	F_0	T^*_C	q
	g	–	s	–
DLS_hor	0.126	2.441	0.326	1
DLS_vert	0.061	–	–	1
LSLS_hor	0.28	2.521	0.350	1.5
LSLS_vert	0.203	–	–	1

6 Modelling

In integral bridges the analysis of soil-structure interaction is essential because of the earth pressures which develop following the thermal expansion and contraction of the deck.

6.1 Soil-Structure Interaction: Method of Analysis

The bridge considered in the study has abutments founded on a single row of piles, then it is not included among structures that can be studied with the *limit equilibrium method*, the first method given by the British Standards (this type of analysis provides formulas to calculate the design value of the earth pressure coefficient for expansion depending on abutment's geometry, and suggests the force distribution with which the designer can simulate the earth pressure acting behind abutments). Moreover the study aims to achieve the maximum length for integral bridges, exceeding the 60 m limit provided by the Design Manual for Roads and Bridges.

Therefore the second method, the *soil-structure interaction method*, has to be chosen, studying the soil-structure interaction through a numerical model that considers the soil properties explicitly.

6.2 Soil Ratcheting Modelling

Integral bridges are structures without joints in the deck that accommodate thermal expansion and contraction by movement of the abutments in and out of the backfill. In granular soils, this repeated backward and forward movement of the abutment causes particle realignment and a consequent increase in the soil stiffness. With the succession of many thermal cycles, pressures become significantly higher than those that would occur with a single thermal cycle and this effect leads to a progressive year-on-year increase in soil pressure behind abutments which is termed *soil ratcheting*.

This phenomenon has to be considered during design and has to be included within the model, as an increase in the soil stiffness results in higher mobilized passive resistance.

The British Standards Institution, MIDAS Civil and Lehane et al. (1999) take into account the increase of the passive earth pressure over the years by multiplying the secant shear stiffness under monotonic loading conditions by the following suggested factors to obtain the operational secant shear stiffness of the granular backfill soil: $f_{cyc,1} = 1.5$ (British Standards Institution), $f_{cyc,2} = 2$ (MIDAS Civil), $f_{cyc,3} = 1.4$ (Lehane et al.).

The three values are very similar, then the value proposed by MIDAS Civil (f_{cyc} = 2) is assumed in the modelling.

6.3 Description of the Model

Time dependent material properties (creep, shrinkage and the variation of modulus of elasticity with time) are automatically applied by MIDAS Civil to concrete.

Girders, slab, piers and foundation piles are modelled using beam elements, while abutments are represented by shell elements. The bridge deck is composed of 4 girders in longitudinal X direction (including longitudinal structural slab) and structural slab in transverse Y direction.

The transverse structural slab allows the collaboration between longitudinal girders. Rigid links between longitudinal girders and transverse structural slab are included to simulate the real deformation mode of the deck in transverse direction (that is the real supporting points of structural slab). Each beam in longitudinal direction represents the precast girder and the collaborating structural slab.

Foundations piles under piers/abutments are simply supported at their base. Springs are positioned along piles using MIDAS' *Pile Springs* (sand, γ = 18 kN/m^3, φ' = 30°). To simulate passive resistance of backfill soil during deck expansion, compression-only springs are positioned at abutments' nodes using MIDAS' *Abutment Springs* (e = 0.3, f_{cyc} = 2).

The numerical model also takes into account construction stages: construction of piles, abutments, piers, and positioning of girders; realisation of bridge deck and nodes. The study takes into account the change both in girders' section and in girders' boundaries.

7 Design of Nodes at Abutments and at Piers

Nodes at abutments and at piers are studied with strut and tie models. The resistant section for design is the portion of the node on abutment/pier and inside precast girders.

Abutment/pier's vertical reinforcement come out from the height at which girders are supported without hindering their positioning. When girders are still simply supported, the structural slab is realized in order to eliminate the contribution of girders' and slab's self weight from the total negative moment. Then node's portion of concrete is cast.

Nodes are subject to both negative bending moment (for permanent and accidental loads) and positive bending moment (for seismic actions).

Figures 8–10 show details of nodes at abutments and at piers.

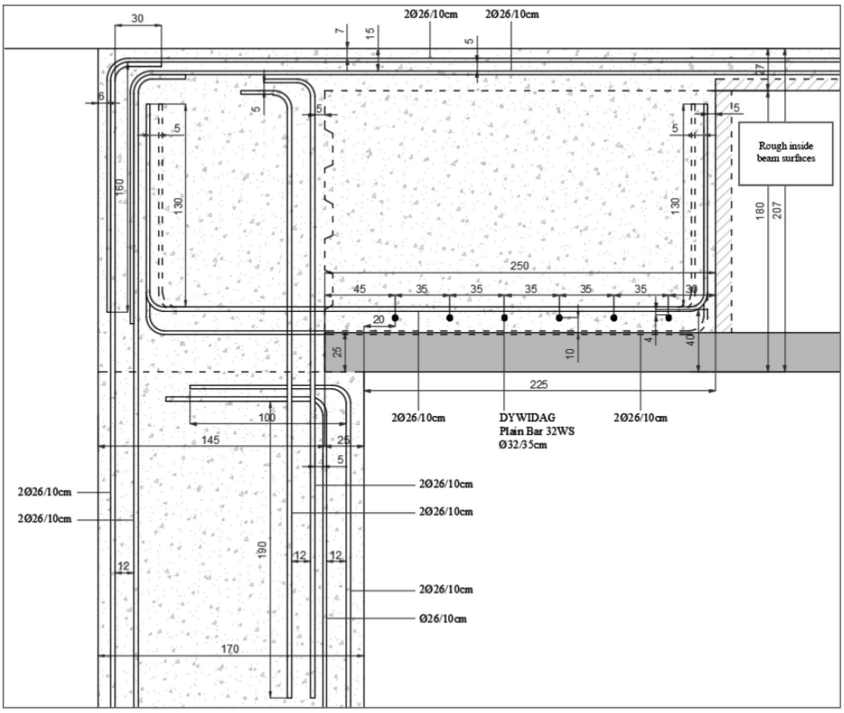

Fig. 8. Node at abutment.

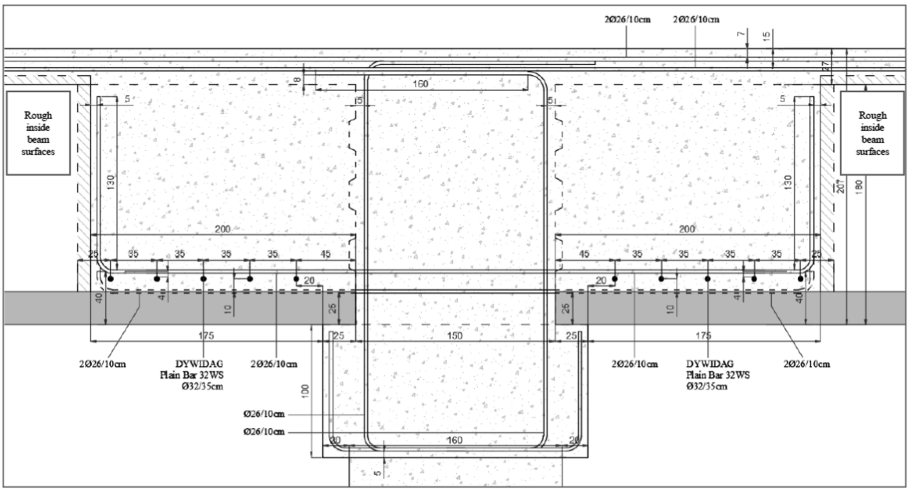

Fig. 9. Node at pier.

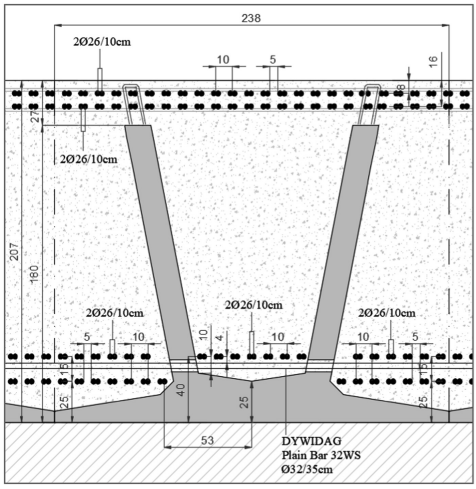

Fig. 10. Final section of girder near abutment.

8 Final Remarks

Integral bridges are one of the most efficient solutions to maintenance problems associated with expansion joints and supports. They lead to a significant reduction in maintenance and construction costs, and the absence of expansion joints allows to eliminate jumps for vehicles accessing or leaving the bridge. However, longitudinal thermal movements of the bridge deck cause the interaction between soil and structure to be studied carefully.

In the present study, the soil-structure interaction is analysed with MIDAS Civil. Results obtained from the model are compared with those obtained from traditional analysis (manual calculation of earth pressure coefficient and determination of stress distribution behind abutments). Manual methods are simplified, then they provide a more conservative solution. Therefore, considering a total length of the bridge equal to 60 m and separating abutment springs from pile springs, MIDAS' results are minor than those obtained from traditional analysis, but the difference is less than 15%.

Furthermore, in integral bridges designers have to consider the phenomenon of soil ratcheting: with the succession of many thermal cycles, the repeated backward and forward movement of the abutment causes an increase in soil stiffness and a progressive year-on-year increase in soil pressure behind abutments. The soil ratcheting is included in the numerical analysis through the cycle factor recommended by MIDAS Civil, that is very similar to those suggested by the British Standards Institution and Lehane.

Moreover, actions that most influence the behaviour of the bridge are the expansion temperature uniform component (with the associated mobilised passive earth pressure) and the longitudinal seismic action.

Substructure's stiffness is a fundamental aspect in integral bridges. In the present study frame abutments are adopted: they support the bridge deck and act as retaining walls for the backfill; they are connected structurally to the deck and they are supported on piled foundations. In integral bridges, abutments with double wall could also be used (Fig. 11): the deck is supported on flexible piles or columns, that are located in front of a retaining wall. Therefore, they overcome the soil-structure interaction problem and they allow the construction of very long integral bridges even in highly seismic areas (bending moments of nodes are reduced by about 20%). On the other hand, we believe that bank pad abutments founded on piles (even if foundations have a single row of piles) do not work properly in long integral bridges: as a matter of fact, horizontal thermal movements of the top of abutment are directly transferred to the head of foundation piles leading to excessive shear forces, while a high frame abutment can absorb a part of thermal movements reducing forces on piles.

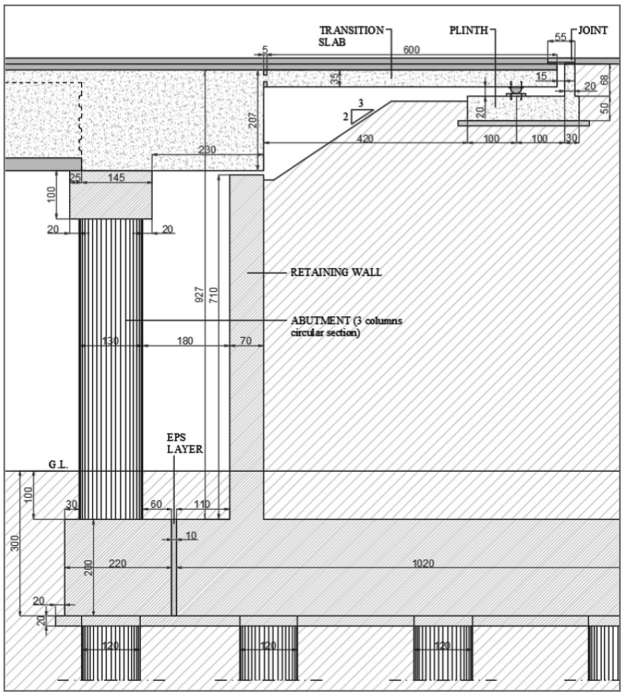

Fig. 11. Abutment with double wall (flexible support abutment).

In conclusion, considering the boundary conditions applied to the present study (that are geometry of structural elements, characteristics of materials, and importance of loads), we believe that a total length of 600 m can be reached with an integral bridge.

References

Design Manual for Roads and Bridges (2003) The design of integral bridges

Dreier D, Burdet O, Muttoni A (2011) Transition slabs of integral abutment bridges. Struct. Eng. Int. 21:2

England GL, Tsang NCM, Bush DI (2000) Integral bridges - a fundamental approach to the time-temperature loading problem. Thomas Telford Ltd, London (UK)

Horvath JS (2000) Integral abutment bridges: problems and innovative solutions using geofoam and other geosynthetics

Lehane BM, Keogh DL, O'Brien EJ (1999) Simplified elastic model for restraining effects of backfill soil on integral bridges. Computers and Structures

FIB Bulletin 75 – New System Performances and Full Scale Tests

T. Ciccone(✉) and L. Civati

Stay-Cable and Post-Tensioning Systems Technical Department, Tensacciai Srl, Milan, Italy
t.ciccone@tensainternational.com

Abstract. FIB Bulletin 75 recommendation has introduced improved performance requirements on corrugated plastic ducts for post-tensioning tendons and also on the entire post-tensioning system. Aim of this article is to describe and analyze critically the most important innovations introduced also with reference to previous FIB Bulletin 7. Special emphasis is given on the full scale testing program carried out recently by Tensa over its post-tensioning tendons in accordance to Annex B of FIB Bulletin 75. A supplementary testing program, made with reference to Florida Department of Transportation 2018 Construction Specifications, is also considered as a reference for further analysis.

Keywords: Post-tensioning systems · Corrugated plastic ducts · Tendons corrosion protection

1 Introduction

FIB Bulletin 75 "Recommendation on Polymer-duct systems for internal bonded post-tensioning", published in December 2014, is a new and improved version of FIB Bulletin 7 "Technical report on Corrugated plastic ducts for internal bonded post-tensioning", dated January 2000.

Corrugated plastic ducts and relevant accessories for post-tensioning systems are becoming more and more important components part of concrete structures around the world.

One of the main reasons for such development is the higher durability granted by such components within the overall performance of the post-tensioning systems and the entire structure.

Several International Recommendations such as PTI / ASBI M50 "Guide Specification for grouted post-tensioning", FIB Bulletin 33 "Durability of post-tensioning tendons" and Florida Department of Transportation "Standard Specifications for Road and Bridge Construction" have set as mandatory the use of corrugated plastic ducts for tendons permanently incorporated within concrete structures, providing medium – high corrosion protection.

Such requirement is further strengthened by the new FIB Bulletin 75 (hereafter called "FIB 75") which provides a clear frame within assessing the minimum required performance not only for the duct itself but also the entire duct system.

M. di Prisco and M. Menegotto (Eds.): ICD 2018, LNCE 42, pp. 530–544, 2020.
https://doi.org/10.1007/978-3-030-23748-6_41

2 Improvements and Lesson Learned

Key advantages and lesson learned in the use of plastic corrugated ducts have been described in the new FIB Bulletin 75 and can be summarized as follows:

- Polypropylene (PP) and Polyethylene (PE) have a different behavior depending on temperature: in principle PP handles higher temperatures than PE while PE better deals with cold temperatures;
- Recycled plastic material affects performance and durability will be significantly reduced;
- Drainage pipe-type plastic ducts are definitely considered not appropriate for post-tensioning applications due first to their insufficient wall thickness and poor wear resistance;
- Electrically Isolated Tendons (EIT) are well considered as a valuable solution for the long-term protection of tendons through full complete encapsulation.

FIB 75 provides also a large amount of information for design purposes such as criteria for selecting the proper Protection Level for tendons, choice of materials, behavior and effects from temperature variation.

There is a number of performance requirements, with reference to FIB Bulletin 7 (hereafter called "FIB 7"), which have been improved and/or introduced.

Most of the acceptance criteria for each test aimed at assessing duct performance have been now split depending on the Protection Level (PL) Type requested for the intended use.

Generally speaking, the higher is the PL, the more severe and stringent are the acceptance criteria for performance testing.

FIB 75 clearly states that, for PL2 and PL3, in order to achieve the desired tendon protection level, full encapsulation of the tendon over its entire length is required.

This means that all auxiliary components such as caps for anchorages, connectors for duct segments and grout connections are integral part of the polymer duct system and hence any assessment of the performance must be done on partially or fully assembled system.

This is why the assessment program is divided between components and systems.

In the following paragraphs descriptions, relevant properties and reference to FIB75 sections will be given.

3 Components Requirements and Assessment Tests

3.1 Dimensional Requirements (Section 6.1 & A.1)

All components need to be precisely defined in terms of geometry, including tolerances. Special care should be given also to different shrinkage of different blends of plastic material, which may affect dimensional tolerances of finished products.

As described later on, since wall thickness plays a crucial role in the duct's performance, measurements of this parameter are very important throughout the entire assessment program.

3.2 Stiffness of Duct (Section 6.2 & A.2)

In order to avoid ducts movements and unexpected bending before and during concreting, it is necessary to determine the maximum permissible spacing of ducts support, strictly correlated to ducts' stiffness.

FIB 75 introduces a more precise and clear testing procedure, aimed at determining minimum supports spacing in a direct way, through force application and deflection measurement.

In the test set-up a load is transversally applied up to reach a deflection of 5 mm from the horizontal. Stiffness is then calculated from the load deflection diagram and support spacing (SS) then determined through a formula.

Previous FIB 7 (that called this requirement as "flexural behavior of duct") was not clear on this and testing procedure was not aimed at determining a direct SS (Fig. 1).

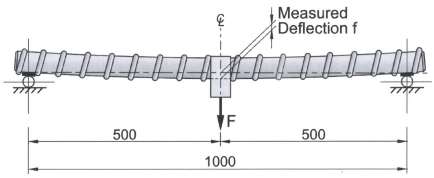

Fig. 1. Stiffness of duct test set-up

3.3 Longitudinal Load Resistance of Duct System (Section 6.3 & A.3)

This requirement is strictly connected to the fact that temperature range, due to direct sunlight and environmental exposure, can definitely induce longitudinal loads to the ducts before concreting.

Ducts' and duct connectors' strength has to be assessed with a dedicated test, aimed at applying a longitudinal load to achieve an elongation of the duct equal to the one given by a 40 °C temperature variation.

This testing condition of 40 °C temperature range has been introduced with FIB 75 while in previous FIB 7 an applied elongation of 8 mm/m was set as default value.

3.4 Lateral Load Resistance of Duct (Section 6.4 & A.4)

Ducts must bear local stresses due to curvature and concrete loads at the support points. These actions must not deform ducts otherwise strands' threading will not be possible.

Testing procedures aim at verifying that duct will not show irreversible transverse deformations of 10% of the duct diameter or 5 mm (whichever is smaller) after the release of the specified load.

3.5 Flexibility of Duct System (Section 6.5 & A.5)

Duct must be flexible enough to allow bending to a curvature radius that will be used during shipping and/or on site.

When bent to a specific radius of curvature, deformation of the duct cross-section should not exceed 5% of the internal duct diameter to allow the installation of pre-stressing steel on site and to confirm that the tendon will remain within the profile envelope.

Since this property is affected by temperature, FIB 75 introduces testing at room, low and high temperatures. Polymers become brittle at low temperatures, with potential cracks while bending, while soften at high temperatures with potential loss of shape (Fig. 2).

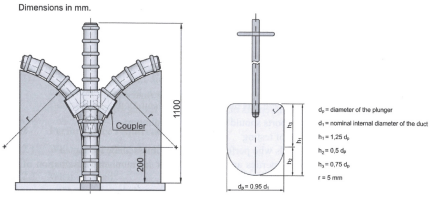

Fig. 2. Flexibility of duct system test set-up

3.6 Leak Tightness of Duct System (Section 6.6 & A.6)

Tightness is a crucial property for the duct system.

Depending on the type of protection level required (PL1 or PL2 / PL3) it must be mortar or leak tight.

In order to simulate in full site conditions, assessment is performed on the same test specimen that has previously successfully passed longitudinal load, lateral load and flexibility testing.

This sequence provides a severe assessment of real performance under site conditions.

For leak tightness assessment, specimen is bent to specified minimum radius of curvature and then is subjected to 0.5 bars positive and then negative pressure to check for air expulsion or water infiltration.

Usually difference between PL2 and PL3 is on the duration of pressure application: 5 against 30 min.

3.7 Concrete Pressure on Duct System (Section 6.7 & A.7)

When concrete is placed, ducts may collapse due to exposure to pressure.

Ducts need to withstand the concrete pressure so that strands can be installed and tensioned properly.

FIB 7 did not have any assessment of this property while FIB 75 identifies also two different performance classes; type I and II.

Type I is for polymer ducts for general use and specifies that the duct system should keep at least a minimum of a 3.0 m in normal-weight concrete head pressure for all types of duct and sizes bent to the specified minimum radius of curvature for field installation.

Type II applies to shallow concrete members and may apply primarily to flat polymer ducts (1 m).

3.8 Wear Resistance of Duct (Section 6.8 & A.8)

This is an extremely important requirement to determine the long-term performance of the duct and the overall durability of the entire post-tensioning system.

Ducts should be sufficiently resistant to wear caused by strands during stressing operations, especially when bent to the minimum radius of curvature defined for the duct size used.

If strands wear through the duct wall

- the integrity of tendons' envelope will be compromised and encapsulation lost;
- friction coefficients will be dramatically underestimated;
- fretting fatigue of tendons may arise due to contact between strands and reinforcing steel.

In order to prevent from potential damages described above, a minimum residual duct wall thickness must remain in place after tendon stressing.

FIB 75 introduces different values for each Protection Level, while previous FIB 7 was asking for not less than 1 mm whatever was the PL considered.

In detail:

- for PL1, minimum residual wall thickness after testing is 1.0 mm;
- for PL2 and PL3, minimum residual wall thickness after testing is 1.5 mm.

In order to reproduce site conditions, a specified force is applied as a clamping force on a single strand to a duct specimen and then the single strand is moved on the polymer duct to simulate the stressing of the tendon.

The clamping force Q applied to the single strand in the test can be related to the actual size of the tendon, the stressing force and the tendon radius of curvature through the equation:

$$Q = 0.7\left(F_{pk}A_p k\ l\right) / R_{min} \tag{1}$$

Where

F_{pk} = specified strength of steel.
A_p = specified cross section of a single tensile element of prestressing steel.
k = cable factor to account for effect of actual number n of tensile elements (strand) inside one duct, according to Oertle (1988). This factor can also be determined as per Weiher (2008).
R_{min} = manufacturer's declared minimum radius of tendon curvature for field installation.

Of course testing is performed to determine minimum radius of curvature by reversal approach: clamping force is gradually increased up to reach minimum wall residual thickness so that by formula (1) R_{min} is calculated.

FIB 75 acknowledges the key role of temperature on this performance and for such reason tests have to be carried out not only at room temperature but also at high temperature (45 °C) (Figs. 3 and 4).

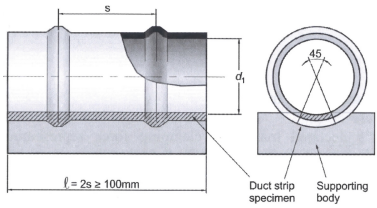

Fig. 3. Wear resistance of the duct test specimen

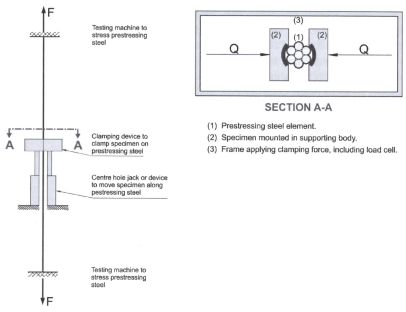

Fig. 4. Wear resistance of the duct test set-up

3.9 Wear Resistance of Duct Under Sustained Load (Section 6.9 & A.9)

This requirement is strictly related to the previous one and it is aimed at taking into account the need of having a duct sufficiently resistant during the time between the stressing and grouting of the tendon.

In fact, after stressing, the duct bears the load given by strands until grouting is performed.

Testing procedure reproduces such condition and calls for a 14 days' time of clamping force applied over duct strips soon after standard wear resistance test has been completed.

This requirement was first introduced by Florida Department of Transportation (hereafter called "FDoT") in year 2007 by requesting to modify basic wear resistance test given in FIB Bulletin 7 and adding a sustained load application of 7 days.

FIB 75 requests a residual wall thickness of 0.5 mm for PL1 tendon and 1 mm for PL2 and PL3.

It has to be noticed that standard PTI / ASBI M50 "Guide Specification for grouted post-tensioning" in year 2012 decided to ask for a sustained load wear resistance test by modifying the old FIB 7 standard wear test and applying load for 7 days, asking for a residual wall thickness of 1.5 mm for duct diameters up to 86 mm and 2 mm for diameters greater than 86 mm.

This procedure asks for half of the time for the load application but sets a higher acceptance criterion for residual wall thickness.

3.10 Bond Behaviour of Duct (Section 6.10 & A.10)

Ducts should be able to provide sufficient bond with the concrete outside and the grout inside the duct.

The assessment procedures for the bond behaviour confirm the ability of the duct to maintain bond when a load of 40% of the tendon ultimate tensile force is applied from the prestressing strand inside the duct into the concrete in a maximum length of 16 duct diameters.

3.11 Precast Segmental Duct Coupler System (Section 6.11 & A.11)

Precast segmental duct couplers, used in precast segmental construction, provide protection from external agents by guaranteeing leak tight continuity of ducts through joints.

Essential functions of these components include gasket compression at a force lower than the temporary prestressing force for segments erections (gasket not acting like a shim), maintaining pressure (3.5 bars for PL2 / PL3 tendons) to prevent intrusion, remaining intact without failure and free of epoxy inside the encapsulation, keeping all components properly attached.

Performance requirement and assessment procedures were not mentioned in FIB 7 while similar but less stringent requirements (2.6 bars) were set in FDoT Standard Specifications for Road and Bridge Construction up to issue 2016.

Assessment procedures require casting concrete blocks where duct segments with couplers are placed. Compressive forces are then applied to put together concrete blocks and pressurization of ducts can start.

Compressive forces should not be greater than 0.175 MPa times the area enclosed by the gasket while, depending on the PL required, system should bear from 1.5 to 3.5 bars for a minimum of 5 min.

3.12 Fracture Resistance of Duct System (Section 6.12 & A.12)

This is an optional performance to be assessed, which was not included in previous FIB 7.

Assessment procedures for the fracture resistance of the duct system confirm that it remains intact with no cracks or perforations during the cyclic crack opening test.

4 Post-Tensioning System Assessment Tests

FIB 75 has also considerably improved details and requirements for the system assessment tests with respect to FIB 7. In detail the new recommendation has created five different assembly tests, previously carried out on the same mock up assembly. In the following paragraphs the new tests are briefly descripted, also as a comparison with outdated ones, and results obtained by Tensa PT system are shown. Moreover further assembly tests required by FDoT are described together with results.

4.1 Leak Tightness of Anchorage-Duct Assembly (Section 7.1 & B.1)

Test is designed to confirm anchorage-duct assembly tightness against mortar in case of PL1, PL2 or PL3 project conditions.

One test is required on a medium anchorage size. Furtherly, FDoT 2018 specs Table 960-3.2.1-1 call for tests for the smaller and bigger size for every type of tendon (i.e. flat, round, external, internal unbonded).

In case of PL1, the sample is filled with water, pressurized with 0.5 bars for 5 min and the loss of water shall be less than 1.5%. In case of PL2 the sample is submerged in water and subjected to 0.5 bars positive and then negative pressures for 5 min (PL3 calls for 30 min); the test is considered successful if there are not air leakages in the first case or water entering in the second case.

This test was not present in FIB 7.

Tensa has successfully carried out this test on the smallest and biggest size for every type of family (see Fig. 5 for the detailed setup used for the internal bonded tendon, Table 1 for details).

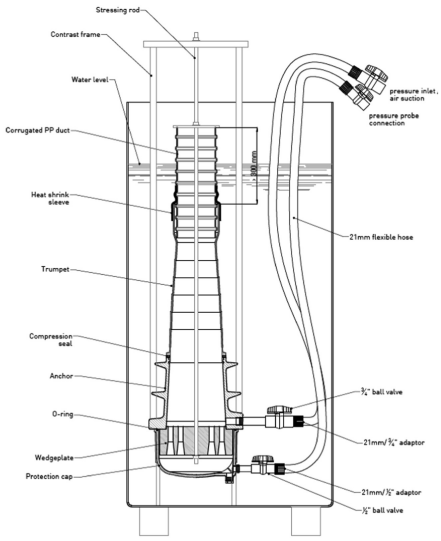

Fig. 5. Detailed set-up for leak tightness test of anchorage-duct assembly (bonded system)

Table 1. Details for leak tightness tests of anchorage-duct assembly/Dettagli delle prove di tenuta ermetica dell'assieme ancoraggio guaina

System	No. of strands	Duct type	Duct dimensions
			mm
4APTS i.b.	4	Corrugated flat	21 × 72
12AMTS i.b.	12	Corrugated	76
31AMTS i.b.	31	Corrugated	130
12AMTS i.u./ext.	12	Smooth HDPE	90
12AMTS ext	12	Smooth steel	90 sch40
31AMTS i.u./ext.	31	Smooth HDPE	140
31AMTS ext.	31	Smooth steel	140 sch40

Moreover the tests have been repeated with steel and HDPE smooth pipes, in order to fulfill FDoT 2018 specifications regarding unbonded systems (Table 960-3.2.1-1). Systems tested are identified as internal bonded (defined i.b.), internal unbonded (defined i.u.) and external (ext.).

4.2 EIT Performance of Duct System (Section 7.2 & B.2)

This test is set to establish if the polymer ducts and accessories can achieve sufficient electrical resistance to meet the assembled duct system EIT on site test. This test is required only for PL3 tendons.

Three tests are required for every duct size: with bare duct, with duct and coupler, with duct and vent.

A basin is filled with tap water and the sample kept submerged for 2 weeks. At the end of this period, the electrical resistance R, the capacitance C and loss factor D are measured every 2 h for 24 h by means of a LCR meter.

The test is considered successful if all the 3 specimens reach a resistance R greater than 2000 kOhm; capacitance C and loss factor D should be consistent with duct material and diameter.

4.3 EIT Performance of Anchorage-Duct Assembly (Section 7.3 & B.3)

This test is aimed at establishing if the anchorage-duct assembly can achieve sufficient electrical resistance to meet the assembled duct system EIT test requirements on site and confirming the stability of eventual coatings on metallic anchorage surface. This test is required only for PL3 tendons.

One test is required on a medium anchorage size.

The anchorage is assembled and a minimum of 1 kN pre-compression between wedge plate and anchor is applied by means of a steel rod. The assembly is positioned inside a tank and filled with saturated $Ca(OH)_2$ solution, then the electrical isolation between steel rod and test frame is confirmed with a LCR meter. The resistance R is measured again after 24 h. At this point the tank is filled with saturated $Ca(OH)_2$

solution and kept as it is for 28 days, measuring the resistance R between steel rod and test frame every 2 days.

The test is considered successful if the resistance R is at least 15 kOhm over the entire test duration, and eventual coatings on metallic anchorage surface remain visually intact.

Tests at paragraph 4.2 and 4.3 are a complete and detailed development of the "Electrical resistance test" described in FIB 7 at Paragraph 4.2.5, that is carried out on a stressed tendon inside a mock-up, before the investigation of the voids takes place. An alternate current is applied between the prestressing steel and rebars and the resistance R is measured: the test is acceptable if R is greater than 1 kOhm.

4.4 Full Scale Duct-System Assembly (Section 7.4 & B.4)

This test is aimed at confirming the compatibility of all the PT system components for the installation with a typical tendon profile, without kinks/discontinuities, according to the method statement. This shall be demonstrated for every installation method.

The set-up is showed in Fig. 6, and one test is required on a medium anchorage size; furtherly FDoT 2018 specs Table 960-3.2.1-1 call for smaller and bigger size for every type of tendon (i.e. flat, round, external, internal unbonded).

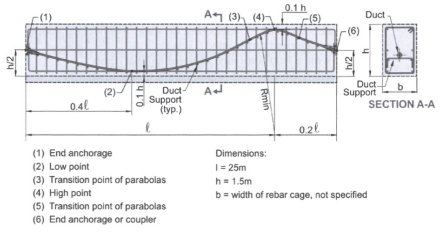

Fig. 6. Set-up for full scale duct-system assembly

This test is required for PL2 and PL3 tendons.

System is assembled following the proper method statement and schemes. The test profile is designed in order to accommodate complete anchorages at both ends, every type of connection of the system and the minimum duct radius in the upper point.

In detail the type of connection used was coupler with heat shrink sleeves for Bonded systems, elastomer boot with band clamps for Unbonded systems, butt welding for both types of system and grout ports welded at upper and lower points.

The system was installed on a 30 m long scaffolding frame: the height of every support was calculated linking the profile of the parabola around the lowest point with the radius of curvature around the highest point, avoiding any type of kinking.

Since at the time of testing corrugated ducts were not yet provided with wear test results (see paragraph 3.8 and 3.9), the minimum radius of curvature have been determined as per FDoT Structural Design Guidelines Table 1.11.4-2. The use of such tight curvature radius brings on the safe side with reference to jobsite use conditions.

The spacing between duct supports must be calculated from the duct stiffness determined as per FIB 75 Section 6.2. (see paragraph 3.2) but, since at the time of testing those tests were not yet completed, the spacing between supports has been defined making reference to maximum support spacing established in FDoT 2018 specs Par. 462-7.2.1.(3).

The number of tests carried out, radius of curvature and support spacing are shown in Table 2.

Table 2. Details for full scale duct-assembly tests

System (no. of strands)	Duct type	Duct dimensions	Radius of curvature/duct support spacing
		mm	mm
4APTS i.b. (4)	Corrugated flat	21 × 72	1829/305
12AMTS i.b. (12)	Corrugated	76	2438/610
31AMTS i.b. (31)	Corrugated	130	3962/610
12AMTS i.u./ext. (12)	Smooth HDPE/steel	90	2438/610
31AMTS i.u./ext. (31)	Smooth HDPE/steel	140	3962 610

After the assembly of all the systems, several measurements have been carried out: check of any kinks or discontinuities, actual tendon profile, ambient and duct temperature at 4 points along the assembly (anchorages, lower and upper points).

Then strands have been threaded inside the assemblies and all the systems have been left exposed to weather for 14 days, continuously monitoring ambient and duct temperatures. As shown in Fig. 7, air temperatures varied between 7 and 35 °C, while ducts' temperatures went from 8 to 54 ° C.

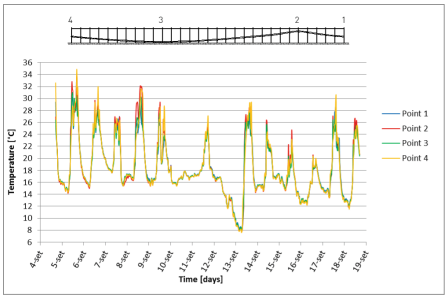

Fig. 7. Diagram showing air temperature variation along tendons during 14 days

At the end of this period the same measures carried out initially were made again: check of any kinks or discontinuities, actual tendon profile and ambient and duct temperatures.

This test can be compared with "Full scale system assembly" described in FIB 7 at Paragraph 4.2.1. The substantial modifications added in FIB 75 are required strand threading and 2 weeks weathering period, simulating a long wait between duct installation and concrete pouring, when weather and sunlight may damage ducts and components and thermal variation may lead to high shortening of ducts and subsequent disconnection of the joints, especially regarding black HDPE pipes.

Tensa has successfully performed this test on the smallest and biggest size for every type of family. Moreover tests have been repeated with steel and HDPE smooth pipes, in order to meet FDoT 2018 specifications Table 960-3.2.1-1 regarding unbonded systems. In the following Figs. 8 and 9 some pictures are shown.

Fig. 8. Picture showing tendons assembled and exposed during the 14 days testing period

Fig. 9. Test general overview

4.5 Leak Tightness of Assembled Duct System (Section 7.5 & B.5)

This test is set to confirm the tightness of the systems previously assembled, after the exposure to environment.

Strand overlengths are cut at both ends in order to allow the installation of the protection caps.

Ambient and duct temperatures are confirmed at both anchorages, lower and upper points.

Then the systems are pressurized with 0.5 bars for 1 h, the pressure is adjusted and the inlet valve is closed. The test is considered successful if the loss of pressure after 5 min is less than 10% of the initial value.

Tensa has successfully carried out this test on smallest and biggest size for every type of family. Moreover the tests have been repeated with steel and HDPE smooth pipes, in order to fulfill FDoT 2018 specifications Table 960-3.2.1-1 regarding unbonded systems. Results and details are given in Table 3.

Table 3. Details and results for leak tightness of assembled duct system tests

System (no. of strands)	Duct type	Pressure loss
		bar
4APTS i.b. (4)	Corrugated flat	0.036
12AMTS i.b. (12)	Corrugated	0.007
31AMTS i.b. (31)	Corrugated	0.014
12AMTS i.u./ext. (12)	Smooth HDPE/steel	0.001
31AMTS i.u./ext. (31)	Smooth HDPE/steel	0.012

5 Fdot Supplementary Tests

Further from FIB 75 tests, FDoT specs 2018 s. 960 regarding post-tensioning introduces other acceptance tests for system to be used with flexible filler, i.e. external and internal unbonded systems.

5.1 External PT System Pressure Tests (FDOT 960–3.2.3)

This test is used to demonstrate that the external systems are suitable to resist to high injection pressures, since in this case the ducts are not embedded in the concrete. The test is required for each system dimension.

The test layout is designed in order to accommodate complete anchorages at both ends and every type of connection of the system.

Anchorages have been embedded into concrete, in order to represent real jobsite conditions, and placed with at least 4.6 m of pipe between each other, using both steel and HDPE types (to simulate also internal unbonded systems). Then they have been kept compressed with a contrast frame: this was necessary due to pressure that pushes away the anchorages since they are not kept in place by stressed strand inside. Assemblies were then filled with water and pressurized at 7 bars for 3 h, the pressure is adjusted and the inlet valve is closed. The test is considered successful if the loss of pressure after 5 min is less than 10% of the initial value.

Tensa has successfully carried out this test on all his external PT systems. Tested systems, results and picture are shown Table 4 and Fig. 10.

Table 4. Details and results for pressure and vacuum tests

System (no. of strands)	Duct dimension	Pressure loss	Vacuum loss
	mm	bar	bar
12AMTS ext. (12)	90	0.138	0.08
19AMTS ext. (19)	110	0.124	0.039
27AMTS ext. (27)	125	0.386	0.039
27AMTS ext. (27)	140	0.076	0.035
31AMTS ext. (31)	140	0.103	0.003

Fig. 10. Test general overview

5.2 Vacuum Test for Internal and External PT System with Flexible Filler (FDOT 960–3.2.4)

This test is designed to demonstrate that the internal and external unbonded PT systems can withstand negative pressure during the vacuum assisted injection with flexible filler.

Test set-up is the same used for the "External PT system pressure test", with the difference that the contrast frame is no more necessary. Test is required for every system dimension.

After the "External PT system pressure test", assemblies have been emptied from water, dried and depressurized with a vacuum pump till 90% of vacuum for 1 h, vacuum has then been adjusted and the inlet valve closed. Test is considered successful if the loss of vacuum after 5 min is less than 10% of the initial value.

Tensa has successfully carried out this test on all his external and internal unbonded PT systems. The system tested and results are shown in Table 4.

6 Conclusions

FIB 75 has introduced several improved performance requirements and assessment methods for corrugated plastic ducts for post-tensioning tendons, aimed also at providing a better work frame within which assess the performance of this important component for PT system. Corrosion protection and durability are the key factors driving the assessment process and must be definitely considered also criteria for designers and owners while choosing a post-tensioning system for a project.

Tensa has performed a long and intensive program for the assessment of its post-tensioning system under requirements of FIB 75 Annex B. Such program has shown how testing parameters and acceptance criteria are stringent and detailed.

Brilliant results have demonstrated that systems are suitable for use in jobsites were severe environmental conditions are expected and PL2 class is requested.

References

FIB Bulletin 7 (2000) Corrugated plastic ducts for internal bonded post-tensioning. International Federation for Structural Concrete *(fib)*

FIB Bulletin 75 (2014) Polymer-duct systems for internal bonded post-tensioning. International Federation for Structural Concrete *(fib)*

PTI/ASBI M50.3-12 (2012) Guide Specification for Grouted Post-Tensioning. Post Tensioning Institute and American Segmental Bridge Institute

Standard Specifications for Road and Bridge Construction (2018) Florida Department of Transportation, January

Stay Cable Multi-tube Saddles, Design and Testing

A. Castiglioni di Caronno and T. Ciccone(✉)

Stay-Cable and Post-Tensioning Systems Technical Department,
Tensacciai Srl, Milan, Italy
t.ciccone@tensainternational.com

Abstract. Saddle systems for stay cables are at the moment one of the preferred solutions in the field of cable stayed bridge design across the world, and this trend seems to increase day by day. The most advanced systems currently available for parallel strand stay cable systems are multi-tube friction saddles, where each single strand runs into an individual pipe and the stay cable differential force is transferred by friction. The structural behaviour of a saddle device is a very complex topic involving several mutually dependent aspects. The development and validation of saddle systems is usually performed in the frame of the design assisted by testing. Full-scale tests have been carried out at the Structural Engineering Laboratory of Politecnico of Milan taking into account current developments of International Recommendations, such as FIB Bulletin 30 and PTI DC 45.1-12, with the aim of characterizing friction, fatigue and static performances of saddles.

Keywords: Multi-tube saddles · Cable-stayed bridges · Full-scale testing

1 Introduction

Nowadays multi-tube saddle systems have become common solutions in cable-stayed and extradosed bridges, mainly as a consequence of the considerable material savings provided in the pylon erection. As a matter of fact, the absence of anchorages at pylon level allows the Designer to reduce the overall dimension of the tower, which turns out to be more slender and, as a consequence, architecturally elegant and graceful.

On the other hand, a stay cable saddle is a complex structural system whose actual behaviour is intrinsically non-linear and strictly dependent on a proper detailing of all its components. Moreover, inspectability, maintenance and replaceability of the stay cable system become more complicated when saddles are installed.

A careful design and manufacturing of the saddle, and an accurate installation procedure are the main keywords for a safe behaviour of the cable stayed bridge.

M. di Prisco and M. Menegotto (Eds.): ICD 2018, LNCE 42, pp. 545–557, 2020.
https://doi.org/10.1007/978-3-030-23748-6_42

2 Saddle Design and Validation

2.1 Design Hints

In general terms, a stay cable saddle is a structural device that allows continuous deviation of the tensile elements from the deck through the tower and back to the deck, as well as transferring the stay-cable unbalanced force into the bridge structure. The most advanced systems available by now are multi-tube saddles, where each single strand runs into an individual pipe and differential stay-cable forces are resisted by friction.

Of course the first key point to be taken in mind when designing a saddle is its geometry, which in many cases is dictated by the configuration chosen for the stay cable system. It is clear that the stress state in the cable is strictly influenced by the saddle. In other words, the uniform tensile stress distribution produced by permanent and live loads over the stay cable cross-section is locally disturbed by bending tensions induced by the curved configuration of the saddle. Such bending stress distribution is difficult to be properly predicted due to the intrinsically non-linear interaction among wires. Many relations are available in literature to compute the bending stress which develops into a curved rope. However, different formulas often lead to completely different results, which are in many cases too conservative.

The maximum bending stress in a bent rope can be computed assuming the same behaviour of a beam to which a curvature is imposed. Let E, d and D be the modulus of elasticity of the material, the diameter of the tensile element and the diameter of the saddle, respectively.

Thus the so-called Reuleaux's formula (1) may be worked out:

$$\sigma_b = E\frac{d}{D} \tag{1}$$

The relation above provides the maximum bending stress inside a rope or a strand under the assumption of perfect interaction between wires composing the rope or the strand. However, this behaviour is only valid when stresses are sufficiently small. For increasing bending stresses, the external wires may slip and the bending stress reduces abruptly.

In the specific case of spirally coiled wires, the Timoshenko's formula (2) provides the bending stress, which is also function of the Poisson's ratio ν and lay angle α.

$$\sigma_b = E\frac{d}{D}\frac{2\cos\alpha}{2+\nu(\cos\alpha)^2} \tag{2}$$

In literature plenty of formulas have been proposed to correct (1) taking into account the actual working condition of a rope. For instance, the Bach's formula (3), used for ropes, introduces an effective modulus of elasticity $E_0 = 3/8E$.

$$\sigma_b = \frac{3}{8} E \frac{d}{D} \tag{3}$$

The Carstarphen's formula (4) modifies the previous one using an effective modulus of elasticity equal to $E_0 = 0.44E$.

$$\sigma_b = 0.44 E \frac{d}{D} \tag{4}$$

Taking into consideration a standard 7-wire, 15.7 mm nominal diameter strand with 5.2 mm nominal diameter external wires helicoidally coiled around the central king wire and a saddle with a 3000 mm radius, the maximum bending stress for each of the previously introduced formulas is summed up in Table 1. It can be seen that, regardless of the used approach, the bending stress is often not negligible.

Table 1. Theoretical bending stress in the saddle

Formula	Bending stress	
	MPa	%GUTS
Reuleaux	510	27%
Timoshenko	507	27%
Bach	191	10%
Carstarphen	225	12%

The stress level computed through the first formula reaches outstanding values which are actually not compatible with the real behaviour of a stay cable. For this reason in literature it has already been proposed to replace the diameter of the 7-wire strand with an equivalent reduced diameter. SETRA Recommendations propose an equivalent diameter of 10 mm, which leads to more reasonable bending stresses in the order of 64% of the previously computed values.

Anyway, the accurate estimate of the maximum bending stress into a strand is a complex topic out of the scope of this paper. It is just worth noting that bending tensions may dramatically affect the behaviour of a bent stay cable and, therefore, shall always be taken into account (Fig. 1).

Secondly, interaction between strand and pipe may produce fretting fatigue phenomena, leading to significant damage of the strand and even collapse. A proper saddle detailing must be carried out in order to avoid any unintentional contact, which may lead to sudden and brittle failure of the strand.

The design of a multi-tube saddle shall investigate all the main aspects characterizing its response, which can be summed up as follows:

1. Mechanical performance:
   a. Transfer of differential stay cable forces;
   b. Fatigue strength;
   c. Static efficiency;

Fig. 1. Multi-tube saddles for 127-strand stay cables stocked in the workshop

2. Functional performance:
   a. Corrosion protection;
   b. Replaceability.

In multi-tube saddles, friction influences the force transmission from the stay-cable to the pylon and may remarkably affect the structural efficiency of the device. As a rule of thumb, the higher the friction, the greater the maximum horizontal load transferred to the pylon. Thus, the friction coefficient developing at the interface between strands and pipes becomes an important design parameter.

The differential force transferred by the cable shall go from the saddle to the pylon. To this purpose, shear connectors (studs or plates) are usually used to improve the stress transfer to concrete, which otherwise would just rely on bonding.

The width of the saddle shall be designed in such a way that, in the most severe load combination, the pressure transmitted to the underlying concrete does not produce concrete cracking or failure.

2.2 Stress State Among Pipes

When designing a multi-tube saddle and the local zone in which it is embedded, a stress analysis should be carried out in order to assess the global state of stress among pipes and under the device.

A 2D linear elastic finite element analysis has been run over the cross-section of both a 37-strand saddle and a 127-strand saddle with the same radius of curvature (3000 mm) and total angle of deviation (60°), assuming that each strand reaches its limit service load (45%GUTS).

The global state of stress under the saddle is quite low, due to the significant diffusion of tensions. The bearing stress reaches approximately peak values of 3.6 MPa and 7.0 MPa for the 37-strand saddle and 127-strand saddle, respectively. Such values may be double-checked by hand computation. Specifically, a 30° stress diffusion rate is assumed from the horizontal cross-section passing through the saddle axis to define the width of redistribution. Let N_{st}, R, B_{red} be the number of strands, the saddle radius and

the width of redistribution, respectively. The bearing pressure may be assessed by means of formula (5), which provides a fair approximation of the stress underneath the saddle:

$$p = \frac{N_{st} 45\% GUTS}{RB_{red}} \tag{5}$$

Specifically pressure of 3.3 MPa and 5.8 MPa can be computed for a 37-strand saddle and a 127-strand saddle, respectively.

Between pipes a more severe state of stress develops: from each tube compressive tensions spread out downward and tensile stresses appear orthogonally to compression lines. Neglecting the upper portion of the saddle, where significant tensile stresses take place due to a model simplification, the principal stresses among lower pipes of the saddle reach values of 1.0 MPa in tension and 5.0 MPa in compression, for the 37-strand saddle, and 2.0 MPa in tension and 10 MPa in compression, for the 127-strand saddle.

A high strength cement mortar is used to withstand both compressive and tensile stresses induced by the strand pressure (Fig. 2).

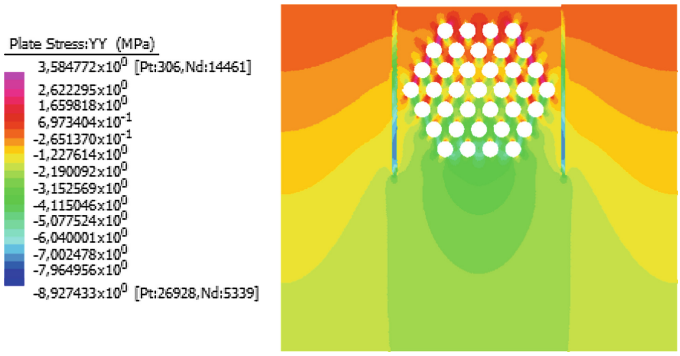

Fig. 2. Vertical stress over the saddle cross-section/Sforzo verticale sulla sezione della sella.

2.3 Code Requirements

An essential assumption of all main International Recommendations is that a stay cable system with a saddle shall exhibit the same performance level of a standard stay cable system, anchored at pylon level through anchorages. This refers to both the mechanical performance and the functional ones, i.e. the saddle system has to ensure corrosion protection and replaceability of any individual strand of the bundle.

The analysis of the structural behaviour of a specific saddle system is a very tough task and involves many co-dependent aspects. For this reason, it cannot be approached from the theoretical point of view only. Development and validation of stay cable saddles is usually carried out in the frame of the so-called design assisted by testing.

Actually, testing plays a crucial role in the evaluation of the structural and functional response of these devices.

Design, testing and installation of saddles are generally performed according to either FIB Bulletin 30 (2005) or PTI DC 45.1-12 (2012), being these two the main International Recommendations addressing stay-cable systems.

FIB Bulletin 30 does not have any specific requirement about friction while PTI Recommendations clearly requires assessing the friction coefficient through testing. However, testing details and conditions are not specified.

According to EN1993-1-11 §6.3.2, the friction phenomenon in the saddle, evaluated through the belt friction equation (capstan equation or Eytelwein's formula), should prevent any slippage. To this purpose the following condition should be met:

$$\max\left\{\frac{F_{Ed1}}{F_{Ed2}}\right\} \leq e^{\frac{\mu\theta}{\gamma_{M,fr}}} \tag{6}$$

where F_{Ed1} and F_{Ed2} = design values of the maximum and minimum force respectively on either side of the cable; μ = coefficient of friction; θ = angle (in radians) of the cable passing over the saddle (deviation angle); $\gamma_{M,fr}$ is the partial factor for friction.

According to Table 2, depending on the code, several partial factors for friction are proposed.

Table 2. Partial safety factor for friction

Codes				
	EC3-1-11	FIB30	PTI DC45	SETRA
$\gamma_{M,fr}$	1.65	1.5	1.54	1.5 with tests
				2.0 without tests

It is reasonable to define the friction coefficient as a mean value, averaged over all the tubes for any specific saddle device. However, Recommendations do not provide any information in that sense.

In addition, current Recommendations do not explain whether or how fatigue may affect the friction coefficient, even though a slight reduction in friction, due to progressive system usage, seems quite reasonable.

Moreover, further and detailed information should also be provided on testing conditions, saddle deviation angles to be tested, and load levels. A need for recommendations improvement on the topic above is however well known; more complete requirements are now under discussion and will be introduced in the next versions of the main International Recommendations on cable stayed bridges.

Secondly, both PTI and FIB recommendations require carrying out a tensile fatigue test, which aims to validate the stay cable behaviour in service conditions. The test shall be performed over a specimen having at least 2 m free length, installed with a 30° inclination against horizontal and subjected to a 10 mrad angular deviation at saddle exits. The saddle must be moved vertically for 2 million cycles between a lower and an

upper configuration corresponding to a stress in the stay-cable equal to 45%GUTS-$\Delta\sigma$ and 45%GUTS, respectively. The general test procedure presented by the two standards is precisely the same, but FIB requirements are a little more stringent. As a matter of fact, FIB recommendation introduces a stress range for parallel-strand stay cable of 200 MPa, greater than the one reported by PTI recommendations, equal to 110 MPa plus 35 MPa through vertical movement of the saddle. Acceptance criteria are the same for both standards (2% maximum wire fractures) while, for small size cables, PTI accepts a slightly greater number of fractures with respect to FIB recommendations (3 instead of 2). In addition, both codes require that no cracking or fracture shall develop in the anchorages material.

For these reasons, a stay-cable saddle fatigue test carried out achieving all FIB requirements satisfies the PTI requirements as well.

At the end of the fatigue test, the static efficiency of the stay-cable system, linked up with its behaviour at the ultimate limit state, shall be tested. FIB Bulletin 30 requires performing a tensile static test in which the stay-cable is symmetrically loaded in order to reach the maximum attainable stress. The stay-cable shall develop a minimum tensile force equal to 95% GUTS or 92% AUTS, whichever is greater.

3 Full-Scale Testing

The TENSA multi-tube saddle system type TSS-T is a steel welded box member, provided with several parallel steel pipes embedded into a high strength cement mortar. The inner surface of each tube is covered with a special high friction compound. Strands are uncoated in their central part to ensure the required friction in the pipes (Fig. 3).

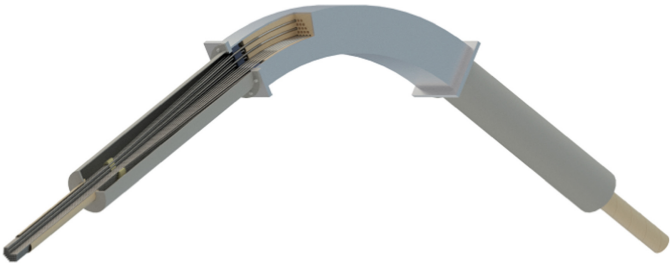

Fig. 3. TENSA multi-tube saddle system TSS-S.

In order to assess the behaviour of the TSS-T saddle system, a wide testing campaign has been developed over a period of almost three years. Most of the tests have been carried out at the Structural Engineering Laboratory of Politecnico of Milan (Italy), following Recommendations described above and introducing additional improvements in testing protocols.

Friction tests were performed over several TSS-T saddle systems, varying both the geometrical configuration and the loading condition. Taking into account all the actual inclinations that a stay cable may have on a bridge, the friction coefficient was measured on saddles with deviation angles ranging between 30° and 150°.

On the other hand, stay-cables were subjected to different initial loads smaller than 50%GUTS, which is the maximum design working load of the stay-cable. In order to properly evaluate the effect of the actual force in the cable, friction was measured on the same saddle for several load levels.

As expected, tests proved that neither the saddle deviation angle nor the stay-cable initial tension affect significantly friction and provided friction coefficients ranging between 0.35 and 0.42, with an average value equal to 0.40.

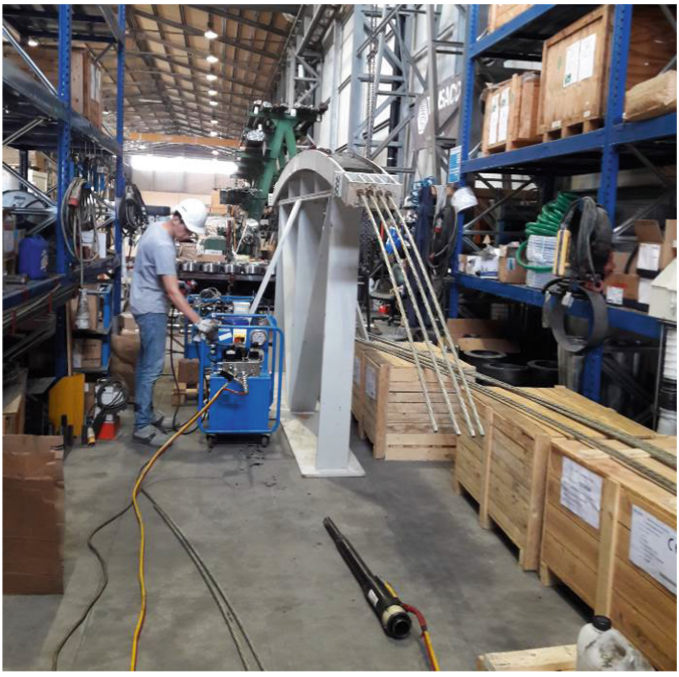

Fig. 4. Friction test carried out over a multi-tube saddle with great radius of curvature (flat saddle)

In order to further analyse the saddle capacity, a full-scale tensile fatigue and static test was performed over a 7-strand saddle system (Figs. 4 and 5).

To this purpose, a 10 ton steel frame has been designed, manufactured and assembled in the laboratory to resist all the loads expected for the test, with the stay-cable configuration as close as possible to the one actually adopted on site. Expensive and dedicated equipment were used to stress the stay-cable and to impose the vertical movement of the saddle. Moreover, all the components generally used in the free length, transition length and anchorage zone of the stay-cable, i.e. deviator disks, wax boxes, etc., were included in the test.

Fig. 5. Friction test carried out over a multi-tube saddle with small radius of curvature.

The real working condition on site was simulated embedding the saddle into a concrete block representing the bridge pylon. In addition, after the stressing phase, the saddle was filled with a protective material able to provide adequate corrosion protection to the strands.

Tensile fatigue test was carried out at 1.20 Hz mean frequency and lasted about 20 days. No wire fracture or damage in the saddle and in any component of anchor heads occurred during testing, as confirmed by a system of accelerometers that the laboratory installed on the sample to continuously monitor the cable state. The test fully met the acceptance criteria introduced by FIB Bulletin 30 and PTI DC.45.1-12.

During the subsequent static tensile test, the 7-strand stay-cable was loaded up to the maximum attainable force and a load corresponding to 97.5% of GUTS and 96.2% AUTS was recorded. The reached load level totally satisfied the acceptance criteria of FIB Bulletin 30. A significant stay-cable elongation, equal approximately to 1.90%, was reached in the final test stages. Because of this corresponded to the end of stroke of jacks, the load level was not further increased and test was stopped.

At the end of static test, no evidence of damage of the saddle system and anchorages was detected. Moreover, after almost one month of direct exposure to atmosphere, no corrosion was noticed over any component of the tested system.

Other friction tests were performed at the end of the static test to estimate the effect of both fatigue and strands' large strain on the friction coefficient. Values ranging from 0.25 to 0.39 were observed.

Such decrease in friction is due to the remarkable usage of the system – i.e. pipes surface and high friction compound – produced by the fatigue test and the subsequent static test. Thus the measured friction coefficients should be considered as minimum values for the ultimate limit state, i.e. lower bound of the actual friction coefficient that the saddle is able to provide. As a consequence of these experimental evidences, a predictable friction coefficient just after the fatigue test may be definitely considered around 0.4 (Fig. 6).

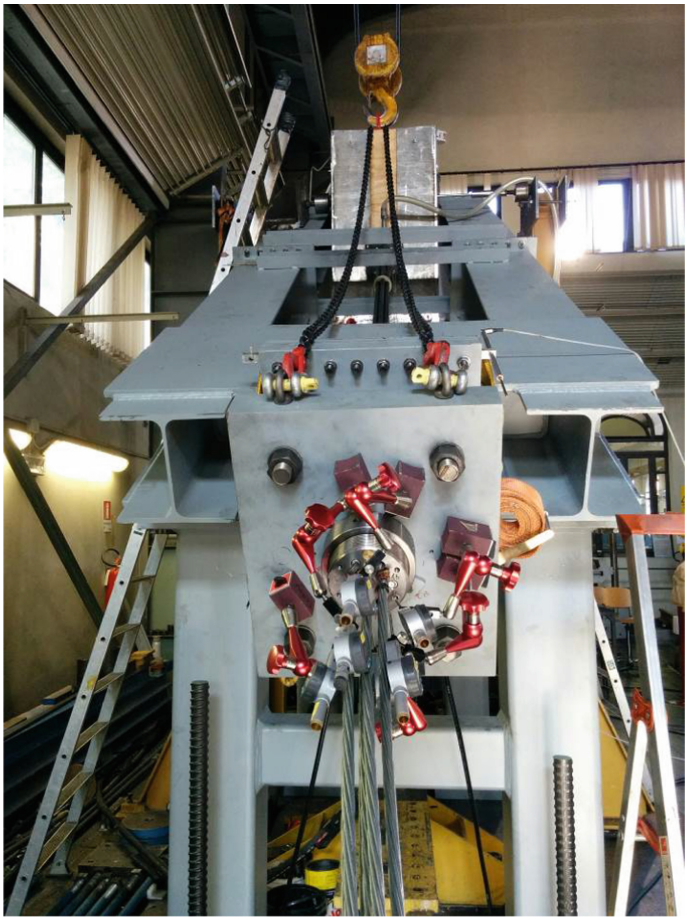

Fig. 6. Tensile fatigue and static test over a multi-tube saddle for 7-strand stay cables

The high performance of the system detected during the tensile fatigue and static tests over the 7-strand saddle system proved that saddle devices are perfectly able to resist fatigue loading – corresponding to traffic loads on the bridge – and, moreover, can be designed not to affect the stay-cable performance in terms of static efficiency. However, the tested saddle was fairly small compared to what is often required and supplied to site.

The increase in dimensions may dramatically affect the actual structural behaviour of a component due to an unavoidable size effect. Additionally, a wider size means higher load levels as well and, in many cases, important deviation of the bundle.

For all these reasons, another tensile and static test was performed on a 37-strand saddle system, again in the Structural Engineering Laboratory of Politecnico of Milan. To this purpose a dedicated 25 ton steel structures was designed, produced and assembled. The impressive load level required by testing according to FIB Bulletin 30 required special dedicated fatigue and tensile equipment with outstanding capacities and a careful and accurate control system. As previously mentioned, the necessity to build in a laboratory a testing set-up as close as possible to the actual site configuration requires imposing important deviations to the bundle. A special attention must be paid to this issue since it can dramatically influence the system performance.

Tensile fatigue test was carried out at 1.55 Hz average frequency and lasted about 15 days. The system of accelerometers installed to monitor the cable during fatigue cycles, recorded several event during the fatigue test. However, as then confirmed during dismantling, only 2 wires broke due to fatigue, while others events corresponded to stabilizing movements from the massive steel structure. Compared to the total amount of 259 wires, the loss of stay cable cross-section due to fatigue was about 0.77%, well below than the 2% limit by FIB Bulletin 30. This important result confirmed the positive fatigue performance of the stay cable system deviated by a saddle device.

During the subsequent static tensile test, the 37-strand stay-cable was again loaded up to the maximum attainable force and a load corresponding to 95.9% GUTS and 93.2% AUTS was recorded. The reached load level totally satisfied the acceptance criteria of FIB Bulletin 30. Due to the notable force imposed to the cable, the test was stopped for safety reason in order to avoid any further dangerous break. A cable elongation equal approximately to 1.53% was reached at the end of the test.

During dismantling two main strand failures have been detected. The first one was located at saddle exit where the resisting cross-section of the strand was reduced due to a fatigue wire break. The other failure has been recorded in the deviation length of the stay cable, close to the deviation system. No evidence of damage of the saddle system and anchorages was detected. Just some negligible steel powder was observed on several strands due to an incipient fretting fatigue phenomenon.

The testing campaign provided a widespread and complete insight into the structural and functional behaviour of multi-tube saddles, accounting for several working conditions. Particularly, the TSS-T saddle system matched all the existing Recommendations requirements, i.e. providing a structural performance equivalent to what expected for a traditional stay-cable system, and gave up satisfactory responses for the conditions not fully described and detailed in the current Recommendations (Fig. 7).

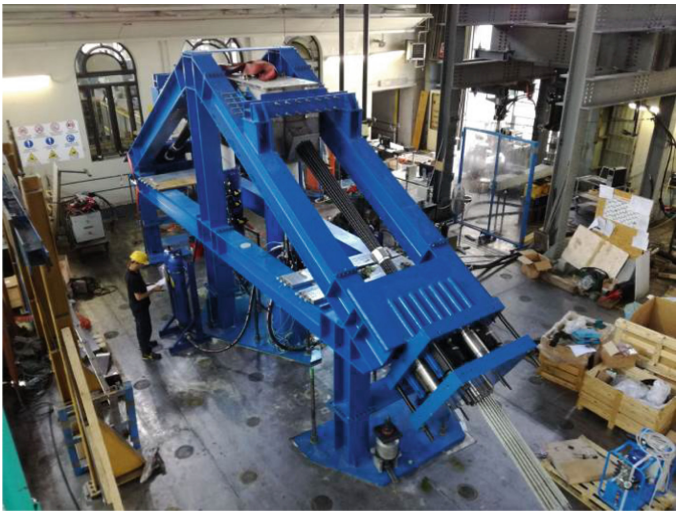

Fig. 7. Tensile fatigue and static test set-up over a multi-tube saddle for 37-strand stay cables

4 Notes on Functional Performance

The current approach to corrosion protection of strands in a stay cable system calls for a multiple barrier approach, which has to be fulfilled in saddles as well. In the TENSA multi-tube saddle, the portion of strands running through the pipes needs to be uncoated in order to ensure proper gripping and, consequently, to reach the required level of friction. Thus the removal of the hdpe sheathing needs to be properly taken into account for assuring an adequate corrosion protection of strands.

The multi-tube saddle has to be designed as a leak tight system. To this aim, welds between steel plates need to be continuous and waterproof so that to provide an involucre which behaves as a physical barrier against the ingress of water. Strands run into individual steel pipes embedded in a high strength cement mortar, which allows both to transfer tensions underneath the saddle and to provide a further barrier against the diffusion of water.

Therefore, the critical zones for the possible ingress of water are the two saddle ends, where strands enter the saddle and the hdpe coating is removed. To ensure the leak tightness of these parts, a system of packed rubber disks is installed and squeezed after stressing in order to recover the clearance between strands and holes, and to seal the ends.

After tightening of the wax box systems, the saddle is injected with a soft protective material which ensures the corrosion protection of uncoated strands. In this way a highly redundant protective system is used to cope with the aggressive action of surrounding environment.

Finally, the TENSA multi-tube saddle allows each strand to be individually replaced whenever required, since each strand runs in a separate channel and can be moved independently of the others. This feature is nowadays crucial to maintain the stay cable without replacing it completely.

5 Conclusions

A wide and expensive testing campaign has been carried out during the last three years in order to develop performing multi-tube saddle systems for stay cables, able to fulfil all requirements introduced by the main International Recommendations. Tests provided a great deal of important and satisfactory results, which gave a complete and clear view of the structural behavior of these devices.

The TENSA multi-tube saddle system type TSS-T proved to be adequate to withstand all the severe loading conditions required by testing, providing at the same time enough friction to avoid any strand slippage and, also, ensuring suitable level of strand corrosion protection.

The positive results obtained in all performed tests provided good confidence in the use of multi-tube saddle systems within cable stayed bridges.

References

Fib Bulletin 30, 2005 Acceptance of stay cable systems using prestressing steels. International Federation for Structural Concrete (fib)

PTI DC-45.1-12, 2012 Recommendations for stay cable design, testing and installation. Post Tensioning Institute

EN1993-1-11, 2006 Design of steel structures; Part 1-11: Design of structures with tension components. CEN

2002 Cable stays: Recommendations of French interministerial commission on Prestressing. SETRA

The Bridge Over the Blue Nile at Mekane Selam - Ethiopia

E. Codacci-Pisanelli[1(✉)] and G. Minisola[2]

[1] Contest - Structural Diagnostic, Rome, Italy
ecp@contest.rm.it
[2] Bonifica Group, Addis Ababa, Ethiopia

Abstract. The present paper reports the description of the construction technologies used during the building of the Blue Nile Bridge at Mekane Selam, in the Amara region in northern Ethiopia. The bridge is part of the second section of the Kombolcha–Gundewein road project, which foresee the upgrading of about 139 km of rural routes to a road in conformity with the DBST standard. The work is carried out using cantilever system with a single-cell frame section of variable height. Unique in its kind for the geographic context in which it is inscribed, the bridge is one of the first examples of prestressed concrete structure in Ethiopia, and the first with cantilever technology. Due to the seismic activity that characterizes the entire area, the design and construction of the work have been carried out in compliance with the anti-seismic regulations of the American Regulations (AASHTO), integrated with the national standards.

Keywords: Blue Nile · Prestressed concrete · Bridge design approach

1 Introduction

The Kombolcha–Gundewein road project includes the construction of two major bridges on the Blue Nile (300 m balanced-cantilever type bridge) and its tributary the Difarsa river (200 m simply supported box girder).

The route crosses the Blue Nile River and gorge. The route section between Mekane Selam on the eastern plateau and Mertole Mariam on the western plateau of the Blue Nile gorge is a new road based on the plateau section on the existing footpaths. The descent and ascent into and out of the blue Nile gorge passes through mountainous and escarpment sections which poses significant environmental as well as design and construction difficulties. The altitude drops from the plateaus to the gorge by 1100 m, this relates to a drop of over 1000 m over a short horizontal alignment.

Due to the steepness of the terrain, the weakness of some of the underlying marl and tuff horizons and the quantities of wet season rainfall, landslides, talus and colluviums slopes predominate in places. Landslides include slope failures in Black Cotton soils, large magnitude rock topples from cliff edges, deep-seated ancient failures and shallow movements in debris. Detailed assessments have been carried out as to the engineering geology of some of these areas for purposes of final alignment and

M. di Prisco and M. Menegotto (Eds.): ICD 2018, LNCE 42, pp. 558–569, 2020.
https://doi.org/10.1007/978-3-030-23748-6_43

earthworks design. Stability checks have been undertaken on retaining walls on hairpin stacks and in talus slope locations. The completions of the bridge link the two riversides, and effectively promote inter-regional exchanges and make the lives of the local people more convenient. In detail the Blue Nile Bridge is Ethiopia's first prestressed concrete segmental bridge and is also the highway bridges with the largest span in Ethiopia. The work has been built using AASHTO standards and new construction technologies. Bridge spans across the Blue Nile, with a design of 76 m + 130 m + 76 m three-span prestressed concrete steel bridge. The total length of the bridge is 294.2 m and the width is 1.3 m + 8.0 m + 1.3 m. During the construction phases, the quality of the materials was checked at the end of each execution phase in order to verify the possibility of running partial pre-compression activities and the completion of the maturation periods required by the AASHTO standards.

Particular attention was also paid to the topographic surveys. The effect produced by the viscosity of the concrete tends to modify the alignments of the work.

Preliminarily, the theoretical configuration of advancement with a slight upward concavity has been defined so as to reach the perfect linearity at the end of the construction phases.

2 Bridge Design Approach

Site visit, knowledge and appreciation of the project site. It was prepared the site visit carried out by the Team Leader with the structural engineer. Then specific surveys were carried out by a responsible for road tracks, a technician for the geotechnical investigations and an expert for hydraulic analysis of the basin and environmental investigations. It was then carried out the inspection of the right bank with analysis of the topography of the terrain and the outcropping geological formations. At the purpose to configure an appropriate solution, were also examined the road layouts next to the area where it is foreseen the construction of the river crossing. Bridge typology selection. After the site visit and the meetings at the city hall, a selection of the structural typology for the river crossing was carried out. This selection comes from project experiences and solutions adopted in similar crossings mainly considering the environmental protection of the area and the respect for style and for the shape of the new structure. The work forms a characterizing element not only of the place but also of the great technological advancement foreseen in the area. The topographic survey of the in area interested to the intervention, including the approaching roads and connection ramps, was carried out very precisely using special equipment. in order to properly design the riverbank solutions and in relation to the various solutions mentioned below, the bathymetric surveys were carried out in the river bed and in significant sections upstream and downstream of the work.

3 Analyzed Solutions

Solution 1 - Suspension bridge without piers in the river bed. The first analysed solution consists of a suspension bridge with a single span crossing the river bed and the embankment road with length of approximately 420 m. This solution is similar to that used in recent bridge made for crossing the Bosporus strait and important and famous structures such as the Golden Gate in San Francisco and Sir Otto Beit Bridge crossing the Zambezi River.

This structural solution allows the building of the foundations in areas outside the banks of the river thereby limiting the cost of construction and the environmental damage produced by foundations made in the river bed. It will also be able to proceed to the realization of the deck for blocks taken from the construction site on the riverbank and moved by means of cables supported by the suspension system. In this way, the erection of the bridge will be carried out without any disturbance or pollution of the river bed (Fig. 1).

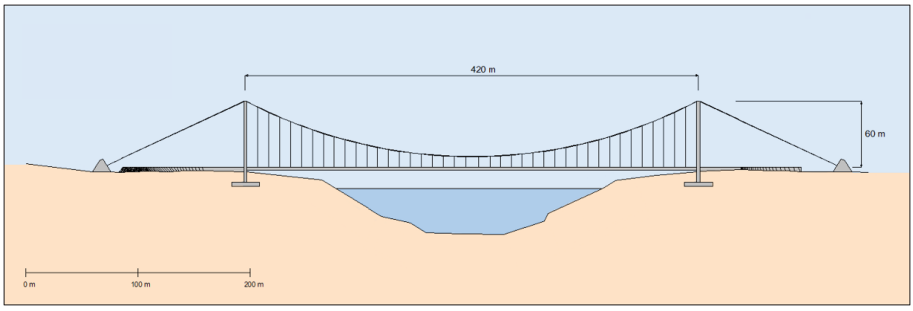

Fig. 1. Solution 1

Solution 2 - Cable stayed bridge without piers in the river bed. The second solution, foreseen a cable-stayed bridge with a single span crossing the river bed and the embankment road. Also in this case the light is approximately 420 m. Compared to the suspension system, the cable-stayed bridge from a technological point of view is easier to build because of its greater simplicity and economy of the stays installation. For the above indicated lengths this solution is recommended because in this way the work can be built more rapidly. Very significant are the bridges made by cable stayed system famous in the world as the Charles Bridge in Boston or the Stoncutter Bridge in Hong Kong. This solution would also widely reported worldwide because it would be the cable-stayed bridge with the largest span of the whole of Africa.

Also in this case this structural solution allows the building of the foundations in areas outside the banks of the river thereby limiting the cost of construction and the environmental damage produced by foundations made in the river bed. It will also be able to proceed to the realization of the deck for blocks taken from the construction site on the riverbank and moved by means of cables supported by the suspension system. In this way, the erection of the bridge will be carried out without any disturbance or pollution of the river bed (Fig. 2).

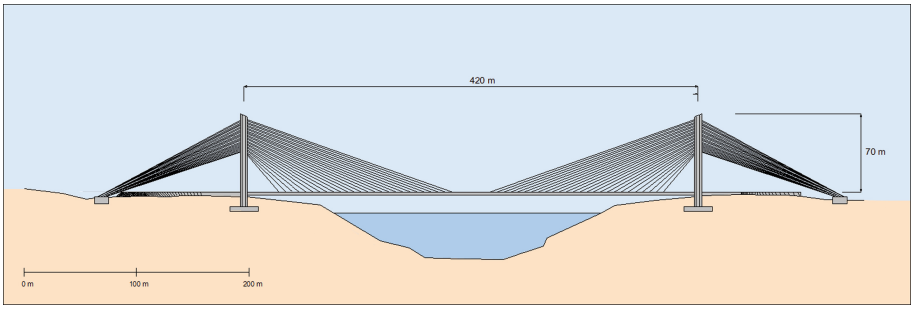

Fig. 2. Solution 2

Solution 3 - Cable stayed bridge with piers in the river bed. The cable-stayed bridge with piers in the river bed is characterized by the aesthetic "spider web" effect generated by cables directly connected between the piers and the deck with linear joints that surround the crossing central span and the approaching spans. For the indicated reason from a general aesthetic point of view the work is more balanced. On the other hand this solution foresees a greater constructive complexity. The lifting and the advancement of the deck segments must be carried out from the piers that are in the river bed. These procedures generate more constructive difficulties and significant increasing of the costs even in presence of spans with more limited lengths. This solution, also foreseen the increasing of the production times. Even in the face of a lower cost of the deck structures due to the lower length of the main span, it is necessary to consider the significant increase of the cost of foundations in the river bed and the added charges related to the complexity of handling systems of the central span segments that must be carried out from the river bed (Fig. 3).

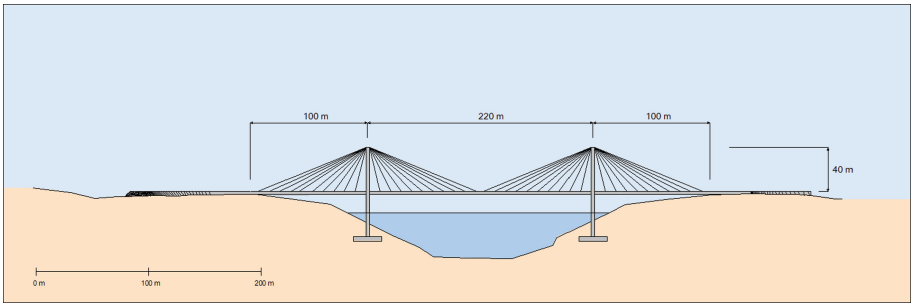

Fig. 3. Solution 3

Solution 4 - Suspension bridge with piers in the river bed. The suspension bridge with piles in the river bed is characterized by the aesthetic effect generated by the sinuosity of continuous suspension cables on the central crossing span and on the approaching spans. For the indicated reason from a general aesthetic point of view the work is more balanced. On the other hand this solution foresees a greater constructive complexity because of the three different span lengths that require higher charges for the structures lifting and timetables for completion. Even in the face of a lower cost of the suspension structures due to the lower length of the main span, it is necessary to consider the significant increase of the cost of foundations in the river bed and the added charges related to the complexity of handling systems of the central span segments (Fig. 4).

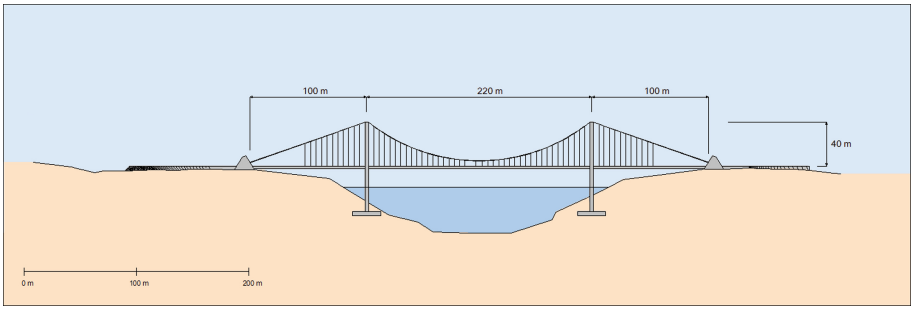

Fig. 4. Solution 4

Solution 5 - Arch Bridge without piers in the river bed. The crossing structure realized by arch bridge with lower deck - unique span, is presented because is a structural solution frequently proposed for lengths less than 500 m. This solution allows the erection of the foundations in the areas outside the river banks limiting the cost of construction and the environmental damage produced by excavations in the river bed.

For the realization of the deck there are however a lot of difficulties because it is necessary to foresee the construction of temporary piers in the river bed or the realization of an articulated system with foot hinges for the rotation of the half-arches of the bridge deck or the construction of temporary external retaining anchors of the arc built with successive blocks. Even if the artistic and aesthetic effect could be more limited comparing a suspension or cable stayed structure having large length, the financial commitment may be more limited. For this reason it is therefore considered appropriate to have a preliminary analysis of this solution also for the purposes of comparison with the structures previously analyzed (Fig. 5).

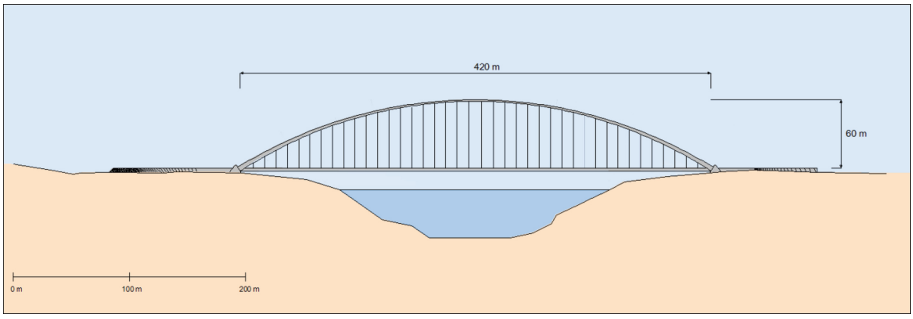

Fig. 5. Solution 5

Solution 6 - Arch Bridge with piers in the river bed. The arch bridge with piers in the river bed is the last analyzed. It is realized by three arches with lower deck.

As above indicated, even in this case there are a lot of difficulties about the construction of the deck with significant increase of the cost of foundations in the river bed and the added charges related to the complexity of handling systems of the span segments.

A proposal was made by the representatives of the Road Authority concerning the possibility to use a structural solution of a continuous prestressed concrete bridge deck (Fig. 6).

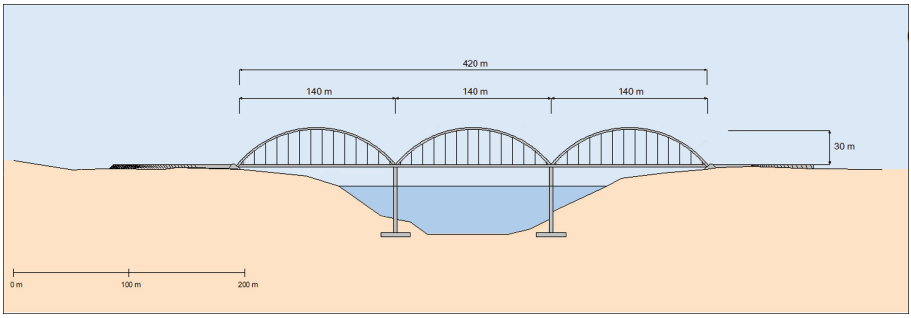

Fig. 6. Solution 6

A comparison was subsequently carried out with reference to the technical and economical realization in terms of cost of construction and operating costs of the work. As a result of careful analysis a solution with concrete bridge deck reinforced with continuous prestressed concrete was adopted (Fig. 7).

Fig. 7. General view of the bridge

4 Structural Solutions

The viaduct deck consists longitudinally of a continuous multi-span performed by a prestressed concrete beam with a constant height and variable inertia from a maximum over the support (abutments and piers) to a minimum at the middle of the spans.

The cross section is a single box girder with an upper large slab with supports the road plane with a variable thickness. The edge section of the viaduct is constant for aesthetical reasons and in order to make easier the construction, shifting and reutilization of the metal formworks.

5 Design Criteria

The viaduct is designed in accordance with the AASHTO "Standard Specification for Highway Bridges" regulations integrated with "Ethiopian Building Code Standard" for what concerns the local seismic requirements. The structural model has been analyzed in static and dynamic modality by using a structural design model with linear and non linear analysis in connection with the seismic design conditions of the area where the viaduct is located. The design calculation model used is tridimensional and the dynamic investigation has been extended to 20 vibrating modalities. The same model has been adopted for wind loads to different load groups and combinations provided by the regulation.

6 Construction Methodology

The construction of the bridge deck has been carried out by phases starting from one abutment and using metal formworks reused for the next spans. At the end of the construction the same formworks will be used for the other viaducts provided in the

Fig. 8. View of the bridge under construction

Fig. 9. View of the bridge under construction

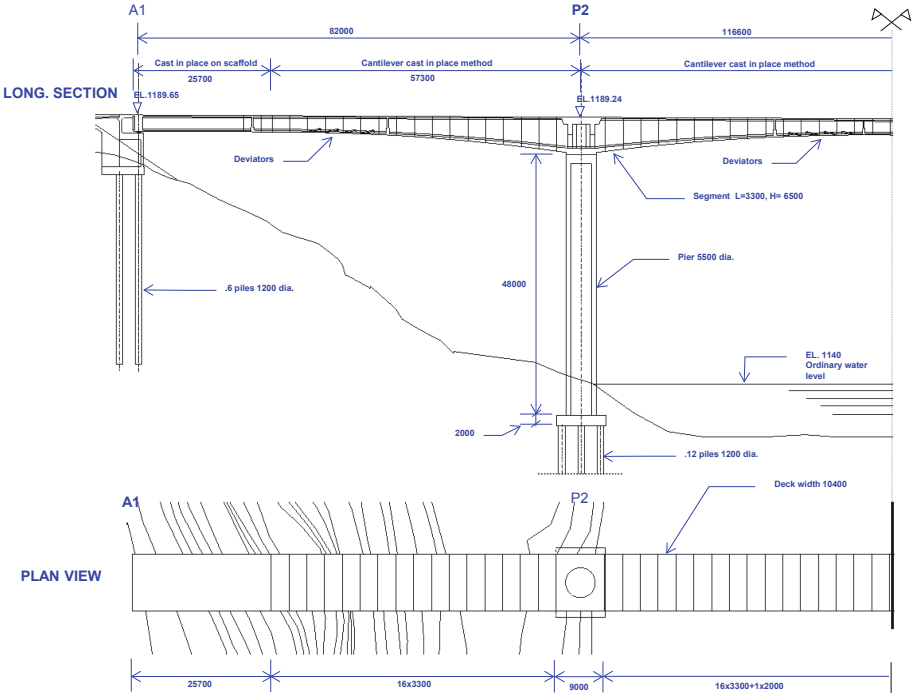

Fig. 10. Long. section and plan view

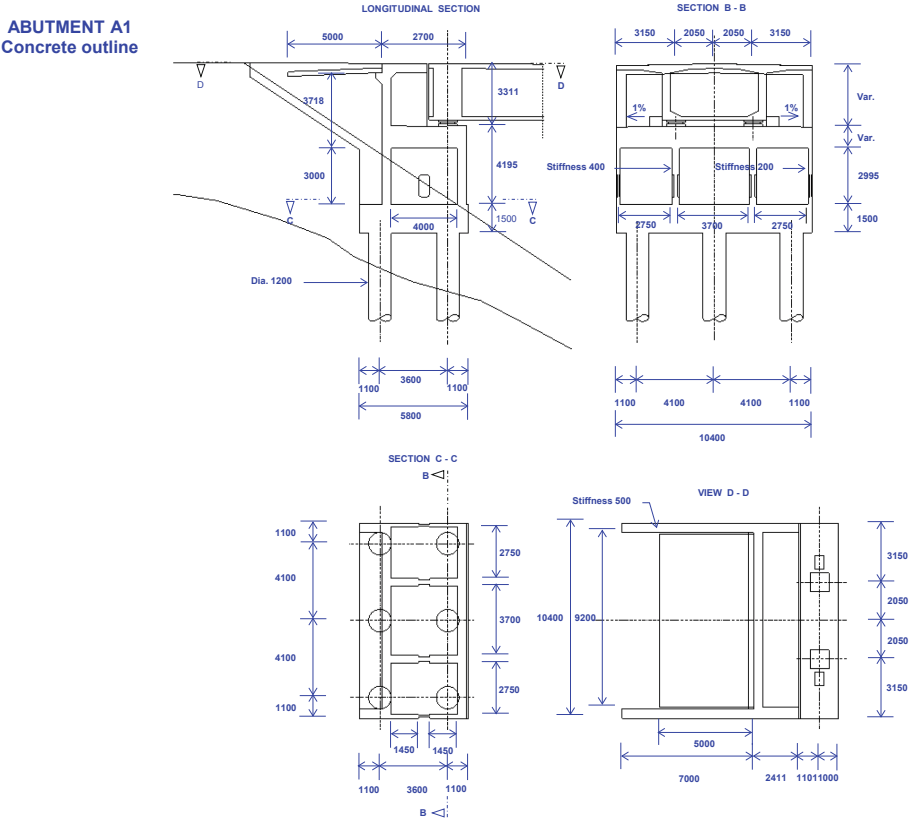

Fig. 11. Abutment cross section

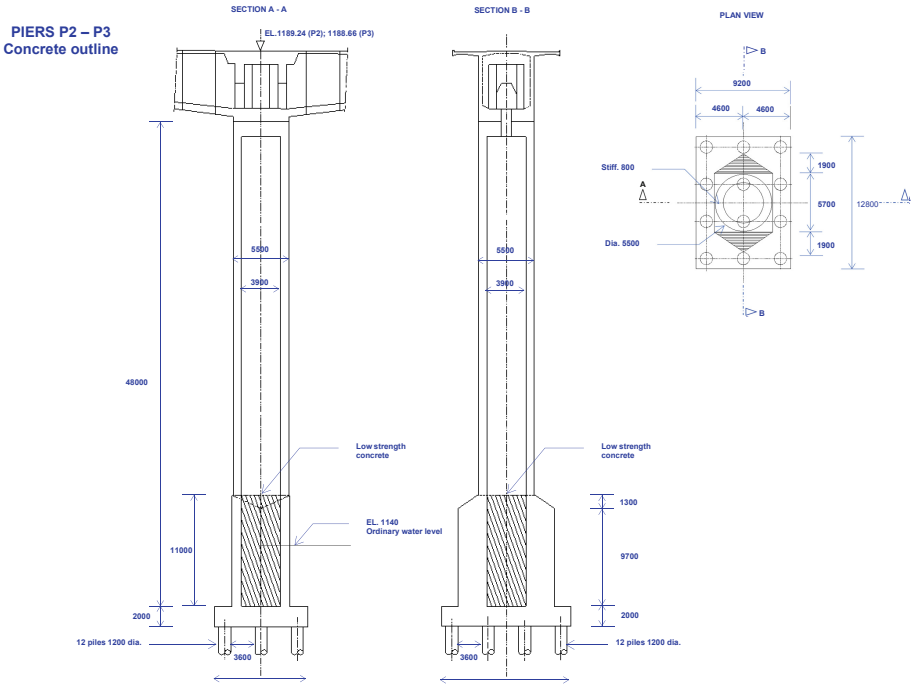

Fig. 12. Pier cross section

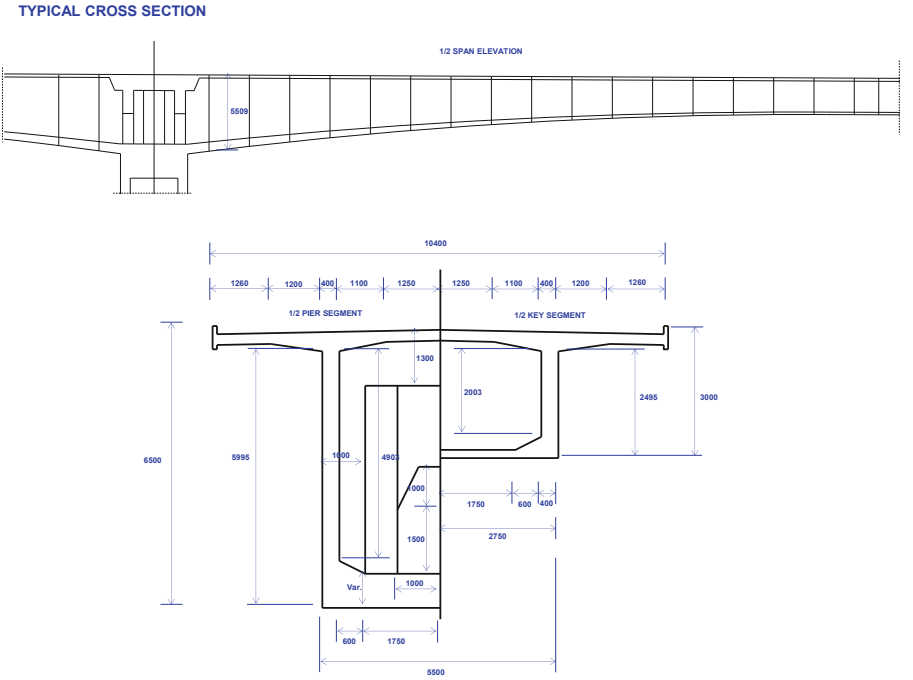

Fig. 13. Deck cross section

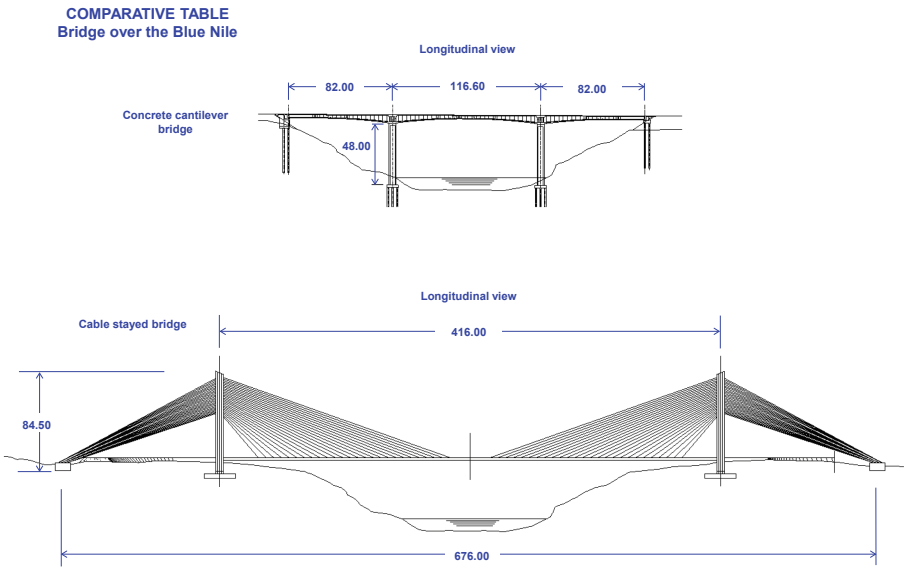

Fig. 14. Comparative table

project. Some tendons are tensioned several times in single phase and made continuous by couplers, others are tensioned in several phases in compliance with the progressing of the concrete casting and in relation with the variation of the stresses. The standard reinforcement, designed according to the shear and torsion stresses, has been shaped in order to allow easy positioning of the longitudinal tendons, without considering complicated work operations.

Particular care has been used for the delayed deformations in order to reach the correct pre-control of the bearings (Figs. 8, 9, 10, 11, 12, 13, and 14).

Flexural Design of Elevated Slabs Made of FRC According to *fib* Model Code 2010: A Case Study

L. Facconi, A. Conforti(✉), F. Minelli, and G. Plizzari

Department of Civil, Environmental, Architectural Engineering and Mathematics (DICATAM), University of Brescia, Brescia, Italy
antonio.conforti@unibs.it

Abstract. Elevated concrete slabs are typically used as columns/piles supported floors in multi-story buildings or industrial facilities. The need to reduce construction time and costs has favoured the use of ever more advanced materials, like Steel Fiber Reinforced Concrete, as an alternative to conventional reinforced concrete. Many research studies and on-site applications have proven that steel fibers can be successfully used to totally substitute the main flexural reinforcement generally placed in conventional reinforced concrete slabs. However, in order to ensure the required minimum structural performance both at ultimate and serviceability loading conditions, the total removal of rebars requires the use of very high steel fiber contents (>70 kg/m^3). However, the use of a proper combination of fibers and conventional rebars, generally known as Hybrid Reinforced Concrete (HRC), may represent a feasible solution to get the required structural performance by minimizing, at the same time, the total amount of reinforcement (fibers+rebars).

This paper focuses on the design of HRC elevated slabs according to the design provisions for FRC structures reported by the *fib* Model Code 2010 and recently introduced also by the Italian structural design code (NTC 2018). A simplified design procedure based on a consolidated design practice is proposed. Emphasis is given to the use of HRC for optimizing the slab reinforcement. A case study of an elevated slab made with synthetic Fiber Reinforced Concrete is used to show the effectiveness of the design procedure.

Keywords: Fibre reinforced concrete · Synthetic fibers · Elevated slabs design · Hybrid Reinforcement · *fib* Model Code 2010

1 Introduction

Post-cracking strength and toughness of concrete can be improved by adding short randomly distributed fibers to the concrete matrix. The resulting composite material is typically referred to as Fiber Reinforced Concrete (FRC). The latter is nowadays recognized as a structural material considered by both international and national structural codes (DAfStb 2012; NTC 2018).

Slabs are typical applications of cast-in-place FRC, as they are used to build industrial pavements (Silfwerbrand 2004), floors for multi-story buildings (Destrée 2004) or

M. di Prisco and M. Menegotto (Eds.): ICD 2018, LNCE 42, pp. 570–584, 2020.
https://doi.org/10.1007/978-3-030-23748-6_44

foundations. Stress redistribution resulting from the high internal redundancy of these structures may allow to exploit the improved post-cracking properties of FRC, leading to a possible reduction of conventional reinforcement. As proved by different research studies (Facconi et al. 2016; Tiberti et al. 2014; Chiaia et al. 2009; Sorelli et al. 2006) fibers may replace either partially or totally the conventional reinforcement, thus providing an important reduction of construction time and costs that generally characterize traditional Reinforced Concrete (RC) structures.

The literature reports experimental tests on FRC elevated slabs performed by different researchers (Gossla 2006; Parmentier et al. 2014; Barros et al. 2012). The latter adopted fibers as the main flexural reinforcement whereas rebars were placed only along the column alignments to prevent the progressive collapse of the structure. Accordingly, ACI 544.6R-15 suggests to reinforce FRC elevated slabs by using steel fibers as the only primary reinforcement in combination with a minimum amount of rebars used as "anti-progressive collapse reinforcement". In spite of the high post-cracking performances achievable by FRC materials nowadays, the tests mentioned above highlighted that the required design capacity of slabs not containing rebars can be achieved only by using steel fiber contents not lower than 70 kg/m^3. On the contrary, the use of a proper combination of fibers with steel reinforcement placed in the most stressed areas of the slab may result in a reduced total amount of fibers and in an improved structural behavior of the overall structure, by considering also the ductility requirements of building codes. The material resulting from the combination of fibers and rebars (Vandewalle 2000; de la Fuente et al. 2012; Mobasher et al. 2015) is herein defined as Hybrid Reinforced Concrete (HRC).

Based on the design requirements reported by *fib* Model Code 2010 (MC2010), the paper presents a simplified procedure for designing HRC elevated slabs. In addition to the bottom reinforcement placed along the column alignments, top rebars are also placed over the columns in order to get the best performance in terms of global capacity of the structure. The method is based on an initial Linear Elastic Finite Element Analysis (LEFEA) that provides the bending moments used for proportioning the Hybrid Reinforcement. Afterwards, a Non-Linear Finite Element analysis (NLFEA), considering the post-cracking tensile behavior of FRC, is carried out for better determining the real bearing capacity of the slab.

The effectiveness of the proposed design approach has been proved by designing a full-scale elevated slab made with synthetic FRC. The main results provided by the design process are reported and discussed in the paper.

2 Description of the Proposed Design Procedure

The proposed design procedure consists of two main stages defined to as "preliminary design stage" and "verification stage". The former concerns the preliminary linear elastic analysis and design of the structure. The latter is performed to verify the structure behavior both at Ultimate Limit State (ULS) and at Serviceability Limit State (SLS) by means of NLFEAs. The following paragraphs describes the main features of the two design stages.

2.1 Preliminary Design Stage (Proportioning)

The preliminary design stage requires the fulfillment of the following steps:

- Choice of the slab thickness (t).
- Choice of mechanical properties of materials.
- Determination of the design loads (E_d). As required by the EN 1990 (2006), all possible combinations of design loads must be considered to obtain the most critical values of the internal actions. The design load results from the following combination:

$$E_d = \sum_{j \geq 1} \gamma_{G,j} \cdot G_{k,j} + \gamma_P \cdot P + \gamma_{Q,1} \cdot Q_{k,1} + \sum_{i > 1} \gamma_{Q,i} \cdot \psi_{0,i} \cdot Q_{k,i} \quad (1)$$

  where G, P and Q represent permanent, pre-stressing and variable actions, respectively; the coefficients γ_G, γ_P, γ_Q are the partial factors for actions; ψ is the factor for the combination of variable actions.
- Determination of the internal actions through LEFEA.
- Design of conventional reinforcement combined with fibers. Based on the results of the LEFEA, the maximum design bending moments ($m_{Ed,x}$, $m_{Ed,y}$) acting in the two orthogonal directions (x and y) can be evaluated as follows:

$$m_{Ed,x} = m_{d,x} \pm \left| m_{d,xy} \right|; \; m_{Ed,y} = m_{d,y} \pm \left| m_{d,xy} \right| \quad (2)$$

where $m_{d,x}$, $m_{d,y}$ are the internal design bending moments in x and y direction whereas $m_{d,xy}$ is the internal design torsional moment.

The contribution to the internal resistance provided by fibers only may be evaluated by using a simplified cross-section model that assumes to represent the ultimate residual tensile strength (f_{Ftu}) with a constant stress distribution below the neutral axis depth (x). The latter is assumed to be a constant parameter equal to 0.1 times the thickness (t) of the slab. The adopted model is represented by the following equation:

$$m_{Rd,FRC} = \frac{1}{2} f_{Ftu,d} \cdot t \cdot (t - x) = 0.45 \cdot f_{Ftu,d} \cdot t^2 \quad (3)$$

where $f_{Ftu,d} = f_{R3k}/(3 \times \gamma_c)$; f_{R3k} is the residual flexural strength at a Crack Mouth Opening Displacement (CMOD) of 2.5 mm according to EN14651(2005); $\gamma_c = 1.5$ is the partial safety factor for FRC according MC2010. The assumed value of the neutral axis depth is representative of lightly reinforced flat slabs.

Additional conventional reinforcement has to be placed in the areas of the slab where the design bending moment (m_{Ed}) is higher than the resisting moment provided by fibers only ($m_{Rd,FRC}$). As a first approximation, the moment distribution provided by the LEFEA may be used to design the additional reinforcement.

The typical regions of the slab that require additional reinforcement are depicted in Fig. 1. For the sake of brevity, the schematic considers only the regions in which additional rebars are required in the x-direction.

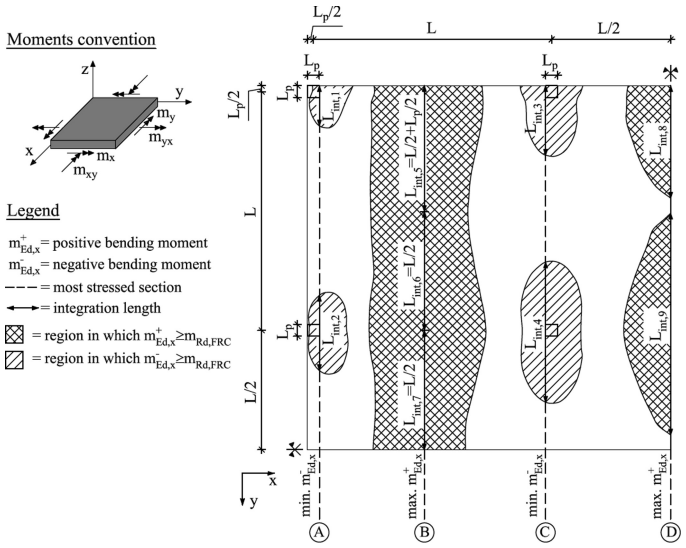

Fig. 1. Typical areas of the slab requiring additional reinforcement in the x-direction

Figure 2 shows the typical envelope curves of bending moments acting in the x-direction along the most critical sections (i.e. section lines A, B, C, D) of the slab. The total area of additional reinforcement can be calculated by integrating the bending moments along the length L_{int}, which is determined by intersecting the envelope curve of bending moments with the resisting moment provided by fibers only (see Fig. 2). Thus, the following relationships can be adopted:

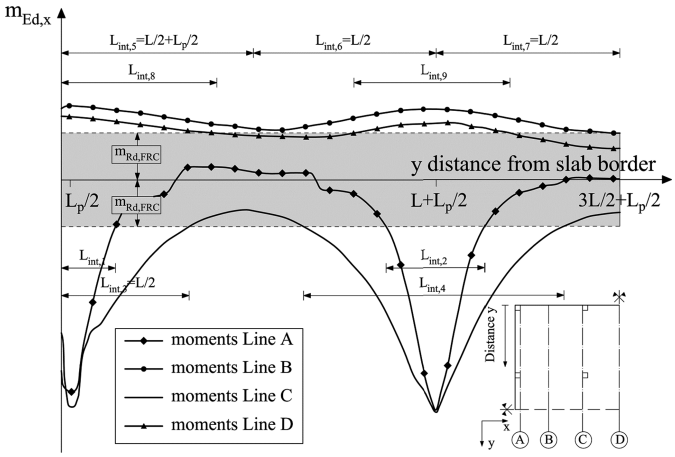

Fig. 2. Typical bending moments acting in the x-direction along the lines A, B, C and D

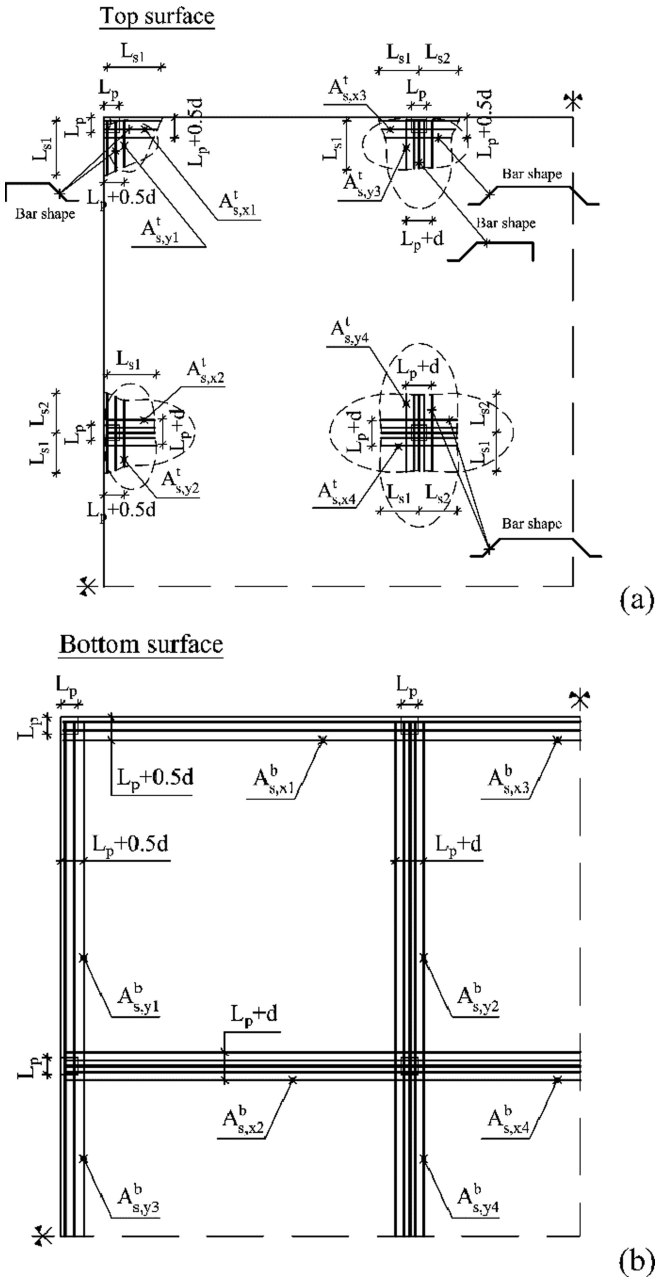

Fig. 3. Proposed layout of conventional top (a) and bottom (b) reinforcement

$$A_{s,x} = \frac{\int_0^{L_{int}} \left(m_{Ed,x} - m_{Rd,FRC}\right) dx}{0.9 \cdot f_{yd} \cdot d}; \quad A_{s,y} = \frac{\int_0^{L_{int}} \left(m_{Ed,y} - m_{Rd,FRC}\right) dy}{0.9 \cdot f_{yd} \cdot d} \tag{4}$$

where $A_{s,x}$ and $A_{s,y}$ are the total required reinforcement areas in x and y-direction, respectively; d is the effective depth of the slab; $f_{yd} = f_{yk}/\gamma_s$, f_{yk} and $\gamma_s = 1.15$ are the design yield strength, the characteristic yield strength and the material safety factor of conventional reinforcing steel, respectively (see MC2010).

The additional top and bottom reinforcement can be placed in the slab according to the layout of Fig. 3. Top reinforcement consists of rebars placed orthogonally over the columns; these bars are bent as shown in Fig. 3a to be easily placed during construction as well as to contribute to the punching shear resistance. Bottom continuum rebars (Fig. 3b) are also placed along the column alignments.

Both top and bottom rebars are spread over a width equal to $L_p+d \leq 2L_p$, where L_p represents the length of the column side. On the contrary, rebars placed along the border of the slab are spread over the width $L_p+0.5d \leq 1.5L_p$ (Fig. 3). According to MC2010 (clause 7.3.5.6), when slabs without shear reinforcement or sufficient deformation capacity are considered, integrity reinforcement has to be adopted. In the proposed reinforcement layout, bottom rebars can also used to prevent the progressive collapse of the structure as they allow to provide continuity between the columns.

No other conventional rebars should be used with the exception of those usually required to control crack formation in correspondence of concrete shafts, staircases, reentrant corners and manholes.

2.2 Verification Stage

In order to verify the Hybrid Reinforcement resulting from the sizing stage, the following procedure can be carried out:

– Perform NLFEAs to determine the global resistance of the structure. The simulations have to implement the tensile constitutive laws of FRC according MC2010 (clause 5.6.4). The design condition for the global safety format proposed by MC2010 (clause 7.11.3) has the following form:

$$E_d \leq R_d = \frac{R_m}{\gamma_R^* \cdot \gamma_{Rd}} \tag{5}$$

where R_d and R_m are respectively the design and mean global resistance of the structure; γ_R^* is the global resistance safety factor; γ_{Rd} is the model uncertainty factor. Different methods can be used to evaluate the design resistance R_d: 1) the probabilistic method (clause 7.11.3.2); 2) the global resistance factor method (clause 7.11.3.3.1); 3) the method of Estimation of a Coefficient of Variation of resistance (ECOV) (clause 7.11.3.3.2). If the global safety condition required by Eq. 5 is not fulfilled, then a tougher FRC or additional reinforcement must be provided until an acceptable safety level is achieved.

- Check the safety and serviceability minimum requirements for FRC structures according MC2010 (see clause 7.7).
- In case the numerical model is not able to simulate punching shear mechanisms, the punching resistance, often critical in flat slabs, must be checked. It is recommended to consider the model reported by MC2010 (clause 7.7.3.5.3) for FRC structures.

3 Design of a FRC Elevated Slab with Synthetic Fibers

In this paragraph, the design method previously described is used to design an elevated slab subjected to uniformly distributed loads, typical of a residential building floor. The Hybrid Reinforcement adopted consists of a combination of rebars and synthetic fibers. The finite element program Diana 10.1 was used to simulate the structure behavior under linear elastic as well as non-linear conditions.

3.1 Preliminary Design of the Structure

The geometry of the elevated slab considered in this work is represented in the schematic of Fig. 4. As one can see, the slab is supported by 16 300x300 mm columns placed with a constant spacing of 6000 mm. The total thickness (t) of the slab is equal to 260 mm.

The loads considered in the slab design include a self-weight ($G_{1,k}$) of 5.0 kN/m^2, a gravity load ($G_{2,k}$) of 4 kN/m^2 and a variable load (Q_k) of 2 kN/m^2. To perform the load combinations according to Eq. 1, the load $G_{2,k}$ was considered as a variable load and thus combined with the related partial safety factor suggested by EN 1990 (2006). The partial safety factor for permanent actions (γ_{G1}) was assumed equal to 1 and 1.35 for favorable and unfavorable actions, respectively. On the contrary, the partial safety factors γ_{G2} and γ_Q were both considered equal to 0 for favorable actions and 1.5 for unfavorable actions. The diagram of the design bending moment envelops ($m_{Ed} = m_{Ed,x} = m_{Ed,y}$) resulting from the LEFEA is shown in Fig. 5. The curves represent the maximum moments detected along the most stressed sections (i.e. Line A, B, C and D) of the slab.

Regarding the mechanical properties of concrete, the mean compressive cubic strength ($f_{cm,cube}$ = 53 MPa) was obtained by testing 150 mm cubes after 28 days of curing whereas the corresponding cylindrical compressive mean (f_{cm} = 44 MPa) and characteristic (f_{ck} = 36 MPa) strengths were assumed as 0.83 $f_{cm,cube}$ and f_{cm}-8 MPa, respectively (see EN 1992-1-1). Likewise, the mean secant Young's modulus (E_{cm}) and the tensile strength (f_{ctm}) were calculated according to the equations proposed by the EN 1992-1-1, i.e. $E_{cm} = 22\cdot(f_{cm}/10)^{0.3}$ = 34300 MPa and $f_{ctm} = 0.3f_{ck}^{2/3}$ = 3.27 MPa. The characteristic value of the tensile strength (f_{ctk} = 2.3 MPa) was assumed to be 30% lower than the corresponding mean value (f_{ctm}). A total of 8 kg/m^3 (fiber volume fraction = 0.89%) of synthetic fibers having a length of 54 mm and an equivalent diameter of 0.68 mm (fiber aspect ratio = 80) were used as a smeared reinforcement for concrete. The behavior in tension of FRC was assessed by testing 6 notched beams (150x150x 500 mm^3) under 3-point bending (3PBT) according EN 14651 (2005). The bending tests provided the nominal stress vs. CMOD (Crack Mouth Opening Displacement) curves depicted in Fig. 6 as well as the mean and characteristic values of

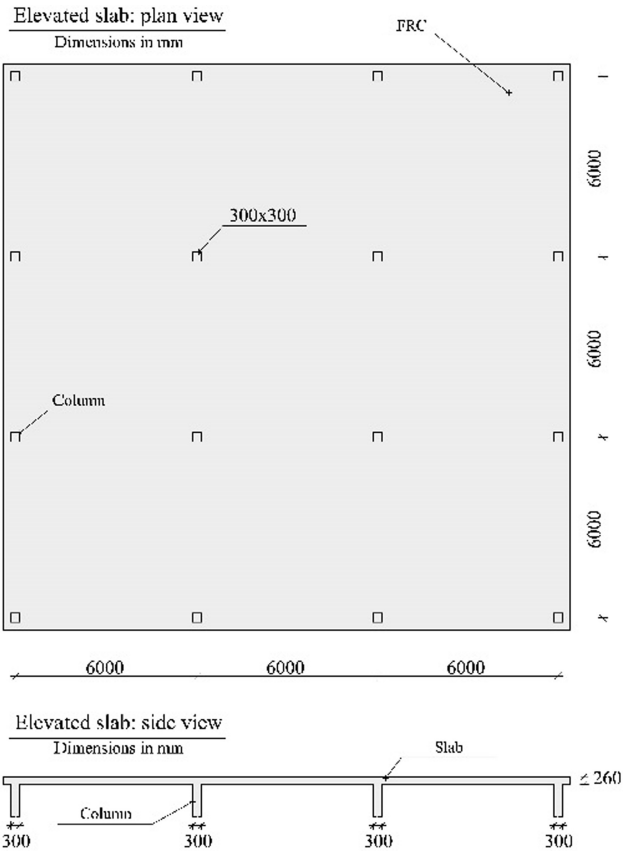

Fig. 4. Geometry of the slab.

the limit of proportionality (f_L) and of the residual stresses (f_{R1}, $f_{R,2}$, $f_{R,3}$, $f_{R,4}$), reported in Table 1. The four residual stresses were determined at CMOD values equal to 0.5, 1.5, 2.5 and 3.5 mm, respectively.

The conventional reinforcement used in combination with fibers was rebars B450C, having an elastic modulus of 210,000 MPa, a characteristic yielding strength of 450 MPa and an ultimate characteristic strength of 517 MPa. According to EN 1992-2 (clause 5.7), to determine the mean tensile strengths, the corresponding characteristic values were multiplied by 1.1.

The main properties of the additional reinforcement designed according to the proposed preliminary design method (see Sect. 2.1) are reported in Table 2. The reinforcement designation refers to the rebar layout depicted in Fig. 3. By considering the FRC properties reported in Table 1, the design resisting moment provided by fibers only (see Eq. 3) resulted to be $m_{Rd,FRC}$ = 12.1 kNm. The total area of conventional reinforcement was calculated by assuming an effective depth (d) of 230 mm. Note that, in order to better assess the effectiveness of the proposed design approach, the integrity reinforcement was not considered to determine the area of bottom rebars.

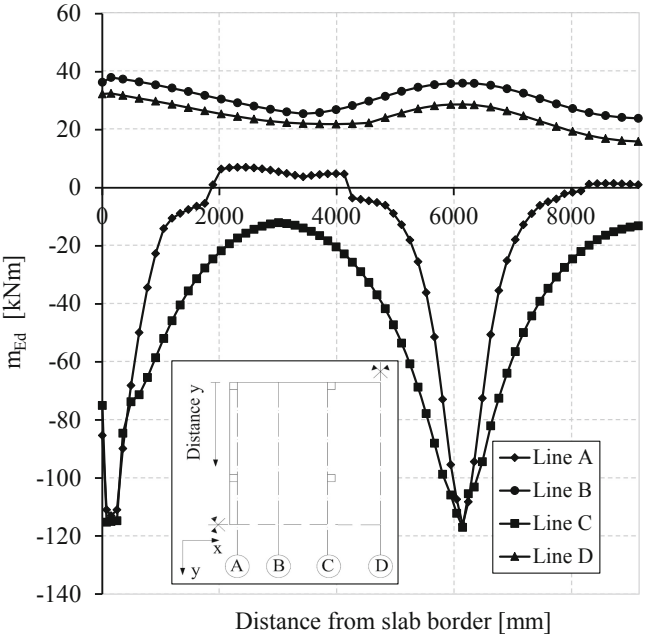

Fig. 5. Envelope of design bending moments resulting from the LEFEA

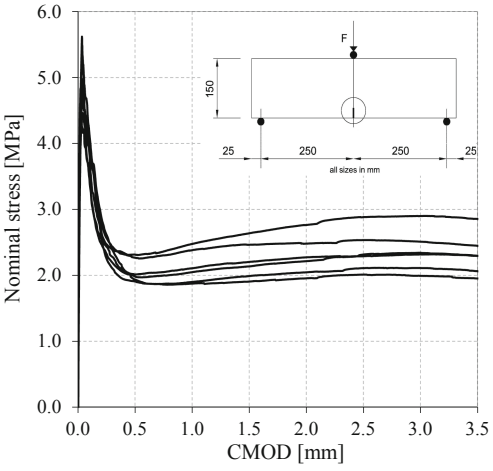

Fig. 6. Nominal tensile stress-CMOD behavior of synthetic FRC resulting from flexural tests according EN 14651(2005).

Table 1. Mechanical properties of FRC in tension

		f_L	f_{R1}	f_{R2}	f_{R3}	f_{R4}
Mean	[MPa]	4.9	2.1	2.2	2.4	2.3
St. Dv.	[MPa]	0.5	0.2	0.3	0.3	0.3
CoV	[%]	10.0	8.0	13.0	13.0	14.0
Charact.	[MPa]	4.1	1.8	1.8	1.8	1.8

Table 2. Properties of additional reinforcement.

Reinforcement type [-]	Bar type [-]	Total bar area [mm^2]	Bar length L_{s1} [m]	Bar length L_{s2} [m]
$A^t_{s,x1} = A^t_{s,y1}$	4Ø16	800	1.0	–
$A^t_{s,x2} = A^t_{s,y3}$	6Ø16	1200	1.0	1.0
$A^t_{s,x3} = A^t_{s,y2}$	4Ø20	1256	1.2	1.2
$A^t_{s,x4}. = A^t_{s,y4}$	8Ø20	2512	1.2	1.2
$A^b_{s,x1} = A^b_{s,y1}$	4Ø16	800	–	–
$A^b_{s,x2} = A^b_{s,y2}$	7Ø16	1400	–	–
$A^b_{s,x3} = A^b_{s,y3}$	3Ø16	600	–	–
$A^b_{s,x4} = A^b_{s,y4}$	4Ø16	800	–	–

3.2 Slab Verification

The verification procedure requires the assessment of the global capacity of the slab containing the Hybrid Reinforcement. Here, to estimate the global design resistance (R_d), the method for the estimation of the coefficient of variation of resistance (V_R) proposed by Cervenka (2008) and reported in the MC2010 (clause 7.11.3.3.2) was adopted. Therefore, the global resistance safety factor reported in the Eq. 5 was calculated by the following relation:

$$\gamma_R^* = \exp(\alpha_R \cdot \beta \cdot V_R) \quad \text{with} \quad V_R = \frac{1}{1.65} \cdot \ln\left(\frac{R_m}{R_k}\right) \tag{6}$$

where $\alpha_R = 0.8$; $\beta = 3.8$ (for a service life of 50 years) corresponds to a failure probability of about 10^{-4}, suitable for residential buildings. R_m and R_k represent the capacity of the structure resulting from the implementation of the mean and characteristic constitutive laws of materials, respectively. The design resistance of the structure is determined according to Eq. 5 by assuming a model uncertainty factor $\gamma_{Rd} = 1.06$.

The finite element model used to simulate the slab (Fig. 7) consists of 4850 eight-node isoparametric flat-shell elements. Vertical rigid constraints (with free rotations) were adopted to reproduce the support of the columns in vertical direction (z-direction). Note that, because of the double symmetry, only a quarter of the whole slab was modelled.

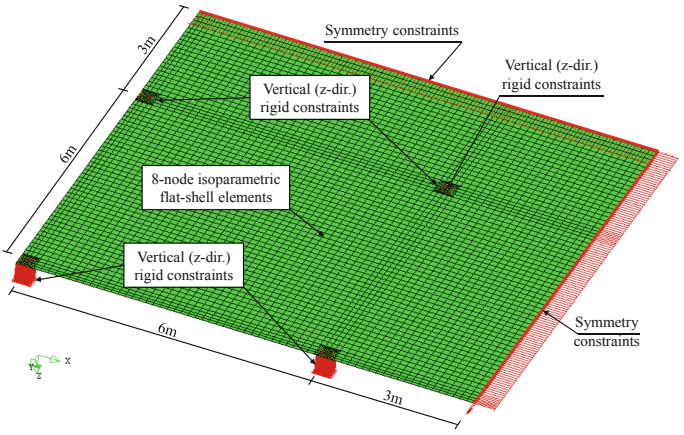

Fig. 7. Finite element model of the elevated slab

In order to represent the fracture behavior of concrete, the "Total Strain Rotating Crack model" implemented in Diana 10.1 was adopted. The compressive behavior of FRC (Fig. 8) was represented by the parabolic uniaxial stress-strain relationship suggested by the MC2010 (clause 5.1.8).

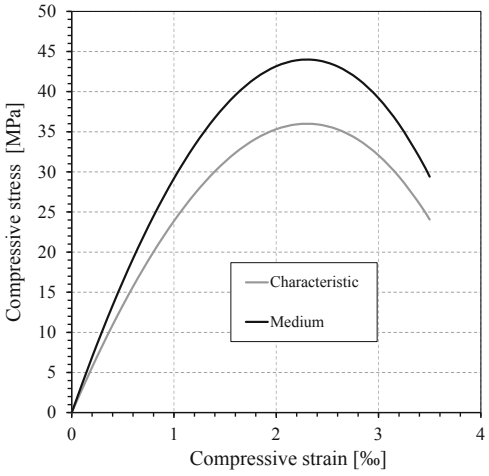

Fig. 8. Medium and characteristic compressive stress-strain constitutive law of FRC.

The bi-linear stress-crack width model reported by MC2010 (clause 5.6.5) was used to represent the post-cracking tensile behavior of FRC. The first descending branch of the constitutive law is conventionally determined by the post-cracking linear response of plain-concrete (i.e., concrete not containing fibers) whereas the second branch

represents the behavior of FRC. On the contrary, the second linear branch is defined by the reference strengths $f_{Fts} = 0.45 \cdot f_{R1}$ and $f_{Ftu} = 0.5 \cdot f_{R3} - 0.2 \cdot f_{R1}$ corresponding to crack width values of 0.5 mm and 2.5 mm, respectively. The mean and characteristic laws implemented in the finite element model are shown in Fig. 9.

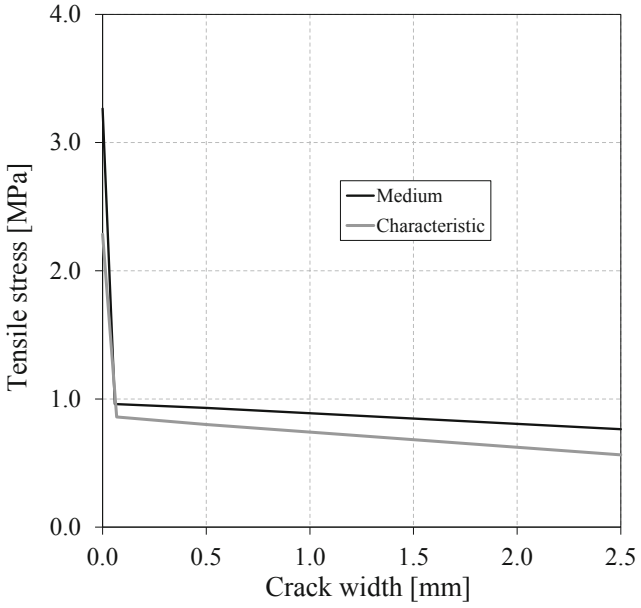

Fig. 9. Medium and characteristic post-cracking tensile stress-crack width laws of FRC.

Note that, in order to change the tensile stress-crack width laws into stress-strain (ε_t) relations, the crack width (w) was smeared over a length L_{ch} (i.e. $\varepsilon_t = w/L_{ch}$) depending on the size $L_{ch} = V_{el}^{1/2}$ (V_{el} = element surface) of shell elements.

Based on the mean and characteristic mechanical properties reported above (see Sect. 2.1), the tensile behavior of reinforcing steel was modelled by the idealized stress-strain diagram reported by MC2010 (clause 5.2.8).

The numerical analyses were carried out by first applying the self-weight and by then increasing the overload up to failure. Only the results obtained from the most critical load combination (i.e. the one considering the self-weight $\gamma_{G1} \cdot G_{1,k} = 1.35 \cdot G_{1,k}$ and the overload $\gamma_Q \cdot (G_2 + Q_k) = \gamma_Q \cdot 6$ kN/m^2 applied all over the surface of the slab) are reported and discussed. Considering that the self-weight was kept constant, the results reported in the following refer to the combination of the permanent and variable load, i.e. $E'_d = 1.5 \cdot (G_{2k} + Q_k) = 9$ kN/m^2.

The diagram of Fig. 10 shows the total overload $E' = G_{2k} + Q_k$ against the maximum deflection detected in the middle of the corner bay of the slab. The two curves refer to the analyses performed with the mean and the characteristic properties of materials, respectively. The diagram and the results reported in Table 3 prove that the adopted Hybrid Reinforcement allowed the slab to reach a design capacity higher than

the design load E'$_d$. In fact, the global safety factor calculated according to Eq. 6 provided a global design resistance (R_d) of 10.4 kN/m^2 which, in turn, allowed to fulfill the minimum safety requirement, i.e. $R_d/E'_d \geq 1$.

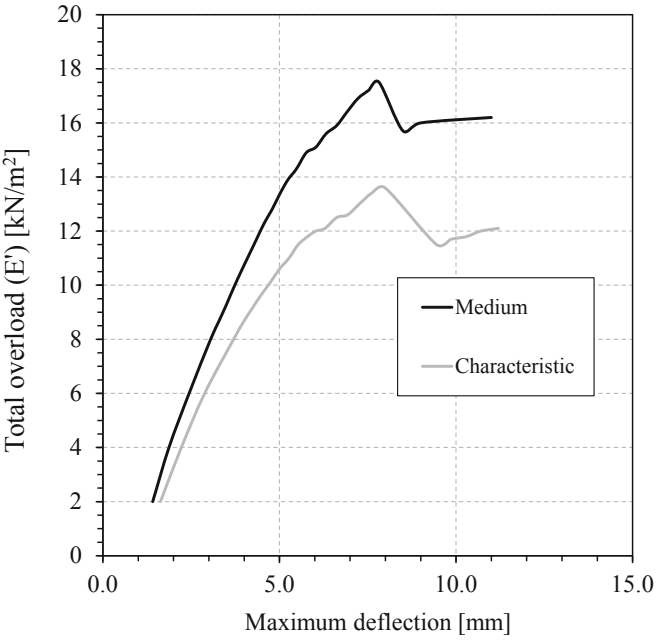

Fig. 10. Total overload – maximum deflection response of the slab

According to the MC2010 (see clause 7.7.2), structure design must fulfill some resistance and serviceability requirements for the expected service life of the structure. Therefore, at least one of the two following conditions must be satisfied:

$$\delta_u \geq 20 \cdot \delta_{SLS} \tag{7}$$

$$\delta_{peak} \geq 5 \cdot \delta_{SLS} \tag{8}$$

where δ_u is the displacement corresponding to the ultimate capacity, δ_{peak} is the displacement at the maximum load and δ_{SLS} is the deflection at the service load determined by performing a linear elastic analysis. In addition to Eqs. 7 and 8, the ultimate load has to be higher than both the first cracking load and the maximum service load. The previous load and deflection values are all derived from the NLFEA performed with mean properties of materials.

Equations 7 and 8 are mandatory for members containing fibers only but, when members containing Hybrid Reinforcement are considered, one may argue whether the classical approach for FRC only would suffice as check. In spite of this, Eqs. 7 and 8 are here adopted for the verification of the slab studied herein. However, other analytical models (Facconi & Minelli 2017) available in the literature could be used for verifying the ULS and SLS compliance.

Table 3. Main results obtained from NLFEAs.

R_m	R_k	γ_R^*	R_d	R_d/E'_d	δ_{peak}	δ_u	δ_{SLS}
[kN/m^2]	[kN/m^2]	[-]	[kN/m^2]	[-]	[mm]	[mm]	[mm]
17.5	13.6	1.6	10.4	1.15	7.8	11	1.4

The service load deflection (δ_{SLS} = 1.4 mm) was determined for a service load (E'_{SLS}) of 6 kN/m^2 whereas the deflection δ_{peak} (Table 3) corresponded to the mean slab capacity R_m. Moreover, the ultimate deflection (δ_u; Table 3) was assumed equal to the maximum deflection predicted by the numerical simulation before of slab collapse. According to the results of the analyses, all the slabs exhibited first cracking right after the application of self-weight.

By considering the deflection values reported in Table 3, it appears that the first code requirement (Eq. 7) is not fulfilled by the structure ($\delta_u/\delta_{SLS} = 7.9 < 20$). However, the value of the deflection at peak allowed to fulfill Eq. 8 ($\delta_{peak}/\delta_{SLS} = 5.6 > 5$). The ultimate load of the slab is higher than both the first cracking load and the service load (E'_{SLS}). Thus, one may conclude that the slab studied herein satisfies the minimum design requirements of MC2010.

4 Concluding Remarks

The paper presents a procedure to design and verify the flexural reinforcement of FRC elevated slabs. The proposed method provides straightforward rules for proportioning the Hybrid Reinforcement by performing a linear elastic analysis of the structure. Moreover, structure verification is carried out by Non-linear finite element analyses including the tensile constitutive law of FRC, as recommended by MC2010.

The proposed designed method has been implemented to design a elevated slab made with synthetic FRC. The numerical results prove the ability of the proposed Hybrid Reinforcement to provide the slab a structural behavior consistent with the safety and serviceability requirements recommended by MC2010.

Since the paper focuses on the proposal of an overall procedure for designing the flexural reinforcement of FRC, in spite of its primary importance, the verification of punching resistance is not considered in the present paper.

Acknowledgements. The Authors are grateful to Ruredil S.p.A. for supporting the experimentation carried out to characterize the synthetic Fiber Reinforced Concrete used in the present study.

References

ACI 544.6R-15, 2015. Report on design and construction of steel fiber-reinforced concrete elevated slabs

Barros JAO, Salehian H, Pires, NMMA, Gonçalves DMF (2012) Design and testing elevated steel fiber reinforced self-compacting concrete slabs. BEFIB2012-Fiber Reinforced Concrete, 2012, 12 pp

Cervenka V (2008) Global safety format for nonlinear calculation of reinforced concrete. Beton- und Stahlbetonbau 103, special edition, Ernst & Sohn:37–42
Chiaia B, Fantilli A, Vallini P (2009) Combining fiber-reinforced concrete with traditional reinforcement in tunnel linings. Eng Struct 31(7):1600–1606
DAfStb COMMITTEE FOR STRUCTURAL CONCRETE 2012. DAfStb guideline on steel fiber reinforced concrete
de la Fuente A, Pujadas P, Blanco A, Aguado A (2012) Experiences in Barcelona with the use of fibres in segmental linings. Tunn Undergr Space Technol 27(1):60–71
Destrée X (2004) Structural Application of Steel Fibers as Only Reinforcing in Free Suspended Elevated Slabs: Conditions—Design Examples. In: Di Prisco M, Plizzari GA, Roberto F (eds) Sixth RILEM symposium on fiber-reinforced concrete (FRC), pp 1073–1082
Diana 10.1. 2016. User's manual. TNO DIANA BV, Delft, The Netherlands
EN 1992-1-1:2005: Eurocode 2. Design of concrete structures. Part 1-1: General rules and rules for buildings
EN 14651:2005. Precast concrete products – test method for metallic fibre concrete – Measuring the flexural tensile strength, European Standard
EN 1992-2:2005. Eurocode 2. Design of Concrete Structures. Part 2: Concrete bridges: design and detailing rules
EN 1990:2006, Eurocode 0 — basis of structural design. European Committee for Standardization, Brussels
Facconi L, Minelli F, Plizzari G (2016) Steel fiber reinforced self-compacting concrete thin slabs – Experimental study and verification against Model Code 2010 provisions. Eng Struct 122(1 September 2016):226–237
Facconi L, Minelli F (2017) Verification of structural elements made of FRC only: A critical discussion and proposal of a novel analytical method. Eng Struct 131:530–541
fib Model Code for Concrete Structures 2010; October 2013. 434 pages. ISBN: 978-3-433-03061-5
Gossla U (2006) Flachdecken aus Stahlfaserbeton. Beton-und Stahlbetonbau 101(Heft 2):94–102 (in German)
Mobasher B, Yao Y, Soranakon C (2015) Analytical solutions for flexural design of hybrid steel fiber reinforced concrete beams. Eng Struct 100(1 October 2015):164–177, ISSN 0141-0296
NTC 2018- Norme Tecniche per le Costruzioni, 2018 (in Italian)
Parmentier B, Van Itterbeeck P, Skowron A (2014) The behavior of SFRC flat slabs: The Limelette full-scale experiments for supporting design model codes. In: Charron JP, Massicotte B, Mobasher B, Plizzari G (eds.) FRC 2014 joint ACI-fib Intl. Workshop – fibre-reinforced concrete: from design to structural applications, Montreal, Canada
Sorelli L, Meda A, Plizzari G (2006) Steel fiber concrete slabs on ground: a structural matter. ACI Struct J 103(4):551–558
Silfwerbrand J (2004) Design of steel fiber-reinforced concrete slabs on grade for restrained loading. In: Di Prisco M, Plizzari GA, Roberto F (eds) Sixth RILEM symposium on fiber-reinforced concretes (FRC), pp 975–984
Tiberti G, Minelli F, Plizzari G (2014) Reinforcement optimization of fiber reinforced concrete linings for conventional tunnels. Compos Part B: Eng, ISSN: 1359-8368 58:199–207
Vandewalle L (2000) Cracking behaviour of concrete beams reinforced with a combination of ordinary reinforcement and steel fibers. Mater Struct 33(3):164–170

An Innovative and Sustainable Wet Joint Between Precast Beam and Columns from the Oil & Gas

V. Colone[1(✉)] and P. Lopriore[2(✉)]

[1] Head of Civil and Structural Section, Technip Italy SpA, Rome, Italy
valerio.colone@TechnipFMC.com
[2] Head of Engineering Department, Technip Italy SpA, Rome, Italy
paolo.lopriore@TechnipFMC.com

Abstract. This innovative joint was conceived for the effective and sustainable construction of precast concrete pipe-rack structures in petrochemical plants. It consists in a cast-in-situ joint between precast beam and column concrete elements, featuring easy in-shop fabrication and on-site assembly, with no scaffolding and minimum formworks. The solution is characterized by high strength and ductile behaviour in the plastic range, by means of loop splices and cast-in-situ concrete with steel fibres. Experimental tests conducted on reduced-scale structures verified that the performance of the prefabricated solution during an earthquake is comparable to, if not better than, that of the corresponding cast-in-situ concrete solution, while fulfilling the American Concrete Institute requirements. This precast concrete solution economically mimics the behaviour of monolithic reinforced concrete frames and has been already successfully implemented in several pipe rack structures in remote seismic zones.

Keywords: Fibre-reinforced concrete · Precast structures · Beam-column joint · Moment frame · Patent

1 Introduction

Oil and gas plants require pipe rack structures to support the process pipelines. These structures are typically built with either steel or reinforced concrete elements or hybrid precast concrete beams and columns with steel bracing to provide the necessary stiffness and strength to resist seismic loads. While modularized pipe racks are made of steel, the structure type for stick-built pipe racks is generally based on considerations related to cost, time for supply and erection of the structures, ease of future maintenance, revamping and expansions. Reinforced concrete is very often preferred to steel for its durability and, where racks are routed across fire-hazardous areas, for its intrinsic fire resistance, which reduces the cost and time for fireproof coating installation. With respect to cost and time, the choice between steel and reinforced concrete depends also on the global and local markets.

Various solutions for precast concrete pipe racks have been implemented in the Oil & Gas industry, ranging from the site pre-casting of entire frames (for smaller racks) to the site assembly of precast elements. Where monolithic behavior of the frames is

M. di Prisco and M. Menegotto (Eds.): ICD 2018, LNCE 42, pp. 585–598, 2020.
https://doi.org/10.1007/978-3-030-23748-6_45

required, then it is usually achieved using mechanical connectors between the re-bars and cast-in-place concrete joints to connect the precast concrete beams and columns.). The very first rack entirely made of shop prefabricated elements was constructed by Technip Italy (formerly TPL) for Brindisi Enichem plant back in 1990 and is still in operation today.

Hence the choice of the right technology for the precast system is of major importance and the aim, for the designer, is to obtain a solution that is capable of obtaining the required performances in terms of load bearing capacity and ductility while minimizing construction manpower, time and costs. This study presents a technical solution able to offer both high strength and ductility in the plastic range, simplicity of construction of the prefabricated elements and ease of assembly on site. The comparison of cyclic tests with imposed displacements up to a drift ratio of 3.5% on a couple of external beam-column joints allowed verifying the structural behavior of the prefabricated solution. The results of the experimental tests showed a seismic performance of the prefabricated joint very similar to that of the 'same' cast-in-place joint.

2 Proposed Wet Joint for Beam Column Connection

The wet joint between precast beams and columns presented in this study has been developed as a standard solution for pipe rack structures, commonly used within worldwide oil and gas plants but it could be also adopted in other continuous precast RC frames. The proposed beam-to-column connection was developed with the following concepts in mind:

1. seismic resistance;
2. safe and quick execution;
3. minimum formworks and no scaffolding (man-lift only);
4. sustainability, thanks to the use of traditional concrete techniques (no mechanical connectors) allowing for the usual construction tolerances and with low-skilled workers (often found at remote locations of the plants).

It has been designed according to the ACI 318 code. An example of the pipe rack structures is shown in Fig. 1. They are generally composed of transversal frames that are repeated along the path of the piping lines at a given spacing. Considering the significant heights that can be reached by such structures is clear the importance of having in seismic-prone regions a moment resisting frame, especially in the transversal direction. The construction of such facilities, which are very often located in remote regions, could turn out to be far too complicated with the traditional cast-in-situ technique. A precast solution would instead allow a much easier building process with reduced construction time and costs.

Assuming initially a cast-in-situ frame, the acting design bending moment of the beam critical section at the beam-column intersection has been evaluated as $M_u = 1100$ kNm. By taking into account the capacity reduction factor for tension controlled failure $\phi = 0.9$, the rectangular beam section 500 mm wide and 900 mm tall has been reinforced with 4 bars of 28 mm diameter and 2 bars with 25 mm diameter placed in the upper

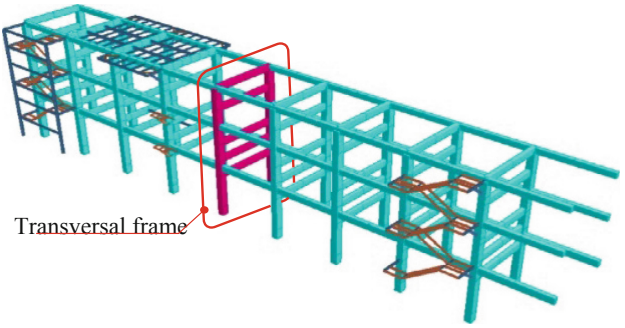

Fig. 1. Example of pipe rack for oil and gas plants. /Esempio di un pipe rack per impianti oil e gas

and lower sides. The nominal bending strength of this section is equal to $M_n = 1233$ kNm.

The joint is basically made of:

1. a beam equipped with U-shaped projecting reinforcement dowels at its ends;
2. a column, equipped with U-shaped projecting reinforcement dowels, which can be overlapped with beam dowels; and a portion that can be completed *in situ* by SFRC;

wherein the cross section of the prefabricated beam (T), at the joint, widens gradually so that it then divides into two prismatic elements with narrow rectangular cross section, referred to as shoulders (S), which define a containment compartment, i.e., a formwork, for the subsequent casting; said containment compartment being accessible and open at the top, at the bottom, and at the front side facing the column (C), wherein said U-shaped re-rods (1 and 3) are arranged in mutually parallel vertical planes (Fig. 2).

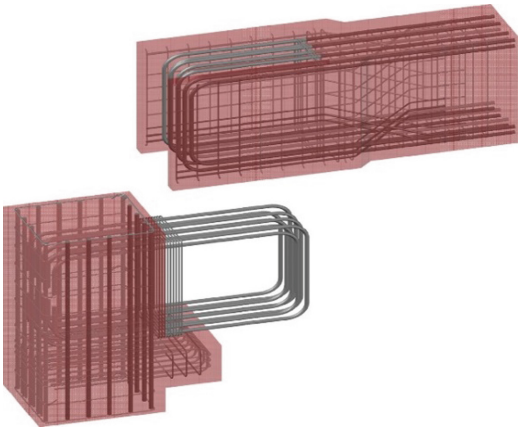

Fig. 2. Protruding rebars from column and beam for the wet joint connection

3 Experimental Program

To compare the precast solution with the corresponding cast-in-situ construction, an experimental program was carried out. Two reduced scale models, the cast-in-situ reference model and the corresponding precast solution, have been designed and built.

The two joint specimens were subjected to a sequence of displacement-controlled cycles according to the provisions of ACI 374.1-05.

The whole apparatus was installed inside a test chamber, delimited by a RC reaction wall. The column was supported by a steel cylinder whose function was that of providing the vertical reaction force without notable horizontal components. The horizontal reaction was instead provided by a stiff steel frame anchored on one side to the rigid RC wall, and on the other side to the lower part of the column using a pinned connection, thus allowing rotation to occur. On the upper part of the column an hydraulic jack attached to the reaction wall was connected to the column using a pinned connection. The jack provided the horizontal force that was used to control the column drift. The beam was connected by means of a pinned restraint to a steel frame. This latter was linked to a rigid steel base that was integral with the floor using a bolted connection. The steel frame applied a restraint to the beam only in the vertical direction allowing at the same time the horizontal movement of the beam itself (see Fig. 3). No notable horizontal restraining force was thus applied to the end of the beam. A second hydraulic ram actuator placed on the top of the column was used to apply a suitable compressive force to the column. The value of this force corresponds to the axial load induced in the column by the permanent loads in the overlying portion of the structure of the pipe rack reduced by a scale factor of 9 to take into account the scale of the specimen. The reaction exerted by the jack was transmitted to the ground by means of two threaded steel rods.

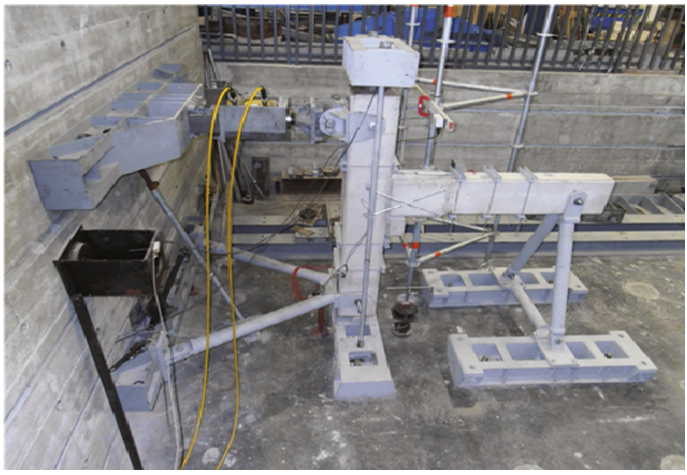

Fig. 3. Picture of the experimental setup before the beginning of precast joint test.

This hydraulic jack was actuated by a manually operated hydraulic pump to impose the predetermined compressive force. In order to minimize the variations in trim during the execution of the tests, it was used a hemispherical head interposed between the vertical actuator and the top of the column. A load cell was installed between the actuator and the column to control and store the time history of the vertical load.

3.1 Testing Procedure

Joint specimens were subjected to a sequence of displacement controlled cycles representative of the drifts expected under earthquake motions and defined in accordance to the ACI standards. The drift sequence, shown in Fig. 4, has been established complying with the following rules:

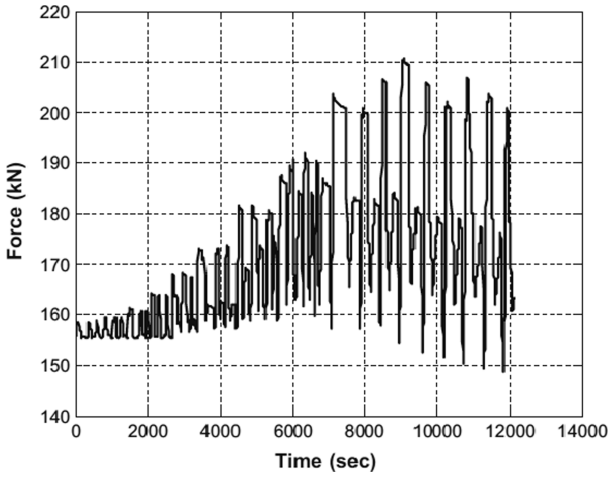

Fig. 4. Time history of the axial force applied on top of the specimen during the experimental test.

1. the initial drift ratio must be within the essentially linear elastic response range;
2. subsequent drift ratios must be not less than one and one quarter times, and not more than one and one-half times the previous drift ratio;
3. three fully reversed cycles must be applied for each drift ratio value.

Testing have been continued with gradually increasing drift ratio until it reached a value of 4.33%.

3.2 Test Results

In the present chapter are presented and analyzed the results of the experimental investigations on the cast-in-situ and precast specimens. Being the objective of this study that of verifying if the precast joint fulfilled the provision of ACI Standards, the tests have been terminated after completing the 4.33% drift cycle. Thus, after having

verified that the third complete cycle at drift ratio of 3.5% presented a peak force not less than 0.75 times the maximum applied force for the same direction, just one more drift ratio at 4.33% has been investigated.

Before going to the main experimental results it is helpful to understand how the vertical force applied on the top of the specimen varied during the experimental test for the imposed horizontal displacement. From Fig. 4 it can be noted that, starting from the initial value of 155 kN (scaled permanent axial load due to the overlying portion of the structure), the force increases as the imposed displacement increases. This behavior corresponds to that occurring in the real structure during an earthquake excitation.

The main findings on the behavior of the joint in comparison with that of the cast-in-situ joint can be drawn observing the force vs. drift responses recorded during both experimental tests, shown in Fig. 5.

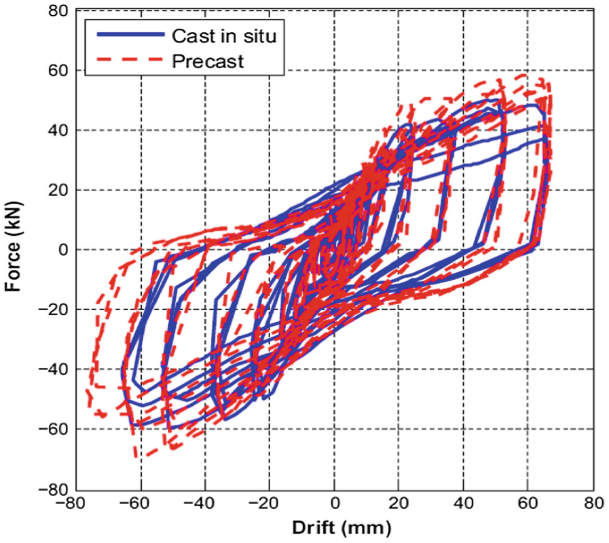

Fig. 5. Force vs drift response of the cast-in-situ (solid curve) and the precast (dashed curve) specimens.

First of all, it can be noted that the drift-load relationship of the precast specimen is very similar to that obtained by other researchers for analogous connections with a stable ductile behavior for drift values in the range 1.5–4.3%. The summary data of the tests are listed in the Table 1.

It is evident that the strength and the ductility of the two specimens are very similar. Indeed, the precast joint behavior (dashed lines) appears to be even more resistant than the cast-in-situ joint (solid lines) without appreciable changes to the ductility of the joint. In fact, the cast-in-situ specimen started yielding under positive drift values with an applied load of roughly 40 kN while the precast joint yielded as a result of the application of a 50 kN horizontal force. A similar observation with slightly higher force values can also be done for negative drift values. The first value is in very good

Table 1. Summary of the test results.

Specimen	Positive displacement		Negative displacement	
	Max load (kN)	Displ. (mm)	Max load (kN)	Displ. (mm)
Cast-in-situ	50.0	51.0	59.5	51.2
Precast	58.1	59.3	69.7	61.4

agreement with that resulting from the calculation in correspondence of the yielding of the beam steel rebars equal to 35.0 kN obtained as the ratio between the nominal bending strength $M_{n,Red} = 47.2$ kNm and the distance L/2 = 1.35 m between the critical section and the beam support. The second one is higher than that expected for the higher compressive strength of the FRC.

The crack patterns observed at the end of the tests for the cast-in-situ and the precast joints are shown in Fig. 6. The cracking pattern inside the joint region for both cases was similar to that obtained for this type of exterior beam-column connections by other researchers. In particular, cracks with an inclination of roughly ±45° on the horizontal have been detected inside the joint region while horizontal cracks have been detected just above and just below the joint region. For the monolithic connection a diffused cracking is present in the critical zone of the beam with very few cracks in the column. A main crack, located in the beam at about 100 mm from the column face, is also visible in the picture. A severe concrete spalling also occurred in the top concrete cover. The precast connection shows an apparent reduced state of cracking in the critical zone but also in this case a main crack, located at roughly 50 mm from the column face, occurred during the tests. Nevertheless, the real state of the cracking occurred in the FRC matrix is not visible since it is hidden by the lateral precast concrete plates used as formworks. The presence of the crack at the beam-column connection can be inferred by looking at Fig. 8b and in particular to the data recorded by the sensors LVDTH1 and LVDTH2. In fact it can be noted that the readings of these sensors are not symmetric with positive values (lengthening) much greater than the negative ones (shortening). The difference between these two values is representative of the main crack amplitude.

The sensors embedded in the specimens allowed to carry out an in-depth analysis of the stress state in the materials. Among the available data, the most interesting ones turned out to be those provided by the VWSG connected to the upper rebars. These data are shown in Fig. 7. The strains recorded by the sensors placed inside the cast-in-situ and the precast beams gradually increased up to a drift ratio of 2.4% corresponding to a top displacement of ±36 mm. Afterward the steel strain has maintained maximum deformation values practically constant up to the end of the tests. This behavior can be ascribed to the yielding of the reinforcing bars within the critical zone. Nevertheless, it should be emphasized that the maximum strain value recorded in the cast-in-situ joint is slightly higher (approx. 2250 με) than that observed in the precast joint (approx. 1750 με).

Most likely this occurred for the overlapping of the rebars in the precast specimen that prevented the yielding of the rebars in the area where they are fully overlapped and caused the yielding of the steel rebars just outside this area.

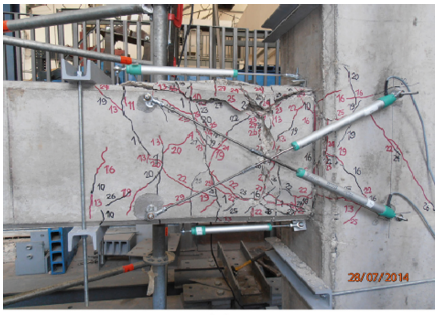

(a)

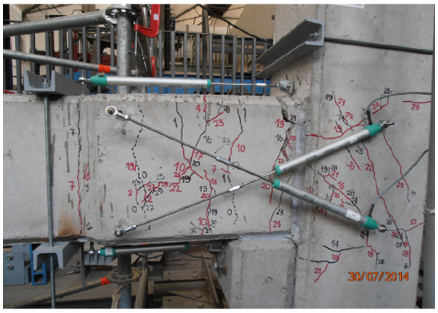

(b)

Fig. 6. Crack patterns at the end of the tests for: (a) the cast-in-situ and (b) the precast joints.

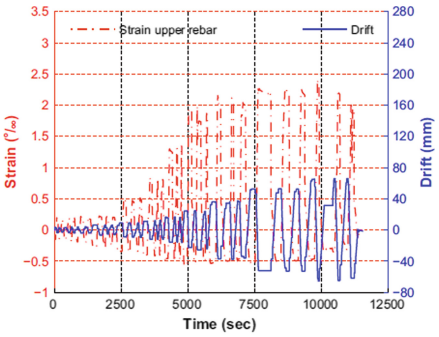

(a)

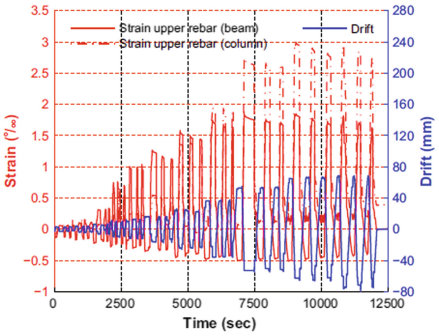

(b)

Fig. 7. Strains recorded in the upper rebars: (a) in the cast-in-situ and (b) in the precast joints.

A confirmation to this thesis has been obtained observing the data gathered from the VWSG placed inside the column, also plotted in the same figure. Values well above the yielding deformation, shown in the Table 2, have been in fact recorded by this sensor.

Table 2. Mechanical properties of the reinforcing steels

Diameter ϕ (mm)	Yielding stress (MPa)	Tensile strength (MPa)	Yielding strain ($\mu\epsilon$)
6		443	
12	453	584	2199
14	466	602	2262

For the precast specimen it can thus be noted that the zone where the yielding of the steel rebars take place is just between the end of the loop coming from the beam and the lateral side of the column, as confirmed by the above mentioned crack pattern.

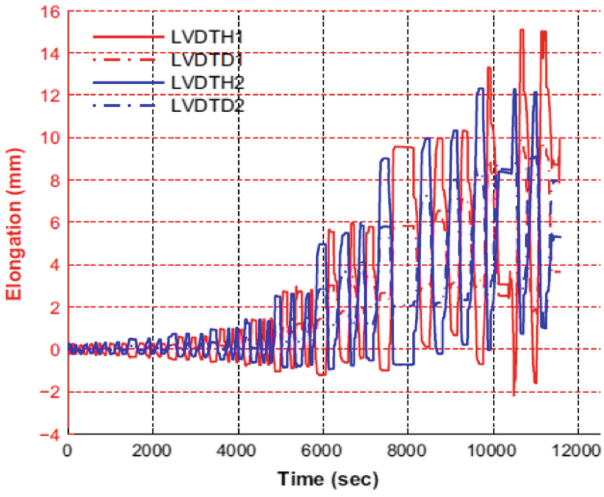

(a)

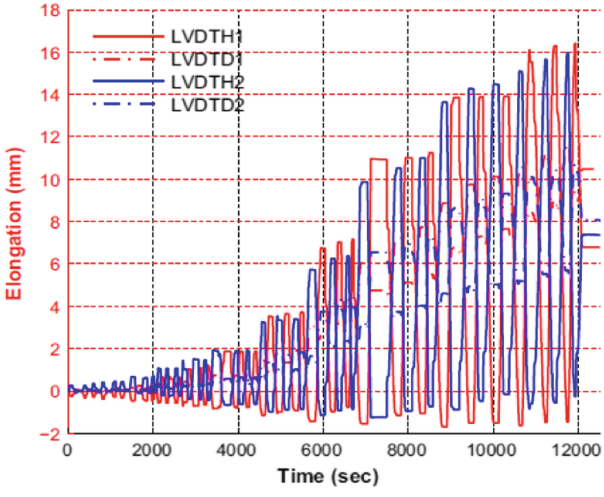

(b)

Fig. 8. Elongation recorded by the LVDTs: (a) in the cast-in-situ and (b) in the precast joints.

This finding also demonstrates the ability of the proposed connection system to transmit the bending moment to the column. Nevertheless, the yielding of the steel rebars can produce tensile cracks inside the column resulting in a not negligible damage of concrete. The use of protruding reinforcing bars with diameter larger than those of the connected beam would avoid this excessive concrete damage inside the joint, inducing the steel yielding to occur only inside the beam as will be shown in the next section by means of FE analysis.

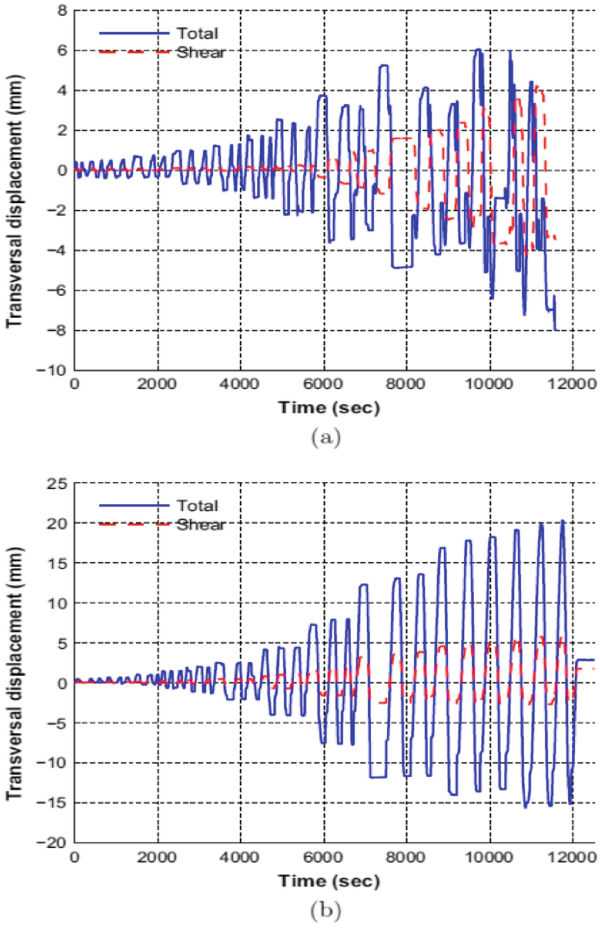

Fig. 9. Total (solid line) and shear (dashed line) transversal deformation: (a) in the cast-in-situ and (b) in the precast joints.

The influence of the shear deformation on the total deformation of the beam critical region can be observed by looking at the data recorded by the PDTs during the experimental tests shown in Fig. 8. The mean transversal displacement of the section placed at 360 mm from the column face can be obtained by using trigonometry equations. This value is made up of the flexural and the shear deformation of the beam critical zone. The contribution of the shear deformation can be extracted from the data recorded by the PDTs according to the method proposed by Massone and Wallace. From the comparison of the two values shown in Fig. 9 it can be deduced that the shear deformation is negligible in the elastic range and for small amount of the damage in the specimens.

The effect produced by the occurrence of the main crack is, instead, relevant as can be deduced by comparing the graphs of Figs. 8 and 9. It can be, in fact, observed that at the same time at which the elongation recorded by LVDTs starts increasing rapidly (due to the formation of the main crack) the shear deformation also starts increasing. This happens after roughly 5800 s for the cast-in-situ specimen (Figs. 8a and 9a) and around 4600 s for the precast specimen (Figs. 8b and 9b). It can, thus, be deduced that the severe cracking reduced in a consistent way the shear stiffness of the joint.

To summarize, the progressive damage and collapse observed in the two types of joint can be judged very similar with the only difference that in the cast-in-situ joint the spalling of the upper concrete cover, probably due to the lower concrete strength and to the absence of the steel fibers with respect to FRC, prevented the attainment of higher lateral forces.

This solution has already been successfully implemented by TechnipFMC for Jebel Ali Refinery in Dubai and for Ethylene Plant in Mexico, a high seismicity region.

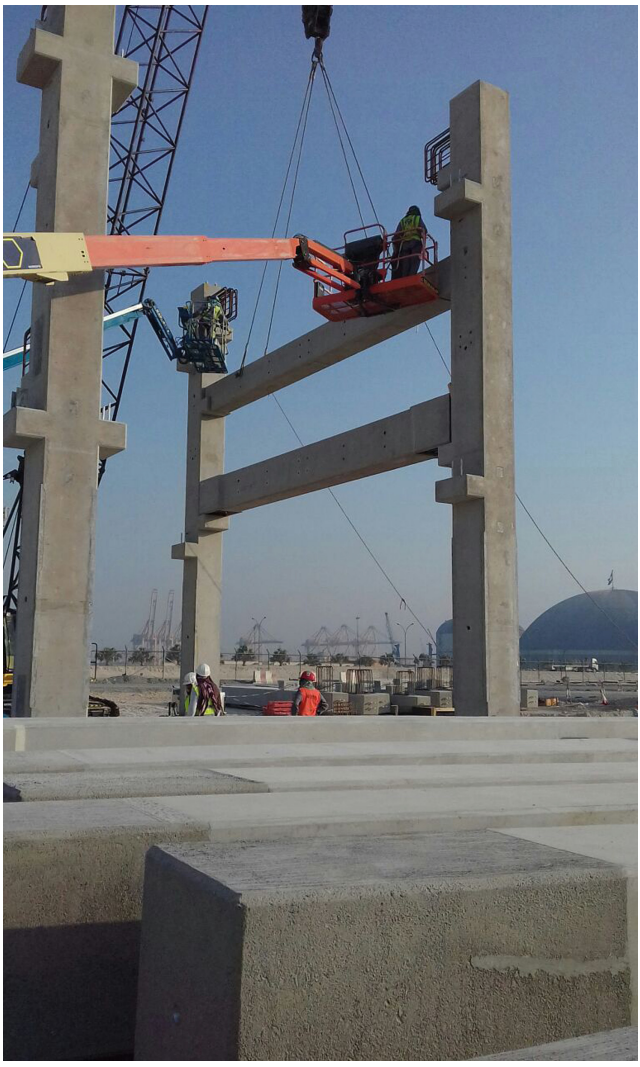

4 Conclusions

This paper presents a technique to use wet beam-to-column connections for precast concrete frames. The technique relies on the prefabrication of beams and columns with protruding hoop-shaped bars that are overlapped in place within a fiber-reinforced concrete cast. Experimental tests on reduced-scale specimens verified the acceptance criteria of ACI 374.1-05. The authors compared the structural behavior of a beam-to-column subassembly created with this technique with that of an equivalent cast-in-place concrete beam-to-column joint. The results of these tests met the acceptance criteria and showed that the two solutions exhibited similar structural behavior. The proposed solution achieved slightly greater strength and stiffness than the cast-in-place concrete solution, without relevant modifications to the joint ductility. This technique, patented worldwide by Technip Italy SpA, allows the construction of seismic resistant monolithic concrete frames, even though made of precast elements.

References

Bellotti P, Menegotto M (1993) Sistema di sostegno ad elementi prefabbricati in c.a. perle tubazioni esterne di un impianto petrolchimico a Brindisi. L' industria italiana del Cemento 5:346–356

Breccolotti M, Gentile S, Tommasini M, Materazzi AL, Bonfigli MF, Pasqualini B, Colone V, Gianesini M (2016) Beam-column joints in continuous RC frames: Comparison between cast-in-situ and precast solutions. Eng Struct 127:129–144

Breccolotti M, Bonfigli MF, Colone V, Luigi A, Materazzi BP, Tommasini M (2017) Wet-joint techniques for the construction of precast concrete pipe rack structures in remote seismic zones. PCI J

Author Index

M. di Prisco and M. Menegotto (Eds.): ICD 2018, LNCE 42, pp. 599–601, 2020.
https://doi.org/10.1007/978-3-030-23748-6